Methylidyne in the Interstellar Medium

by

Erin Marie Dailey

(Under the Direction of Loris Magnani)

Abstract

Methylidyne (CH) is one of the most common molecules in the interstellar medium, and is an excellent tracer of molecular hydrogen using optical observations. Unfortunately, radio observations of CH at 3.3 GHz require long integration times and, for analysis, the excitation temperature ($T_{\rm ex}$) must be known or assumed. The excitation temperature of the ground state, hyperfine, main line transition of CH at 3335 MHz is often assumed to be -15 K (Rydbeck et al. 1976).

Based on comparisons of radio and optical/uv observations from the literature, using $T_{\rm ex} = -15$ K for the 3335 MHz line may be overestimating the CH column density on average. By comparing the N(CH)/N(H_2) ratio and N(CH)/E(B-V) ratio for both data sets, we determine $T_{\rm ex}$ may be approximately -4 K on average. We calculated the excitation temperature of the CH main line at 3335 MHz for 16 lines of sight with optical/UV and radio observations of CH, and we found $T_{\rm ex}$ varies significantly between the lines of sight. For example, for HD 24534, $T_{\rm ex} = -3.1$ K, while for HD 24398 $T_{\rm ex} = -27$ K.

CH production in the ISM is closely linked to the production of H_2, so we compare CH observations with CO in the diffuse clouds MBM 16 and MBM 53. In MBM 16, CH is able to trace the CO-faint gas

which surrounds a CO-bright clump. In CH the molecular gas in the sampled region is roughly uniform, but the CO observations suggests there is a compact clump surrounded by far less dense gas, a suggestion which is not supported by HI and extinction observations. CH and CO observations in MBM 53 seem to also support that CH is able to trace CO-faint gas, but due to the faint CH 3335 MHz signal, CH is able to trace gas surrounding CO-bright gas only if the column density of H_2 is greater than $\sim 10^{20}$ cm^{-2}. In very diffuse regions of MBM 53, CO was able to be detected, but the signal was too faint for CH to be detected with the integration times used.

INDEX WORDS: [ISM: clouds, ISM: molecules, ISM: lines and bands]

Methylidyne in the Interstellar Medium

by

Erin Marie Dailey

B.S., University of North Georgia, 2014

A Dissertation Submitted to the Graduate Faculty of the

University of Georgia in Partial Fulfillment of the Requirements for the Degree.

Doctor of Philosophy

Athens, Georgia

2021

Methylidyne in the Interstellar Medium

by

Erin Marie Dailey

Major Professor: Loris Magnani

Committee: Jean-Pierre Caillault

Robin Shelton

Electronic Version Approved:

Ron Walcott

Vice Provost for Graduate Education and Dean of the Graduate School

The University of Georgia

August 2021

Dedication

To my cat Nix.

Contents

[1] Dailey, E.M., Magnani, L., and Doppel, J.E. Submitted to Monthly Notices of the Royal Astronomical Society, 04/07/2020

[2] Dailey E.M., Smith A.J., Magnani L., Andersson B-G., Reach W.T. Accepted by Monthly Notices of the Royal Astronomical Society. Reprinted here with permission of the publisher.

List of Figures

List of Tables

Chapter 1

Introduction

Although the regions between stars in the night sky appear to contain nothing, they are far from empty. This seemingly vacant void, known as the interstellar medium (or ISM), is filled with baryonic matter, radiation, cosmic rays, magnetic fields, and neutrinos. There is also non-baryonic dark matter which does not interact with the objects we are interested in studying and so will be ignored for the remainder of this thesis. The ISM is home to a large amount of baryonic matter, about an order of magnitude less than the mass contained in stars, but still on the order of 10^{10} solar masses[1] for a galaxy like the Milky Way. In large spiral galaxies the ISM accounts for approximately 10% of the total baryonic mass. The ISM is composed of a nearly homogeneous mixture of gas and dust, with a mass ratio of gas to dust of approximately 100 to 1. The gas is about $3/4$ hydrogen and $1/4$ helium by mass with less than 1% in metals (elements heavier than helium according to astronomical parlance). The conditions in the ISM vary greatly across space, with a wide range of densities and temperatures from 10^{-3} particles cm^{-3} at 10^6 K in the hot ionized medium to 10^7 cm^{-3} at 10 K inside dense molecular cores. Some regions of the colder ISM are exposed

[1] The unit of mass in the ISM is typically the solar mass, equal to 1.988×10^{30} kg and denoted by the symbol $M_\odot$

to harsh radiation which breaks apart molecules shortly after they are formed, while others are shielded, allowing for complex molecules to form. The ISM is divided into 4 equilibrium phases, the hot ionized medium (HIM), the warm ionized medium (WIM), the warm neutral medium (WNM), and the region of interest in this dissertation, the cold neutral medium (CNM). A fifth component, not in pressure equilibrium, is mostly molecular and is even colder and denser than the CNM.

1.1 Molecular Clouds in the Interstellar Medium

In the denser regions of the cold neutral medium, harsh dissociative radiation is absorbed by both H_2 molecules and dust, creating "pockets" of material known as molecular clouds. This molecular medium is composed of very large objects known as giant molecular clouds with $M \geq 10^5$ $M_\odot$, and smaller entities known as diffuse clouds, translucent clouds, and dark (or dense) clouds. This categorization scheme for the smaller clouds was devised by Van Dishoeck and Black (1989) who defined clouds based on the line of sight extinction, where objects with an extinction (A_V) less than 2 mag are diffuse clouds, clouds with an extinction greater than 10 mag are dark clouds, and clouds in between are translucent clouds. The bounds of the cloud types are not consistent through the literature. For example, Magnani and Shore (2017) defined molecular clouds with line of sight extinction less than 1 mag as diffuse clouds, those with an extinction greater than 5 mag as dark clouds, and those in between as translucent clouds. The complex structure of the ISM, the long path lengths and the great variation in radiation and magnetic fields make it difficult to determine characteristic properties of the local cloud conditions for a classification system based on the line of sight extinction through the cloud. For example, a dark line of sight may be the sum of many diffuse clouds aligned so they effectively overlap from our point of view, instead of being due

to a single dark cloud. Additionally, a dark cloud will be encased in an envelope of less dense diffuse and translucent gas, visible distinctly at the edges of a dark cloud. Another classification system by Snow and McCall (2006) classifies the objects based on the local conditions in the cloud, where the different cloud types are classified by the local abundance ratios of H to H_2 and C^+ to CO. The density and temperature of the diffuse to dark clouds range from 10 cm^{-3} and 100 K to 10^7 cm^{-3} and 10 K. In this thesis we will be primarily focused on diffuse and translucent clouds.

Diffuse clouds are divided into diffuse atomic and diffuse molecular clouds, although in both objects A_V is less than 1 and/or the majority of carbon is in C+ ions, depending on the classification scheme described above. Diffuse atomic clouds are, as the name suggests, primarily composed of hydrogen and helium atoms, and any molecules which form are quickly dissociated by the ambient radiation field so the equilibrium abundance remains very low. For example, molecular hydrogen typically accounts for less than 10% of the hydrogen in this region. The destruction of H_2 molecules in the diffuse atomic clouds gradually attenuates the radiation field in the cloud, at least at the wavelengths capable of dissociating molecular hydrogen. The attenuated radiation field allows the H_2 to "self-shield", a situation when there is enough sacrificial molecular hydrogen produced to absorb the majority of the incoming dissociating radiation thereby shielding the interior regions from dissociating radiation (see figure 1.1). The dust in the ISM also absorbs UV radiation, further attenuating the radiation field and aiding in molecule formation by providing nucleation sites for the formation of H_2. The cloud is referred to as a diffuse molecular cloud once more than 10% of the hydrogen is contained in H_2. While this region is shielded from much of radiation which dissociates H_2, there are enough photons that can dissociate other molecules, such as CO. With the large abundance of molecular hydrogen and the reduced radiation field, other molecules

such as CH can be produced in larger quantities. Within diffuse clouds, the hydrogen density ranges between 10 to 500 cm^{-3}, and the temperature ranges from 30 to 100 K.

As the radiation field becomes more attenuated, carbon increasingly becomes bound into neutral carbon and CO instead of carbon ions. The region where the majority of carbon is no longer in carbon ions and up to the point where 90% of the carbon is in CO, is referred to as the translucent regime (Snow and McCall 2006). Within this region, the hydrogen density increases, ranging between approximately 500 to 5000 cm^{-3} and the temperature drops to between approximately 50 to 15 K. Similar to self-shielding of molecular hydrogen, CO becomes self-shielding in the translucent cloud region as the radiation field is gradually attenuated in the wavelengths which dissociate CO. The self-shielding of CO is assisted by the overlap in frequency ranges of the radiation which dissociates H_2 and CO, which greatly helps increase the abundance of CO. Dense clouds are regions of a cloud where almost all (greater than 90%) of the carbon is in CO. In dense clouds the density is (unsurprisingly) much higher than the surrounding regions, often exceeding 10^4 cm^{-3}. The temperature continues to drop because molecules are excellent coolants, and ranges between 10 to 50 K. Within these dense regions, stars are sometimes able to form when a dense region becomes gravitationally unstable and collapses.

Each of the clouds categories listed above is surrounded by lower extinction gas. For example, a dark cloud is surrounded by a translucent region which, in turn, is surrounded by a layer of diffuse molecular gas, which is again surrounded by a layer of diffuse atomic gas. Therefore, any observation of the translucent material from outside the cloud will not only see the translucent material in the heart of the cloud, but will also see the diffuse layers which surround it.

1.2 Tracing Molecular Gas

The most abundant molecule in the ISM, by at least four orders of magnitude, is molecular hydrogen (H_2). Composed of two hydrogen atoms, the molecule is the simplest and lightest form a neutral molecule can be. Unfortunately, H_2 is very difficult to observe directly as it is symmetric and thus has no permanent dipole moment, which means the electric dipole rotational and vibrational transitions are not allowed, leaving the slower quadrupole transitions . Earth's atmosphere is opaque in ultraviolet, necessitating space observatories to observe molecular hydrogen's electronic transitions in the Lyman and Werner bands. In addition, ultraviolet absorption observations of H_2 are limited to nearby diffuse and translucent clouds with background early-type stars. Molecular hydrogen may also be observed in absorption via the infrared rotational lines, although the gas needs to be warm ($T \gtrsim 80$ K) in order to be detectable, leaving most of cold molecular clouds invisible in these transitions (Habart et al. 2005).

The next most abundant molecule is carbon monoxide (CO). CO, significantly heavier than H_2, is asymmetrical and has a permanent dipole moment, which means that, unlike H_2, electric dipole rotational and vibrational transitions are allowed. The rotational levels are arranged in a simple ladder structure with the J = $1-0$ ground rotational state as 115.3 GHz, the J = $2-1$ at 230.5 GHz, the J = $3-2$ at 345.8 GHz, and so on. It is the most commonly used tracer of molecular hydrogen as its abundance (as high as 10^{-4} in dense molecular cores) makes the lower rotational levels bright and thus does not require long integration times for detection (typically on the scale of minutes with modern 3-mm receivers). The velocity integrated antenna temperature for CO (defined in this thesis as W(CO)) is nearly linear with N(H_2) over a wide range of conditions in the ISM (Pety, Liszt, and Lucas 2011). For the last four decades Pat Thaddeus, Tom Dame, and coworkers have been mapping the sky using the J = $1-0$ line at 115.271

GHz in a survey that at the time of writing was still ongoing (see, e.g., Dame, Hartmann, and Thaddeus 2001; or the group's website[2]). The two lowest rotational lines are almost always optically thick, which would normally prevent them from being used as a mass tracer. However, W(CO) can be employed in this fashion for reasons that are complex, but have been primarily attributed either to an empirical linear relation between the CO luminosity and W(CO) (Solomon, et al. 1987), or the size-linewidth relationship (Larson 1981) likely stemming from turbulence in the clouds (Maloney 1990). The CO X-factor [X(CO) defined as $N(H_2)/W(CO)$] is used to convert the observed quantity, W(CO), to $N(H_2)$, and is determined to be $2 \pm 0.6 \times 10^{20}$ cm^{-2}/ K km s^{-1} for dark and diffuse gas (Bolatto, Wolfire and Leroy 2013). CO electronic lines may also be observed in absorption in ultraviolet (e.g., Sheffer, Federman, and Andersson 2003).

Another common tracer, hydroxyl (OH), is the third most abundant molecule in the interstellar medium and is considered to be an excellent tracer of diffuse molecular gas (Magnani and Shore 2017). It was first detected by observations of the 1667 and 1665 MHz lines in Cassiopeia A by Weinreb et al. (1963), making it the first molecule to be detected by radio observations. It is among the few molecules which can be observed in visible wavelengths (e.g., Crutcher and Watson 1976) and radio wavelengths. The ground state of OH has 4 hyperfine transitions, with the main transitions at 1665 and 1667 MHz and the satellite lines at 1612 and 1721 MHz. Since these lines are at approximately 1.7 GHz, close to the HI line at 1.4 GHz, OH has the situational advantage of being observable simultaneously with the HI line at 1.4 GHz for most modern L-band receivers. For example, the L-band receiver on the Arecibo 305-m telescope had a bandwidth wide enough to allow for both species to be simultaneously observed.

[2] https://lweb.cfa.harvard.edu/mmw/MilkyWayinMolClouds.html

The HI data used in chapter 7 was collected at the same time as the OH observations for the MBM 53 molecular cloud.

Methylidyne (CH) at low extinctions is an excellent tracer for H_2 but is unfortunately hampered by a weak signal strength in the hyperfine, ground state transitions at 3.3 GHz requiring long integration times. These lines are optically thin and the excitation temperature needs to be known or assumed for determinations of N(CH) (see, e.g., Magnani and Shore 2017). Additionally, the receiver required (S-high, or upper S band) is seldom a part of the arsenal of low frequency receivers at radio observatories. For example, the only one in operation at a single dish telescope in the western hemisphere at the time of writing being at Arecibo (no longer in operation after the platform collapsed in late 2020). As this molecule is the primary focus of this dissertation, it will be discussed in greater detail throughout the rest of this work.

Cyanogen (CN) is the last of the 4 major molecules that are observable in radio and optical wavelengths, it has a very strong correlation with HCN and HNC, and has been used to determine the cosmic microwave background radiation temperature at 2.7 mm (Liszt and Lucas 2001). However, the abundance of CN varies greatly with respect to H_2, preventing it from being useful as a tracer of H_2 (van Dishoeck and Black 1989). CN, along with CH and CH^+, were the first molecules found in the interstellar medium as interstellar absorption lines superimposed on the spectra of background stars (Dunham 1937, McKellar 1940, Adams 1941, Douglas and Herzberg 1941).

Recent work has shown that Hydrogen Fluoride (HF) is also able to effectively trace H_2 (Gerin, Neufeld, Goicoechea 2016), and has been predicted to be capable of detecting molecular gas at H_2 column densities of less than 10^{19} cm^{-2} (Neufeld, Wolfire, Schilke 2005). Due to the small moment of inertia for the molecule, it is difficult to detect HF from ground based observatories (Neufeld et al. 2010). It was first

detected using the far infrared J = $(2-1)$ transition at 2463.43 GHz (Neufeld et al. 1997), and was later observed using the J = $(1-0)$ line at 1232.48 GHz (Neufeld et al. 2010) and the near infrared $\nu = 1-0$ R(0) and R(1) lines at 2.499385 μm and 2.475876 μm (Indriolo et al. (2013). It may also be observed in the ultraviolet (Tashiro, Ubachs, and Zare 1989). Finally, the 4.83 GHz line of Formaldehyde (H_2CO) is able to trace the lower density core regions of diffuse and translucent molecular clouds (Magnani and Shore 2017), although it tends to trace denser gas than the CO$(1-0)$ line at 115 GHz or the OH and CH hyperfine, main line transitions.

On average, the gas-to-dust ratio in the ISM is fairly constant, so the column density of molecular hydrogen may also be determined from extinction or color excess along with observations of neutral atomic hydrogen (HI) to obtain the column density of H_2. Up to a color excess of 0.5 mag, Bohlin, Savage, and Drake (1978) determined the ratio of total neutral hydrogen to color excess to be N(H) / E(B-V) = 5.8×10^{21} atoms cm^{-2} mag^{-1} (where N(H) = N(HI) + 2 N(H_2)) using a sample of 100 stars. We explore this issue further in chapter 2. Extinction may be determined from dust maps such as the recalibrated SFD dust maps (Schlafly and Finkbeiner 2011). In the absence of HI observations, the extinction sets an upper limit on the amount of H_2 along a line of sight. Unfortunately, the dust maps do not contain any velocity information so the determined H_2 column density will not contain any kinematic information.

Complicating the above discussion, Grenier, Casandjian, and Terrier (2005) demonstrated that HI and CO observations of the ISM do not account for a significant amount of the atomic and molecular gas, discovering clouds of "HI and CO-dark" gas. They claimed that the amount of molecular gas missed by CO$(1-0)$ observations was equivalent to that detected by the large scale surveys. To discover the HI and CO dark gas, they used gamma rays with energies greater than 100 MeV as a tracer of the gas. The HI observations used were from the Leiden/Dwingeloo survey (Burton and Hartmann 1994) along

with observations below $\delta = -30^{\circ}$ from Dickey and Lockman (1990). HI was assumed to be optically thin, so the presence of HI-dark gas could suggest that the 1420 MHz HI line is not always optically thin. However, Grenier et al. (2005) used CO observations from the Dame, Hartman, and Thaddeus (2001) survey which has integration times between 20 to 300 seconds. This is insufficient for detecting faint diffuse clouds which may require much longer integration times (e.g. Donate and Magnani 2017). Although H_2 that is unable to be traced by CO is expected to some extent (figure 1.1 shows that H_2 will begin forming in relatively large quantities before CO becomes abundant enough to be visible in radio observations with practical integration times), producing regions around CO-bright gas that contain H_2 but cannot be seen in CO observations, the amount of this dark gas is under intense debate (see discussion in Magnani and Shore 2017).

1.3 CH in the Interstellar Medium

The molecule Methylidyne (CH) was detected in the ISM early in the 20^{th} century by Dunham (1937), although he could not identify the absorption line at 4300 Å. The molecule was soon identified by Swings & Rosenfeld (1937), making it the first molecule discovered in the ISM. The violet 4300.3 Å line of CH is from the CH A-X band (Weselak et al. 2014), and is actually two closely spaced lines [4300.3235 and 4300.3030 Å (Black and van Dishoeck 1988)] which can be seen individually under some conditions (e.g., Crane 1995, discussed further in chapter 4). The 4300.3 Å main lines can often become saturated, so the lines from the B-X band are usually observed as well. The B-X band gives rise to 3 lines in the low ultraviolet at 3890.217, 3886.409, and 3878.774 Å (Weselak et al. 2014). Observation of the A-X and

B-X bands of CH have shown that the column density of CH is well correlated with the column density of H_2 (e.g., Weselak 2019; also see chapter 2 of this dissertation).

The development of radio astronomy in the 1950s opened up the possibility of detecting rotational and hyperfine emission lines from cold molecular gas. The first molecule to be detected through radio emission was Hydroxide (OH) via its 18 cm lines (Weinreb et al. 1963). Despite the early detection of CH in optical observations, the radio lines of CH were not detected until approximately 4 decades after its optical detection because of the difficulty in predicting the frequency of the 3 GHz CH transitions. The CH 3 GHz lines were estimated indirectly by measuring the spacing between the two A-X band lines at 4300.3 Å, for example, Baird and Bredohl (1971) measured the separation of the lambda-doubled ground state to be 3374 ± 20 MHz. Direct laboratory measurements of the CH radio lines were difficult due to complications associated with producing and maintaining a large enough sample of a highly reactive gas for the 3 GHz radio emission to be detectable (Evenson, Radford, and Moran 1971). Late estimates of the 3 GHz line of CH, before it was detected in 1973, used the separation of the more easily detected 4300 Å lines to determine the separation of the lambda doubled levels of the ground state. It was finally detected by Rydbeck, Elldér, and Irvine (1973), making CH one of the few molecules, along with OH, CN, and CO which is readily detectable in optical and radio observations. Astronomical observations of CH provided the most accurate measurements of the ground state hyperfine energy levels up until measurements conducted by Truppe et al. (2014).

This thesis will be primarily focused on the hyperfine levels of the ground state of CH at 9 cm. The rotational levels of CH are split by spin-orbit interaction, so each N level is split into two states, with $J = N \pm 1/2$ (Herzberg 1971). The lowest energy level is the N=1, J=1/2 level, which is further split into two levels due to Λ-doubling. The level splitting is caused by the interaction between the rotation

of the molecule and the orbital motion of the electrons splitting the energy level into two levels, each level corresponding to one of the two directions of rotation of the electrons around the internuclear axis (Herzberg 1971). The two levels have opposite parities, where the upper level has a negative parity, and the lower level has a positive parity. The upper and lower levels of the Λ-doubled ground state are then further split by hyperfine splitting, with F = J ± 1/2. This results in the ground state of CH having four levels (see figure 1.2) at 0 eV, 5.671×10^{-8} eV, 1.355×10^{-5} eV, and 1.385×10^{-5} eV. There are three allowed transitions, the main line F = $(1 \rightarrow 1)$ at 3335.479 MHz, and the two satellite lines F = $(1 \rightarrow 0)$ and F = $(0 \rightarrow 1)$ at 3349.193 MHz and 3263.793 MHz respectively (Truppe et al. 2014). The transition F = $(0 \rightarrow 0)$ is absolutely forbidden by selection rules. (Herzberg 1971). The levels of the ground state transitions are shown in figure 1.2.

The radio lines of CH originating from the ground state hyperfine levels have been used as a tracer for the notoriously elusive molecular hydrogen, due to a robust linear relation between the column density of CH and H_2 (see Chapter 2). However, while optical observations are able to directly determine the column density of CH, determining the column density using radio observations requires knowing or assuming the excitation temperature.

1.3.1 CH Excitation Temperature

Excitation temperature ($T_{\rm ex}$) is a representation of the relative populations of two quantum states, defined as

$$T_{\rm ex} = -\Delta E / {\rm k_b} [ln((n_{\rm u} g_{\rm l})/(n_{\rm l} g_{\rm u})]^{-1} \tag{1.1}$$

where ΔE is the difference in energy between the two states, $\mathrm{k_b}$ is the Boltzmann constant, n_u and n_l are the densities of the particles in the upper and lower states, and g_u and g_l are the statistical weights of the upper and lower states. Despite its name, excitation temperature, it is only related to the physical temperature when the gas is in thermodynamic equilibrium. T_ex can even be negative in some cases if the upper state is more populated than the lower state, such as in a maser, and this situation is very common for the 3335 MHz main CH line (e.g., Rydbeck et al. 1976; Hjalmarson 1977; Genzel et al. 1979). As n_u and n_l are terms in the ratio of the population of the upper and lower states, they may be replaced with an easily measured quantity, column density, N_u and N_l. As a consequence of using the column densities instead of the density for determining T_ex, the excitation temperature determined by column densities is an "average" T_ex, based on the sum of the upper and lower states through a region and does not represent the local population ratio in a cloud.

The excitation temperature for the CH ground state main line transition at 3335 MHz has been measured before along many lines of sight using a variety of methods. For example, Rydbeck et al. (1976), Hjalmarson et al. (1977), and Genzel et al. (1979) used on-off radio observations of continuum sources to determine T_ex for the main line and satellite lines (described in more detail in chapter 4). Lien (1984) and Jura and Meyer (1985) used optical observations to determine T_ex for a few lines of sight toward stars. Lien (1984) also used a hybrid method using both optical and radio observations T_ex. Each of these methods will be discussed in more detail in chapter 3 of this thesis.

1.4 Column Density from Radio Frequency Observations

Column density is a measurement of the number of particles along a line of sight within a given unit area. In professional astronomical work, the default units are CGS so column density (denoted by N) is measured in particles cm^{-2}. The relationship between molecules which are absorbing a background continuum and an observable quantity like the column density is based on expressing the absorption coefficient for a given transition and the number of molecules in that state with the optical depth of the transition (e.g. Magnani and Shore 2017). We may express this as

$$\int \tau_{ij} \mathrm{d}v = 0.75 N_{\mathrm{l}} \lambda^3 A_{ij} (1 - \exp[-\mathrm{h}\nu(\mathrm{k_B}\, T_{\mathrm{ex}})^{-1}])(8\pi)^{-1} \tag{1.2}$$

which comes from the solution of the radiative transfer equation in the limit where h$\nu \ll$ kT and the quantum mechanical description of the absorption coefficient, where λ is the wavelength of the emitted radiation. T_{ex} is the excitation temperature of the transition, A_{ij} is the emission coefficient of the F = $i \rightarrow j$ transition, and N_{l} is the column density of the lower half of the ground state Λ-doublet. The radiative transfer equation may be written as

$$T_{\mathrm{A}} = \eta_{\mathrm{B}} (1 - \exp[-\tau])[J(T_{\mathrm{ex}}) - J(T_{\mathrm{bg}})] \tag{1.3}$$

where T_{A} is the antenna temperature, η_{B} is the beam efficiency, τ is the optical depth, T_{ex} is the excitation temperature, T_{bg} is the background temperature, and $J(T)$ is (hν/k)(exp[(hν/(kT)$-$1])$^{-1}$. At the

Rayleigh-Jeans limit ($h\nu \ll kT$), $J(T_{ex})$ becomes T_{ex} and $J(T_{bg})$ becomes T_{bg}, so that

$$T_A = \eta_B(1 - \exp[-\tau])[T_{ex} - T_{bg}] \tag{1.4}$$

A_{ij} is determined by equation 9 from Pickett et al. (2003) using data for the ground state CH transitions from the Jet Propulsion Laboratory Molecular Spectroscopy Database:

$$A_{ij} = I_{ij}(T)\nu^2(Q/g)(\exp[-E_l/(k_B T)] - \exp[-E_u/(k_B T)])^{-1} \times 2.7964 \times 10^{-16}\,\mathrm{sec}^{-1} \tag{1.5}$$

where I_{ij} is the line intensity, Q is the rotation-spin partition function, g is the degeneracy of the state, E_l and E_u are the energies of the lower and upper levels respectively, k_B is the Boltzmann constant, and T is the temperature. The emission rate does not change significantly between $30 - 300$ K. For the 3335 MHz, F = 1→1 main line, $A_{11} = 2.0456\ s^{-1}$. For the 3264 MHz, F = 0→1 satellite line, $A_{01} = 2.8761\ s^{-1}$. For the 3349 MHz, F = 1→0 satellite line, $A_{10} = 1.0359\ s^{-1}$.

Assuming a small optical depth and Rayleigh-Jeans limit,

$$(1 - \exp[-\tau]) \approx \tau \tag{1.6}$$

$$J(T) = (h\nu/k)(\exp[(h\nu/(kT) - 1])^{-1} \approx T \tag{1.7}$$

$$T_A = \eta_B\tau[T_{ex} - T_{bg}] \tag{1.8}$$

Plugging this into equation 1.2 results in

$$(\eta_{\rm B}[T_{\rm ex} - T_{\rm bg}])^{-1} \int T_{\rm A} {\rm d}v = 0.75 N_{\rm l} \lambda^3 A_{ij} {\rm h}\nu ({\rm k_B}\, T_{\rm ex})^{-1} (8\pi)^{-1} \tag{1.9}$$

$$N_{\rm l} \approx N({\rm CH})/2 \tag{1.10}$$

$$N(CH) = [(16\pi/0.75)(\lambda^3 A_{ij} {\rm h}\nu)^{-1} {\rm k_B}]\, T_{\rm ex} (\eta_{\rm B}[T_{\rm ex} - T_{\rm bg}])^{-1} \int T_{\rm A} {\rm d}v \tag{1.11}$$

For each of the three ground state lines the column density can be written in terms of the excitation temperature, the background temperature, and the intensity of the line as:

$${\rm N(CH)}_{3335} = (2.82 \times 10^{14})\, T_{\rm ex} (\eta_{\rm B}[T_{\rm ex} - T_{\rm bg}])^{-1} \int T_{\rm A} {\rm d}v \tag{1.12}$$

$${\rm N(CH)}_{3264} = (1.92 \times 10^{14})\, T_{\rm ex} (\eta_{\rm B}[T_{\rm ex} - T_{\rm bg}])^{-1} \int T_{\rm A} {\rm d}v \tag{1.13}$$

$${\rm N(CH)}_{3349} = (5.61 \times 10^{14})\, T_{\rm ex} (\eta_{\rm B}[T_{\rm ex} - T_{\rm bg}])^{-1} \int T_{\rm A} {\rm d}v \tag{1.14}$$

Given the value of the constants, $T_{\rm A}\ {\rm d}v$ are in units of K km s^{-1} and N(CH) is in cm^{-2}. As none of the transitions go between the same states, each line may have a different excitation temperature.

1.5 Outline of Thesis

After this introduction, the outline of this thesis is as follows: chapter 2 focuses on the relation between the CH column density and both color excess and H_2 column density for optical and radio observations separately using data collected from the literature. Chapter 3 is a paper that was published in MNRAS

(Dailey et al. 2020) and discusses the excitation temperature of the CH 3335 MHz transition for 16 lines of sight in a sample of translucent and dark molecular clouds. Chapter 4 examines the method of determining $T_{\rm ex}$ by radio/optical observations toward stars and radio on/off observations of continuum sources. The question of whether or not the CH 3335 MHz line can trace a diffuse and translucent low-density molecular component surrounding a clump that is seen with CO($1-0$) is explored in chapter 5. Chapter 6 compares CH observations with CO and OH observations in MBM 53, a diffuse cloud with very low expected H_2 column densities. In chapter 7 we study a collection of very high signal to noise HI data collected by Donate and Magnani while they were studying OH in MBM 53 (Donate, White and Magnani 2019). In chapter 8 we discuss the computational project studying the excitation of the CH ground state using the 3D-PDR code (Bisbas et al. 2012). Finally, this thesis concludes in chapter 9 with a brief summary of the results and prospects for future work.

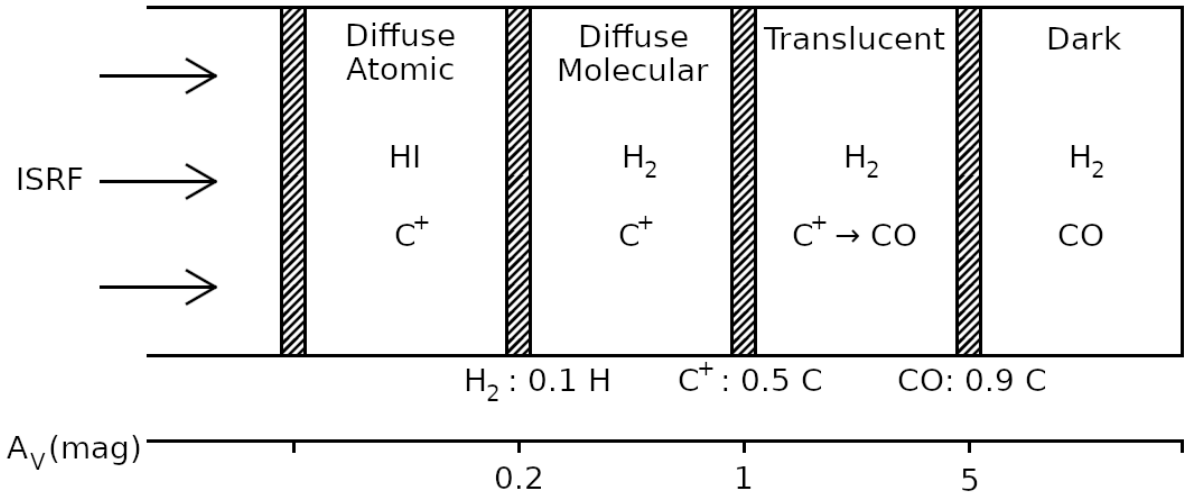

Figure 1.1: Photodissociation Region Schematic

The sections of the photodissociation region are shown, according to the characteristics described by Snow and McCall (2006) and Magnani and Shore (2017). The area separating each section is labeled with the characteristics that separate them, for example, the transition between translucent and dark clouds is labeled with CO accounting for 90 percent of the local carbon, and $A_V = 5$ mag to account for the two ways to categorize the cloud.

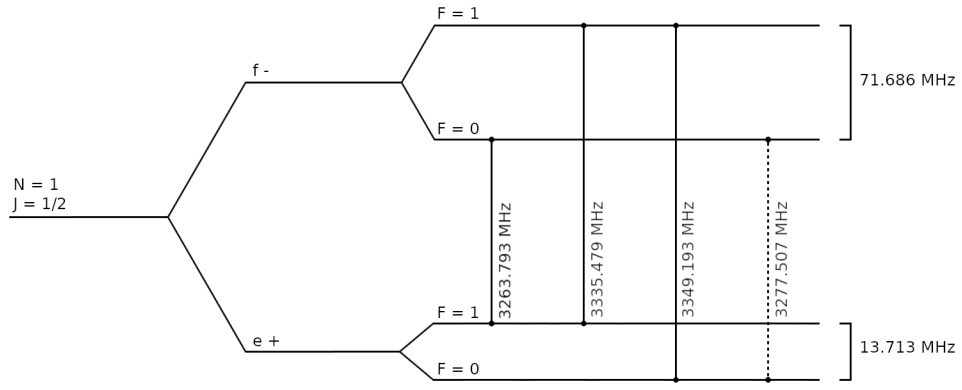

Figure 1.2: CH Ground State Structure

Diagram of the hyperfine structure of the CH ground state. The F = $(1 \rightarrow 1)$, F = $(1 \rightarrow 0)$, and F = $(0 \rightarrow 1)$ transitions are marked with solid lines, and the forbidden F = $(0 \rightarrow 0)$ transition is marked with a dotted line. The frequency separation of the hyperfine splitting is marked on the right. The spacing of the energy levels is not to scale. The allowed transition frequencies were determined by Truppe et al. (2014).

Chapter 2

The Relation Between CH, Colour Excess, and Hydrogen [1]

[1]Dailey, E.M., Magnani, L., and Doppel, J.E. Submitted to Monthly Notices of the Royal Astronomical Society, 04/07/2020

Abstract

The relationship between N(CH) and $E(B-V)$ is studied along with the relation between N(CH) and N(H_2), distinguishing between two common methods for obtaining the three quantities. The first method relies on optical and UV absorption lines of CH and reddening data to stars behind diffuse molecular clouds, and the second relies on observations of the 3335-MHz, ground state, hyperfine, main line transition of CH and dust column densities [calibrated to $E(B-V)$] based on infrared data. The two methods sample different galactic environments and lead to different slopes for N(CH)/$E(B-V)$ and N(CH)/N(H_2). We argue that the stellar method yields more reliable estimates for N(CH), and use that to determine the average excitation temperature for the 3335-MHz transition. Using optical and UV data from the literature, we determine N(H_{tot})/$E(B-V)$ = 5.78 $\pm$ 2.33 $\times$ 10^{21} cm^{-2} mag^{-1}. In contrast, radio observations of the HI 21-cm line for $15,385$ lines of sight at $|b| \geq 30^{\circ}$, yield a value of $7.8 \pm 3.1 \times 10^{21}$ cm^{-2} mag^{-1}, similar to that of Liszt (2014a). We find the N(HI)/$E(B-V)$ ratio begins to decrease at lower $E(B-V)$ in the outer Galaxy compared to the inner Galaxy.

2.1 Introduction

One of the principal goals of molecular spectroscopy of the ISM is to determine the column density of molecular hydrogen using transitions of molecules that are more easily detectable. Optical and radio surveys of CH in diffuse and translucent clouds have found that the column density of CH is proportional to that of H_2 up to $A_B \leq 5$ mag [e.g., Danks, Federman, & Lambert (1984); Mattila (1986); Weselak (2019)]. In a related study, Lang & Willson (1978) determined, using primarily radio observations of CH at 9 cm (optical observations were used in place of non-detection upper limits of the 3335-MHz CH transition) that, at low colour excess [$E(B-V) \leq 0.6$ mag], the column density of CH is proportional to $E(B-V)$, but the slope decreases for high colour excess lines of sight through dark clouds. Similarly, Mattila (1989) observed several lines of sight through dark clouds and determined there is no single N(CH) versus colour excess relationship from diffuse to dark molecular clouds. These findings were extended by Liszt & Lucas (2002) who compiled an extensive set of optical and radio CH observations and found that even at relatively low colour excess [$E(B-V) \leq 2$ mag] there was no single-valued or linear relationship between N(CH) and $E(B-V)$.

Optical studies of the CH optical and UV lines in absorption lead directly to N(CH) (e.g., Lien 1984). Radio observations of the ground state, hyperfine, transitions at 9 cm can also lead to N(CH), but only if the excitation temperature, T_{ex}, is known or assumed. Traditionally, for the 3335-MHz main line, it is assumed that $|T_{ex}| \gg T_{bg}$ where T_{bg} is the background temperature at 3.3 GHz, in which case N(CH) is proportional to the velocity-integrated brightness temperature of the line. However, that assumption has been called into question (Lien 1984; Dailey et al. 2020). To address the issue, Dailey et al. (2020) combine optical and radio measurements for the same lines of sight to solve for T_{ex} of the

3335-MHz transition. But for this method to work, it is assumed that the two techniques produce the same value of N(CH) for a given line of sight. This assumption can be tested by comparing N(CH) versus $E(B-V)$ studies using optical and radio observations. Moreover, this ratio, when coupled with the $N(H_{tot})$[2]$/E(B-V)$ ratio, leads directly to the CH abundance that can then be studied as a function of gas density or molecular fraction. Although there is more consensus in the $N(H_{tot})/E(B-V)$ ratio than is the case for CH, there are studies that possibly indicate a latitude dependence (e.g, Knapp & Kerr 1974), and breaks in the slope at low extinction (e.g., Liszt 2014b). However, the many studies that look at global gas-to-dust ratios involve different techniques and parameters which need to be considered.

In this paper the relationships of CH and $N(H_{tot})$ with colour excess are determined from data in the literature paying particular attention to factors such as whether the CH column density is obtained from radio or optical observations, the Galactic latitudes being considered, and whether or not the line of sight in question terminates at a stellar surface. The latter criterion involves the path length, which we will distinguish as (1) *stellar*, meaning the lines of sight for both quantities truncate at the star, or (2) *galactic*, where the lines of sight extend through the Galactic disk and even into the cold neutral gas of the halo. Clearly, the two methods probe different Galactic environments. Besides the path length, the stellar method probes a column of nearly infinitesimal solid angle whereas the galactic method probes regions of angular size on the order of 1 to 10 arcminutes.

The paper is organized as follows: §2 discusses some of the results of previous studies of the column density of hydrogen or CH versus the colour excess distinguishing between the various methodologies used in establishing the relationships. In §3 we describe the data sets from the literature that are used to obtain our results. In compiling the HI, CH, and $E(B-V)$ data we emphasize homogeneity and

[2] $N(H_{tot}) = N(HI) + 2N(H_2)$

high-quality observations. The relations between hydrogen and colour excess under various criteria are obtained in §4 and compared to the previous work, and the same is done for CH in §5. Section 6 explores the relation between N(CH) and H_2 distinguishing between the different techniques used to obtain the two quantities. The results of our investigation are discussed in §7.

2.2 Previous work

We briefly review some of the previous work in establishing the $N(H_{tot})/E(B-V)$ ratio (which we will alternatively refer to as the "gas to dust ratio"). This review is not meant to be comprehensive but highlights previous results that we will address directly with our data.

2.2.1 N(H_{tot}) versus Colour Excess

In two classic studies analyzing UV absorption line data from the *Copernicus* satellite, Savage et al. (1977) and Bohlin, Savage, & Drake (1978) established a relation between $N(H_{tot})$ and $E(B-V)$. Surveying over 100 stellar lines of sight, they obtained N(HI) from Lα and $N(H_2)$ from the J=0 and J=1 rotational levels of the ground vibrational state, which allowed them to determine $N(H_{tot})$ accurately for the path length to the star. This technique is what we refer to as the stellar method. Combining these data with well-established $E(B-V)$ values for each of the program stars, they obtained the classic result

$$N(H_{tot})/E(B-V) = 5.8 \times 10^{21} \ \ \mathrm{atoms\,cm^{-2}\,mag^{-1}} \tag{2.1}$$

This program was continued by Diplas & Savage (1994) using *IUE*. Their study was limited to HI and resulted in a slope of 4.93×10^{21} atoms cm^{-2} mag^{-1} (we drop the units in the rest of the paper for brevity).

Later, Rachford et al. (2002) used data from the *FUSE* satellite to get nearly the same slope (5.6×10^{21}) as Bohlin et al. (1978). These studies differed in the space-borne telescopes and spectrometers used and in the stellar sample. Moreover, in all cases, the relevant line of sight only traversed a limited portion of the Galactic plane, ending at the stellar surface.

A different approach (i.e., the galactic method described in §1) was taken by Liszt (2014a) who used the Schlegel, Finkbeiner, & Davis (1998) dust maps with $6'$ resolution to estimate $E(B-V)$ for lines of sight where data from low- and high-resolution 21 cm surveys (with $36'$ and $4'$ resolution, respectively) provided N(HI). Lines of sight with $|b| \geq 20^\circ$ and $E(B-V) \leq 0.1$ mag were chosen to avoid opacity effects and regions with significant molecular gas. Thus, for this study, N(HI) is effectively N($\mathrm{H_{tot}}$). The slope he obtained, 8.3×10^{21}, is greater than the ones obtained previously at higher colour excesses using the stellar method. A break in slope (to lower values) for $E(B-V) \geq 0.1$ mag is noted in a subsequent paper (Liszt 2014b) and is attributed to the onset of $\mathrm{H_2}$ formation. He also notes that the ratio decreases to $5-6 \times 10^{21}$ for $|b| < 30^\circ$ for all $E(B-V)$, but, interestingly, the opposite trend occurs for $|b| \leq 20^\circ$ and $E(B-V) \leq 0.075$ mag [see Figure 5 from Liszt (2014b)].

Liszt's result as far as the latitude dependence for unrestricted values of $E(B-V)$, is reminiscent of the early work by Knapp & Kerr (1974) which, using the reddening towards globular clusters and HI 21 cm observations, found an increase in the N(HI)/$E(B-V)$ ratio as a function of $|b|$ with values as low as 4×10^{21} at $|b| \sim 10^\circ$ and as high as 4×10^{22} at $|b| \sim 75^\circ$.

A study using the galactic method by Lockman & Condon (2005) examined a small field ($3^\circ \times 3^\circ$) at high Galactic latitude using the 100-meter GBT. The beam size of the GBT ($9.4'$) is smaller than that used by the Leiden-Argentina-Bonn (LAB) survey (Kalberla et al. 2005) which forms the basis for many of the gas to dust studies using the galactic method. Moreover, the GBT beam is relatively free of stray radiation

without needing to resort to bootstrapped corrections. Their study revealed that, when HI high-velocity data is excluded in determining the gas-to-dust ratio, the correlation between N(HI) and $E(B-V)$ is tighter and the slope (i.e, the gas to dust ratio) is shallower. This implies that high-latitude studies using the galactic method with sightlines extending into the Galactic halo might show a larger gas-to-dust ratio when regions with HVCs are considered (see discussion in §7).

2.2.2 N(CH) versus Colour Excess or Extinction

Many studies have examined the relationship between N(CH) and either colour excess or extinction; they are reviewed by Mattila (1986), Magnani & Onello (1995), and Liszt & Lucas (2002). Here we focus on some of the issues discussed by previous work that we will address in this paper. Liszt & Lucas (2002) summarize many previous optical observations of CH absorption at $\lambda 4300$ and CH emission using the 3335-MHz ground state, hyperfine, main line. Their Figure 1 shows N(CH) as a function of $E(B-V)$ and indicates that for $E(B-V) \leq 0.3$ mag there is no single linear relationship. Even if only data using the stellar method are considered, there may be two separate relationships one with clearly higher values of N(CH) at a given colour excess. Liszt & Lucas (2002) argue that the difference involves the presence of substantial molecular gas along the line of sight. If this is present, as indicated, for example, by the detection of the CO$(1-0)$ transition, then there is substantially more (factor of 3) N(CH) than for those lines of sight with similar colour excess but no CO emission. This result can also be seen in Figure 12b of Penprase et al. (1993) which shows N(CH) versus $E(B-V)$ using the stellar method for three data sets: Two from Danks et al. (1984; 1990) based on observations to stars behind traditional diffuse clouds; and their own CH spectroscopic data towards stars located behind or near high-latitude molecular clouds. The possibility of significant molecular gas towards stars in the Penprase et al. (1993) sample is much

higher than towards the Danks et al. (1984; 1990) sample. Thus, there are two distinct relationships for N(CH)/$E(B-V)$ depending on whether or not the line of sight contains significant molecular gas.

2.3 The CH, hydrogen, and colour excess data sets

The data we use to derive the various gas to dust ratios are divided into two groups, depending on whether they were compiled using the stellar or galactic method. The stellar method uses lines of sight with high quality $A-X$ or $B-X$ band observations of CH and corresponding observations of H_2 with uncertainties listed in the literature. The stellar CH column densities are from Weselak (2019), Mookerjea (2016), Smoker et al. (2014), Dahlstrom et al. (2013), Thorburn (2003), and Andersson, Wannier & Crawford (2002); in the case of duplicate lines of sight, the column density from the latest paper takes precedence. The 87 lines of sight are shown in Table 2.1, where the first column lists the target star, and the second and third columns give the galactic longitude and latitude of the corresponding line of sight. Column 4 lists the CH column density, column 6 lists the colour excess, column 8 lists the HI column density, and column 10 lists the H_2 column density. All uncertainties and upper limits listed are for 1σ.

The second group, based on the galactic method, is comprised of observations compiled from the literature of the ground-state, hyperfine, main line transition of CH at 3335 MHz which were collected using the defunct NRAO 43-m telescope to ensure a data set with a homogeneous beam size. Additionally, to be included in this data set, the publication must also list column density uncertainties. The radio CH data includes a total of 83 observations from Mattila (1986), Lang & Willson (1978), Mattila (1989), Magnani, Sandell, & Lada (1992), Magnani & Onello (1993), and Liszt & Lucas (2002). As the colour

excess is determined from Schlafly et al. (2011), observations with a line of sight along the galactic plane ($|b| < 5^\circ$) are not included.

The colour excess and N(HI) are used to determine N(H_2), using the relation

$$N(H_2) = [5.78 \pm 2.33 \times 10^{21}\ E(B-V) - N(HI)]/2 \quad \mathrm{cm}^{-2} \tag{2.2}$$

where the value of the slope is justified in §4. Because of the high standard deviation in the gas to dust ratio and the subtraction of N(HI), it is possible to get a negative value for N(H_2), as was the case for one line of sight in the sample. The column density uncertainty covers positive values as well, so the point is kept. The HI column densities are determined from EBHIS[3] and GASSIII[4], and are assumed to have 3 percent errors[5]. The assumed uncertainties in N(HI) are dwarfed by the 40 percent standard deviation in the N(H_{tot})/$E(B-V)$ relation. The colour excess is determined from the SFD dust maps (Schlafly & Finkbeiner 2011). The data are listed in Table 2.2, where column 1 lists the name of the line of sight, and columns 2 and 3 lists the galactic longitude and latitude of each line of sight. Column 4 lists the CH column density, column 6 lists the colour excess, and column 7 lists the calculated molecular hydrogen column density.

All of the data that are used for linear fits in this paper have measured or estimated uncertainties, so the fitting is done with weighted orthogonal distance regression (WODR)[6], since it is one of the best methods for determining a fit line using data with x and y uncertainties (Wu & Yu 2018). The non-detections are considered to be half of the original one sigma limit, and the uncertainties are half of the one sigma limit.

[3]Effelsberg-Bonn HI Survey (Winkel et al. 2016)
[4]Parkes Galactic All-Sky Survey III (Kalberla & Haud 2015; McClure-Griffiths et al. 2009)
[5]see website: https://www.astro.uni-bonn.de/hisurvey/AllSky_profiles/
[6]The linear fits are made in Python using the ODR package of the SciPy Python library (Virtanen et al. 2020).

For determining the gas to dust ratio using the galactic method, we use the Magnani et al. (2000) and Hartmann, Magnani, & Thaddeus (1998) high-latitude CO($1-0$) surveys. Those authors sampled with an $8'$ beam the high-latitude sky ($|b| \geq 30°$) every degree in latitude and longitude for all points that rose to an elevation $\geq 30°$ from Cambridge, MA, the site of the CO observations. This led to a data set with more than 10000 points in the northern Galactic hemisphere and nearly 5000 in the south. Only 170 lines of sight of the total $15,555$ lines of sight had CO($1-0$) emission. Thus, for the remaining lines of sight we can ignore the contribution from N(H_2) and obtain a robust estimate of the N(HI)/$E(B-V)$ ratio. The HI data come from the Leiden-Argentina-Bonn survey (Kalberla et al. 2005) and the $E(B-V)$ data are from the Schlafly & Finkbeiner (2014) dust maps. The beam sizes vary from $6'$ for the Schlafly & Finkbeiner (2014) data to $36'$ for the 21 cm observations. We averaged the Schlafly & Finkbeiner (2014) data to $18'$ resolution in a compromise to matching the HI and CO data ($8'$) resolution.

2.4 The N(H_{tot}) / $E(B-V)$ ratio revisited

We begin by determining the gas to dust ratio using the galactic method for $|b| \geq 30°$. Figure 2.1 shows the general relationship between N(HI) and $E(B-V)$ for all $15,385$ points in our data set along with the best fit line. Our value, 7.2×10^{21}, is more consistent with that of Liszt (2014a) than with the Bohlin et al. (1978) value that was derived with the stellar method. Figure 2.2 shows the same data but for $E(B-V)$ ≤ 0.8 mag for a more direct comparison with the work of Liszt (2014a). Our value, 7.8×10^{21}, is fairly close to his (8.3×10^{21}). Figures 2.3 and 2.4 break down the data for the inner and outer Galaxy. The two data sets show slightly different slopes (8.4×10^{21} for the outer Galaxy and 7.0×10^{21} for the inner), perhaps indicating a difference in the gas to dust ratio, averaged over large scales, at high Galactic latitudes.

More intriguingly, the inner Galaxy data ($270^\circ \leq \ell \leq 90^\circ$) show a break in the slope at a higher colour excess (~ 0.7 mag) in the inward data set compared to the outward data set (~ 0.4 mag)[7].

Our study and the previous ones described in §2 use four basic approaches to analyzing their data sets: The atomic hydrogen is determined either for a line of sight that truncates on a star (stellar method), or continues through the entire Galactic disk and even the lower halo (galactic method). The other pair of options in organizing the data involved a latitude cutoff so that the data are either along the Galactic plane or at high Galactic latitudes. The latitude cutoffs are chosen somewhat arbitrarily at $|b| \leq 20^\circ$ or 30° for low latitude and $|b| \geq 20^\circ$ or 30° for high Galactic latitudes. The N($\mathrm{H_{tot}}$)/$E(B-V)$ slope for each of the studies categorized as just described is shown in Table 2.3.

The other data set involves the stellar method, uses substantially less points and includes lines of sight with latitudes $|b| < 24^\circ$, as well as lines of sight with detectable levels of molecular hydrogen. The sample of stars is listed in Table 2.1.

Figure 2.5 shows the total hydrogen column density versus the colour excess, with 1σ error bars. Assuming the intercept is negligible, the relation

$$N(H_{\mathrm{tot}})/E(B-V) = 5.78 \pm 2.33 \times 10^{21}\ \mathrm{cm^{-2}\ mag^{-1}} \tag{2.3}$$

is determined from the fit for colour excess between 0.07 and 1.08 mag, where the uncertainty is the standard deviation of the fit. Our value is virtually the same as that from Bohlin et al. (1978), with the two data sets sharing 38 of the 87 lines of sight.

[7] The color excess values of 0.7 and 0.4 mag in the submitted version of the paper should be 0.07 and 0.04 mag.

Figure 2.6 illustrates the effect the fractional abundance of H_2, f(H_2)[8], has on the N(H_{tot})/$E(B-V)$ relationship. It appears the lines of sight with a high fractional abundance of H_2 have a slightly reduced N(H_{tot})/$E(B-V)$. This may suggests that gas and dust in regions with high amounts of H_2 may produce increased reddening, lowering the gas to dust ratio. However, because this data set does not include many observations with a fractional H_2 abundance greater than 0.5, this conclusion is tentative and warrants further investigation.

2.5 N(CH) versus $E(B-V)$

Observations of the 9 cm ground state CH hyperfine transitions require assuming or knowing the excitation temperature to determine the column density, while observations of the optical and UV A-X and B-X CH absorption lines do not. Assuming that the two methods are sampling similar material on average, we can estimate the CH excitation temperature by comparing N(CH) versus $E(B-V)$ for the two types of observations. The CH column density can be determined from radio observations of the 3335-MHz emission line by:

$$N(CH) = 2.82 \times 10^{11} (\eta_{\rm B})^{-1} [T_{\rm ex}/(T_{\rm ex} - T_{\rm bg})]\ W(CH) \tag{2.4}$$

where W(CH) is the velocity integrated antenna temperature of the 3335-MHz line, $\eta_{\rm B}$ is the beam efficiency, and $T_{\rm bg}$ is the background temperature at 3.3 GHz. If $T_{\rm ex}$ is much greater than $T_{\rm bg}$, then the factor, $[T_{\rm ex}/(T_{\rm ex} - T_{\rm bg})] \equiv F_{\rm T}$, approaches 1 and N(CH) can be determined directly from the observed W(CH). However, $|T_{\rm ex}|$ has previously been determined to not be much greater than $T_{\rm bg}$ for several lines

[8] f(H_2) = 2 N(H_2)/N(H_{tot})

of sight [e.g., Lien (1984); Jura & Meyer (1985); Dailey et al. (2020)] , indicating that the CH excitation temperature cannot always be assumed to be much greater than the background temperature.

By comparing stellar and galactic plots of N(CH) versus $E(B-V)$, with the latter using the assumption $|T_{\rm ex}| \gg T_{\rm bg}$, we can see how the two CH-to-dust relationships directly compare. If the slopes of the stellar and galactic relationships do not match, then the likely culprit would be the assumption for $T_{\rm ex}$. We can then vary the factor $F_{\rm T}$ until the galactic slope more closely matches the stellar one.

Unfortunately, the comparison between the galactic and stellar data is somewhat problematic. The stellar data are collected over an almost infinitesimal beam that extends only to the star, while the galactic data are all from the NRAO 43-m radio telescope which had a $9'$ beam at 3.3 GHz. Additionally, the colour excess for the stellar observations is also determined from a nearly infinitesimal beam that extends only to the background source, while the galactic colour excess is determined from a $6'$ beam and extends all along the line of sight. Comparisons between the two data sets are further complicated by the differing fractional abundances of H_2. N(CH) has a strong correlation with N(H_2) (e.g. Liszt & Lucas 2002; Weselak 2019), but N(H_2) only partially contributes to N($H_{\rm tot}$), which is correlated with $E(B-V)$ (e.g. §4; Bohlin et al. 1978). Therefore, as the galactic data set contains lines of sight with an average f(H_2) greater than that for the stellar data set, the galactic N(CH) estimate for a given $E(B-V)$ may be greater than the stellar one due at least in part to the variation in f(H_2) instead of problems with estimating $T_{\rm ex}$.

Figure 2.7 shows N(CH)/$E(B-V)$ versus f(H_2) for the stellar data, and Figure 2.8 is the same for the galactic data. The N(CH)/$E(B-V)$ galactic relation does not appear to have any strong relation with f(H_2)[9], while the stellar data indicate a trend between an increasing N(CH)/$E(B-V)$ ratio and f(H_2), which has also been noted by Fan et al. (2017). Similarly, N(H_2)/$E(B-V)$ versus f(H_2) for the stellar

[9] defined for galactic data as f(H_2) = 1 - N(HI)/N($H_{\rm tot}$)

data is shown in Figure 2.9, and a clear dependence on f(H_2) is evident. In contrast, N(CH)/$E(B-V)$ for the galactic data shows no such dependence, despite the strong correlation between N(CH) and H($_2$). Galactic values of f(H_2) rely on an estimate of N(H_{tot}) from the relation given in equation 2.2, which may be the reason that Figure 2.8 does not show the same behaviour as Figures 2.7 and 2.9.

Figure 2.10 shows the stellar CH column densities versus colour excess for the 87 lines of sight in Table 2.1, with $E(B-V)$ between 0.01 and 1.08 mag. The stellar observations show a CH column density versus colour excess relation:

$$N(CH) = [(6.82 \pm 4.82) \times E(B-V) - (0.61 \pm 1.18)] \times 10^{13} \tag{2.5}$$

at least up to 1.08 mag colour excess, or A_V = 3.35 mag (assuming R_V = 3.1). This is similar to the relation determined by Lang & Willson (1978), N(CH)/$E(B-V)$ = 6.3×10^{13} $E(B-V)$ for $E(B-V)$ less than 0.6 mag. Liszt & Lucas (2002) determined there is no single relation between N(CH) and $E(B-V)$ below 0.3 mag due to the difference in N(CH) at similar $E(B-V)$ in lines of sight through typical diffuse gas or low colour excess H_2-rich gas. Our interpretation is somewhat similar in that, while there is a single N(CH)/$E(B-V)$ relation that continues to low colour excess in Figure 2.10, the standard deviation of the fit is large and at $\sim$ 0.2 mag the standard deviation is approximately equal to the N(CH) values predicted by the fit line.

If only the stellar observations with f(H_2) $> 1/3$ are sampled (Figure 2.11), the N(CH)/$E(B-V)$ relation is:

$$N(CH) = [(7.95 \pm 4.91) \times E(B-V) - (0.78 \pm 1.70)] \times 10^{13} \tag{2.6}$$

and if only observations with f(H_2) $< 1/3$ are sampled (Figure 2.12):

$$N(CH) = [(4.95 \pm 4.23) \times E(B-V) - (0.33 \pm 0.87)] \times 10^{13} \quad (2.7)$$

The stellar data sample has a fairly low average f(H_2) of 0.28 overall, and the galactic data average is 0.51. Only including stellar lines of sight with f(H_2) greater than $1/3$ results in f(H_2)$_{\text{average}}$ = 0.48. To reduce the discrepancy in the N(CH)/$E(B-V)$ relation due to the different average f(H_2) of the stellar and galactic data, the N(CH)/$E(B-V)$ relation for f(H_2) $> 1/3$ will be used as it better matches the galactic data set.

Figure 2.13 shows the radio derived CH column densities versus the colour excess for the 69 lines of sight within the same range of colour excess as Figure 2.10. The CH column densities are determined from the published antenna temperatures and line widths, the uncertainty of the CH column density assumes that the uncertainties of the antenna temperature and line width are uncorrelated. Fourteen of these lines of sight are non-detections, approximately 20 percent of the observations. The N(CH)/$E(B-V)$ relation for galactic observations is:

$$N(CH) = [(15.87 \pm 11.26) \times E(B-V) - (2.37 \pm 4.92)] \times 10^{13} \quad (2.8)$$

for colour excess up to 1.08 mag. If the range of colour excess is increased to 1.5 mag, the slope of the N(CH)/$E(B-V)$ relation is

$$N(CH) = [(15.08 \pm 10.74) \times E(B-V) - (2.19 \pm 4.99)] \times 10^{13} \quad (2.9)$$

with the addition of 6 observations. In both cases, the relation between N(CH) and $E(B-V)$ derived from the galactic data set is much steeper than the relation derived from the stellar data. Since the galactic N(CH) was calculated using the assumption $|T_{\rm ex}| \gg T_{\rm bg}$, it is likely that this assumption is not valid for the majority of the lines of sight in the sample. Extending the range of colour excess to 20 mag (see Figure 2.14) adds a small group of observations with CH column densities close to what was seen in Figure 2.13 but at much higher colour excess. These points have clearly lower column densities than the best fit line would indicate, a behaviour noted before by, e.g., Mattila (1986). At high extinctions, indicative of dense molecular gas, the CH abundance decreases relative to the colour excess as more complex carbon molecules are produced and CH is no longer a good tracer of the molecular gas (or the dust).

Several of the galactic lines of sight are within the 1σ standard deviation of the stellar fit line and therefore may have an excitation temperature greater than the background. However, the majority of the lines of sight have CH column densities greater than expected from the stellar data set, so $\rm T_{ex}$, on average, is likely not much greater than $\rm T_{bg}$, and $F_{\rm T}$ cannot be assumed to be approximately 1. By adjusting $F_{\rm T}$ until the slope of the data in Figure 2.13 is equal to the slope of the data in Figure 2.10, we can estimate the average $F_{\rm T}$ of the galactic data set. Figure 2.15 shows the galactic column density of CH versus colour excess for when $F_{\rm T}$ = 0.521 (equivalent to an average $\rm T_{ex}$ = -3.05 K), leading to a similar slope as the stellar data set shown in Figure 2.10. When accounting for the 1σ standard deviation; error of both stellar and galactic fits, $F_{\rm T} = 0.52 \pm 0.48; 0.07$. With the inclusion of galactic lines of sight with $E(B-V)$ up to 1.5 mag, $F_{\rm T}$ increases slightly to $0.55 \pm 0.53; 0.07$.

2.6 N(CH) versus N(H_2)

Figure 2.16 shows N(CH) versus N(H_2) for the stellar lines of sight in Table 2.1 with the fits excluding the outlying point, Herschel 36. The N(CH)/N(H_2) ratio is $4.75 \pm 2.20 \times 10^{-8}$, where the uncertainty is the standard deviation of the fit slope. This value is similar to the CH abundance obtained by Liszt & Lucas (2002), $4.3 \pm 1.9 \times 10^{-8}$.

Figure 2.17 shows the radio-derived CH column densities in relation to the calculated H_2 column densities (using equation 2.2). The substantial uncertainty for N(H_2) is a result of the accumulating uncertainties of both N(HI) observations and $E(B-V)$, along with the high standard deviation in the N(H_{tot})/$E(B-V)$ relation.

The slope of the best fit line for the stellar data set ($47.5 \pm 22.0 \times 10^{12}$) is less than the slope for the galactic data set ($87.3 \pm 61.1 \times 10^{12}$), which could suggest that, similar to the result from §5, F_T = 0.57 $\pm$ 0.48; 0.07 (see Figure 2.18). If the fit accounts for observations with N(H_2) up to 4×10^{21} cm^{-2}, F_T increases to 0.72 (T_{ex} = -7.2 K). The standard deviation of the galactic data is large, especially at low N(H_2), which may be due to overestimated non-detections. At higher N(H_2), the standard deviation is not much greater than the standard deviation of the stellar data, possibly due to varying excitation temperature, or the indirect method used to estimate the molecular hydrogen column density.

Figures 2.19 and 2.20 show the CH abundance as a function of f(H_2) for both the stellar and galactic methods. The stellar CH to H_2 fraction appears to be constant above approximately 0.2, but at low f(H_2), the N(CH) to N(H_2) fraction increases as f(H_2) decreases. No clear trend is noticeable in Figure 2.20 but the variation in the ratio seems to be greater at low values of f(H_2), perhaps because of the larger uncertainties at low f(H_2) due to determining f(H_2) using N(HI) and $E(B-V)$ instead of N(H_2).

2.7 Discussion

Our result in determining N(HI)/$E(B-V)$ using the galactic method shows a larger slope than the stellar studies at very low colour excess; consistent with Liszt (2014a,b) and Lockman & Condon (2005), who use high-latitude data and the galactic method. With the $E(B-V)$ values restricted to less than 0.08 mag (see Figure 2.2), the same colour excess cutoff as Liszt (2014a), our slope is close to his result (7.8×10^{21} for our data compared to 8.3×10^{21} for his study). The value of N(HI)/$E(B-V)$ is dependent on the longitude of the observations; toward the inner Galaxy N(HI)/$E(B-V)$ = $7.0 \pm 3.7 \times 10^{21}$ cm^{-2} mag^{-1}, while for the outer Galaxy N(HI)/$E(B-V)$ is $8.4 \pm 4.5 \times 10^{21}$ cm^{-2} mag^{-1}. Because the gas and dust are well-mixed (Spitzer 1978), whether the sight-lines terminate on nearby stars or extend throughout the disk should not affect the ratio for low galactic latitude. This is confirmed by the left-hand column of Table 2.3. However, once the sight-lines extend into the halo (i.e., non-truncated lines of sight at high Galactic latitude), the temperatures of the halo produce an environment that is less conducive to high dust densities. A study of the gas-to-dust ratio by Reach, Heiles, & Bernard (2015) does report that the ratio increases at higher temperatures. Moreover, Lockman & Condon (2005) note that lines of sight that extend to the halo have greater column densities of atomic hydrogen because of the widespread presence of high- and intermediate-velocity atomic clouds (e.g., Wakker & van Woerden 1997). Thus, one would expect the N(HI)/$E(B-V)$ slope to increase for non-truncated lines of sight at high Galactic latitudes - as confirmed by Lockman & Condon (2005), Liszt (2014a), and our work.

For the inner and outer Galaxy, the slopes of the N(HI) versus $E(B-V)$ relation are similar, however both relations (shown in Figures 2.3 and 2.4) have a break in the slope, at $E(B-V) \approx 0.07$ mag for the inner Galaxy compared to 0.04 mag for the outer Galaxy. Liszt (2014a) also notes a break in his data

at 0.075 mag and attributes this to the onset of H_2 formation. In light of this, our results may indicate that significant H_2 formation begins at lower $E(B-V)$ in the outer Galaxy perhaps due to the lower interstellar radiation field there.

If, instead of the galactic method, the stellar method is used, then the results tend to have lower slopes and they all cluster between $4-6\times10^{21}$. The stellar N(H_{tot})/$E(B-V)$ relation uses observations with high colour excess relative to the galactic N(HI)/$E(B-V)$ relation, which uses observations at very low colour excess. The N(H_{tot})/$E(B-V)$ relation using WODR for 87 stellar lines of of sight produces a similar relation to what was determined by Bohlin et al. (1978) and Diplas & Savage (1994) (see Table 2.3.)

The N(CH)/$E(B-V)$ ratio is, on average, lower using the stellar method compared to the galactic one. This has been observed previously (e.g. Lang & Willson 1978) for a reduced number of lines of sight. We note that the stellar observations were often along lines of sight with low f(H_2) compared with the galactic observations, but it is unlikely this fully accounts for the discrepancy in N(CH) between the two methods. Assuming the remaining discrepancy is due to using the wrong value of T_{ex} in equation 2.4, we determine that F_T can be assumed to be at least $0.52\pm0.48;0.07$ on average (equivalent to an average T_{ex} = -3.05 K). However, due to the discrepancy in the average f(H_2) between the data sets, the average F_T is likely higher than 0.52. The estimated standard deviation in the excitation temperature is large, consistent with previous estimates of the excitation temperature that result both in a high F_T, such as suggested by Rydbeck et al. (1976) (T_{ex} = -15 K) and Genzel et al. (1979) (T_{ex} = -60 K), and in a low F_T, such as Lien (1984), Jura & Meyer (1985).

We find that F_T required to reconcile the N(CH) versus N(H_2) data for the two methods is slightly larger (0.57), but the large uncertainty in the calculated N(H_2) results in a high standard deviation for

the fit. Additionally, there is a substantial decrease in the slope when additional observations with higher N(H_2) are included. The average $F_{\rm T}$ increases to 0.72 when accounting for the additional galactic observations, however this higher value is based on $E(B-V)$ well beyond the range of the stellar observations. At higher N(H_2) values, the CH abundance drops as more complex carbon-bearing molecules are formed (e.g., Mattila 1986).

Assuming the excitation temperature is -15 K, -60 K, or a value much greater than the background temperature may accurately determine N(CH) for some lines of sight, but overall will likely lead to an overestimated N(CH). We tentatively estimate that the average $F_{\rm T}$ is approximately $0.57 \pm 0.48; 0.07$ for lines of sight with $E(B-V)$ less than 1.08 mag and N(H_2) less than 1.5×10^{21} cm^{-2}.

Liszt & Lucas (2002) note that, at very low extinctions, there are two distinct N(CH)/$E(B-V)$ relationships depending on whether or not the line of sight in question has significant molecular gas (determined by the presence of the CO($1-0$) line). We see one relationship for N(CH)/$E(B-V)$, with a large scatter for the points with $E(B-V) < 0.2$ mag. Given the uncertainties in determining N(CH) by radio means, the column density and CH abundance are most reliably determined from optical and UV absorption data. Column densities derived from the CH 3335-MHz line should not automatically assume that that $|T_{\rm ex}| \gg T_{\rm bg}$. However, these observations are still valuable for detecting the presence of molecular gas in low density, low extinction molecular clouds, and, perhaps most importantly, for determining the kinematics of this gas.

Acknowledgements

This research has made use of the SIMBAD database, operated at CDS, Strasbourg, France. This research has made use of the NASA/IPAC Extragalactic Database (NED) which is operated by the Jet Propulsion Laboratory, California Institute of Technology, under contract with the National Aeronautics and Space Administration. This research also made use of the Python packages SciPy (Virtanen et al. 2020) and Matplotlib (Hunter 2007).

We acknowledge support from the Center for Undergraduate Research Opportunities (CURO) at the University of Georgia.

Data Availability

The data used in this article are available on request.

Line of Sight	l	b	N(CH) 10^{12} cm^{-2}	ref	$E(B-V)$ mag	ref	N(HI) 10^{21} cm^{-2}	ref	N(H_2) 10^{21} cm^{-2}	ref
HD 886	109.43	−46.68	1.10 ± 0.38	a	0.01 ± 0.01	b	0.11 ± 0.02	b	> 0.0000002	b
HD 2905	120.84	00.14	13.52 ± 0.92	c	0.33 ± 0.05	b	1.91 ± 0.39	b	0.19 ± 0.06	b
HD 12323	132.91	−05.87	7.04 ± 1.41	c	0.23 ± 0.02	d	1.51 ± 0.31	e	0.21 ± 0.04	e
HD 21856	156.32	−16.75	6.90 ± 0.76	c	0.17 ± 0.02^f	c	1.10 ± 0.22	g	0.11 ± 0.04	h
HD 22951	158.92	−16.70	12.54 ± 0.92	c	0.27 ± 0.03	b	1.10 ± 0.33	b	0.29 ± 0.09	b
HD 23180	160.36	−17.74	22.24 ± 2.91	c	0.31 ± 0.03	b	0.66 ± 0.14	b	0.40 ± 0.11	h
HD 24398	162.29	−16.69	22.30 ± 2.61	c	0.31 ± 0.03	b	0.63 ± 0.12	b	0.47 ± 0.15	b
HD 24534	163.08	−17.14	39.58 ± 3.00	c	0.59 ± 0.06	b	0.54 ± 0.07	b	0.83 ± 0.08	i
HD 24760	157.35	−10.09	1.13 ± 0.48	c	0.07 ± 0.01	d	0.25 ± 0.05	j	0.03 ± 0.02	h
HD 24912	160.37	−13.11	14.56 ± 1.37	c	0.33 ± 0.05	b	1.12 ± 0.21	b	0.34 ± 0.09	b
HD 27778	172.76	−17.39	39.93 ± 4.10	c	0.37 ± 0.03	b	0.89 ± 0.31	b	0.62 ± 0.09	b
HD 30614	144.07	14.04	10.28 ± 0.28	c	0.30 ± 0.05	b	0.93 ± 0.19	b	0.22 ± 0.06	b
HD 34078	172.08	−02.26	79.27 ± 4.79	c	0.52 ± 0.05	b	1.58 ± 0.40	b	0.76 ± 0.26	b
HD 36861	195.05	−12.00	2.56 ± 0.32	c	0.15 ± 0.03	b	0.65 ± 0.18	b	0.01 ± 0.004	b
HD 37022	209.01	−19.38	< 0.64	c	0.34 ± 0.03	b	3.47 ± 0.88	b	> 0.0004	h
HD 37903	206.85	−16.54	10 ± 2	k	0.35 ± 0.03	b	1.48 ± 0.34	b	0.83 ± 0.11	b
HD 40111	183.97	00.84	2.42 ± 0.45	c	0.20 ± 0.03	b	1.07 ± 0.22	b	0.05 ± 0.02	b
HD 41117	189.69	−00.86	19.16 ± 1.72	c	0.45 ± 0.06	b	2.51 ± 0.87	b	0.49 ± 0.11	b
HD 42087	187.75	01.77	19.61 ± 1.56	c	0.36 ± 0.06	b	2.45 ± 0.62	b	0.33 ± 0.09	b
HD 43384	187.99	03.53	28.92 ± 2.01	c	0.58 ± 0.03	b	1.86 ± 1.29	b	0.74 ± 0.24	b
HD 46202	206.31	−02.00	17 ± 3	k	0.49 ± 0.03	b	3.80 ± 1.31	b	0.48 ± 0.07	b
HD 47129	205.87	−00.31	14.64 ± 0.84	c	0.36 ± 0.03	b	1.51 ± 0.38	b	0.35 ± 0.11	b
HD 48099	206.21	00.80	6.90 ± 0.56	c	0.27 ± 0.06	b	1.58 ± 0.29	b	0.19 ± 0.05	b
HD 53367	223.71	−01.90	44 ± 4	k	0.74 ± 0.06	b	2.09 ± 1.44	b	1.10 ± 0.13	b
HD 53975	225.68	−02.32	3.10 ± 0.14	c	0.21 ± 0.03	b	1.26 ± 0.23	b	0.02 ± 0.001	b
HD 54662	224.17	−00.78	12.50 ± 0.56	c	0.35 ± 0.05	b	1.70 ± 0.39	b	0.10 ± 0.03	b
HD 79186	267.36	02.25	10.36 ± 0.43	a	0.30 ± 0.04^f	e	1.58 ± 0.33	b	0.52 ± 0.11	b
HD 92740	287.17	−00.85	8.20 ± 1.63	a	0.33 ± 0.04^f	h	2.19 ± 0.50	b	0.09 ± 0.03	b
HD 108639	300.22	01.95	< 1.21	l	0.34 ± 0.04^f	l	2.24 ± 0.46	b	0.09 ± 0.01	b
HD 110432	301.96	−00.20	17.18 ± 0.84	c	0.51 ± 0.06	b	0.71 ± 0.24	b	0.44 ± 0.04	b

Line of Sight	l	b	N(CH) 10^{12} cm^{-2}	ref	$E(B-V)$ mag	ref	N(HI) 10^{21} cm^{-2}	ref	N(H_2) 10^{21} cm^{-2}	ref
HD 112244	303.55	06.03	6.62 ± 0.42	c	0.29 ± 0.06	b	1.20 ± 0.22	b	0.14 ± 0.03	b
HD 113904	304.67	−02.49	2.82 ± 0.28	c	0.18 ± 0.02^{f}	c	1.20 ± 0.24	g	0.07 ± 0.02	h
HD 115071	305.76	00.15	8.21 ± 0.34	l	0.54 ± 0.07^{f}	l	2.40 ± 0.55	b	0.49 ± 0.10	b
HD 115455	306.06	00.22	16.67 ± 1.45	l	0.49 ± 0.06^{f}	l	2.57 ± 0.53	b	0.38 ± 0.08	b
HD 135591	320.13	−02.64	5.21 ± 0.28	c	0.18 ± 0.01	d	1.20 ± 0.28	m	0.06 ± 0.01	h
HD 137595	336.72	18.86	12.08 ± 2.90	l	0.27 ± 0.03^{f}	l	1.00 ± 0.14	b	0.36 ± 0.05	b
HD 141637	346.10	21.71	1.90 ± 0.24	c	0.15 ± 0.03	b	1.51 ± 0.28	b	0.02 ± 0.01	b
HD 143275	350.10	22.49	2.75 ± 0.89	a	0.17 ± 0.03	b	1.02 ± 0.19	b	0.03 ± 0.01	b
HD 144217	353.19	23.60	2.86 ± 0.25	c	0.19 ± 0.03	b	1.07 ± 0.20	b	0.07 ± 0.01	b
HD 144470	352.45	22.77	4.65 ± 0.28	c	0.22 ± 0.03	b	1.51 ± 0.31	b	0.11 ± 0.02	b
HD 144965	339.04	08.42	14.25 ± 1.93	l	0.35 ± 0.04^{f}	l	1.17 ± 0.16	b	0.59 ± 0.09	b
HD 145502	354.61	22.70	5.21 ± 0.28	c	0.24 ± 0.03	b	1.58 ± 0.44	b	0.08 ± 0.02	b
HD 147165	351.31	17.00	4.44 ± 0.21	c	0.41 ± 0.04	b	2.40 ± 0.44	b	0.06 ± 0.02	h
HD 147683	344.86	10.09	22.22 ± 1.62	l	0.48 ± 0.06^{f}	l	2.57 ± 0.47	b	0.48 ± 0.13	b
HD 147888	353.65	17.71	24.64 ± 1.69	c	0.47 ± 0.03	b	3.98 ± 0.92	b	0.30 ± 0.03	b
HD 147933	353.69	17.69	25.60 ± 1.70	n	0.48 ± 0.03	b	4.27 ± 0.88	b	0.37 ± 0.10	b
HD 148184	357.93	20.68	35.43 ± 0.42	c	0.52 ± 0.06	b	1.35 ± 0.31	b	0.43 ± 0.14	b
HD 148605	353.10	15.80	0.99 ± 0.42	c	0.13 ± 0.03	b	0.46 ± 0.08	b	0.01 ± 0.002	b
HD 149038	339.38	02.51	13.94 ± 0.42	c	0.24 ± 0.03^{f}	c	1.00 ± 0.20	g	0.28 ± 0.10	h
HD 149404	340.54	03.01	27.08 ± 1.84	c	0.68 ± 0.06	b	2.51 ± 0.81	b	0.62 ± 0.06	b
HD 149757	006.28	23.59	26.06 ± 0.28	c	0.32 ± 0.03	b	0.49 ± 0.11	b	0.44 ± 0.06	b
HD 150898	329.98	−08.47	5.35 ± 0.27	c	0.11 ± 0.01	d	0.90 ± 0.18	g	0.06 ± 0.03	h
HD 151804	343.62	01.94	8.73 ± 0.56	c	0.35 ± 0.04^{f}	c	1.20 ± 0.36	g	0.18 ± 0.05	h
HD 152234	343.46	01.22	18.02 ± 0.70	c	0.41 ± 0.05	b	2.09 ± 0.58	b	0.27 ± 0.09	b
HD 152236	343.03	00.87	27.24 ± 3.04	c	0.68 ± 0.06	b	5.89 ± 1.76	b	0.54 ± 0.15	b
HD 152408	344.08	01.49	14.08 ± 0.56	c	0.45 ± 0.06^{f}	c	1.80 ± 0.54	g	0.24 ± 0.01	h
HD 154368	349.97	03.22	61.75 ± 4.1	c	0.78 ± 0.04	b	1.00 ± 0.12	b	1.45 ± 0.23	b
HD 155806	352.59	02.87	8.03 ± 0.28	c	0.23 ± 0.01	d	1.20 ± 0.36	g	0.08 ± 0.03	h
HD 163758	355.36	−06.10	6.47 ± 0.76	a	0.35 ± 0.04^{f}	o	1.70 ± 0.70	b	0.07 ± 0.02	b
HD 164353	029.73	12.63	6.34 ± 0.28	c	0.10 ± 0.01^{f}	c	1.00 ± 0.40	g	0.18 ± 0.12	h

Table 2.1: Continued

Line of Sight	l	b	N(CH) 10^{12} cm^{-2}	ref	$E(B-V)$ mag	ref	N(HI) 10^{21} cm^{-2}	ref	N(H_2) 10^{21} cm^{-2}	ref
HD 164794	006.01	−01.20	11.90 ± 2.50	n	0.31 ± 0.05	b	1.95 ± 0.31	b	0.13 ± 0.04	b
HD 164816	006.06	−01.20	7.59 ± 0.39	p	0.30 ± 0.04^{f}	p	1.51 ± 0.45	b	0.11 ± 0.01	b
HD 165246	006.40	−01.56	6.46 ± 0.15	p	0.40 ± 0.05^{f}	p	2.57 ± 0.41	b	0.14 ± 0.03	b
HD 167264	010.46	−01.74	6.61 ± 0.76	a	0.34 ± 0.04^{f}	h	1.41 ± 0.42	b	0.19 ± 0.04	b
HD 167971	018.25	01.68	30 ± 3	k	1.08 ± 0.06	b	3.98 ± 2.75	b	0.71 ± 0.20	b
HD 168076	016.94	00.84	30 ± 5	k	0.74 ± 0.06	b	4.47 ± 2.37	b	0.48 ± 0.09	b
HD 170740	021.06	−00.53	22.00 ± 1.40	n	0.48 ± 0.03	b	1.10 ± 0.38	b	0.72 ± 0.13	b
HD 179406	028.23	−08.31	19.95 ± 0.44	c	0.33 ± 0.03	b	1.70 ± 0.59	b	0.54 ± 0.09	b
HD 184915	031.77	−13.29	7.74 ± 0.28	c	0.17 ± 0.01	d	0.80 ± 0.24	g	0.20 ± 0.07	h
HD 186994	078.62	10.06	4.0 ± 0.8	k	0.17 ± 0.03	b	0.79 ± 0.35	b	0.04 ± 0.004	b
HD 192639	074.90	01.48	28 ± 5	k	0.66 ± 0.06	b	2.09 ± 0.58	b	0.49 ± 0.06	b
HD 198478	085.75	01.49	19.95 ± 1.84	a	0.54 ± 0.06	b	2.09 ± 0.77	b	0.74 ± 0.26	b
HD 199579	085.70	−00.30	26 ± 4	k	0.37 ± 0.06	b	1.10 ± 0.28	b	0.34 ± 0.03	b
HD 203064	087.61	−03.84	11.11 ± 0.28	c	0.25 ± 0.03^{f}	c	1.00 ± 0.30	g	0.19 ± 0.07	h
HD 203938	090.56	−02.23	42.84 ± 3.41	c	0.74 ± 0.04	b	3.02 ± 1.04	b	1.00 ± 0.14	b
HD 206267	099.29	03.74	31.68 ± 1.88	c	0.53 ± 0.05	b	2.00 ± 0.69	b	0.72 ± 0.07	b
HD 207198	103.14	06.99	41.72 ± 4.48	c	0.62 ± 0.06	b	2.19 ± 0.86	b	0.68 ± 0.06	b
HD 207538	101.60	04.67	47.53 ± 4.00	c	0.64 ± 0.04	b	2.19 ± 0.60	b	0.83 ± 0.11	b
HD 209975	104.87	05.39	12.67 ± 0.42	c	0.36 ± 0.03	b	1.48 ± 0.31	b	0.12 ± 0.04	b
HD 210121	056.88	−44.46	35.90 ± 2.50	n	0.40 ± 0.04	b	0.43 ± 0.15	b	0.56 ± 0.16	b
HD 210839	103.83	02.61	36.00 ± 2.45	c	0.57 ± 0.05	b	1.41 ± 0.39	b	0.69 ± 0.06	b
HD 217035	110.25	02.86	37.31 ± 2.11	c	0.76 ± 0.10^{f}	c	2.88 ± 0.80	q	0.90 ± 0.03	r
HD 218376	109.95	−00.78	11.12 ± 0.42	c	0.25 ± 0.03	b	0.81 ± 0.17	b	0.14 ± 0.05	b
HD 218915	108.06	−06.89	8.51 ± 4.12	a	0.29 ± 0.04^{f}	o	1.29 ± 0.39	b	0.14 ± 0.03	b
HD 224572	115.55	−06.36	8.87 ± 0.28	c	0.19 ± 0.03	b	0.62 ± 0.11	b	0.17 ± 0.05	h
HD 281159	160.49	−17.80	53 ± 4	k	0.85 ± 0.05	b	2.45 ± 1.70	b	1.23 ± 0.54	b
Herschel 36	005.97	−01.17	74.13 ± 5.12	p	0.87 ± 0.03	b	8.91 ± 3.08	b	0.15 ± 0.04	b

a) Smoker et al. (2014), b) Fan et al. (2017), c) Weselak (2019), d) Bowen et al. (2008), e) Cartledge et al. (2004),
f) Colour excess uncertainty is estimated by the average uncertainty of the non-zero colour excesses in Fan et al. (2017) and Bowen et al. (2008). g) Bohlin et al. (1978), h) Savage et al. (1977), i) Rachford et al. (2002),
j) Lacour et al. (2005), k) Thorburn (2003), l) Andersson et al. (2002), m) Fruscione et al. (1994), n) Mookerjea (2016),
o) Burgh, France, & McCandliss (2007), p) Dahlstrom et al. (2013), q) Diplas & Savage (1994), r) Pan et al. (2005)

Table 2.1: Continued

Table 2.2: Galactic Data

Line of Sight	l	b	N(CH)	ref	$E(B-V)$	N(H_2)
			10^{12} cm^{-2}		mag	10^{21} cm^{-2}
L1590 −18, −18	195.39	−16.99	62.0 ± 6.1	a	0.773 ± 0.077	1.55 ± 0.93
L1590 −18, −9	195.25	−16.91	166.3 ± 8.9	a	1.395 ± 0.140	3.38 ± 1.68
L1590 −18, 0	195.12	−16.83	84.1 ± 8.0	a	0.570 ± 0.057	1.00 ± 0.68
L1590 −18, 9	194.99	−16.75	75.2 ± 8.0	a	0.483 ± 0.048	0.73 ± 0.58
L1590 −18, 18	194.85	−16.67	81.8 ± 7.5	a	0.631 ± 0.063	1.11 ± 0.76
L1590 −9, −18	195.47	−16.86	83.2 ± 8.9	a	0.675 ± 0.068	1.22 ± 0.81
L1590 −9, −9	195.34	−16.78	122.2 ± 6.6	a	1.126 ± 0.113	2.54 ± 1.35
L1590 −9, 0	195.20	−16.71	113.7 ± 7.1	a	0.795 ± 0.080	1.60 ± 0.95
L1590 −9, 9	195.07	−16.63	99.6 ± 6.1	a	0.654 ± 0.065	1.19 ± 0.79
L1590 −9, 18	194.94	−16.55	79.9 ± 6.6	a	0.731 ± 0.073	1.35 ± 0.88
L1590 0, −9	195.42	−16.66	117.9 ± 6.6	a	0.835 ± 0.084	1.67 ± 1.00
L1590 0, 0	195.28	−16.58	108.1 ± 7.5	a	0.925 ± 0.092	1.94 ± 1.11
L1590 0, 9	195.15	−16.50	87.0 ± 4.7	a	0.835 ± 0.084	1.67 ± 1.00
L1590 0, 18	195.02	−16.42	110.9 ± 5.6	a	0.902 ± 0.090	1.80 ± 1.08
L1590 9, −9	195.50	−16.53	96.8 ± 8.5	a	0.843 ± 0.084	1.68 ± 1.01
L1590 9, 0	195.36	−16.45	128.7 ± 8.0	a	0.872 ± 0.087	1.77 ± 1.05
L1590 9, 9	195.23	−16.37	111.3 ± 9.4	a	0.992 ± 0.099	2.10 ± 1.19
L1590 9, 18	195.10	−16.29	58.8 ± 8.9	a	0.946 ± 0.095	1.93 ± 1.14
L1590 18, −9	195.58	−16.40	46.5 ± 6.6	a	0.626 ± 0.063	1.06 ± 0.75
L1590 18, 0	195.45	−16.32	92.1 ± 8.0	a	0.822 ± 0.082	1.61 ± 0.99
L1590 18, 9	195.31	−16.25	141.4 ± 8.9	a	1.265 ± 0.127	2.87 ± 1.52
L1590 18, 18	195.18	−16.17	59.7 ± 5.6	a	0.995 ± 0.099	2.02 ± 1.19
L1590 27, 9	195.39	−16.12	118.9 ± 5.2	a	1.080 ± 0.108	2.31 ± 1.30
L1590 27, 18	195.26	−16.04	77.6 ± 7.5	a	0.977 ± 0.098	1.95 ± 1.17
L1780 −18, −9	358.67	36.87	> 20.0	a	0.159 ± 0.016	0.05 ± 0.19
L1780 −18, 0	358.81	36.97	> 20.0	a	0.145 ± 0.014	0.02 ± 0.17
L1780 −9, −18	358.66	36.65	> 20.0	a	0.197 ± 0.020	0.14 ± 0.24
L1780 −9, −9	358.80	36.76	60.2 ± 5.6	a	0.372 ± 0.037	0.65 ± 0.45
L1780 −9, 0	358.94	36.86	66.7 ± 7.1	a	0.417 ± 0.042	0.79 ± 0.50
L1780 −9, 18	359.22	37.06	> 20.0	a	0.141 ± 0.014	0.01 ± 0.17
L1780 0, −18	358.78	36.54	23.0 ± 4.2	a	0.232 ± 0.023	0.23 ± 0.28
L1780 0, −9	358.92	36.65	54.5 ± 6.6	a	0.412 ± 0.041	0.75 ± 0.50
L1780 0, 0	359.06	36.75	113.2 ± 5.2	a	0.552 ± 0.055	1.17 ± 0.66
L1780 0, 9	359.20	36.85	51.2 ± 7.1	a	0.308 ± 0.031	0.48 ± 0.37
L1780 0, 13.5	359.27	36.90	7.5 ± 4.7	a	0.224 ± 0.022	0.24 ± 0.27
L1780 0, 18	359.34	36.65	> 20.0	a	0.158 ± 0.016	0.06 ± 0.19
L1780 9, −18	358.91	36.43	> 20.0	a	0.215 ± 0.021	0.17 ± 0.26
L1780 9, −9	359.05	36.53	32.0 ± 5.6	a	0.327 ± 0.033	0.50 ± 0.39
L1780 9, 0	359.19	36.64	110.4 ± 6.1	a	0.511 ± 0.051	1.05 ± 0.61
L1780 9, 9	359.32	36.74	38.1 ± 5.6	a	0.296 ± 0.030	0.45 ± 0.36
L1780 9, 18	359.46	36.84	> 20.0	a	0.156 ± 0.016	0.05 ± 0.19

Table 2.2: Continued

Line of Sight	l	b	N(CH)	ref	$E(B-V)$	N(H_2)
			10^{12} cm^{-2}		mag	10^{21} cm^{-2}
L1780 18, −9	359.17	36.42	> 20.0	a	0.264 ± 0.026	0.30 ± 0.32
L1780 18, 0	359.31	36.52	40.0 ± 4.7	a	0.374 ± 0.037	0.64 ± 0.45
L1780 18, 9	359.45	36.62	> 20.0	a	0.207 ± 0.021	0.18 ± 0.25
L1780 27, −9	359.29	36.31	> 25.1	a	0.231 ± 0.023	0.20 ± 0.28
L1780 27, 0	359.43	36.41	> 15.0	a	0.233 ± 0.023	0.22 ± 0.28
L134C	4.18	35.75	99.2 ± 9.4	a	0.811 ± 0.081	1.90 ± 0.97
L134	4.21	35.56	109.5 ± 9.9	a	0.865 ± 0.086	2.06 ± 1.04
HD21483	158.87	−21.30	57.1 ± 12.3	b	0.890 ± 0.089	2.02 ± 1.07
HD23180	160.37	−17.74	80.7 ± 13.3	b	3.526 ± 0.353	9.60 ± 4.23
HD24534	163.08	−17.14	40.6 ± 10.1	b	0.379 ± 0.038	0.79 ± 0.46
HD147701	352.25	16.84	40.1 ± 12.3	b	0.894 ± 0.089	1.96 ± 1.07
ρ Oph	353.74	17.63	41.7 ± 10.1	b	1.129 ± 0.113	2.61 ± 1.35
ζ Oph	6.28	23.59	20.3 ± 5.5	b	0.494 ± 0.049	0.87 ± 0.59
Pal2	170.49	−8.98	168.0 ± 19.1	c	1.075 ± 0.107	1.73 ± 1.29
NGC6121	351.00	15.97	> 3.8	c	0.439 ± 0.044	0.55 ± 0.53
NGC6287	00.13	11.97	88.2 ± 13.8	c	0.695 ± 0.070	1.30 ± 0.84
NGC6325	00.99	8.00	55.8 ± 11.1	c	0.833 ± 0.083	1.33 ± 1.00
NGC6402	21.30	14.78	80.0 ± 17.6	c	0.421 ± 0.042	0.47 ± 0.51
NGC6517	19.23	6.77	32.9 ± 10.0	c	1.071 ± 0.107	1.88 ± 1.29
NGC6539	20.80	6.78	45.1 ± 11.8	c	0.967 ± 0.097	1.50 ± 1.16
L1551	178.93	−20.05	65.0 ± 4.2	d	0.772 ± 0.077	1.48 ± 0.93
RNO91	359.57	23.03	83.4 ± 2.0	d	0.369 ± 0.037	0.36 ± 0.44
RcrA	359.93	−17.85	62.0 ± 4.1	d	1.371 ± 0.137	3.67 ± 1.65
B335	44.93	−6.56	13.0 ± 0.5	d	0.283 ± 0.028	-0.14 ± 0.34
A	170.79	−36.22	32.5 ± 9.6	e	0.589 ± 0.059	0.82 ± 0.71
B	170.64	−36.33	22.5 ± 14.3	e	0.638 ± 0.064	0.94 ± 0.77
C	170.49	−36.44	20.7 ± 9.6	e	0.625 ± 0.063	0.90 ± 0.75
B0212 + 735	128.93	11.96	65.5 ± 5.1	f	0.668 ± 0.067	0.60 ± 0.80
B0415 + 379	161.68	−8.82	149.2 ± 2.2	f	1.462 ± 0.146	2.87 ± 1.75
B0433 + 295	170.58	−11.66	112.4 ± 5.2	f	0.866 ± 0.087	1.94 ± 1.04
B0459 + 252	177.73	−9.91	73.9 ± 3.4	f	0.793 ± 0.079	1.03 ± 0.95
B0528 + 134	191.37	−11.01	61.2 ± 6.1	f	0.760 ± 0.076	1.03 ± 0.91
B0736 + 017	216.99	11.38	9.0 ± 3.3	f	0.121 ± 0.012	0.00 ± 0.15
B0954 + 658	145.75	43.13	> 10.1	f	0.106 ± 0.011	0.07 ± 0.13
B2200 + 420	92.59	−10.44	> 4.4	f	0.291 ± 0.029	0.00 ± 0.35

a) Mattila (1986), non detections assume a line width of 1 km/s. b) Lang & Willson (1978) c) Mattila (1989), non detections assume a line width of 2.5 km/s. d) Magnani et al. (1992) e) Magnani & Onello (1993) f) Liszt & Lucas (2002)

Table 2.3: Gas-to-dust ratios

Latitude	stellar method	ref.	galactic method	ref.
$\|b\| \leq 20°$	5.4×10^{21}	a,b	$5 - 6 \times 10^{21}$	c
	4.7×10^{21}	d,b		
$\|b\| \geq 20°$	5.9×10^{21}	a,b	7.2×10^{21}	e
	4.0×10^{21}	d,b	7.8×10^{21}	f
			10.0×10^{21}	g
			8.3×10^{21}	h
all $\|b\|$	5.8×10^{21}	a		
	4.9×10^{21}	d		
	5.6×10^{21}	i		
	5.8×10^{21}	j		

a) Bohlin et al. (1978), N(H_{tot}) to $E(B-V)$
b) Calculated using the published data with known and estimated uncertainties
c) Liszt (2014b), $|b| \leq 30°$, N(HI) to $E(B-V)$
d) Diplas & Savage (1994), N(HI) to $E(B-V)$
e) this work; $|b| \geq 30°$, N(HI) to $E(B-V)$
f) this work; only using lines of sight with $E(B-V) \leq 0.08$ mag, N(HI) to $E(B-V)$
g) Lockman & Condon (2005), N(HI) to $E(B-V)$
h) Liszt (2014a), N(HI) to $E(B-V)$
i) Rachford et al. (2002), N(H_{tot}) to $E(B-V)$
j) this work

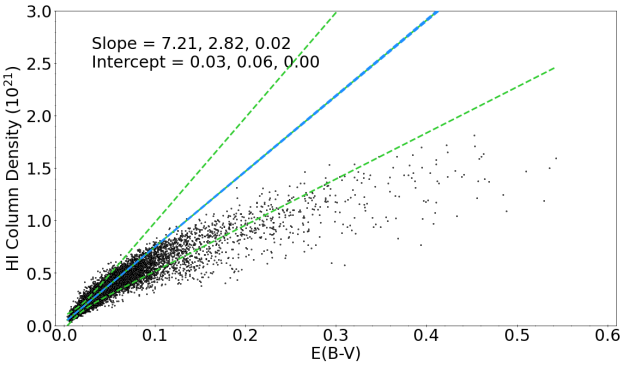

Figure 2.1: The relationship between N(HI) (cm^{-2}) and $E(B-V)$ (mag) for more than $15,000$ points at Galactic latitudes $> 30°$ and $< -30°$ (see text). The atomic hydrogen data are from the LAB all sky survey (Kalberla et al. 2005). The $E(B-V)$ values are from Schlafly & Finkbeiner (2014). The slope and y-intercept of the best fit line are given in the top left corner in units of 10^{21}, along with the 1σ standard deviations and 1σ standard errors. The solid green line is the relation in equation 2.2, with the dashed green lines representing the 1σ standard deviation and the dashed blue lines representing the 1σ standard error. The slope decreases notably at a colour excess ≈ 0.7 mag.

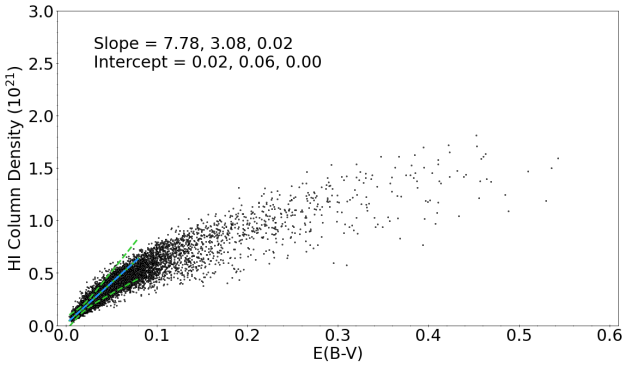

Figure 2.2: Same as Figure 2.1 but only for those line of sight with $E(B-V) \leq 0.08$ mag for a more direct comparison with the work of Liszt (2014a).

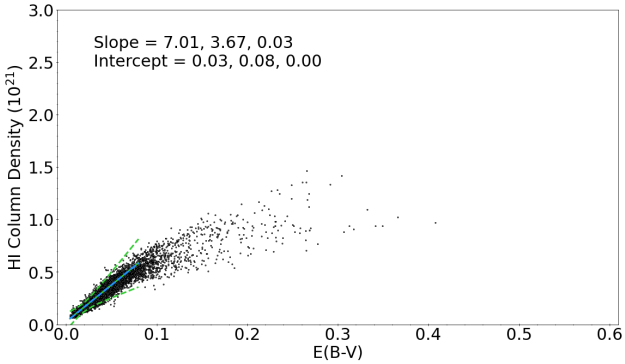

Figure 2.3: Same as Figure 2.2 for lines of sight with galactic longitude between 270° and 90° (i.e., the inner Galaxy). The slope decreases notably at a colour excess ≈ 0.07 mag.

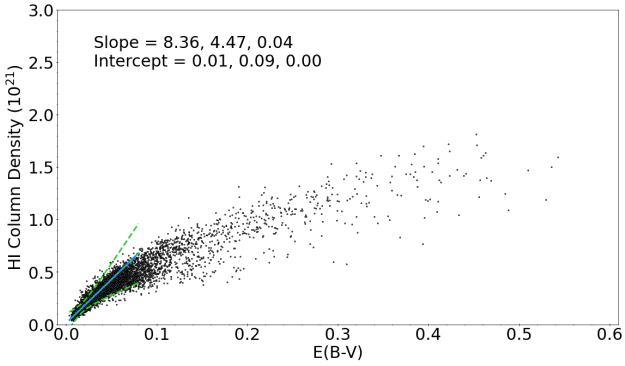

Figure 2.4: Same as Figure 2.2 except limited to galactic longitudes between 90 and 270 (i.e., the outer Galaxy). The slope decreases sharply at a colour excess ≈ 0.04 mag.

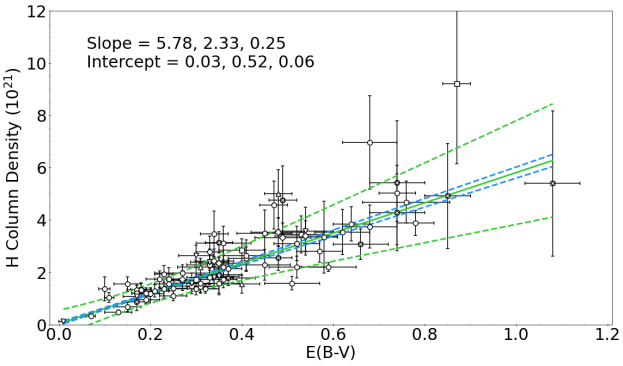

Figure 2.5: $N(H_{tot})$ (cm^{-2}) versus $E(B-V)$ (mag) for the lines of sight to the stars in Table 2.1 (see text). The green dashed line is the 1σ confidence interval of the standard deviation and the blue dashed line for the standard error. The slope and y-intercept of the best fit line are given in the top left corner, along with the 1σ standard deviations and 1σ standard errors in units of 10^{21}. The data points with CH column densities from Weselak (2019) are marked with circles, those from Mookerjea (2016) are marked with upright triangles, Smoker (2014) data points are marked with inverted triangles, Dahlstrom (2013) data points are marked with squares, Thorburn (2003) data points are marked with X, and Andersson et al. (2002) data points are marked with diamonds.

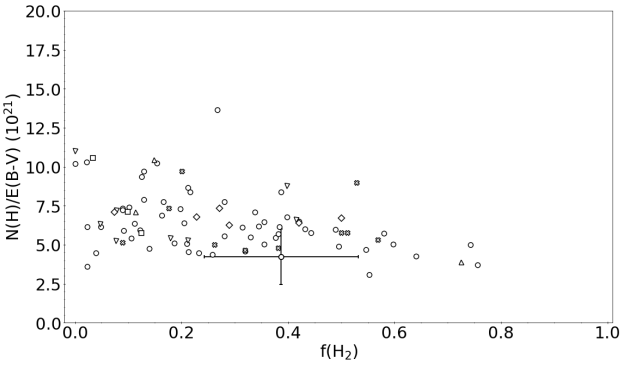

Figure 2.6: $N(H_{tot})/E(B-V)$ [cm^{-2} mag^{-1}] versus f(H_2) for the lines of sight plotted in Figure 2.5. Data points are marked the same manner as Figure 2.5.

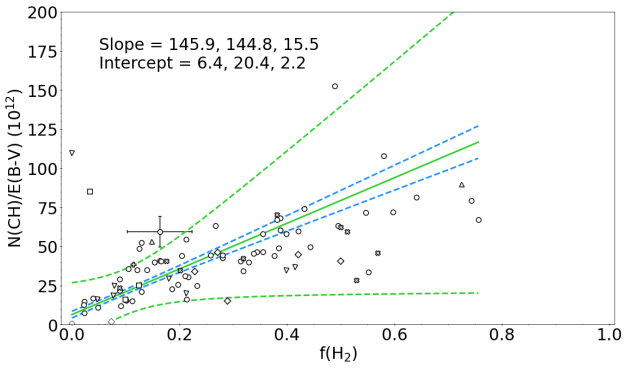

Figure 2.7: N(CH)/$E(B-V)$ versus f(H_2) for the stellar data set. Data points are marked the same way as Figure 2.5. The slope and y-intercept of the best fit line are given in the top left corner, along with the 1σ standard deviations and 1σ standard errors in units of 1×10^{12}. Sample error bars are shown for one of the data points.

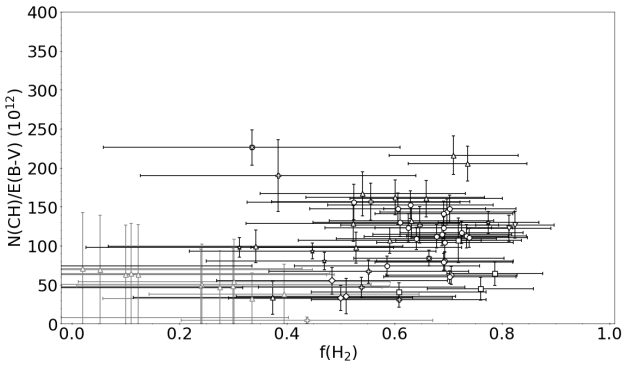

Figure 2.8: N(CH)/$E(B-V)$ versus f(H_2) for the galactic data set. L1590 data points from Mattila (1986) are marked by circles, L1780 data from Mattila (1986) by upright triangles, L134 data from Mattila (1986) by inverted triangles, Lang & Willson (1978) data by squares, Mattila (1989) data by plus signs, Magnani et al. (1992) data by X, Magnani & Onello (1993) data by diamonds, and Liszt & Lucas (2002) data by stars.

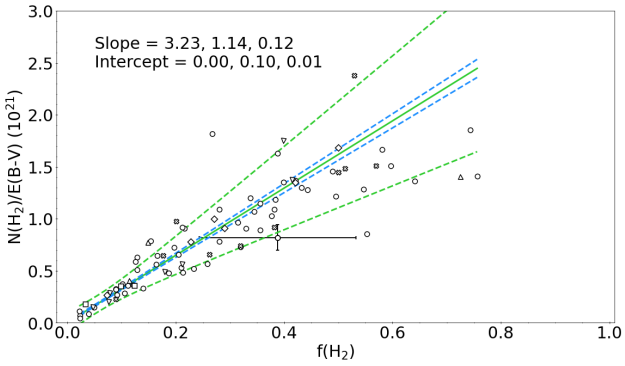

Figure 2.9: The N(H_2)/$E(B-V)$ ratio versus f(H_2) for the stellar data set. The slope and y-intercept of the best fit line are given in the top left corner, along with the 1σ standard deviations and 1σ standard errors in units of 10^{21}. Data points are marked the same way as Figure 2.5.

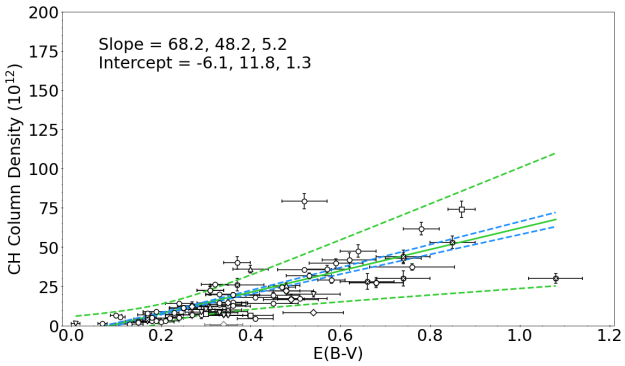

Figure 2.10: N(CH) determined from optical data versus $E(B-V)$ for the lines of sight to the stars in Table 2.1. The slope and y-intercept of the best fit line are given in the top left corner, along with the 1σ standard deviations and 1σ standard errors in units of 1×10^{12}. Data points are marked the same way as Figure 2.5.

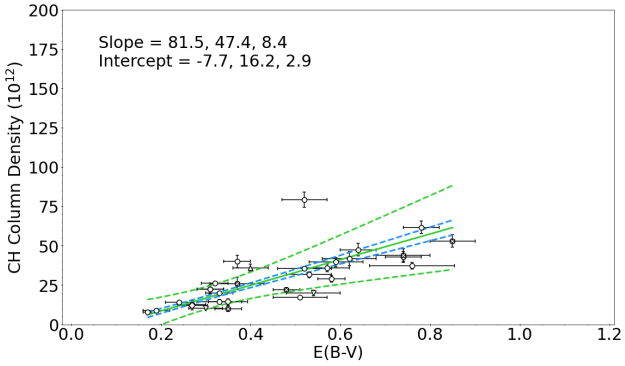

Figure 2.11: N(CH) versus $E(B-V)$ for the stellar data set, f(H_2) greater than $1/3$. The slope and y-intercept of the best fit line are given in the top left corner, along with the 1σ standard deviations and 1σ standard errors in units of 10^{12}. Data points are marked in the same way as Figure 2.5.

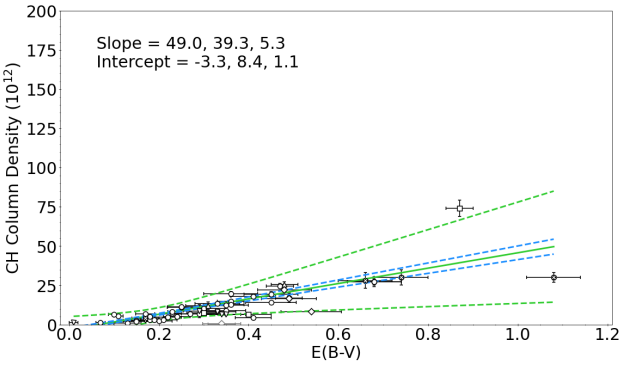

Figure 2.12: Same as Figure 2.11 for f(H_2) less than $1/3$.

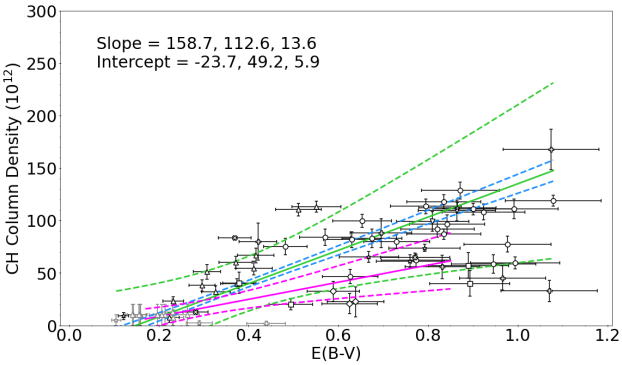

Figure 2.13: N(CH) (cm^{-2}) determined from radio data versus $E(B-V)$ (mag) for lines of sight with colour excesses less than 1.08 mag to allow for comparison with the optical data. The slope and y-intercept of the best fit line are given in the top left corner, along with the 1σ standard deviations and 1σ standard errors in units of 10^{12}. Data points are marked the same way as Figure 2.7. The magenta solid and dashed lines show the fit line and 1σ standard deviations from Figure 2.11.

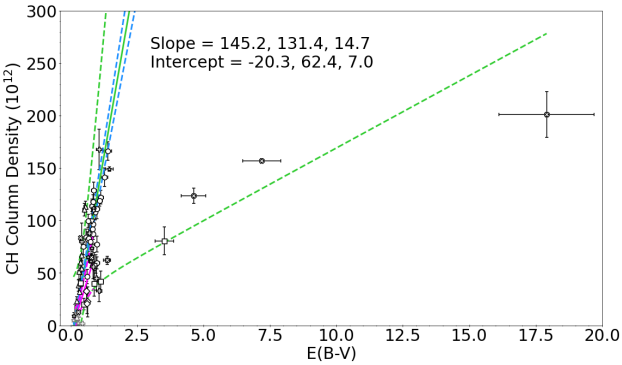

Figure 2.14: Same as Figure 2.13, but $E(B-V)$ is extended to 20 mag. The turnover in slope is expected (e.g., Mattila 1986) as the CH abundance decreases significantly in dense molecular gas.

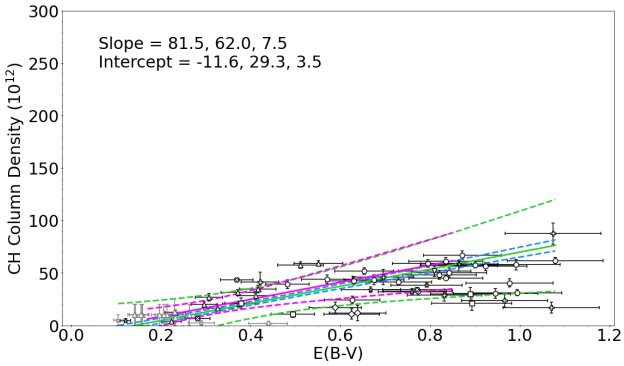

Figure 2.15: Similar to Figure 2.13, except the CH column densities for the radio data are determined assuming $F_{\rm T} = 0.521$ (see §5).

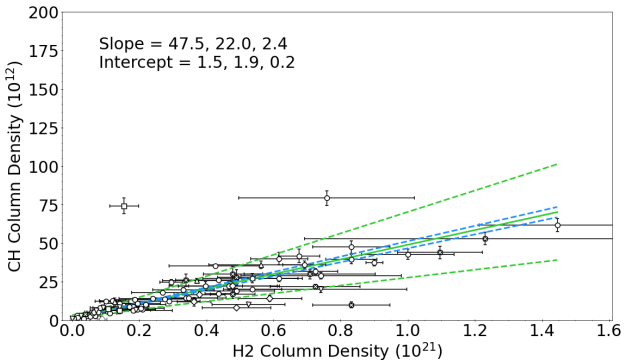

Figure 2.16: N(CH) (cm^{-2}) compared with N(H_2) (cm^{-2}) for the lines of sight to the stars in Table 2.1. Herschel 36 is an outlier so it is not accounted for in determining the fit. The slope and y-intercept of the best fit line are given in the top left corner, along with the 1σ standard deviations and 1σ standard errors. Data points are marked the same way as Figure 2.4.

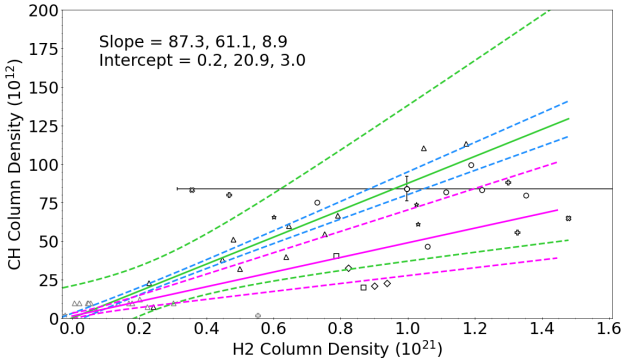

Figure 2.17: N(CH) (cm^{-2}) compared with N(H_2) (cm^{-s}) using the galactic method. Data points are marked the same way as figure 2.7, and the magenta solid and dashed lines show the fit line and 1σ standard deviations from figure 2.16.

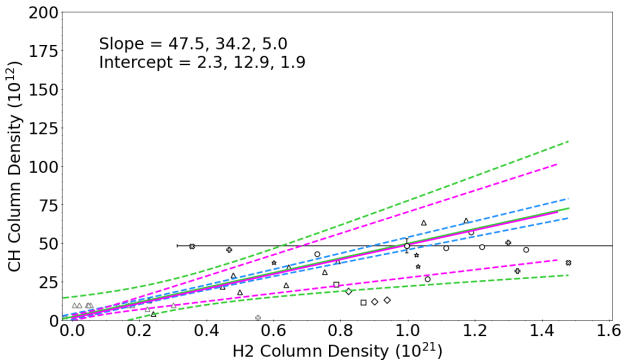

Figure 2.18: Similar to Figure 2.17, except the CH column densities are determined assuming $F_{\mathrm{T}} = 0.574$. Data points are marked the same way as Figure 2.7.

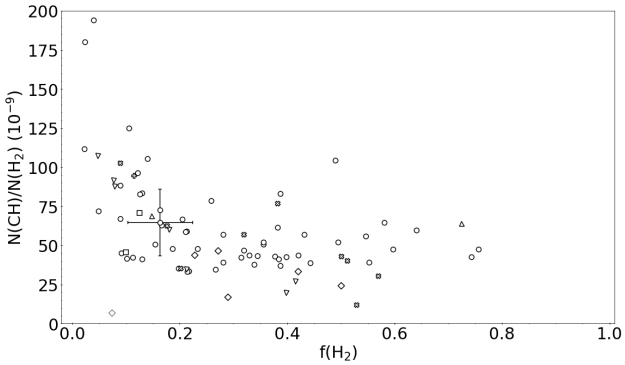

Figure 2.19: N(CH)/N(H_{tot}) versus f(H_2) for the stellar data set. Data points are marked the same way as Figure 2.4.

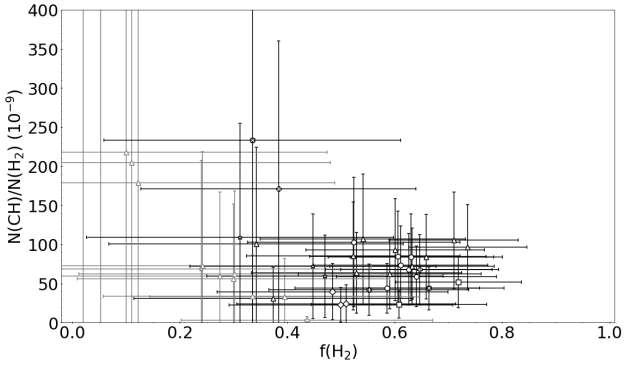

Figure 2.20: N(CH)/N(H_{tot}) versus f(H_2) for the galactic data set. Data points are marked the same way as figure 2.7.

Chapter 3

Excitation Temperature of the 3335 MHz Line [1]

[1] Dailey E.M., Smith A.J., Magnani L., Andersson B-G., Reach W.T. Accepted by Monthly Notices of the Royal Astronomical Society. Reprinted here with permission of the publisher.

Abstract

Molecular hydrogen is the main constituent of dense molecular clouds, but is expected to also be a dominant constituent in many environments where CO can no longer be seen, the so-called 'CO-dark molecular gas'. Based on comparisons of ultraviolet spectroscopy of H_2 and optical line observations (4300 Å), CH is a prime candidate to trace H_2. Since the optical line (and the UV lines at 3143, 3890, 3878 Å) require bright background sources, (and the CH N=2 $\leftarrow$ 1 ground state rotation line at 149 μm requires space-based, or stratospheric, observations) the hyperfine structure transition at 3335 MHz is a potentially important tool for probing the CO-dark molecular gas. However, the excitation of this transition is complicated, and has often been found to be inverted, making column density determinations uncertain. To clarify the potential use of the 3.3-GHz line as a proxy for H_2, we have observed the CH 3335 MHz line with the Arecibo 305-m radio telescope along 16 lines of sight towards stars with existing measurements of the 4300-Å line. By comparing the CH column densities from optical and UV absorption lines to the CH radio emission line we can derive the excitation temperature ($T_{\rm ex}$) of the 3335-MHz transition. We obtain a wide range of excitation temperatures for nine lines of sight, including some with $|T_{\rm ex}| < 5$ K. The common assumption that $T_{\rm ex}$ for the 3335-MHz line is always much larger than the background temperature ($T_{\rm bg}$) is not always warranted and can lead to significant errors in the value of N(CH).

3.1 Introduction

The most commonly used tracer of molecular hydrogen in the interstellar medium (ISM) is the J=1-0 transition of CO at 115 GHz. It has long been clear from both observations (e.g., Federman et al. 1980) and theory (Federman, Glassgold & Kwan 1979; van Dishoeck & Black 1986, 1988) that H_2 is, because of significant self-shielding in the Lyman and Werner bands, less prone to photodissociation than CO and hence will survive to smaller column densities. Until recently, the assumption was made that the transition region between molecular gas with N(CO) too low for detection at 115 GHz and that with detectable CO(1-0) emission was relatively thin and contained little mass (e.g., Andersson & Wannier 1993), or consisted of a minor population of diffuse molecular clouds (e.g., Lada & Blitz 1988; van Dishoeck & Black 1989).

With the lack of detectable CO emission, other species were proposed as tracers of this transitional gas, including OH (Wannier et al. 1993; Barriault et al. 2010; Cotten et al. 2012; Allen et al. 2012, Allen, Hogg & Engelke 2015; Xu et al. 2016; Tang et al. 2017; Li et al. 2018) and CH (Sandell, Stevens & Heiles 1987; Magnani & Onello 1993; Xu & Li 2016). In particular, the latter has been found to be a reliable tracer of H_2 over several orders of magnitude of N(H_2) using the optical 4300-Å line (e.g., Sheffer & Federman 2007), the 3335 MHz hyperfine, Λ-doubled, F=1-1 transition (Mattila 1986), and recently through the N=2 $\leftarrow$ 1 ground state rotation line at 149 μm (Wiesemeyer et al. 2018).

The possible existence of substantial molecular gas in the ISM that is not spectroscopically detectable via the CO(1-0) emission line was discussed by Grenier, Casandjian & Terrier (2005). By using a combination of colour-corrected dust maps, gamma-ray data from EGRET, and N(HI) and CO(1-0) emission maps, they identified regions with substantial gas column density not traced by the HI or CO data. At

mid to high latitudes these regions appear to form extensive halos surrounding local molecular clouds (cf. Andersson & Wannier 1993) and are believed to represent a molecular component currently referred to as 'CO-dark molecular gas' (for brevity, we will refer to this gas as CO-dark gas, acknowledging that fully atomic or ionized gas is, of course, by definition, also 'CO-dark'). Based on estimates in Grenier et al. (2005) CO-dark gas was thought, on galactic scales, to contribute about an equal molecular mass to that detected through CO(1-0) emission. However, subsequent studies have substantially decreased the estimated CO-dark gas balance (e.g., Donate & Magnani 2017).

The CH molecule was one of the first found in the ISM (Dunham & Adams 1937a, b) via the 4300-Å line in the A-X band. Studies of this line towards background early-type stars reveal that there is a good correlation between N(CH) and N(H_2) (e.g., Federman 1982; Danks, Federman & Lambert 1984; Sheffer et al. 2008). In addition to the 4300-Å line, the B-X band offers the 3886-Å and 3890-Å lines as agents for determining robust values for N(CH) (e.g., Chaffee 1974, 1975; Weselak et al. 2008). Studies of this type were used by Mattila (1986) to establish the low extinction ($A_V \lesssim 3$ mag) end of his empirical relation between N(CH) and N(H_2). For low extinctions the N(CH)/N(H_2) ratio is very robust at $4.3 \pm 1.9 \times 10^{-8}$ (Liszt & Lucas 2002), and thus N(CH) can lead to reliable estimates of N(H_2).

In addition to optical and UV observations of interstellar absorption lines towards early-type stars, a recent paper by Wiesemeyer et al. (2018) proposes that the N=2 $\leftarrow$ 1 ground state transition of CH at 149 μm can also be used to obtain N(CH) and, consequently, N(H_2). The absorption line connects the N=1, J=1/2 ground state to the N=2, J=3/2 states comprised of two triplets of hyperfine structure lines. The lines are thin and unsaturated and arise in low density molecular gas. However, while the Galaxy is more transparent at infrared than optical wavelengths, the atmosphere is not and observations of these lines require space/stratospheric observatories.

In the radio regime, the $^2\Pi_{1/2}$, J=1/2, ground state, lambda doubled, hyperfine, F=1-1 main line at 3335.479 MHz (Truppe et al. 2014) provides a reasonable alternative to CO or OH for tracing low density molecular gas. The two other hyperfine components of this transition are 3263.793 MHz (F=0-1) and 3349.193 MHz (F=1-0) (Truppe et al. 2014). Under normal excitation conditions, these satellite lines are one half the intensity of the main line.

N(CH) is obtained from the velocity-integrated antenna temperature of the 3335-MHz line [W(CH) $\equiv (\eta_{\rm B})^{-1} \int T_{\rm A} {\rm d}v$ (mK km s^{-1})] using an equation from Liszt & Lucas (2002):

$$\mathrm{N(CH)} = 2.82 \times 10^{11} (\eta_{\rm f})^{-1} [T_{\rm ex}/(T_{\rm ex} - T_{\rm bg})] \, \mathrm{W(CH)} \tag{3.1}$$

where $\eta_{\rm B}$ is the beam efficiency of the telescope, $\eta_{\rm f}$ is the filling factor of molecular gas in the beam, $T_{\rm ex}$ is the excitation temperature, and $T_{\rm bg}$ is the background temperature. At 3.3 GHz, $T_{\rm bg} \approx 2.8$ K (e.g. Fixsen et al. 2011). If $|T_{\rm ex}| \gg T_{\rm bg}$, then N(CH) is directly proportional to W(CH). Early measurements showed that the 3335-MHz transition was inverted with $T_{\rm ex}$ ranging from -9 to -60 K (Rydbeck et al. 1976; Hjalmarson et al. 1977; Genzel et al. 1979). Specifically, Rydbeck et al. (1976) used on-off observations of Perseus and Orion Arm clouds towards Cassiopeia A to determine $T_{\rm ex} = -15 \pm 5$ K. Shortly thereafter, Lang & Willson (1978) used this value to determine N(CH) in a comparison of column densities from radio and optical observations. They found that the radio and optical column densities differed by less than a factor of two, with the ratio of $N_{\rm radio}/N_{\rm optical} = 1.68 \pm 0.34$ lending credence to the idea that the factor $T_{\rm ex}/(T_{\rm ex} - T_{\rm bg})$ could be considered to have a value near unity. Moreover, the resulting N(CH) values were linear with the colour excess for $E(B-V) < 0.6$ mag, for both the optical and radio observations. Genzel et al. (1979) used on-off observations similar to Rydbeck et al. (1976) and found $T_{\rm ex} = -60 \pm 30$

K for the 3335-MHz line from dust clouds 3C123 and L1500. On the basis of these results, most radio astronomers derive N(CH) directly from W(CH) (3335) assuming $T_{\rm ex}$ = -15 ± 5 K, $T_{\rm ex}$ = -60 ± 30 K, or $|T_{\rm ex}| \gg T_{\rm bg}$.

In a key paper, Lien (1984) also compared radio and optical column densities of CH for a few lines of sight traversing diffuse or translucent gas. He found that $T_{\rm ex}$ from radio and optical observations were in the range of approximately 6 to 25 K with one line of sight where $T_{\rm ex}$ is approximately -4 K, while $T_{\rm ex}$ from optical and ultraviolet observations were approximately -1 or 1 K. Not surprisingly, the column densities of the observed lines of sight derived using $T_{\rm ex}$ in this range are often significantly different than under the assumption $|T_{\rm ex}| \gg T_{\rm bg}$. In addition to differing excitation temperatures, Lien (1984) attributed the reasons for the discrepancy in column density to several additional factors: In deriving $\rm N(CH)_{radio}$, both a filling factor, $\eta_{\rm f}$, and $T_{\rm ex}$ have to be assumed. Moreover, $\rm N(CH)_{optical}$ measures the column density only to the star, whereas $\rm N(CH)_{radio}$ traces gas along the entire line of sight. If there is substantial CH beyond the target star for the absorption lines studies, then a direct comparison of the column densities between the two techniques would not be fruitful. Finally, the beam size of the radio observations is on the order of arc minutes compared with the nearly infinitesimal solid angle of the optical line of sight. Thus, variations in cloud structure on small scales can produce discrepancies in the column densities estimated from the two methods.

Lien (1984) also proposed that if the above issues aside from the value of $T_{\rm ex}$ could be resolved, then replacing $\rm N(CH)_{radio}$ with the more robust $\rm N(CH)_{optical}$ estimate would allow one to solve Equation 3.1 directly for $T_{\rm ex}$. In this paper, we calculate $T_{\rm ex}$ by this technique. We detected CH 9 cm emission for 9 of the 16 lines of sight in our sample for which optical and UV CH absorption lines are available. We then examine whether the conditions described above can permit us to determine $T_{\rm ex}$ for the given line

of sight. The paper is organized as follows: §3.2 describes the radio observations we made to compare with the optical ones from the literature. The results are described in §3.3, and some of the problems encountered in deriving $T_{\rm ex}$ are discussed in §3.4. The individual lines of sight are discussed is §3.5, and the paper closes with a summary.

3.2 Observations

The CH observations for this project were made between 2017 August and December, using the Arecibo 305-m radio telescope. We used the upper S-band receiver which produced system temperatures of $\sim$30 K on the sky with a beam size at 3335 MHz of 1.3×1.5 arcmin elongated in azimuth. At Arecibo we measured the beam efficiency by observing extragalactic continuum sources. Our observations were made before and after Hurricane Maria which struck the island of Puerto Rico on 2017 September 20. The damage done by the hurricane to the facilities at Arecibo significantly changed the beam efficiency. At 3335 MHz, $\eta_{\rm B}$ was 0.57 ± 0.02 before the hurricane and 0.40 ± 0.04 after.

The spectrometer was the Wideband Arecibo Pulsar Processor (WAPP) divided into 8 boards configured to observe the CH lines at 3 GHz (9 cm) with a bandwidth of 1.5625 MHz for each section resulting in a velocity coverage of 141 km s^{-1} and a resolution of 0.07 km s^{-1} per channel (before smoothing) for the 3335-MHz line. The CH 3335-MHz line was in boards 1 and 2 (for redundancy), the 3349-MHz line was in boards 3 and 4, and the 3264-MHz line was in boards 5 and 6. Boards 7 and 8 were centred on 3139 MHz and 3195 MHz, respectively, in an unsuccessful effort to detect H_2CS and CH_3CHO. Each final spectrum consisted of between 5 and 24 five-minute scans taken in ON-source mode only. A

sixth order baseline was removed from the summed spectrum to produce the spectra shown in Figure 3.1. Typical rms noise levels were between $9 - 22$ mK for a velocity resolution of 0.069 km s^{-1}.

3.3 Results

We observed 16 lines of sight towards early-type stars behind or within molecular clouds. The stars are listed in Table 3.1 along with their coordinates, spectral types, distances to the stars, and distances to the cloud in the line of sight to the star (if known). We detected the 3335-MHz main line for 9 lines of sight. In Table 3.2 we list the Gaussian-fit parameters (antenna temperature, $T_{\rm A}$; FWHM, Δv; and $v_{\rm LSR}$) for all CH detections including 1σ uncertainties. Nondetections are listed as 2σ upper limits in $T_{\rm A}$.

Table 3.3 lists the colour excess, $E(B-V)$, for the entire line of sight from Schlafly & Finkbeiner (2011) in column 2. The colour excess along the line of sight to the star is listed in column 3, and is determined from the B and V colours of the star from Oja (1991, 1993), Hg et al. (2000), and Ducati (2002), and the unreddened $B-V$ for the spectral type of the star listed in Table 3.1 from Fitzgerald (1970). Column 4 has W(CH) for the 3335-MHz line as derived by summing the antenna temperature per channel over the line profile. The uncertainty in W(CH) is calculated using

$$\sigma_{\rm I} = \sqrt{N}\sigma_{\rm T}\Delta v_{\rm c} \tag{3.2}$$

where $\sigma_{\rm T}$ is the uncertainty in the antenna temperature, N is the number of channels the line extends over, and $\Delta v_{\rm c}$ is the width of each channel (e.g. Mangum & Shirley 2015). Column 5 lists N(CH) derived from equation 3.1, and columns 6 and 7 list the values of $T_{\rm ex}$ and its uncertainties. For lines of sight with no radio detection, the range of $T_{\rm ex}$ is calculated for the range of values below the 2σ upper limit of the

velocity-integrated antenna temperature. As shown in Figure 3.2, in cases where W(CH) is fairly large but the corresponding optically determined N(CH) is small, the range of $T_{\rm ex}$ can be well constrained.

We list in Table 3.4 the velocity-integrated brightness temperatures from the literature in column 2 compared to our observations in column 4 and, in column 5, N(CH) from our data assuming $T_{\rm ex}/(T_{\rm ex} - T_{\rm bg})$ = 1. Column 6 lists the value of N(CH) as determined from optical observations in the literature.

Using the technique described in §3.1, we determine $T_{\rm ex}$ for the 9 lines of sight where we have values of $\rm W(CH)_{radio}$. The uncertainties for the excitation temperature are determined in two ways: First, formal uncertainties using standard error propagation analysis are listed in column 6 of Table 3.3. For the second method, assuming $\eta_{\rm f}$ = 1, we can express $T_{\rm ex}$ as

$$T_{\rm ex} = T_{\rm bg}[D/(D-1)] \tag{3.3}$$

where D is

$$D = \rm N(CH)[W(CH) \times (2.82 \times 10^{11})]^{-1}. \tag{3.4}$$

For values of D approaching 1, the value of $T_{\rm ex}$ becomes singular. Thus a calculation of the uncertainties based on error propagation becomes indeterminate. For those lines of sight where $\rm N(CH)_{optical}$ and $\rm W(CH)_{radio}$ lead to values of D approaching 1, we can determine the range of $T_{\rm ex}$ based on $D \pm 1\sigma$.

3.3.1 Comparison with previous observations

We compare our values of the velocity integrated brightness temperature, W(CH), obtained with a ~ 1.4 arcmin beam to the data presented by Lang & Willson (1978) and Willson (1981) with a $\sim$ 9 arcmin

beam (see Table 3.4). Due to the large discrepancy in beam sizes, inconsistencies with the results of Lang & Willson (1978) and Willson (1981) are likely attributable to structure in the two beams and underscore the importance of minimizing the radio beam when comparing the radio and optical observations. Twelve of sixteen of our lines of sight were observed by Liszt (2008) for the ^{12}CO J=1-0 line at 115.3 GHz using the ARO 12-m telescope, with a beam size of 65 arcsec. He detected CO emission from 7 of 12 lines of sight included in Table 3.1, with each detection/nondetection mirrored by our CH results in Table 3.2.

3.4 Problems in determining $T_{\rm ex}$

The excitation temperature is derived by the method described in the introduction but several concerns must be addressed. We assume that $\eta_{\rm f}$ is 1.0; should there be significant structure on the scale of 10^{-2} pc, then optical and radio comparisons would be unprofitable.

For three of the nine lines of sight with radio detections, the 1σ uncertainty from the measurements of the optical and radio CH lines extends over the singularity in Equation 3.3. Lien (1984) first pointed out this issue in his calculations of the excitation temperature. The excitation temperature rapidly increases in both positive and negative value as it approaches this singularity. Consequently, accurate measurements are required in order to calculate $T_{\rm ex}$ accurately. For the remaining six lines of sight, the range of optical and radio 1σ uncertainty does not result in an excitation temperature that approaches the singularity, and the values of $T_{\rm ex}$ are between $-3.1 < T_{\rm ex} < 10$ K.

We primarily used parallax measurements and cloud distance measurements from literature shown in Table 1 to determine the position of the star relative to the cloud. Secondarily, we used colour excess of the line of sight to the star compared with the colour excess of the full line of sight as shown in Table 3.3

to determine if the optical and radio observations are observing equivalent material. For five lines of sight, the star is behind the cloud according to the cloud distance determined from Ĉernis (1993), Kenyon et al. (1994), Arce et al. (2011), Zucker et al. (2018), and Zucker et al. (2019). In these instances we can assume that the optical and radio beam are sampling the same molecular column.

The remaining four stars with radio detections are either within or very close to the cloud, or we lack information on the cloud distance and the colour excess is unreliable for the line of sight. The proximity to the cloud means that the CH column detected in the optical may not be equivalent to that detected in radio. In addition, dust extinction is a cumulative quantity, making it hard to attribute the entire value solely to a single molecular cloud in front of the star. Ĉernis (1993) and Zucker et al. (2018) have shown the extinction along a line of sight can occur in discrete increments due to intervening clouds. For example, Ĉernis (1993) discusses two dust layers in the direction of IC348, at 160 ± 20 and 260 ± 20 pc, and with A_V = 0.71 ± 0.27 and 2.0 ± 0.6 mag, respectively.

3.4.1 Alternate measurements of $T_{\rm ex}$

In addition to the method described in §3.2, we also use the method described in Lien (1984) to determine the excitation temperatures towards a few of our lines of sight using optical data from Jura & Meyer (1985), Weselak et al. (2008), Weselak et al. (2014), and Weselak (2019). The excitation temperature is calculated by using the 3886-Å line to derive the upper column density ($N_{\rm u}$) and the 3890-Å line to derive the lower column density ($N_{\rm l}$) of the lambda-doubled levels. With values for $N_{\rm u}$ and $N_{\rm l}$, $T_{\rm ex}$ may be determined using an equation from Lien (1984):

$$T_{\rm ex} = 0.16[ln(N_{\rm l}/N_{\rm u})]^{-1} \tag{3.5}$$

The uncertainties for the excitation temperature are determined in two ways: First, using formal propagation of error, and secondly using the range of column density $N \pm 1\sigma$ for the 3886 and 3890 Å lines to find informal limits to the excitation temperature. The results are shown in Table 3.5 with columns 2 and 3 listing the values for the column density of the upper and lower levels according to various observers (column 4). Column 5 has the ratio of $N(CH)_l$ and $N(CH)_u$. Column 6 has the calculated T_{ex} from equation 3.3, and column 7 has the range of T_{ex} determined using the $\pm 1\sigma$ range as described above. For the majority of these lines of sight, there is a singularity in the range of excitation temperatures which causes a large range of values of T_{ex}. However, there is some overlap between the ranges of T_{ex} for a given line of sight. For example, the line of sight to ζ Per has the range $-1.12 > T_{ex} > -2.41$ K in common between the five data sets.

3.5 Discussion

Rydbeck et al. (1976) found $T_{ex} = -15 \pm 5$ K by making on-off observations of the CH 3335 MHz line towards Cas A. Calculating T_{ex}, using optical observations or a combination of optical and radio observations, consistent with $T_{ex} = -15 \pm 5$ K requires very accurate measurements of N_l/N_u or D. Figure 3.3 shows that the rapid change in slope near the singularity (at D or $N_l/N_u = 1$) necessitates increasingly accurate measurements of D or N_l/N_u if a reliable range of T_{ex} is to be derived. For example, the ratio of the lower and upper column densities determined from optical observations in Table 3.5 has average uncertainties of ± 0.13, for average values of $N_l/N_u \approx 1$. This then limits the range of T_{ex} to 1.3 K $> T_{ex} > -1.1$ K. Reproducing the calculation of T_{ex} as determined by Rydbeck et al. (1976) ($T_{ex} = -15 \pm 5$ K) by the ratio of lower and upper column densities requires $N_l/N_u = 0.9894^{+0.0026}_{-0.0053}$, necessitating

highly accurate measurements of $N_{\rm l}/N_{\rm u}$. By using a combination of optical and radio measurements, reproducing the Rydbeck et al. (1976) value would require $D = 0.8427^{+0.0345}_{-0.0614}$.

Hjalmarson et al. (1977) determined $T_{\rm ex} = -9 \pm 4$ K using on-off observations with the Onsala Space Observatory 25.6-m telescope (15 arcmin beam at 3.3 GHz) toward 3C123 near the dark cloud L1500, consistent with $T_{\rm ex} = -15$ (+10,−30) K determined by Rydbeck et al. (1976). However, we derive $T_{\rm ex} = -3$ K using the line and continuum values given by Hjalmarson et al. (1977) and their equation 3.3. Liszt & Lucas (2002) determined $T_{\rm ex} = -10.7 \pm 3.2$ K towards 3C123 using observations with the NRAO 43-m telescope, with a beam size of approximately 9 arcmin, consistent with $T_{\rm ex} = -9 \pm 4$ K from Hjalmarson et al. (1977) despite the varying beam sizes. The values from Liszt and Lucas (2002) and Hjalmarson et al. (1977), whether $T_{\rm ex} = -9$ K or -3 K, differ greatly from the value from Genzel et al. (1979) determined using the Effelsberg 100-m telescope (4 arcmin beam at 3.3 GHz) for the same line of sight, $T_{\rm ex} = -60 \pm 30$ K.

We now discuss our results for each of our detections.

3.5.1 HD 21483

The parallax data from SIMBAD gives a distance of 533 ± 32 pc for HD 21483, placing it behind an intervening portion of the Perseus clouds at 284^{+8}_{-5} pc (Zucker et al. 2019). The colour excesses to the star and along the line of sight are 0.52 and 0.89 ± 0.14 mag, respectively, which along with the cloud and star distances suggests that the radio and optical beams are sampling approximately the same molecular material. Using the optical column density from Thorburn et al. (2003), we find $T_{\rm ex} = -35 \pm 69$ K. However, the 1σ uncertainty in D encompasses the singularity, resulting in a large range of $T_{\rm ex}$ (from the 1σ uncertainty in D) with $T_{\rm ex} > 48$ K, $T_{\rm ex} < -11$ K.

3.5.2 HD 23180 (o Persei)

The parallax data from SIMBAD gives a distance of 344 ± 86 pc for HD 23180, which places it close to the IC348 region at 321 ± 10 pc (Ortiz-León et al. 2018). However, Arce et al. (2011) state that HD 23180 is likely within ~ 1 pc of the cluster. The colour excess of the star and along the line of sight are 0.31 and 3.49 ± 0.56 mag, respectively, which along with the cloud and star distances likely indicate that a considerable portion of the molecular gas extends beyond the star. Due to the star's proximity to the cloud, it is likely that the radio observations are sampling CH behind the star which cannot be seen by the optical observations. Using the optical column density from Weselak et al. (2014), we find $T_{\rm ex} = -0.73 \pm 0.09$ K.

This star has been studied by Jura & Meyer (1985) who find the excitation temperature using optical observations of the CH B-X lines. They find $T_{\rm ex} = 3.7$ K, but the uncertainty of the upper and lower column densities encompasses the singularity in Equation 3.3. The range of values for $T_{\rm ex}$ are inconsistent with the excitation temperature we find, likely due to the component of the cloud behind the star.

3.5.3 HD 281159

The parallax data for HD 281159 from SIMBAD gives a distance of 152 ± 94 pc, likely placing it in front of an intervening portion of the IC348 region at 321 ± 10 pc (Ortiz-León et al. 2018). The small parallax distance likely means the absorption measured in the optical is from the foreground clouds at 169^{+2}_{-3} pc (Zucker et al. 2018). The colour excess of the star and along the line of sight are 0.84 and 8.90 ± 1.42 mag respectively, which along with the cloud and star distances likely indicate that the radio velocity-integrated brightness temperature is sampling more of the cloud than the optical measurement. Our $\mathrm{W(CH)_{radio}}$

value does not agree within 4σ with the velocity-integrated brightness temperature from Willson (1981), likely indicating that the CH distribution has structure at scales of a few arcminutes. Using the optical column density from Thorburn et al. (2003), we find $T_{\rm ex} = -0.86 \pm 0.15$ K. Due to the stars proximity to the cloud, it is likely that the radio observations are sampling CH behind the star which is not seen by the optical observations.

3.5.4 HD 23478

The parallax distance for HD 23478 is 288 ± 5 pc, placing it at about the same distance as an intervening portion of the Perseus clouds at 299^{+10}_{-8} pc (Zucker et al. 2019). The colour excess of the star and along the line of sight are 0.24 and 0.56 ± 0.09 mag respectively, which along with the cloud and star distances could possibly indicate that the radio estimate is sampling more of the cloud than the optical. Using the optical column density from Sheffer & Federman (2007), we find $T_{\rm ex} = -1.2 \pm 0.3$ K.

3.5.5 HD 24398 (ζ Persei)

The parallax distance for HD 24398 is 230 ± 10 pc, placing it behind an intervening portion of the Taurus clouds at $140 - 170$ pc (Kenyon et al. 1994, Zucker et al. 2018). The colour excesses of the star and along the line of sight are 0.31 and 0.27 ± 0.04 mag, respectively, which suggests that the radio and optical beams are sampling approximately the same molecular gas. Using the optical column density from Weselak et al. (2014), we find $T_{\rm ex} = -27 \pm 58$ K.

The line of sight to this star has been studied before in order to determine the excitation of the CH main line. Lien (1984) determined $T_{\rm ex}$ from the optical column densities of the upper and lower populations of the lambda-doubled ground state, and also through a comparison of the optical and radio measurements.

By using the upper and lower populations of the Λ doublet of the B-X system, he determined $T_{\rm ex}$ = -0.54 $\pm$ 0.30 K, with a range of $-2.3 < T_{\rm ex} < -0.3$ K, which does not agree with our $T_{\rm ex}$ estimate. Lien also found $T_{\rm ex}$ = -3.7 K through a comparison of the optical and radio measurements using a method similar to the one described in §3.2, which is outside our range of $T_{\rm ex}$. Jura & Meyer (1985) determined $T_{\rm ex}$ from the optical column densities of the upper and lower populations obtaining $T_{\rm ex}$ = -1.3 K, and Liszt & Lucas (2002) similarly determined $T_{\rm ex} \approx -3$ K.

All but one of the above estimates for $T_{\rm ex}$ are between approximately -4 and -1 K. Our result for the range of $\rm T_{ex}$, where $\rm T_{ex} > 34$ K and $\rm T_{ex} < -7.2$ K is not consistent with other determinations at the 1σ level. However, given all of the above estimates, the often used assumptions, $T_{\rm ex}$ = -15 ± 5 K, $T_{\rm ex}$ = -60 ± 30 K, and $|T_{\rm ex}| \gg T_{\rm bg}$ may not be valid for this line of sight.

3.5.6 HD 24534 (X Persei)

The parallax data from SIMBAD gives a distance of 810 ± 37 pc, placing it behind an intervening portion of the Taurus clouds at $140 - 170$ pc (Kenyon et al. 1994, Zucker et al. 2018). The colour excesses to the star and along the line of sight are 0.42 and 0.38 ± 0.06 mag respectively, which along with the cloud and star distances suggests that the radio and optical beams are sampling approximately the same molecular material. Using the optical column density from Weselak et al. (2008) we find $T_{\rm ex}$ = $-3.1 \pm$ 0.5 K. Due to the star being far behind the cloud, and no discontinuity in the uncertainty, we find that the assumption $|T_{\rm ex}| \gg T_{\rm bg}$ is clearly invalid for this line of sight.

This star has been studied before in order to determine the excitation of the CH main line. Lien (1984) determined $T_{\rm ex}$ from the optical column densities of the upper and lower populations, and also through a comparison of the optical and radio measurements. By using the upper and lower populations

of the Λ doublet, he determined $T_{\rm ex} = -0.63 \pm 0.73$ K, with a range of $T_{\rm ex} > 0.5$ K, $T_{\rm ex} < -0.2$ K, which is consistent with our $T_{\rm ex}$ estimate. He also found $T_{\rm ex} = 7.6$ K through a comparison of the optical and radio measurements, which is outside our range of $T_{\rm ex}$. However, his radio measurements were made with a beam size of 9 arcmin, which is the likely reason for the discrepency between our results.

3.5.7 HD 26571

The parallax data from SIMBAD gives a distance of 274 ± 8 pc for HD 26571, likely placing it behind the Taurus clouds at 140 ± 10 pc (Kenyon et al. 1994). The colour excesses to the star and along the line of sight are 0.29 and 0.41 ± 0.07 mag respectively, which along with the cloud and star distances suggests that the radio and optical beams are possibly sampling approximately the same molecular material. Using the optical column density from Thorburn et al. (2003), we find $T_{\rm ex} = -1.8 \pm 0.7$ K. Due to the star being behind the cloud, and the data not causing a discontinuity in the uncertainty, our $T_{\rm ex}$ estimate is robust. We find that the often used assumptions, $T_{\rm ex} = -15 \pm 5$ K, $T_{\rm ex} = -60 \pm 30$ K, and $|T_{\rm ex}| \gg T_{\rm bg}$, are clearly invalid for this line of sight.

3.5.8 HD 27778

The parallax data from SIMBAD gives a distance of 224 ± 2 pc for HD 27778, likely placing it behind the Taurus clouds at 140 ± 10 pc (Kenyon et al. 1994). The colour excesses to the star and along the line of sight are 0.36 and 0.53 ± 0.08 mag respectively, which along with the cloud and star distances suggests that the radio and optical beams are possibly sampling approximately the same amount of molecular material. Using the optical column density from Weselak et al. (2008), we find $T_{\rm ex} = -55$ K. However, the 1σ

uncertainty in D encompasses the singularity, resulting in a large range of $T_{\rm ex}$ (from the 1σ uncertainty in D) $T_{\rm ex} > 27$ K, $T_{\rm ex} < -10$ K.

3.5.9 HD 183143

While HD 183143 is at 2435 ± 269 pc, there are no estimates of the intervening cloud's distance. However the colour excess values imply that a translucent cloud is intervening. The colour excess of the star and along the line of sight are 1.29 and 3.40 ± 0.54 mag respectively, which could possibly indicate that the radio velocity-integrated brightness temperature is sampling more of the cloud than the optical measurement. Unfortunately, the star is at $|\mathrm{b}| < 5^\circ$, so the colour excess along the line of sight is unreliable (Schlegel et al. 1998). Using the optical column density from Thorburn et al. (2003), we find $T_{\rm ex}$ = 10 $\pm$ 7 K.

3.6 Summary

Observations of the CH 3335 MHz line have been used since 1976 to determine N(H_2) directly from W(CH) usually by assuming $T_{\rm ex}$ = -15 ± 5 K from Rydbeck et al. (1976), $T_{\rm ex}$ = -60 ± 30 K from Genzel et al. (1979), or $|T_{\rm ex}| \gg T_{\rm bg}$ (e.g. Magnani, Sandell & Lada 1992). Lien (1984) explored other ways of determing $T_{\rm ex}$ from optical and radio data and obtained values inconsistent with $|T_{\rm ex}| \gg T_{\rm bg}$. We observed 16 lines of sight in the CH 3335 MHz line, and detected emission from 9 of them. By combining our radio results with optically derived values for N(CH), we solved for the excitation temperature of the transition, $T_{\rm ex}$. Unfortunately, this method for determining $T_{\rm ex}$ is often problematic because of the differences in how the column density of CH is calculated from optical and radio observations. Primarily, the molecular material sampled by optical observations only extends to the star, requiring the star to be behind

the cloud in order for the molecular material sampled in optical and radio to be approximately equivalent. In addition, the differences in the angular sizes of the two sampled regions could cause problems if the CH is not smoothly distributed.

Our results described in §3.5 imply $T_{\rm ex}$ varies significantly over the 9 lines of sight. For a line of sight such as HD 21483 where the 1σ uncertainty in D (see §3.3) encompasses the singularity in equation 3.3, $|T_{\rm ex}|$ is possibly much greater than $T_{\rm bg}$. However, for other lines of sight where the 1σ uncertainty in D does not encompasses the singularity, the range of $T_{\rm ex}$ includes values of $T_{\rm ex}$ which are inconsistent with $|T_{\rm ex}| \gg T_{\rm bg}$. We determined $T_{\rm ex} = -1.8 \pm 0.7$ K for the line of sight HD 26571, which is inconsistent with the assumptions $T_{\rm ex} = -15 \pm 5$ K, $T_{\rm ex} = -60 \pm 30$ K, and $|T_{\rm ex}| \gg T_{\rm bg}$. The line of sight to HD 24534, with $T_{\rm ex} = -3.1 \pm 0.5$ K, is also inconsistent.

Assuming $T_{\rm ex} = -15 \pm 5$ K, $T_{\rm ex} = -60 \pm 30$ K, or $|T_{\rm ex}| \gg T_{\rm bg}$ for all lines of sight can lead to overestimates or underestimates of the column density. For example, for HD 26571, with $T_{\rm ex} = -1.8 \pm 0.7$ K, the column densities calculated assuming $|T_{\rm ex}| \gg T_{\rm bg}$ will cause N(CH) to be overestimated by approximately a factor of 2.6. Similarly, assuming $T_{\rm ex} = -15$ K will cause an overestimation of approximately a factor of 2.2.

Although the CH 3335 MHz transition provides a reliable way to study the kinematics and distribution of low-density molecular gas, the conversion of W(CH) to N(CH) may not be as straightforward as has often been assumed. Converting the observations to N(CH) requires accurate measurements of $T_{\rm ex}$. In the absence of such measurements, the normal assumptions about the value of $T_{\rm ex}$ can lead to significant errors in N(CH). Radio astronomers who use the 3335-MHz line as a surrogate for H_2 should interpret their results allowing for the possibility that the assumption $|{\rm T_{ex}}| \gg {\rm T_{bg}}$ may not hold for some or all of their observations.

Acknowledgements

The Arecibo Observatory is operated by SRI International under a cooperative agreement with the National Science Foundation (AST-1100968), and in alliance with Ana G. Méndez-Universidad Metropolitana, and the Universities Space Research Association. This work has made use of data from the European Space Agency (ESA) mission Gaia (https://www.cosmos.esa.int/gaia), processed by the Gaia Data Processing and Analysis Consortium (DPAC, https://www.cosmos.esa.int/web/gaia/dpac/consortium). Funding for the DPAC has been provided by national institutions, in particular the institutions participating in the Gaia Multilateral Agreement. This research has made use of the SIMBAD database, operated at CDS, Strasbourg, France, and the NASA/IPAC Extragalactic Database (NED) which is operated by the Jet Propulsion Laboratory, California Institute of Technology, under contract with the National Aeronautics and Space Administration. W. T. Reach and B-G Andersson acknowledge support from NASA contract NNA17BF53C to the Universities Space Research Association (USRA).

We thank the referee, Harvey Liszt, for comments which rectified an error in the calculation of the uncertainties and greatly improved the presentation. We also would like to thank Steve Shore for helpful discussions and comments on the manuscript.

Table 3.1: Target Stars Data and Distances

HD number	Name	Spectral Type	R.A. (2000) $h\ m\ s$	Dec (2000) $^\circ\ '\ ''$	ℓ deg	b deg	$d_{\rm star}$ pc	$d_{\rm cloud}$ pc
HD 21483	–	B3III[a]	03 28 46.7	+30 22 31.2	158.9	−21.3	533 ± 32[b]	284^{+8}_{-5}[c]
HD 21856	–	B1V[a]	03 32 40.0	+35 27 42.2	156.3	−16.8	465 ± 24[b]	–
HD 23180	*o* Per	B1III[d]	03 44 19.1	+32 17 17.7	160.4	−17.7	344 ± 86[e]	321 ± 10[f]
HD 281159	–	B5V[g]	03 44 34.2	+32 09 46.3	160.5	−17.8	152 ± 94[e]	321 ± 10[f,h]
HD 23408	20 Tau	B7III[i]	03 45 49.6	+24 22 03.9	166.2	−23.5	118 ± 4[e]	–
HD 23478	–	B3IV[j]	03 46 40.9	+32 17 24.7	160.8	−17.4	288 ± 5[b]	299^{+10}_{-8}[c]
HD 24398	ζ Per	B1Ib[k]	03 54 07.9	+31 53 01.1	162.3	−16.7	230 ± 10[e]	$140 - 170$[l,m]
HD 24534	X Per	O9.5III[n]	03 55 23.1	+31 02 45.0	163.1	−17.1	810 ± 37[b]	$140 - 170$[l,m]
HD 24912	ξ Per	O7.5III(n)((f))[o]	03 58 57.9	+35 47 27.7	160.4	−13.1	382 ± 74[e]	–
HD 26571	V1137 Tau	B8III[p]	04 12 51.2	+22 24 48.5	172.4	−20.6	274 ± 8[b]	140 ± 10[l]
HD 27778	62 Tau	B3V[i]	04 23 59.8	+24 18 03.5	172.8	−17.4	224 ± 2[b]	140 ± 10[l]
HD 34078	AE Aur	O9.5V[o]	05 16 18.1	+34 18 44.3	172.1	−02.3	406 ± 11[b]	–
HD 37367	–	B2IV-V[k]	05 39 18.3	+29 12 54.8	179.0	−01.0	989 ± 167[b]	–
HD 43818	11 Gem	B0II[a]	06 19 19.3	+23 28 09.9	188.5	+03.9	2570 ± 300[b]	–
HD 164353	67 Oph	B5I[q]	18 00 38.7	+02 55 53.6	029.7	+12.6	566 ± 159[b]	–
HD 183143	–	B6Ia[r]	19 27 26.6	+18 17 45.2	053.2	+00.6	2440 ± 270[e]	–

a) Wenger et al. (2000); b) Distance based on parallax from Gaia Collaboration, Prusti et al. (2016) and Gaia Collaboration, Brown et al. (2018); c) Zucker et al. (2019); d) Morgan & Keenan (1973); e) Distance based on parallax from the Hipparcos Catalogue (van Leeuwen 2007); f) Ortiz-León et al. (2018); g) Mora et al. (2001); h) Distance to the cloud with highest extinction - foreground clouds at 169^{+2}_{-3} pc likely contribute to the absorption in the optical (Zucker et al. 2018); i) Pesch (1967); j) Hiltner (1956); k) Lesh (1968); l) Kenyon, Dobrzycka & Hartmann (1994); m) Zucker et al. (2018); n) Slettebak (1982); o) Sota et al. (2011); p) Hube (1970); q) van Belle & von Braun (2009); r) Stock, Nassau & Stephenson (1960)

Table 3.2a: Radio CH Observations 3335.5 GHz

Line of Sight	Integration Time	$T_{\rm A}$ (3335.5)	Δv	$v_{\rm LSR}$
	min	mK	km s^{-1}	km s^{-1}
HD 21483	35^a	45.7 ± 17.2	1.35 ± 0.51	5.69
HD 21856	90^b	< 22.8	–	–
HD 23180	25^a	75.7 ± 21.7	1.81 ± 0.52	8.41
HD 281159	60^b	115.5 ± 12.6	1.48 ± 0.16	8.66
		24.0 ± 12.6	5.69 ± 2.99	7.23
HD 23408	120^b	< 18.3	–	–
HD 23478	120^b	13.9 ± 9.3	1.63 ± 1.10	9.56
		16.4 ± 9.3	4.81 ± 2.74	8.25
HD 24398	50^a	26.0 ± 14.6	1.77 ± 0.99	7.60
HD 24534	75^a	44.8 ± 12.3	0.77 ± 0.21	7.55
		23.0 ± 12.3	4.88 ± 2.61	6.58
HD 24912	70^b	< 25.3	–	–
HD 26571	105^b	28.4 ± 10.2	2.12 ± 0.76	10.50
HD 27778	50^a	17.0 ± 14.7	4.73 ± 4.11	5.70
HD 34078	50^b	< 30.8	–	–
HD 37367	90^b	$[20.5 \pm 10.9]$	$[2.91 \pm 1.54]$	[0.25]
HD 43818	55^b	< 27.7	–	–
HD 164353	45^a	< 32.0	–	–
HD 183143	30^a	31.2 ± 18.9	1.39 ± 0.84	24.36

Brackets indicate a tentative detection. Spectra for each line of sight are shown in Figure 3.1.
a) $\eta_{\rm B} = 0.57 \pm 0.02$ – see §3.2
b) $\eta_{\rm B} = 0.40 \pm 0.04$ – see §3.2

Table 3.2b: Radio CH Observations 3349.2 GHz

Line of Sight	Integration Time	$T_{\rm A}$ (3349.2)	Δv	$v_{\rm LSR}$
	min	mK	km s^{-1}	km s^{-1}
HD 21483	35^a	28.2 ± 17.6	2.60 ± 1.63	5.51
HD 21856	90^b	< 22.8	–	–
HD 23180	25^a	37.1 ± 20.8	3.33 ± 1.87	8.19
HD 281159	60^b	79.0 ± 12.7	1.74 ± 0.28	8.50
		17.8 ± 12.7	2.85 ± 2.03	5.14
HD 23408	120^b	< 17.1	–	–
HD 23478	120^b	14.0 ± 9.4	4.57 ± 3.05	8.74
HD 24398	50^a	16.8 ± 14.5	2.29 ± 1.97	6.72
HD 24534	75^a	22.5 ± 11.6	1.97 ± 1.02	7.24
HD 24912	70^b	< 25.4	–	–
HD 26571	105^b	$[14.0 \pm 10.2]$	$[2.24 \pm 1.63]$	[10.10]
HD 27778	50^a	< 29.8	–	–
HD 34078	50^b	< 30.9	–	–
HD 37367	90^b	< 20.1	–	–
HD 43818	55^b	< 27.2	–	–
HD 164353	45^a	< 32.7	–	–
HD 183143	30^a	< 37.4	–	–

Brackets indicate a tentative detection. Spectra for each line of sight are shown in Figure 3.1.
a) $\eta_{\rm B} = 0.57 \pm 0.02$ – see §3.2
b) $\eta_{\rm B} = 0.40 \pm 0.04$ – see §3.2

Table 3.2c: Radio CH Observations 3263.8 GHz

Line of Sight	Integration Time	$T_{\rm A}$ (3263.8)	Δv	$v_{\rm LSR}$
	min	mK	km s^{-1}	km s^{-1}
HD 21483	35^a	21.5 ± 18.3	4.02 ± 3.41	6.01
HD 21856	90^b	< 22.6	–	–
HD 23180	25^a	51.6 ± 22.4	1.63 ± 0.71	8.37
HD 281159	60^b	73.9 ± 13.0	1.84 ± 0.32	8.63
HD 23408	120^b	< 18.1	–	–
HD 23478	120^b	13.6 ± 9.2	5.20 ± 3.53	8.60
HD 24398	50^a	< 30.9	–	–
HD 24534	75^a	$[21.5 \pm 12.4]$	$[1.21 \pm 0.70]$	[7.43]
HD 24912	70^b	< 26.7	–	–
HD 26571	105^b	$[12.9 \pm 10.3]$	$[2.31 \pm 1.84]$	[10.09]
HD 27778	50^a	< 29.1	–	–
HD 34078	50^b	< 30.2	–	–
HD 37367	90^b	< 21.2	–	–
HD 43818	55^b	< 27.4	–	–
HD 164353	45^a	< 31.5	–	–
HD 183143	30^a	< 41.7	–	–

Brackets indicate a tentative detection. Spectra for each line of sight are shown in Figure 3.1.
a) $\eta_{\rm B} = 0.57 \pm 0.02$ – see §3.2
b) $\eta_{\rm B} = 0.40 \pm 0.04$ – see §3.2

Table 3.3: Column Densities and Excitation Temperatures derived from our data

Line of Sight	$E(B-V)^a_{full}$	$E(B-V)^b_{star}$	W(CH)$^c_{\rm radio}$ mK km s^{-1}	N(CH)$^d_{\rm radio}$ 10^{12} cm^{-2}	$T^e_{\rm ex}$ K	$T^f_{\rm ex}$ K
HD 21483	0.89 ± 0.14	0.52	149 ± 19	42.1 ± 5.3	-35 ± 69	$T_{\rm ex} > 48, T_{\rm ex} < -11$
HD 21856	0.28 ± 0.04	0.17	< 60.7	< 17.1	-	$T_{\rm ex} > 2.8, T_{\rm ex} < -2.7$
HD 23180	3.49 ± 0.56	0.31	327 ± 31	92.2 ± 8.8	-0.73 ± 0.09	$-0.64 > T_{\rm ex} > -0.82$
HD 281159	8.90 ± 1.42	0.84	801 ± 86	226 ± 24	-0.86 ± 0.15	$-0.72 > T_{\rm ex} > -1.0$
HD 23408	0.59 ± 0.09	0.05	< 48.6	< 13.7	-	$T_{\rm ex} > 2.8, T_{\rm ex} < -0.28$
HD 23478	0.56 ± 0.09	0.24	215 ± 30	60.6 ± 8.4	-1.2 ± 0.3	$-1.0 > T_{\rm ex} > -1.5$
HD 24398	0.27 ± 0.04	0.31	76.5 ± 15.6	21.6 ± 4.4	-27 ± 58	$T_{\rm ex} > 34, T_{\rm ex} < -7.2$
HD 24534	0.38 ± 0.06	0.42	260 ± 20	73.2 ± 5.7	-3.1 ± 0.5	$-2.6 > T_{\rm ex} > -3.7$
HD 24912	0.26 ± 0.04	0.33^g	< 67.4	< 19.0	-	$T_{\rm ex} > 2.8, T_{\rm ex} < -11$
HD 26571	0.41 ± 0.07	0.29	182 ± 27	51.4 ± 7.5	-1.8 ± 0.7	$-1.2 > T_{\rm ex} > -2.6$
HD 27778	0.53 ± 0.09	0.36	135 ± 24	38.0 ± 6.6	-55 ± 197	$T_{\rm ex} > 27, T_{\rm ex} < -10$
HD 34078	1.95 ± 0.31^h	0.52	< 82.0	< 23.1	-	$5.7 > T_{\rm ex} > 2.8$
HD 37367	1.32 ± 0.21^h	0.37	< 58.1	< 16.4	-	$T_{\rm ex} > 2.8, T_{\rm ex} < -40$
HD 43818	0.97 ± 0.16^h	0.58	< 73.7	< 20.8	-	$T_{\rm ex} > 2.8, T_{\rm ex} < -4.2$
HD 164353	0.18 ± 0.03	0.12	< 59.9	< 16.9	-	$T_{\rm ex} > 2.8, T_{\rm ex} < -1.0$
HD 183143	3.40 ± 0.54^h	1.29	129 ± 31	36.4 ± 8.8	10 ± 7	$89 > T_{\rm ex} > 6.7$

a) Calculated using A_V from the NED Extinction Calculator using data from Schlafly & Finkbeiner (2011) with $E(B-V) = A_V/3.1$

b) Calculated by method described in §3.3.

c) W(CH) determined with a nonparametric fit of the data. 2σ upper limits of W(CH) calculated using W(CH) = $1.066(T_{\rm A}\Delta v)/(\eta_{\rm B})$ assume Δv = 1 km s^{-1}.

d) N(CH)$_{\rm radio}$ assuming that $T_{\rm ex} \gg T_{\rm bg}$.

e) Uncertainties based on formal error propagation.

f) Uncertainties based on the $\pm 1\sigma$ range in D as described in §3.3.

g) Thorburn et al. (2003)

h) Unreliable colour excess, $|b| < 5^\circ$ (Schlegel, Finkbeiner & Davis 1998)

Table 3.4: Data from literature

Position	$W(CH)^{a}_{radio}$ Literature mK km s^{-1}	Ref	$W(CH)^{b}_{radio}$ This Paper mK km s^{-1}	$N(CH)^{c}_{radio}$ This Paper 10^{12} cm^{-2}	$N(CH)_{optical}$ Literature 10^{12} cm^{-2}	Ref
HD 21483	203 ± 44	d	149 ± 19	42.1 ± 5.3	39 ± 3	e
HD 21856	-		< 60.7	< 17.1	6.90 ± 0.76	f
HD 23180	286 ± 47	d	327 ± 31	92.2 ± 8.8	19.00 ± 0.22	g
HD 281159	391 ± 32	h	801 ± 86	226 ± 24	53 ± 4	e
HD 23408	< 71.1	h	< 48.6	< 13.7	1.5 ± 0.6	i
HD 23478	-		215 ± 30	60.6 ± 8.4	18.3 ± 0.7	j
HD 24398	139 ± 14	h	76.5 ± 15.6	21.6 ± 4.4	19.52 ± 0.24	g
HD 24534	134 ± 14	h	260 ± 20	73.2 ± 5.7	38.49 ± 0.60	k
HD 24912	< 88.8	h	< 67.4	< 19.0	11.99 ± 0.34	g
HD 26571	84.4 ± 21.6	h	182 ± 27	51.4 ± 7.5	20 ± 4	e
HD 27778	-		135 ± 24	38.0 ± 6.6	36.14 ± 0.36	k
HD 34078	< 107	h	< 82.0	< 23.1	70.80 ± 0.44	g
HD 37367	-		< 58.1	< 16.4	12.0 ± 2.4	l
HD 43818	-		< 73.7	< 20.8	11.3 ± 2.2	l
HD 164353	-		< 59.9	< 16.9	4.4 ± 2.2	i
HD 183143	-		129 ± 31	36.4 ± 8.8	50 ± 3	e

a) $W(CH)_{radio}$ calculated using η_B, T_A and Δv, from references in column 3. $W(CH) = 1.066(T_A \Delta v)/(\eta_B)$. For 2σ upper limits, Δv is assumed to be 1 km s^{-1}.
b) Same as column 4 of table 3.3.
c) Radio column densities assume $T_{ex} \gg T_{bg}$.
d) Lang & Willson (1978)
e) Thorburn et al. (2003)
f) Weselak (2019)
g) Weselak et al. (2014)
h) Willson (1981)
i) Federman (1982)
j) Sheffer & Federman (2007)
k) Weselak et al. (2008)
l) Sheffer et al. (2008)

Table 3.5: $T_{\rm ex}$ from optical measurements from the literature

Position	$N_{\rm u}$ (3886) 10^{12} cm^{-2}	$N_{\rm l}$ (3890) 10^{12} cm^{-2}	Ref	$N_{\rm l}$ / $N_{\rm u}$	$T_{\rm ex}^{a}$ K	$T_{\rm ex}$ Range^{b} K
HD 23180	8.91 ± 0.24	9.30 ± 0.32	*c*	1.04 ± 0.05	3.73 ± 3.81	$T_{\rm ex} > 1.54, -8.53 > T_{\rm ex}$
	9.82 ± 0.70	12.97 ± 0.70	*d*	1.32 ± 0.12	0.57 ± 0.19	$1.04 > T_{\rm ex} > 0.39$
	9.89 ± 0.70	10.62 ± 0.91	*e*	1.07 ± 0.12	2.25 ± 3.51	$T_{\rm ex} > 0.71, -1.84 > T_{\rm ex}$
	10.54 ± 1.29	11.46 ± 1.51	*f*	1.09 ± 0.19	1.91 ± 4.11	$T_{\rm ex} > 0.47, -0.93 > T_{\rm ex}$
HD 24398	20.5 ± 0.4	18.1 ± 0.5	*c*	0.88 ± 0.03	-1.29 ± 0.32	$-0.96 > T_{\rm ex} > -1.96$
	10.05 ± 0.47	9.82 ± 0.70	*d*	0.98 ± 0.08	-6.69 ± 23.8	$T_{\rm ex} > 1.73, -1.12 > T_{\rm ex}$
	11.54 ± 0.84	11.04 ± 0.95	*e*	0.96 ± 0.11	-3.61 ± 9.19	$T_{\rm ex} > 1.41, -0.78 > T_{\rm ex}$
	11.60 ± 1.17	10.55 ± 1.33	*f*	0.91 ± 0.15	-1.69 ± 2.90	$T_{\rm ex} > 1.22, -0.49 > T_{\rm ex}$
HD 24534	18.94 ± 1.87	19.28 ± 1.05	*d*	1.02 ± 0.11	8.91 ± 56.0	$T_{\rm ex} > 0.91, -1.21 > T_{\rm ex}$
	19.85 ± 2.36	19.46 ± 1.51	*f*	0.98 ± 0.14	-7.99 ± 56.7	$T_{\rm ex} > 0.88, -0.75 > T_{\rm ex}$
HD 24912	6.73 ± 0.94	6.76 ± 0.98	*e*	1.00 ± 0.20	36.0 ± 1630	$T_{\rm ex} > 0.55, -0.57 > T_{\rm ex}$
	7.20 ± 1.31	8.59 ± 1.58	*f*	1.19 ± 0.31	0.91 ± 1.33	$T_{\rm ex} > 0.29, -0.83 > T_{\rm ex}$
HD 27778	18.00 ± 2.10	17.88 ± 2.10	*d*	0.99 ± 0.16	-23.2 ± 556	$T_{\rm ex} > 0.70, -0.66 > T_{\rm ex}$
	16.90 ± 2.06	16.20 ± 2.8	*e*	0.96 ± 0.20	-3.78 ± 18.9	$T_{\rm ex} > 0.65, -0.46 > T_{\rm ex}$
	22.79 ± 1.82	16.90 ± 2.24	*f*	0.74 ± 0.11	-0.53 ± 0.28	$-0.31 > T_{\rm ex} > -1.75$
HD 34078	37.87 ± 0.70	37.16 ± 0.70	*d*	0.98 ± 0.03	-8.38 ± 11.6	$T_{\rm ex} > 8.74, -2.83 > T_{\rm ex}$
	45.80 ± 2.58	41.90 ± 3.58	*e*	0.91 ± 0.09	-1.80 ± 2.07	$T_{\rm ex} > 2.79, -0.71 > T_{\rm ex}$
	39.16 ± 3.06	39.54 ± 1.75	*f*	1.01 ± 0.09	16.5 ± 152.8	$T_{\rm ex} > 1.19, -1.44 > T_{\rm ex}$

a) Uncertainties based on formal error propagation.
b) Uncertainties based on technique we described in §3.4.1.
c) Jura & Meyer (1985)
d) Weselak et al. (2008)
e) Weselak et al. (2014)
f) Weselak (2019)

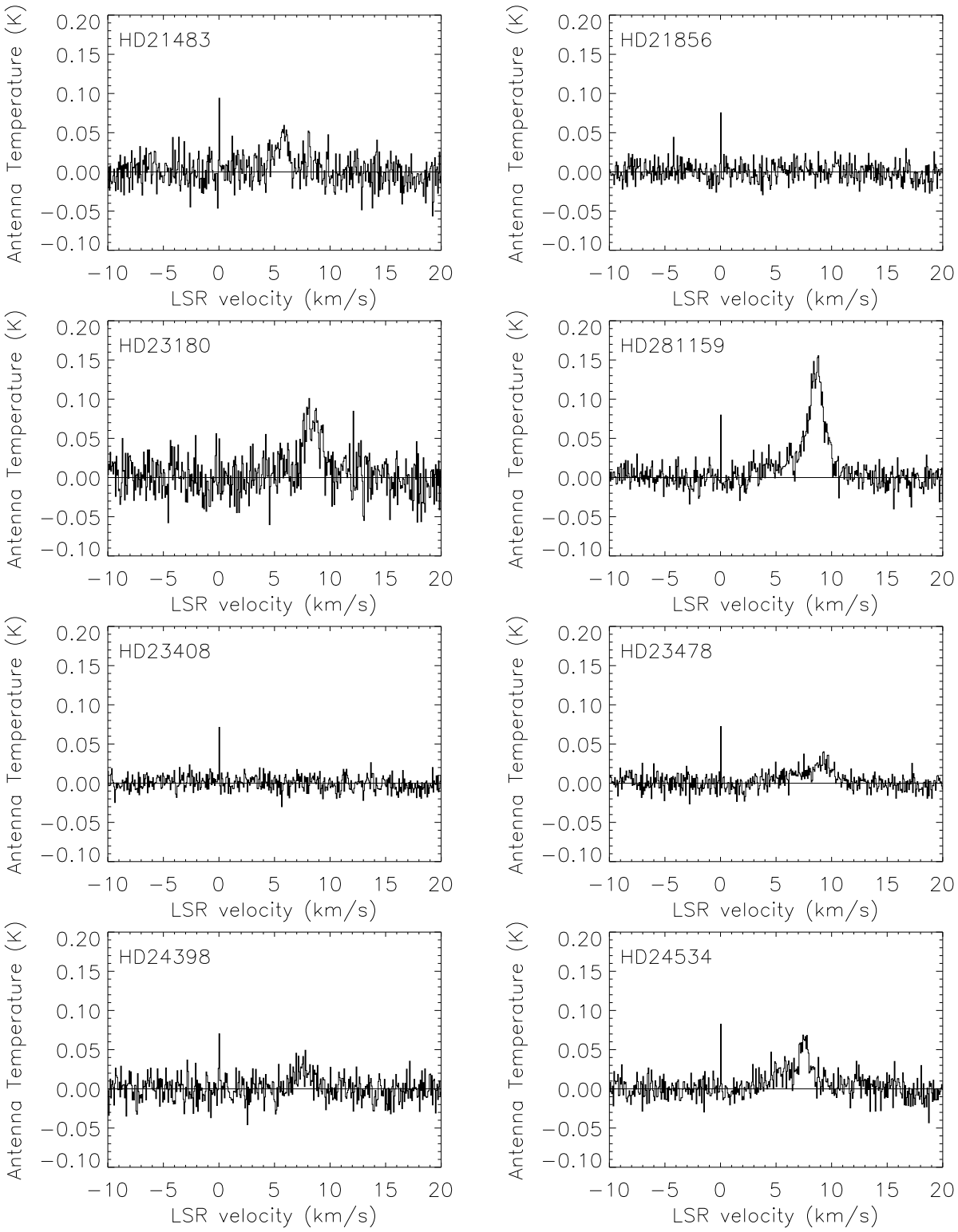

Figure 3.1a: CH 3335 MHz spectra for the first 8 lines of sight in Table 3.1. The spike sometime visible at $v_{\rm LSR} = 0.0$ km s^{-1} is due to internal interference.

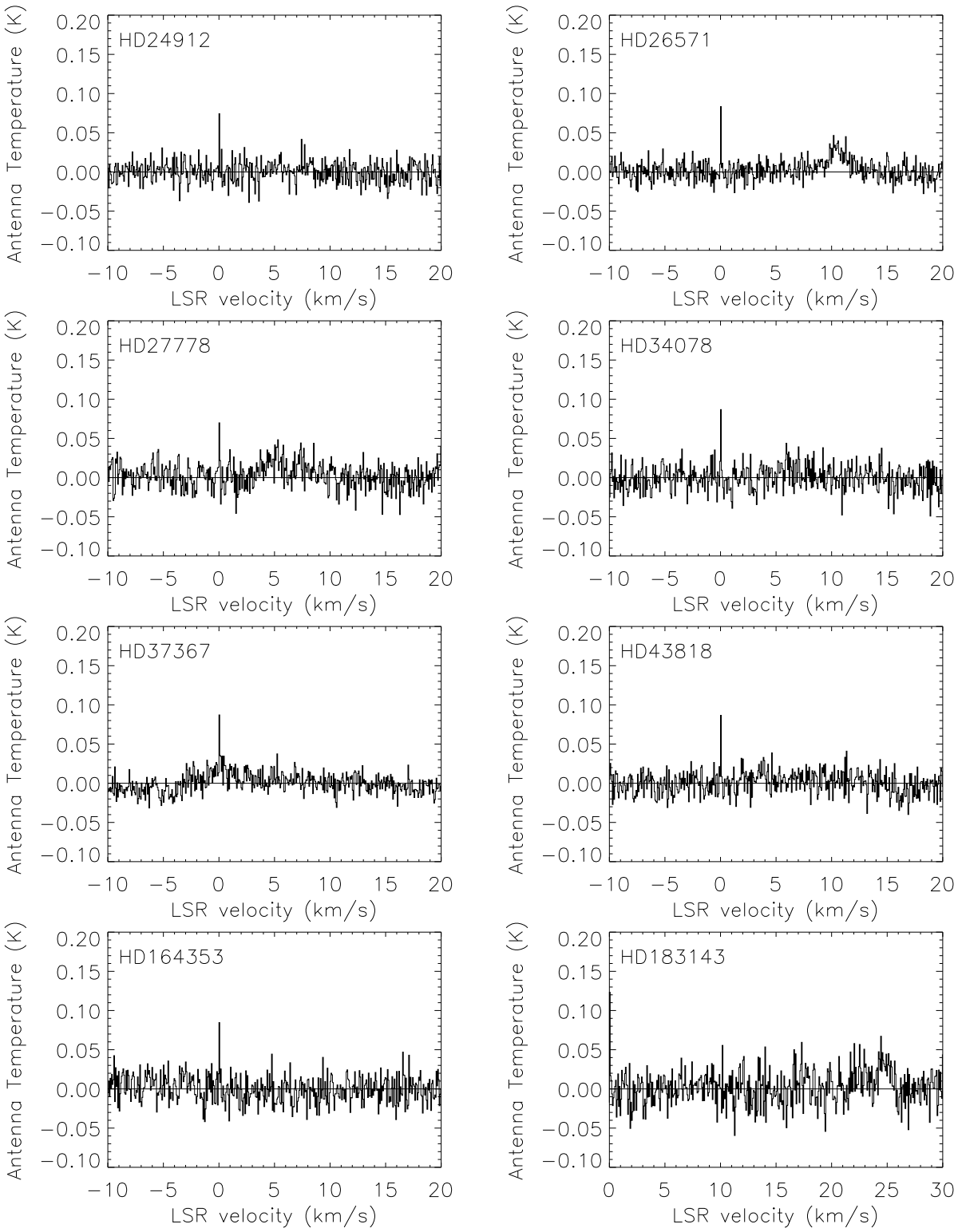

Figure 3.1b: Same as Figure 3.1*a* for the remaining 8 lines of sight in Table 3.1.

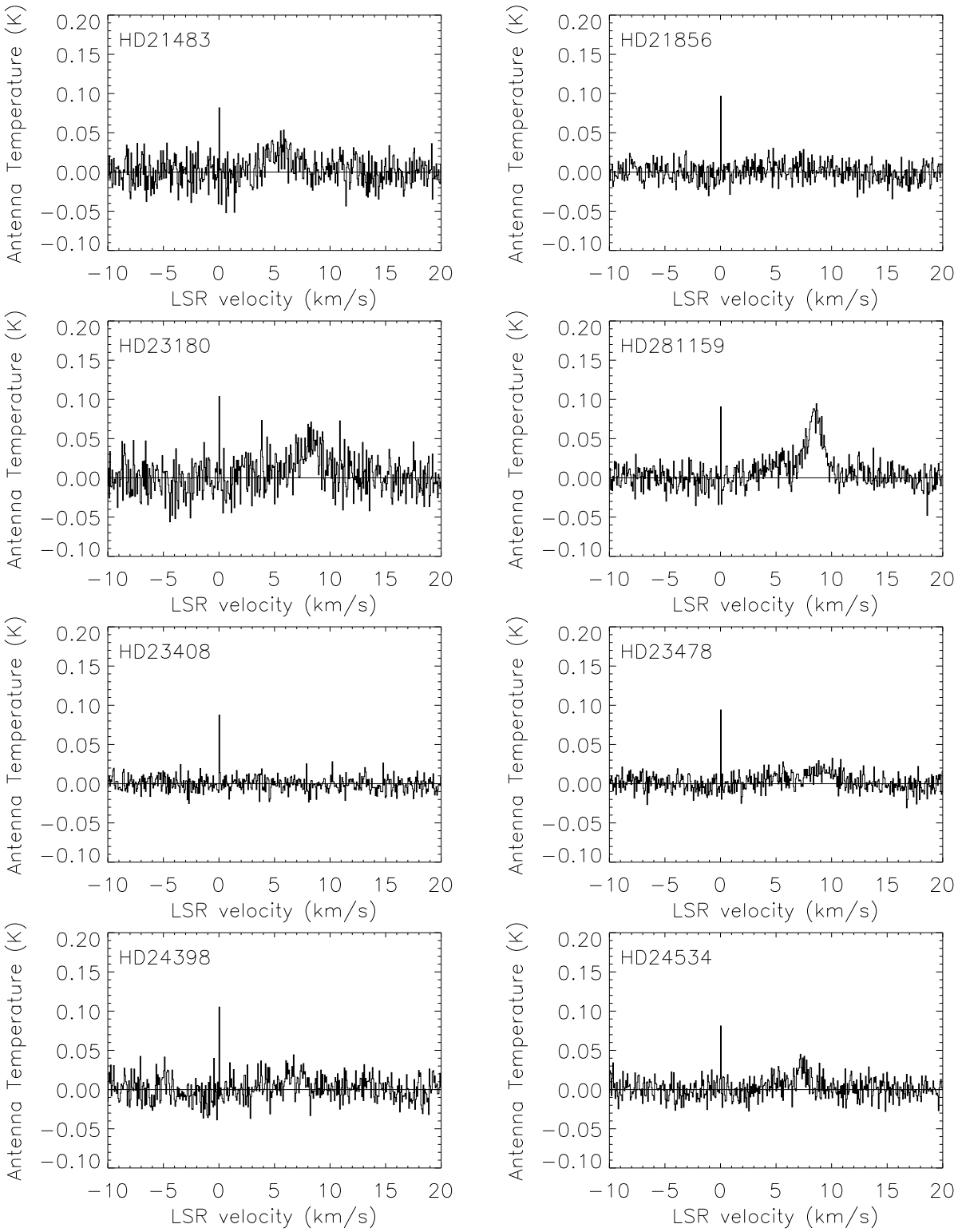

Figure 3.1c: CH 3349 MHz spectra for the first 8 lines of sight in Table 3.1. The spike sometime visible at $v_{\rm LSR} = 0.0$ km s^{-1} is due to internal interference.

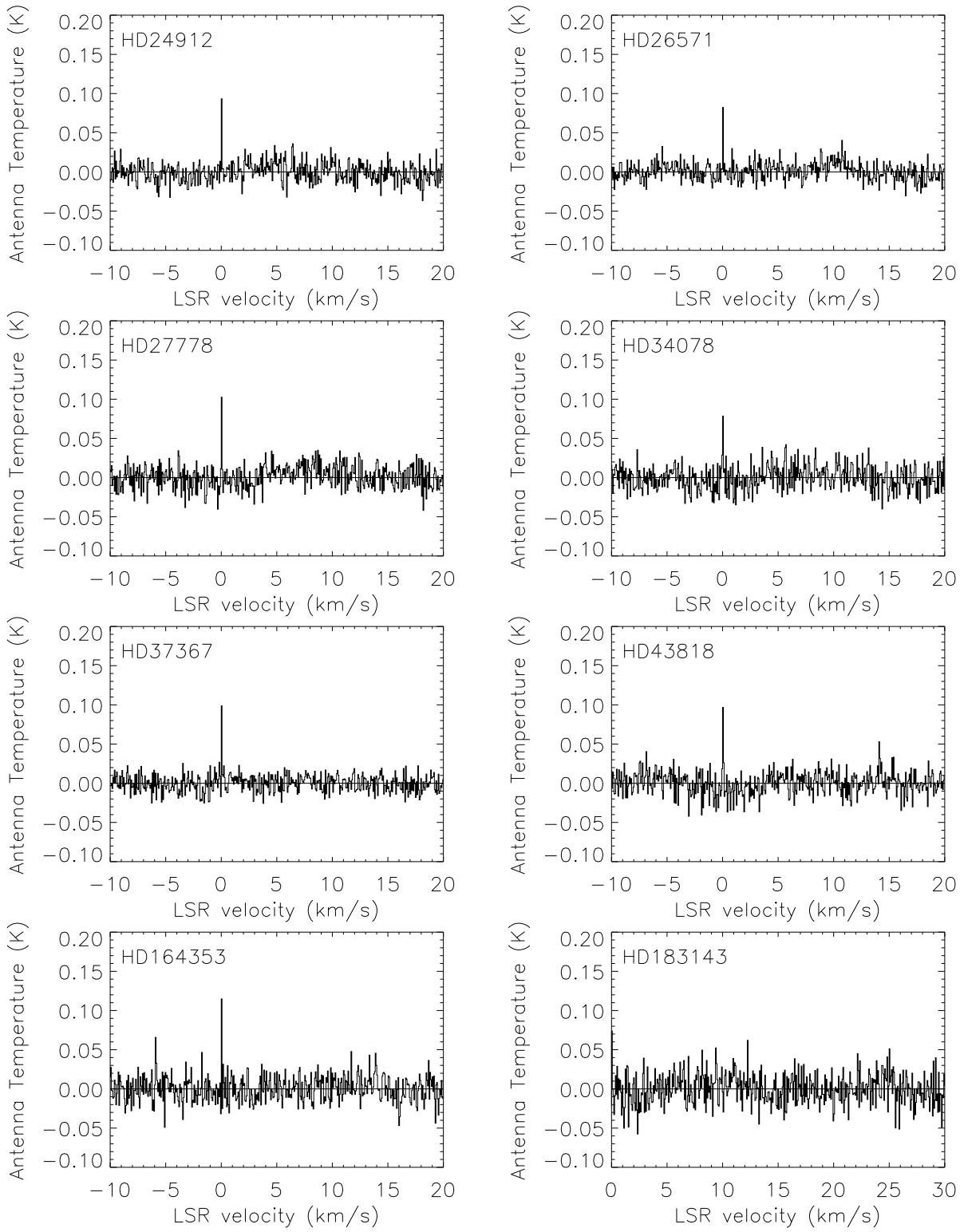

Figure 3.1d: Same as Figure 3.1*c* for the remaining 8 lines of sight in Table 3.1.

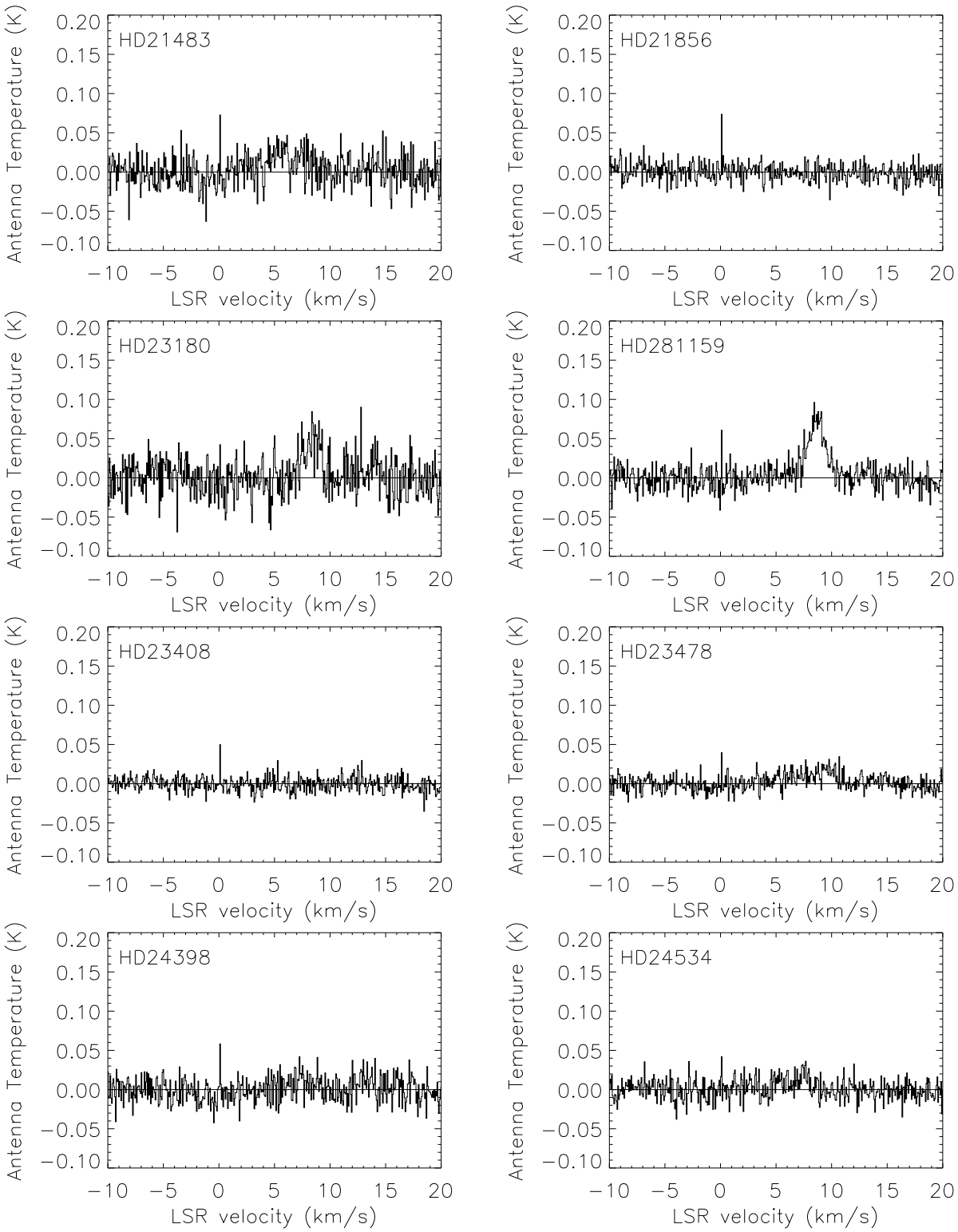

Figure 3.1e: CH 3264 MHz spectra for the first 8 lines of sight in Table 3.1. The spike sometime visible at $v_{\rm LSR} = 0.0$ km s^{-1} is due to internal interference.

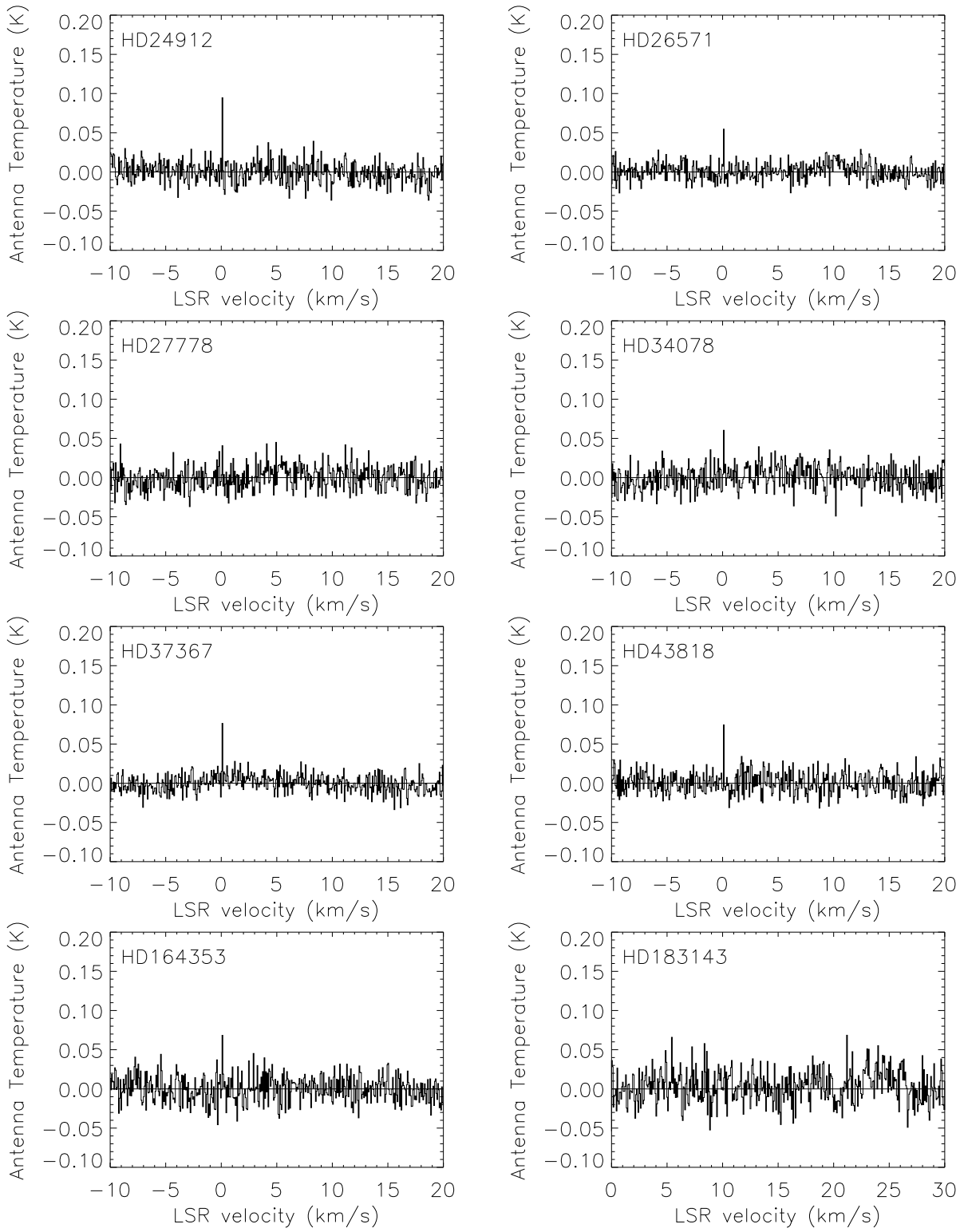

Figure 3.1f: Same as Figure 3.1*e* for the remaining 8 lines of sight in Table 3.1.

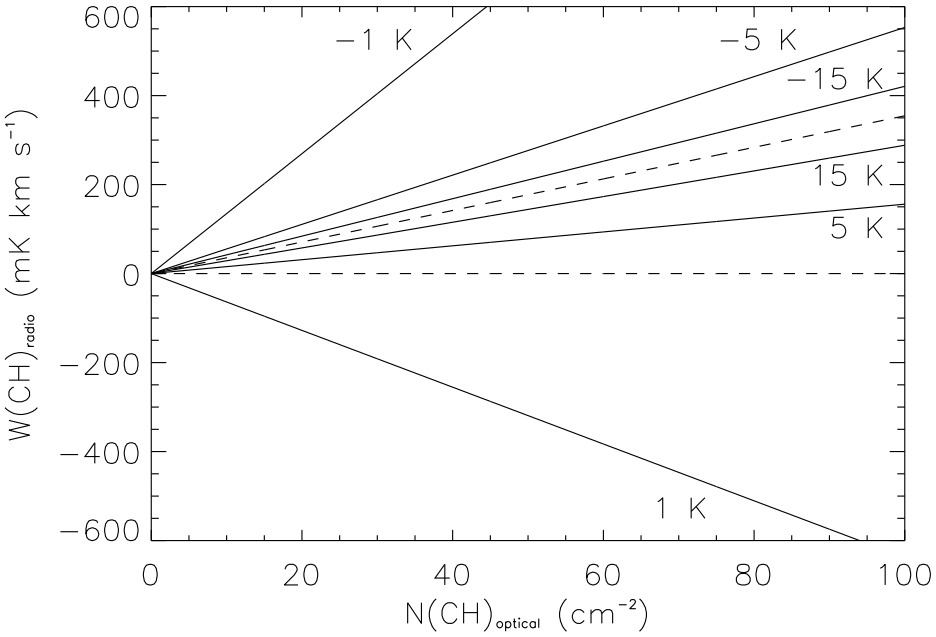

Figure 3.2: Plot of $W(CH)_{radio}$ as a function of $N(CH)_{optical}$ ($\times 10^{12}$) for various T_{ex}. The upper dotted line is for large T_{ex}, when $T_{ex}/(T_{ex} - T_{bg}) = 1$. The lower dotted line at $T_{ex} = 2.8$ K shows the transition from emission to absorption, at which there is no detectable radio signal and $T_{ex}/(T_{ex} - T_{bg})$ is undefined. The plot assumes $\eta_f = 1$ and $T_{bg} = 2.8$ K. See discussion in §3.3.

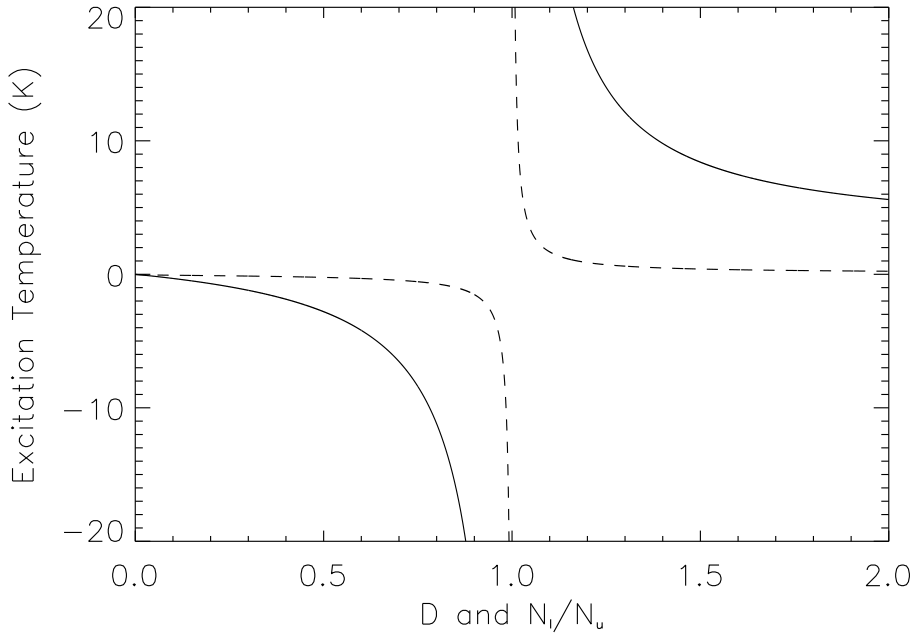

Figure 3.3: Plot of T_{ex} as a function of the ratio of the population in the lower and upper levels of the lambda-doubled CH ground state (dashed lines) and the function $D = N(CH)(\eta_f)[W(CH)\times(2.82 \times 10^{11})]^{-1}$ (solid lines). See discussion in §3.5.

Chapter 4

Other methods of determining $T_{\rm ex}$

In addition to the methods of determining $T_{\rm ex}$ described in Chapter 3, there are three other ways to do so which are discussed in this chapter. One uses on/off measurements of the 3.3 GHz lines towards a radio continuum source. Another involves determining the population of the upper and lower lambda-doubled halves of the blended 4300 Å line. Observations of the B-X band lines may also be used to determine $T_{\rm ex}$ (Lien 1984; Jura and Meyer 1985), but this method will not be discussed further in this chapter.

On and off source observations towards radio continuum sources were used by Rydbeck et al. (1976) to determine the often-used result for the 3335 MHz line that $T_{\rm ex} = -15$ K, and the technique has been used by Hjalmarson et al. (1977) and Genzel et al. (1979) to determine the excitation temperature of the CH main line and satellite lines. They found the main line excitation temperature to be inverted with an absolute magnitude greater than the background, from $T_{\rm ex} = -9$ K (Hjalmarson et al. 1977) to $T_{\rm ex} = -60$ K (Genzel et al. 1979). Crane, Lambert, and Sheffer (1995) were able to detect the two components of the blended 4300 Å line due to the high resolution of the observations along with the narrow signal,

but they did not attempt to determine the excitation temperature and instead fit the spectra as if both of the levels had equal column densities.

4.1 Determining $T_{\rm ex}$ using on/off measurements

In single-dish radio astronomy, the line and continuum measurements on and off of a continuum source behind a molecular cloud can be used to solve for the excitation temperature. Here, we determine the excitation temperature of the CH 3335 MHz line using on-source/off-source radio line and continuum measurements, similar to the method used in Genzel et al. (1979). We begin with the radiative transfer equation:

$$dI_\nu/ds = -k_\nu\, I_\nu + j_\nu \tag{4.1}$$

where I_ν is the intensity (ergs s^{-1} cm^{-2} sr^{-1} Hz^{-1}), k_ν is the absorption coefficient in units of cm^{-1} and j_ν is the emission coefficient (ergs s^{-1} cm^{-3} sr^{-1} Hz^{-1}). Assuming the source function S_ν = j_ν/k_ν is constant, we can solve for the intensity as a function of the optical depth as

$$I_\nu(\tau_\nu) = I_\nu(0)\, e^{-\tau_\nu} + S_\nu(1 - e^{-\tau_\nu}). \tag{4.2}$$

The brightness temperature, $T_{\rm b}$, if h$\nu \ll$ k$T_{\rm b}$, is defined as

$$I_\nu = 2\nu^2 c^{-2} k T_{\rm b} \tag{4.3}$$

For blackbody radiation the intensity is equal to B_ν, the blackbody intensity function:

$$B_\nu = 2h\nu^3 c^{-2}(e^{h\nu/(kT)} - 1)^{-1} \tag{4.4}$$

In the case of optically thick thermal radiation, the source function S_ν is equal to B_ν. Applying this approximation to equation 4.2 results in the standard solution of the radiative transfer equation if h$\nu \ll$ kT_b in terms of the brightness temperature.

$$T_{\rm b}(\tau_\nu) = T_{\rm b}(0)e^{-\tau_\nu} + T(1 - e^{-\tau_\nu}) \tag{4.5}$$

T is the temperature of the gas in its capacity for absorbing and re-emitting radiation, and this is the excitation temperature, $T_{\rm ex}$. $T_{\rm b}(0)$ is the background temperature $T_{\rm bg}$, and is a combination of the cosmic microwave background, the galactic thermal and non-thermal background, and any background continuum sources. At low frequencies, the brightness temperature is the antenna temperature of the line, so assuming that $T_{\rm bg}$ is the same for the on and off source scans, the on-source radio brightness temperature is given by equation 4.6, and the off-source radio brightness temperature is given by equation 4.7:

$$T_{\rm ON,L} = (T_{\rm ex} - T_{\rm bg} - T_{\rm ON,C})(1 - e^{-\tau}) \tag{4.6}$$

$$T_{\rm OFF,L} = (T_{\rm ex} - T_{\rm bg} - T_{\rm OFF,C})(1 - e^{-\tau}) \tag{4.7}$$

$T_{\rm ON,L}$ is the on-source brightness temperature of the line, and $T_{\rm ON,C}$ is the on-source brightness temperature of the background continuum source. The background temperature is assumed to be 2.8 K. τ is the optical depth, assumed to be the same for both on and off sources line of sight. Similar to the

on-source temperatures, $T_{\mathrm{OFF,L}}$ is the off-source brightness temperature of the line, and $T_{\mathrm{OFF,C}}$ is the off-source brightness temperature of the background continuum source. Assigning L=$T_{\mathrm{OFF,L}}/T_{\mathrm{ON,L}}$ and C=$T_{\mathrm{OFF,C}}/T_{\mathrm{ON,C}}$, we rewrite equation 4.6 and 4.7 to solve for T_{ex},

$$T_{\mathrm{ex}} = T_{\mathrm{bg}} - (L - C)(1 - L)^{-1} T_{\mathrm{ON,C}} (\eta_b)^{-1} \tag{4.8}$$

Where η_b is the beam efficiency. In the case of our 9 cm CH observations from Arecibo, prior to hurricane Maria, η_b = 0.57 ± 0.02 (see discussion in Chapter 3).

4.1.1 Observations

We used the quasar QSO J$0530 + 13$ behind the cloud LDN 1573 as the background continuum source. The observations consisted of on and off source observations with J$0530 + 13$ as the on and J$0530 + 13$N as the off source located 1.5' north of the on position (the beam size at 3.3 GHz is 1.3×1.5 arcmin elongated in azimuth). The background continuum source is not in the direction of the OFF scans, so $T_{\mathrm{OFF,C}}$ = 0 K and $T_{\mathrm{ON,C}}$ is determined by subtracting the baseline temperature of the ON scans by the OFF scans. Therefore, C = 0 and $T_{\mathrm{ON,C}}$ = 11.7 K. The parameters of our detections are shown in Table 4.1. Plugging in those values in equation 4.8 gives T_{ex} = -21.0 ± 11.2 K for the 3335 MHz line, which is consistent with the excitation temperature determined by Rydbeck et al. (1976), and correlates to F_{T} = 0.88[1] where T_{bg} = 2.8 K.

[1] F_{T} = [T_{ex}/(T_{ex}-T_{bg})]

4.2 Synthetic High-Resolution Profiles of the 4300 Å Line

The Methylidyne (CH) 4300.3132 Å transition is not a single line, but a blend of two lines that sample the upper and lower lambda-doubled $X^2\Pi$ ground state. The upper line is the R_{2e} line at 4300.3030 Å (Black and van Dishoeck 1988), which is between the upper N=2, J=3/2, $A^2\Delta$ state and the lower N=1, J=1/2, $X^2\Pi$ state. The lower line is the R_{2f} line at 4300.3235 Å (Black and van Dishoeck 1988), which is between the lower N=2, J=3/2, $A^2\Delta$ state and the upper N=1, J=1/2, $X^2\Pi$ state. Due to the closeness of the lines, it is difficult to resolve each line separately. Crane et al. (1995) were able to distinguish between the two blended components by using a spectrometer at the 2.7 meter telescope at the W. J. McDonald Observatory on Mt. Locke, Texas, which had a resolution of 0.004 Å, or 0.28 km s^{-1}. Even with the high resolution provided by the spectrometer, they were only able to detect the individual lambda-doubled components from 2 of the 20 stars they observed, which had very narrow CH components. They assumed the ratio of the upper and lower column densities would be equal to one when there were two peaks 1.43 km s^{-1} apart.

In the rare cases where the lines are able to be resolved separately and the column densities of both lines can be determined accurately, then the excitation temperature of the lambda doublet may be determined from the ratio of the column densities of the two lines. The population in each of the hyperfine states for the upper and lower halves is unknown, so it is not possible to determine the excitation temperature of an individual hyperfine line. The excitation temperature is that of the lambda-doubled ground state.

In order to explore whether observations of the split 4300 Å line can be used to determine $T_{\rm ex}$for the 3335 MHz line, synthetic spectra are created to determine how effective fitting gaussians to the spectra is at

determining the "true" excitation temperature of the doublet. The equation for the excitation temperature is:

$$N_u/N_l = N_r^{-1} = g_u/g_l e^{-E/kT_{\rm ex}} \tag{4.9}$$

where N is the column density, and g is the statistical weight of the upper and lower levels in question. N_r is the ratio of the column densities of the lower and upper halves of the doublet (N_r = $\mathrm{N}_l/\mathrm{N}_u$). E is the energy difference between the upper and lower levels and k is the Boltzmann constant, $E/\mathrm{k} \approx 0.16$ K for the Λ-doubled CH 3335 MHz line (Lizst and Lucas 2002). The ratio of the statistical weights of the upper and lower states is assumed to be $g_\mathrm{u}/g_\mathrm{l} = 1$.

There is a singularity when N_u = N_l, but this is not always an issue as $|T_{\rm ex}| \gg T_{\rm bg}$ near the singularity, and when $T_{\rm ex}$ is applied to the equation for the column density,

$$N(CH) = 2.82 \times 10^{11} (\eta_f \eta_B)^{-1} [T_{\rm ex}/(T_{\rm ex} - T_{\rm bg})]\, W_{CH} \tag{4.10}$$

for the radio column density, $T_{\rm ex}$/($T_{\rm ex}$ - $T_{\rm bg}$) ≈ 1. Unfortunately, the noise in the data may cause N_u and N_l to be equal within 1σ error, while $T_{\rm ex}$ is not much greater than the background. If we assume that the threshold for when $|T_{\rm ex}| \gg T_{\rm bg}$ is at $T_{\rm ex} = -11$ K ($F_{\rm T} \approx 0.8$), then the threshold occurs for N_r = $\mathrm{N}_l/\mathrm{N}_u$ = 0.986. If the column densities are similar, the noise of the data is a significant factor in determining moderately high $T_{\rm ex}$.

The column densities of the upper and lower halves of the doublet are determined using the following equation from Weselak et al. (2008):

$$N(CH) = 1.13 \times 10^{20}(EW/f\lambda^2) \tag{4.11}$$

where EW is the equivalent width, and λ is the wavelength of the line. The oscillator strength is f, and is equal to 506×10^{-5} for the CH 4300 Å line (Larsson and Siegbahn 1983, Weselak et al. 2014).

4.2.1 Gauss Fitting Procedure

Two types of synthetic spectra will be considered, both based on the observation of λ Cep by Crane et al. (1995). The first will test the ability of the gauss fitting program in determining the excitation temperature on an isolated, single line with a width of 0.7 km s^{-1} and an equivalent width of 6.1 mÅ. The second will test the gaussfitting program when there are two overlapping lines (as seen in λ Cep) by including the other wider line with a width of 2.8 km s^{-1} and an equivalent width of 10.4 mÅ. Both of the lines are split by lambda doubling, but the twin peaks are not visible in the second line due to the velocity width of each component.

We test 4 excitation temperatures for both spectra types, so there are 8 sets total. While the excitation temperature of the doublet is for the lambda-doubled ground state, we use excitation temperatures of the CH main line as examples. Rydbeck et al. (1976) determined $T_{\rm ex} = -15$ K through On-Off observations of the supernova remnant 3C461, and similarly Genzel et al. (1979) determined $T_{\rm ex} = -60$ K by observing the cloud L1500 and the source 3C123. For lower excitation temperatures, $T_{\rm ex} = -4$ K is representative of $F_{\rm T} = 0.57$ (see chapter 2), and $T_{\rm ex} = -1$ K represents a large difference in the upper and lower states, similar to what has been determined in Lien (1984). To better simulate actual observations, noise is generated from a normal distribution multiplied by 0.01, resulting in an average rms of 0.0101. A control

set is created without noise to ensure that the fitting process is able to recreate the initial conditions. Additionally, another set of noisy data is tested, where the noise simulates a line of sight which has been oberved for a longer amount of time. The noise is reduced by a factor of $\sqrt{10}$, resulting in an average rms of 0.0032. Each set will have 5 trials and 1 control, for a total of 40 trials with 8 controls.

The fitting program uses the Python packages PySpecKit (Ginsburg and Mirocha 2011) for the gauss fitting, Matplotlib (Hunter 2007) for the creating the plots, and numpy (Harris et al. 2020). The gauss fitting requires guesses in order to create the fits, and the doublet peaks seen in both the simple and complex spectra are guessed to be at -13.7 and -12.3 km s^{-1}. The width of both halves are tied together as they both arise from the same cloud component, and the separation is locked at 1.4292 km s^{-1}. The secondary component seen in the complex spectra is guessed to be at -12 km s^{-1}, and is fitted using a single gaussian, attempts to fit with a doublet similar to the thinner peaks often resulted in one peak having an amplitude of 0 relative brightness.

4.2.2 Results

The synthetic spectra are shown in figures 4.1 through 4.5. With the simple doublet spectra shown in figure 4.1, the control spectrum was able to effectively reproduce the gaussian profiles and the excitation temperature. The column densities and excitation temperatures are listed in table 4.2. Even in the control spectra, the difficulty of accurately determining the excitation temperature for high $T_{\rm ex}$ is apparent, with $T_{\rm ex}$ = -15 K becoming -14.99 K and $T_{\rm ex}$ = -60 K becoming -59.88 K due to the extreme sensitivity of $T_{\rm ex}$ to changes in N$_r$. The sensitivity of $T_{\rm ex}$ increasing as N$_r$ increases becomes a limiting factor on the ability to determine $T_{\rm ex}$ due to the noise in the data. In the default case with an approximate rms of

0.0101, the only group which was able to output a similar excitation temperature as the control was the $T_{\rm ex} = -1$ K group.

At higher $|T_{\rm ex}|$, such as $T_{\rm ex} = -4$ K, the uncertainty of N_r (≈ 0.080) encompasses the singularity at $\mathrm{N}_r = 1$. To measure higher $|T_{\rm ex}|$, the noise needs to be reduced. Reducing the noise by a factor of $\sqrt{10}$, simulating observing for 10 times longer, allows for higher $|T_{\rm ex}|$ to be accurately determined. The column densities and excitation temperatures of the simple doublet with reduced noise are listed in table 4.3, and the spectra are shown in figure 4.2. With the reduced noise, $T_{\rm ex} = -1$ and -4 K are able to be effectively measured, but higher magnitude excitation temperatures still limited by the noise. The uncertainty of N_r in the reduced noise spectra is approximately 0.026 on average, which is too large when attempting to determine $T_{\rm ex}$ when $T_{\rm ex} = -15$ K ($\mathrm{N}_r = 0.989$) and $T_{\rm ex} = -60$ K ($\mathrm{N}_r = 0.997$). To reduce the noise enough to reproduce the excitation temperature at -15 K, the line of sight would need to be observed for at least 60 times longer than the original spectra to reduce the uncertainty so that the singularity at $\mathrm{N}_r = 1$ is not encompassed by the 1σ uncertainty. For the $T_{\rm ex} = -60$ K case, the line of sight would need to be observed for approximately 700 times longer than the default spectra.

Crane et al. (1995) did not observe a single velocity component in the line of sight to λ Cep, but rather two overlapping components. Column densities and excitation temperatures of the two component spectra are listed in table 4.4, and the spectra are shown in figure 4.3. Including the second component at -12 km s^{-1}, the excitation temperatures from the control spectra are higher in magnitude than the original $T_{\rm ex}$. Similar to the simple doublet spectra with the default noise, the high uncertainty makes it difficult to determine the excitation temperatures when N_r is close to 1. The reduced noise spectra are shown in figure 4.4, and in table 4.5 the column densities and excitation temperatures are listed. It shows similar results as the single component spectra, the uncertainty is reduced enough so the excitation

temperature is able to be determined for cases with low N_r, such as for $T_{ex} = -1$ K and -4 K. However, N_r is elevated across all of the control cases, which may be due to the second component being fit with a single gaussian component instead of two. The fitting program did not fit the second component, but if the second component is included then it could account for the elevated N_r.

To test this, the spectra shown in figure 4.5 are similar to the reduced noise two component spectra, except the -12 km s^{-1} component is moved to -14 km s^{-1}. Table 4.6 shows the column densities and excitation temperatures of the trials. In the control tests of each T_{ex} groups, N_r is reduced. If the broad component is assumed to be a single gaussian component instead of two, whichever half of the doublet is centered on the peak of the broad component will have the amplitude inflated by the fitting program. If the broad component's center is near the lower CH component at ≈ -13.7 km s^{-1}, the derived $|T_{ex}|$ is reduced, and if it is near the upper CH component at ≈ -12.3 km s^{-1}, $|T_{ex}|$ is elevated.

4.3 Conclusion

The on/off source method discussed in section 4.1 is capable of determining T_{ex} when $|T_{ex}| \gg T_{bg}$, but is limited to lines of sight with strong background continuum sources. In contrast, excitation temperatures measured by observations of the 4300 Å doublet are highly sensitive to the rms of the spectrum. To measure T_{ex} when $|T_{ex}| \gg T_{bg}$, N_r will be close to one (≈ 0.99), necessitating long observation times to produce spectra with low enough noise to allow accurate determinations of N_r. If the line has multiple components, attempts to fit gaussians to the data will likely need to account for the doublet in each of the components. The excitation temperature of the 3.3 GHz doublet may be determined from the 4300 Å

doublet, but requires very high signal to noise to accurately measure the difference between the amplitude of the doublet components, and is limited to lines of sight with a background star.

Table 4.1: Radio CH Observations

Position		J0530 + 13	J0530 + 13N
R.A. (2000)	$^h\ ^m\ ^s$	05 30 56.4	05 30 56.4
Dec (2000)	$^\circ\ '\ ''$	+ 13 31 55.1	+ 13 33 25.1
l		191.368	191.346
b		−11.012	−10.999
$T_{\rm A}$ (3335.5)	mK	86.9 ± 20.25	46.7 ± 13.8
Δv	km s^{-1}	0.57 ± 0.13	1.09 ± 0.32
v$_{LSR}$	km s^{-1}	9.62	9.67
$T_{\rm A}$ (3349.2)	mK	80.0 ± 19.8	54.7 ± 14.3
Δv	km s^{-1}	0.72 ± 0.18	0.61 ± 0.16
v$_{LSR}$	km s^{-1}	9.52	9.49
$T_{\rm A}$ (3263.8)	mK	63.3 ± 20.5	38.2 ± 13.3
Δv	km s^{-1}	0.73 ± 0.24	1.65 ± 0.57
v$_{LSR}$	km s^{-1}	9.71	9.73
$T_{\rm C}$	mK	40.2 ± 0.23	28.5 ± 0.16

Table 4.2: Simple Doublet Parameters

$T_{ex} = -1$ K				
Trial	N(CH)$_{upper}$ 10^{12} cm^{-2}	N(CH)$_{lower}$ 10^{12} cm^{-2}	N$_r$	T_{ex} K
Control	3.98	3.39	0.852	-1.00
Trial 1	3.93 ± 0.22	3.49 ± 0.22	0.886 ± 0.074	-1.32
Trial 2	3.94 ± 0.21	3.33 ± 0.21	0.846 ± 0.071	-0.96
Trial 3	4.14 ± 0.22	3.46 ± 0.22	0.836 ± 0.069	-0.89
Trial 4	4.04 ± 0.22	3.50 ± 0.22	0.866 ± 0.071	-1.11
Trial 5	3.79 ± 0.22	3.39 ± 0.22	0.895 ± 0.077	-1.45
$T_{ex} = -4$ K				
Trial	N(CH)$_{upper}$ 10^{12} cm^{-2}	N(CH)$_{lower}$ 10^{12} cm^{-2}	N$_r$	T_{ex} K
Control	3.76	3.61	0.961	-4.00
Trial 1	4.09 ± 0.24	3.66 ± 0.24	0.894 ± 0.077	-1.43
Trial 2	3.92 ± 0.22	3.58 ± 0.22	0.913 ± 0.076	-1.76
Trial 3	3.35 ± 0.22	3.69 ± 0.22	1.101 ± 0.096	1.66
Trial 4	3.81 ± 0.21	3.59 ± 0.21	0.943 ± 0.077	-2.73
Trial 5	3.80 ± 0.22	3.46 ± 0.22	0.911 ± 0.078	-1.71
$T_{ex} = -15$ K				
Trial	N(CH)$_{upper}$ 10^{12} cm^{-2}	N(CH)$_{lower}$ 10^{12} cm^{-2}	N$_r$	T_{ex} K
Control	3.70	3.66	0.989	-14.99
Trial 1	3.75 ± 0.21	3.61 ± 0.21	0.962 ± 0.079	-4.14
Trial 2	3.68 ± 0.23	3.63 ± 0.23	0.985 ± 0.087	-10.41
Trial 3	3.78 ± 0.22	3.70 ± 0.22	0.980 ± 0.081	-8.06
Trial 4	3.40 ± 0.21	3.51 ± 0.21	1.033 ± 0.088	4.90
Trial 5	3.57 ± 0.21	3.75 ± 0.21	1.048 ± 0.085	3.42
$T_{ex} = -60$ K				
Trial	N(CH)$_{upper}$ 10^{12} cm^{-2}	N(CH)$_{lower}$ 10^{12} cm^{-2}	N$_r$	T_{ex} K
Control	3.69	3.68	0.997	-59.88
Trial 1	3.56 ± 0.21	3.71 ± 0.21	1.042 ± 0.087	3.90
Trial 2	3.71 ± 0.22	3.54 ± 0.22	0.955 ± 0.082	-3.47
Trial 3	3.67 ± 0.22	3.91 ± 0.22	1.065 ± 0.089	2.53
Trial 4	3.63 ± 0.22	3.71 ± 0.22	1.022 ± 0.087	7.25
Trial 5	3.85 ± 0.22	3.71 ± 0.22	0.962 ± 0.080	-4.14

Table 4.3: Simple Doublet Parameters, Low Noise

$T_{\rm ex} = -1$ K				
Trial	N(CH)$_{upper}$ 10^{12} cm^{-2}	N(CH)$_{lower}$ 10^{12} cm^{-2}	N$_r$	$T_{\rm ex}$ K
Control	3.98	3.39	0.852	-1.00
Trial 1	3.99 ± 0.07	3.36 ± 0.07	0.843 ± 0.023	-0.94
Trial 2	3.97 ± 0.07	3.38 ± 0.07	0.851 ± 0.023	-0.99
Trial 3	3.92 ± 0.07	3.34 ± 0.07	0.851 ± 0.023	-0.99
Trial 4	3.96 ± 0.07	3.36 ± 0.07	0.849 ± 0.023	-0.98
Trial 5	3.97 ± 0.07	3.39 ± 0.07	0.854 ± 0.023	-1.01
$T_{\rm ex} = -4$ K				
Trial	N(CH)$_{upper}$ 10^{12} cm^{-2}	N(CH)$_{lower}$ 10^{12} cm^{-2}	N$_r$	$T_{\rm ex}$ K
Control	3.76	3.61	0.961	-4.00
Trial 1	3.72 ± 0.07	3.59 ± 0.07	0.966 ± 0.026	-4.68
Trial 2	3.69 ± 0.07	3.59 ± 0.07	0.974 ± 0.027	-6.04
Trial 3	3.72 ± 0.07	3.59 ± 0.07	0.964 ± 0.026	-4.41
Trial 4	3.77 ± 0.07	3.54 ± 0.07	0.937 ± 0.025	-2.48
Trial 5	3.76 ± 0.07	3.67 ± 0.07	0.975 ± 0.026	-6.43
$T_{\rm ex} = -15$ K				
Trial	N(CH)$_{upper}$ 10^{12} cm^{-2}	N(CH)$_{lower}$ 10^{12} cm^{-2}	N$_r$	$T_{\rm ex}$ K
Control	3.70	3.66	0.989	-14.99
Trial 1	3.74 ± 0.07	3.67 ± 0.07	0.980 ± 0.027	-8.06
Trial 2	3.76 ± 0.07	3.64 ± 0.07	0.966 ± 0.026	-4.61
Trial 3	3.67 ± 0.07	3.65 ± 0.07	0.996 ± 0.026	-36.46
Trial 4	3.74 ± 0.07	3.67 ± 0.07	0.979 ± 0.026	-7.72
Trial 5	3.73 ± 0.07	3.70 ± 0.07	0.993 ± 0.027	-22.73
$T_{\rm ex} = -60$ K				
Trial	N(CH)$_{upper}$ 10^{12} cm^{-2}	N(CH)$_{lower}$ 10^{12} cm^{-2}	N$_r$	$T_{\rm ex}$ K
Control	3.69	3.68	0.997	-59.88
Trial 1	3.66 ± 0.07	3.72 ± 0.07	1.012 ± 0.027	9.11
Trial 2	3.64 ± 0.07	3.65 ± 0.07	1.003 ± 0.027	53.23
Trial 3	3.63 ± 0.07	3.72 ± 0.07	1.025 ± 0.028	6.59
Trial 4	3.65 ± 0.07	3.69 ± 0.07	1.012 ± 0.027	13.29
Trial 5	3.69 ± 0.07	3.63 ± 0.07	0.983 ± 0.027	-9.24

Table 4.4: Complex Doublet Parameters

$T_{ex} = -1$ K				
Trial	$N(CH)_{upper}$ 10^{12} cm^{-2}	$N(CH)_{lower}$ 10^{12} cm^{-2}	N_r	T_{ex} K
Control	3.96	3.38	0.854	−1.01
Trial 1	4.18 ± 0.23	4.14 ± 0.23	0.991 ± 0.079	−17.50
Trial 2	3.75 ± 0.21	3.43 ± 0.21	0.915 ± 0.076	−1.81
Trial 3	3.93 ± 0.22	3.52 ± 0.22	0.894 ± 0.075	−1.42
Trial 4	4.37 ± 0.23	3.59 ± 0.23	0.823 ± 0.069	−0.82
Trial 5	3.88 ± 0.21	3.72 ± 0.21	0.959 ± 0.077	−3.84
$T_{ex} = -4$ K				
Trial	$N(CH)_{upper}$ 10^{12} cm^{-2}	$N(CH)_{lower}$ 10^{12} cm^{-2}	N_r	T_{ex} K
Control	3.75	3.61	0.963	−4.26
Trial 1	3.68 ± 0.22	3.62 ± 0.22	0.983 ± 0.084	−9.40
Trial 2	3.72 ± 0.21	3.43 ± 0.21	0.921 ± 0.075	−1.95
Trial 3	3.23 ± 0.21	2.97 ± 0.21	0.920 ± 0.086	−1.92
Trial 4	3.50 ± 0.22	3.33 ± 0.22	0.951 ± 0.085	−3.18
Trial 5	3.97 ± 0.22	3.62 ± 0.22	0.912 ± 0.074	−1.74
$T_{ex} = -15$ K				
Trial	$N(CH)_{upper}$ 10^{12} cm^{-2}	$N(CH)_{lower}$ 10^{12} cm^{-2}	N_r	T_{ex} K
Control	3.69	3.66	0.992	−19.67
Trial 1	3.29 ± 0.22	3.85 ± 0.22	1.170 ± 0.103	1.021
Trial 2	3.42 ± 0.21	3.47 ± 0.21	1.016 ± 0.090	10.32
Trial 3	3.15 ± 0.21	3.43 ± 0.21	1.089 ± 0.101	1.87
Trial 4	3.96 ± 0.21	4.08 ± 0.21	1.030 ± 0.078	5.36
Trial 5	4.32 ± 0.24	4.34 ± 0.24	1.004 ± 0.078	38.93
$T_{ex} = -60$ K				
Trial	$N(CH)_{upper}$ 10^{12} cm^{-2}	$N(CH)_{lower}$ 10^{12} cm^{-2}	N_r	T_{ex} K
Control	3.68	3.68	1.000	−1370.19
Trial 1	4.07 ± 0.24	4.44 ± 0.24	1.091 ± 0.086	1.84
Trial 2	3.20 ± 0.21	3.48 ± 0.21	1.086 ± 0.095	1.94
Trial 3	3.81 ± 0.22	3.73 ± 0.22	0.979 ± 0.081	−7.41
Trial 4	3.84 ± 0.21	3.67 ± 0.21	0.954 ± 0.076	−3.36
Trial 5	3.36 ± 0.21	3.76 ± 0.21	1.119 ± 0.094	1.42

Table 4.5: Complex Doublet Parameters, Low Noise

$T_{ex} = -1$ K				
Trial	$N(CH)_{upper}$ 10^{12} cm^{-2}	$N(CH)_{lower}$ 10^{12} cm^{-2}	N_r	T_{ex} K
Control	3.96	3.38	0.854	−1.01
Trial 1	3.87 ± 0.07	3.44 ± 0.07	0.889 ± 0.024	−1.36
Trial 2	3.95 ± 0.07	3.42 ± 0.07	0.865 ± 0.024	−1.10
Trial 3	4.07 ± 0.07	3.37 ± 0.07	0.828 ± 0.023	−0.85
Trial 4	4.04 ± 0.07	3.45 ± 0.07	0.853 ± 0.023	−1.01
Trial 5	3.75 ± 0.07	3.04 ± 0.07	0.811 ± 0.023	−0.76
$T_{ex} = -4$ K				
Trial	$N(CH)_{upper}$ 10^{12} cm^{-2}	$N(CH)_{lower}$ 10^{12} cm^{-2}	N_r	T_{ex} K
Control	3.75	3.61	0.963	−4.26
Trial 1	3.74 ± 0.07	3.61 ± 0.07	0.965 ± 0.026	−4.54
Trial 2	3.83 ± 0.07	3.70 ± 0.07	0.965 ± 0.026	−4.44
Trial 3	3.77 ± 0.07	3.63 ± 0.07	0.963 ± 0.026	−4.21
Trial 4	3.70 ± 0.07	3.56 ± 0.07	0.962 ± 0.026	−4.11
Trial 5	3.94 ± 0.07	3.72 ± 0.07	0.943 ± 0.025	−2.74
$T_{ex} = -15$ K				
Trial	$N(CH)_{upper}$ 10^{12} cm^{-2}	$N(CH)_{lower}$ 10^{12} cm^{-2}	N_r	T_{ex} K
Control	3.69	3.66	0.992	−19.67
Trial 1	3.67 ± 0.07	3.73 ± 0.07	1.016 ± 0.027	10.04
Trial 2	3.72 ± 0.07	3.67 ± 0.07	0.988 ± 0.026	−13.66
Trial 3	3.68 ± 0.07	3.72 ± 0.07	1.011 ± 0.027	14.28
Trial 4	3.56 ± 0.07	3.59 ± 0.07	1.008 ± 0.028	20.91
Trial 5	3.51 ± 0.07	3.60 ± 0.07	1.025 ± 0.028	6.56
$T_{ex} = -60$ K				
Trial	$N(CH)_{upper}$ 10^{12} cm^{-2}	$N(CH)_{lower}$ 10^{12} cm^{-2}	N_r	T_{ex} K
Control	3.68	3.68	1.000	−1370.19
Trial 1	3.87 ± 0.07	3.83 ± 0.07	0.988 ± 0.026	−13.74
Trial 2	3.73 ± 0.07	3.82 ± 0.07	1.022 ± 0.027	7.35
Trial 3	3.60 ± 0.07	3.65 ± 0.07	1.013 ± 0.027	12.08
Trial 4	3.67 ± 0.07	3.66 ± 0.07	0.996 ± 0.027	−36.93
Trial 5	3.64 ± 0.07	3.69 ± 0.07	1.014 ± 0.027	11.79

Table 4.6: Complex Doublet Parameters, Low Noise, Reversed

$T_{\text{ex}} = -1$ K				
Trial	N(CH)_{upper} 10^{12} cm^{-2}	N(CH)_{lower} 10^{12} cm^{-2}	N_r	T_{ex} K
Control	3.99	3.39	0.850	-0.98
Trial 1	4.00 ± 0.07	3.44 ± 0.07	0.860 ± 0.023	-1.06
Trial 2	4.03 ± 0.07	3.36 ± 0.07	0.834 ± 0.022	-0.88
Trial 3	3.95 ± 0.07	3.23 ± 0.07	0.817 ± 0.022	-0.79
Trial 4	4.10 ± 0.07	3.55 ± 0.07	0.866 ± 0.023	-1.11
Trial 5	3.88 ± 0.07	3.39 ± 0.07	0.875 ± 0.023	-1.20
$T_{\text{ex}} = -4$ K				
Trial	N(CH)_{upper} 10^{12} cm^{-2}	N(CH)_{lower} 10^{12} cm^{-2}	N_r	T_{ex} K
Control	3.76	3.60	0.958	-3.76
Trial 1	3.80 ± 0.07	3.53 ± 0.07	0.928 ± 0.025	-2.14
Trial 2	3.58 ± 0.07	3.41 ± 0.07	0.951 ± 0.026	-3.20
Trial 3	3.77 ± 0.07	3.50 ± 0.07	0.928 ± 0.025	-2.15
Trial 4	3.77 ± 0.07	3.55 ± 0.07	0.942 ± 0.025	-2.67
Trial 5	3.78 ± 0.07	3.64 ± 0.07	0.963 ± 0.026	-4.20
$T_{\text{ex}} = -15$ K				
Trial	N(CH)_{upper} 10^{12} cm^{-2}	N(CH)_{lower} 10^{12} cm^{-2}	N_r	T_{ex} K
Control	3.70	3.66	0.987	-12.07
Trial 1	3.78 ± 0.07	3.67 ± 0.07	0.970 ± 0.026	-5.18
Trial 2	3.56 ± 0.07	3.54 ± 0.07	0.994 ± 0.027	-25.24
Trial 3	3.82 ± 0.07	3.77 ± 0.07	0.988 ± 0.026	-13.42
Trial 4	3.80 ± 0.07	3.73 ± 0.07	0.981 ± 0.026	-8.37
Trial 5	3.77 ± 0.07	3.73 ± 0.07	0.989 ± 0.026	-14.40
$T_{\text{ex}} = -60$ K				
Trial	N(CH)_{upper} 10^{12} cm^{-2}	N(CH)_{lower} 10^{12} cm^{-2}	N_r	T_{ex} K
Control	3.69	3.67	0.995	-30.52
Trial 1	3.68 ± 0.07	3.63 ± 0.07	0.986 ± 0.026	-11.44
Trial 2	3.65 ± 0.07	3.57 ± 0.07	0.978 ± 0.026	-7.33
Trial 3	3.87 ± 0.07	3.86 ± 0.07	0.997 ± 0.026	-57.40
Trial 4	3.73 ± 0.07	3.70 ± 0.07	0.993 ± 0.026	-24.12
Trial 5	3.75 ± 0.07	3.78 ± 0.07	1.009 ± 0.027	18.49

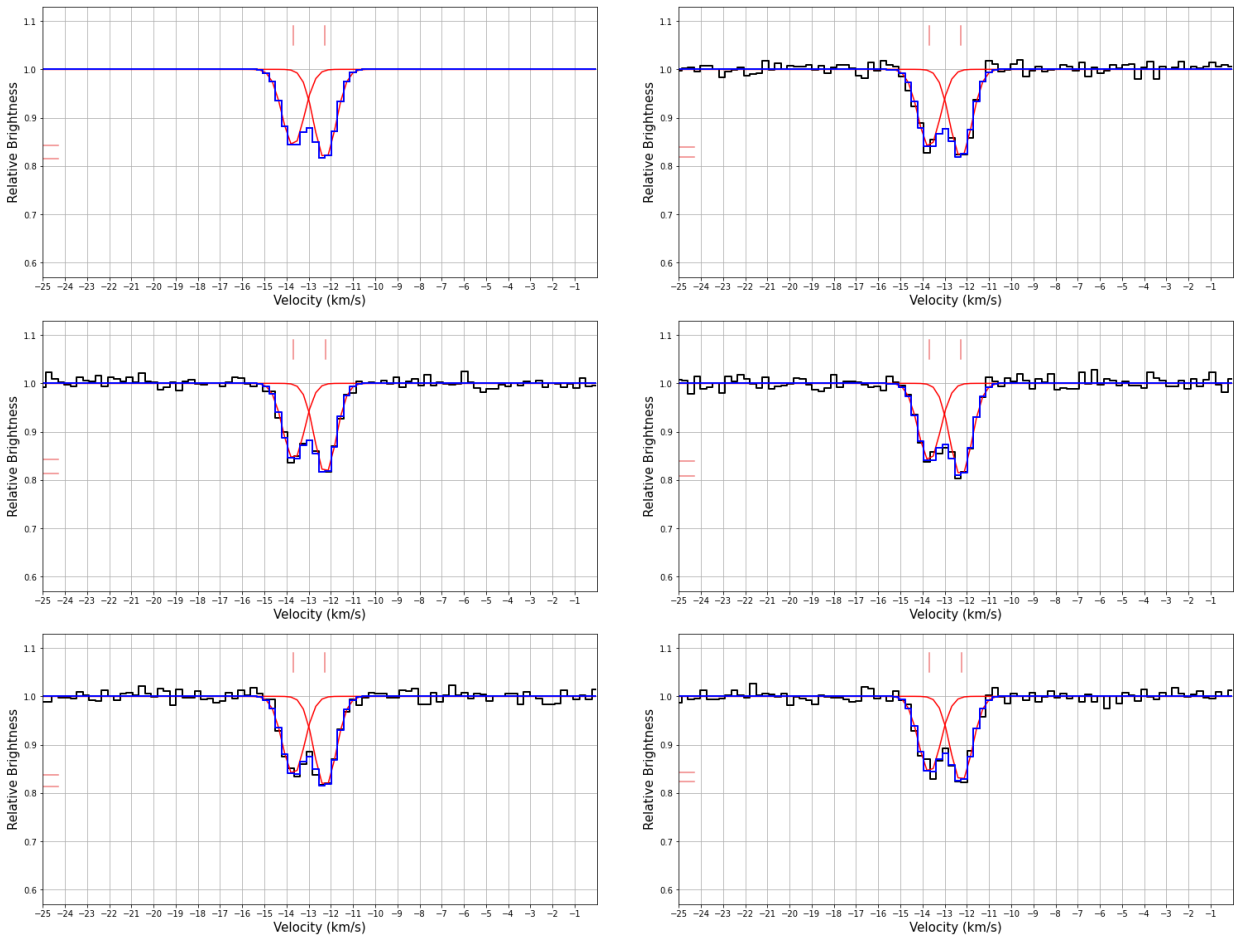

Figure 4.1a: Simple Doublet Spectra, -1 K

Spectra of the single component 4300 Å doublet with an excitation temperature of -1 K. The top-left image shows the control spectrum without noise, while the remaining spectra have an average rms of approximately 0.0101.

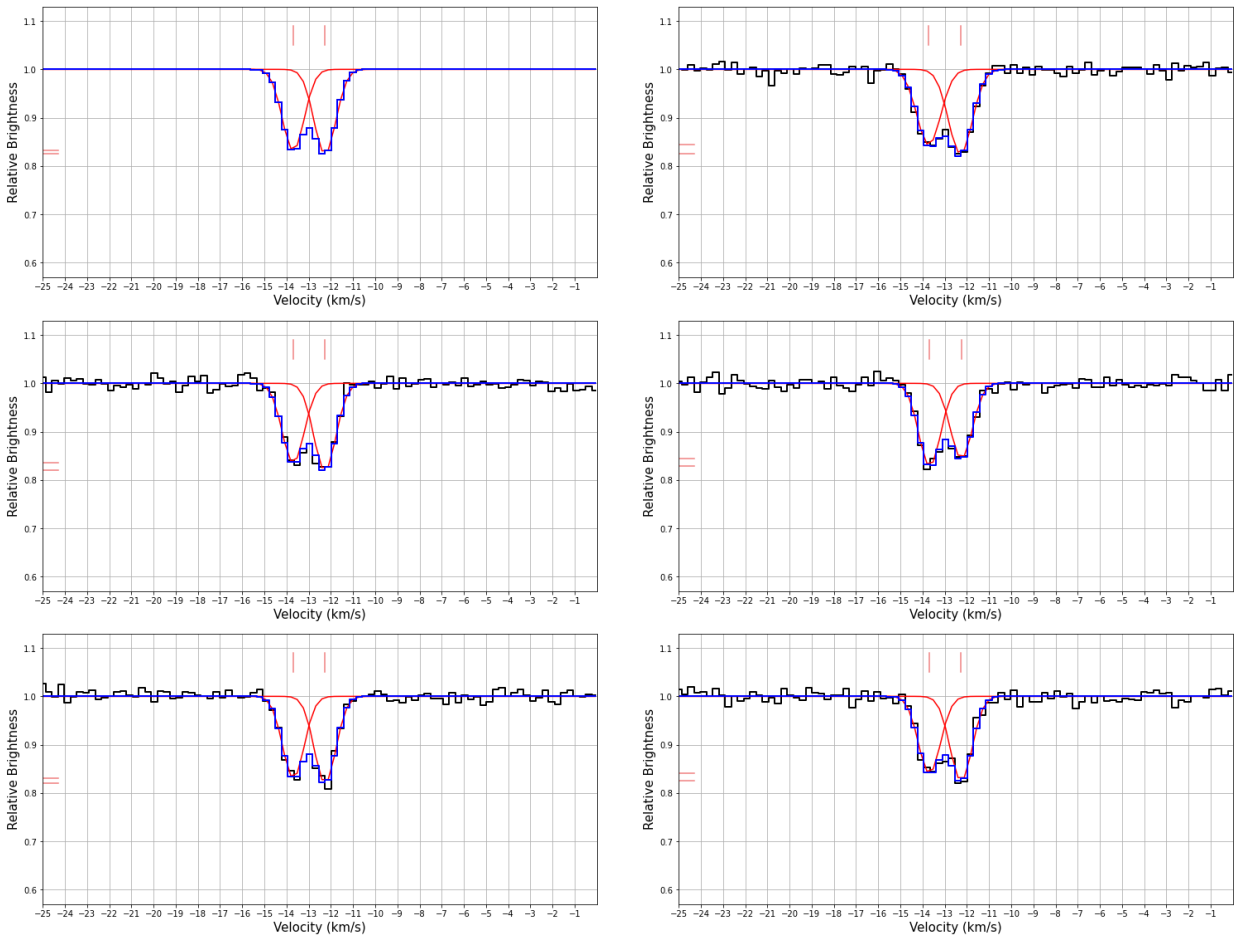

Figure 4.1b: Simple Doublet Spectra, -4 K

Spectra of the single component 4300 Å doublet with an excitation temperature of -4 K. The top-left image shows the control spectrum without noise, while the remaining spectra have an average rms of approximately 0.0101.

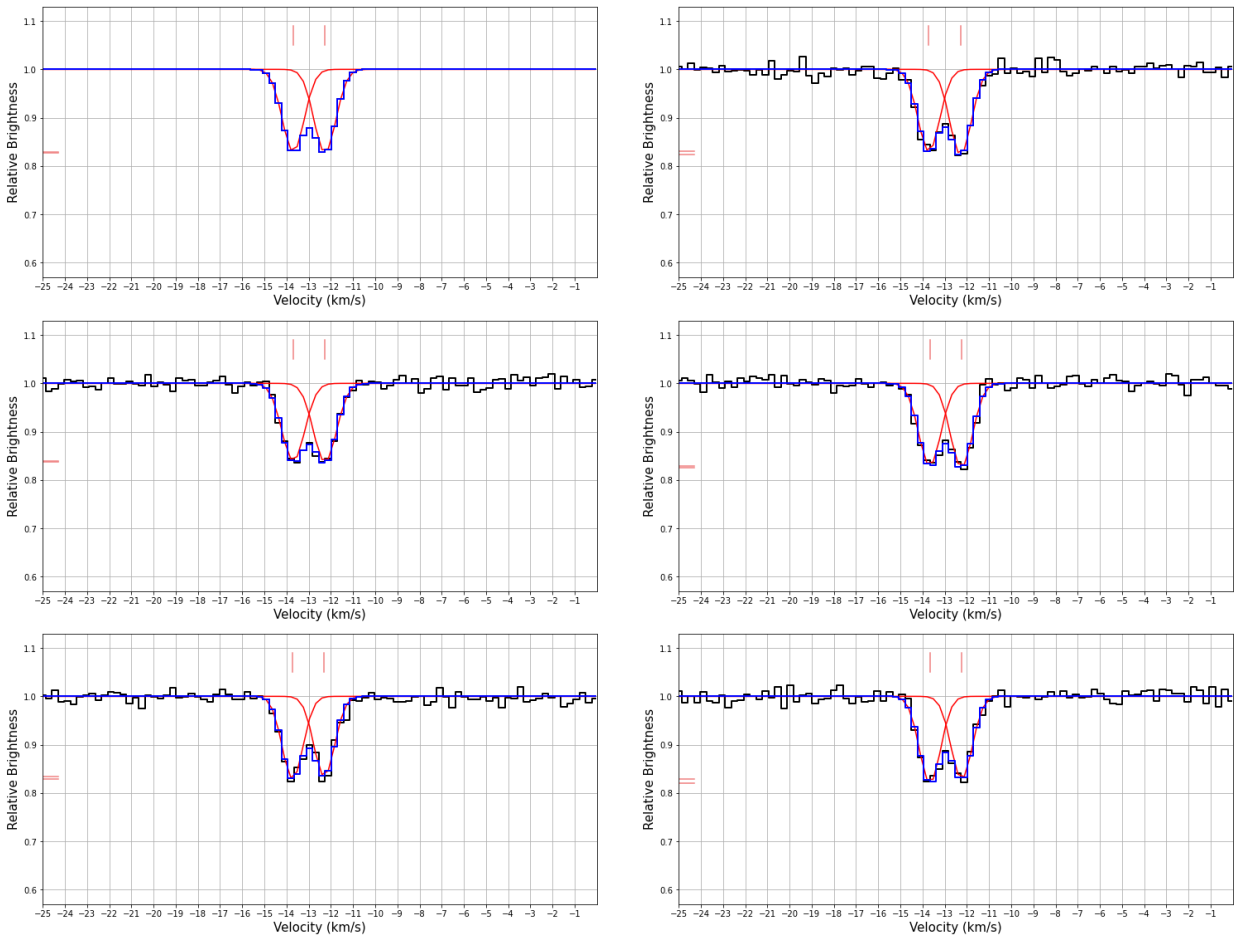

Figure 4.1c: Simple Doublet Spectra, −15 K

Spectra of the single component 4300 Å doublet with an excitation temperature of −15 K. The top-left image shows the control spectrum without noise, while the remaining spectra have an average rms of approximately 0.0101.

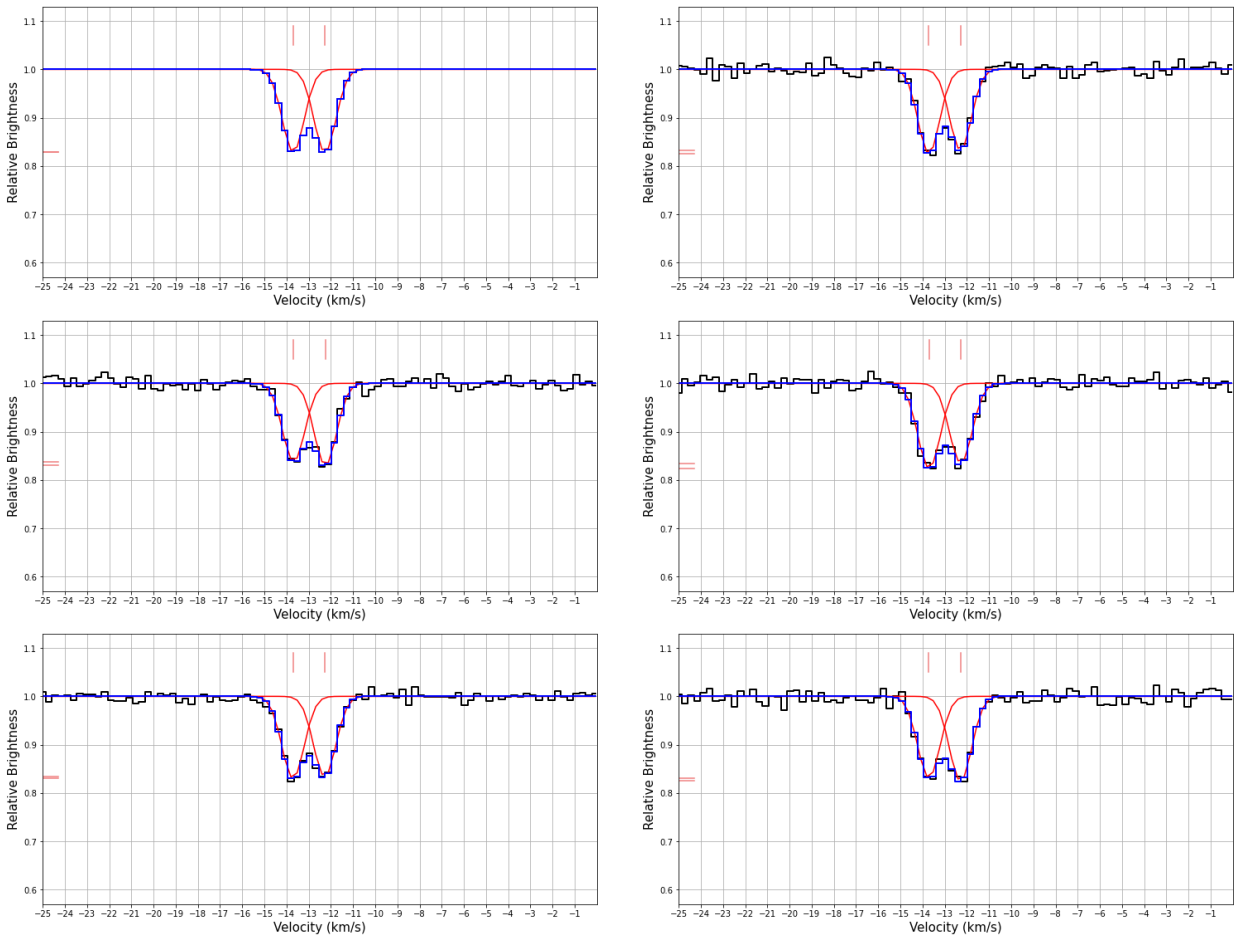

Figure 4.1d: Simple Doublet Spectra, −60 K

Spectra of the single component 4300 Å doublet with an excitation temperature of −60 K. The top-left image shows the control spectrum without noise, while the remaining spectra have an average rms of approximately 0.0101.

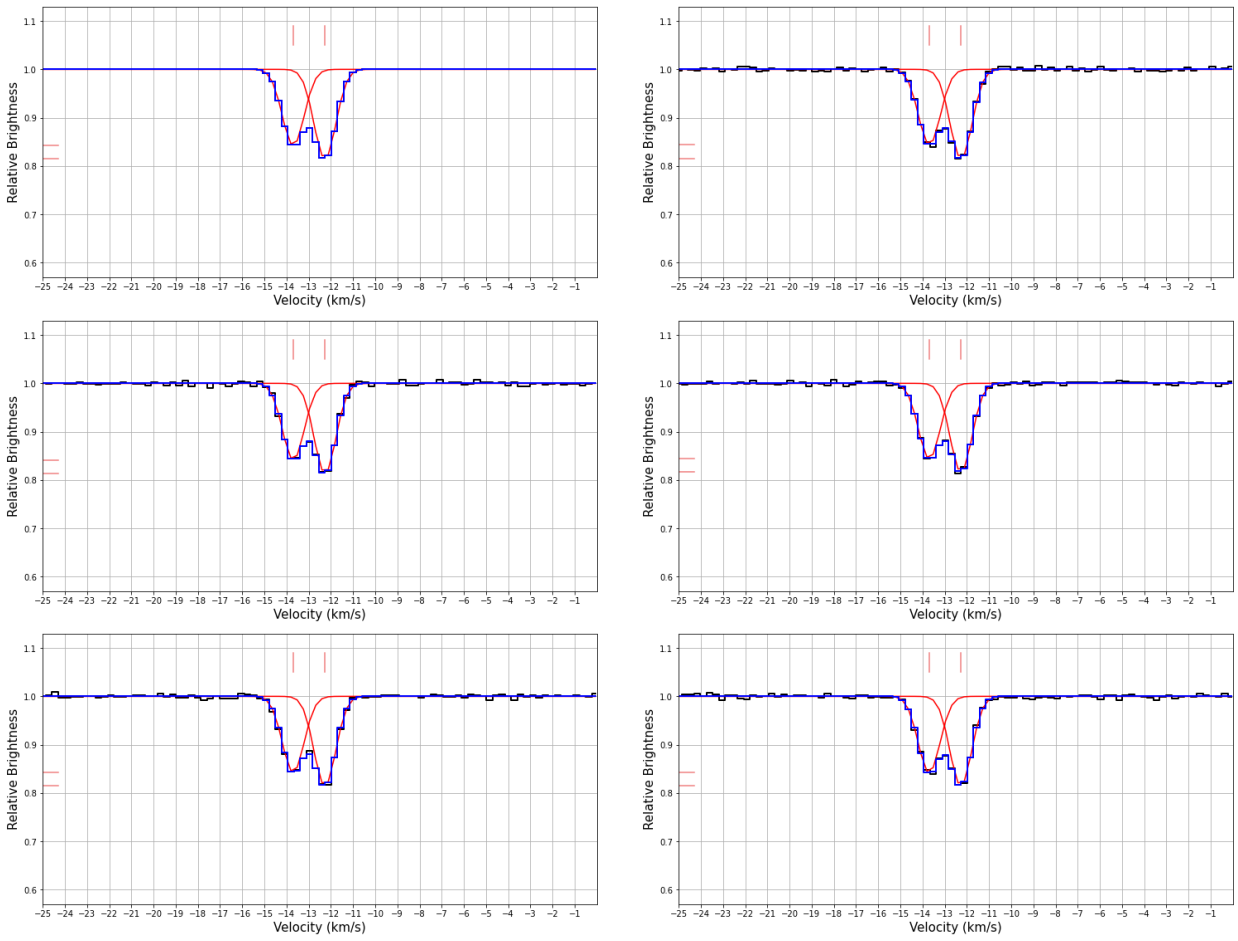

Figure 4.2a: Simple Doublet Spectra, -1 K, low noise

Spectra of the single component 4300 Å doublet with an excitation temperature of -1 K. The top-left image shows the control spectrum without noise, while the remaining spectra have an average rms of approximately 0.0032.

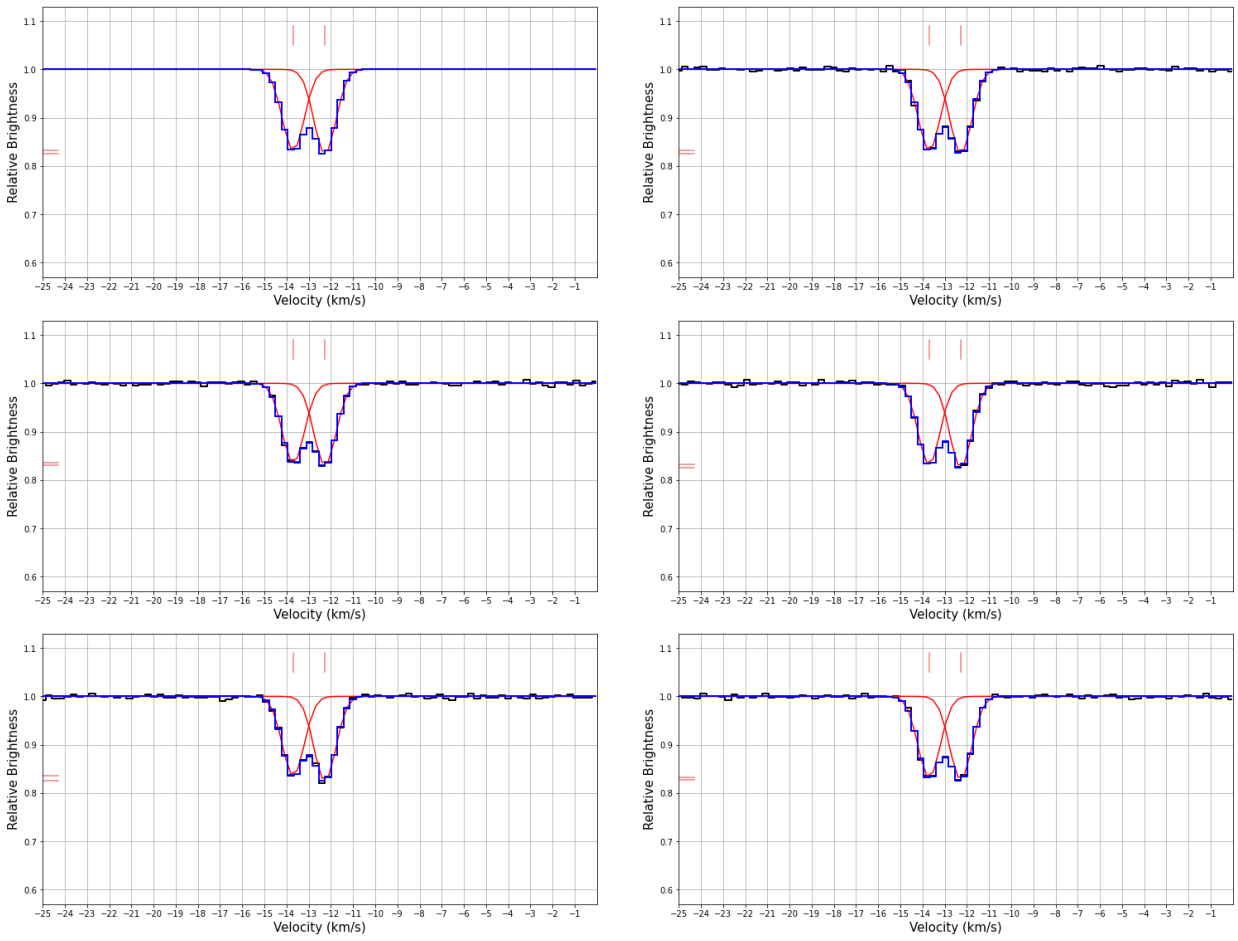

Figure 4.2b: Simple Doublet Spectra, -4 K, low noise

Spectra of the single component 4300 Å doublet with an excitation temperature of -4 K. The top-left image shows the control spectrum without noise, while the remaining spectra have an average rms of approximately 0.0032.

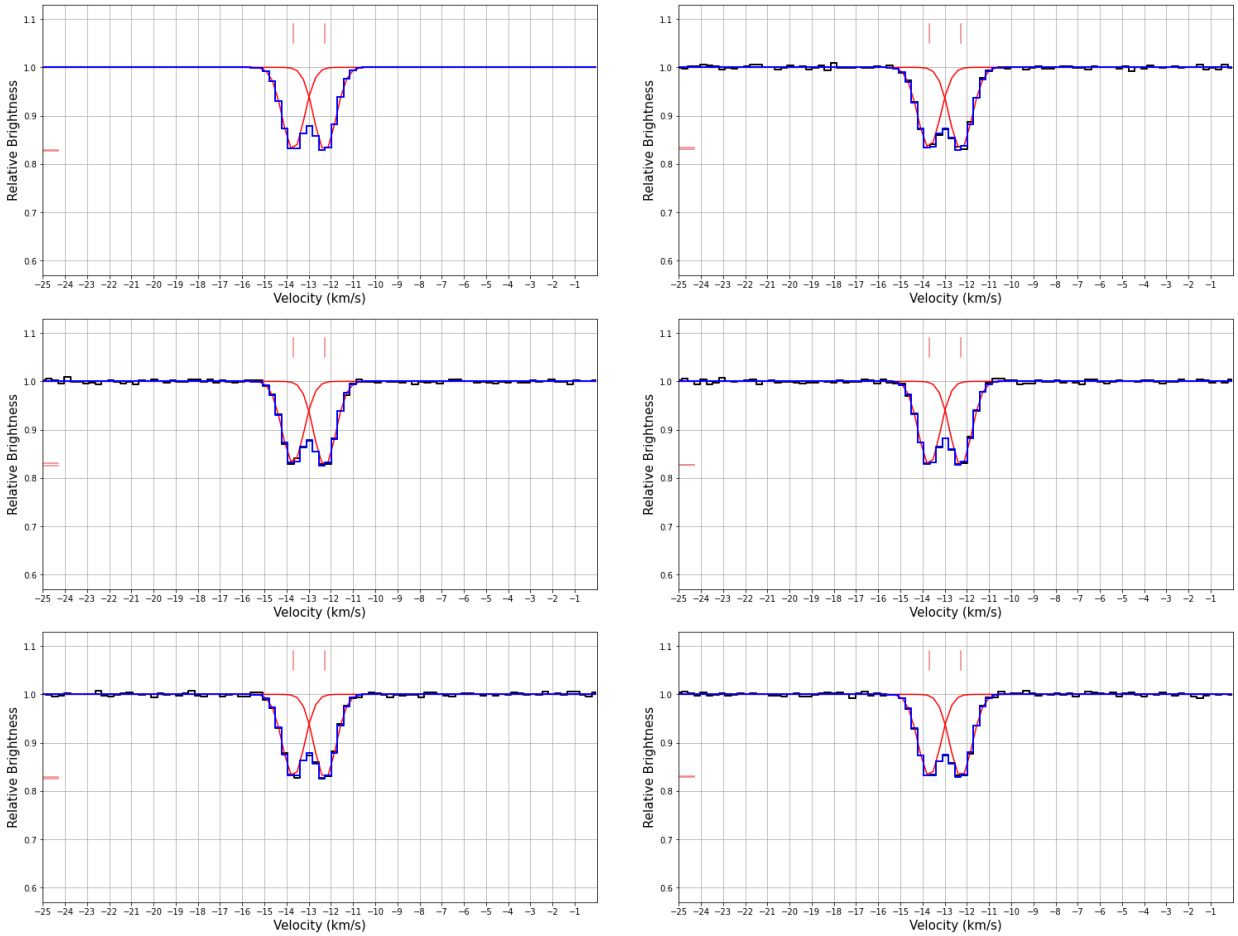

Figure 4.2c: Simple Doublet Spectra, −15 K, low noise

Spectra of the single component 4300 Å doublet with an excitation temperature of −15 K. The top-left image shows the control spectrum without noise, while the remaining spectra have an average rms of approximately 0.0032.

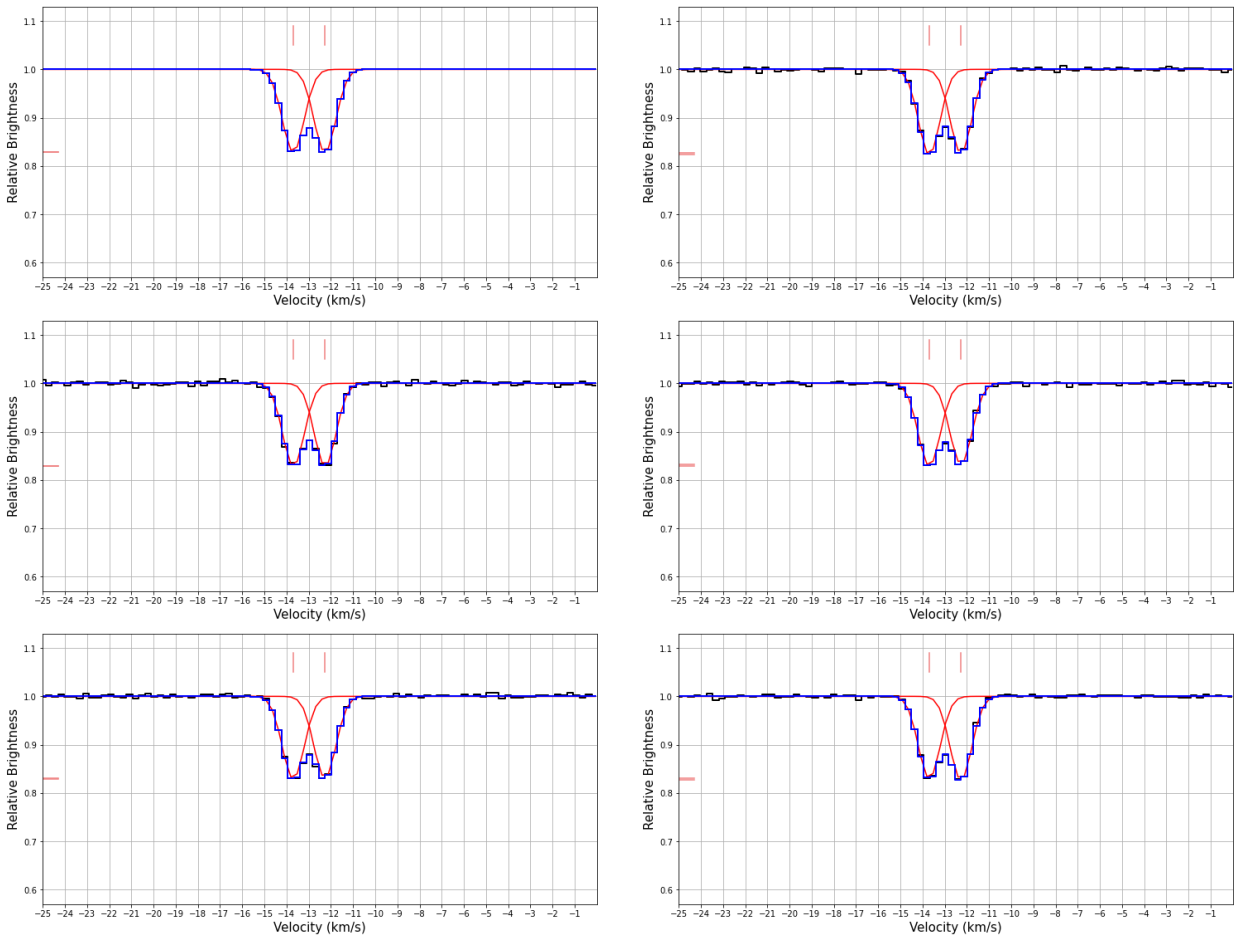

Figure 4.2d: Simple Doublet Spectra, −60 K, low noise

Spectra of the single component 4300 Å doublet with an excitation temperature of −60 K. The top-left image shows the control spectrum without noise, while the remaining spectra have an average rms of approximately 0.0032.

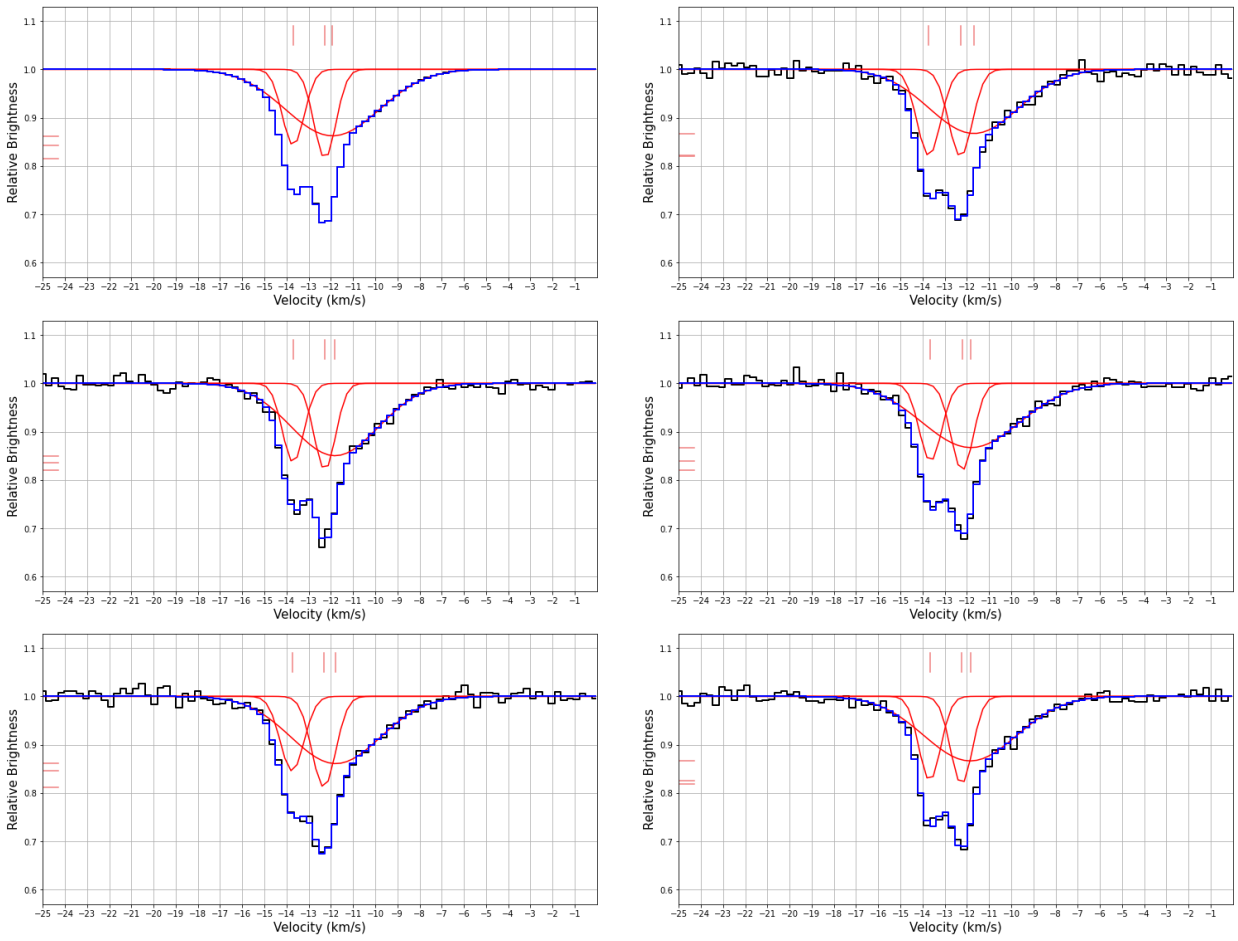

Figure 4.3a: Complex Doublet Spectra, -1 K

Spectra of the two component 4300 Å doublet with an excitation temperature of -1 K. The top-left image shows the control spectrum without noise, while the remaining spectra have an average rms of approximately 0.0101.

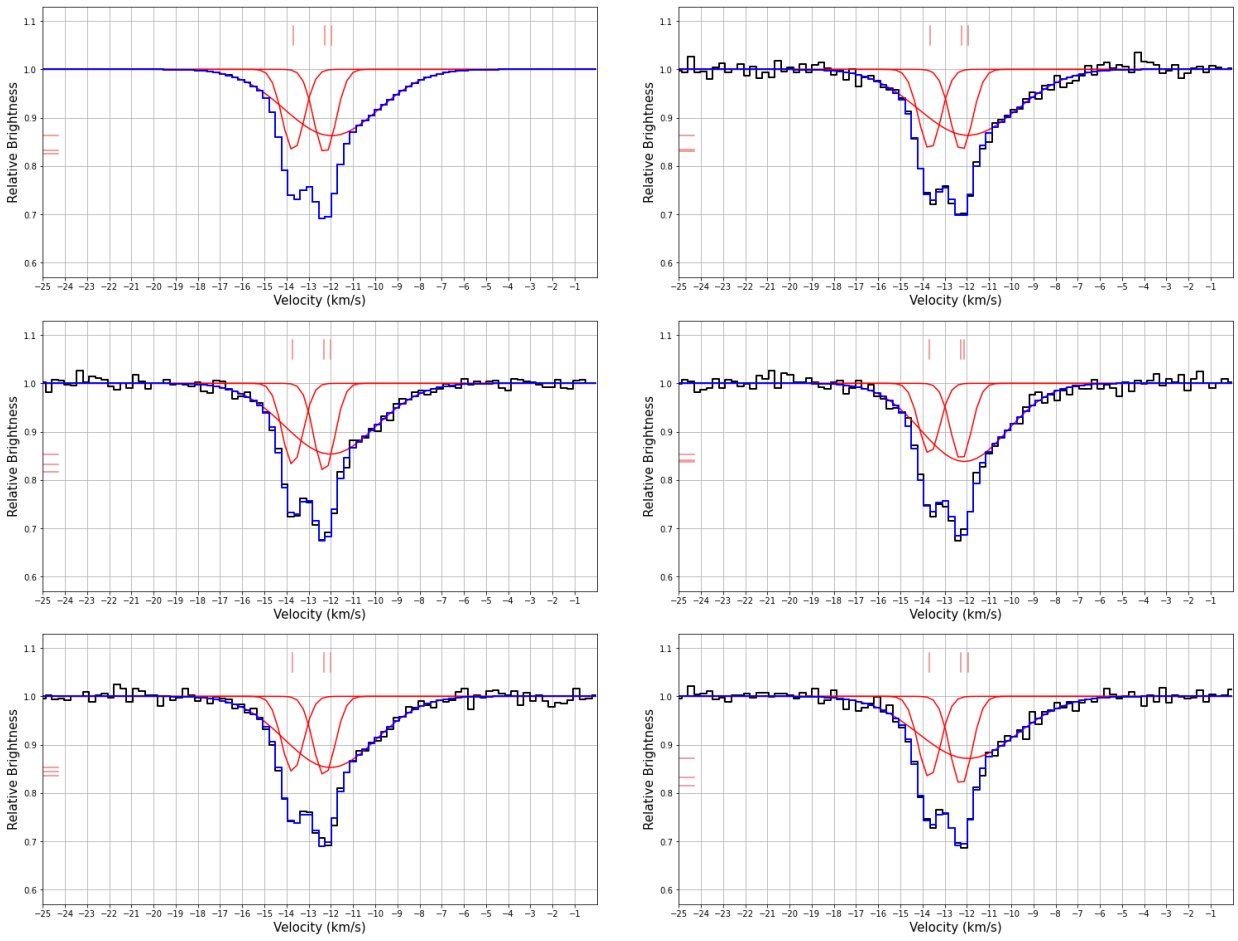

Figure 4.3b: Complex Doublet Spectra, -4 K

Spectra of the two component 4300 Å doublet with an excitation temperature of -4 K. The top-left image shows the control spectrum without noise, while the remaining spectra have an average rms of approximately 0.0101.

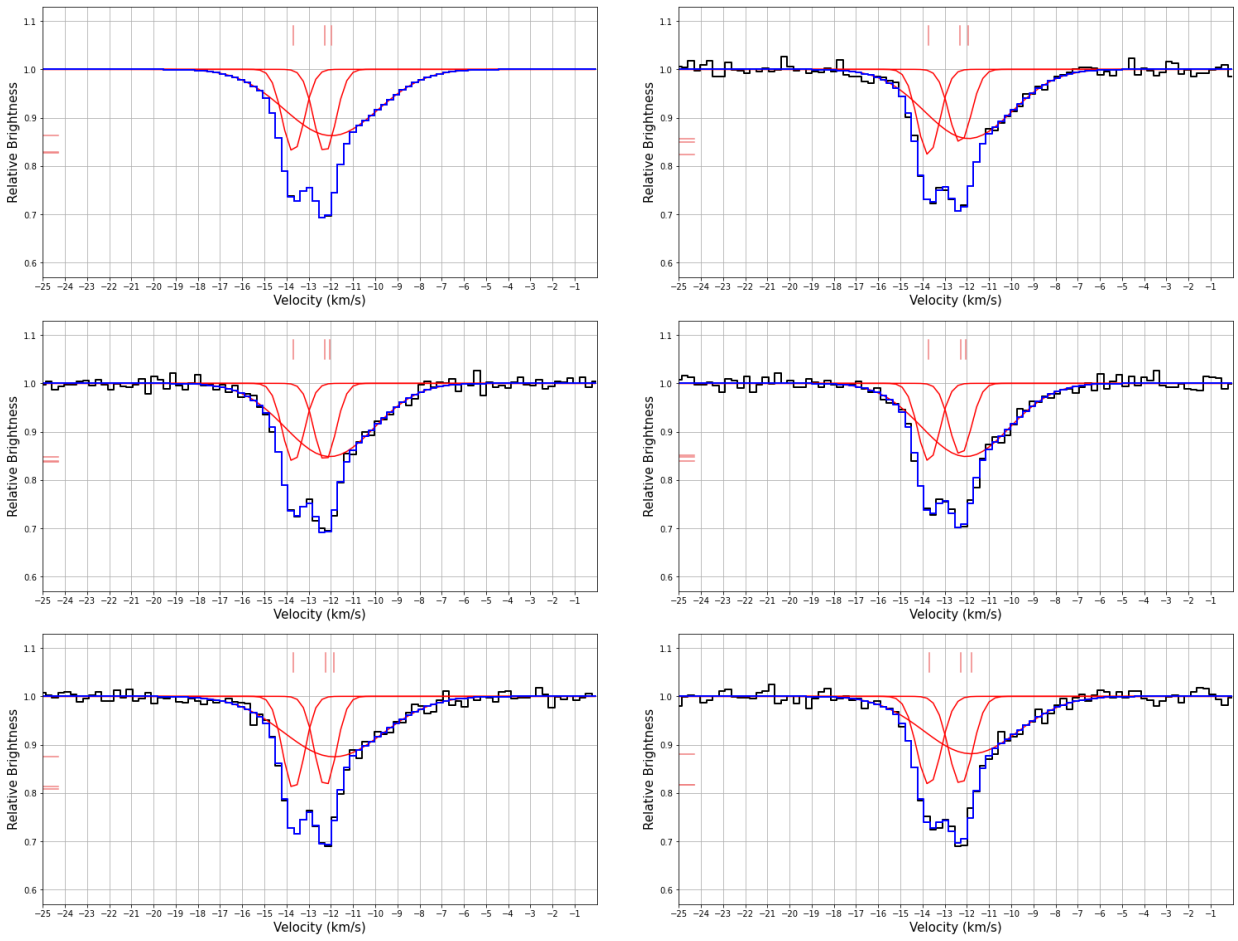

Figure 4.3c: Complex Doublet Spectra, −15 K

Spectra of the two component 4300 Å doublet with an excitation temperature of −15 K. The top-left image shows the control spectrum without noise, while the remaining spectra have an average rms of approximately 0.0101.

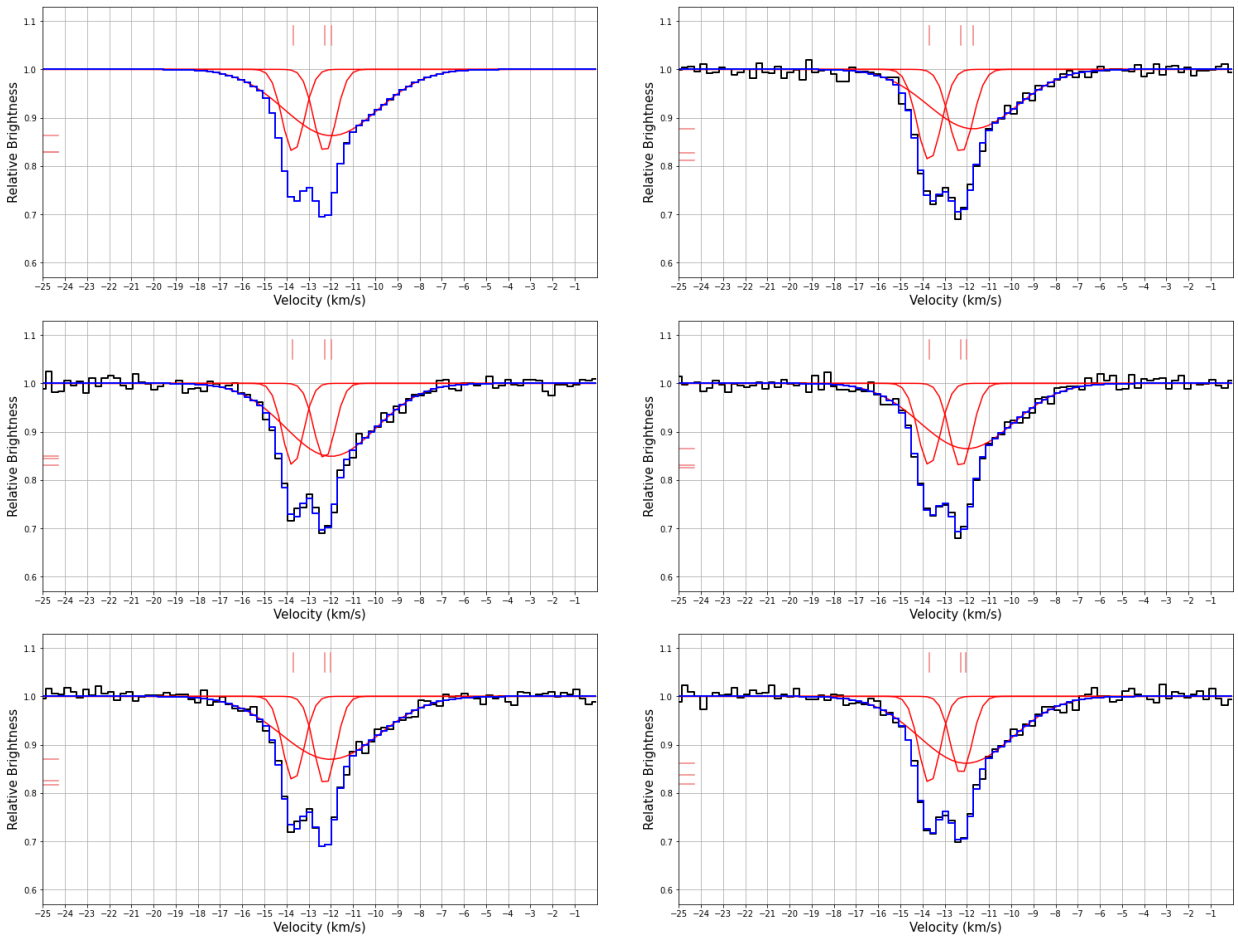

Figure 4.3d: Complex Doublet Spectra, −60 K

Spectra of the two component 4300 Å doublet with an excitation temperature of −60 K. The top-left image shows the control spectrum without noise, while the remaining spectra have an average rms of approximately 0.0101.

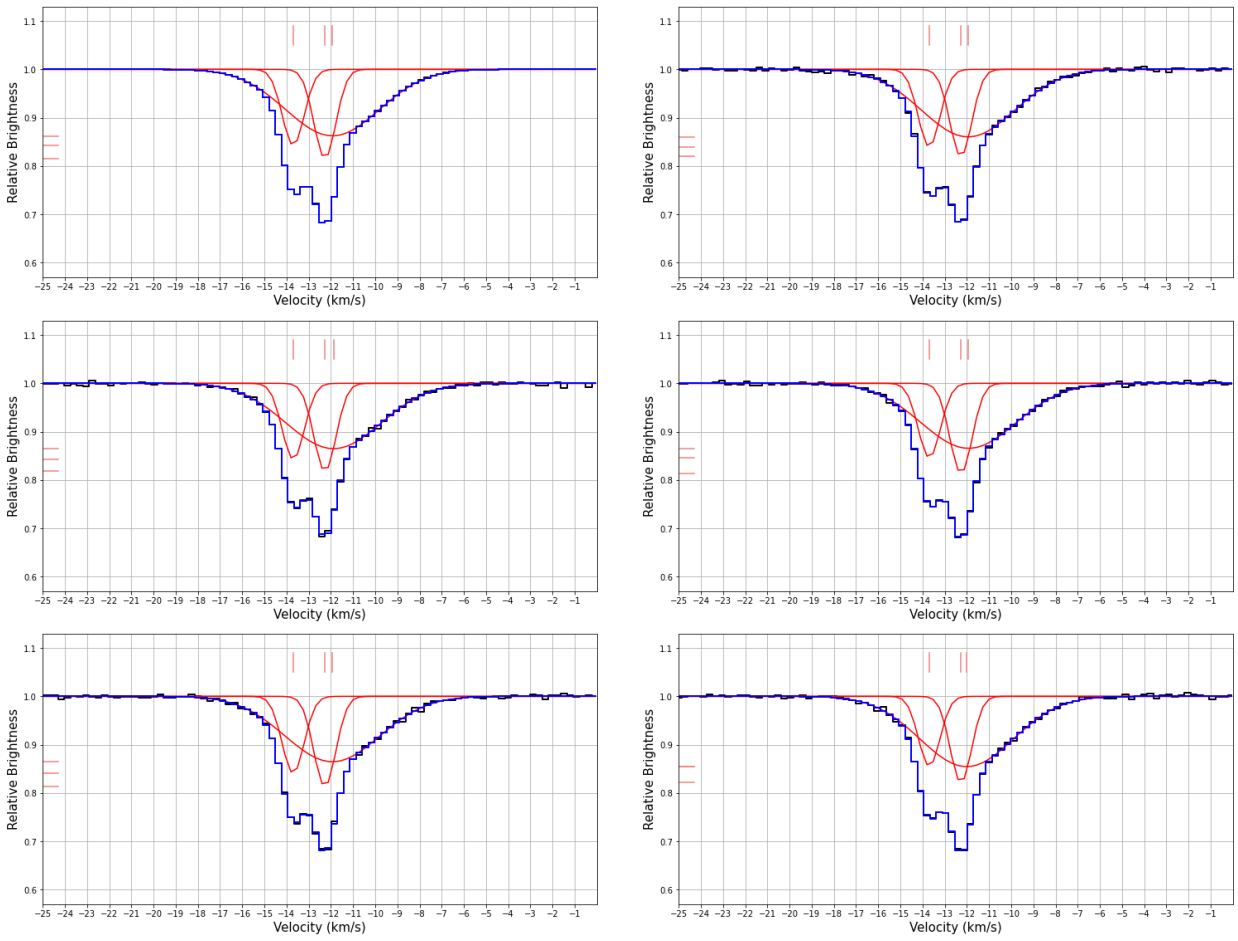

Figure 4.4a: Complex Doublet Spectra, -1 K, low noise

Spectra of the two component 4300 Å doublet with an excitation temperature of -1 K. The top-left image shows the control spectrum without noise, while the remaining spectra have an average rms of approximately 0.0032.

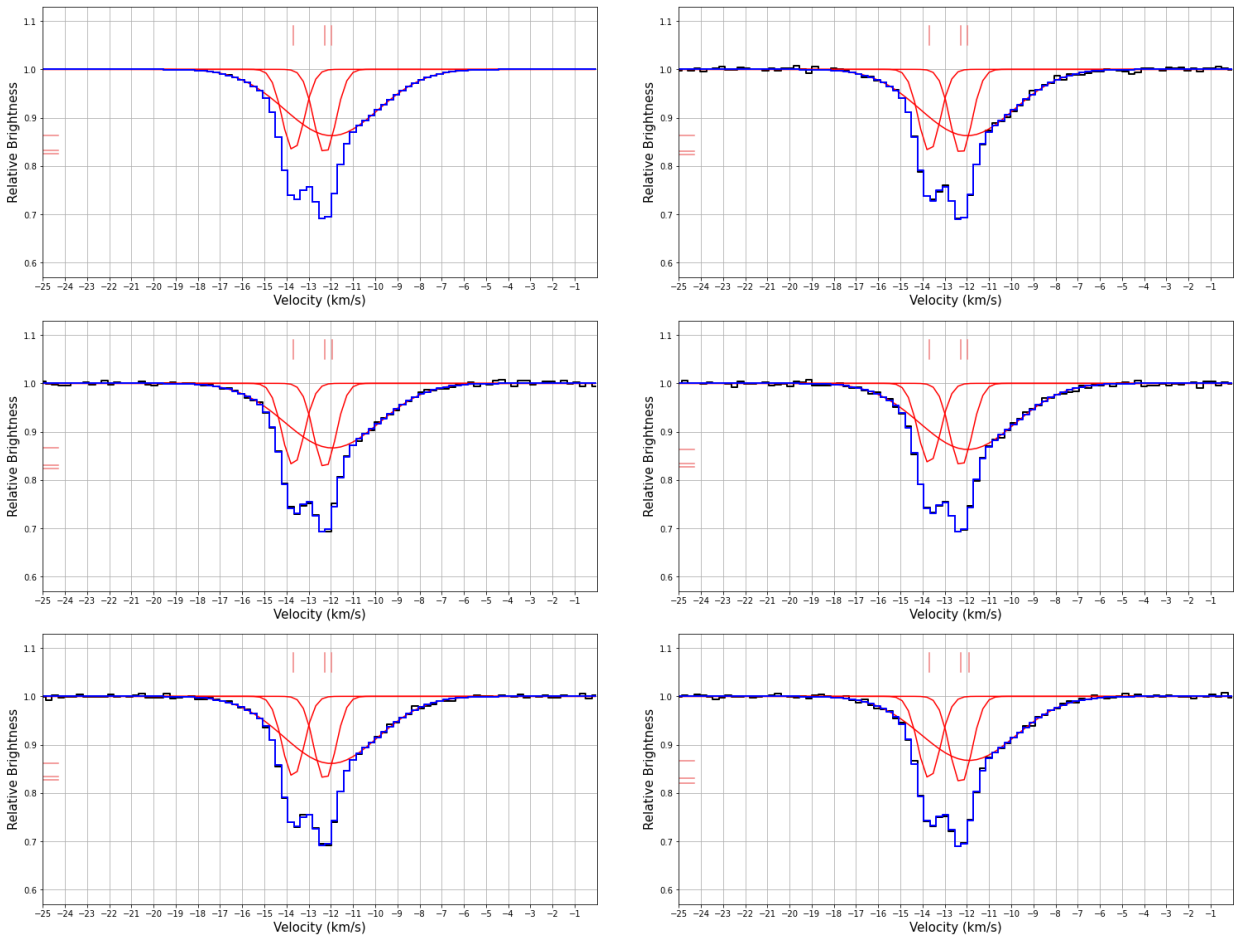

Figure 4.4b: Complex Doublet Spectra, -4 K, low noise

Spectra of the two component 4300 Å doublet with an excitation temperature of -4 K. The top-left image shows the control spectrum without noise, while the remaining spectra have an average rms of approximately 0.0032.

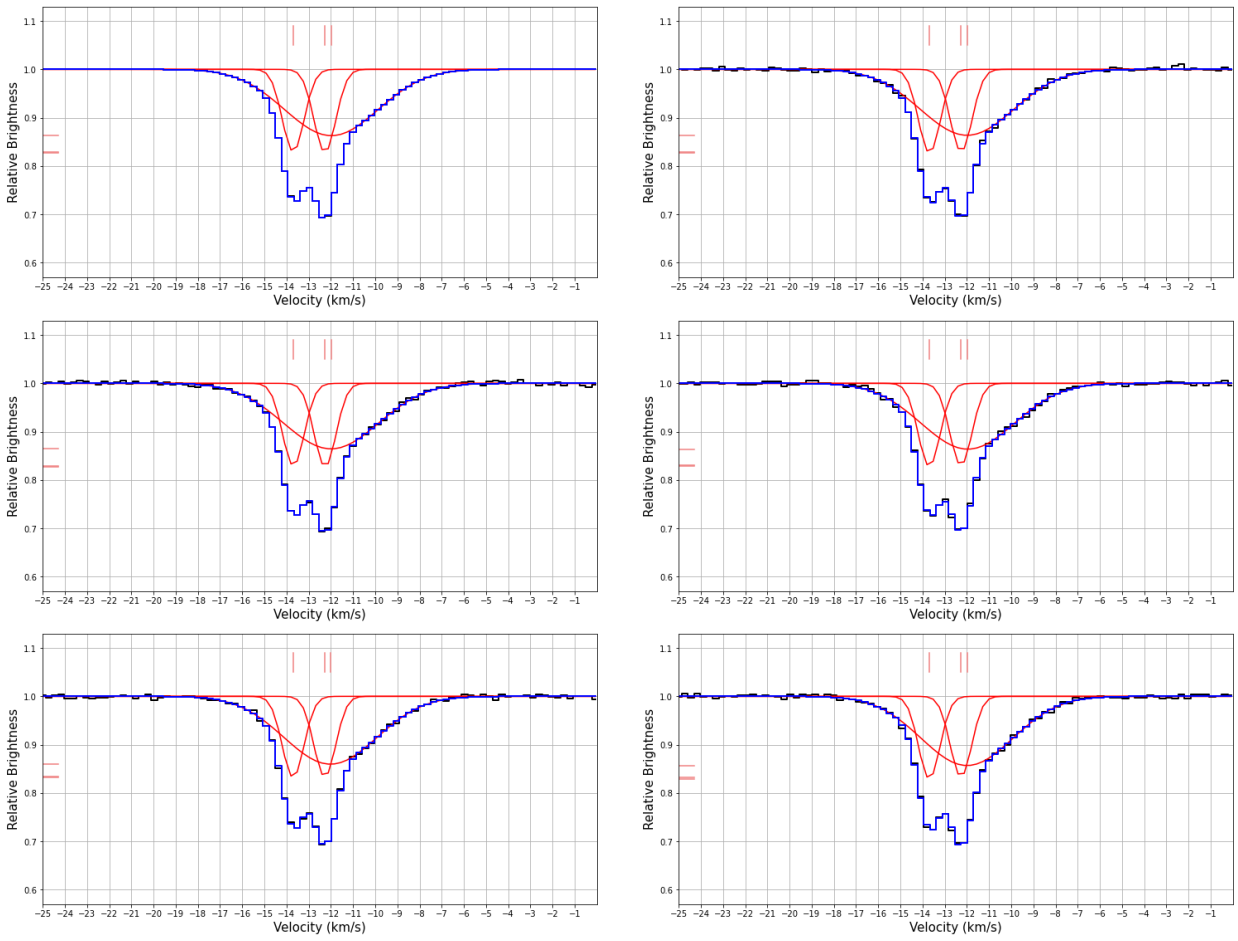

Figure 4.4c: Complex Doublet Spectra, -15 K, low noise
Spectra of the two component 4300 Å doublet with an excitation temperature of -15 K. The top-left image shows the control spectrum without noise, while the remaining spectra have an average rms of approximately 0.0032.

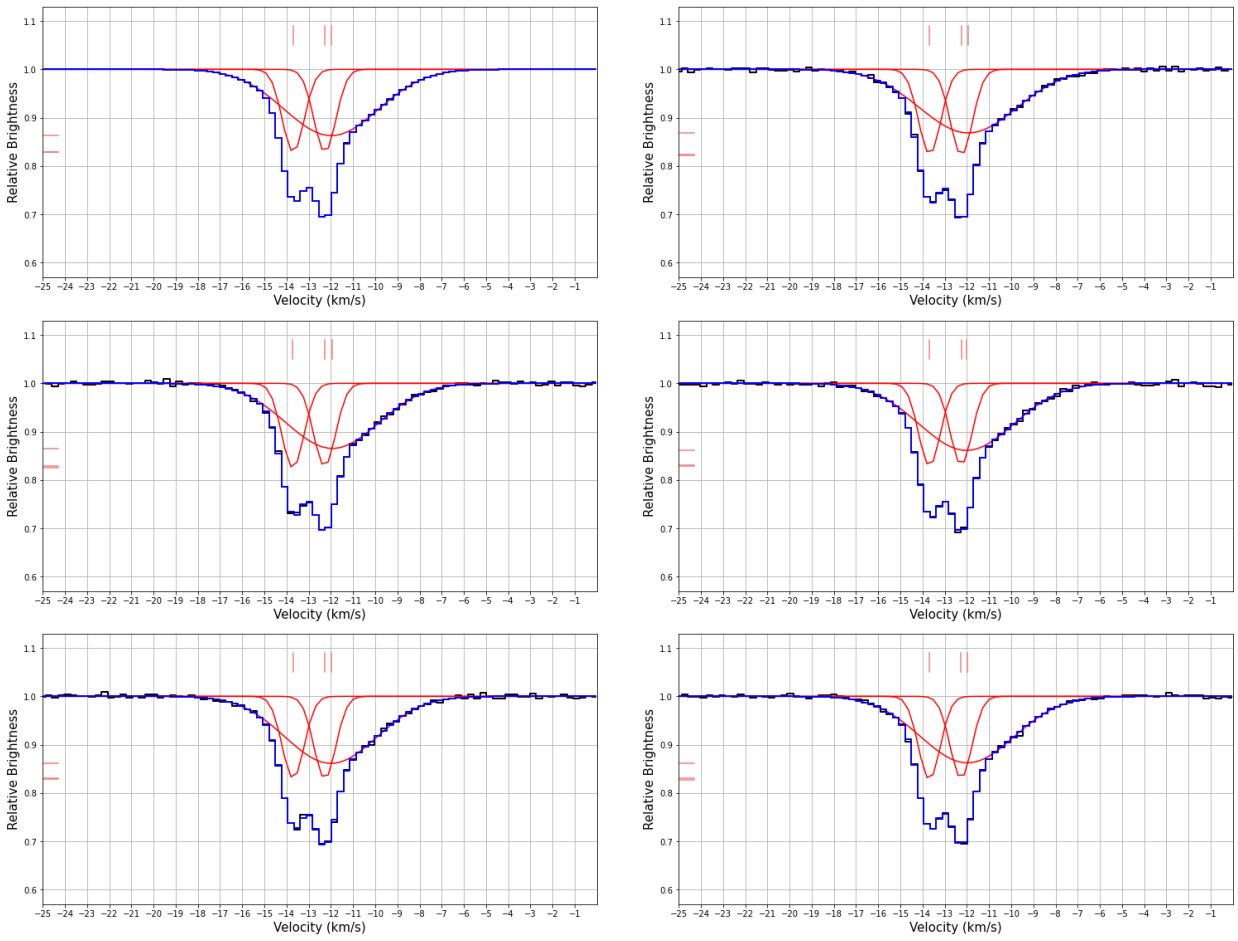

Figure 4.4d: Complex Doublet Spectra, −60 K, low noise

Spectra of the two component 4300 Å doublet with an excitation temperature of −60 K. The top-left image shows the control spectrum without noise, while the remaining spectra have an average rms of approximately 0.0032.

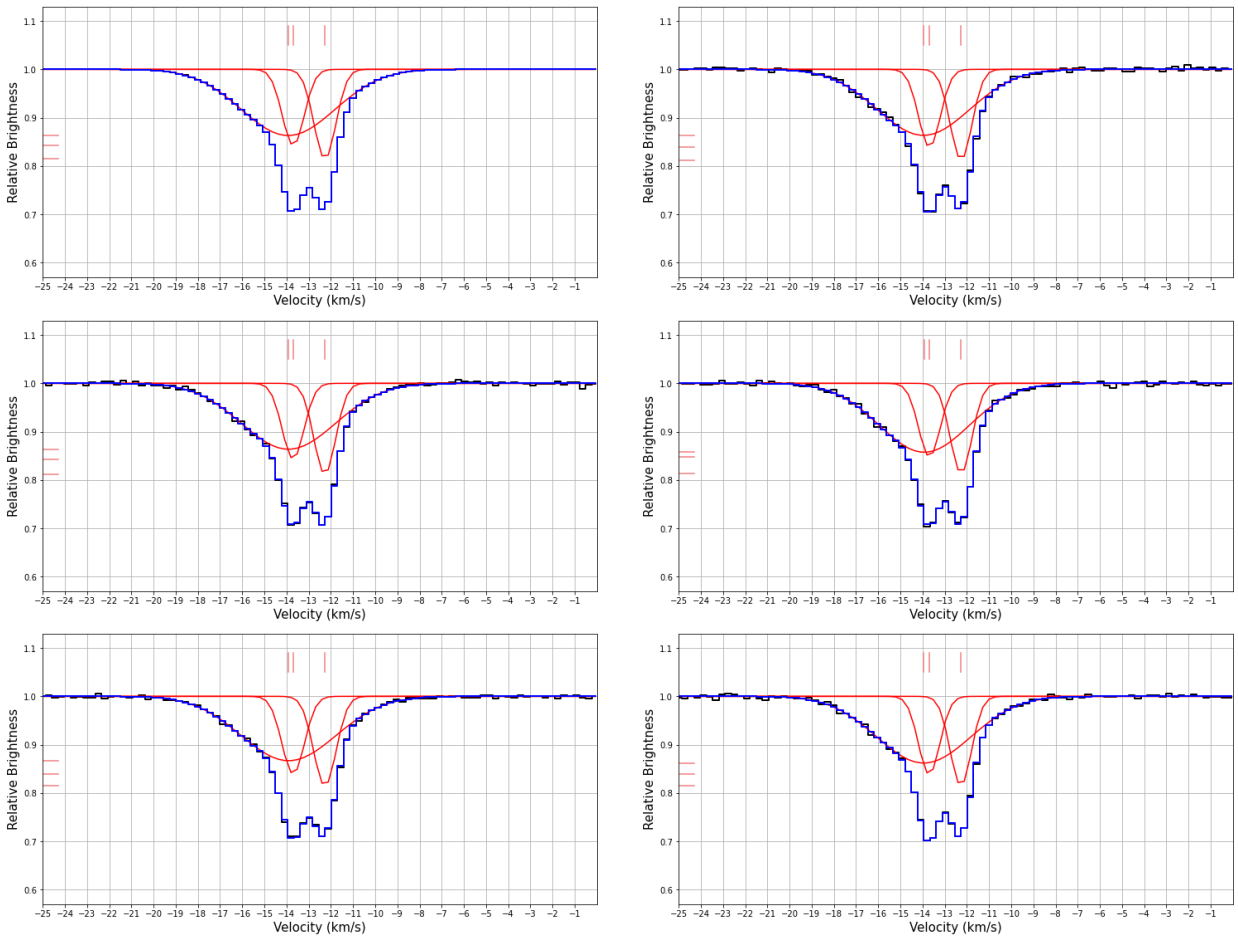

Figure 4.5a: Reversed Complex Doublet Spectra, -1 K, low noise
Spectra of the reversed two component 4300 Å doublet with an excitation temperature of -15 K. The top-left image shows the control spectrum without noise, while the remaining spectra have an average rms of approximately 0.0032.

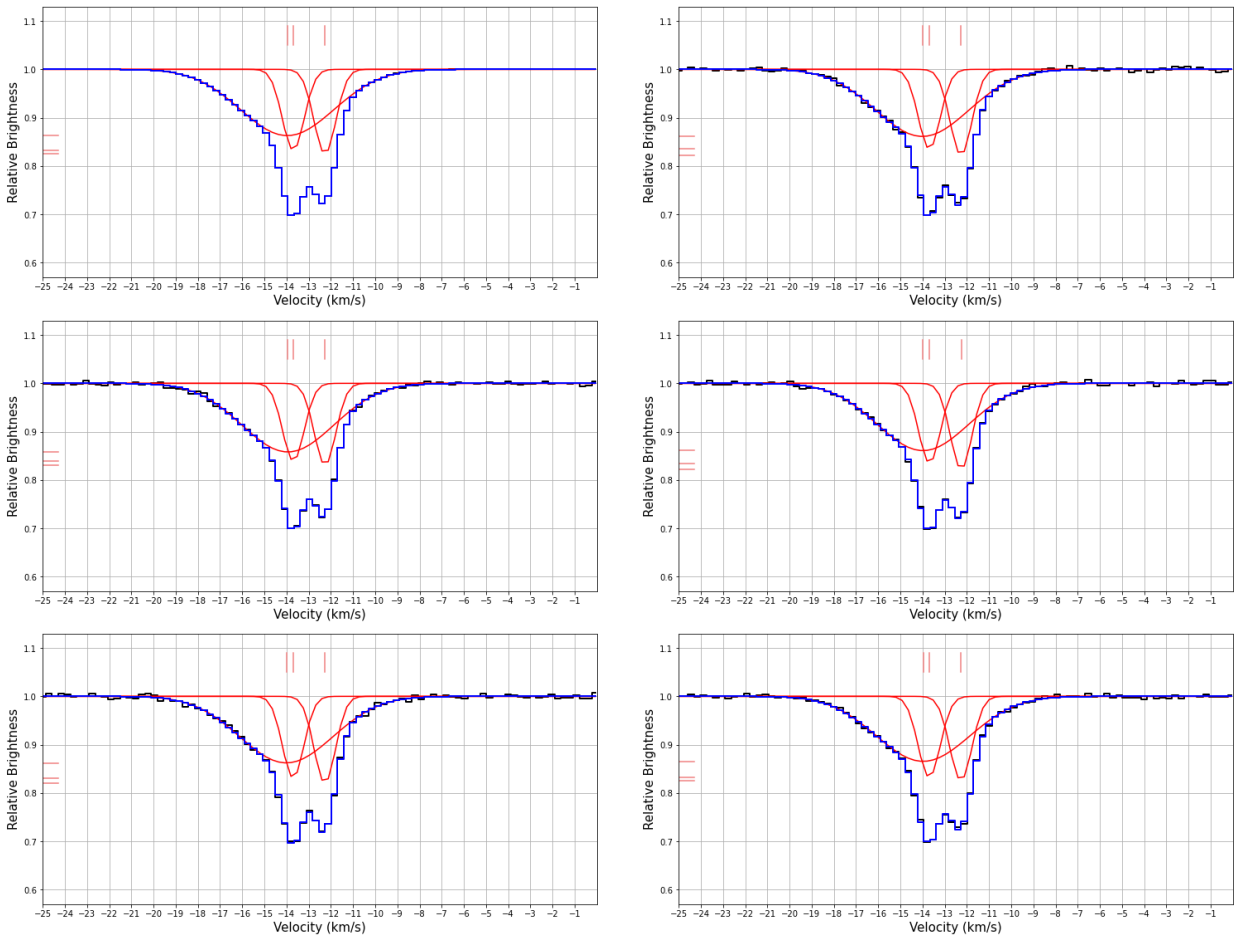

Figure 4.5b: Reversed Complex Doublet Spectra, -4 K, low noise
Spectra of the reversed two component 4300 Å doublet with an excitation temperature of -15 K. The top-left image shows the control spectrum without noise, while the remaining spectra have an average rms of approximately 0.0032.

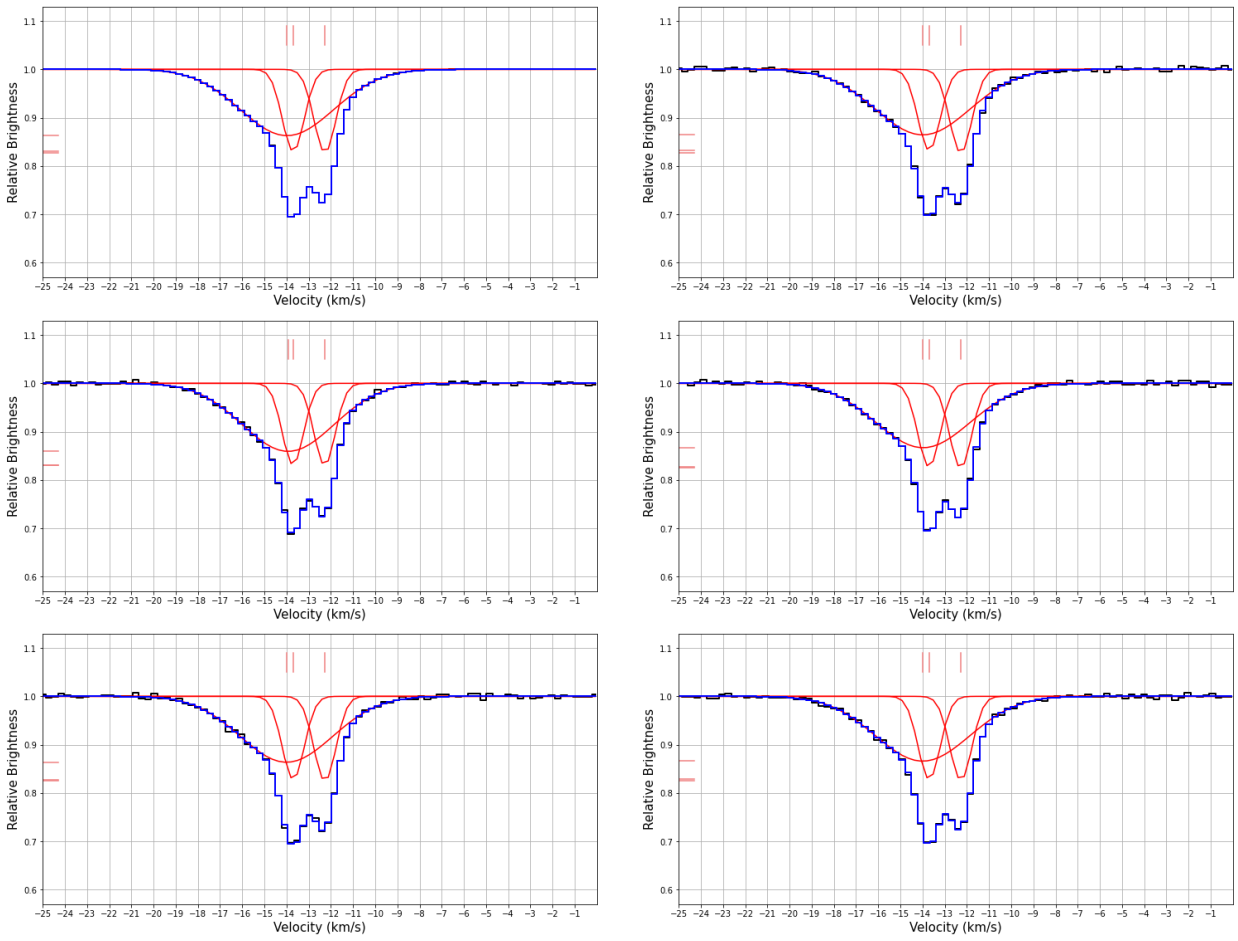

Figure 4.5c: Reversed Complex Doublet Spectra, −15 K, low noise
Spectra of the reversed two component 4300 Å doublet with an excitation temperature of −15 K. The top-left image shows the control spectrum without noise, while the remaining spectra have an average rms of approximately 0.0032.

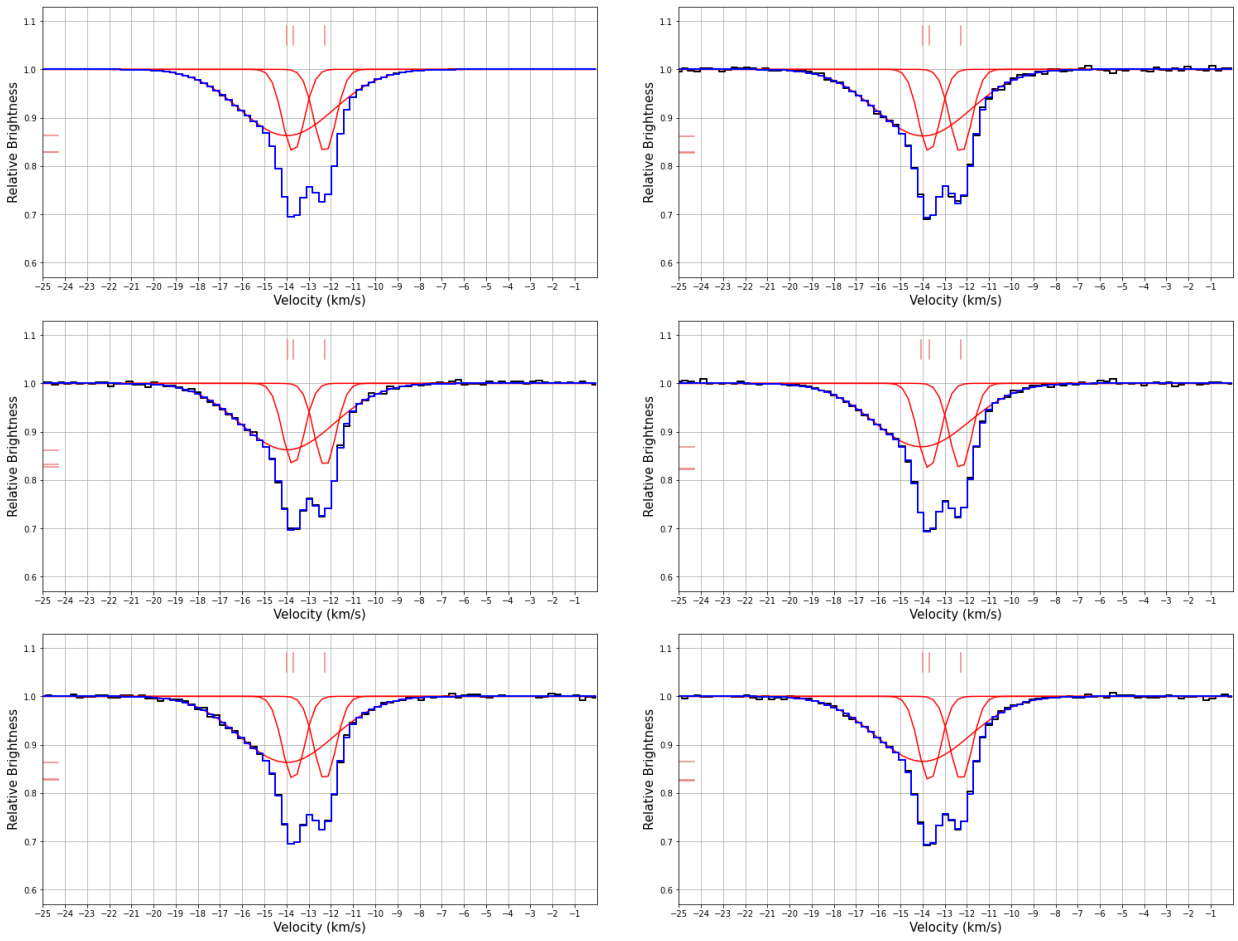

Figure 4.5d: Reversed Complex Doublet Spectra, −60 K, low noise
Spectra of the reversed two component 4300 Å doublet with an excitation temperature of −60 K. The top-left image shows the control spectrum without noise, while the remaining spectra have an average rms of approximately 0.0032.

Chapter 5

Methylidyne and Carbon Monoxide Emission in MBM 16

5.1 Introduction

MBM 16 is one of the larger high-latitude molecular clouds from the Magnani, Blitz, and Mundy (1985) catalog. It is located in Aries and is about 20° southeast of the Taurus-Auriga dark cloud complex. A CO($1-0$) map of the entire cloud can be found in Magnani et al. (2003). Analysis by Truong, Magnani, and Hartmann (1997) determined that the cloud has a mass of 320 ± 190 $M_\odot$, and that it is not gravitationally bound. Early estimates of the cloud distance placed the cloud nearby, with Hobbs et al. (1988) estimating the distance to be $60 - 95$ pc, while Kuntz, Snowden, and Verter (1997) estimated the distance to be 100 pc. Recently, estimates based on the extinction to stars with known distances have shown that MBM 16 is further away than originally thought. Schlafly et al. (2014) determined that the cloud is 147^{+10}_{-9} pc away, and Zucker et al. (2019) have determined that it is further away at 170 ± 8

pc, which would increase the estimated mass by a factor of 5, compared to the mass at 80 pc. There is a small clump of CO-bright gas at an RA, Dec of approximately 03:19:04, 11:30:52 (J2000) which was identified by Magnani (1987) and is not visible in the dust maps by Schlegel, Finkbeiner, and Davis (1998) and Schlafly and Finkbeiner (2011) (see figure 5.1). The clump, if defined as the region with CO($1-0$) antenna temperature greater than 1.5 K, covers a 4 by 7 arcminute area (Magnani et al. 1990), which at 170 pc corresponds to a 0.6 by 1.0 pc region.

CH and CO observations of MBM 16 at 3.3 GHz and 115 GHz show that the CH lines are wider than CO lines observed in the same area. In this chapter, CH and CO observations of the clump in MBM 16 are compared to determine if the two molecules trace the same gas or if they trace different portions of the cloud. It is possible that CH traces the warm diffuse gas surrounding the clump and does not trace the colder gas inside of the clump well, due to CH being used to create more complex molecules in shielded, opaque, high-density regions. N(CH) increases with N(H_2) linearly up to approximately $4-5\times10^{21}$ cm^{-2} , where N(CH) will level off (Mattila 1986; also see figure 5.2). CO is able to trace gas at higher N(H_2) column densities, and the colder gas in the clump will cause less thermal line broadening in the CO spectra relative to the CH spectra, which likely samples the warmer diffuse gas surrounding the clump.

5.2 Observations

The data used in this chapter were collected using the Arecibo 305-m radio telescope as part of projects A1659 and A1708 in 2002. This data were taken by Loris Magnani and Raymond Chastain but were never analyzed or published. The observations used the Interim Correlator with a bandwidth of 0.781 MHz and 1024 channels. For all of the lines of sight except cn2 (see Table 5.1), the center frequency is set

to 3335.7 MHz for boards 1 and 2. The positions along the north-south and east-west axes of the clump described above are listed in table 5.1 and shown in figure 5.1. With the cn2 position, the center frequency for boards 1 and 2 is 3335.5 MHz. The CH main hyperfine line is at 3335.479 MHz, so cn2 has the correct velocity for that frequency, but the observed peak from cn2 does not align with other observations of the cloud (which are at the correct frequency). The observed peaks using a center frequency of 3335.7 MHz align with previous observations in the literature (Magnani et al. 2003). Thus, the cn2 velocities are adjusted by 17.96 km s^{-1} to account for the 0.2 MHz change in the center frequency, but the spectrum in figure 5.3 is not adjusted. Boards 3 and 4 are centered inconsistently in frequency between the various days of the observations, sometimes even for an individual line of sight, and are ignored for this chapter. Those boards were originally meant to trace the satellite or search for other molecular species in the frequency range of the receiver.

5.3 Results

Table 5.2 contains the CH derived data, with the first column listing the observed lines of sight. The second column is the velocity-integrated antenna temperature, W(CH), determined from the number of channels the line occupies and the sum of the channels (e.g., Mangum and Shirley 2015). W(CH) is adjusted by the beam efficiency, $\eta_{\rm b}$, is 0.6 ± 0.1. The fourth, fifth, and sixth columns are the antenna temperature, line width, and the center velocity of the line as determined from a gaussian fit. The CH column density, N(CH), is in column 7 and is calculated using equation 3.1, where $[T_{\rm ex}/(T_{\rm ex} - T_{\rm bg})]$ is considered to be 0.57 ± 0.07[1]. The filling factor is assumed to be 1. The H_2 column density is in column 8, and is converted from the CH column density with the ratio obtained in figure 2.18, N(CH)/N(H_2)

[1]The reason for this value is discussed in chapter 2.

$= 4.75 \pm 3.42 \times 10^{-8}$. The standard deviation of the slope accounts for the variation in the excitation temperature and the spread in N(CH)/N(H_2).

CO observations of MBM 16 from table 2 of Magnani et al. (1990) are used to compare with the CH data, and the data are reproduced in table 5.3. Similar to table 5.2, the first column lists the lines of sight, the second lists W(CO), the fourth lists the antenna temperatures, the fifth lists the line widths, and the sixth lists the line center velocities. However, W(CO) is determined by:

$$W(CO) = 1.066\, T_{\rm R}\, \Delta v \tag{5.1}$$

where the uncertainty of W(CO) assumes that the uncertainty in $T_{\rm R}$ and Δv are uncorrelated. The rms values for each of the lines of sight are not provided in the literature on a case-by-case basis, so a value corresponding to the middle of the published range (0.115 K) is used for all of the lines of sight. The CO-derived N(H_2) is calculated by:

$$N(H_2) = W(CO)\, X_{\rm CO} \tag{5.2}$$

where $X_{\rm CO}$ is the CO X-factor, and is assumed to be $2.0 \pm 0.6 \times 10^{20}$ K^{-1} km^{-1} s cm^{-2} (Bolatto, Wolfire, and Leroy 2013).

Excluding the CH lines of sight MBM 16 ce4, ce3, cn2, and cs2, the area covered by the remaining lines of sight is similar to the area covered by the CO observations (see figure 5.1). Within this area, the CH column densities are somewhat uniform, in stark contrast with the CO observations, which sharply peak in the central line of sight and then decrease markedly from the center. The values of W(CO) at either end of the right ascention strip are more than an order of magnitude lower than the central position.

CH-derived N(H_2) within the area averages at $6.86 \pm 1.97 \times 10^{20}$ cm^{-2}, less than half of the CO-derived N(H_2) at the center. At the outer lines of sight, 3'W0'N and 3'E0'N, the CO-derived H_2 column density is at 1.40 ± 0.83 and $1.27 \pm 0.58 \times 10^{20}$ cm^{-2}, lower than the column density of H_2 derived by CH. However, due to the large standard deviation in the CH-derived H_2 column densities, the CO-derived N(H_2) for the outer lines of sight is consistent with some of the lower CH-derived N(H_2). For the CH and CO observations to be consistent with one another at the outer region, the excitation temperature of CH would need to be very small, closer to zero than -1 K. Alternatively, adjusting the value of X_{CO} to 1.0×10^{20} K^{-1} km^{-1} s cm^{-2} would bring the CO-derived N(H_2) fairly close to the CH-derived column densities. The line widths for those two lines of sight are similar to the CH line widths, while the other CO lines of sight have line widths that are approximately half of the width as the outer two points.

The CO lines, despite the narrow line width, cover the velocities from approximately 6.8 to 9.0 km s^{-1}, similar to the CH lines, which indicates that the CO line is likely tracing two distinct components of gas. The narrow width of the gaussians fit to the CO lines show that the CO is tracing colder gas than the CH observations, which indicates that CO is likely tracing the cold, dense gas in the clump. The similar velocity coverage of the CO and CH spectra shows that a portion of the CO line is tracing the warm, diffuse gas which is also traced by CH. It appears like both sets of observations are able to observe the diffuse region surrounding the clump, but CH more effectively traces the material outside of the clump while CO more effectively traces the material inside of the clump. CH is not entirely unable to trace the material at the clump, but the velocity component which is likely associated with the clump correlates with a much smaller H_2 column density compared to the CO-derived H_2 column density.

A direct comparison of N(H_2) derived from observations of CH and CO would involve comparing the overlapping positions. These positions are MBM 16 cw1 and 2'W0'N, MBM 16 cn1 and 0'W2'N,

MBM 16 c and 0'W0'N, and MBM 16 ce1 and 2'E0'N. The outer lines of sight at MBM 16 cw1, cn1, and ce1 all have lower CO-derived N(H_2) than CH-derived N(H_2), but both of the N(H_2) values are consistent with each other. At the center line of sight, the CO-derived N(H_2) is larger than the CH-derived N(H_2), with a H_2 column density which is a factor of 2 greater and is large enough that the two values are not consistent with each other.

The difference between the CO and CH observations could be interpreted as a change in the CH excitation temperature or a value of X_{CO} lower than the usual ISM value. However, for the former case, the excitation temperature would have to vary between -1 K and much greater than the background temperature (i.e., 2.74 K). An estimate of N(H_2) can be determined from the extinction and N(HI) from the GALFA survey (Peek et al. 2018) using the N(H)/$E(B-V)$ relation in equation 2.2. The results are listed in Table 5.3, using the same lines of sight as the CH observations. The beam size of both the N(HI) survey and the extinction are larger than the CH and CO beams, but this method can still provide an estimate of N(H_2) which can provide a reference value to compare with the CH- and CO-derived N(H_2). The values for N(H_2) determined from N(HI) and extinction suggests the CH is tracing the gas more effectively than CO. CH-derived N(H_2) is reduced due to using an average excitation temperature, but if the excitation temperature is assumed to be much greater than the background temperature then the two sets of N(H_2) values are similar in magnitude (see table 5.3). For both the N(HI)-extinction derived N(H_2) and CH-derived N(H_2), the column densities are fairly constant relative to the CO observations. While this can be attributed to a larger sampled area and larger beam sizes smoothing over small features, CH does not show a sharp peak in N(H_2) in the central line of sight. CH may have a varying excitation temperature in this region of MBM 16, but it is unlikely that the excitation temperature varies significantly, enough to account for this difference.

Complicating the comparison between CH and CO is the uncertain value of X_{CO} for converting W(CO) to N(H_2). Magnani and Onello (1995) show that the X_{CO} value for MBM 16 varies over the face of the cloud, but this conclusion was based on using CH to calibrate W(CO). Based on N(H_2) derived from N(HI) and extinction, it appears that the CH 3335 MHz is tracing the gas and the varying X_{CO} is likely due to the high CO X-factors indicating regions where CO is not adequately self-shielding and is partially broken up by the interstellar radiation field.

5.4 Mass of MBM 16 clump

The mass of molecular hydrogen within a 13.4 by 9.4 arcminute region of MBM 16 is determined using CH observations. It can be estimated using the following equation:

$$M = N(H_2)\, A\, \mu\, m_H \tag{5.3}$$

where N(H_2) is the average column density of H_2 over the entire region in cm^{-2}, A is the area of the region in cm^2, defined as the solid angle Ω multiplied by the distance to the cloud squared. m_H is the mass of a hydrogen atom in kg and μ is considered to be 2 to adjust the mass to represent molecular hydrogen, ignoring the slight change in mass from the bonding of the two hydrogen atoms. The distance to MBM 16 is 170 ± 8 pc (Zucker et al. 2019), so the area of the 13.4 by 9.4 arcminute region is 2.93×10^{36} cm^2. N(H_2) is the average of the calculated molecular hydrogen column density from each of the lines of sight.

The average CH-derived N(H_2) is $6.58 \pm 1.53 \times 10^{20}$ cm^{-2}, so the mass of H_2 in this portion of MBM 16 is 3.25 ± 0.81 $M_\odot$. Based on N(H_2) derived from N(HI) and the extinction discussed above,

the excitation temperature may be larger than average, so if $T_{\rm ex}$ is set so $F_{\rm T} = 1$, then the average N(H_2) is $12.41 \pm 2.88 \times 10^{20}$ cm^{-2}[2] corresponding to a H_2 mass of 6.13 ± 1.54 $M_\odot$.

Using equation 5.3, the mass of the 3 by 4 arcminute clump can be determined with CO $(1-0)$ observations from Magnani et al. (1990). Sampling only the five center observations, the average N(H_2) = $14.9 \pm 2.01 \times 10^{20}$ cm^{-2}. From this the mass of the molecular hydrogen in the clump is determined to be 0.70 ± 0.12 $M_\odot$.

The clump in MBM 16 covers a 4 by 7 arcminute area of the cloud (Magnani et al. 1990). Using the average N(H_2) of the 5 inner CO lines of sight, the mass of H_2 is 1.63 ± 0.27 $M_\odot$. The mass of the same area determined using the CH-derived H_2 column density using only the inner 5 CH lines of sight, the mass of H_2 in the area is 0.73 ± 0.26 $M_\odot$. Since $T_{\rm ex}$ is expected to be much greater than $T_{\rm bg}$, the mass of H_2 in the area if $F_{\rm T} = 1$ is 1.38 ± 0.48 $M_\odot$, consistent with the mass of H_2 in the area determined from CO.

While CO traces the gas in the middle of the "clump" as well as CH, it struggles to trace the CO-faint gas surrounding that small region. The CO-faint gas surrounding the clump is still easily visible in the CH 3335 MHz line, which may indicate that in some cases, CH is able to trace CO-faint gas more effectively than CO in regions where there is a relatively large amount of H_2.

5.5 Conclusion

It appears that CH 3335 MHz line and the CO$(1-0)$ line at 115 GHz do not always trace the same gas. For this particular clump in MBM 16, CH is able to effectively trace the diffuse gas which encompasses the clump, which is poorly traced by CO. This could be due to CO only being fully self-shielding in the

[2] When $F_{\rm T} = 1$, N(CH)/N(H_2) = $4.75 \pm 2.20 \times 10^{-8}$.

central region of the observations, while H_2 is self shielding beyond the area where the clump is observed. The excitation temperature of the CH 3335 MHz transition in the region, based on comparison with the expected N(H_2), is larger than what is predicted from the average F_T determined in chapter 2. Thus, CH may be an effective tracer of CO-faint gas when the expected column density of H_2 is large (on the order of 10^{21} cm^{-2}).

Table 5.1: Observations Parameters

CH 3335 MHz Line

Observation	Integration Time sec	R.A. (2000) $h\ m\ s$	Dec (2000) $\circ\ '\ ''$	ℓ deg	b deg
MBM 16 c	6000	03 19 04	11 30 52	170.66	−37.32
MBM 16 ce1	900	03 18 56	11 30 52	170.63	−37.34
MBM 16 ce2	2400	03 18 48	11 30 53	170.60	−37.37
MBM 16 ce3[a]	5100	03 19 28	11 30 50	170.75	−37.26
MBM 16 ce4[a]	5700	03 19 36	11 30 50	170.78	−37.23
MBM 16 cw1	3000	03 19 12	11 30 51	170.69	−37.30
MBM 16 cw2	5100	03 19 20	11 30 51	170.72	−37.28
MBM 16 cn1	9000	03 19 04	11 32 52	170.63	−37.30
MBM 16 cn2	6000	03 19 04	11 34 52	170.60	−37.27
MBM 16 cs1	6000	03 19 04	11 28 52	170.69	−37.35
MBM 16 cs2	5100	03 19 04	11 26 52	170.72	−37.37

CO$(1-0)$ Line (Magnani et al. 1990)

Observation	R.A. (2000) $h\ m\ s$	Dec (2000) $\circ\ '\ ''$	ℓ deg	b deg
3'W 0'N	03 19 16	11 30 51.1	170.70	−37.29
2'W 0'N	03 19 12	11 30 51.3	170.69	−37.30
1'W 0'N	03 19 08	11 30 51.5	170.67	−37.31
0'W 2'N	03 19 04	11 32 51.7	170.63	−37.30
0'W 1'N	03 19 04	11 31 51.8	170.64	−37.31
0'W 0'N	03 19 04	11 30 51.8	170.66	−37.32
0'W 1'S	03 19 04	11 29 51.8	170.67	−37.33
1'E 0'N	03 19 00	11 30 52.0	170.64	−37.33
2'E 0'N	03 18 56	11 30 52.2	170.63	−37.34
3'E 0'N	03 18 52	11 30 52.4	170.61	−37.36

a) These lines of sight were mislabeled during the original observations.

Table 5.2: Radio CH 3.3 GHz Observations

Line of Sight	W(CH)	rms	T_A	Δv	v_{LSR}	N(CH)	N(H_2)
	mK km s^{-1}	mK	mK	km s^{-1}	km s^{-1}	10^{12} cm^{-2}	10^{20} cm^{-2}
MBM 16 c	220.2 ± 37.2	9.7	49.9 ± 9.7	0.41 ± 0.08	8.13	35.4 ± 7.4	7.45 ± 5.59
			40.7 ± 9.7	2.58 ± 0.61	7.45		
MBM 16 ce1	192.1 ± 36.0	28.0	38.9 ± 28.0	2.54 ± 1.83	7.10	30.9 ± 6.9	6.50 ± 4.90
MBM 16 ce2	185.0 ± 32.6	16.2	40.6 ± 16.2	2.57 ± 1.02	7.08	29.7 ± 6.4	6.26 ± 4.70
MBM 16 ce3	162.3 ± 28.0	10.9	39.3 ± 10.9	1.93 ± 0.53	7.44	26.1 ± 5.5	5.49 ± 4.12
MBM 16 ce4	92.7 ± 16.5	10.3	36.4 ± 10.3	1.51 ± 0.43	7.26	14.9 ± 3.2	3.14 ± 2.36
MBM 16 cw1	200.3 ± 34.6	14.4	48.9 ± 14.4	2.26 ± 0.66	7.65	32.2 ± 6.8	6.78 ± 5.09
MBM 16 cw2	252.0 ± 42.4	9.5	48.0 ± 9.5	2.71 ± 0.53	7.45	40.5 ± 8.4	8.53 ± 6.40
MBM 16 cn1	223.7 ± 37.8	9.0	43.4 ± 9.0	2.54 ± 0.52	7.34	36.0 ± 7.5	7.57 ± 5.67
MBM 16 cn2	257.1 ± 43.4	9.6	34.8 ± 9.6	4.17 ± 1.15	7.00	41.3 ± 8.6	8.70 ± 6.52
MBM 16 cs1	146.2 ± 25.0	9.7	39.4 ± 9.7	2.34 ± 0.58	7.45	23.5 ± 5.0	4.95 ± 3.71
MBM 16 cs2	206.9 ± 35.4	11.1	38.7 ± 11.1	3.15 ± 0.91	7.32	33.3 ± 7.0	7.00 ± 5.25

Table 5.3: Radio CO($J = 1 - 0$) Observations

Line of Sight	W(CO)	rms[a]	$T_{\rm R}$	Δv	$v_{\rm LSR}$	N(H_2)
	K km s^{-1}	K	K	km s^{-1}	km s^{-1}	10^{20} cm^{-2}
3'W 0'N	0.699 ± 0.355	0.115	0.32 ± 0.12	2.05 ± 0.74	7.61	1.40 ± 0.83
2'W 0'N	1.754 ± 0.121	0.115	2.35 ± 0.12	0.70 ± 0.03	8.08	3.51 ± 1.08
1'W 0'N	5.779 ± 0.133	0.115	7.04 ± 0.12	0.77 ± 0.01	7.95	11.56 ± 3.48
0'W 2'N	1.591 ± 0.130	0.115	1.99 ± 0.12	0.75 ± 0.04	8.16	3.18 ± 0.99
0'W 1'N	7.502 ± 0.133	0.115	9.14 ± 0.12	0.77 ± 0.01	8.16	15.00 ± 4.51
0'W 0'N	8.343 ± 0.149	0.115	9.10 ± 0.12	0.86 ± 0.01	8.05	16.69 ± 5.01
0'W 1'S	8.060 ± 0.144	0.115	9.11 ± 0.12	0.83 ± 0.01	7.66	16.12 ± 4.84
1'E 0'N	7.462 ± 0.149	0.115	8.14 ± 0.12	0.86 ± 0.01	8.15	14.92 ± 4.49
2'E 0'N	2.343 ± 0.101	0.115	3.79 ± 0.12	0.58 ± 0.02	8.11	4.69 ± 1.42
3'E 0'N	0.636 ± 0.220	0.115	0.47 ± 0.12	1.27 ± 0.31	7.59	1.27 ± 0.58

CO observations are from Magnani et al. 1990.

a) The rms value is the middle of the range of rms given for MBM 16 observations.

Table 5.4: Estimated N(H_2)

Line of Sight	A_V	N(HI)	N(H_2)	CH-N(H_2)[a]
	mag	10^{20} cm^{-2}	10^{20} cm^{-2}	10^{20} cm^{-2}
MBM 16 c	2.396	17.04	13.82 ± 5.74	13.07 ± 6.19
MBM 16 ce1	2.480	17.58	14.33 ± 5.95	11.40 ± 5.42
MBM 16 ce2	2.524	17.83	14.61 ± 6.07	10.99 ± 5.21
MBM 16 ce3	2.046	16.51	10.82 ± 4.49	9.63 ± 4.56
MBM 16 ce4	2.002	17.10	10.11 ± 4.20	5.50 ± 2.61
MBM 16 cw1	2.273	16.61	12.89 ± 5.35	11.89 ± 5.63
MBM 16 cw2	2.136	16.26	11.78 ± 4.89	14.96 ± 7.08
MBM 16 cn1	2.334	16.96	13.28 ± 5.52	13.28 ± 6.28
MBM 16 cn2	2.259	17.28	12.42 ± 5.52	15.26 ± 7.22
MBM 16 cs1	2.379	16.92	13.72 ± 5.70	8.68 ± 4.11
MBM 16 cs2	2.300	17.00	12.94 ± 5.38	12.28 ± 5.81

The uncertainty of the extinction is 10 percent (Schlafly et al. 2011), and the uncertainty in N(HI) is assumed to be negligible compared to the standard deviation in the N(H)/$E(B-V)$ ratio.

a) N(H_2) derived from N(CH), where $F_{\rm T}$ is assumed to be 1.

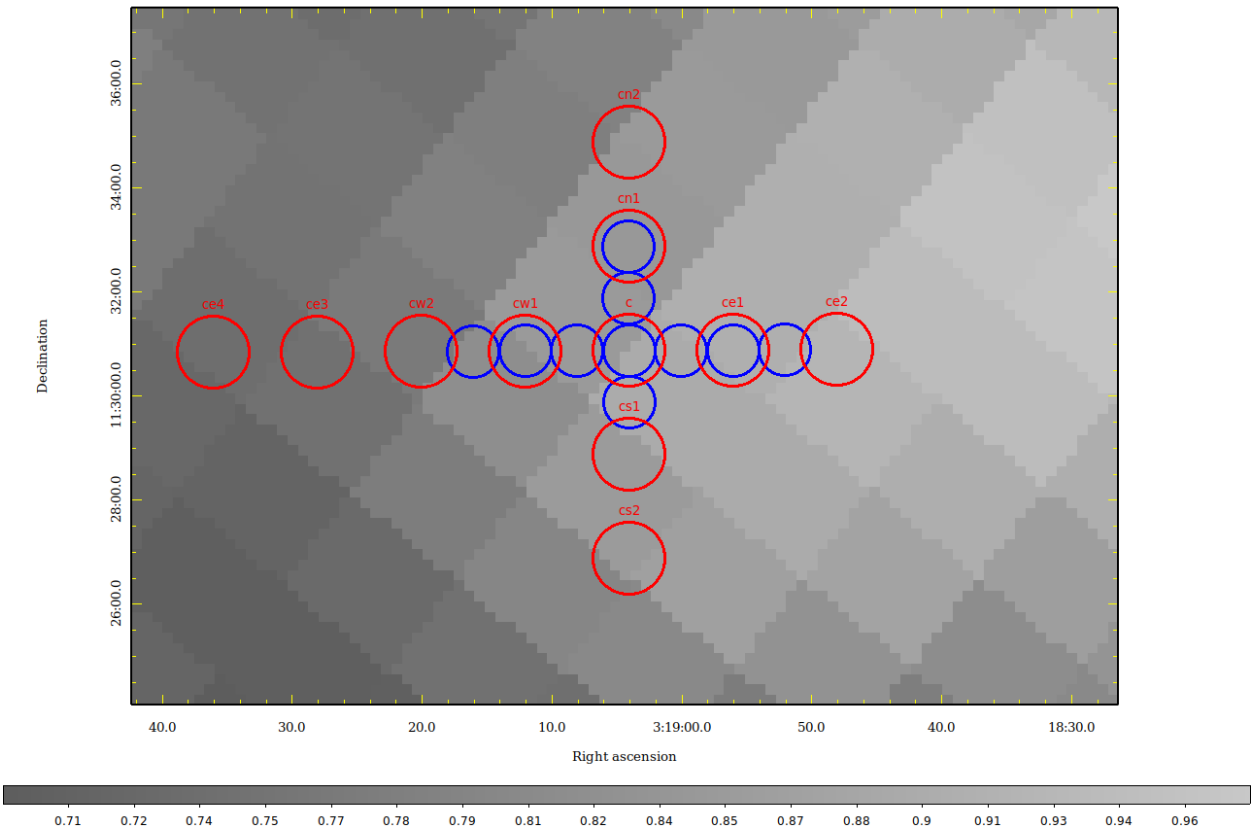

Figure 5.1: Map of the MBM 16 Clump

Map of the locations of the CH and CO observations. The greyscale background shows the extinction from the SFD dust map (Schlegel et al. (1998)). The observations are centered on the clump which is not well traced by the dust. The CH observations are shown with red 1.4 arcminute circles, and have the line of sight labeled above the marker because a few of them were mislabeled in the original observations. CO(J = 1 − 0) lines of sight from Magnani et al. (1990) are indicated with 1 arcminute blue circles. The CO clump itself can be seen in figures 1 and 4 of Magnani et al. (1990).

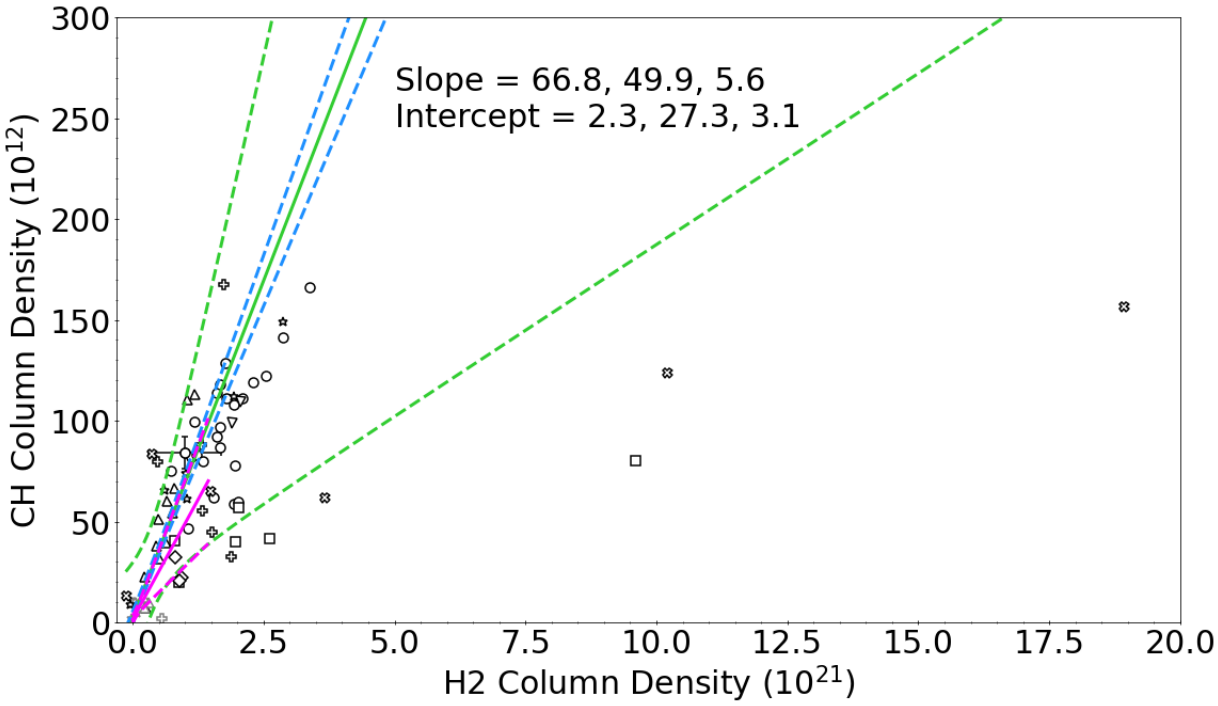

Figure 5.2: N(CH) vs. N(H_2)

Plot of N(CH) vs N(H_2) created using the data described in chapter 2. The CH column densities assume that $F_T = 1$ (see discussion in chapter 2). At higher H_2 column densities, the CH column density no longer increases and levels off as CH molecules are consumed in chemical reactions that produce more complex molecules.

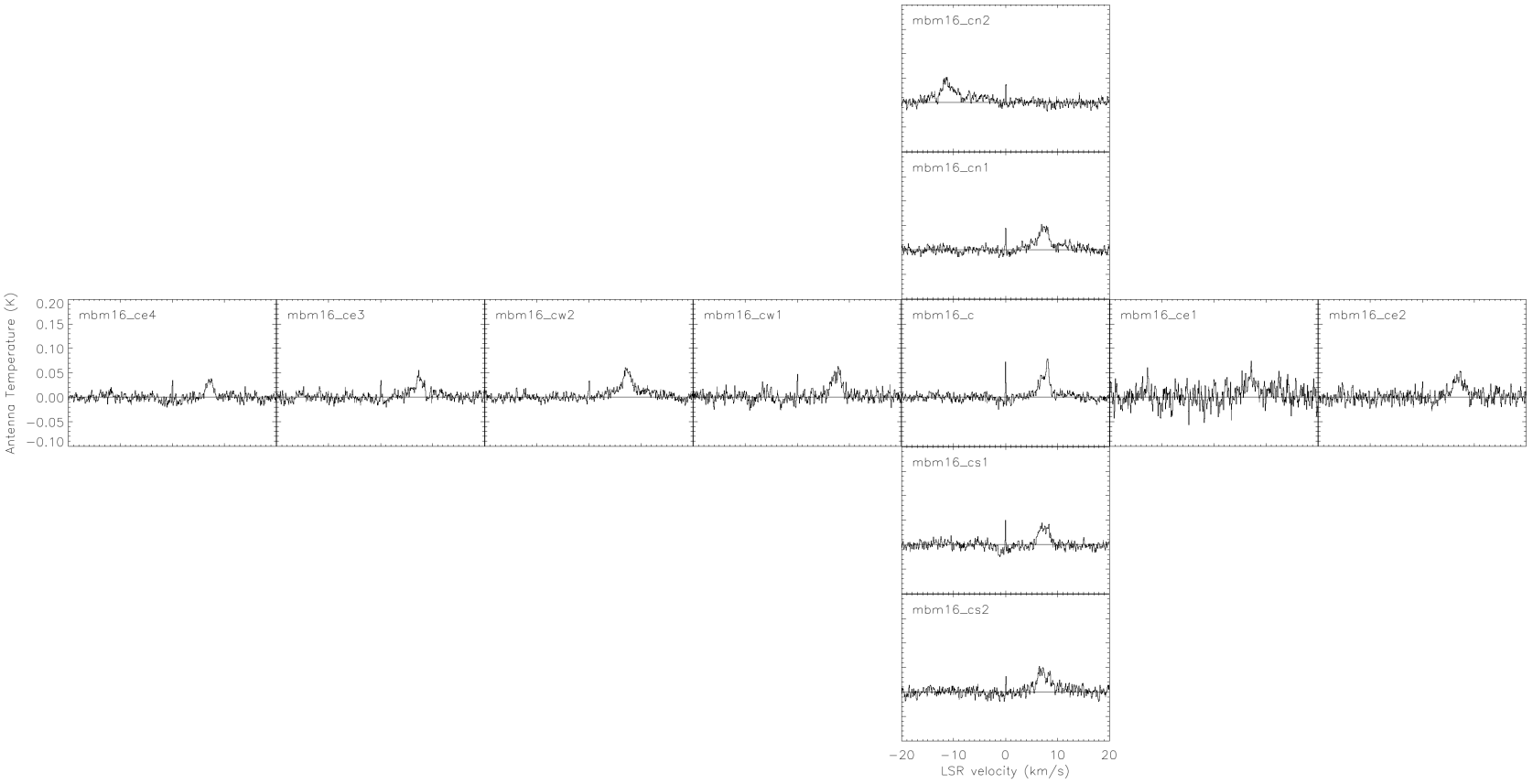

Figure 5.3: MBM 16 CH Spectra

Spectra for the CH 3335 MHz observations shown in figure 5.1. The spectra have been smoothed using hann smoothing once for the figures only (i.e., the data in table 5.2 are based on the original data). Spectra for the CO observations can be found in Magnani et al. (1990). The velocity difference between MBM 16 cn2 and the other spectra was caused by using an incorrect center frequency during the original observations.

Chapter 6

Methylidyne in Pegasus

6.1 Introduction

A large molecular complex was found in Pegasus by Magnani, Blitz and Mundy (1985) and individual clouds in the complex were named MBM 53, 54, and 55. A complete map of the region was made in CO($1-0$) by Yamamoto et al. (2003). This high-latitude molecular cloud complex is the largest structure of its kind in the southern Galactic hemisphere at b $< -30°$.

Grenier, Casandjian, and Terrier (2005), using gamma ray and infrared data, discovered molecular gas surrounding CO clouds and in between dense cores and atomic clouds not seen by the CO surveys, demonstrating that the molecular gas traced by the traditional CO($1-0$) observations may not reveal all of the molecular gas in a given region. This 'missing' gas was called dark gas, but is now called CO-dark gas or CO-faint gas and it is associated with the outer regions of molecular clouds that are unable to be detected by low-sensitivity CO surveys. This gas is thought to be molecular or, possibly, HI due to optical depth considerations. To some extent this limitation of the CO surveys was previously known, as noted

in the description of photodissociation regions in chapter 1.1 of this dissertation, and in the previous chapter, where the CH 3335 MHz line is able to trace a CO-faint component of a clump in MBM 16. Any photodissociation region will have sections in the outer layers of the molecular cloud where the molecular hydrogen is able to self-shield and therefore is produced in relatively large quantities, while CO is not yet self-shielding leading to relatively low column densities ($\lesssim 10^{15}$ cm^{-2}) that make it difficult to detect in emission, if it can be detected at all.

Donate and Magnani (2017) observed a portion of MBM 53 with high-sensitivity CO observations (with typical rms values in the 20-30 mK range) in an attempt to account for at least some of the molecular portion of dark gas in the region by looking for weak CO emission at cloud edges. There, CO surveys are unable to detect weak CO signals due to the large noise that accompanies the relatively short observation times used to complete the surveys (for example, Dame, Hartman and Thaddeus 2001). Another commonly used tracer of lower density molecular gas are the 18 cm main lines of OH. Donate, White, and Magnani (2019) observed MBM 53 using 18 cm OH observations to search for dark gas and to compare the effectiveness of CO and OH as tracers of dark gas. For similar integration times of CO and OH, they determined CO is more effective than OH at tracing the extent of the diffuse molecular gas, but the assumptions made about the CO X-factor in very low extinction clouds makes CO unreliable relative to OH observations as a means to determine the amount of molecular gas present.

To build upon the previous work, this chapter describes observations of the CH 9 cm lines in MBM 53. Originally, we were awarded 45 hours of Arecibo time (project A3340) to observe in CH a subset of the lines of sight observed in OH by Donate, White, and Magnani (2019) and in CO by Donate and Magnani (2017). While some of the planned 40 lines of sight were observed, the recent collapse of the Arecibo 305-m telescope prevented us from completing the project. The CH signals we had detected

are very weak, so instead of focusing on the detection of dark gas, this chapter will focus primarily on comparing the CH observations with observations of CO and OH along with estimates of N(H_2) from extinction and N(HI).

6.2 Observations

The CH observations for project A3340 were made using the Arecibo 305-m radio telescope from July to October 2019. We used the upper S-band receiver with a beam size at 3.3 GHz of 1.3×1.5 arcmin elongated in azimuth. Our beam efficiency was 0.4 ± 0.04 as measured by monitoring quasars of known flux. The relatively low efficiency was a consequence of the damage done to the reflector by hurricane Maria in 2017 (see discussion in chapter 3). The spectrometer was the Wideband Arecibo Pulsar Processor (WAPP) divided into 8 boards, with boards 1, 2, 5, and 6 having a bandwidth of 1.5625 MHz and boards 3, 4, 7, and 8 having a bandwidth of 3.125 MHz. The boards are configured to observe the CH 3.3 GHz lines, with boards 1, 3, 6, and 8 centered on the CH main line at 3335.48 MHz. The satellite lines were observed on the remaining boards; boards 2 and 4 observed the lower satellite line at 3263.79 MHz and boards 5 and 7 observed the upper satellite line at 3349.19 MHz. Due to issues with WAPP 2 failing due to then-unresolved power issues, early observations taken before September 2019 do not have the observations from the original boards 3 and 4, with boards 5, 6, 7, and 8 becoming boards 3, 4, 5, and 6 in the later observation run.

Donate and Magnani (2017) observed MBM 53 along many of the same lines of sight as the CO observations from part of the Southern Galactic High-Latitude Survey by Magnani et al. (2000), but the telescopes used in the two projects had different beam sizes. Donate and Magnani (2017) used the Arizona

Radio Observatory (ARO) 12-m telescope and Magnani et al. (2000) used the Harvard-Smithsonian CFA (HSCFA) 1.2-m telescope. Consequently, at the CO$(1-0)$ frequency, the beam sizes are very different (55 arcseconds and 504 arcseconds). To roughly sample the same solid angle of the sky as the HSCFA 1.2-m telescope using the ARO 12-m telescope, Donate and Magnani (2017) observed 13 lines of sight within each of the Magnani et al. (2000) CO beams, illustrated in figure 6.1 by the smallest green circles. Due to the small beam size of the CO beams from the ARO 12-m telescope, the 13 CO beam pattern only covers approximately 15 percent of the HSCFA CO beam. The 13 CO beams are spread out enough so while they do not sample a large fraction of the HSCFA beam, they are still able to sample small areas across the beam. To simplify the comparison of the CH observations to previous CO $(1-0)$ observations by Magnani et al. (2000) and Donate and Magnani (2017), the same 13 line of sight pattern used in Donate and Magnani (2017) was used for our project. The CH observations were made using the now unoperational Arecibo 305-m radio telescope with a beam size of approximately 84 arcminutes. The 13 CH beams observe approximately 36 percent of the HSCFA CO beam, roughly 2.3 times the solid angle observed by the CO beams. The discrepancy between the CO and CH beam sizes results in the CO beam from the ARO 12-m telescope only observing approximately 43 percent of the solid angle covered by the CH beams from the Arecibo 305-m telescope. For most of the rest of this chapter it is assumed that the two beams are sampling the same region. However, we note that the two beams are not the same size and the CH beam is also over sampling a small region around each of the CO observations observed from the ARO 12-m telescope.

The target region, MBM 53, is 259 ± 12 parsecs away from the solar system (Zucker et al. 2019). At this distance, the HSCFA CO beam samples a region of the cloud 0.633 ± 0.029 pc across, the ARO

CO beam samples a region of the cloud 0.069 ± 0.003 pc across, and the AO CH beam samples a region of the cloud 0.106 ± 0.005 pc across.

6.3 Results

Figure 6.2 shows a map of the detections from the Southern Galactic High-Latitude Survey (Magnani et al. 2000), the deep CO $(1-0)$ survey in MBM 53 by Donate and Magnani (2017), the OH 18 cm survey in MBM 53 by Donate, White, and Magnani (2019), and the CH observations from observing project A3340. With the limited time available, complete or mostly complete observations were collected for only 15 of the 40 proposed lines of sight for the CH project. Of the 15, only 3 of them had clear CH detections visible in the full observation spectra. Four other lines of sight have detections or tentative detections, but the poor baseline makes it difficult to determine the column density for low signal-to-noise data. Each of the CH detections and tentative detections occur in a location where CO had been detected by Donate and Magnani (2017) and OH at 18 cm had also been detected (Donate, White, and Magnani 2019).

The detections and nondetections for the full sets of CH are shown in table 6.2. The extinction is shown in column 3, and is determined from the corrected SFD dust maps (Schlafly and Finkbeiner 2011; Schlegel, Finkbeiner, and Davis 1998). The filling factor shown in column 4 is the number of lines of sight, out of 13, with CO detections (Stricklan 2019). The fifth column lists W(CH) for each 3335 MHz detection as determined from board 6 for observations made after or during September 2019, and board 4 if observations were made before September 2019. The column density is listed in column 6, and assumes that $F_{\mathrm{T}} = 0.57 \pm 0.07$, and the center velocity of the peak is listed in the last column.

The naming convention used for each of the observations (listed in the first column of each table) is the galactic longitude followed by the latitude preceded by 'G'. There are no decimal points or negative signs, so an observation at $l = 92.4°$, $b = -32°$ would be G92432. To simplify the comparison between the CH dataset and the datasets by Magnani et al. (2000) and Donate and Magnani (2017) we observed at 13 points within the beam of several of the Magnani et al. (2000) lines of sight as described in 6.2. Each of the 13 lines of sight will be referred to as a "component" observation, and each of the spectra made up of 13 components will be referred to as a "full" observation.

Stricklan (2019), using the CO $(1 - 0)$ observations from Donate and Magnani (2017), examined each of the 13 component observations separately. The low filling factor of the full (8.4 arcminute) beam in many of the lines of sight in MBM 53 leads to the summed spectra being diluted, possibly making it difficult to detect CO over the relatively large beams from the Magnani et al. (2000) survey if the emission occurred in only 1 or 2 components. Additionally, she found the average linewidth of the CO signals was 0.948 km s^{-1}. Given that the velocity resolution of the Magnani et al. (2000) survey was 0.65 km s^{-1}, some weak, narrow signals may have eluded detection.

From the CH data there are three detections at G92434, G92431, and G92433. There are also detections in G93534, G93532, and G93531, however the poor baseline in the spectra makes it difficult to determine the strength of the detection. One position, G99031, had tentative detections in 2 of the 5 subgroups (see below).

6.3.1 CH Sub Groups

In an attempt to determine how the CH observations vary within each of the full observations, each full observation is broken into 5 sub groups, each composed of 5 component observations. The individual

component observations are not analyzed due to how weak the CH lines are in MBM53, and even in the regions with the strongest signal to noise, it is difficult to detect CH. Each of the sub observations is composed of 5 components, sub 1 contains components 1, 6, 7, 10, 11, sub 2 contains 1, 4, 5, 11, 13, sub 3 contains 1, 8, 9, 12, 13, sub 4 contains 1, 2, 3, 10, 12, and sub 5 contains 1, 2, 4, 6, 8. Figure 6.1 shows the numbered components.

Each of the full observations was divided into 5 sub observations, and the spectra are shown along with the full observations in figure 6.3. G92434 appears to have a detection in each of the 5 sub observations, which matches Stricklan (2019) who detected CO in all 13 of the components. G92433 has a weak detection for the full observation, but with the increased noise of the sub observations it is difficult to determine which of them have CH detections and which do not. Sub groups 1 and 2 may have weak detections. CO was only detected in one of the 13 lines of sight, so a CH detection in sub group 1 could be tracing CO-faint gas. Despite 4 CO detections present in G92432, there is no CH detection in the full observation, and there are no visible CH detections in any of the sub groups. G92431 has a relatively strong double peak detection at -5.07 and -7.77 km s^{-1}, and each of the 5 sub observations have CH detections as well. Stricklan (2019) detected CO in 3 of the 13 component lines of sight, which means that sub group 4 has a CH detection where CO is not seen (see figure 6.4a). G92430 does not have a detection in the full observation, but in sub observation 2, there may be a weak CH detection. This possible CH detection in sub observation 2 does not agree with the location of the CO detection in component 7 from Stricklan (2019).

The line of sight G93534 has a detection, but it is difficult to determine W(CH) due to the poor baseline. There appears to be a detection in each of the sub groups, which means that sub group 2 shows the detection of CH in an area where CO is not detected. G93533 does not have detections in the full

observation or any of the sub observations. Both G93532 and G93531 have poor baselines which make it difficult to determine if any of the sub groups have detections; G93532 may have detections in sub observations 1 and 5 and G93531 may have a detection. Line of sight G99031 appears to have a tentative detection in sub groups 4 and 5, but both of the possible lines are very small relative to the noise. G94634, G94633, G94632, G94631, and G99033 do not have detections in the full observation or any of the sub observations.

6.3.2 CO-ON, CO-OFF Groups

Stricklan (2019) discussed the filling factor of each of the full observations with the CO data of Donate and Magnani (2017). The number of components out of 13 where CO was detected in her thesis is listed in table 6.2, column 4. To directly compare the CO and CH data within the individual lines of sight, the CH data is divided into two groups, one group will contain all of the observations of the component lines of sight where there were CO detections, and the other will contain the lines of sight where there were no CO detections. Figure 6.4 shows the spectra for the CO-detection segregated CH observations for all regions where there is a CO detection and there is CH data, with the exception of G92434 as it was completely filled by CO detections and G92433 and G92430 as there is only one CO detection in each line of sight so there would not be a large enough sample to get any usable data. In figure 6.5 we show the CO detections often do not fill the CH sub regions they occupy, for example G92431 and G93534.

G92432 had CO detections in 4 of the 13 component lines of sight. Just like with the CH full observation and sub group spectra, neither of the two groups had any CH detections.

The CO-ON spectra for G92431 shows a signal for CH, but with only 3 of 13 line of sight components contributing to the ON spectra the noise is too high to claim there are 2 velocity components. The CO-

OFF spectra for G92431 also shows a CH signal with 2 velocity components. The presence of CH at detectable levels in regions where CO was not detected could suggests the line of sight samples a section of the photodissociation region where CH is able to form to detectable levels, but CO is culled by interstellar radiation. Alternatively, it may be a result of the CO-OFF CH spectra being summed together so there is a detectable signal in CH, while in Stricklan (2019), only the individual component lines of sight were considered and they were not summed together, so there is no confirmation on whether there is a CO signal visible if all of the CO-OFF components were summed.

G93534, G93532, and G93531 each had poor baselines which made it difficult to determine if there is a CH detection in the spectra. However, in each of the CO-detection segregated CH spectra for this group, the signal is higher in the CO-ON CH spectra than in the CO-OFF CH spectra, indicating that there is at least a signal in the CO-ON spectra, if not both spectra. Additionally, in G93532 and G93531, the baseline is close to the zero line in the CO-OFF CH spectra. The CO-ON spectra for G93532 contains spectra from 5 of the 13 components, and has a velocity integrated antenna temperature 137.1 ± 45.3 mK km s^{-1} greater than the CO-OFF CH spectra within the velocity range -2 to -15 km s^{-1}. If we assume the increase in the antenna temperature within -2 to -15 km s^{-1} is due to CH within the lines of sight where CO is observed, then the CH detected will have a wider velocity distribution than the accompanied CO, which has a narrow signal with a width of 1.46 km s^{-1}.

The line of sight G93531 had CO detections in 10 of the 13 component lines of sight. Unfortunately, the information that can be gathered from the difference of the CO-ON and CO-OFF CH observations of G93531 is greatly limited by the strong discrepancy in the integration time of the two spectra. The CO-ON CH spectrum has a stronger velocity integrated antenna temperature 43.0 ± 49.6 mK km s^{-1}

greater than the CO-OFF CH spectrum, but the high uncertainty makes it difficult to be certain if there is CH detected along the line of sight.

G93534 had CO detections in 6 of the 13 component lines of sight. The CO-ON CH spectrum for G93534 has a velocity-integrated antenna temperature 119.0 ± 44.8 mK km s^{-1} greater than the CO-OFF CH spectrum within the velocity range -2 to -12 km s^{-1}, which likely indicates there is CH in at least the CO-ON lines of sight. Additionally, there is a possible CH detection in the CO-OFF lines of sight as well. In support of the possibility of CH in the CO-OFF spectrum of G93534, there is a peak at -4.89 km s^{-1}, which is very close to the CO peak at -4.21 km s^{-1} (Donate and Magnani 2017) along with a much flatter baseline than the full spectra shown in figure $6.3f$. If the CH peak in the CO-OFF observations of G93534 are due to CH, then this line of sight could be similar to G92431 where CH is visible and CO is not detected.

G94632 had CO detections in 4 of the 13 component lines of sight, G94634 had CO detections in 2 of the 13 component lines of sight, G99031 had CO detections in 6 of the 13 component lines of sight, but none of them have any CH detections in either group.

The lack of CH detections in groups with clear CO $(1-0)$ emission is puzzling in light of the evidence that the CH 3335 MHz line can trace low-density molecular gas (Magnani and Onello 1993, Johannson 1979, Sandell, Stevens, and Heiles 1987) and the results of chapter 6. Furthermore, when CH is detected in the sub groups, it tends to trace regions which do not contain CO detections, like in G92431 and G93534. When CH is detected with a steady baseline, it seems to be able to trace gas which is not seen in CO, similar to what is seen in chapter 5 with MBM 16. This will be discussed in section 6.5.

6.4 CO X-Factor and N(H_2)

X_{CO}, the CO X-factor, is a conversion factor which allows the molecular hydrogen column density to be estimated directly from the CO column density, and is suggested to be $2 \pm 0.6 \times 10^{20}$ cm^{-2} K^{-1} km^{-1} s for most Galactic applications (Bolatto, Wolfire, and Leroy 2013). It is defined as

$$X_{CO} = N(H_2)/W(CO) \tag{6.1}$$

where W(CO) is the velocity-integrated CO($1-0$) line profile. Using the CH-derived H_2 column density determined in this work along with the column densities of CO from Donate and Magnani (2017), the CO X-factor can be determined for each line of sight. N(H_2) in equation 6.1 is determined by converting the CH column density into H_2 column density, using a CH-H_2 conversion factor, where the CH column density is determined assuming F_T = 0.57 ± 0.07. The conversion factor used is

$$N(CH)/N(H_2) = 4.75 \pm 3.42 \times 10^{-8} \tag{6.2}$$

which is the value determined from the adjusted radio CH observations in chapter 2. Using this conversion factor allows the CO X-factor to be calculated, the results are shown in column 7 of table 6.3.

As a comparison, the CO X-factor is also calculated from the extinction along the line of sight and the HI column density using equation 2.2, and OH observations from Donate, White, and Magnani (2019). N(HI) is determined from an 8.4 arcminute area of the GALFA survey (Peek et al. 2018) for each line of sight, and the extinction is determined from corrected SFD dust maps (Schlegel et al. 1998; Schlafly and Finkbeiner 2011). The column density of H_2 is determined using equation 2.2, with the assumption that

R_V = 3.1. OH-derived N(H_2) for lines of sight with OH detections are listed in column 5 of table 6.3. The column density of OH is calculated using the following equation in Donate, White, and Magnani (2019):

$$N(OH) = 2.24 \times 10^{14}\, \eta_{\rm f}^{-1}\, [T_{\rm ex}/(T_{\rm ex} - T_{\rm bg})] \int T_{\rm A}\, dv\ \ cm^{-2} \tag{6.3}$$

where the beam filling factor $\eta_{\rm f}$ = 1, $T_{\rm ex}$ = 5 K, and $T_{\rm bg}$ = 3.3 K. To convert N(OH) to N(H_2), the relation N(OH)/N(H_2) = $1.05 \pm 0.14 \times 10^{-7}$ (Weselak et al. 2010) is used.

G92434 had the largest CO signal and the largest CH signal, and has an X-factor of $1.48 \pm 1.11 \times 10^{20}$ cm^{-2} K^{-1} km^{-1} s, which is in agreement with the suggested CO X-factor, $2 \pm 0.6 \times 10^{20}$ from Bolatto et al. (2013). When determined from the extinction and N(HI), $X_{\rm CO}$ is instead 0.67 ± 0.57 cm^{-2} K^{-1} km^{-1} s. OH observations predicts higher N(H_2) levels than any of the other methods for all lines of sight with OH detections, and for G92434, N(H_2) is about twice the amount of the CH- or CO-derived N(H_2). If the excitation temperature is assumed to be 20 K instead of 5 K, N(H_2) is reduced by about 41 percent, which could account for the high OH-derived N(H_2). The center velocity for CH and CO are similar, suggesting the two are tracing the same velocity component of the cloud. However, the width of the CH line was significantly wider than the CO line, with the CH line being approximately $2 - 3$ times greater than the CO line width, which may again suggest the CH is tracing a warmer, more diffuse region of the cloud than the CO. Donate and Magnani (2017) reported two velocity components for this line of sight, at -7.48 and -7.27 km s^{-1}, and given the low signal to noise inherent with observations of low extinction clouds and the width of the CH signal, the two velocity components would be difficult to separate in the CH spectra. For the 13 individual component observations, Stricklan (2019) found the center velocities to range from -6.99 to -8.18 km s^{-1}, and each of the observations had a narrow signal

of less than 2 km s^{-1} width. As a comparison, the CH sub observations range between -7.25 and -9.27 km s^{-1}, and each had a relatively wide signal with a width of approximately 5 km s^{-1}, as seen in table 6.4 and figure 6.3.

G92433 and G92431 have CH signals approximately half as strong as the signal in G92434, but the CO signal is roughly an order of magnitude less than the signal in G92434. For these two full observation lines of sight, the CH-derived CO X-factors are much higher, at about $9.3 - 9.7 \times 10^{20}$ cm^{-2} K^{-1} km^{-1} s. This same behavior of having large CH-derived X_{CO} is carried over with the nondetections, however this may be due to the roughly constant W(CH) upper limit and the varying W(CO). X_{CO} is lower when determined from extinction and N(HI), at approximately $4.5 \pm 3.9 \times 10^{20}$ for both lines of sight, which is consistent with X_{CO} suggested by Bolatto et al. (2013). The remaining lines of sight with CO detections, with the exception of G99031, all have A_V, N(HI)-derived X_{CO} which are in agreement with the mentioned suggested value. Therefore it seems like CO effectively traces the amount of N(H_2) in MBM53, while CH is overestimating N(H_2) for the majority of the lines of sight.

6.5 Conclusion

Due to the long integration times typically associated with observations of the CH 3.3 GHz lines, along with the very low amount of H_2 in the cloud, it appears like CH is a poor tracer of the diffuse gas in MBM53. For the full observation lines of sight, CO and OH detections always accompanied CH detections, but CH detections were not always present with CO or OH detections. CH and OH also typically predict high N(H_2) in MBM53 compared with CO and extinction. Determining N(H_2) from extinction or CO seems to lead to similar estimates, most of which are consistent with the CO X-factor suggested

by Bolatto et al. (2013). This may suggest that CO is effective at tracing the gas in MBM53 and that the abundances of OH and CH may be higher in the sampled sections of MBM 53 than in the average cloud. Alternatively, the CO X-factor and the gas-to-dust ratio could be higher than normal in this cloud.

Within the individual full lines of sight, the comparison between CH and CO becomes a little more complicated. CO is detected in lines of sight where CH is not detected, due to the CO($1-0$) line being much stronger than the CH 3.3 GHz line. However, in lines of sight where the baseline was steady and relatively strong CH lines were detected, CH was sometimes detected in the areas without CO detections. The CO-OFF spectra of G93534 and G92431 show CH detections tracing a CO-faint component of the gas. The larger width of the CH lines also may suggest that CH is tracing warmer gas which is not visible in CO, similar to what was seen in MBM 16 (see chapter 5).

When CH was detected, it usually predicted large N(H_2) relative to N(H_2) determined from N(HI) and extinction, which could mean that the excitation temperature is inverted and close to zero, contrary to the prediction of the excitation temperature in chapter 5. Similar to what is seen in the CH lines of sight in MBM 16, CH in MBM 53 seems to trace the molecular gas in the cloud which is not seen in CO. However, due to the much lower extinction and lower H_2 column density across the observed region in MBM 53, it is difficult to detect CH without extremely long integration times in some areas, limiting the ability of CH to detect CO-faint gas. CO appears to be a more effective tracer of very faint diffuse molecular gas where the brightness of the CO($1-0$) line makes CO easy to detect, but there is likely gas surrounding areas where CO is detected which can be detected with CH, if given an adequete integration time.

The intriguing results of this chapter and chapter 5 underscore why CH 3.3 GHz observations, although very time intensive, have been pursued over the last 5 decades. Clearly more data are needed to resolve definitively the issues and questions that have been raised.

Table 6.1: Pegasus Survey Comparison

Survey Molecule	CO[a] (2000)	CO[b] (2017)	OH[c] (2019)	CH (2021)
Detections / Lines of Sight	5 / 50	20 / 50	11 / 38	7 / 15

The above table shows the number of detections and tentative detections within the region shown in figure 6.2 instead of the full region some of the surveys cover.

a) Magnani et al. (2000)

b) Donate and Magnani (2017)

c) Donate, White, and Magnani (2019)

Table 6.2: CH Full Observations 3335.5 GHz

Line of Sight	Int. Time min	A_V mag	Filling Factor[a]	W(CH) mK km s^{-1}	N(CH) 10^{12} cm^{-2}	v_{LSR} km s^{-1}
G92434	125	0.626	13	193.4 ± 26.9	31.1 ± 5.8	-7.99
G92433	120	0.404	1	87.8 ± 17.8	14.1 ± 3.3	-8.46
G92432	130	0.413	4	< 98.8	< 15.9	–
G92431	130	0.516	3	137.0 ± 20.3	22.0 ± 4.2	-6.51
G92431[b]	130	0.516	3	71.7 ± 12.8	11.5 ± 2.5	-5.07
G92431[c]	130	0.516	3	64.9 ± 12.4	10.4 ± 2.4	-7.77
G92430	130	0.383	1	< 105.0	< 16.9	–
G93534	170	0.615	6	$[174.9 \pm 27.1$[d]$]$	$[28.1 \pm 5.6]$	–
G93533	80	0.445	0	< 125.9	< 20.2	–
G93532	125	0.461	5	< 98.8[d]	< 15.9	–
G93531	135	0.437	10	< 95.3[d]	< 15.3	–
G94634	130	0.574	2	< 105.2	< 16.9	–
G94633	60	0.419	0	< 149.7	< 9.6	–
G94632	60	0.511	4	< 148.6	< 9.6	–
G94631	60	0.201	0	< 149.8	< 24.1	–
G99033	120	0.198	0	< 107.0	< 17.2	–
G99031	75	0.349	6	< 177.1	< 28.5	–

As all of our detections are weak, non-detections are 1 σ velocity-integrated antenna temperatures instead of 2 σ and assume the width is 4.5 km s^{-1}. A width of 4.5 km s^{-1} is approximately the average of the widths of the signal in G92434, G92433, and G92431, which were chosen to be samples to represent the width of a potential detection due to having a detection and a somewhat steady baseline. In the absence of a CH detection, the upper limit of the CO X-factor is determined from the upper limit of W(CH). The excitation temperature is assumed to be a value where $F_T = 0.57 \pm 0.07$ (see chapter 2 for more details). The uncertainty is the standard error.

a) Number of components detected (out of 13) within the larger region in Figure 6.1.

b) component 1

c) component 2

d) Possible detection by inspection; poor baseline makes W(CH) difficult to specify

Table 6.3: CH Full Observations 3335.5 GHz

Line of Sight	$N(H_2)_{A_V}$ 10^{20} cm^{-2}	$N(H_2)_{CH}$ 10^{20} cm^{-2}	$N(H_2)_{CO}$ 10^{20} cm^{-2}	$N(H_2)_{OH}$ 10^{20} cm^{-2}	X_{CO}(OH) 10^{20}	X_{CO}(CH) 10^{20}	$X_{CO}(A_V)$ 10^{20}
G92434	2.96 ± 1.23	6.54 ± 4.86	8.82 ± 0.38	15.89 ± 5.24	3.60 ± 1.20	1.48 ± 1.11	0.67 ± 0.57
G92433	1.43 ± 0.59	2.97 ± 2.25	0.64 ± 0.23	9.29 ± 3.25	29.04 ± 14.66	9.28 ± 7.81	4.46 ± 3.85
G92432	1.56 ± 0.65	< 3.34	0.84 ± 0.14	–	–	< 7.96	3.70 ± 3.08
G92431	2.20 ± 0.91	4.63 ± 3.45	0.96 ± 0.14	9.32 ± 3.15	19.42 ± 7.17	9.66 ± 7.34	4.58 ± 3.91
G92431[b]		2.43 ± 1.82	0.70 ± 0.12			6.93 ± 5.35	–
G92431[c]		2.20 ± 1.66	0.26 ± 0.08			16.90 ± 13.78	–
G92430	0.67 ± 0.28	< 3.55	0.66 ± 0.26	–	–	< 10.77	2.03 ± 1.69
G93534	2.91 ± 1.21	$[5.92 \pm 4.42$[d]$]$	2.24 ± 0.16	18.79 ± 5.78	16.77 ± 5.30	5.28 ± 3.96	2.60 ± 2.22
G93533	0.72 ± 0.30	< 4.26	–	–	–	–	–
G93532	2.30 ± 0.95	< 3.34[d]	1.00 ± 0.12	7.39 ± 2.27	14.78 ± 4.86	< 6.69	4.59 ± 3.82
G93531	1.66 ± 0.69	< 3.23[d]	2.52 ± 0.23	4.07 ± 2.07	3.23 ± 1.67	< 2.56	1.32 ± 1.10
G94634	2.67 ± 1.11	< 3.56	2.98 ± 0.47	9.99 ± 3.50	6.70 ± 2.58	< 2.39	1.79 ± 1.49
G94633	0.85 ± 0.35	< 2.03	–	–	–	–	–
G94632	1.62 ± 0.67	< 2.01	0.86 ± 0.08	–	–	< 4.68	3.78 ± 3.14
G94631	-0.20 ± -0.08	< 5.07	–	–	–	–	–
G99033	-0.26 ± -0.11	< 3.62	–	–	–	–	–
G99031	0.37 ± 0.16	< 5.99[d]	2.54 ± 0.36	6.03 ± 2.40	4.75 ± 2.00	< 4.72	0.29 ± 0.24

As all of our detections are weak, non-detections are 1 σ velocity-integrated antenna temperatures instead of 2 σ and assume the width is 4.5 km s^{-1}. A width of 4.5 km s^{-1} is approximately the average of the widths of the signal in G92434, G92433, and G92431, which were chosen to be samples to represent the width of a potential detection due to having a detection and a somewhat steady baseline. In the absence of a CH detection, the upper limit of the CO X-factor is determined from the upper limit of W(CH). The excitation temperature is assumed to be a value where $F_{\rm T} = 0.57 \pm 0.07$ (see chapter 2 for more details). The uncertainty is the standard error. All X-factors have units of cm^{-2} K^{-1} km^{-1} s.

a) Number of components detected (out of 13) within the larger region in Figure 6.1.

b) component 1

c) component 2

d) Possible detection by inspection; poor baseline makes W(CH) difficult to specify

Table 6.4: CH Component Observations 3335.5 GHz

Line of Sight	Integration Time	W(CH)	N(CH)	$v_{\rm LSR}$
	min	mK km s^{-1}	cm^{-2}	km s^{-1}
G92434	125	193.4 ± 26.9	31.1 ± 5.8	-7.99
G92434 1	45	293.8 ± 42.6	47.2 ± 7.6	-7.74
G92434 2	45	208.6 ± 36.4	33.5 ± 6.3	-7.95
G92434 3	50	190.0 ± 34.3	30.5 ± 5.9	-9.27
G92434 4	50	167.4 ± 33.0	26.9 ± 5.6	-7.64
G92434 5	50	192.4 ± 34.8	30.9 ± 6.0	-7.25
G92433	130	87.8 ± 17.8	14.1 ± 3.3	-8.46
G92433 1	50	106.6 ± 27.7	17.1 ± 4.9	-7.59
G92433 2	50	141.1 ± 29.9	22.7 ± 5.5	-8.25
G92433 3	50	$[69.6 \pm 28.3]$	$[11.2 \pm 4.8]$	–
G92433 4	50	$[66.6 \pm 27.2]$	$[10.7 \pm 4.6]$	–
G92433 5	50	$[63.8 \pm 25.2]$	$[10.2 \pm 4.2]$	–
G92431	130	137.0 ± 20.3	22.0 ± 4.2	-6.51
G92431 1	50	176.3 ± 30.4	28.3 ± 6.0	-6.84
G92431 2	50	169.1 ± 29.3	27.2 ± 5.8	-6.39
G92431 3	50	129.7 ± 27.3	20.8 ± 5.1	-6.17
G92431 4	50	153.4 ± 28.5	24.7 ± 5.5	-6.02
G92431 5	50	138.4 ± 27.4	22.2 ± 5.2	-6.71
G92431[a]	130	71.7 ± 12.8	11.5 ± 2.5	-5.07
G92431[a] 1	50	83.0 ± 19.4	13.3 ± 3.5	-5.50
G92431[a] 2	50	95.6 ± 19.4	15.4 ± 3.6	-5.01
G92431[a] 3	50	88.8 ± 19.2	14.3 ± 3.5	-5.69
G92431[a] 4	50	93.0 ± 19.3	14.9 ± 3.6	-4.94
G92431[a] 5	50	$[63.3 \pm 17.9]$	$[10.2 \pm 3.1]$	–
G92431[b]	130	64.9 ± 12.4	10.4 ± 2.4	-7.77
G92431[b] 1	50	92.9 ± 19.8	14.9 ± 3.7	-7.90
G92431[b] 2	50	71.7 ± 18.4	11.5 ± 3.3	-7.95
G92431[b] 3	50	44.1 ± 17.6	7.1 ± 3.0	-8.57
G92431[b] 4	50	61.8 ± 18.0	9.9 ± 3.1	-7.81
G92431[b] 5	50	$[71.7 \pm 18.2]$	$[11.5 \pm 3.2]$	–
G93534	130	174.9 ± 27.1	28.1 ± 5.6	-5.09
G93534 1	50	178.0 ± 39.2	28.6 ± 7.2	-5.26
G93534 2	50	107.8 ± 35.6	17.3 ± 6.1	-5.00
G93534 3	50	212.2 ± 41.2	34.1 ± 7.8	-4.60
G93534 4	50	$[318.7 \pm 47.7]$	$[51.2 \pm 9.9]$	–
G93534 5	50	$[234.2 \pm 40.0]$	$[37.6 \pm 7.9]$	–

Non-detections have the 2 σ velocity-integrated antenna temperatures assuming the width is 4.5 km s^{-1}.
a) component 1
b) component 2

Table 6.5: CO Segregated CH Observations 3335.5 GHz

Line of Sight	Integration Time min	W(CH) mK km s^{-1}	N(CH) cm^{-2}	$v_{\rm LSR}$ km s^{-1}
G92431 ON	30	150.4 ± 35.1	24.2 ± 6.4	$-3, -10$
G92431 OFF	100	106.2 ± 20.0	17.1 ± 3.8	$-3, -10$
G92431 Δ		44.2 ± 40.4	7.1 ± 7.4	$-3, -10$
G93531 ON	95	193.5 ± 29.3	31.1 ± 6.1	$-5, -18$
G93531 OFF	30	150.5 ± 40.1	24.2 ± 7.1	$-5, -18$
G93531 Δ		43.0 ± 49.6	6.9 ± 9.3	$-5, -18$
G93532 ON	50	247.5 ± 38.2	39.8 ± 7.8	$-2, -15$
G93532 OFF	75	110.4 ± 24.4	17.7 ± 4.5	$-2, -15$
G93532 Δ		137.1 ± 45.3	22.0 ± 9.0	$-2, -15$
G93534 ON	80	173.4 ± 34.6	27.9 ± 6.5	$-2, -12$
G93534 OFF	85	54.4 ± 28.4	8.7 ± 4.7	$-2, -12$
G93534 Δ		119.0 ± 44.8	19.1 ± 8.0	$-2, -12$

Non-detections have the 2 σ velocity-integrated antenna temperatures assuming the width is 1 km s^{-1}.

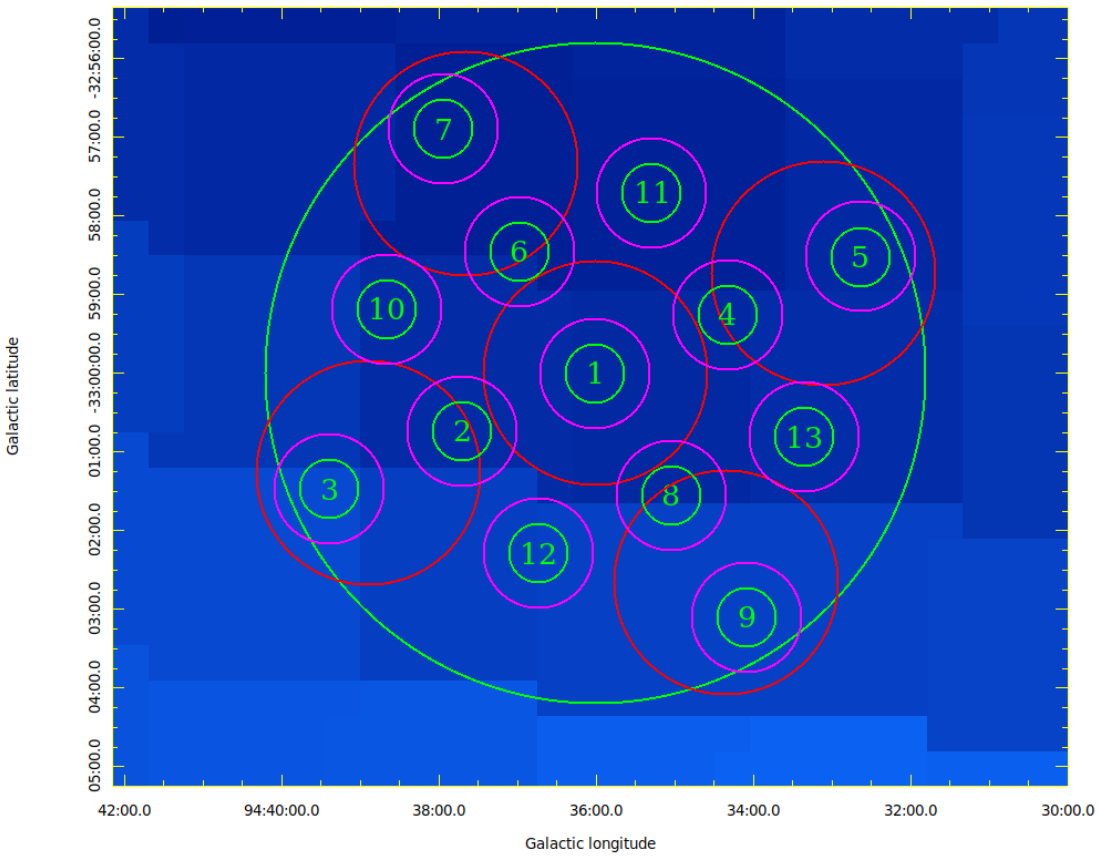

Figure 6.1: Beam Pattern
Pattern of the 13 component beams for each main line of sight. The outer green circle represents the Harvard-Smithsonian CFA 1.2-m telescope CO beam at 115 GHz (8.4'). The 13 small green circles represent the Arizona Radio Observatory 12-m telescope CO beam at 115 GHz (55"), and the 13 magenta circles represent the Arecibo Observatory 305-m telescope CH beam at 3.3 GHz (1.4'). The 5 larger magenta circles represent the Arecibo Observatory 305-m telescope OH beam at 1.7 GHz (2.85').

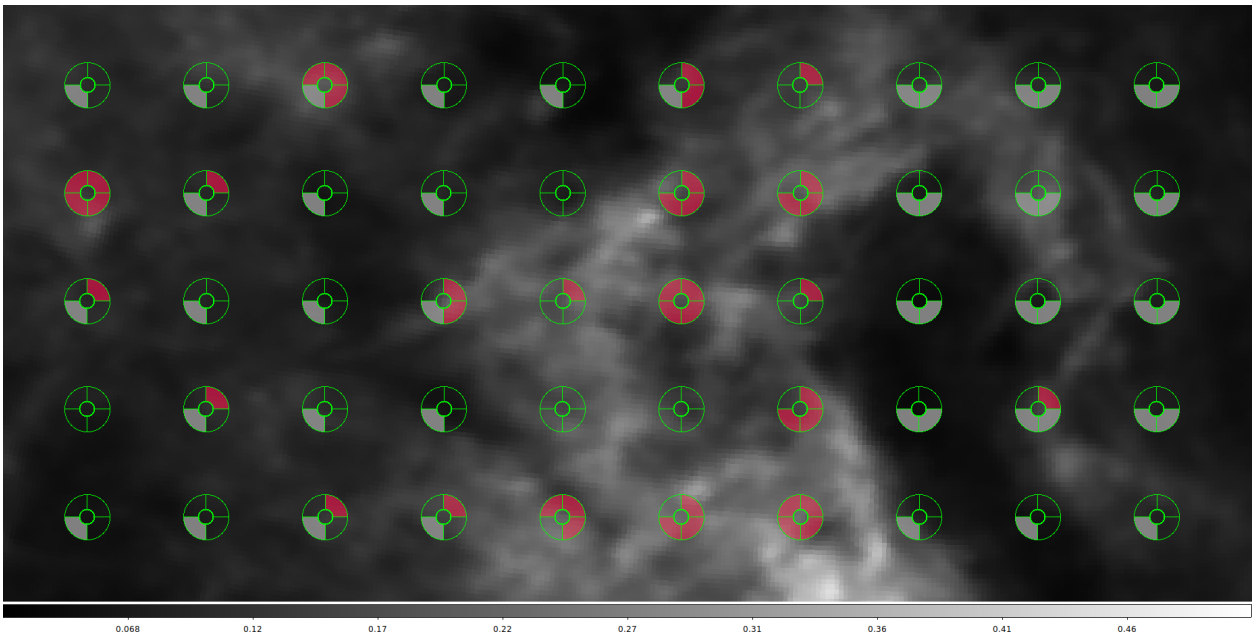

Figure 6.2: Detection Map
Dust map of MBM 53 from Schlegel, Finkbeiner, and Davis (1998) with the locations of CO (1.2-m), CO (12-m), OH, and CH observations and detections. The map shows the locations from Galactic longitudes $99.0°$ to $89.1°$ and latitudes $-30°$ to $-34°$, left to right, top to bottom. Each location shows 4 quadrants, either red, grey, or empty. The upper left quadrant is for the CO (1.2-m) data, the upper right is for CO (12-m) data, the lower left is for the CH data, and the lower right is for the OH data. If the quadrant is red then there is a detection or tentative detection, if it is empty then there is no detection, and is the quadrant is grey than there is no data or not enough data. The inner circle is to scale with the size of the Harvard-Smithsonian CFA 1.2-m telescope CO beam at 115 GHz (8.4').

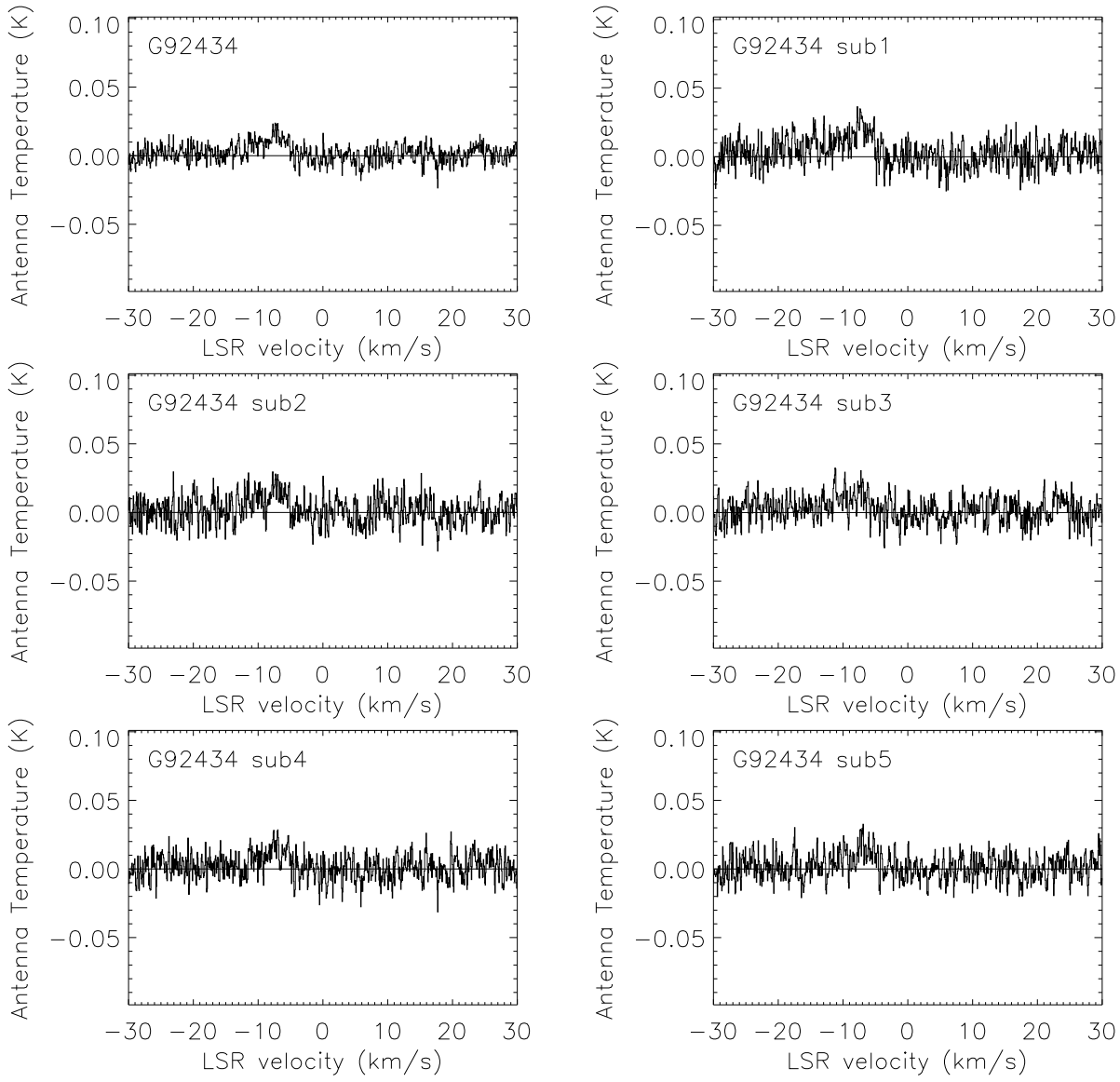

Figure 6.3a: G92434 Component Clusters
Full line of sight and component sub groups 1 through 5.

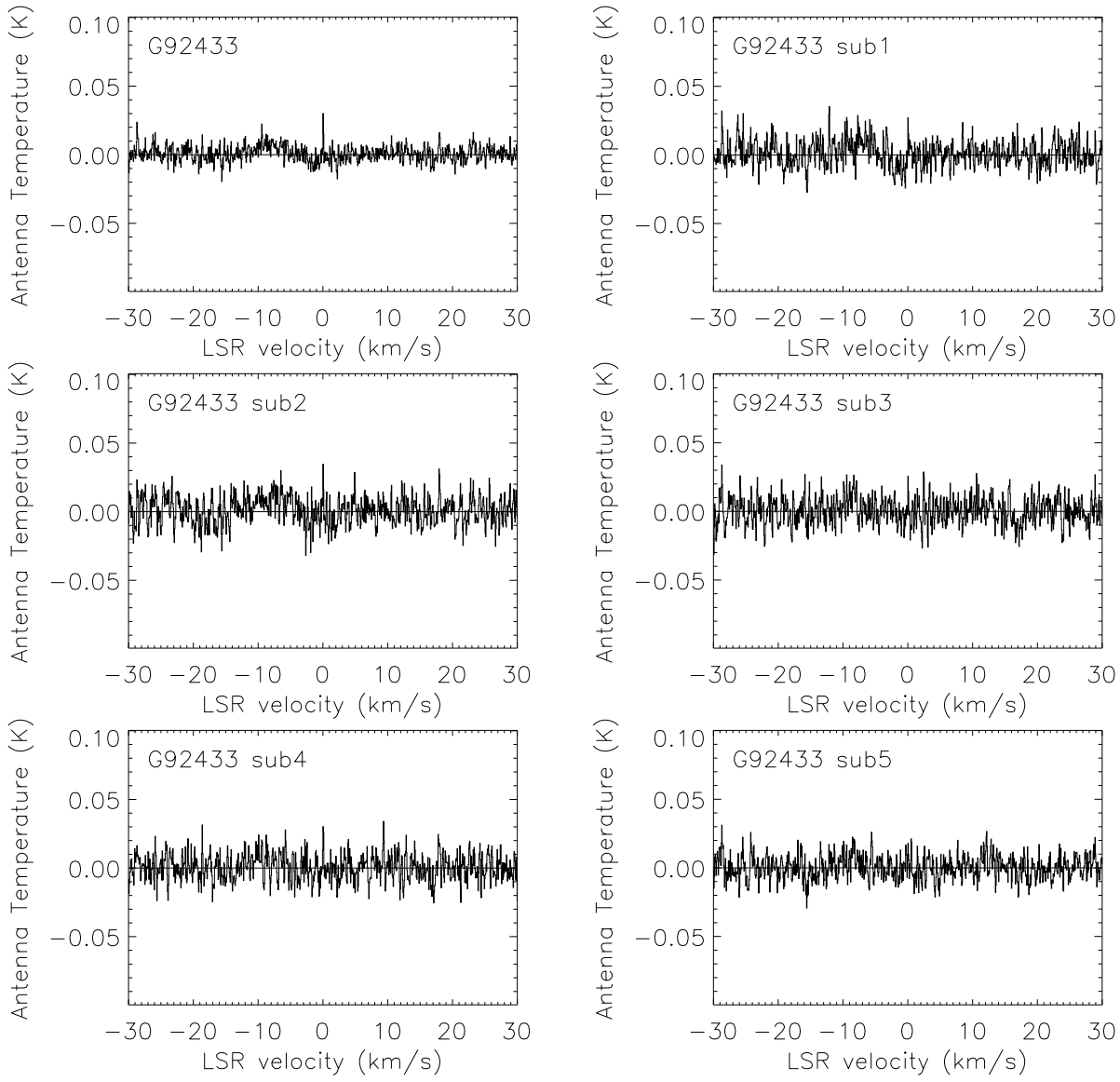

Figure 6.3b: G92433 Component Clusters
Full line of sight and component sub groups 1 through 5.

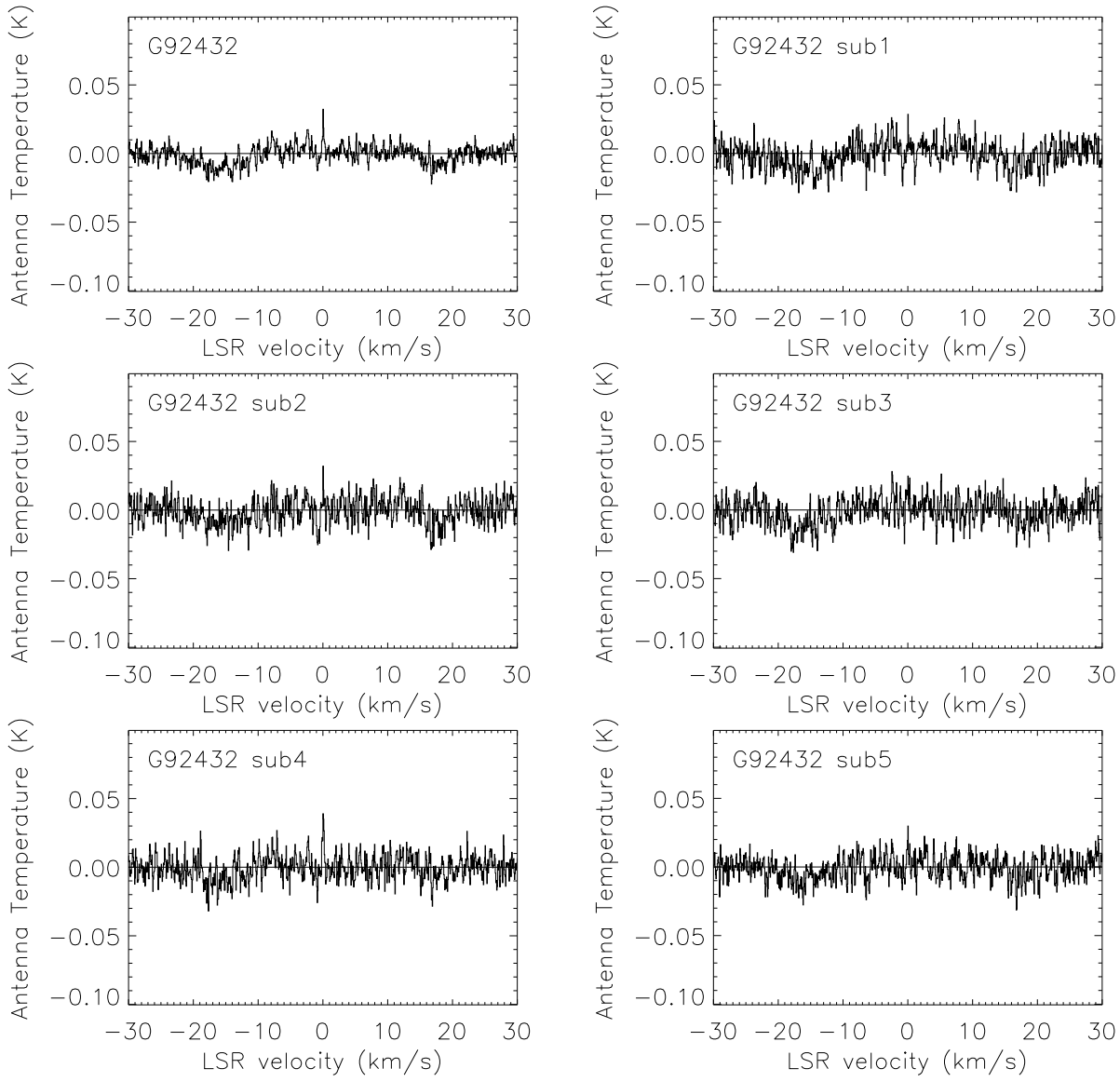

Figure 6.3c: G92432 Component Clusters
Full line of sight and component sub groups 1 through 5.

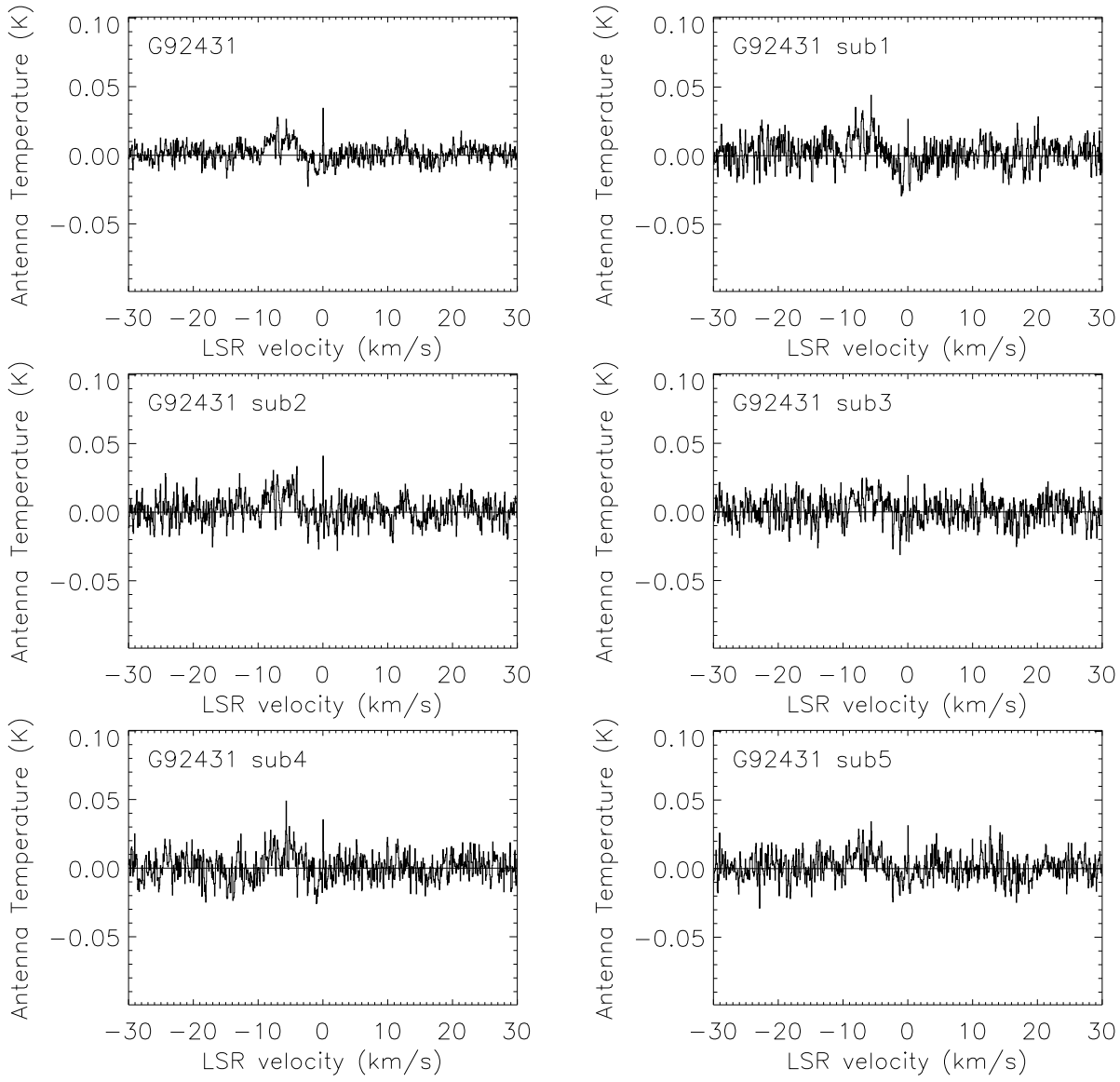

Figure 6.3d: G92431 Component Clusters
Full line of sight and component sub groups 1 through 5.

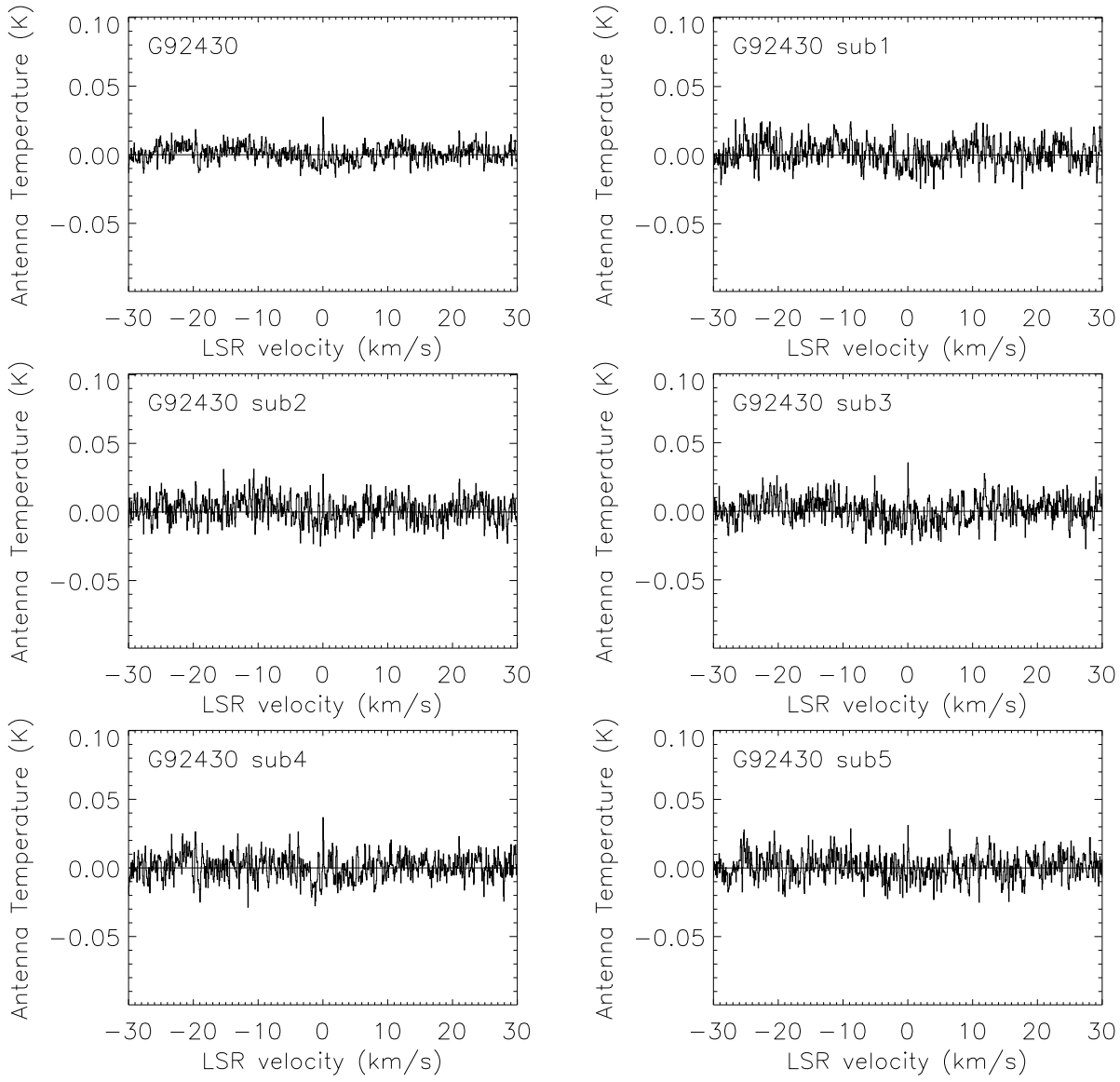

Figure 6.3e: G92430 Component Clusters
Full line of sight and component sub groups 1 through 5.

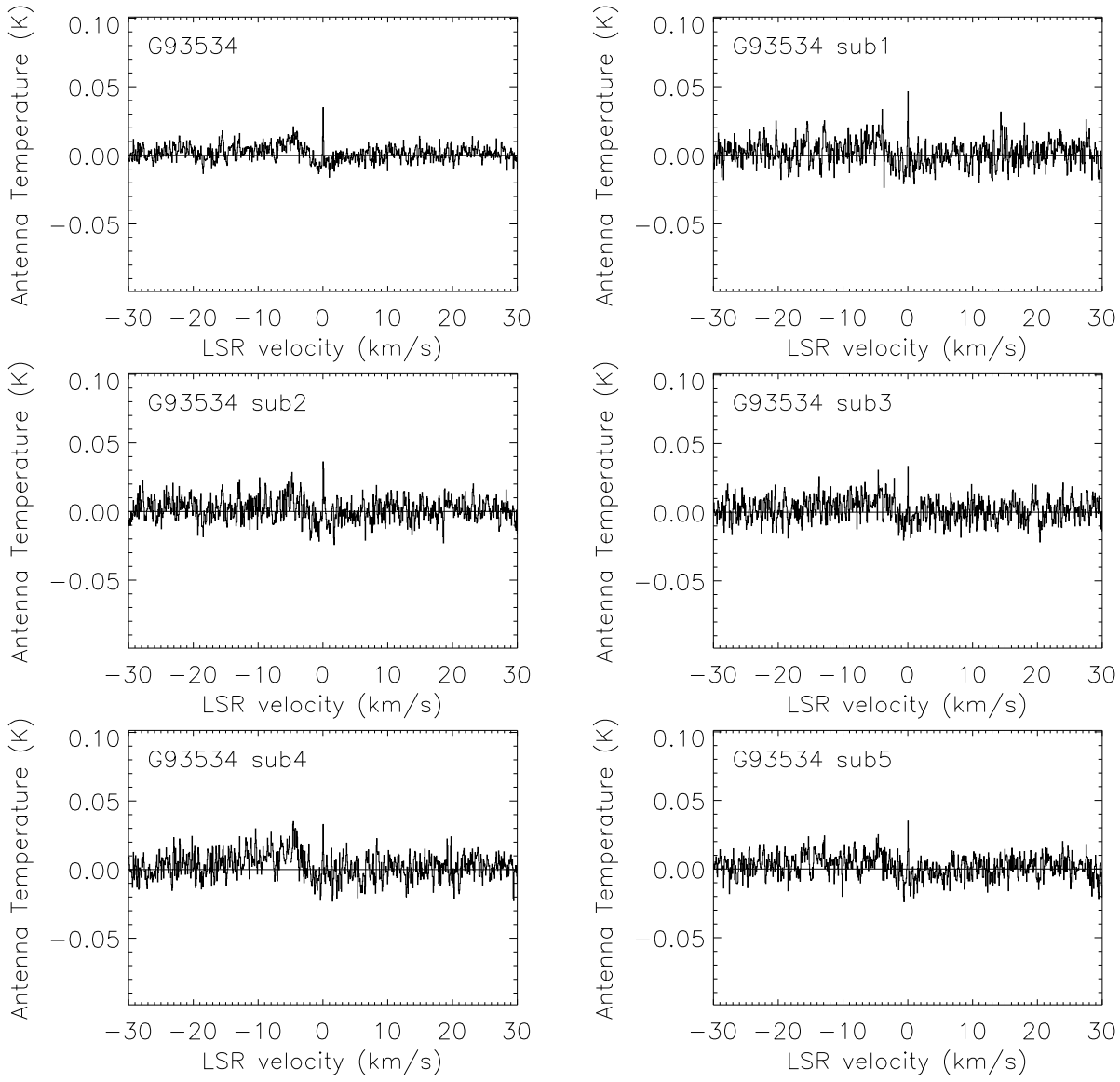

Figure 6.3f: G93534 Component Clusters
Full line of sight and component sub groups 1 through 5.

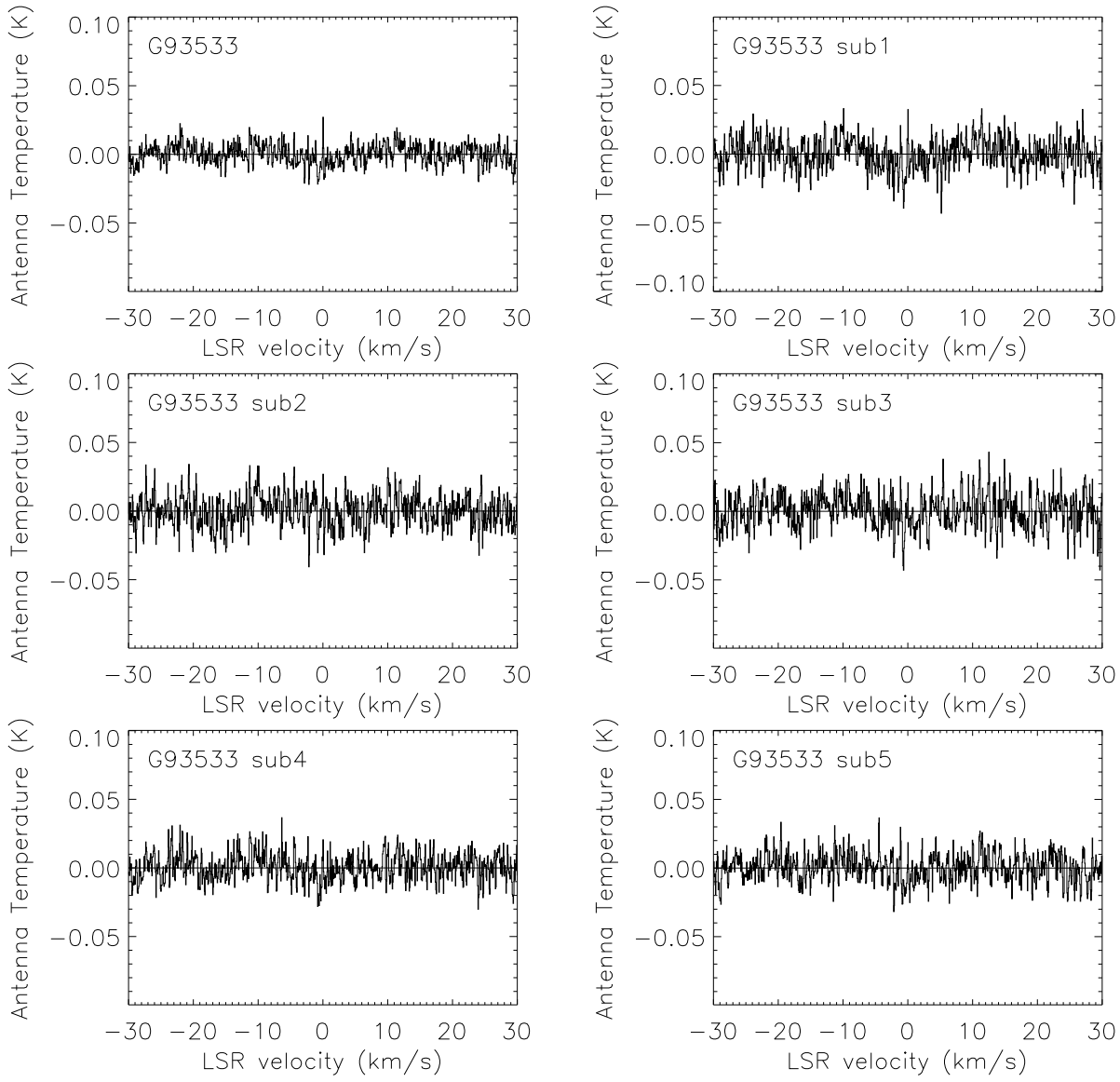

Figure 6.3g: G93533 Component Clusters
Full line of sight and component sub groups 1 through 5.

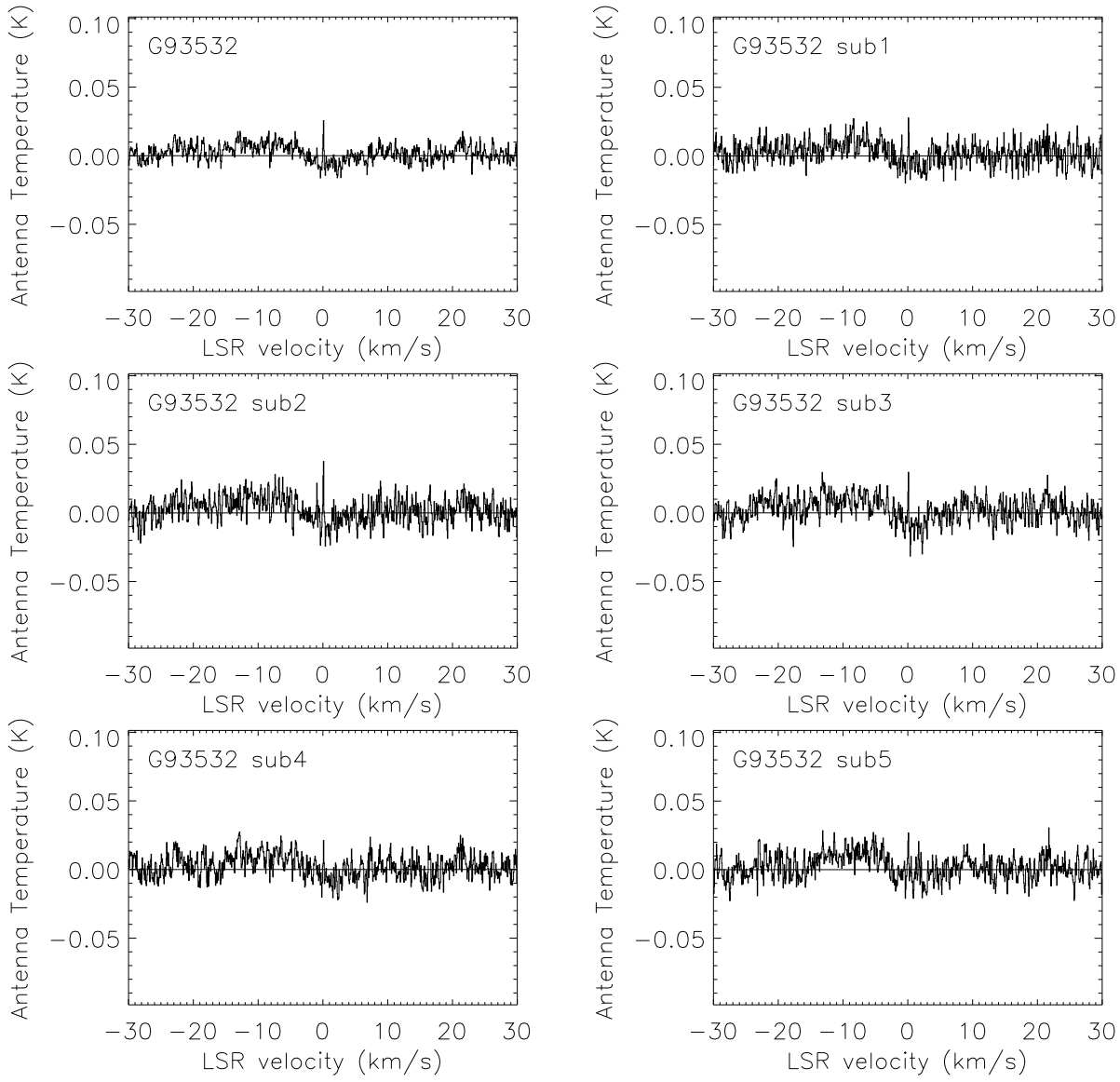

Figure 6.3h: G93532 Component Clusters
Full line of sight and component sub groups 1 through 5.

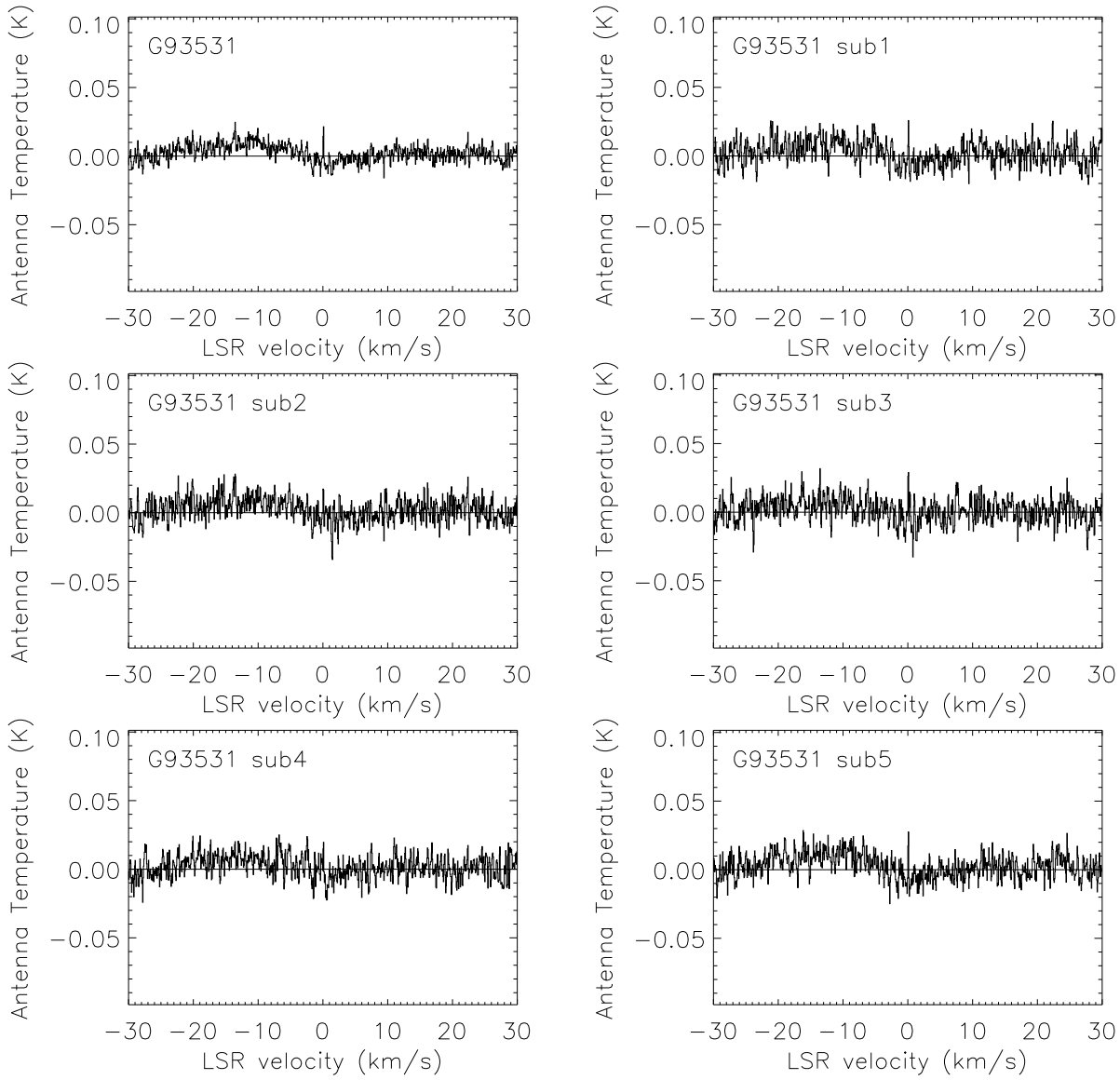

Figure 6.3i: G93531 Component Clusters
Full line of sight and component sub groups 1 through 5.

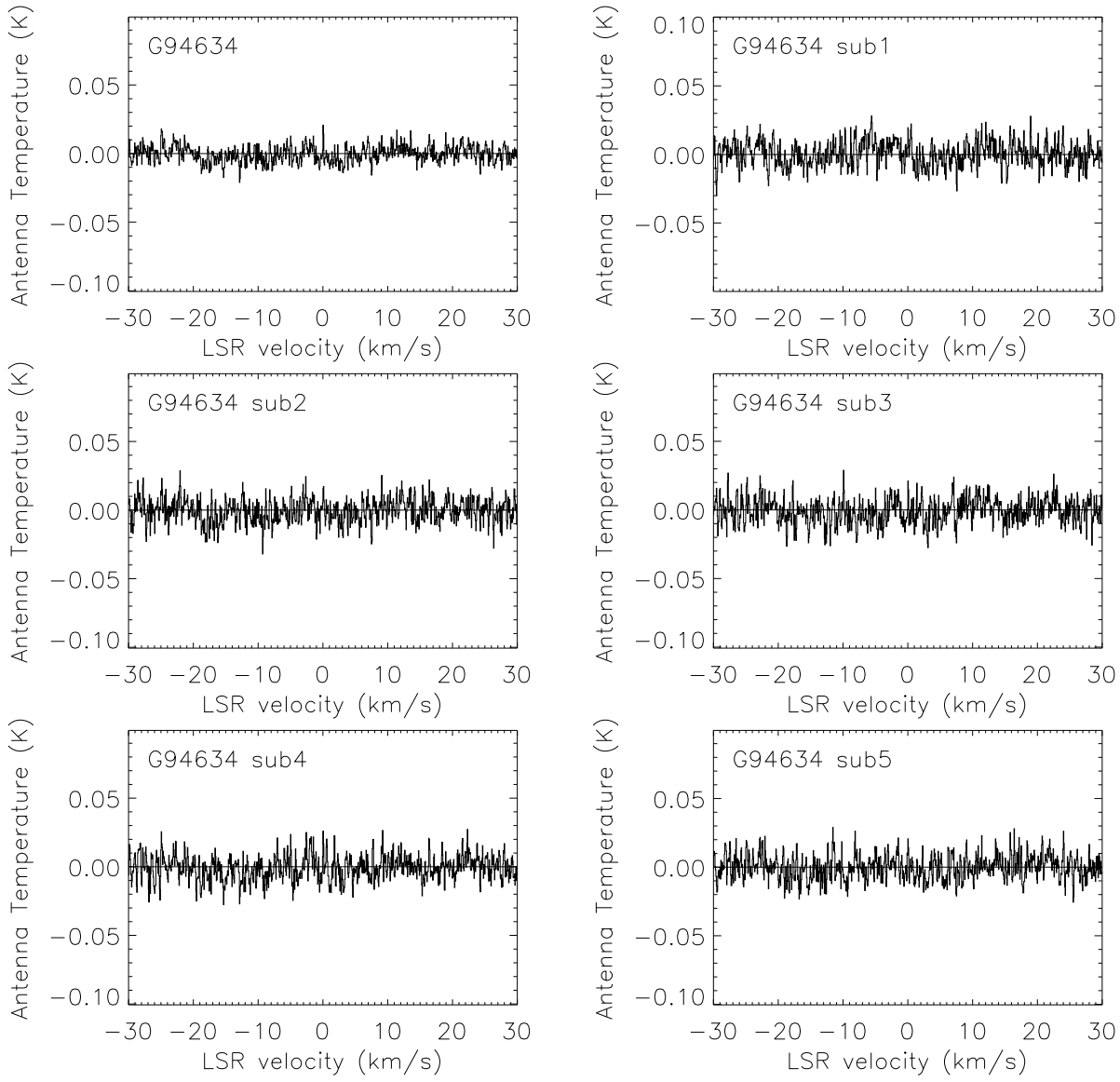

Figure 6.3j: G94634 Component Clusters
Full line of sight and component sub groups 1 through 5.

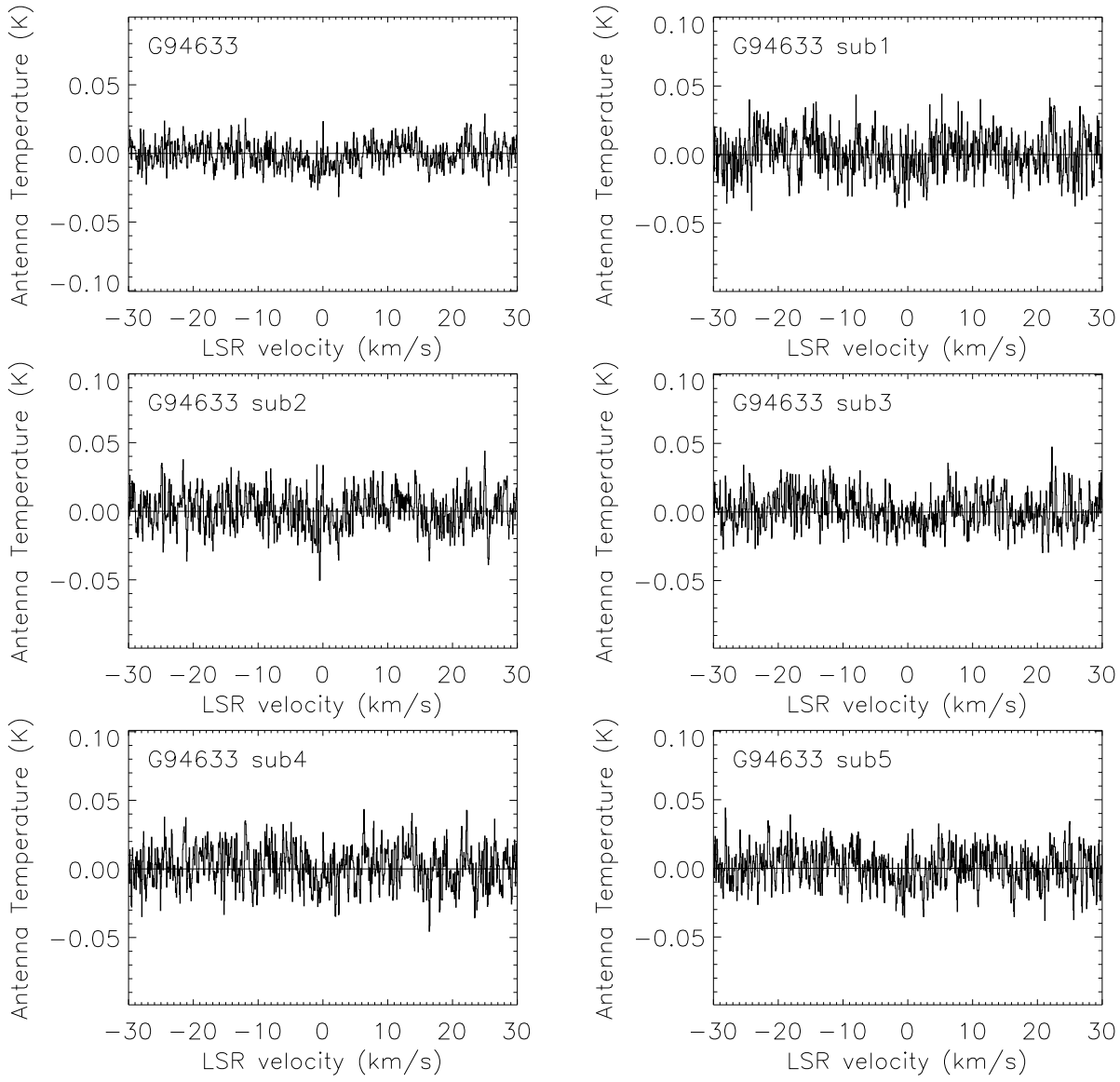

Figure 6.3k: G94633 Component Clusters
Full line of sight and component sub groups 1 through 5.

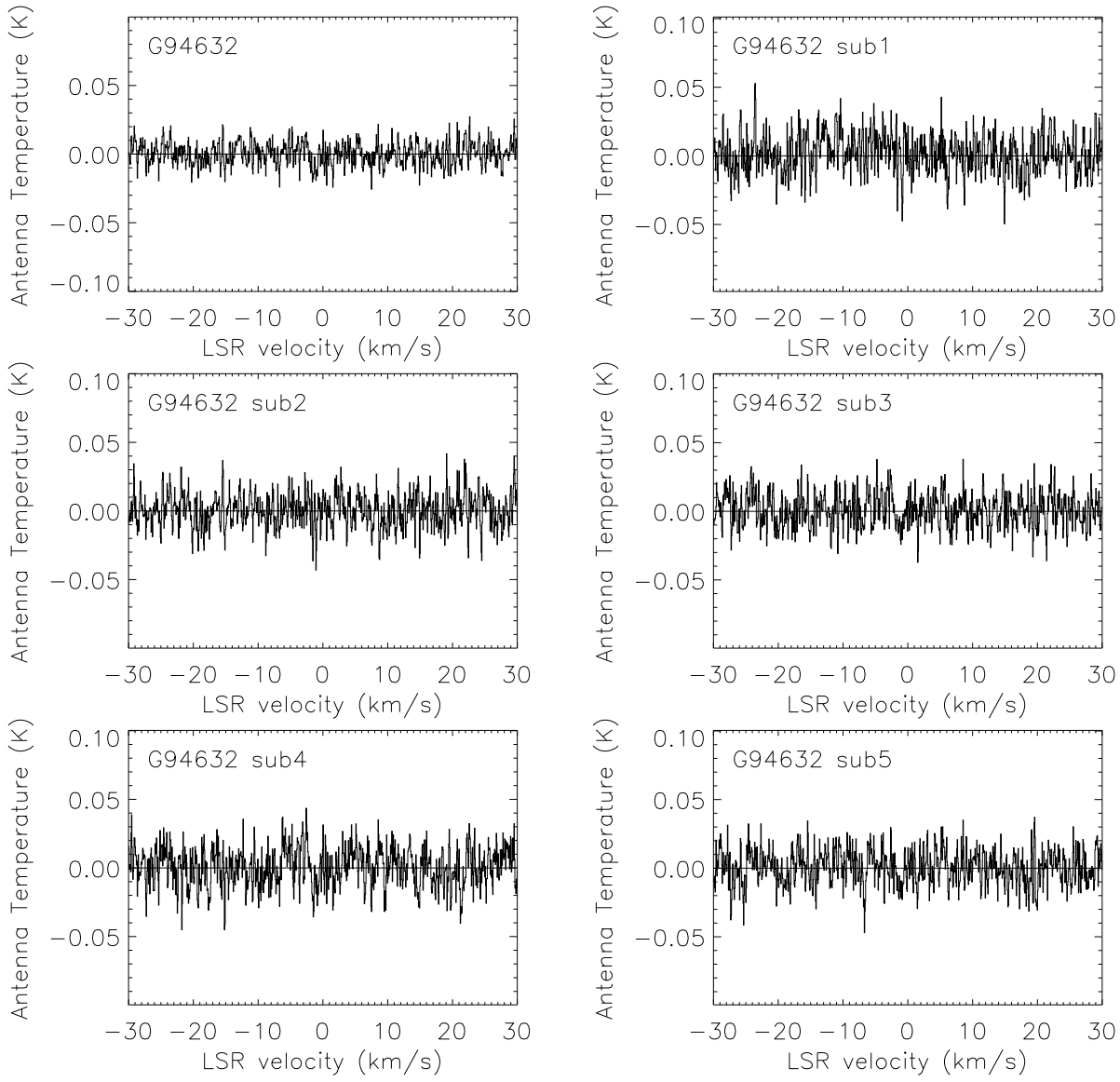

Figure 6.31: G94632 Component Clusters
Full line of sight and component sub groups 1 through 5.

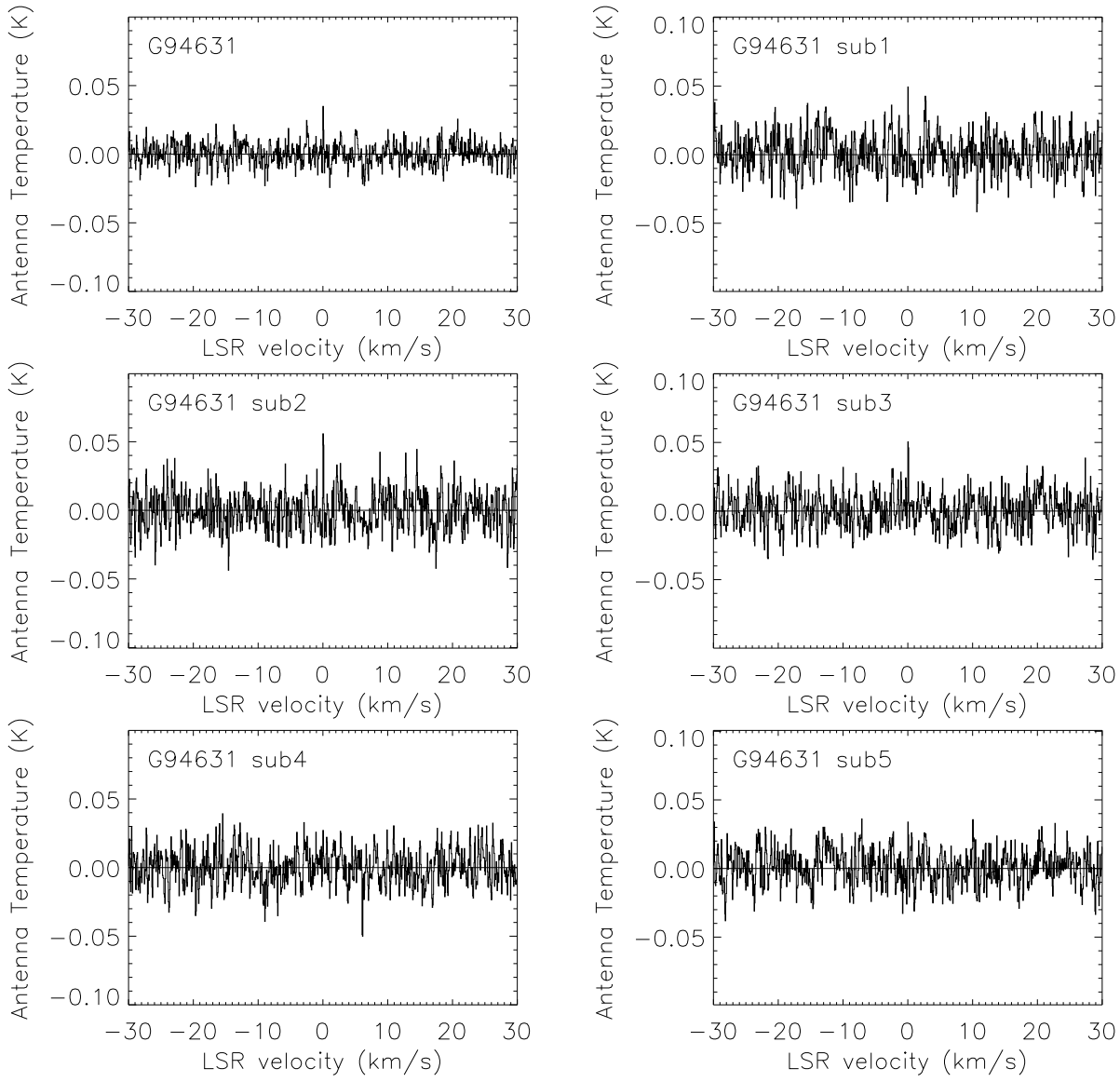

Figure 6.3m: G94631 Component Clusters
Full line of sight and component sub groups 1 through 5.

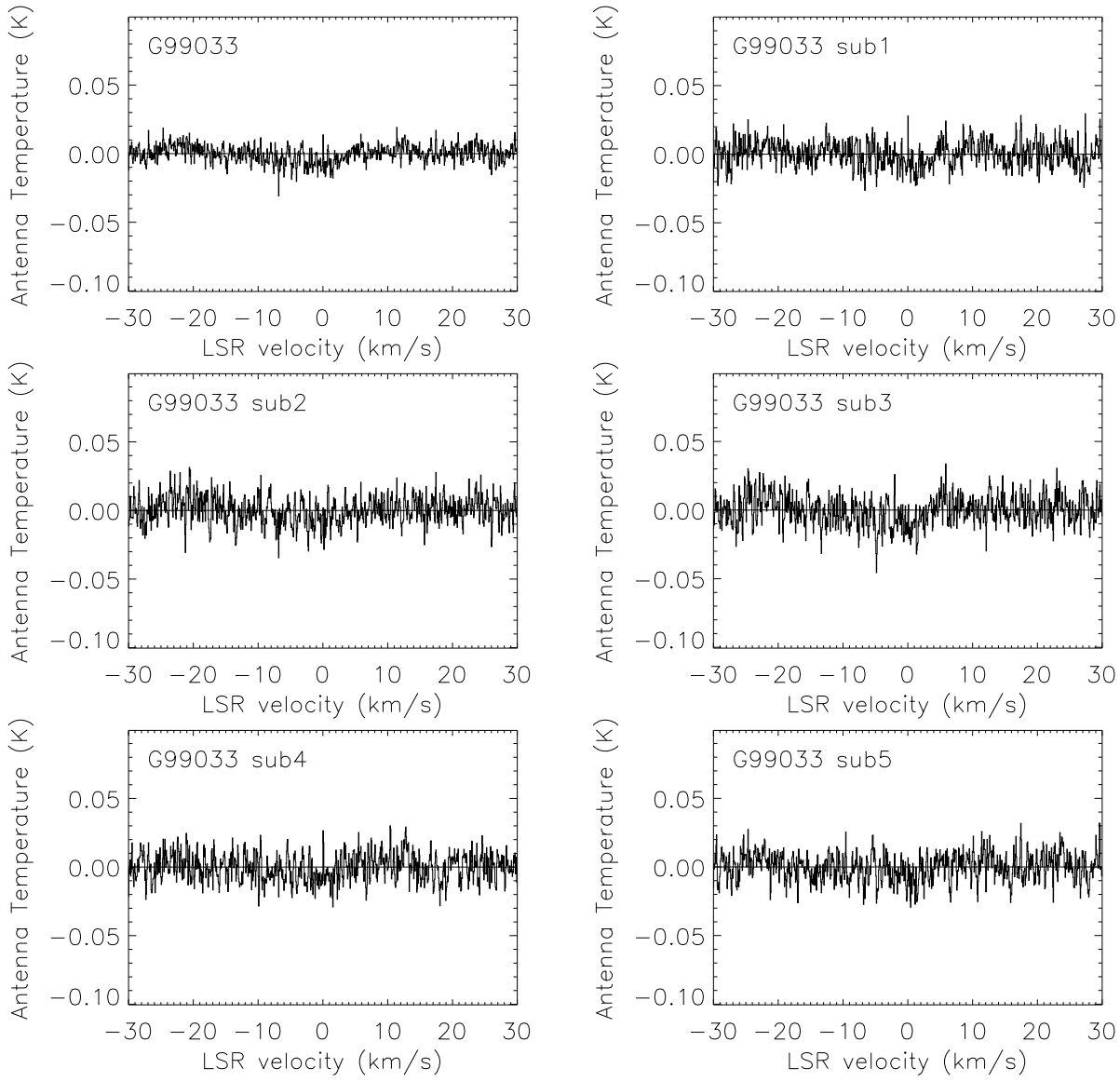

Figure 6.3n: G99033 Component Clusters
Full line of sight and component sub groups 1 through 5.

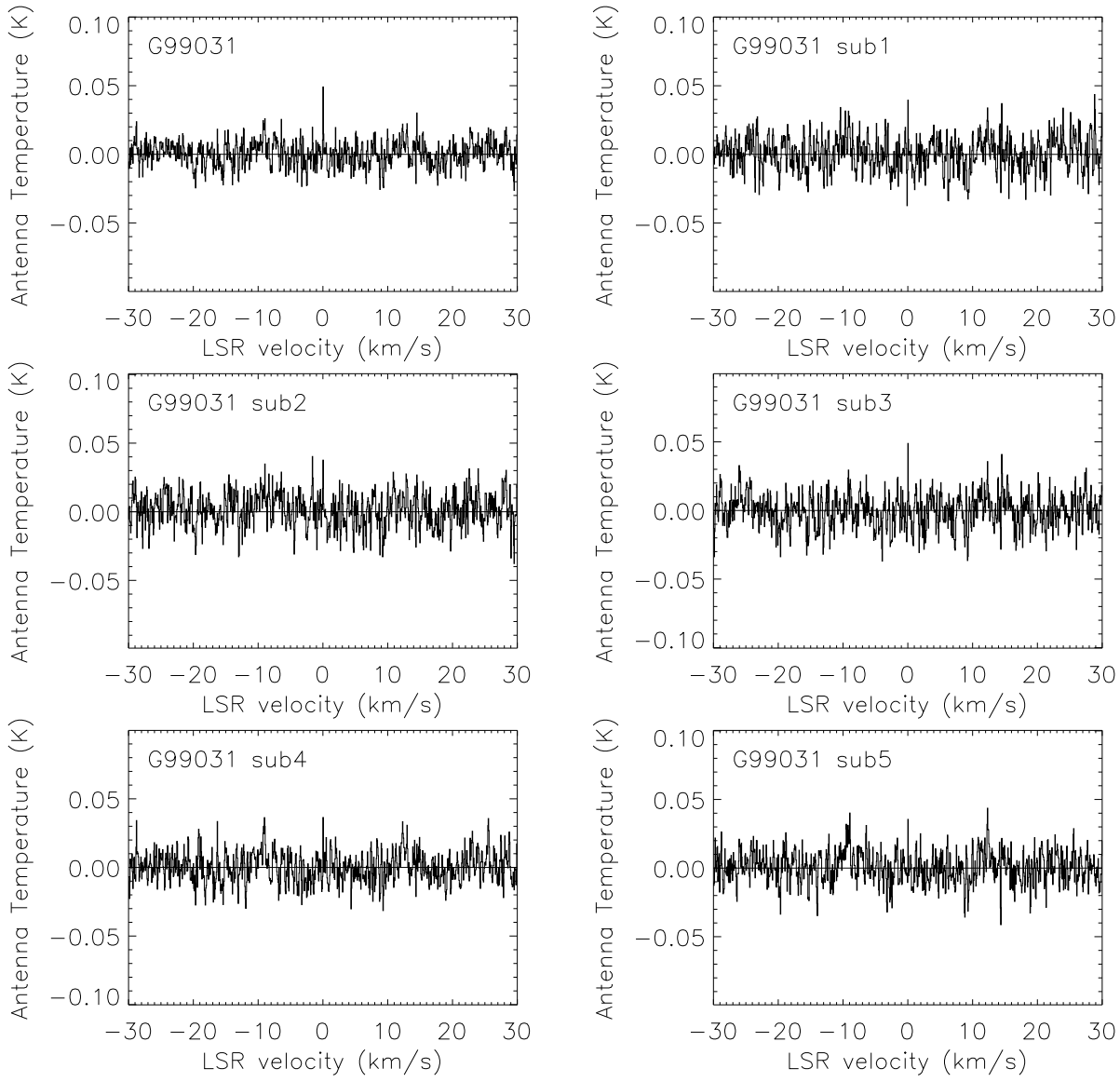

Figure 6.30: G99031 Component Clusters
Full line of sight and component sub groups 1 through 5.

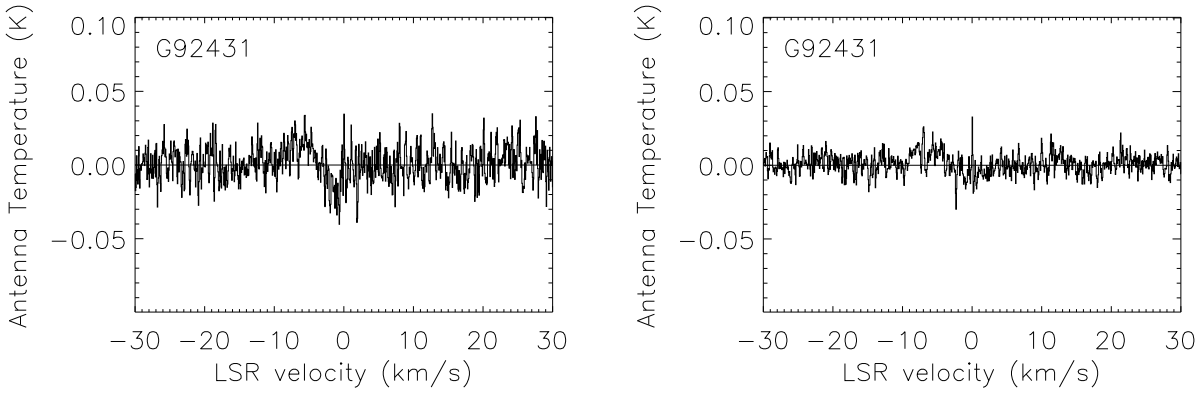

Figure 6.4a: CO Detection Segregated Observations G92431
The left figure shows the CH observations in the lines of sight where CO was detected, and the right figure shows the combined CH observations in the lines of sight where CO was not detected (Stricklan 2019).

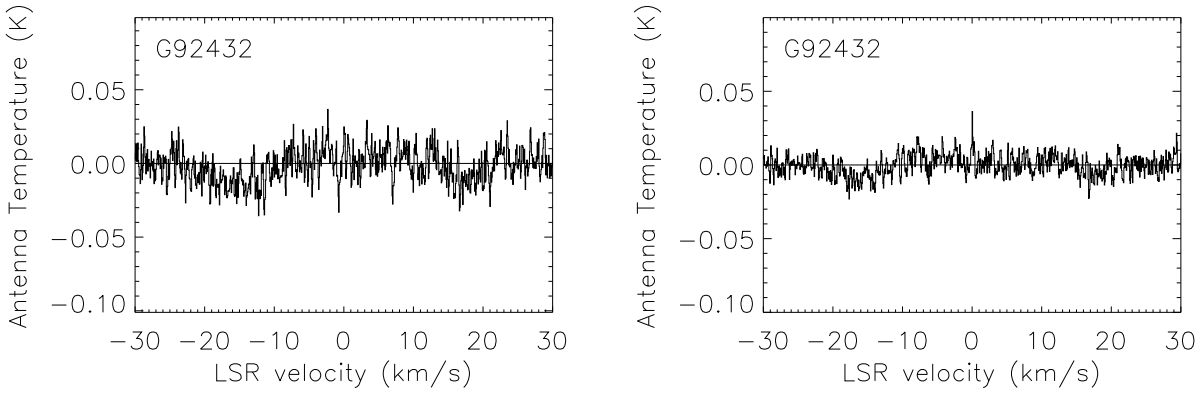

Figure 6.4b: CO Detection Segregated Observations G92432
The left figure shows the CH observations in the lines of sight where CO was detected, and the right figure shows the combined CH observations in the lines of sight where CO was not detected (Stricklan 2019).

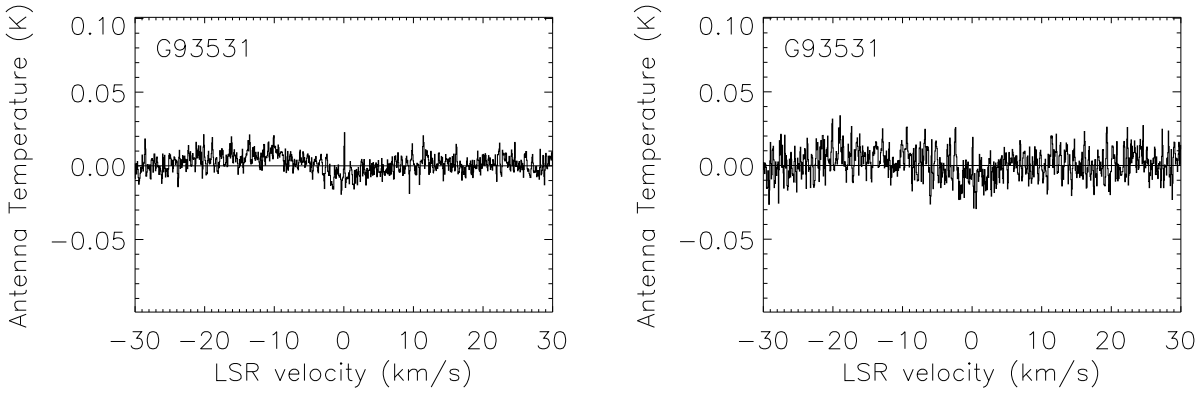

Figure 6.4c: CO Detection Segregated Observations G93531
The left figure shows the CH observations in the lines of sight where CO was detected, and the right figure shows the combined CH observations in the lines of sight where CO was not detected (Stricklan 2019).

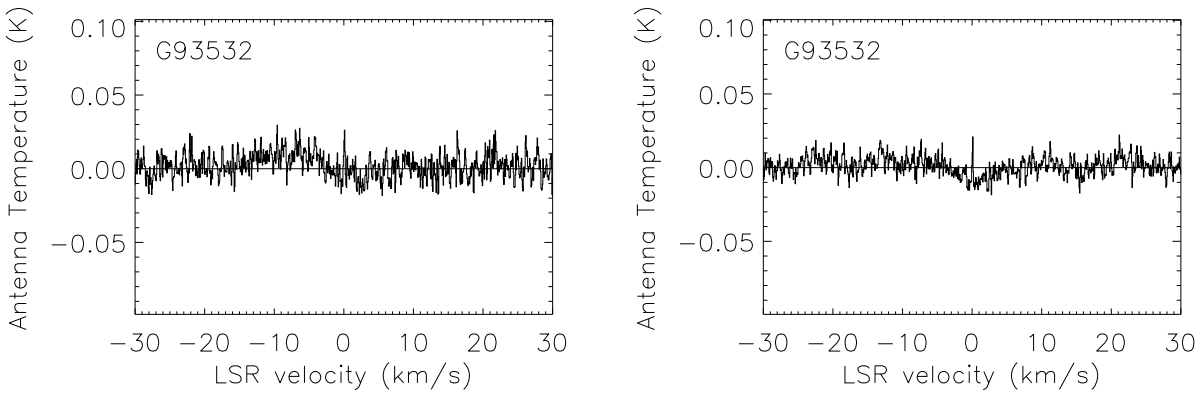

Figure 6.4d: CO Detection Segregated Observations G93532
The left figure shows the CH observations in the lines of sight where CO was detected, and the right figure shows the combined CH observations in the lines of sight where CO was not detected (Stricklan 2019).

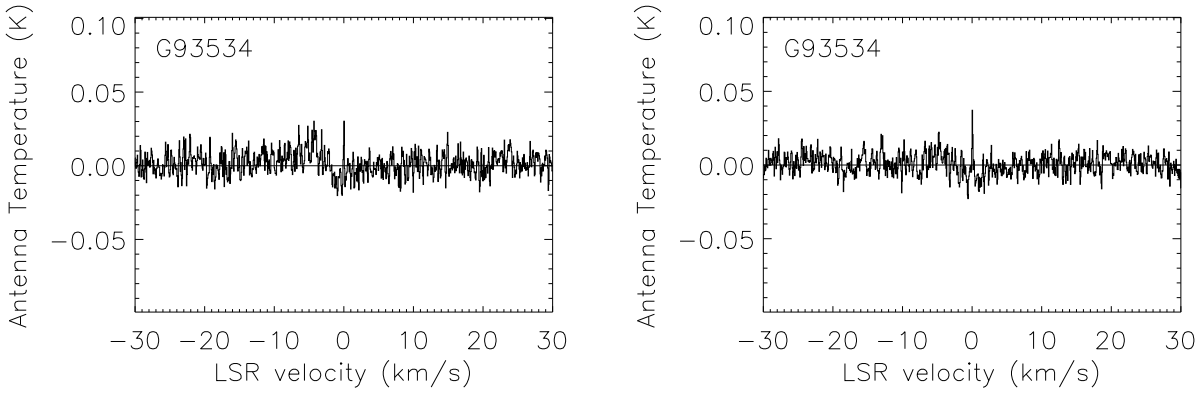

Figure 6.4e: CO Detection Segregated Observations G93534
The left figure shows the CH observations in the lines of sight where CO was detected, and the right figure shows the combined CH observations in the lines of sight where CO was not detected (Stricklan 2019).

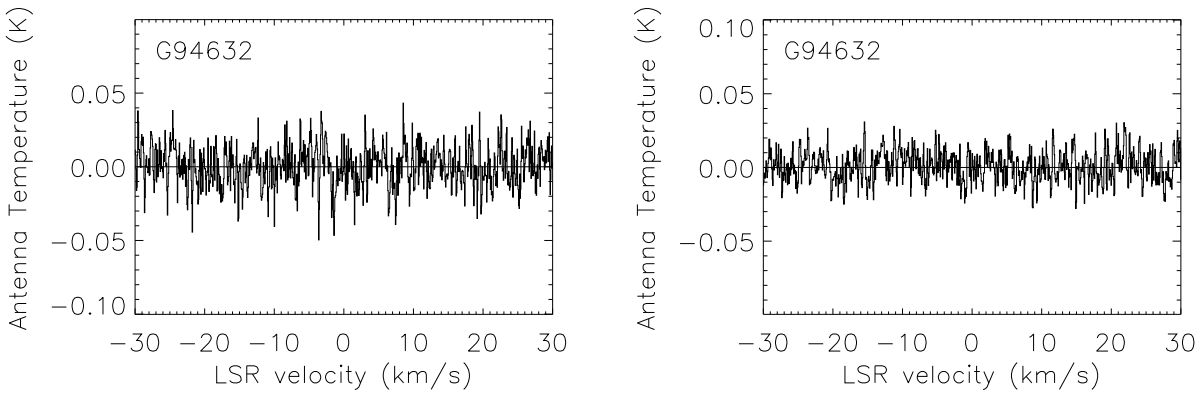

Figure 6.4f: CO Detection Segregated Observations G94632
The left figure shows the CH observations in the lines of sight where CO was detected, and the right figure shows the combined CH observations in the lines of sight where CO was not detected (Stricklan 2019).

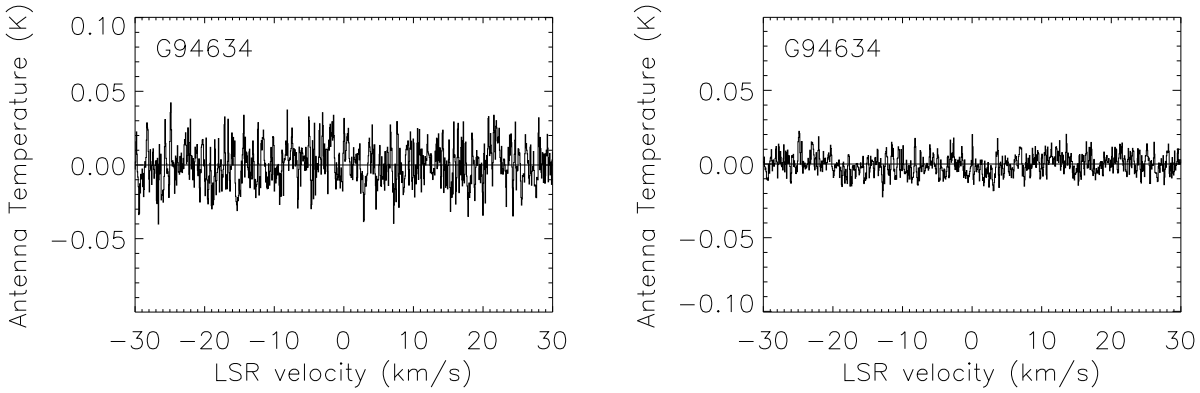

Figure 6.4g: CO Detection Segregated Observations G94634
The left figure shows the CH observations in the lines of sight where CO was detected, and the right figure shows the combined CH observations in the lines of sight where CO was not detected (Stricklan 2019).

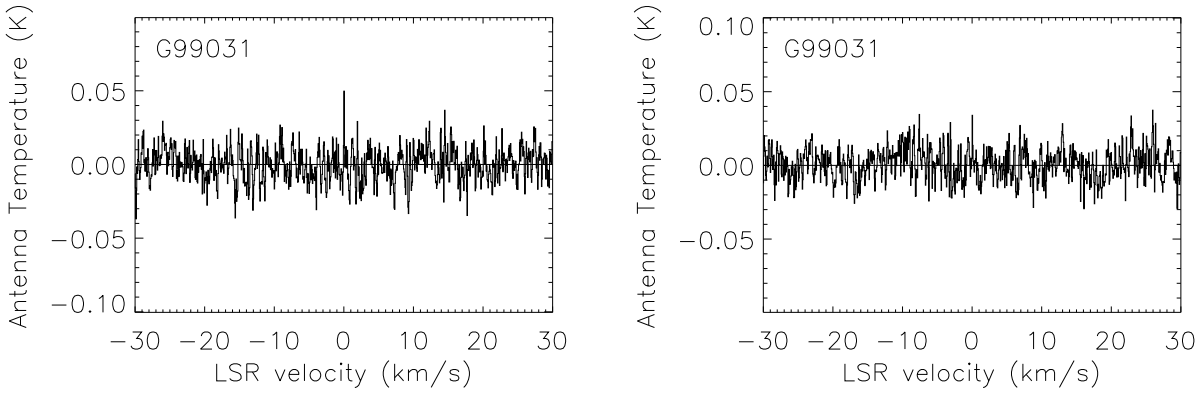

Figure 6.4h: CO Detection Segregated Observations G99031
The left figure shows the CH observations in the lines of sight where CO was detected, and the right figure shows the combined CH observations in the lines of sight where CO was not detected (Stricklan 2019).

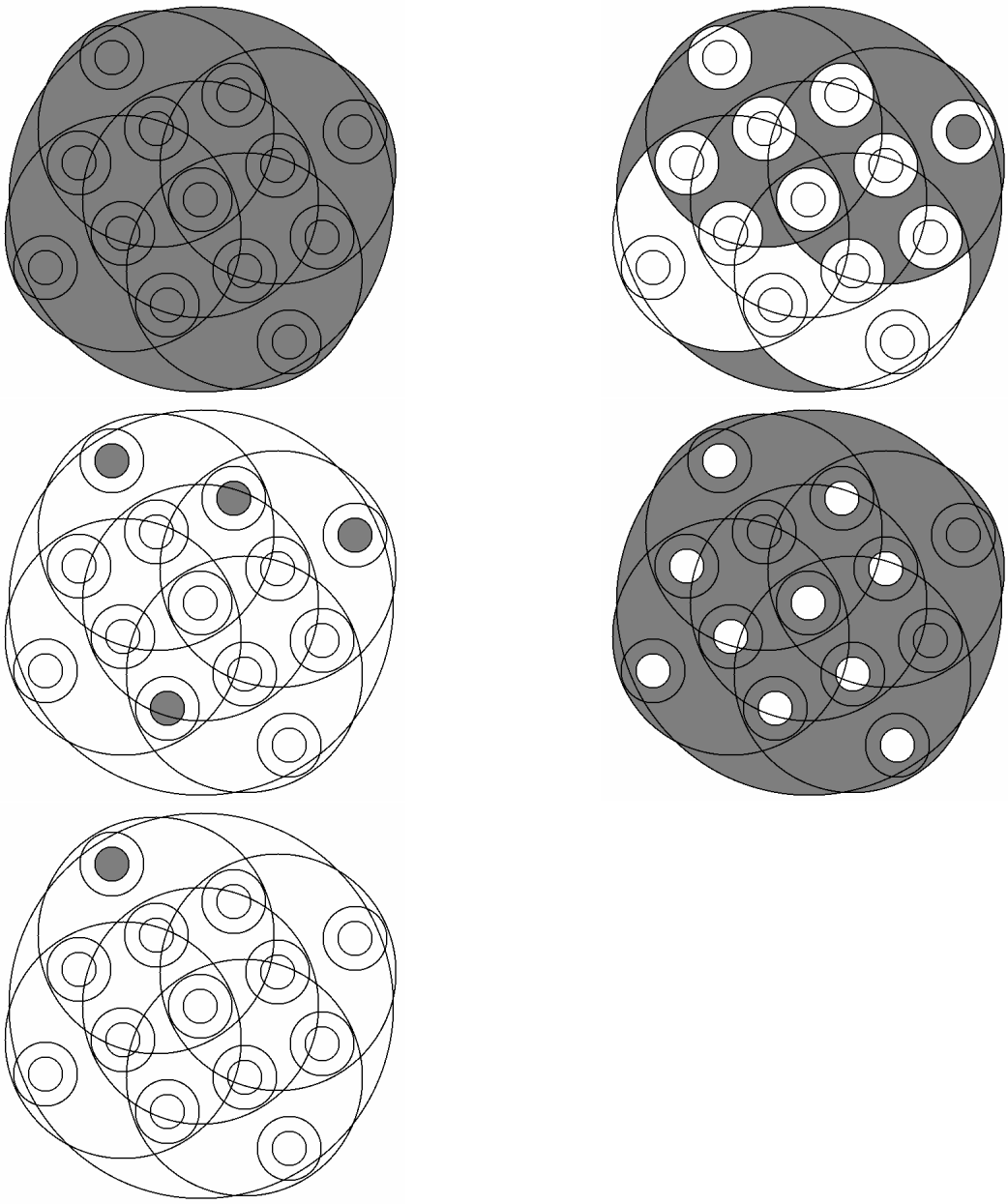

Figure 6.5a: G924 Detection Maps
The maps show, descending left to right, G92434, G92433, G92432, G92431, and G92430. The areas filled in are regions with detections or tentative detections. The small circles represent the CO 55 arcsecond beam, and is filled in if there is a CO detection. The circles encompasing CO beams represent the CH CO-ON and CO-OFF observations and are filled in if there is a CH detection in the CO-ON or CO-OFF spectra. The five midsized circles represent the five groups of CH spectra, and it is filled in if there is a CH detection in the group. The outer circle represents the CH full observation, and is filled in if there is a CH detection.

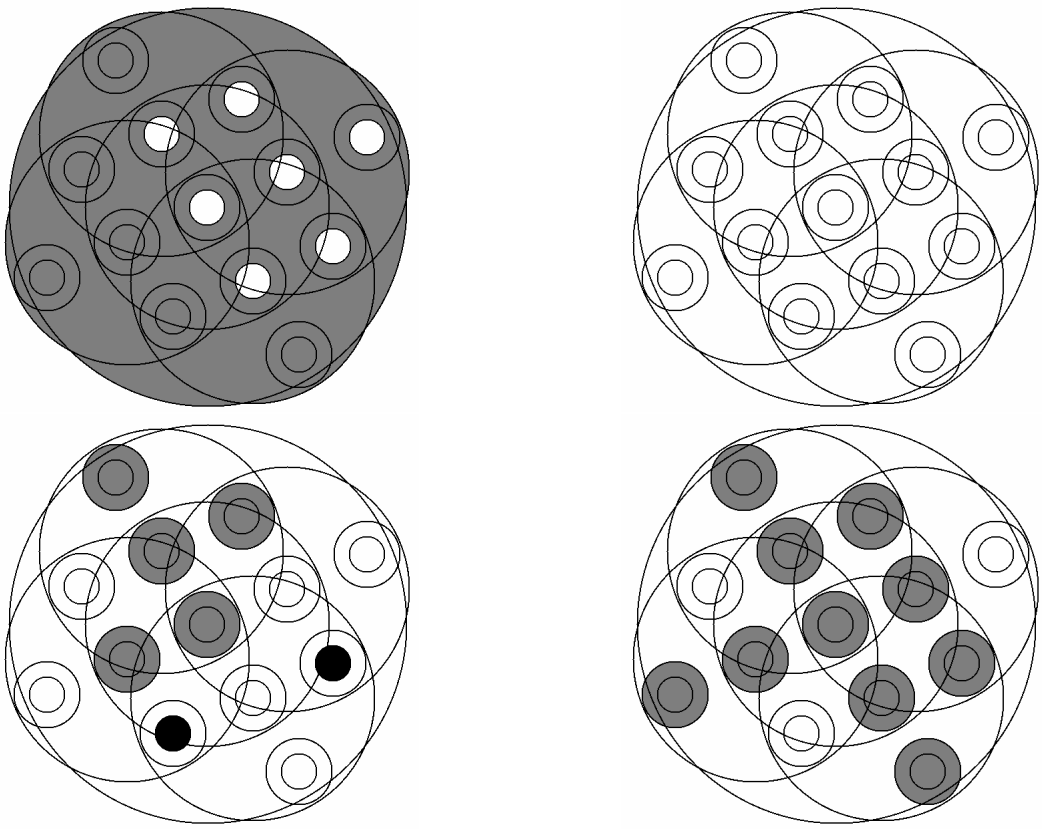

Figure 6.5b: G935 Detection Maps
The maps show, descending left to right, G93534, G93533, G93532, and G93531. The areas filled in are regions with detections or tentative detections. The small circles represent the CO 55 arcsecond beam, and is filled in if there is a CO detection. The circles encompasing CO beams represent the CH CO-ON and CO-OFF observations and are filled in if there is a CH detection in the CO-ON or CO-OFF spectra. The five midsized circles represent the five groups of CH spectra, and it is filled in if there is a CH detection in the group. The outer circle represents the CH full observation, and is filled in if there is a CH detection. The points marked in black are lines of sight without observations.

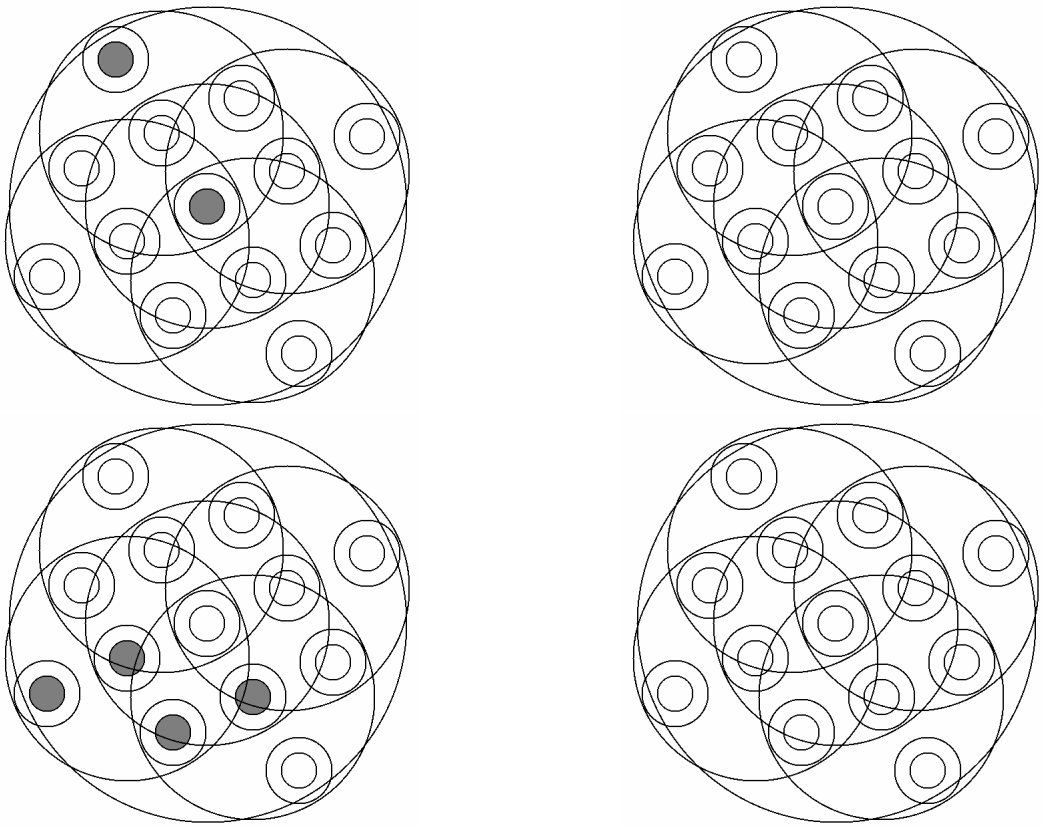

Figure 6.5c: G946 Detection Map
The maps show, descending left to right, G94634, G94633, G94632, and G94631. The areas filled in are regions with detections or tentative detections. The small circles represent the CO 55 arcsecond beam, and is filled in if there is a CO detection. There were no CH detections in any of these lines of sight.

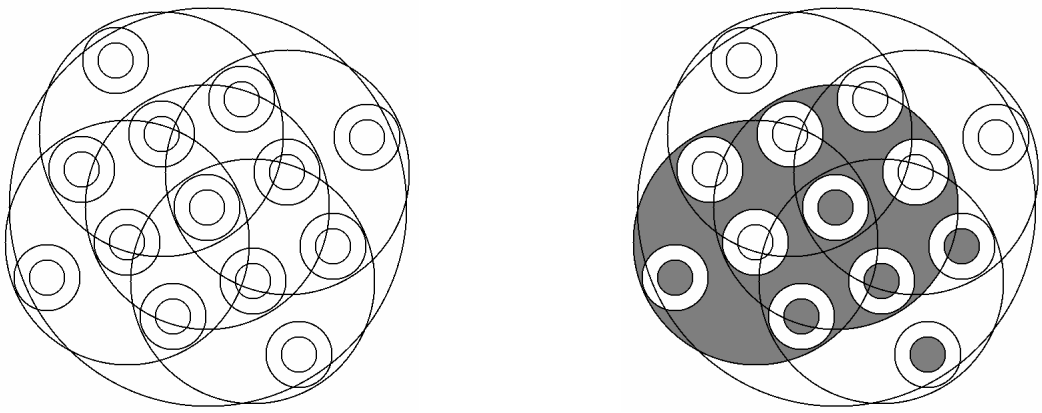

Figure 6.5d: G990 Detection Map
The maps show, left to right, G99033 and G99031. The areas filled in are regions with detections or tentative detections. The small circles represent the CO 55 arcsecond beam, and is filled in if there is a CO detection. The five midsized circles represent the five groups of CH spectra, and it is filled in if there is a CH detection in the group.

Chapter 7

Neutral Atomic Hydrogen Line Profiles in Pegasus

7.1 Introduction

The principal reason for studying CH in low-density, low-extinction clouds is that it may trace the lowest density molecular component, possibly including a component that is not usually traced by the CO $(1-0)$ line. In chapter 5, we noted that CH in MBM 16 appears to be more effective in tracing diffuse gas compared to high signal-to-noise CO $(1-0)$ observations while the situation in MBM 53 described in chapter 6 is more complicated. Even if the CH 3.3 GHz line only sporadically traces the low-density molecular component of an interstellar cloud, observations of any species at the atomic/molecular interface is critical for understanding how diffuse molecular clouds form out of the ambient gas. In this chapter, the atomic/molecular interface will be examined from the atomic side using never-published observations of the 21-cm HI line in MBM53. We attempt to determine if the HI profile shows the presence of molecular

gas through self-absorption, and we make use of the very high signal to noise of our 21-cm data to see if there are any very broad HI components present in the spectra. Additionally, we compare our high signal-to-noise observations with observations from HI surveys, such as EBHIS (Winkel et al. 2016) and GALFA (Peek et al. 2011; Peek et al. 2018).

In diffuse cloud regions, neutral atomic hydrogen makes up a significant fraction of the total hydrogen in the region. Unlike molecular hydrogen, which is very difficult to detect in the cold ISM, atomic hydrogen is trivially easy to detect, and can be observed in most lines of sight after a few seconds with a good L-band receiver. It was the first radio spectral line detected (Ewen and Purcell 1951) and is the strongest non-masing spectral line in the ISM. The line originates from the spin-flip transition connecting the upper to lower halves of the hyperfine-split ground state.

Due to the short integration time required to obtain usable spectra, there have been many HI surveys completed. The entire sky was surveyed in HI in the Leiden/Argentine/Bonn (LAB) Survey (Kalberla et al. 2005) by combining the Leiden/Dwingeloo Survey (LDS - Hartmann and Burton 1997) and the Instituto Argentino de Radioastonomía (IAR) Survey (Arnal et al. 2000 and Bajaja et al. 2005). The Hartmann and Burton (1997) survey observed the northern sky above a declination of -30° using the Netherlands Foundation for Research in Astronomy 25-m telescope. The survey velocity resolution was 1.25 km s^{-1} with a velocity coverage from -450 to 400 km s^{-1} and an rms of 0.09 K (Kalberla et al. 2005). The IAR survey by Arnal et al. (2000) and Bajaja et al. (2005) observed the southern sky below a declination of -25°, using the Instituto Argentino de Radioastonomía 30-m telescope. The final data release in 2005 (Bajaja et al. 2005) lists the survey velocity resolution to be 1.27 km s^{-1} with a velocity coverage from -450 to 400 km s^{-1} and an rms of 0.07 K. A more detailed comparison between the two surveys is in table 1 of Kalberla et al. (2005).

The Effelsberg-Bonn HI Survey (EBHIS) (Winkel et al. 2016) used the 100-m telescope at Effelsberg to survey the sky above a declination of $-5°$. The survey had an rms of 0.09 K and a velocity resolution of 1.29 km s^{-1} over a velocity range from -600 to 600 km s^{-1}. The beam size was significantly improved compared to the LAB survey, where the EBHIS survey has a beam size of 10.8 arcminutes while the LAB survey has a beam size of 36 arcminutes (Winkel et al. 2016). The southern sky below a declination of $1°$ was surveyed by the Parkes Galactic All-Sky Survey (GASS) using the 64-m Parkes telescope (McClure-Griffiths et al. 2009). This survey had a velocity resolution of 0.82 km s^{-1} with a velocity range from -470 to 470 km s^{-1}, a low rms of 0.057 K, and a beam size of 16.1 arcminutes (Winkel et al. 2016). Similar to the LAB survey, the HI4PI survey (HI4PI Collaboration et al. 2016) combines EBHIS and GASS to create a single survey that covers the entire sky.

Lastly, the GALFA survey (Peek et al. 2011 and Peek et al. 2018) was conducted using the 305-m telescope at Arecibo Observatory with an exceptional (for HI) 4 arcminute angular resolution. The survey covered velocities from -650 to 650 km s^{-1} with a resolution of 0.184 km s^{-1}, but had an unremarkable 0.15 K rms. Due to the geometry of the telescope, the survey viewed only the sky within the narrow declination range of $-1.28°$ and $37.95°$.

7.2 Observations

The data used in this section uses previously unused data from Arecibo project A3021 conducted by Donate and Magnani in 2016 from January to July. The backend used was the Wideband Arecibo Pulsar Processor (WAPP) configured for 8 boards, with 1.5625 MHz bandwidth, 9-level sampling, and 2048 channels each. Boards 2 and 4 observed the HI 1420.406 MHz line, while the remaining boards were

used to observe the 1.7 GHz OH lines for a separate project eventually published by Donate, White, and Magnani (2019). The OH and HI data were taken to sample the 8 arcminute beam of the Magnani et al. (2000) CO survey and comprise of 5 observations for each position in MBM 53 (see chapter 6 and figure 7.1). The beam efficiency at 1420 MHz was approximately 0.69 ± 0.07. The individual points were observed for approximately 10 minutes each, resulting in an average rms of 0.032 K. The beam size of the observations is 3.58 arcminutes. To account for stray radiation, the data is normalized using the EBHIS observations, which reduces the measured column densities to about 79 percent of the original value. Combining the component observations of each main line of sight results in an average rms of approximately 0.018 K. The rms of the combined observations is much lower than that of the other HI surveys; GASS, which has an rms of 0.057 and has the lowest rms of the surveys listed above, has an rms that is ~ 3 times greater than that from our combined observations described below.

7.3 Results

The baseline was determined by selecting the best baseline from a variety of conditions for each individual component line of sight[1], and was always chosen to be second order. Due to the signal covering large portions of the spectrum for each line of sight, the regions chosen to fit the baseline were always at the ends of the spectra. Each of the spectra covers a velocity range of about 233 km s^{-1} across 1448 channels. For the positive velocities, the number of channels chosen to fit the baseline is either 100, 200, 300, or 400, approximately 16 to 64 km s^{-1}. For the negative side, the number of channels chosen to fit the baseline is either 100, 200, or 300, approximately 16 to 48 km s^{-1}.

[1]See chapter 6 for the definition of a "component" line of sight.

To account for stray radiation, the data is normalized using the EBHIS data (Winkel et al. 2016). The column densities of our HI data are calculated from the unadjusted spectra, and the magnitude of the brightness temperature of each channel is reduced by a flat percentage to reduce N(HI) to match the EBHIS values. To determine N(HI), equation 2 from HI4PI Collaboration et al. (2016) was used, with the integrated intensity determined from equation C1 in Mangum and Shirley (2015),

$$N_{HI} = 1.823 \times 10^{18} \int T_{B,sum} \Delta v_c \tag{7.1}$$

where $T_{\rm B,sum}$ is the sum of the brightness temperature in each channel within the line where $\eta_b = 0.69$, and Δv_c is the velocity width of each channel. With a 1.5625 MHz bandwidth, the velocity width per channel at 1420.406 MHz is 0.161 km/s. Equation 7.1 assumes the HI emission is optically thin.

The stray radiation correction factor averages at about 0.79, so on average about 21 percent of the signal is from stray radiation. This varies across the Pegasus cloud, with a maximum 28 percent of the signal from stray radiation, and a minimum 8 percent. Typically, the higher correction factors are at higher galactic latitude; i.e., -30° and -31° usually have less stray radiation than the lines of sight at galactic latitude -34° and -33°.

7.4 HI Summed Lines of Sight

Each set of up to 5 component lines of sight within each of the main lines of sight[2] are combined, in order to mimic the CO beam from the Southern Galactic High-Latitude Survey (Magnani et al. 2000).

[2] Arrangement of the components is shown in figure 7.1

Figure 7.2 shows an example of the 5 component lines of sight along with the spectrum of the combined components.

Similar to the CO and CH observations in chapter 6, there are small variations in the component observations in each full line of sight, and some have components which are not shared with the rest of the group. One of the largest variations in G92434 is the velocity component at approximately 40 km s^{-1} in G9243402 and G9243404. In the summed line of sight for G92434, the 40 km s^{-1} feature has been reduced from combining the spectra. However, the feature at -30 km s^{-1} in G9243402 is smoothed over enough in the summed spectrum that it is no longer easily visible.

7.5 HI Gaussian Decomposition

Gaussian fits were applied to each of the summed lines of sight in order to examine the velocity structure of HI. There is not a single combination of gaussians which can be used to fit the data uniquely in an observed spectrum, but we attempt to fit the spectra with as few gaussians as possible. The examined spectra are corrected for stray radiation by a simple zeroth order reduction in the brightness temperature, but some of the velocity components may be wholly or partially due to stray radiation, since it does not increase the brightness temperature in each channel equally.

In order to reduce, but unfortunately not eliminate, our own biases in the gaussian fitting process, we used an automatic gaussian fitting program based on the pyspeckit Python package (Ginsburg and Mirocha 2011). Pyspeckit is built to use user inputs to select the initial guesses used to fit the data, but the process has been automated by using the residual data from successively applied gaussians until the sum of every 11 channel group of the residual data is below a specified level. For each channel, the channel

brightness temperature is added to the sum of the 5 channel brightness temperatures on either side of the channel for a sum of the 11 channels to prevent the program from attempting to fit high-temperature individual channels. At the ends of the spectra where there are not 5 channels to one side of a channel, the missing channels are substituted with a brightness temperature of 0 K. In the case of the plots in figure 7.3 and 7.4, the threshold is at 0.50 K. The plots are made using Matplotlib (Hunter 2007).

Gaussians are added one at a time, selecting the midpoint point of the 11 channel group with the highest summed brightness temperature to select an amplitude and center for the guess. In each iteration, all of the gaussians which have been added are fit based on the guesses. After the first gaussian is applied, the amplitude guess uses the amplitude from the initial data set at the location of the midpoint of the 11 channel group. The guess for the width is a function of the amplitude guess and the absolute sum of all residual temperatures. The simulation assumes that 11 channel groups on the residuals is a good basis to determine the guesses to use to apply gaussian fits, and requires that the residual baseline is flat enough to be below the summed temperature threshold. This method is effective in automatically applying gaussian fits to a curve as long as the channel width is small compared to the width of the signals. The EBHIS data have wide channels so this fitting method is not effective. Instead of selecting the center point of the 11 channel group with the highest brightness temperature, the highest individual point is selected.

A mosaic of all of the spectra is shown in figure 7.3, which illustrates how the shape of the HI lines changes across the sampled portion of MBM 53. Figures for each of the 35 combined lines of sight are shown in figure 7.4. The data are shown in black and the combined gaussian fit in blue. The red gaussians are each of the component gaussians, and each of the gaussians has the center marked by a red line underneath the data.

Across most of the spectra, the majority of the HI signal is between -10 and 0 km s^{-1}. There are a few interesting features which arise in single spectra, such as the several lines of sight which include gaussian components which are at high negative velocities, near approximately -50 km s^{-1}, and they are discussed further in section 7.7. The majority of the velocity components are negative, however there are a few lines of sight with positive velocity components with centers at greater than 10 km s^{-1}, with G99030, G97931, and G96831 having a distinct peak between 20 and 30 km s^{-1}. For most of these positive velocity components, the feature is short and wide like in G95733, which could indicate the presence of warm and/or turbulent gas.

The 21-cm line is able to trace neutral atomic hydrogen in the warm neutral medium (WNM) and cold neutral medium (CNM). The CNM is where molecular clouds form and is very cold, around 10 - 100 K, so emission lines originating from this gas will be narrow. Rearranging an equation from Alexander (2008) which converts the line width to temperature

$$T = 40\,(\sigma_{FWHM}/2.355)^2 \tag{7.2}$$

to the following equation

$$\sigma_{FWHM} = 2.355 * (T/40)^{1/2} \tag{7.3}$$

allows us to convert the temperature to the width of a line widened by the thermal doppler broadening. The CNM will be considered to have temperatures less than 200 K to match the boundary stated in Audit and Hennebelle (2005), which means that the FWHM will be below 5.3 km s^{-1}. The boundary temperatures between the different categories will be rounded up for each case, so the boundary will be at 6 km s^{-1}.

The WNM accounts for 60 percent of HI in the ISM (Heiles and Troland 2003), and contains gas between 5000 to 9600 K (Audit and Hennebelle 2005; Magnani and Shore 2017), which corresponds to FWHM between $\sim$ 27 km s^{-1} and $\sim$ 37 km s^{-1}. Between the WNM and the CNM is the thermally unstable warm neutral medium, which accounts for at least 48 percent of the WNM[3] (Heiles and Troland 2003). The amount of gas in the thermally unstable WNM is directly related to the amount of turbulence in the ISM; as the amount of turbulence increases, so does the amount of gas in the thermally unstable WNM (Audit and Hennebelle 2005). Gazol et al. (2001) simulated the galactic disk, and found that about half of the total mass is in the thermally unstable WNM. The boundaries for each of the categories will be at FWHM = 6, 27, and 37 km s^{-1}. The lines with FWHM above 37 km s^{-1} are from unknown sources (Haud and Kalberla 2007), and may be from improper baseline fitting, instrumental effects, or, possibly, stray radiation.

Generally, each of the HI spectra consists of several smaller components, some of which are seen as the small "bumps" on the signal. The distribution of the gaussian component widths of the fits shown in figures 7.3 and 7.4 is shown in figure 7.5a, where each of the bins has a width of 1 km s^{-1}. The gaussian structure of the spectra suggests that each of the lines of sight contains several velocity components, with the majority of the components being thin with widths of less than 6 km s^{-1}. These components with narrow widths are likely from gas in the cold neutral medium. The most populated bin is the one for widths between 2 and 3 km s^{-1}, which is not much greater than the velocity resolution of the surveys which are combined to create the LAB survey. There are also approximately 22 components which have widths that are less than 2 km s^{-1}. The number of components in each bin beyond 6 km s^{-1} is low, usually not exceeding 10 components, but overall, about 45 percent of the components have widths greater than

[3]In Heiles and Troland (2003) the lower limit of the WNM was 500 K.

6 km s^{-1}. Some of these wide components have extreme widths, and almost 30 velocity components throughout MBM 53 have widths in excess of 37 km s^{-1}. The equivalent kinetic temperature of this component would be in excess of 9874 K, which makes the interpretation that this component arises from neutral atomic gas unlikely. This is discussed in the next section. These extremely wide components only make up about 7 percent of the total components, approximately the amount determined from the LAB survey data in Haud and Kalberla (2007) for components with FWHM of $\sim$ 42 km s^{-1}.

The summed velocity integrated brightness temperature for each of the bins is shown in figure 7.5b, which better represents the distribution of the gas in the cloud compared to figure 7.5a. Out of each of the 4 velocity width groups, the second group, representing the thermally unstable WNM, components contribute the most to the overall brightness temperature. Approximately 52 percent of the HI in the sampled lines of sight is in the warm neutral medium, which is consistent with the simulation in Gazol et al. (2001). Despite having relatively few components per bin, the components from the warm neutral medium and unstable region tend to have high velocity-integrated HI brightness temperatures. Heiles (2001) and Heiles and Troland (2003) find that the thermally unstable HI accounts for at least 48 percent of the warm neutral medium. In the sampled area of MBM 53, it appears that the thermally unstable HI accounts for 86 percent of the WNM. About 30 percent of the HI in the sampled lines of sight is in the CNM. The extremely wide components with widths above 37 km s^{-1} contribute little of the brightness temperature to the overall signal, but make up about the same amount of the signal as the thermally stable WNM, making up $\sim$ 9 percent of the total.

It does not appear like there is evidence of self-absorption in the HI spectra of MBM 53, when compared with the CO spectra from Donate and Magnani (2017). This is not surprising given that MBM53 is a diffuse molecular cloud.

7.5.1 Comparison with Previous Surveys

Our data are compared with spectra from the GALFA survey (Peek et al. 2018) and EBHIS (Winkel et al. 2016) to determine if the high signal-to-noise, high resolution data collected in A3021 are able to detect components of the ISM that were not seen in prior surveys. Spectra of positions G96830, G94632, and G95731 are collected from our observations and the GALFA spectra, which are from the GALFA spectra are from the GALFA-HI DR2 Wide data cubes by Peek (2017). The observation coordinates do not quite line up, so the closest observation to our center line of sight is used. To reduce the GALFA data, the Python package Astropy (Astropy Collaboration et al. 2013; Astropy Collaboration et al. 2018) was used along with Numpy (Harris et al. 2020). The EBHIS data was collected from HI Profile Search[4]. Both sets of spectra had gaussians fit using the method described in section 7.5, but the threshold brightness temperature varies between each line of sight. The spectra from each of the data sets for each of the sampled lines of sight are shown in figure 7.6, and the threshold brightness temperature is listed for each spectrum.

The lower signal to noise of the GALFA spectra makes the low brightness velocity components difficult to separate, and so the GALFA spectra sometimes do not detect the small, narrow components and the very wide, short components which are seen in the A3021 spectra. In the intermediate velocity component of G96830, the GALFA spectrum does not detect a very wide component, which is seen in both the A3021 and EBHIS spectra. The low velocity resolution of the EBHIS spectra results in less gaussian components than the other two sets, and the fitting program does not pick out the narrow components.

[4]see website: https://www.astro.uni-bonn.de/hisurvey/AllSky_profiles/

Due to having high signal to noise and high resolution, the A3021 spectra are able to detect small features in the HI profiles which are not detected in GALFA or EBHIS, either due to poor resolution or poor signal to noise. For example, there are small "bumps" on the positive side of the signal near ~ 8 km s^{-1} in G94632 and G96830 which are seen in only the A3021 data set. These small features are smoothed over by the low resolution in the EBHIS spectra and are undetectable due to the high noise in the GALFA spectra. The A3021 data adds several velocity components to the fits that are not included in the other spectra, and many of them are narrow features. Due to the high noise or poor resolution smoothing over the features in the spectra, the GALFA and EBHIS spectra may be overestimating the amount of HI in the warm neutral medium and underestimating the amount that is in the cold neutral medium.

The high signal to noise data presented in this chapter show that there is HI velocity structure in the ISM which is missed by the fully sampled surveys. Thus, there is still a reason for a high-resolution, high-sensitivity HI survey of local atomic gas.

The GALFA and EBHIS spectra may indicate that the shallow features seen in some lines of sight at $\sim$ 30 km s^{-1} may be due to improperly fit baselines, as those features are not seen in the EBHIS or GALFA spectra. On the negative side of the spectra, however, the GALFA and EBHIS spectra show that the shallow features from very wide velocity components seen in the A3021 spectra are likely real.

The distribution of the component widths of the GALFA velocity components is shown in figure 7.7a. Despite the poor signal to noise present in the GALFA data, the distribution of the component widths is similar to what is seen in the much higher signal to noise A3021 data, but the overall number of components is greatly reduced. Figure 7.7b shows the summed velocity-integrated brightness temperature [W(HI)] of the components in each bin, similar to figure 7.5b. In the GALFA data, the thermally unstable WNM is even more dominant, with nearly 60 percent of the total HI in this temperature range, and 90

percent of the HI in the WNM is in the thermally unstable WNM. 26 percent of the HI is in the CNM, slighly less than the amount determined from the A3021 data. The extremely wide width components contibute about the same amount of the signal compared to the A3021 data, contributing ~ 8 percent of it. Assuming that the velocity components that are isolated using gaussian decomposition are actual HI components, then the high signal to noise and high resolution of the A3021 data shows that gaussian decomposition of the GALFA survey is overestimating the contribution of the unstable WNM to the overall signal, and that MBM 53 contains more gas in the cold neutral medium and the stable WNM than suggested by the GALFA survey. The EBHIS data are not compared this way due to the poor velocity resolution of the data.

In both the A3021 and GALFA data there is present very wide HI components (> 54 km s^{-1}) which cannot be produced by warm HI. The equivalent temperature of such a wide component would be greater than $21,000$ K so HI emission from such gas would be unphysical. This component has been seen before (e.g. Haud and Kalberla 2007) and is present even in HI spectra from the GBT (Lockman, private communication). Its origin remains mysterious and could be purely instrumental (e.g. stray radiation or poor baseline fitting), although its continual detection at high sensitivities makes the idea of poor baseline fitting less tenable.

7.6 Map Comparisons

The poorly sampled map of HI column density from project A3021 was compared to HI surveys, specifically GALFA-DR2 (Peek et al. 2018) shown in figure 7.8 and Hartmann and Burton (1997), shown in figures 7.9 and 7.10. The observation time per individual line of sight was usually 600 seconds, and the

rms per combined line of sight on average was approximately 0.018 K. Usually the number of individual scans contributing to a combined line of sight was 10.

The GALFA survey used the Arecibo 305-m radio telescope and therefore has a resolution of approximately 4 arcminutes, the same as our individual observations. While the rms is comparitively poor at 150 mK, the map is fully sampled between -1 and 38 degrees declination. Figure 7.7 shows a comparison between the GALFA survey and our observations. From the figure it is clear that our poorly sampled data misses much of the HI variations between each grid point. Although there is large-scale agreement between the two data sets, the GALFA survey is rich in detailed small-scale structure.

Additionally, in figures 7.9 and 7.10, we compare our HI observations to the observations by Hartmann and Burton (1997), using figures from Yamamoto et al. (2003). The observations were collected using the 25-m radio telescope at the Netherlands Foundation for Research in Astronomy and observed on a half degree grid. From the two figures the two data sets agree with each other fairly well, likely because our poor sampling matching the poor resolution of the Hartmann and Burton (1997) observations.

Figure 7.11 contains four comparison plots, using HI observations collected from A3021, CO observations from Donate and Magnani (2017), and extinction measurements from the corrected SFD dust maps (Schlafly and Finkbeiner 2011; Schlegel, Finkbeiner, and Davis 1998). Although the extinction has better sampling than the HI and CO data, we only use the extinction at the HI and CO lines of sight. The upper left plot shows a contour map of the HI column density ($\times 10^{20}$ cm^{-2}) in the background, with a line contour map in the foreground showing the visual extinction (A_{V}). The two data sets agree fairly well, likely due to the low amount of H_2 in the cloud relative to HI. The upper right plot shows a contour map of the extinction in the background, and in the foreground there is a map of the estimated H_2 column density (10^{20} cm^{-2}) determined from the CO velocity-integrated antenna temperature and $X_{\mathrm{CO}} = 2 \times$

10^{20} (see chapter 6). The bottom left plot compares the estimated H_2 column density determined from A_V using the relation from Bohlin et al. (1978) in the background and from CO (with $X_{CO} = 2 \times 10^{20}$) in the foreground. Similar to the plot of the extinction and CO-derived N(H_2), the two sets of N(H_2) are somewhat consistent in terms of regions with high or low N(H_2), however, the two methods do not agree very well on how much H_2 is present. This could be due to CO in most of the lines of sight not being adequately shielded from the interstellar radiation field, or due to the uncertainty present in both data sets. The background of the bottom right plot shows the total hydrogen ($\times 10^{20}$ cm^{-2}) determined from our HI observations, H_2 estimated from CO observations, and the foreground is the extinction. These two maps are consistent with each other, similar to the N(HI) and extinction map.

7.7 HI Velocity Channel Maps

Velocity channel maps in figure 7.12 show the sum brightness temperature for each 5 km s^{-1} section. In addition to the low velocity clouds seen in each of the spectra, there were also some intermediate velocity clouds observed with center velocities between -40 and -60 km s^{-1}. The intermediate velocity clouds are most prominent at positions G96830 and G95731, in agreement with what is seen in figure 7.3. This intermediate velocity cloud appears intermittenly across the observed region, mostly as a very short peak at or below 1 K with a wide velocity dispersion. The intermediate velocity cloud is most visible at G96830, G96831, and G95731, where the cloud appears to have at least two velocity components. A detailed map of this cloud should be made with the GBT or the FAST radio telescopes.

,

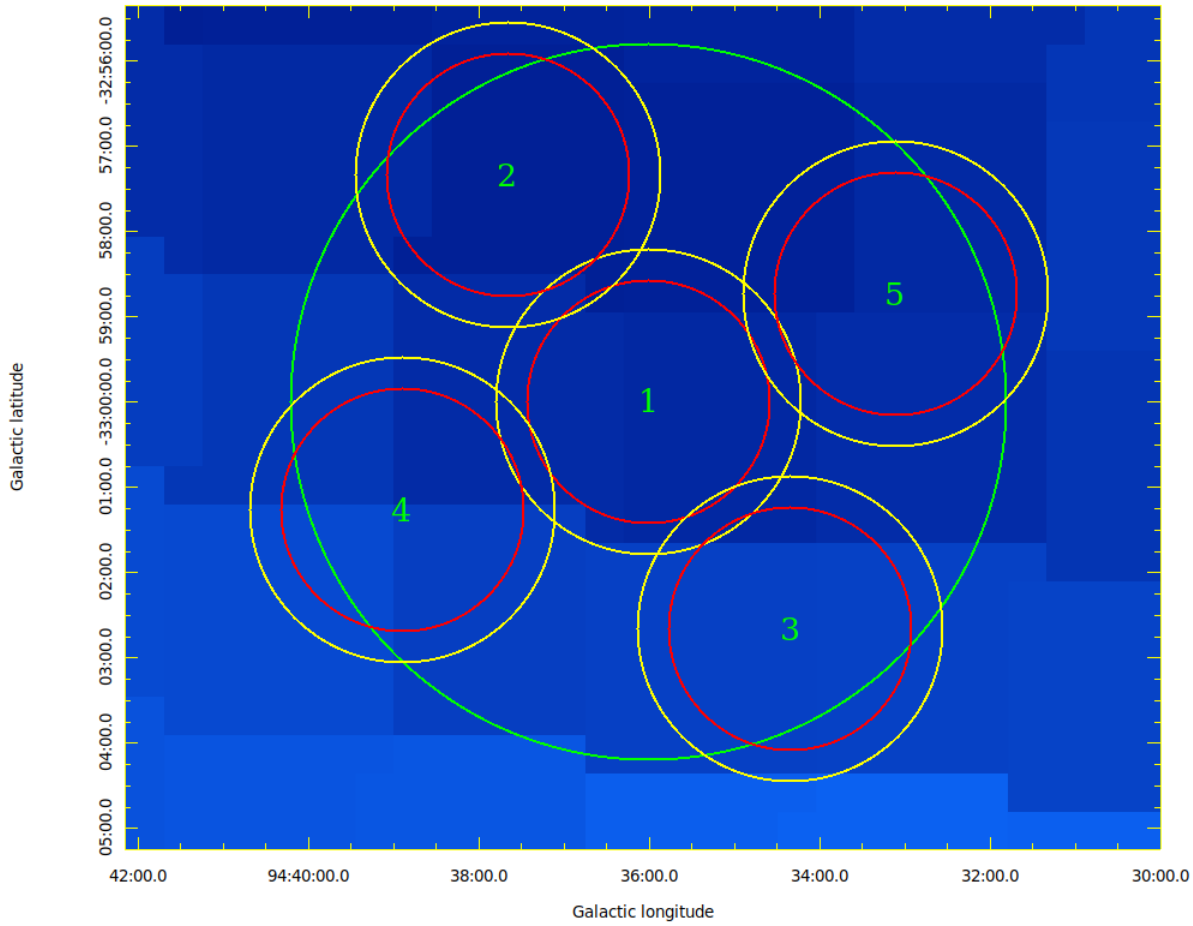

Figure 7.1: A3021 Beam Pattern

The outer green circle represents the Harvard CFA 1.2-m telescope CO beam at 115 GHz (8.4') used in the Magnani et al. (2000) CO $(1-0)$ survey. The 5 red circles represent the Arecibo Observatory 305-m telescope OH beam at 1.7 GHz (2.85') described by Donate, White, and Magnani (2019), and the 5 yellow circles represent the Arecibo Observatory 305-m telescope HI beam at 1.4 GHz (3.58').

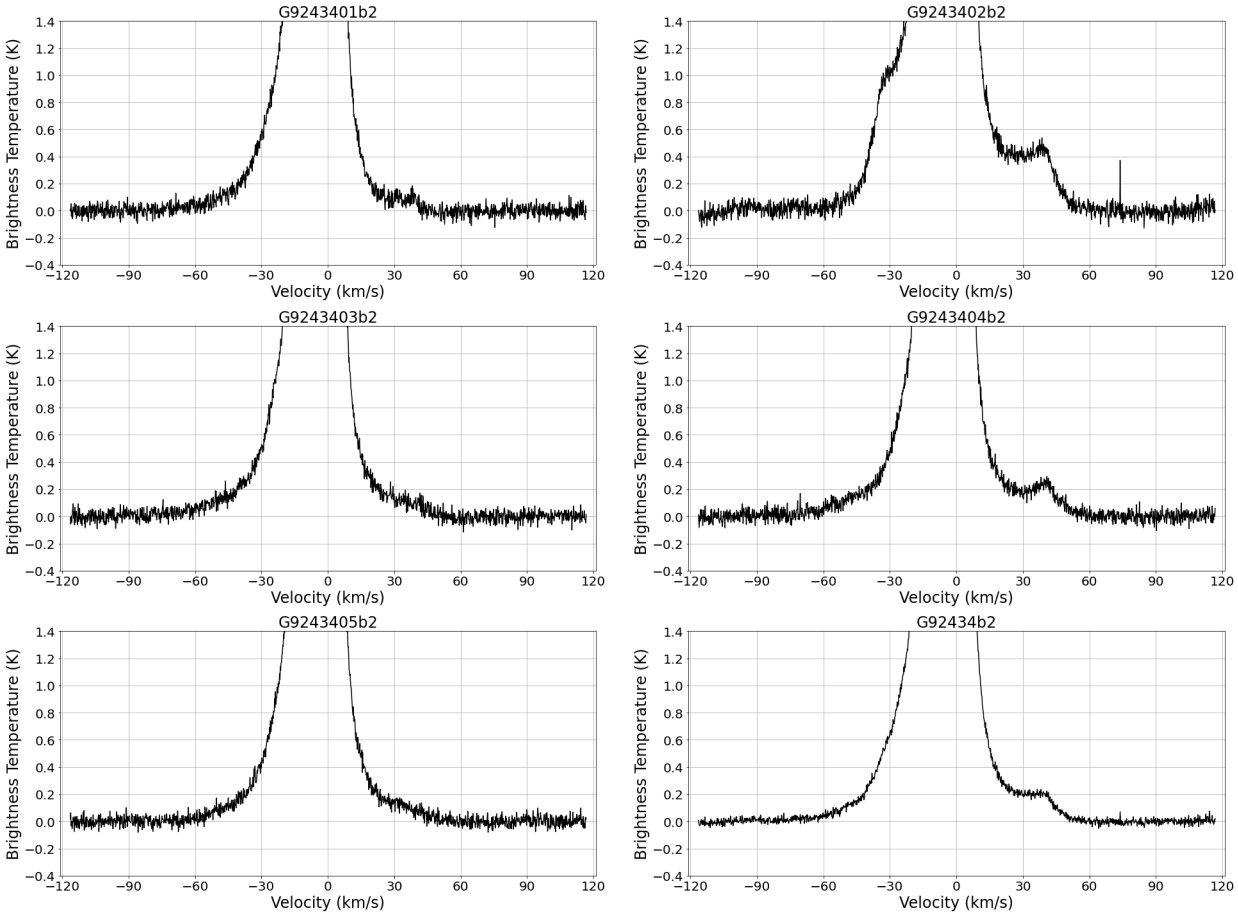

Figure 7.2: G92434 Component Baselines

Component lines of sight which are summed in order to create the composite lines of sight used throughout this chapter, in order to mimic the 8.4' beam used for the Southern Galactic High-Latitude Survey (Magnani et al. 2000). The bottom right spectrum shows all of the components summed together.

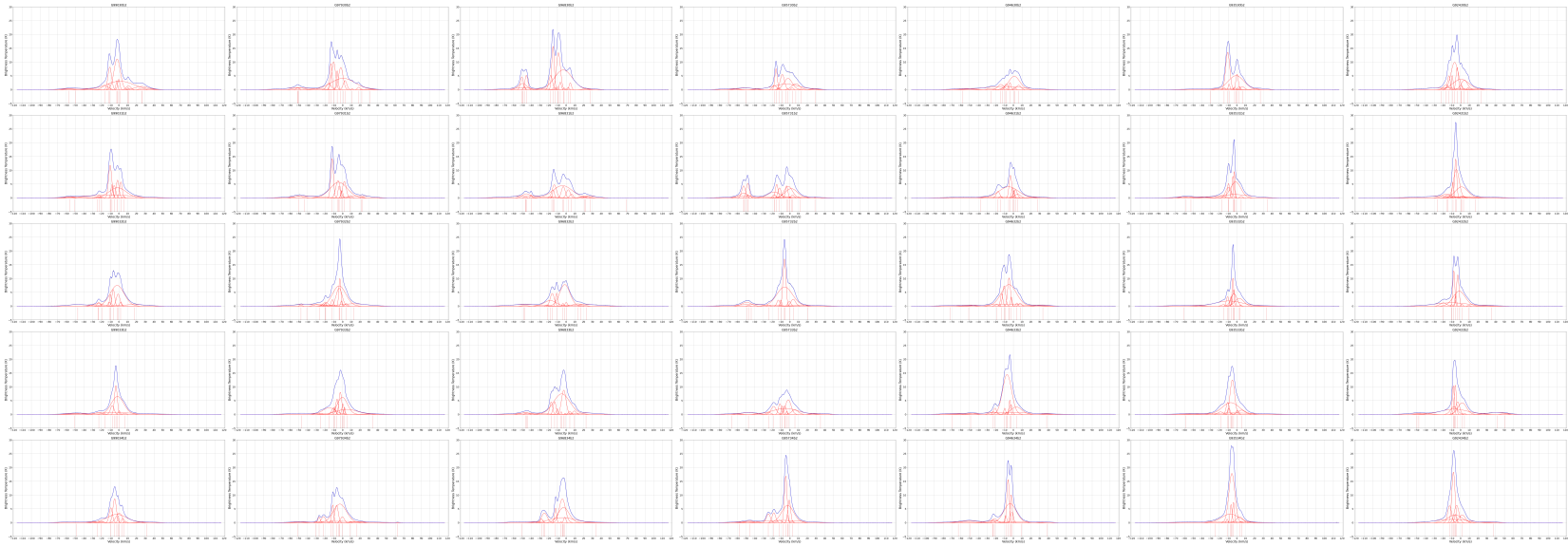

Figure 7.3: Plots of Gaussian Fits

Summed HI spectra for the sampled positions in Pegasus [see figure 7.4 for the galactic coordinates]. Spectra have been reduced to account for stray radiation. In the digital version, zoom in for more detail.

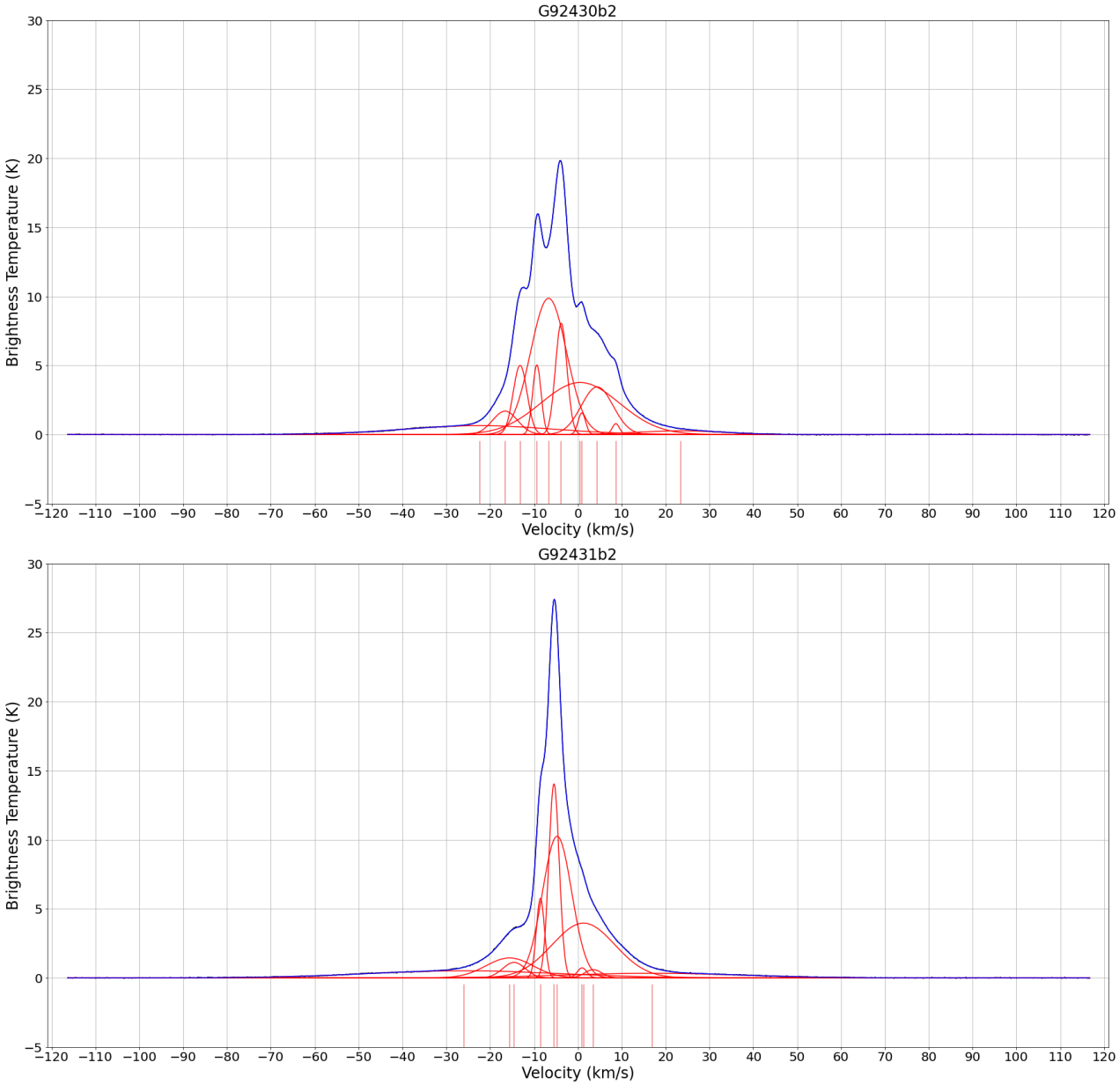

Figure 7.4a: Plots of Gaussian Fits: 92.4
Positions $l = 92.4°$, $b = -30°$ (top) and $b = -31°$ (bottom).

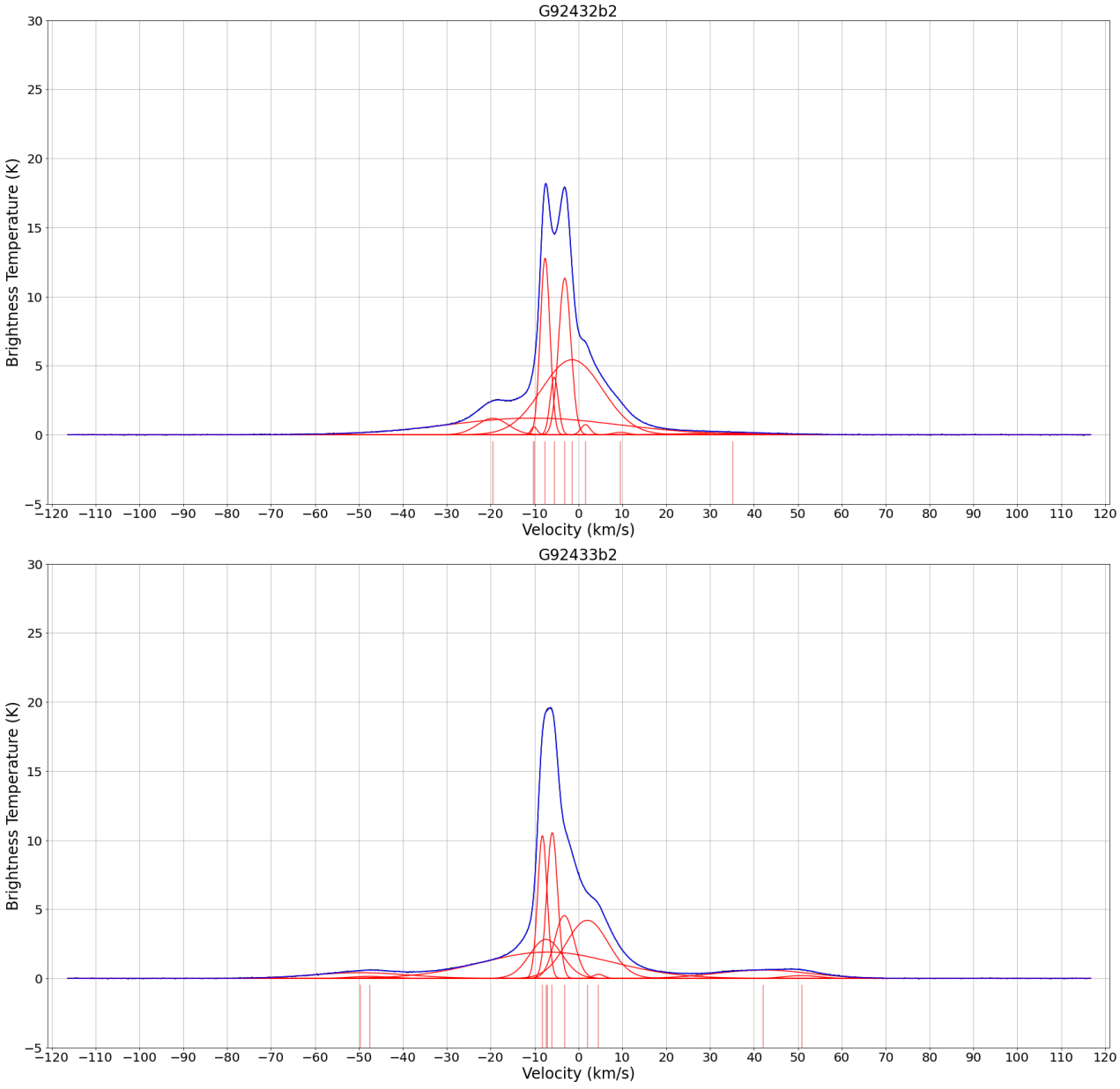

Figure 7.4b: Plots of Gaussian Fits: 92.4
Positions $l = 92.4°$, $b = -32°$ (top) and $b = -33°$ (bottom).

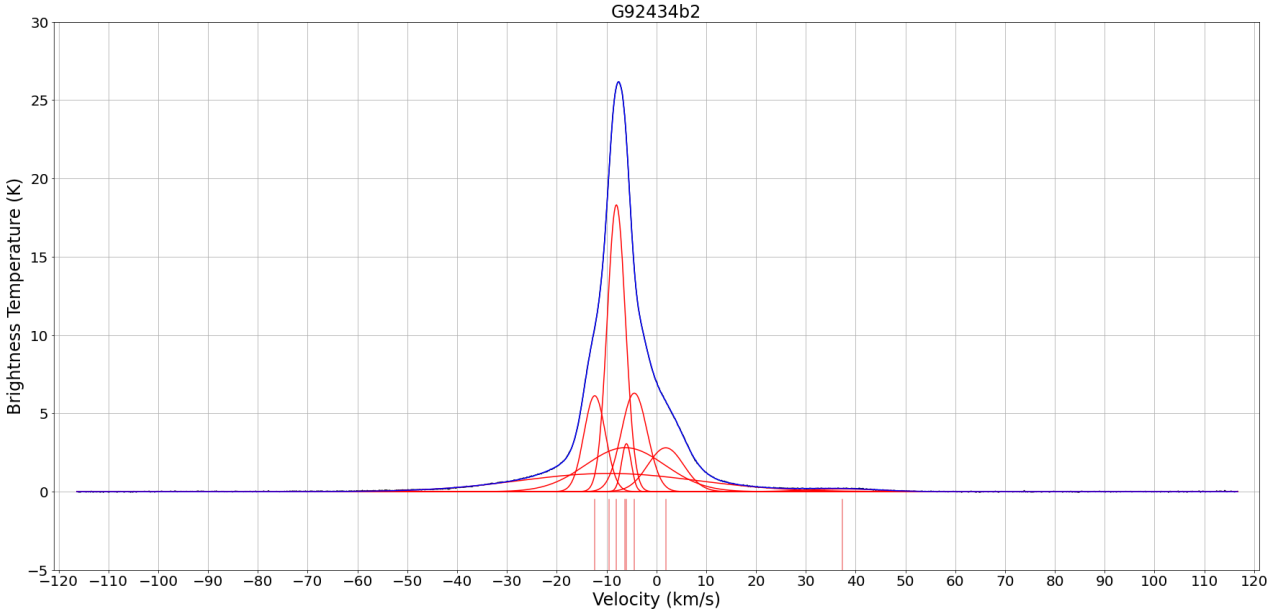

Figure 7.4c: Plots of Gaussian Fits: 92.4

Positions $l = 92.4°$, $b = -34°$.

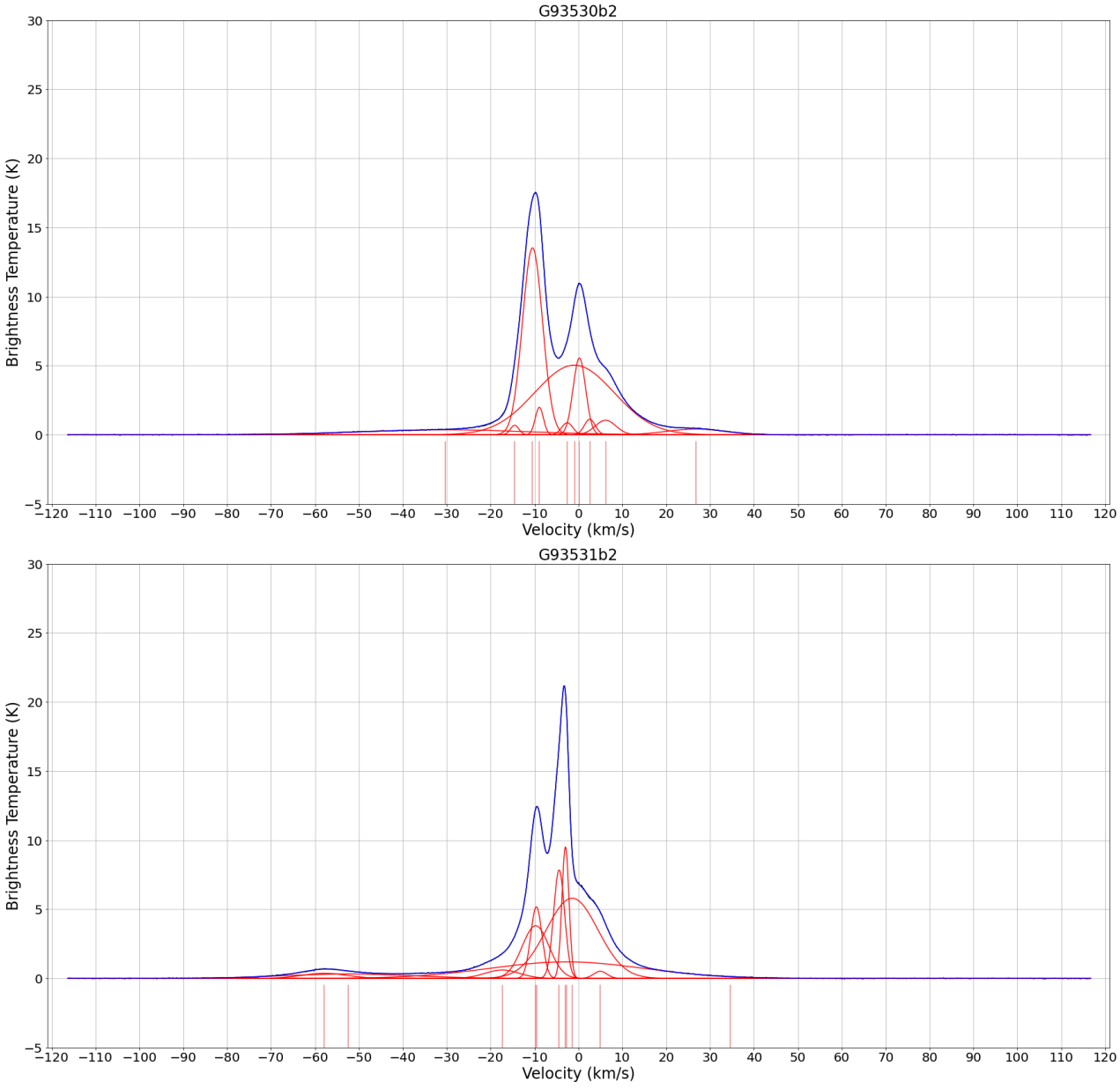

Figure 7.4d: Plots of Gaussian Fits: 93.5
Positions $l = 93.5°$, $b = -30°$ (top) and $b = -31°$ (bottom).

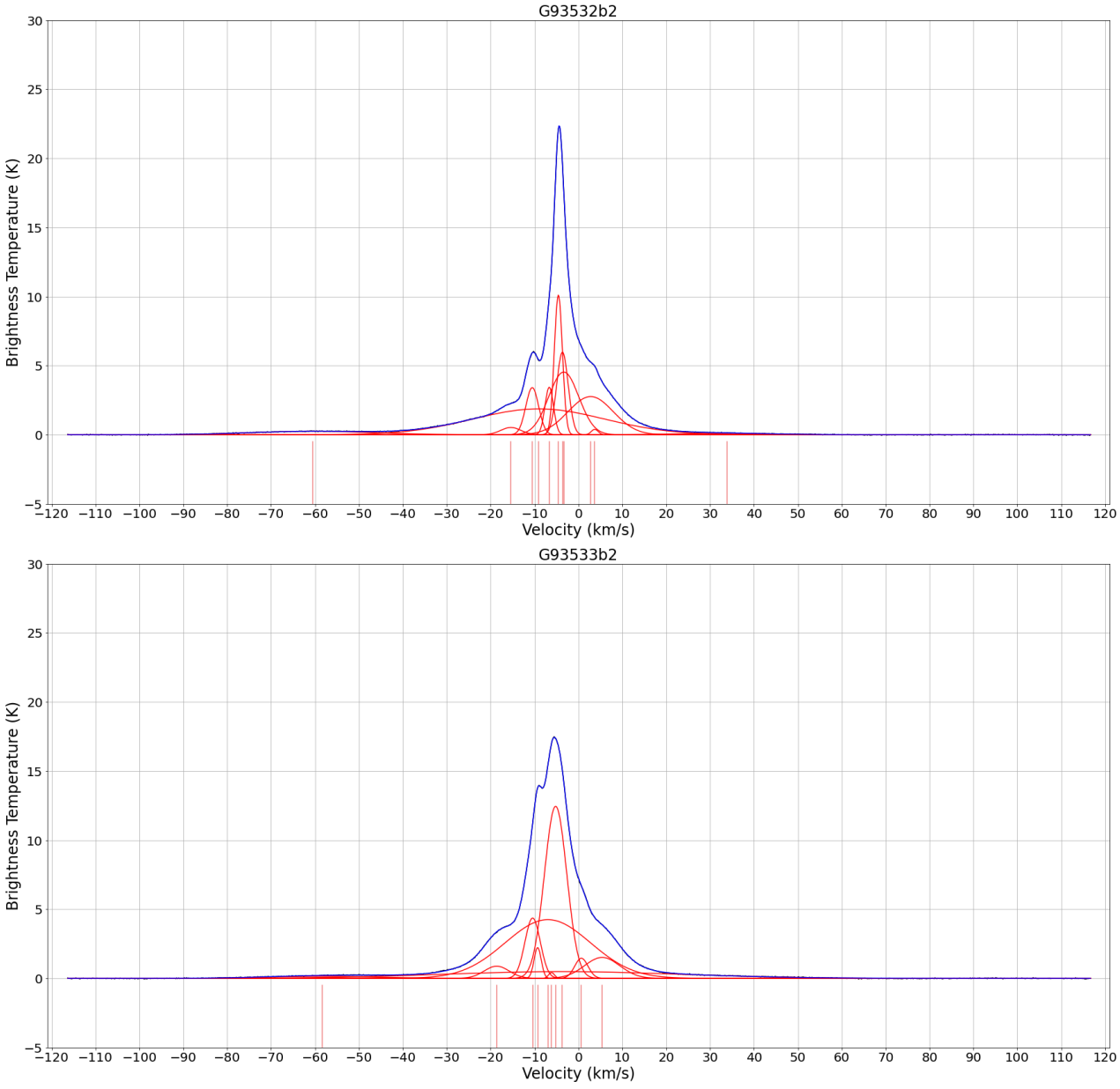

Figure 7.4e: Plots of Gaussian Fits: 93.5
Positions $l = 93.5°$, $b = -32°$ (top) and $b = -33°$ (bottom).

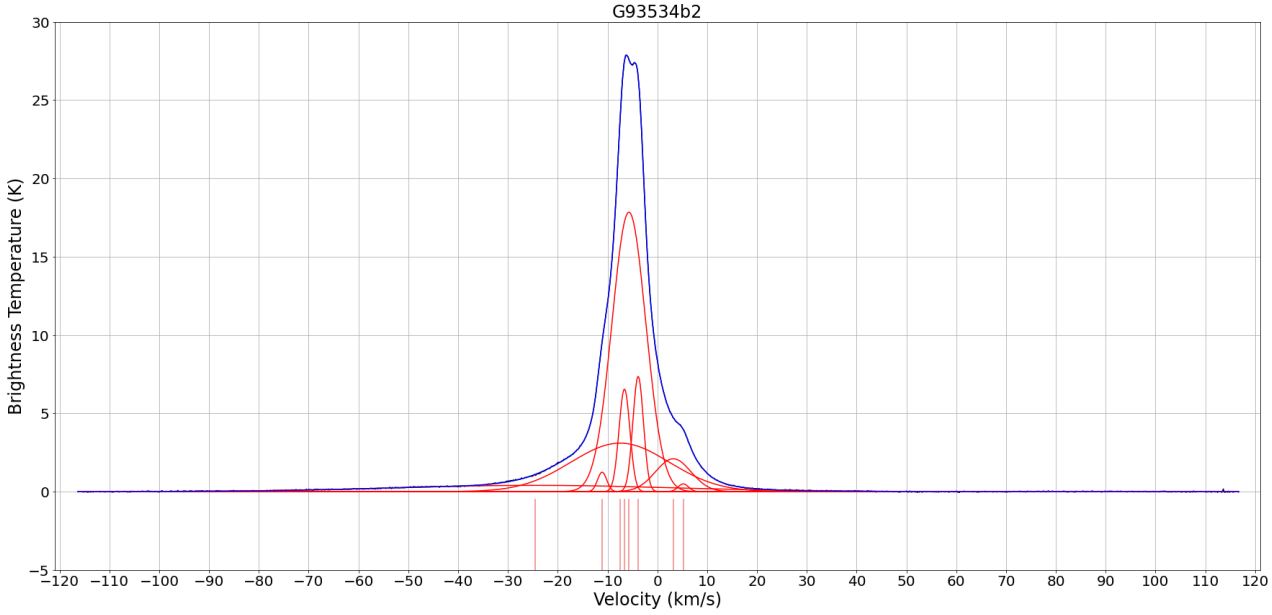

Figure 7.4f: Plots of Gaussian Fits: 93.5

Positions $l = 93.5°$, $b = -34°$.

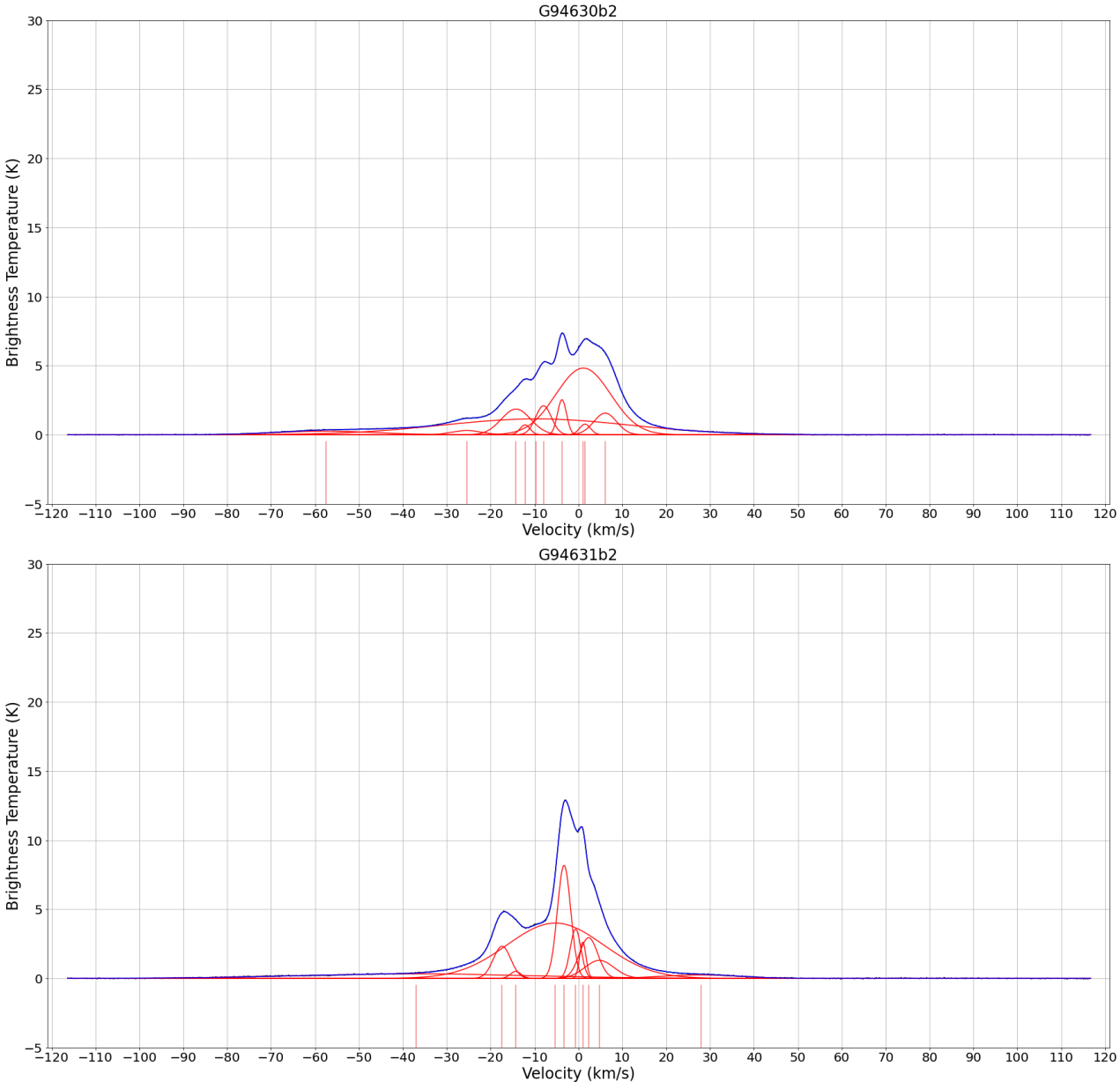

Figure 7.4g: Plots of Gaussian Fits: 94.6
Positions $l = 94.6°$, $b = -30°$ (top) and $b = -31°$ (bottom).

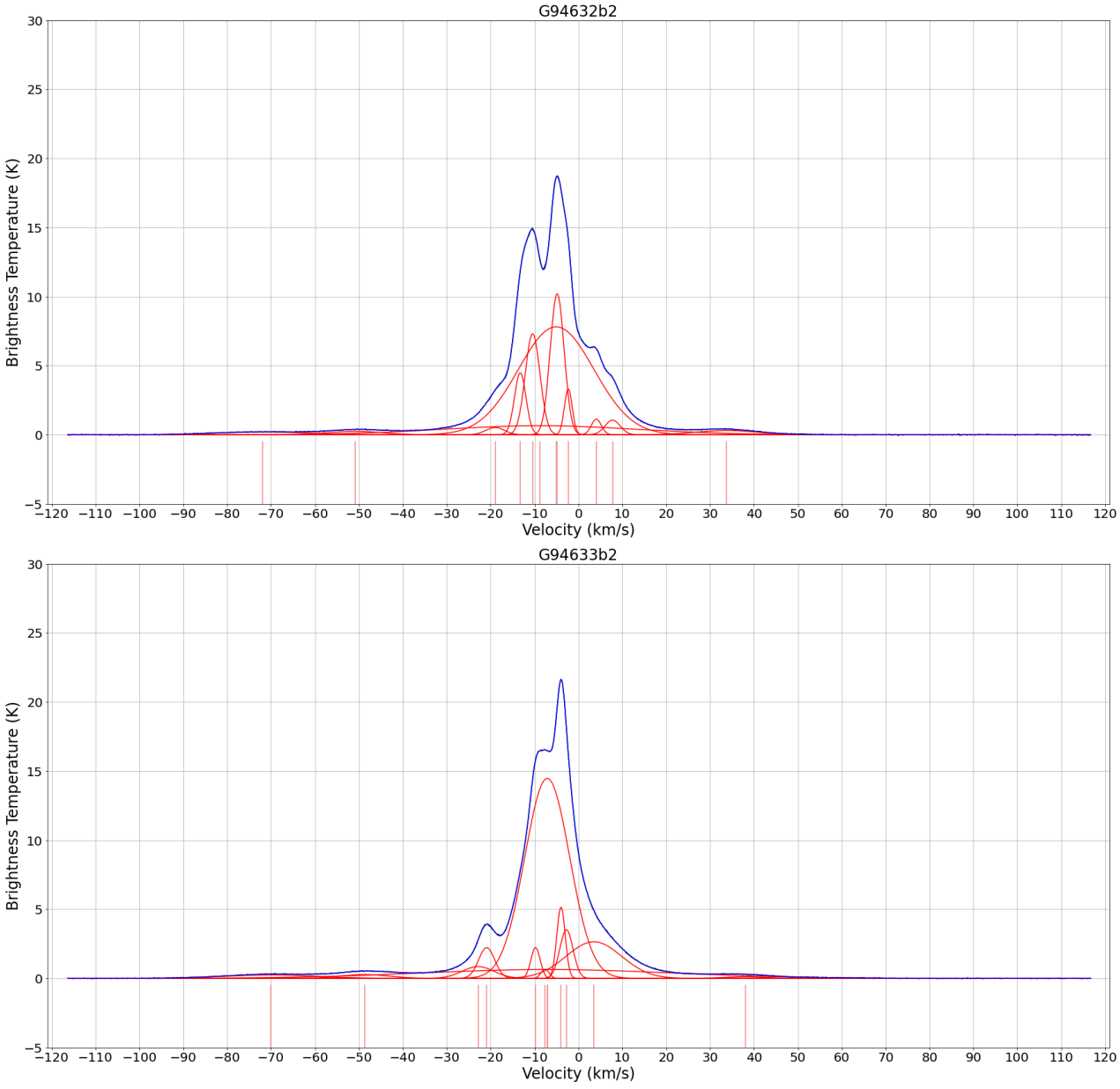

Figure 7.4h: Plots of Gaussian Fits: 94.6
Positions $l = 94.6°$, $b = -32°$ (top) and $b = -33°$ (bottom).

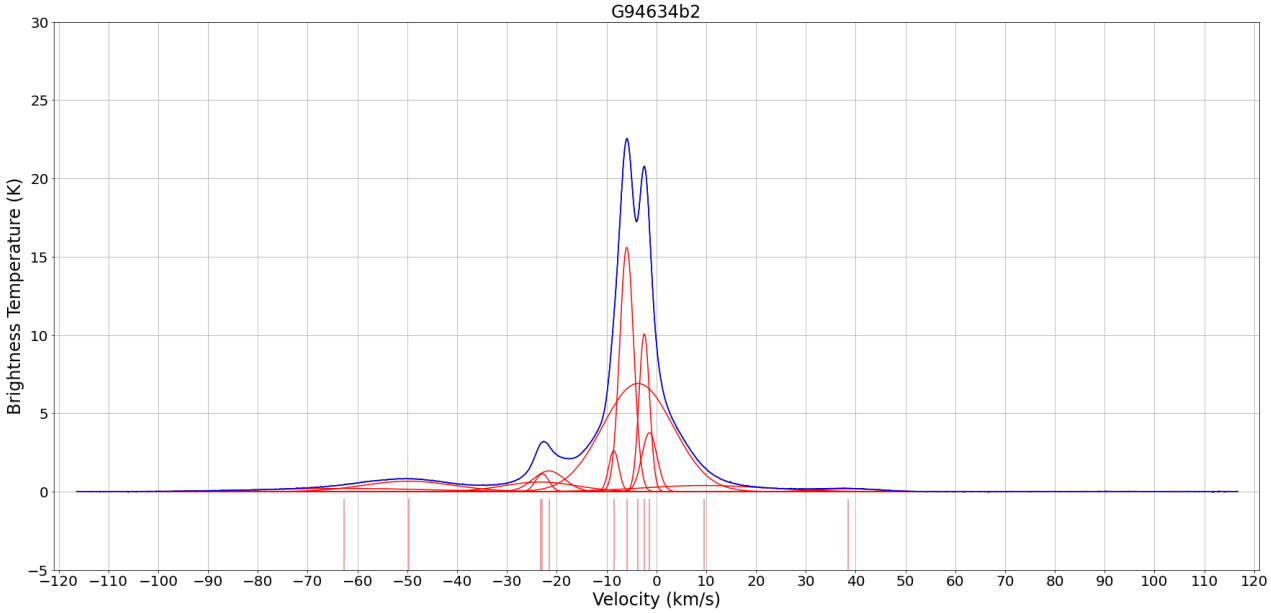

Figure 7.4i: Plots of Gaussian Fits: 94.6

Positions $l = 94.6°$, $b = -34°$.

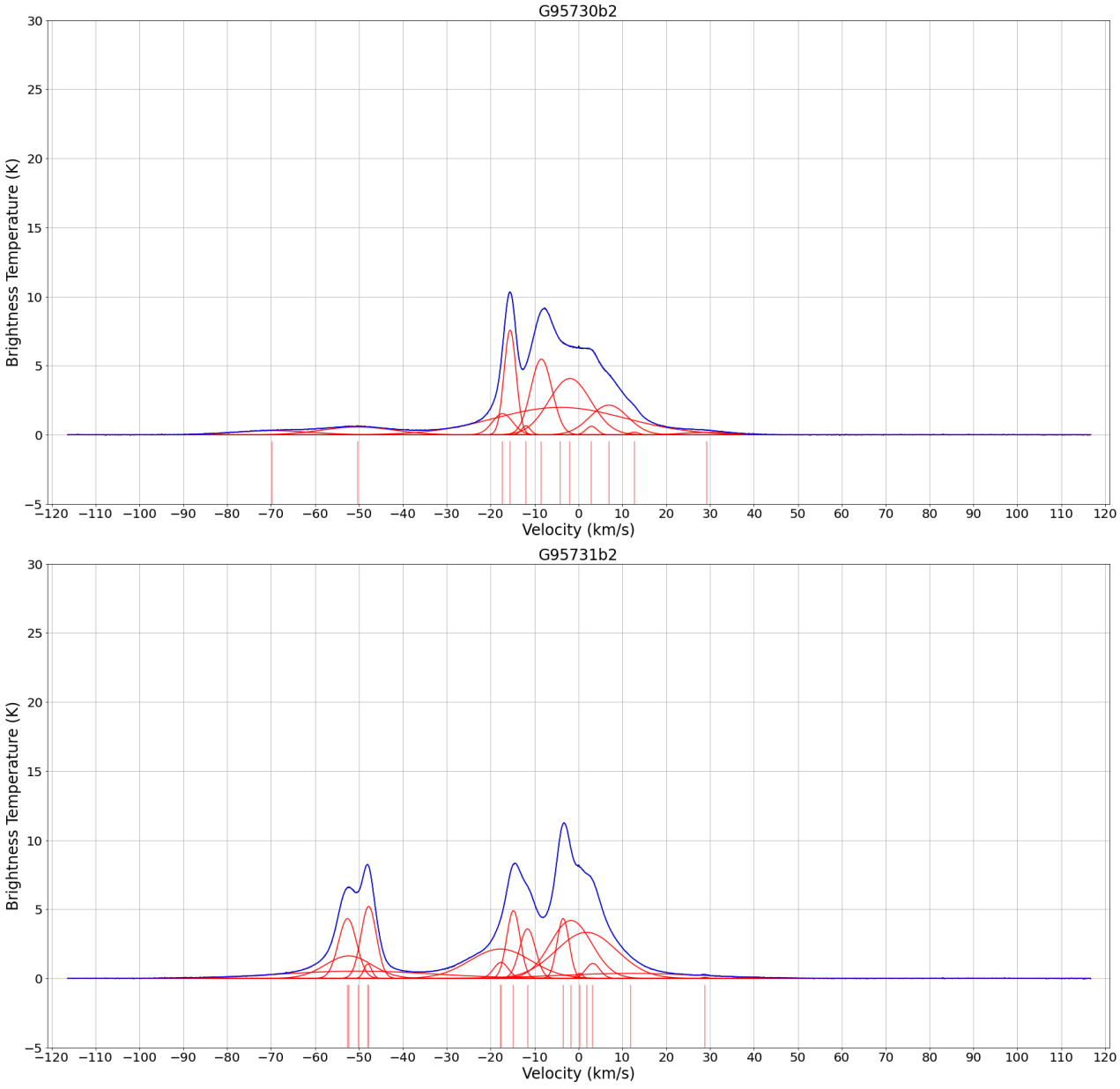

Figure 7.4j: Plots of Gaussian Fits: 95.7
Positions $l = 95.7°$, $b = -30°$ (top) and $b = -31°$ (bottom).

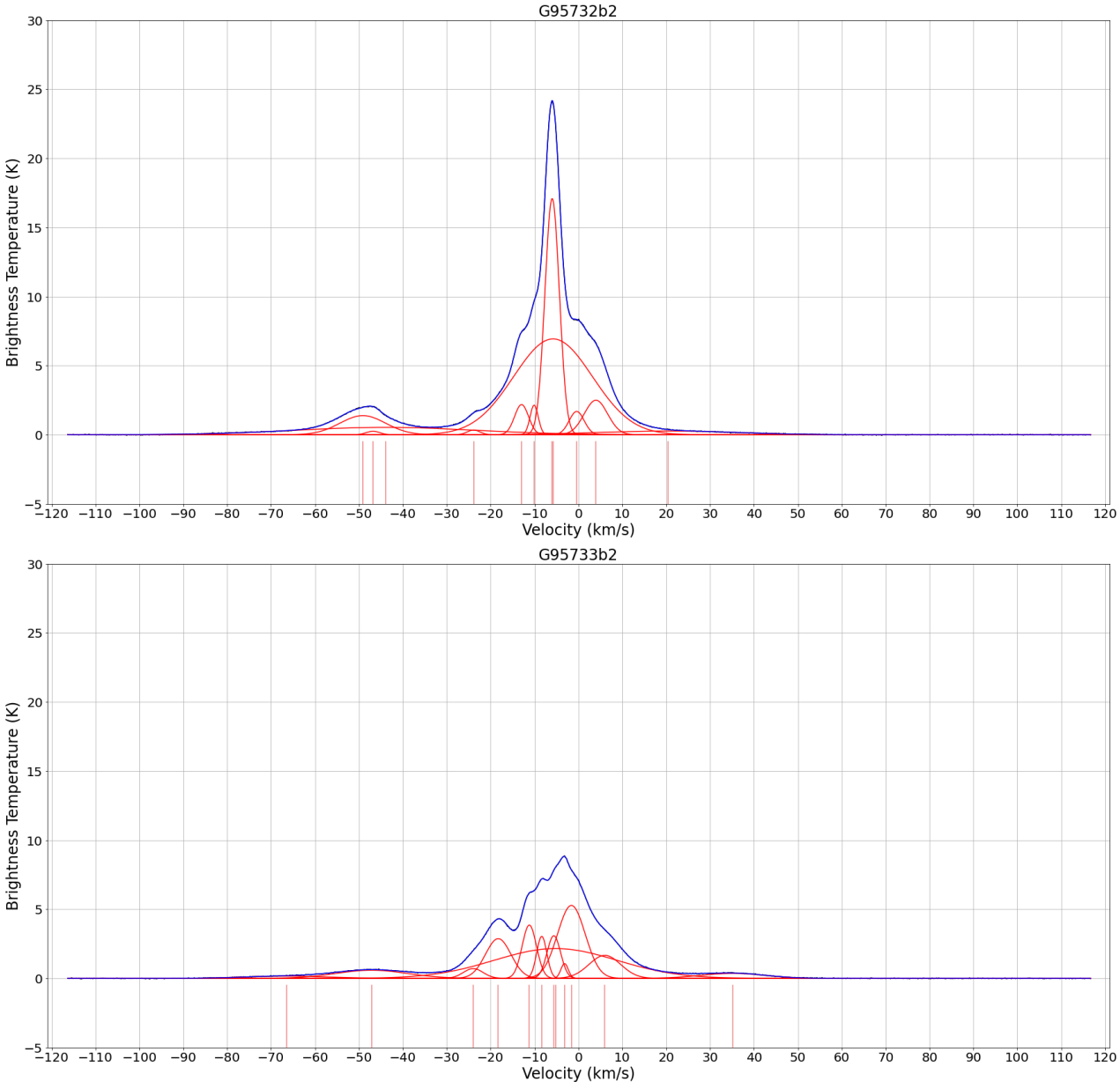

Figure 7.4k: Plots of Gaussian Fits: 95.7
Positions $l = 95.7°$, $b = -32°$ (top) and $b = -33°$ (bottom).

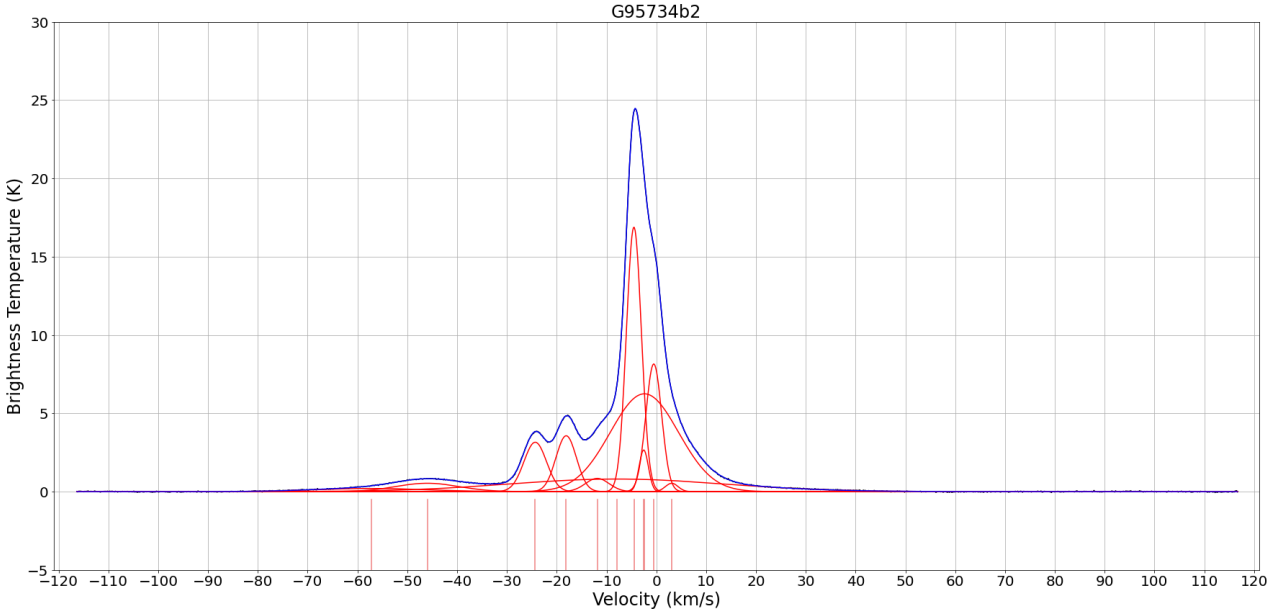

Figure 7.4l: Plots of Gaussian Fits: 95.7

Positions $l = 95.7°$, $b = -34°$.

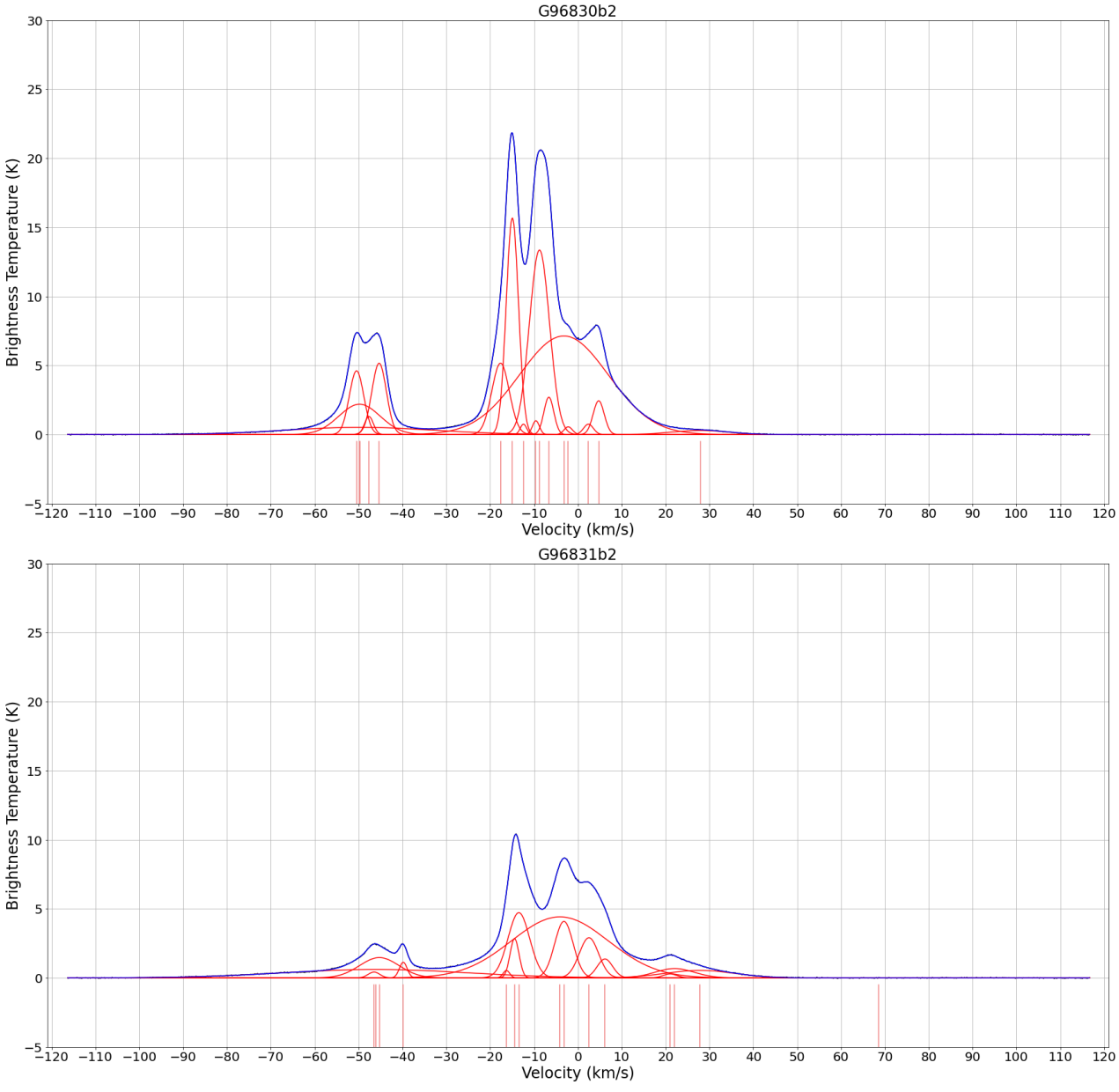

Figure 7.4m: Plots of Gaussian Fits: 96.8
Positions $l = 96.8°$, $b = -30°$ (top) and $b = -31°$ (bottom).

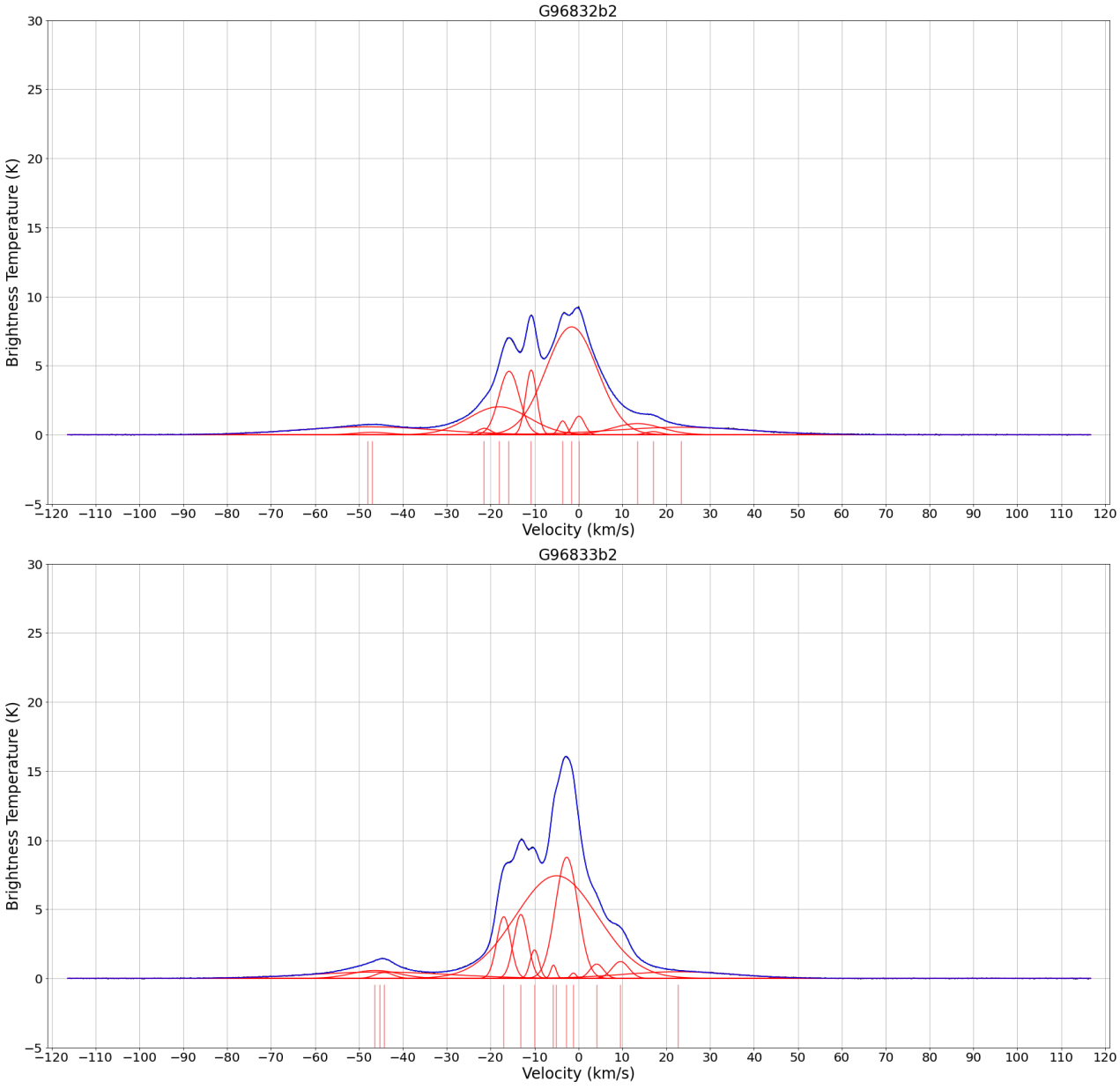

Figure 7.4n: Plots of Gaussian Fits: 96.8
Positions $l = 96.8°$, $b = -32°$ (top) and $b = -33°$ (bottom).

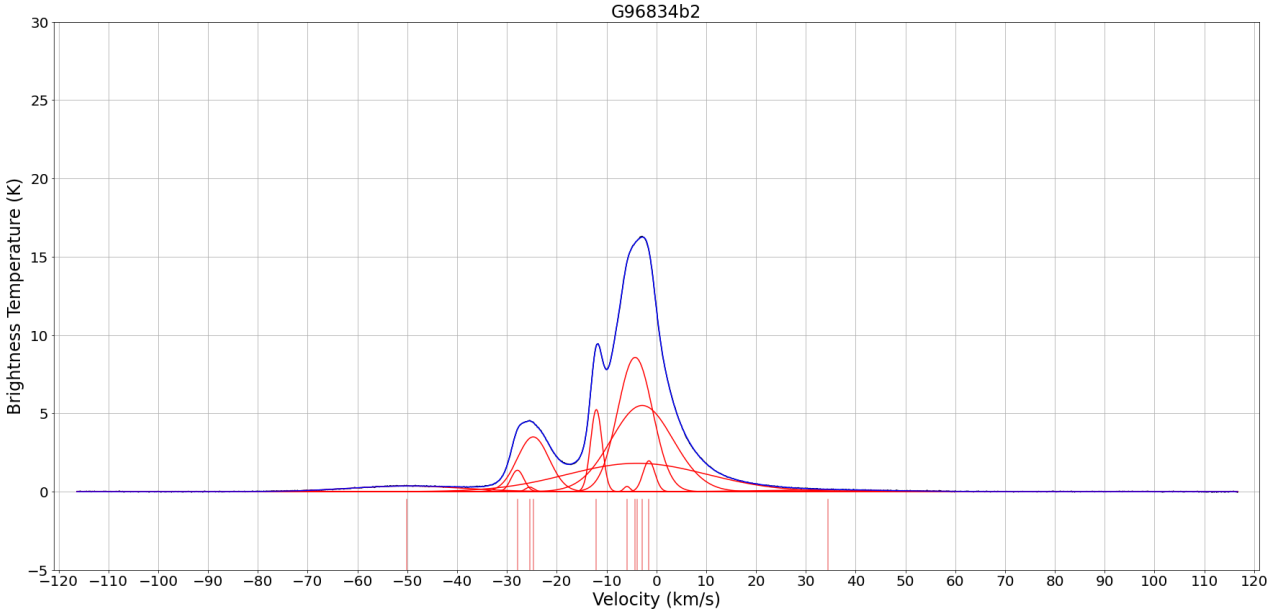

Figure 7.40: Plots of Gaussian Fits: 96.8

Positions $l = 96.8°$, $b = -34°$.

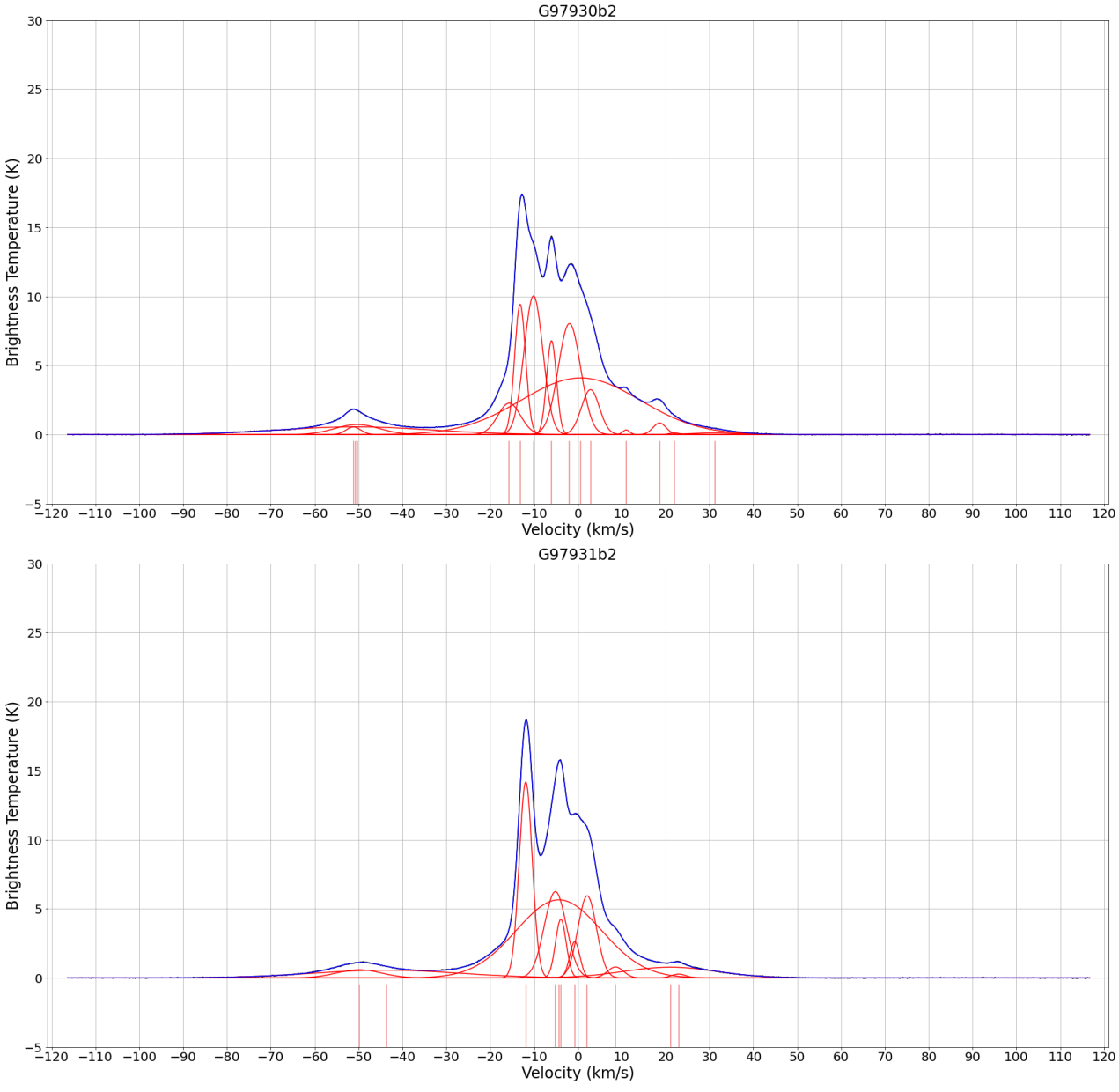

Figure 7.4p: Plots of Gaussian Fits: 97.9
Positions $l = 97.9°$, $b = -30°$ (top) and $b = -31°$ (bottom).

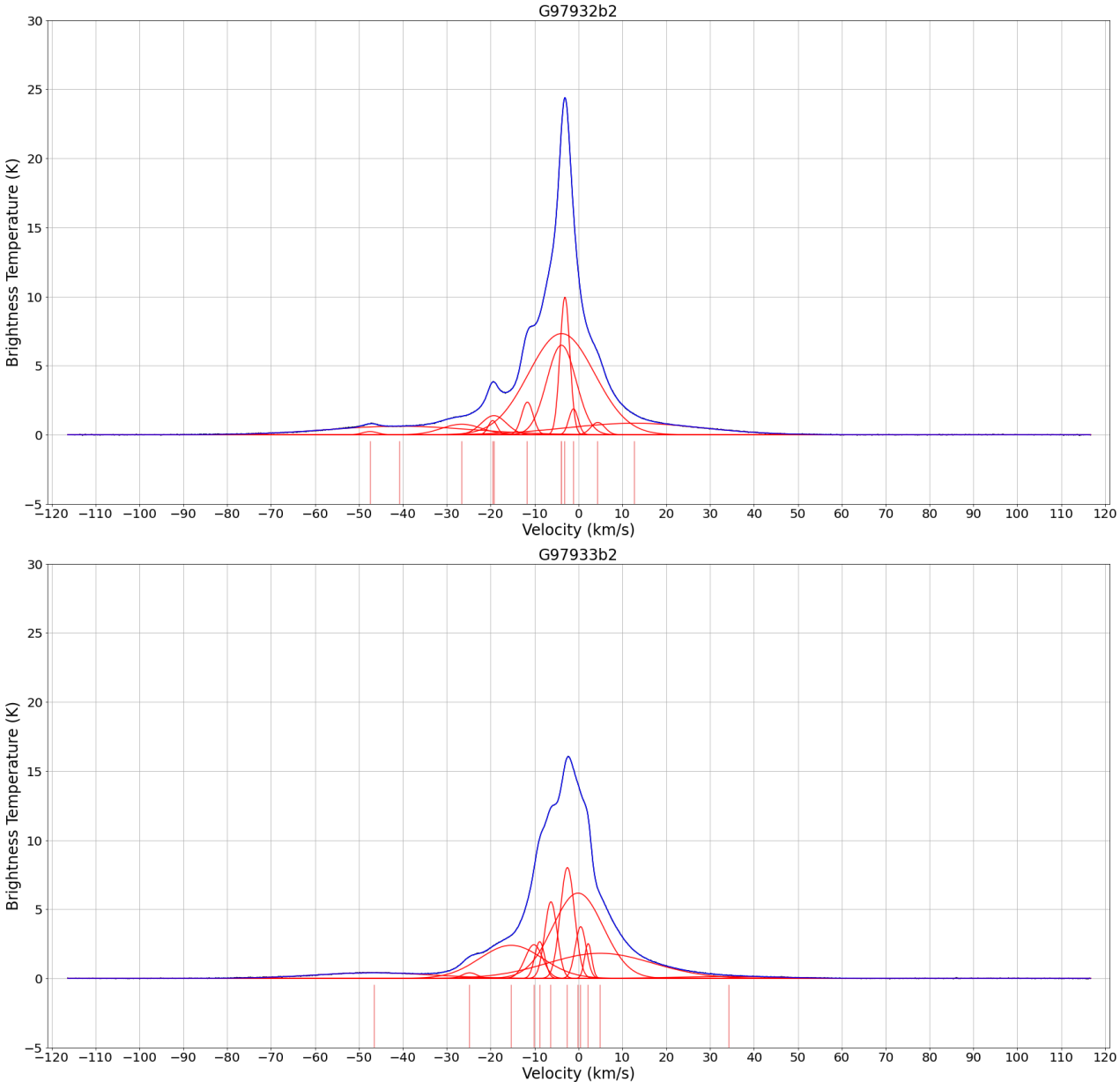

Figure 7.4q: Plots of Gaussian Fits: 97.9
Positions $l = 97.9°$, $b = -32°$ (top) and $b = -33°$ (bottom).

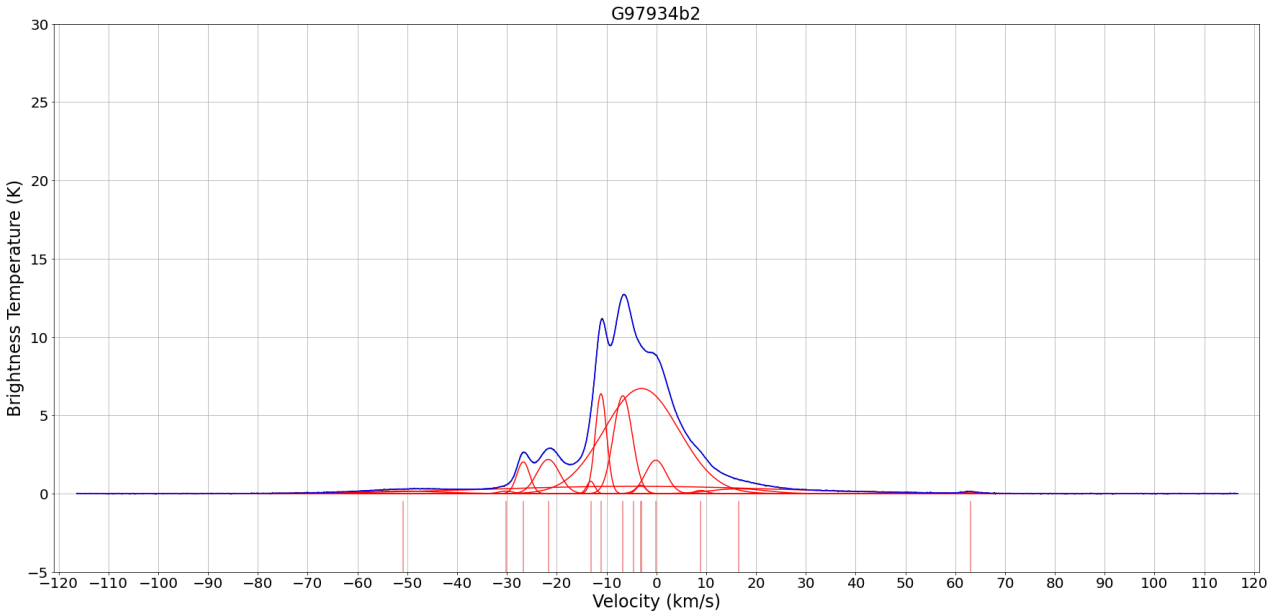

Figure 7.4r: Plots of Gaussian Fits: 97.9

Positions $l = 97.9°$, $b = -34°$.

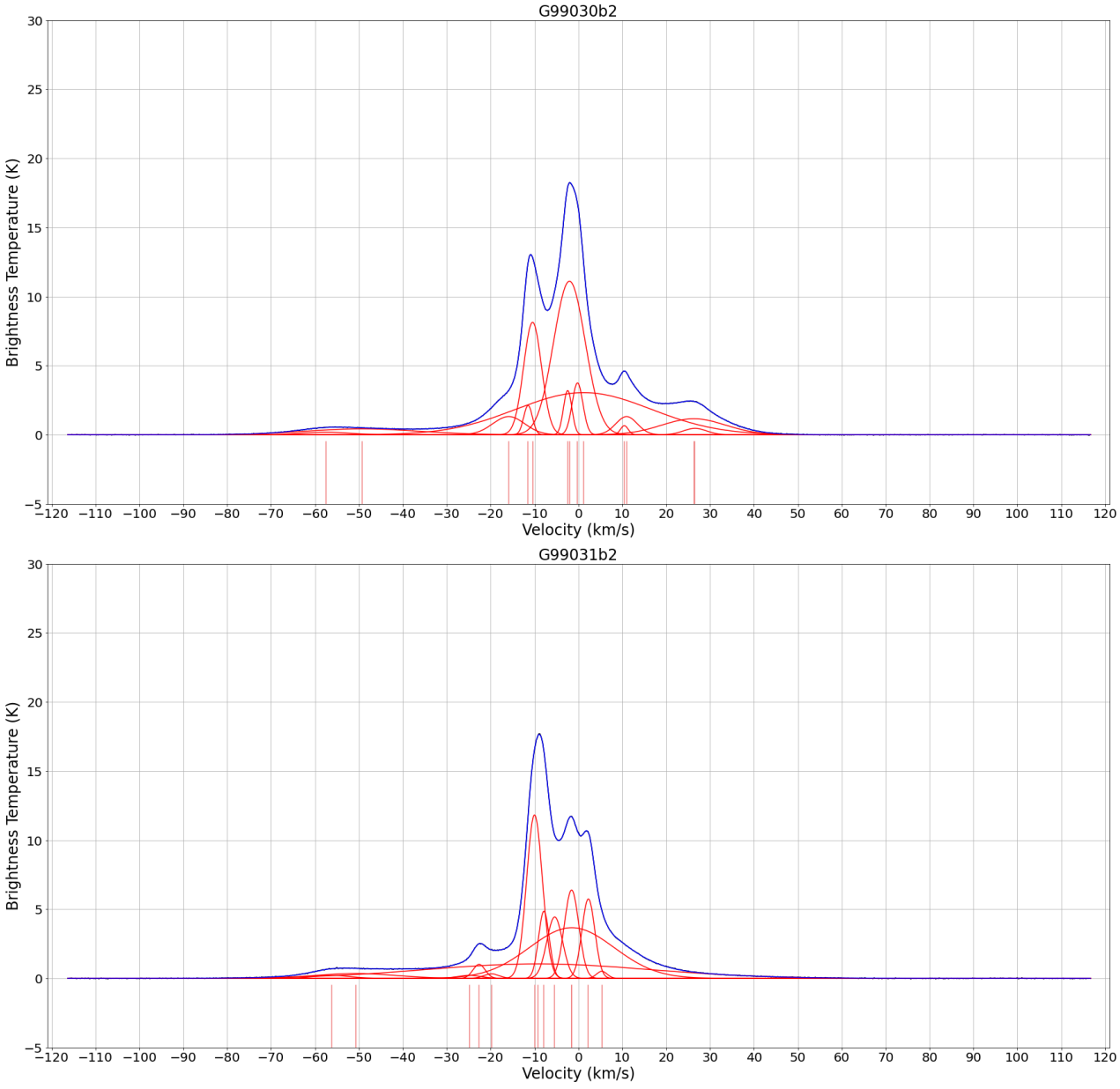

Figure 7.4s: Plots of Gaussian Fits: 99.0
Positions $l = 99.0°$, $b = -30°$ (top) and $b = -31°$ (bottom).

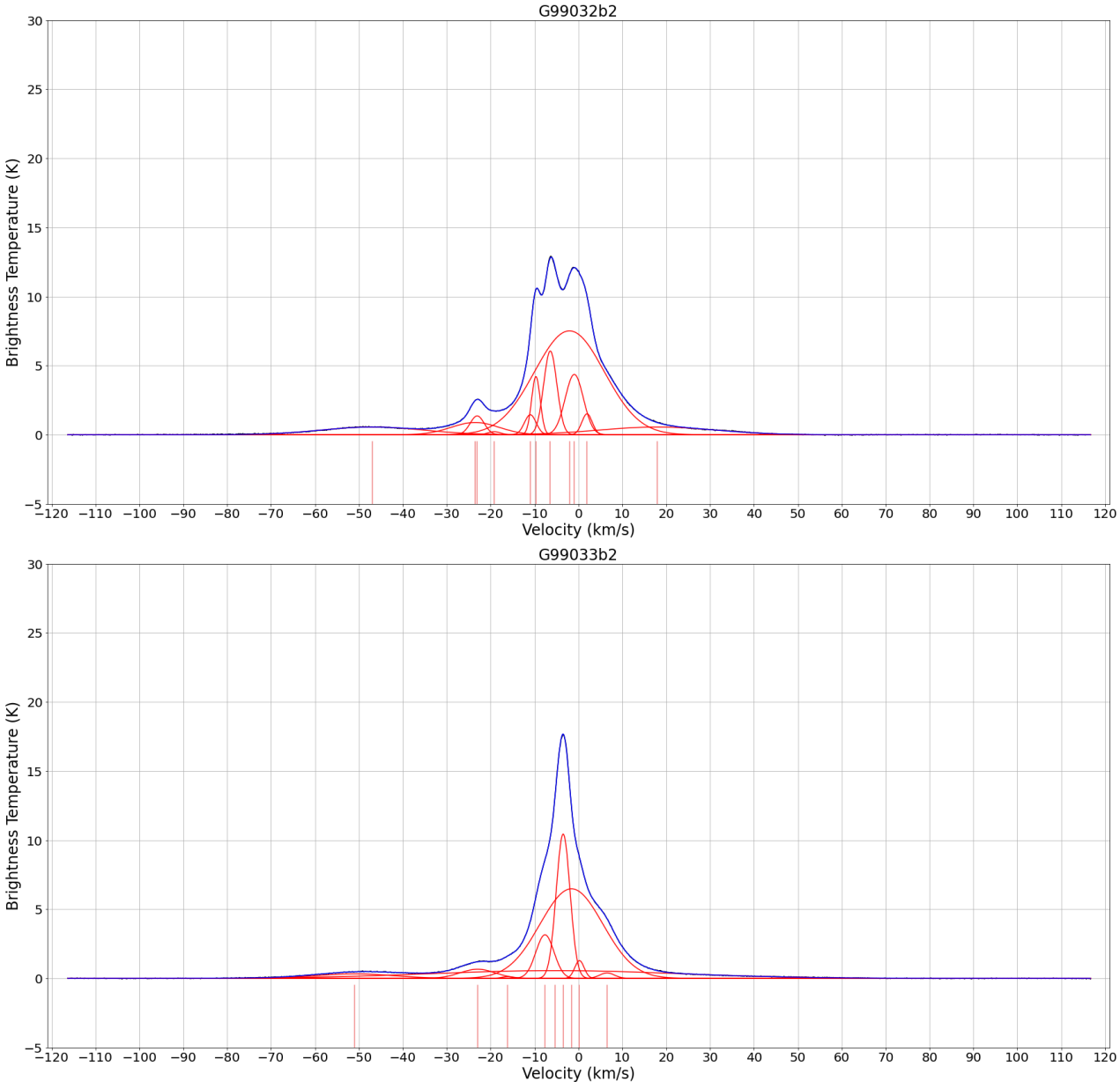

Figure 7.4t: Plots of Gaussian Fits: 99.0
Positions $l = 99.0°$, $b = -32°$ (top) and $b = -33°$ (bottom).

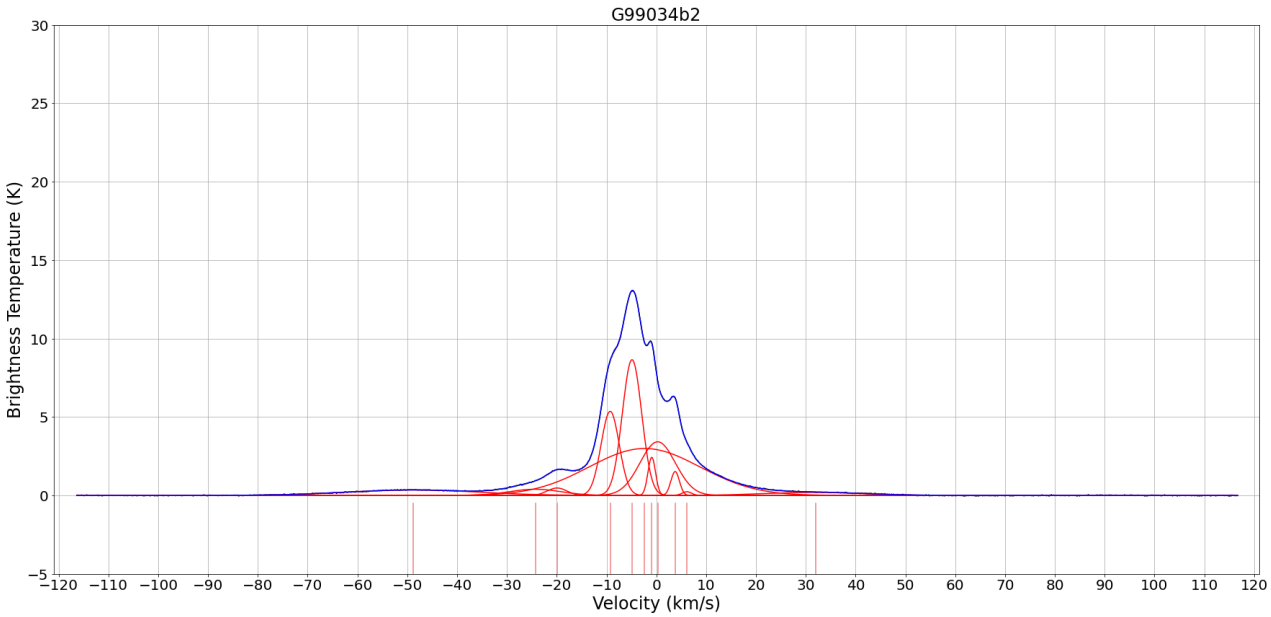

Figure 7.4u: Plots of Gaussian Fits: 99.0
Positions $l = 99.0°$, $b = -34°$.

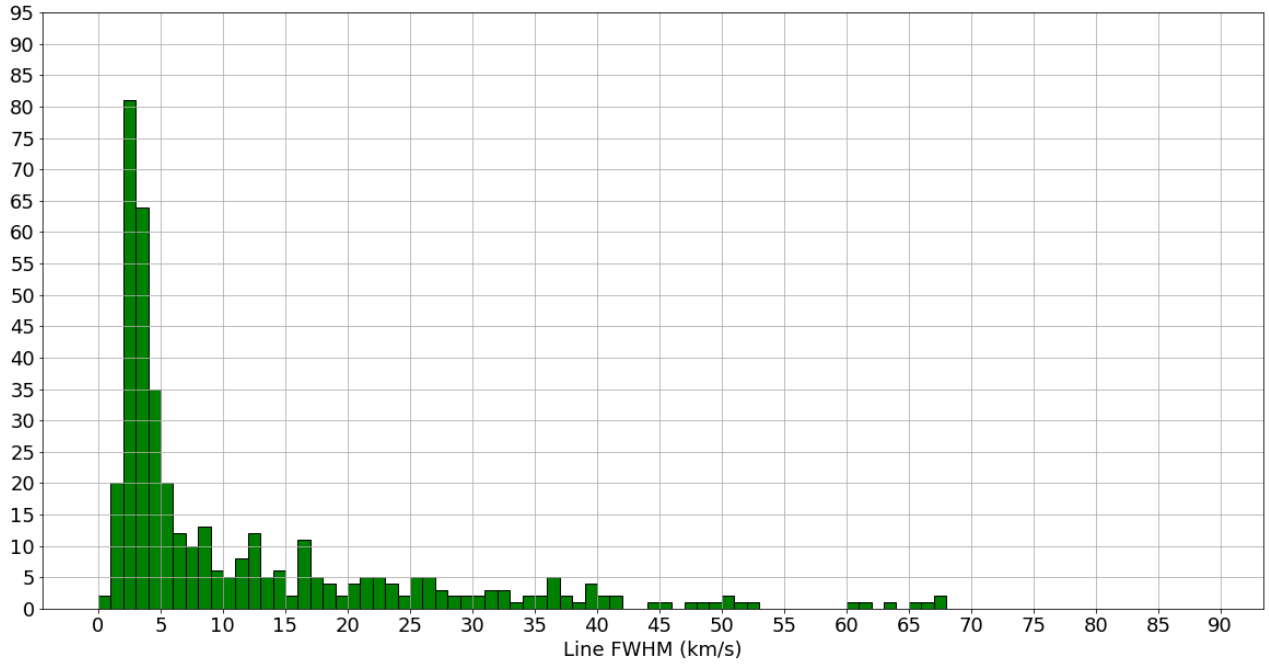

Figure 7.5a: A3021 Component Width Distribution
Histogram of the number of gaussians fit to the spectra shown in figures 7.3 and 7.4 as a function of the FWHM of each gaussian fit.

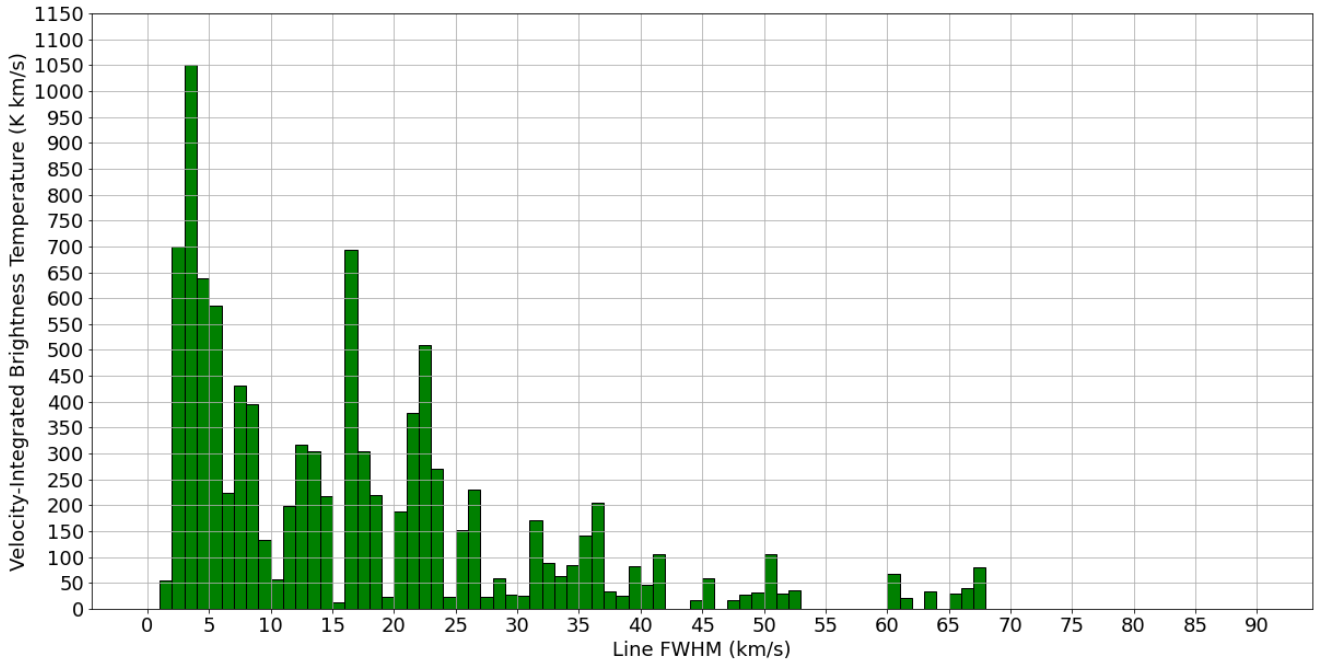

Figure 7.5b: A3021 Component Width W(HI)

Bar plot of the sum of the velocity-integrated brightness temperature of the 21-cm HI line of each bin in figure 7.5a.

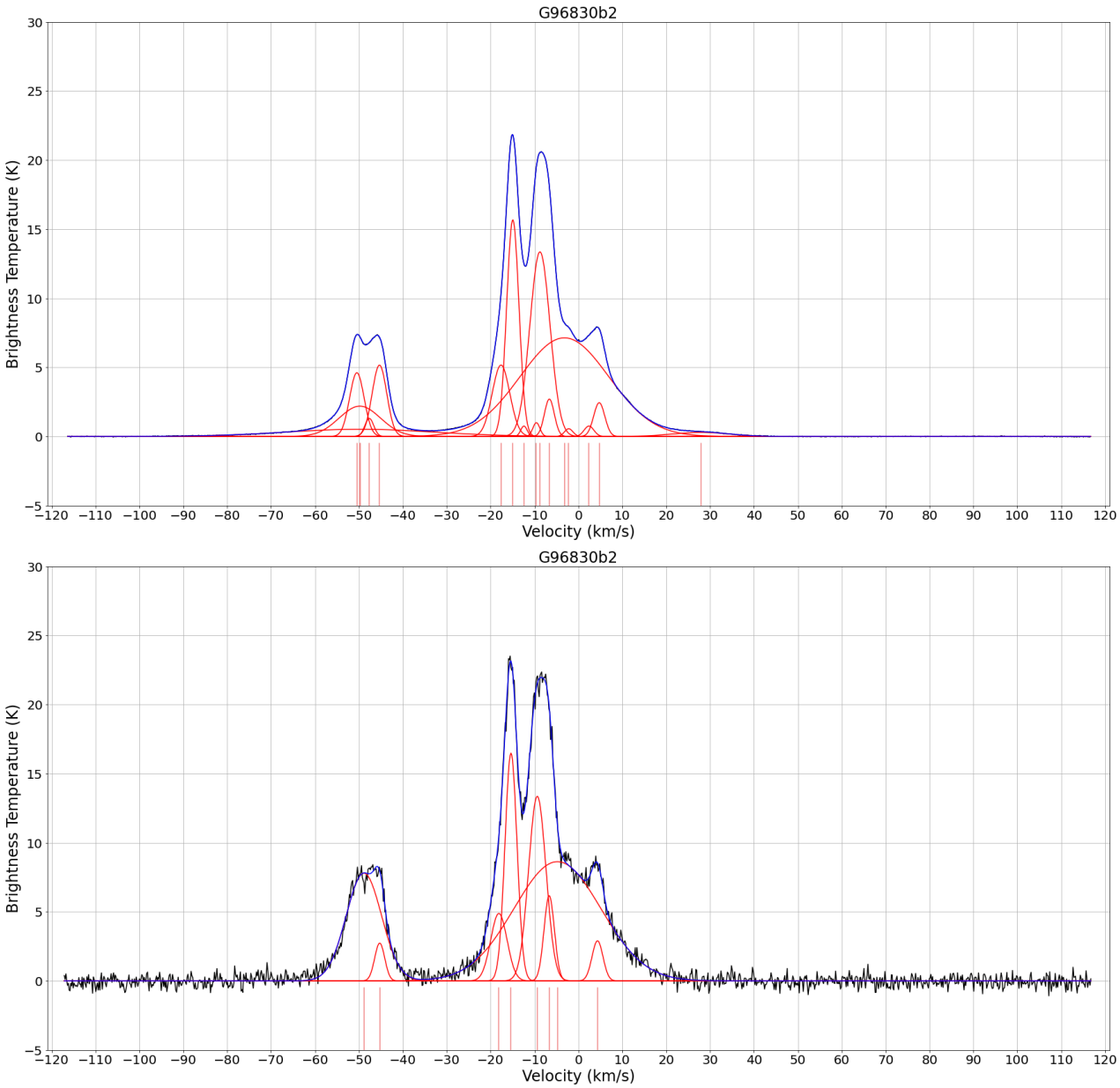

Figure 7.6a: Plots of G96830

Upper plot is the fit data from A3021 with a threshold value of 0.50 K, and the lower plot is the data from the GALFA survey (Peek et al. 2018) with a threshold value of 6 K.

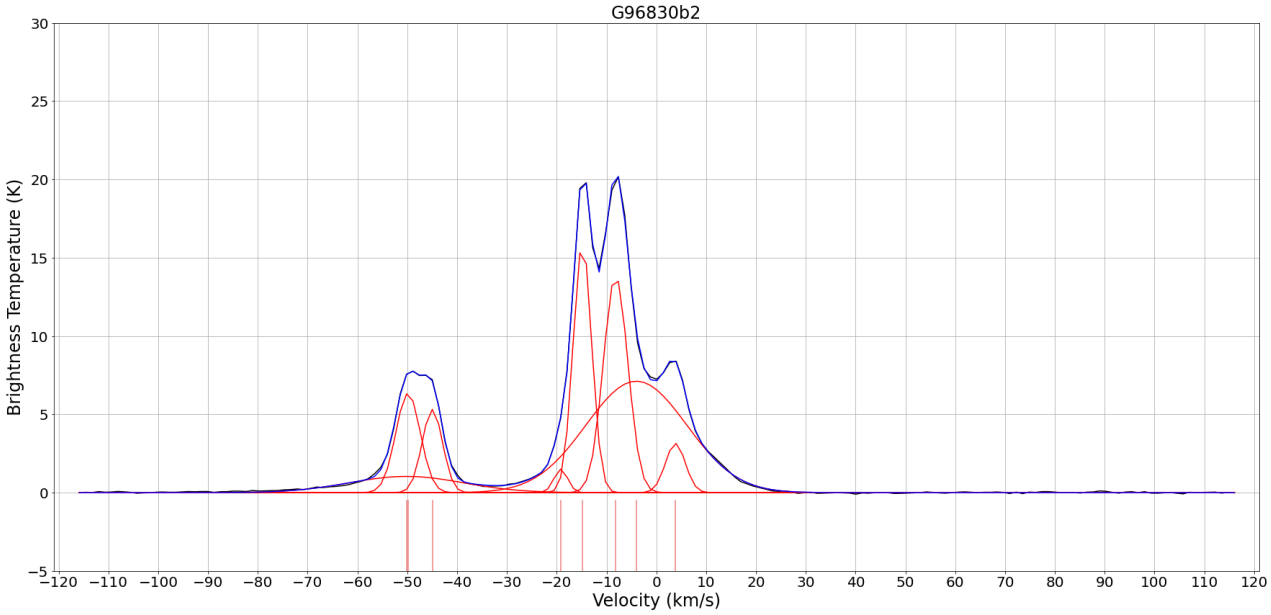

Figure 7.6b: Plot of G96830
Data are from EBHIS (Winkel et al. 2016) with a threshold value of 0.40 K.

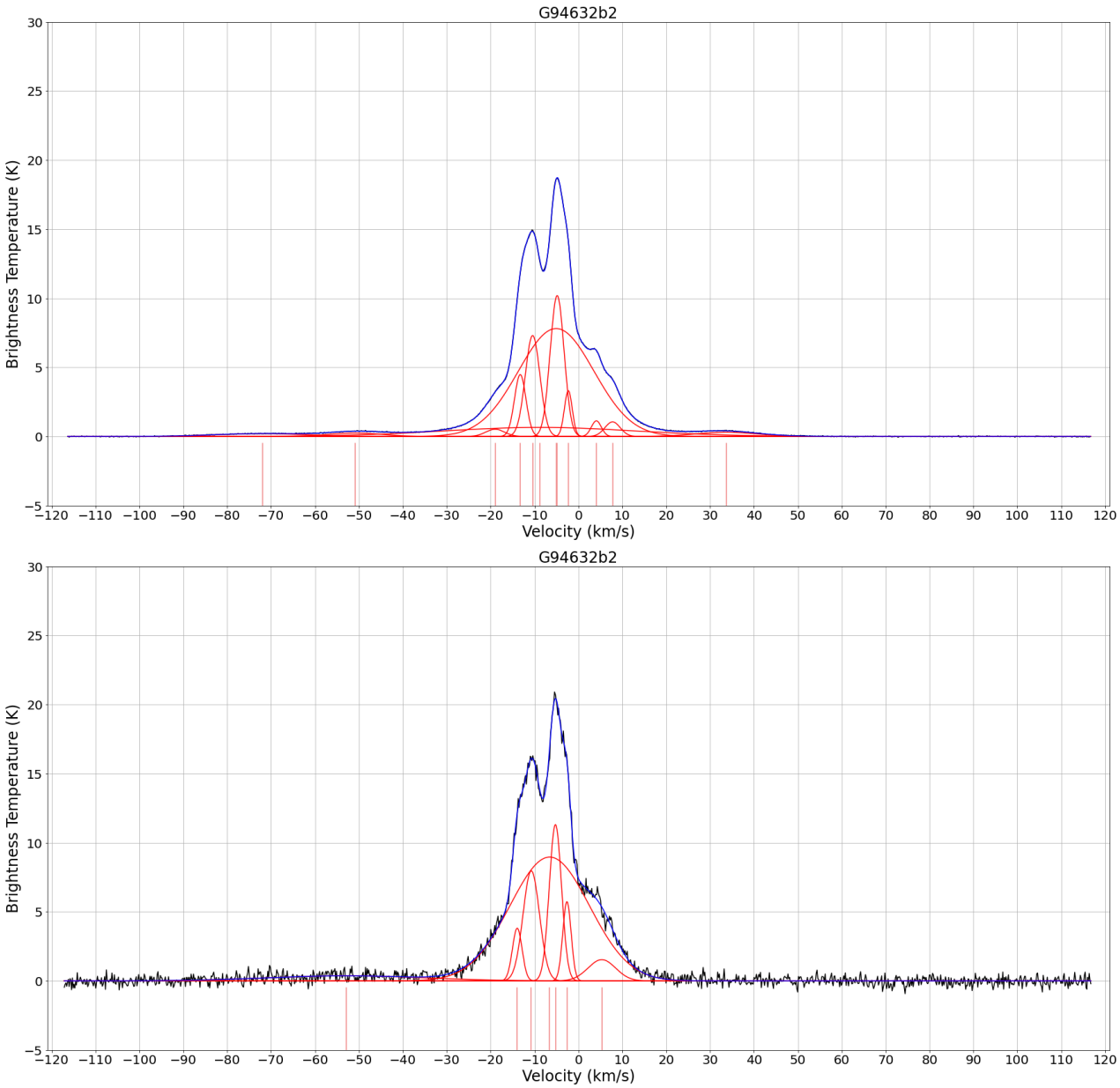

Figure 7.6c: Plots of G94632
Upper plot is the fit data from A3021 with a threshold value of 0.50 K, and the lower plot is the data from the GALFA survey (Peek et al. 2018) with a threshold value of 5 K.

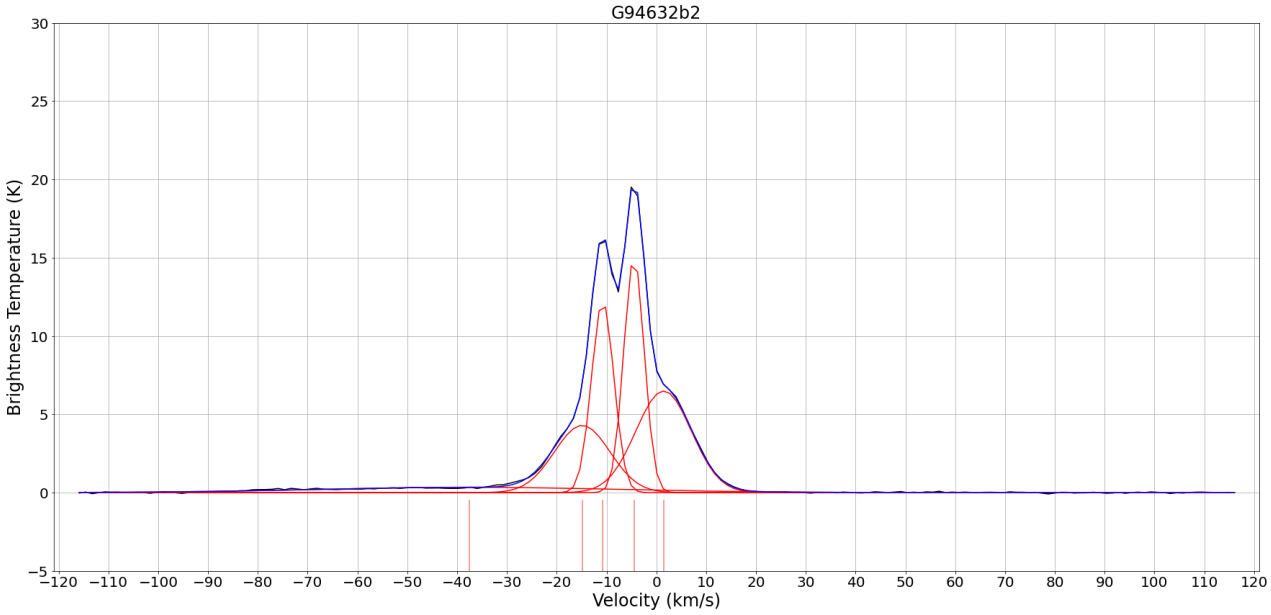

Figure 7.6d: Plot of G94632
Data are from EBHIS (Winkel et al. 2016) with a threshold value of 0.30 K.

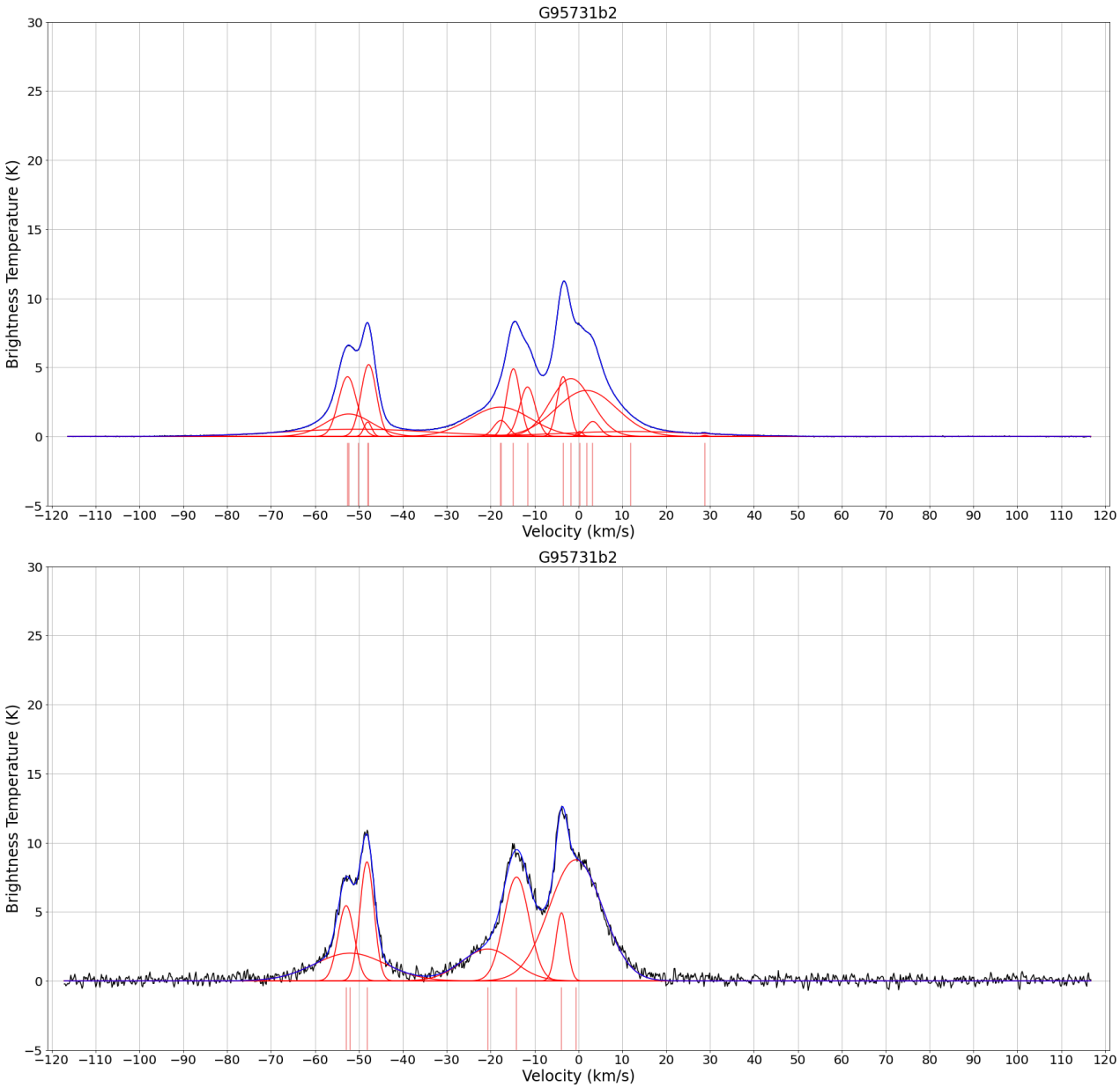

Figure 7.6e: Plots of G95731
Upper plot is the fit data from A3021 with a threshold value of 0.50 K, and the lower plot is the data from the GALFA survey (Peek et al. 2018) with a threshold value of 5 K.

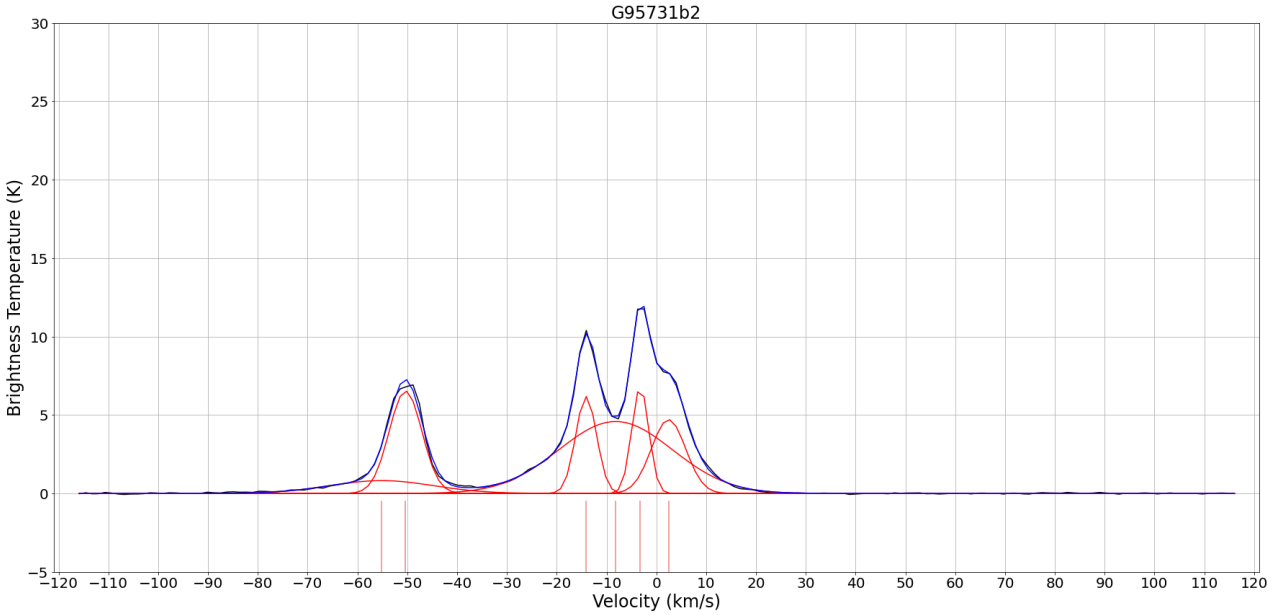

Figure 7.6f: Plot of G95731
Data are from EBHIS (Winkel et al. 2016) with a threshold value of 0.55 K.

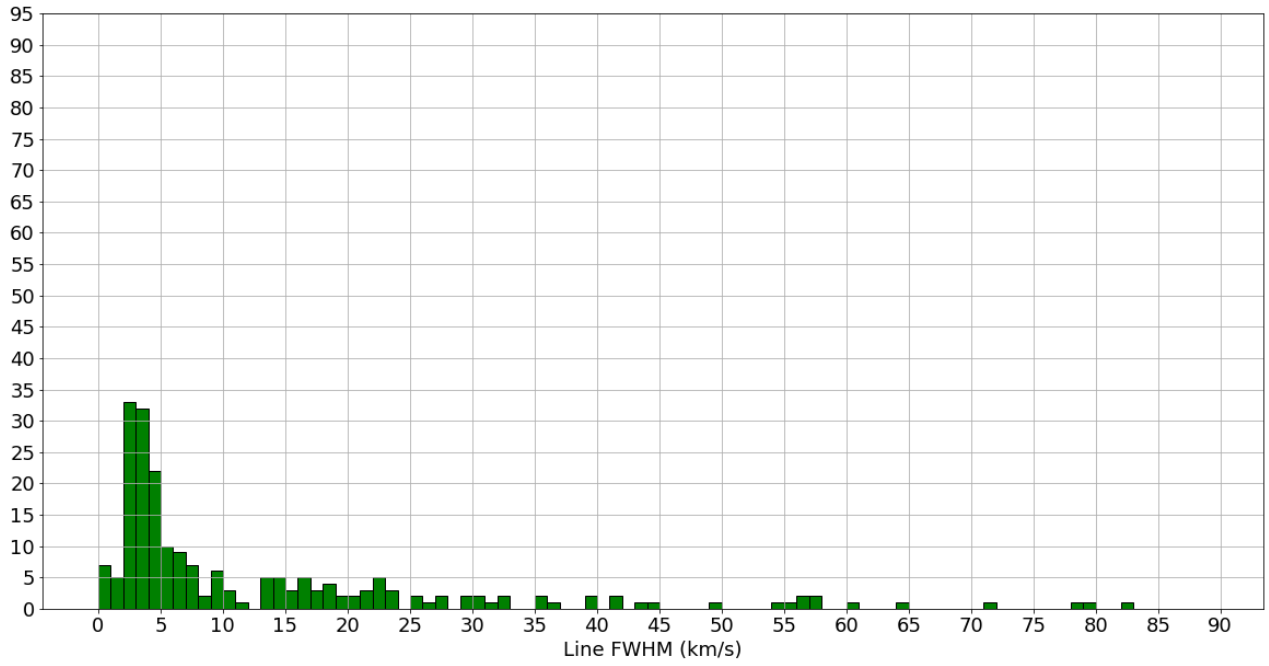

Figure 7.7a: GALFA Component Width Distribution
Same as 7.5a except using data from the GALFA survey (Peek et al. 2018).

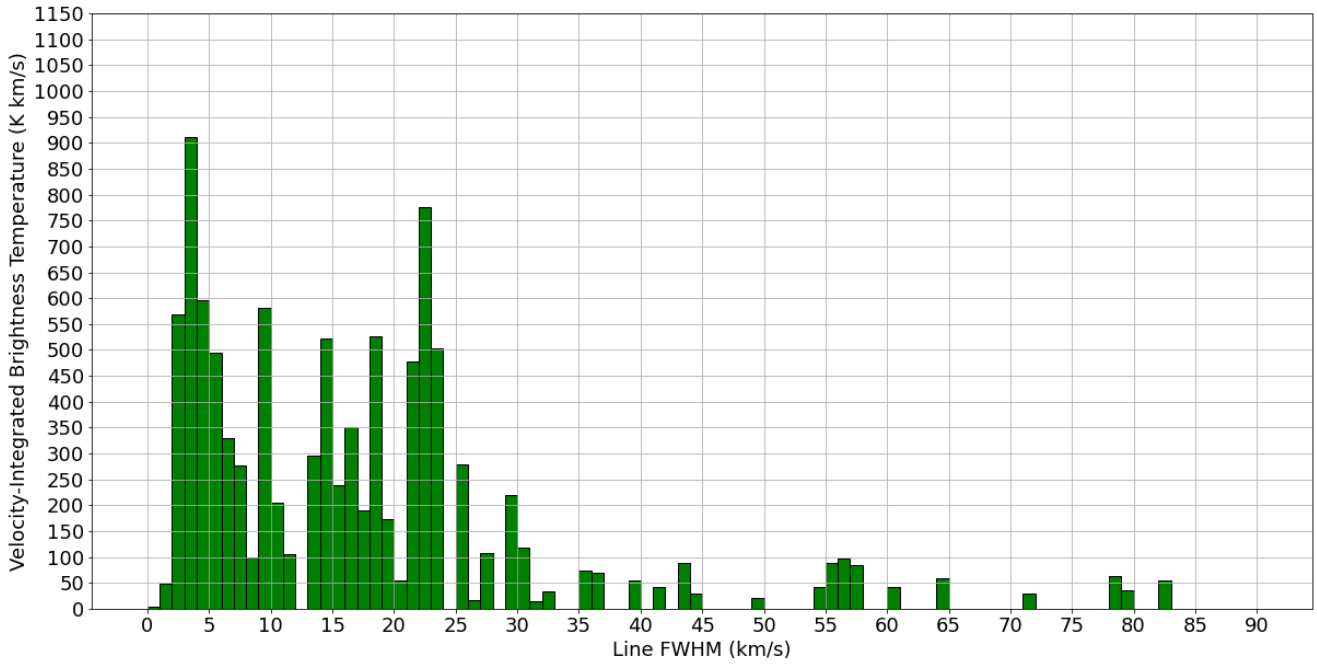

Figure 7.7b: GALFA Component Width W(HI)
Same as 7.5b except using data from the GALFA survey (Peek et al. 2018).

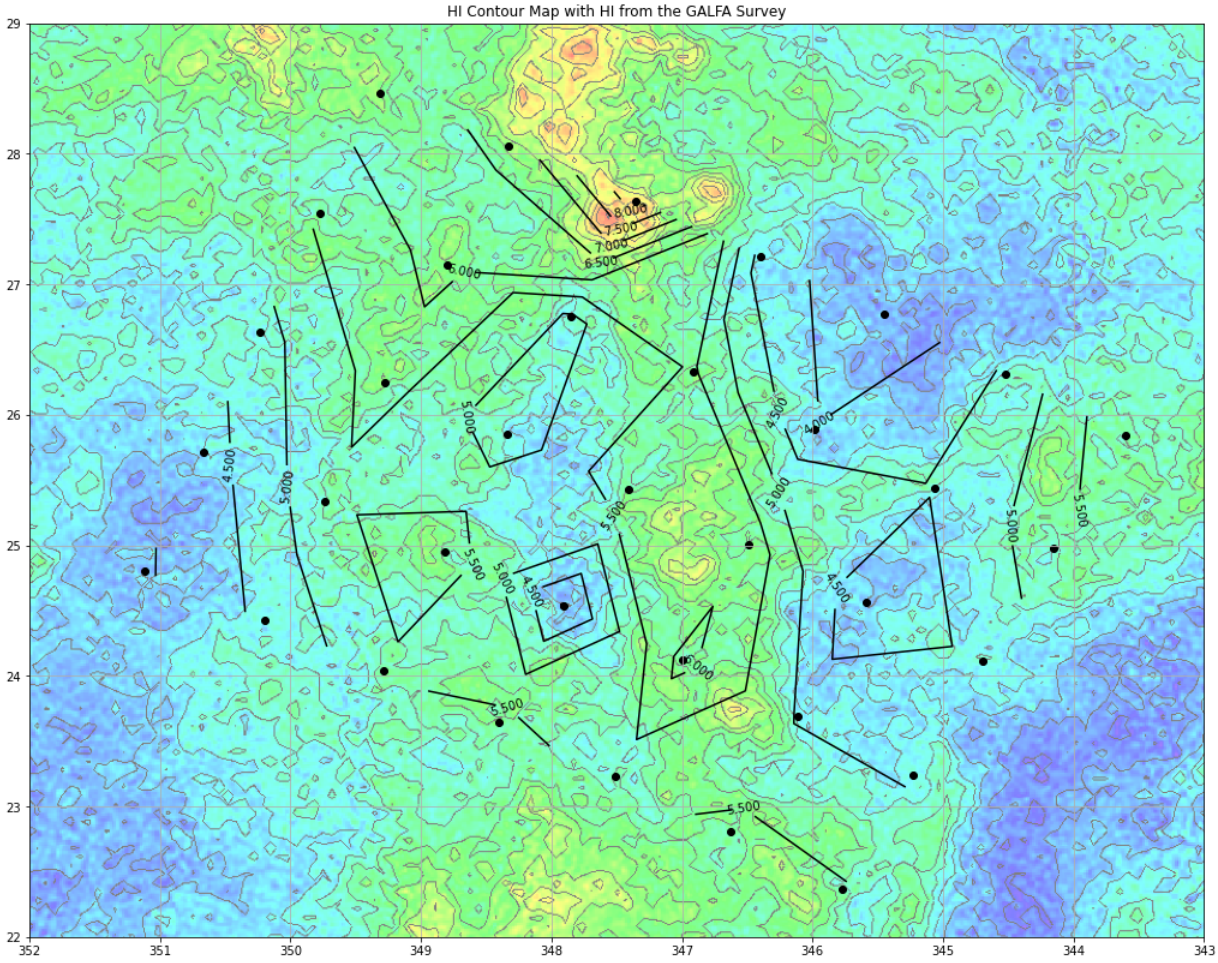

Figure 7.8: GALFA and A3021

HI column density is in units of 10^{20} cm^{-2}. The horizontal axis is right ascension, and the vertical axis is declination in 2000 coordinates. The black foreground contour lines are based on the HI 1420 MHz line data collected on board 2 of the project A3021 observations, and the background is from the GALFA survey. The contour lines in both are in steps of 0.5×10^{20} cm^{-2} from 10^{20} to 10^{21} cm^{-2}.

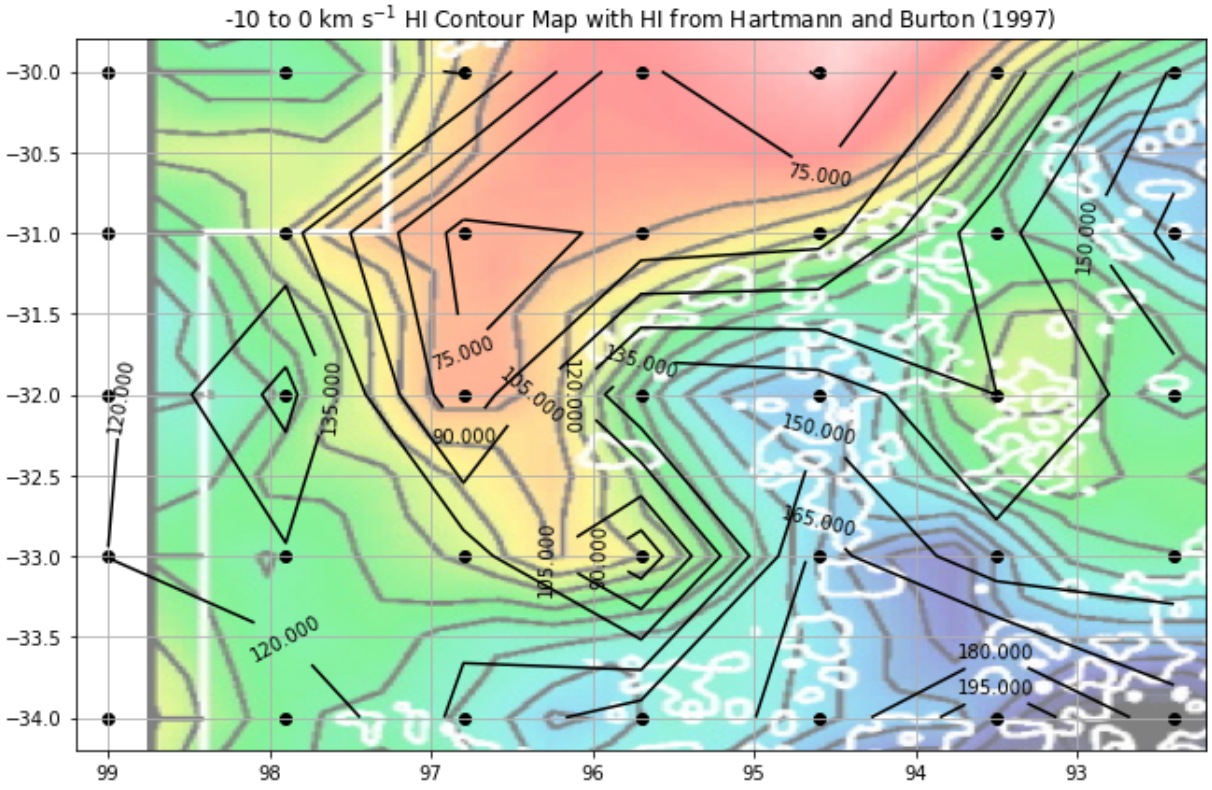

Figure 7.9: GALFA and A3021

HI velocity-integrated beam temperature is in K km s^{-1}. The horizontal axis is galactic longitude, and the vertical axis is galactic latitude. The black foreground contour lines are based on the HI 1420 MHz line data collected on board 2 of project A3021. The background is a portion of figure 6 from Yamamoto et al. (2003), using the data from Hartmann and Burton (1997) between −11 and 0 km/s. The foreground data are between −10 and 0 km/s.

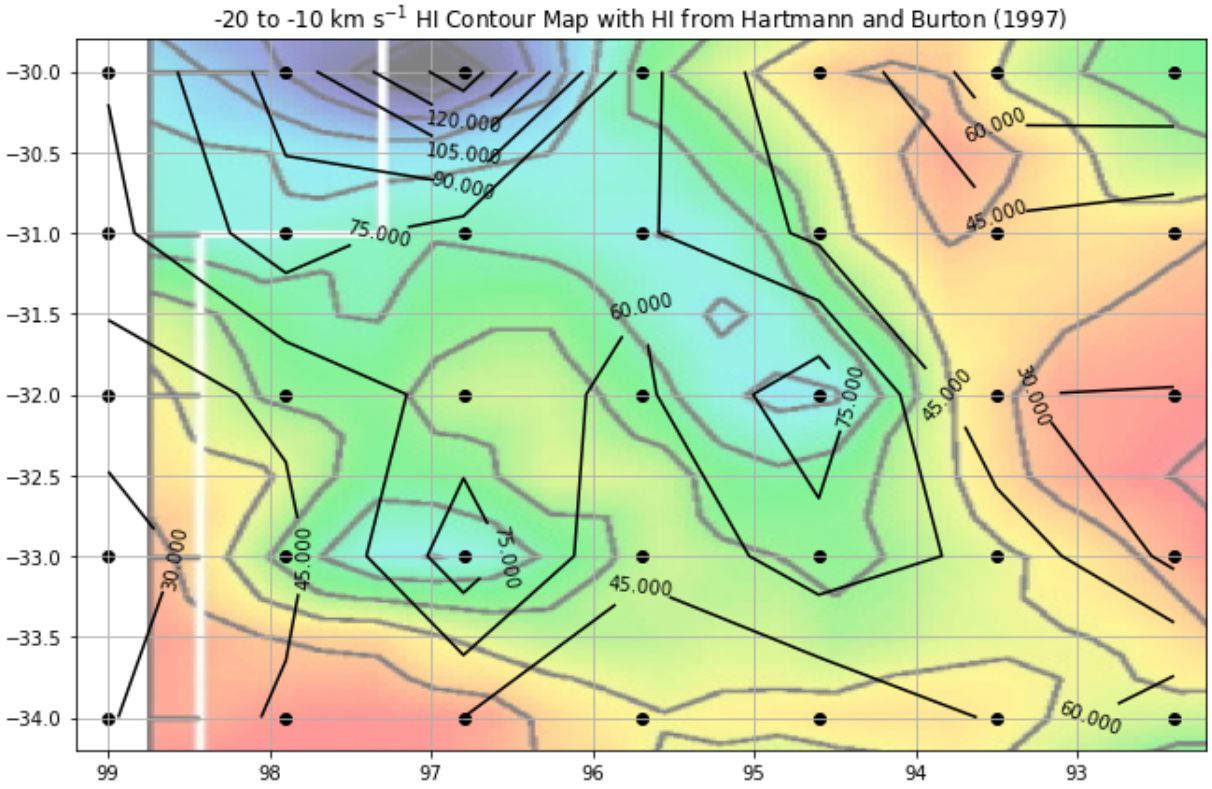

Figure 7.10: GALFA and A3021

HI velocity-integrated beam temperature is in K km s^{-1}. Again, the horizontal axis is galactic longitude, and the vertical axis is galactic latitude. The black foreground contour lines are based on the HI 1420 MHz line data collected on board 2 of project A3021. The background is a portion of figure 8 from Yamamoto et al. (2003), using the data from Hartmann and Burton (1997) between −20 and −12 km/s. The foreground data are between −20 and −10 km/s.

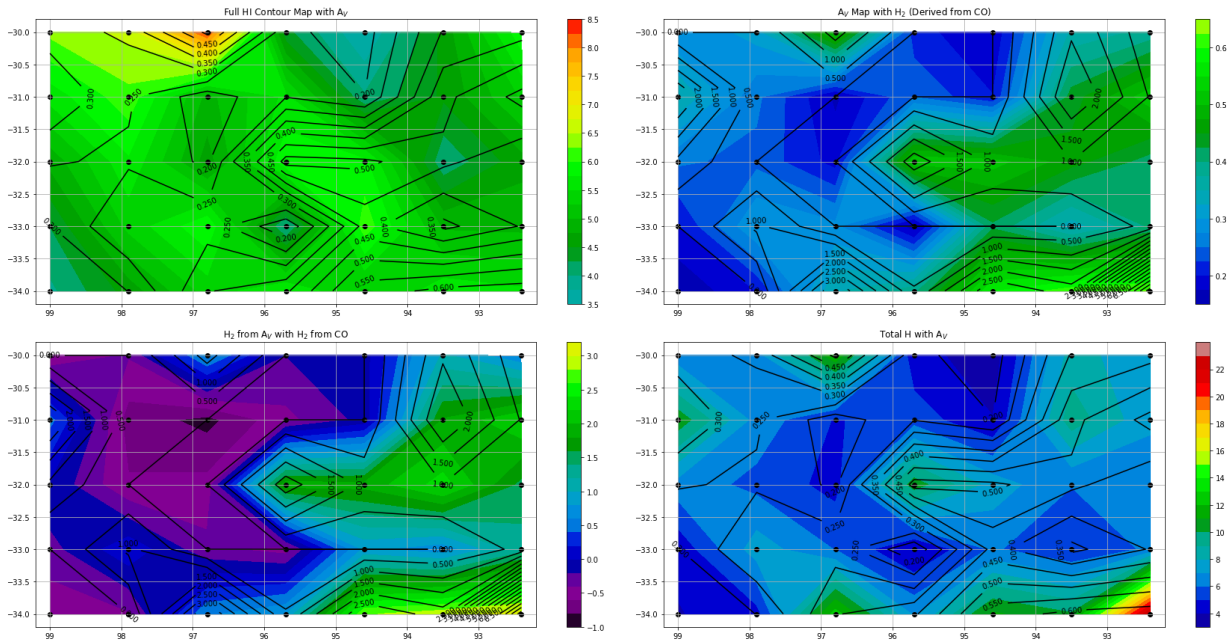

Figure 7.11: Comparison Contour Plots

HI column density is in units of 10^{20} cm^{-2}. Extinction is in units of mag. CO velocity integrated beam temperature is in units of K km s^{-1}. See section 7.6 for details.

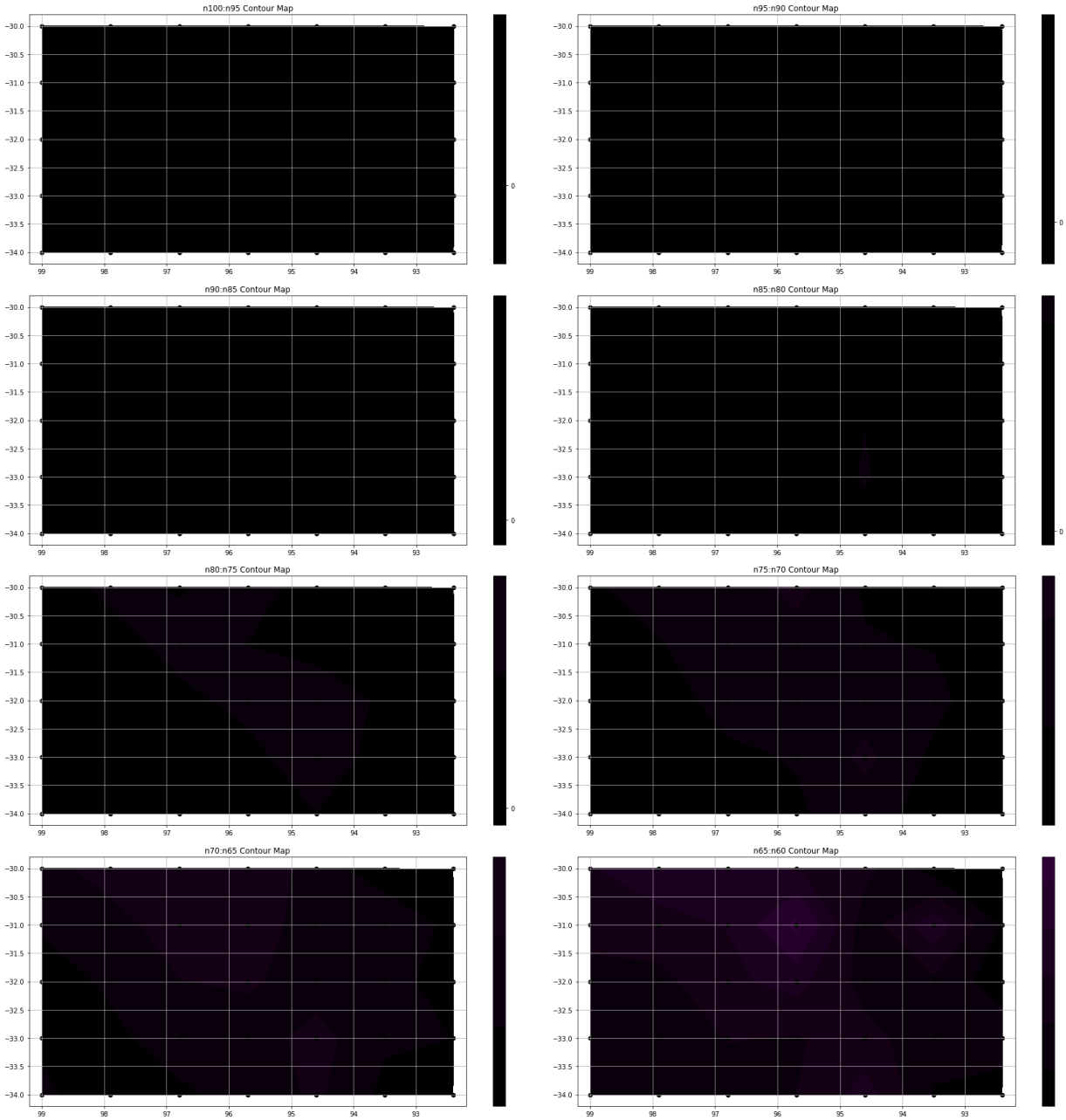

Figure 7.12a: Contour Plots of N(HI) from -100 to -60 km/s

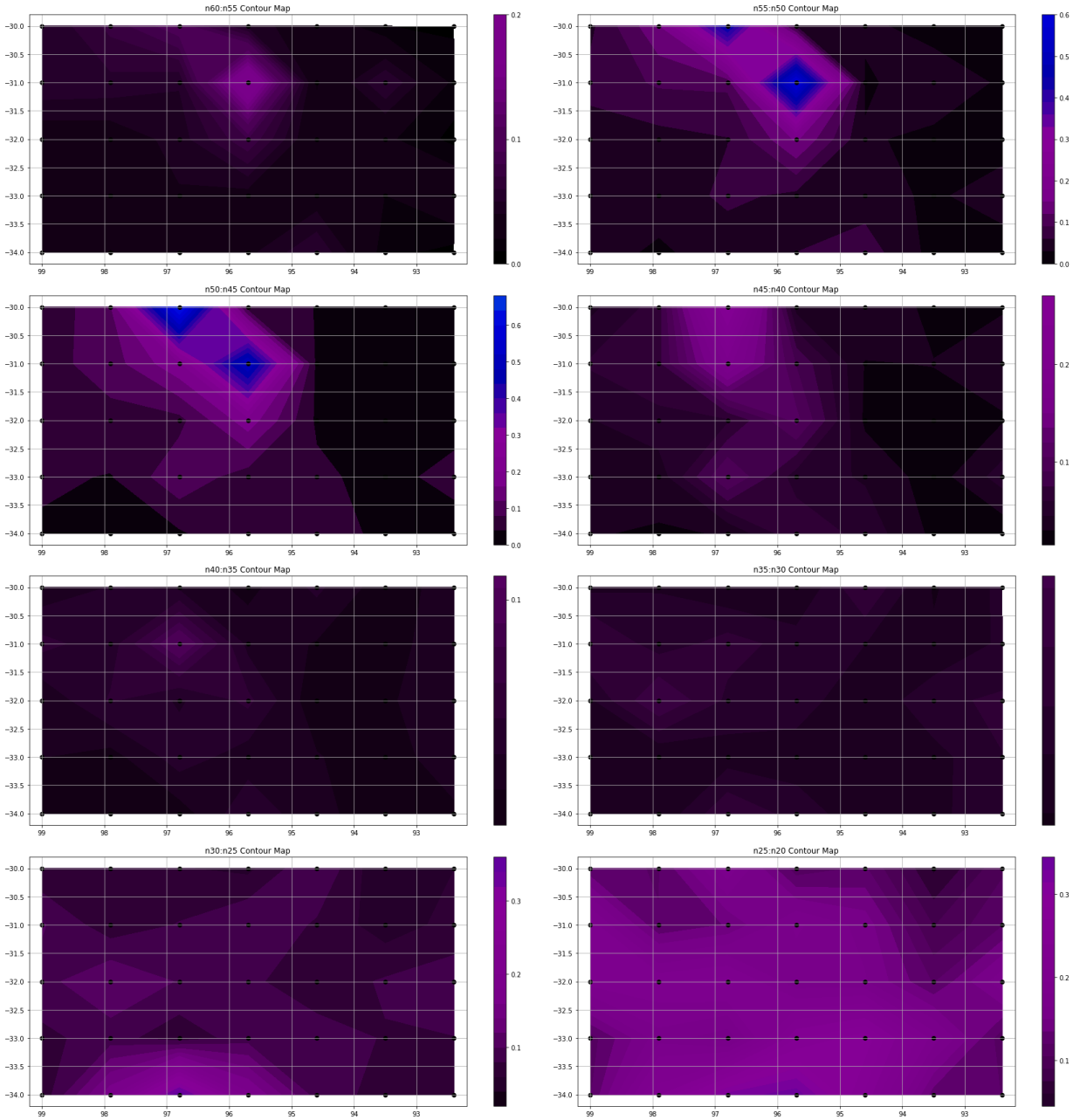

Figure 7.12b: Contour Plots of N(HI) from -60 to -20 km/s

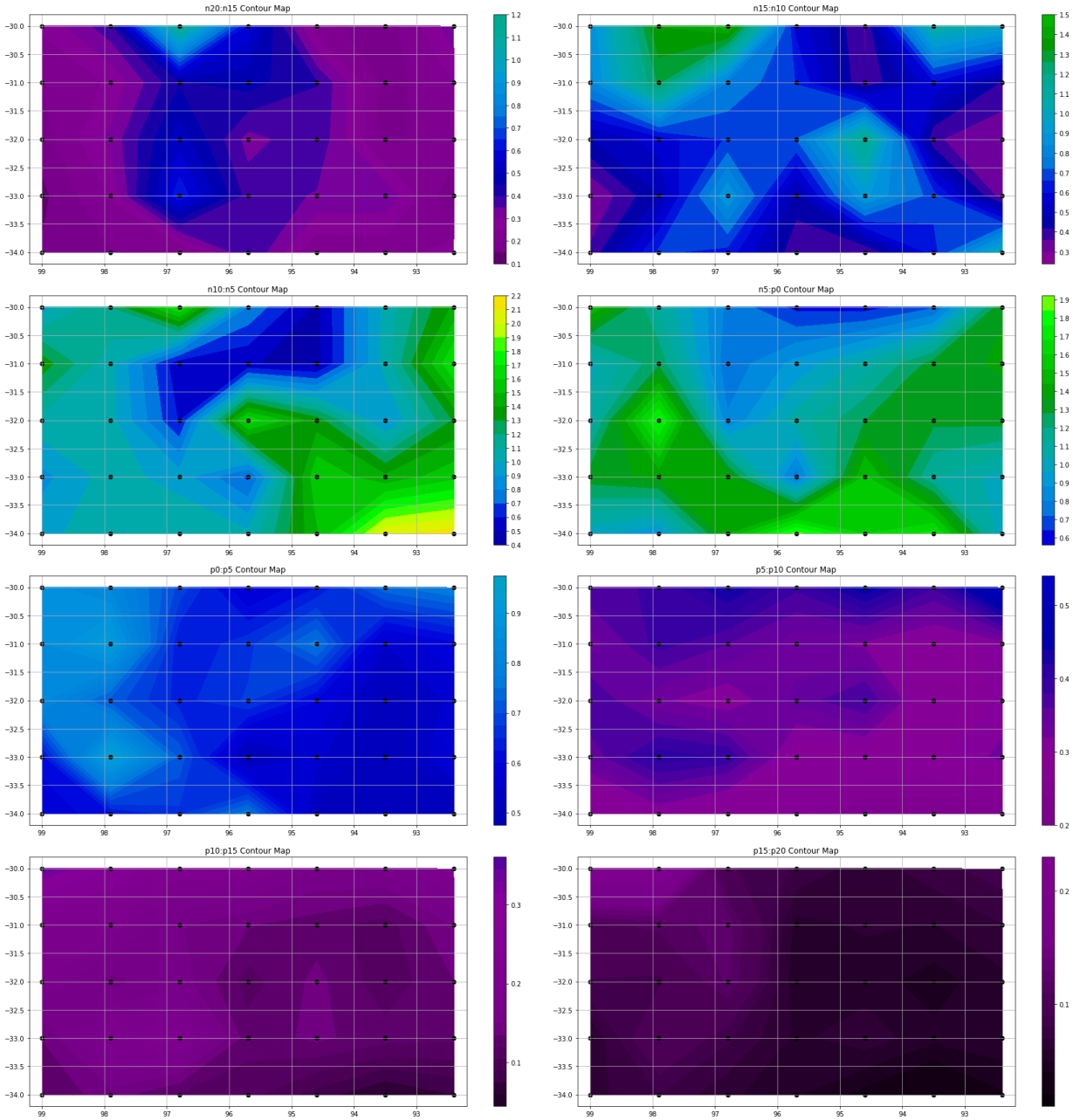

Figure 7.12c: Contour Plots of N(HI) from -20 to 20 km/s

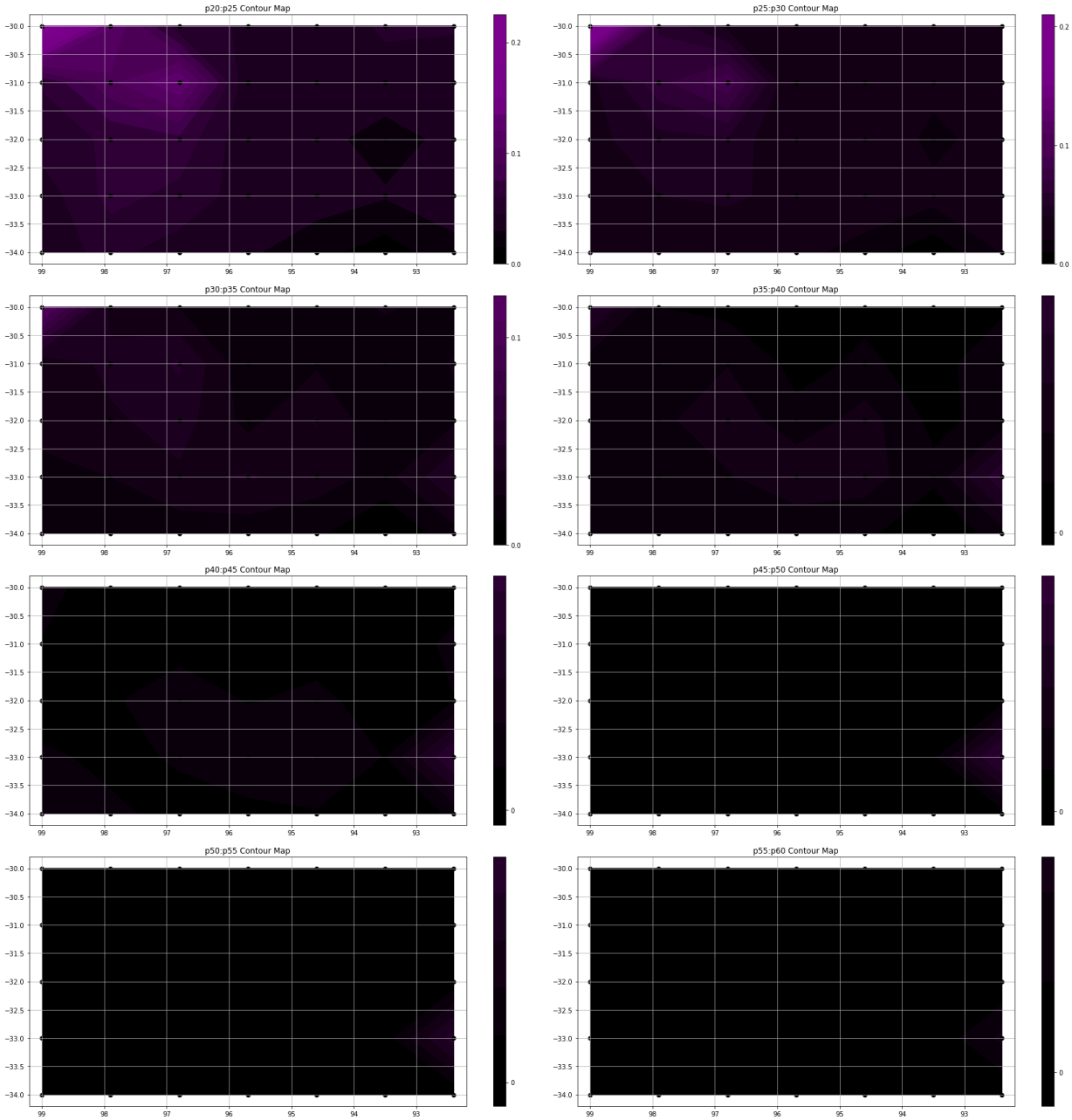

Figure 7.12d: Contour Plots of N(HI) from 20 to 60 km/s

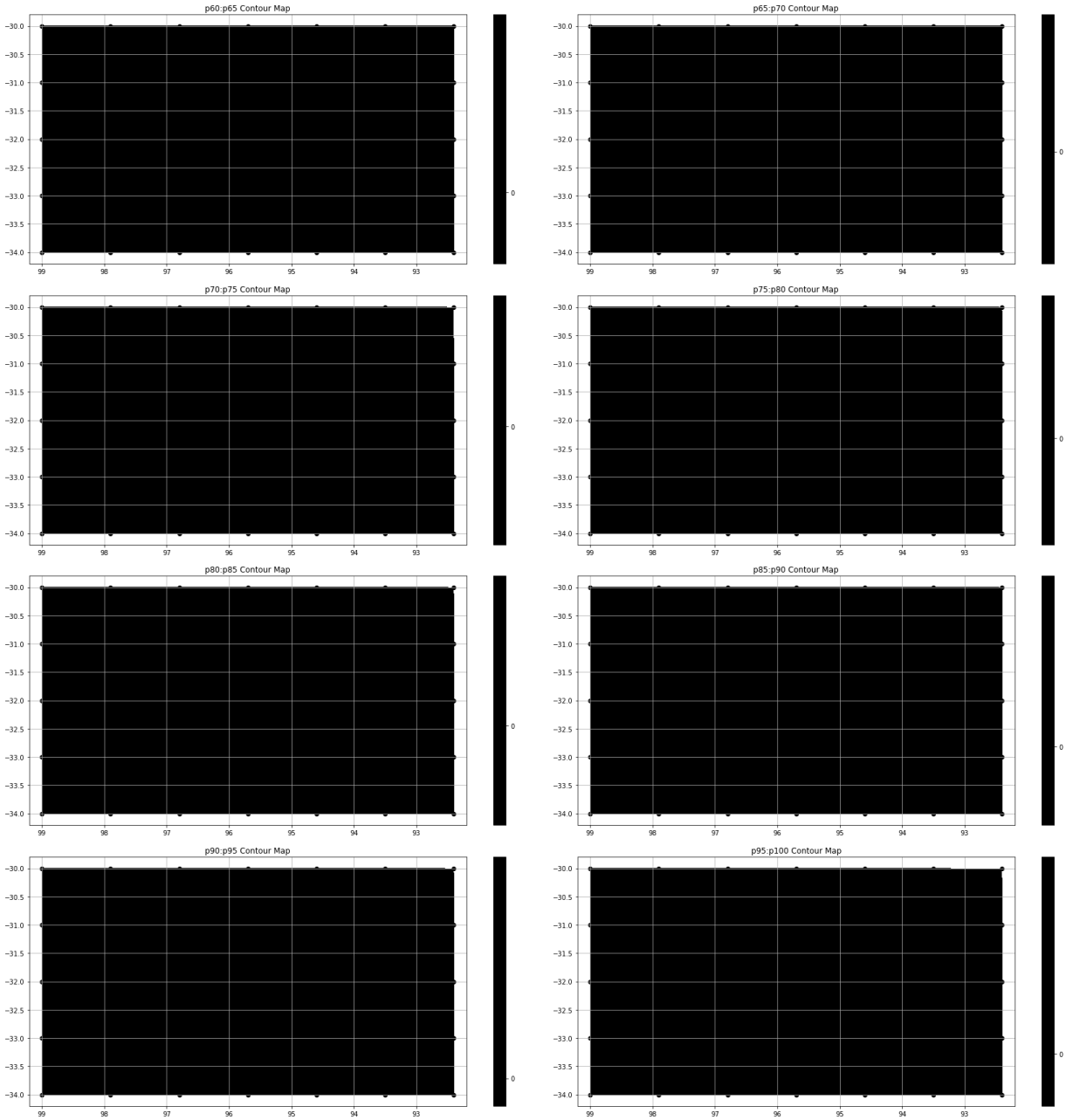

Figure 7.12e: Contour Plots of N(HI) from 60 to 100 km/s

Chapter 8

Methylidyne PDR Model

8.1 Introduction

Numerical simulations of photodissociation regions can help to improve our understanding of how the abundances and excitation conditions for the relevant atomic and molecular species vary as a function of depth into the photodissociation region. Because molecular clouds can be thought of as PDRs (e.g. Magnani and Shore 2017), this is the first step in understanding how these molecular clouds form from larger atomic structures in the ISM. In this chapter we study how CH is treated in a photodissociation region model. We have seen in Chapters 3 and 4 how $T_{\rm ex}$ has been determined using on−off radio observations (e.g. Rydbeck et al. 1976, Hjalmarson et al. 1977, Genzel et al. 1979), optical observations of O and B type stars (e.g. Lien 1984, Jura and Meyer 1985), and optical observations of O and B type stars with radio observations of the same line of sight (e.g. Lien 1984, Dailey et al. 2020). If we assume that $T_{\rm ex}$ determined through each of the methods is the excitation temperature of the main line of the CH ground state, then $T_{\rm ex}$ varies greatly due to the differing physical conditions in each cloud. Thus,

assuming a uniform $T_{\rm ex}$ for all clouds would cause significant errors in the derived column density if the variations in physical conditions (i.e. density, radiation field, gas-to-dust ratio, metallicity) are not accounted for. Bertojo et al. (1976) predicted that $T_{\rm ex}$ for the ground state doublet would vary depending on the conditions within the cloud using collisional models, and determined $T_{\rm ex}$ changes significantly with a change in density and/or temperature.

In order to further explore how $T_{\rm ex}$ depends on the conditions within the cloud, we used a modified version of the 3D-PDR code developed by Bisbas et al. (2012). The code was modified by Thomas Bisbas (2020, private communication) to add CH into the cooling function calculations. With the addition of CH as a coolant, the code calculates the populations of the energy levels of CH using the rate coefficients from Dagdigian (2018), with H and H_2 colliders published on the LAMDA database (Schöier et al. 2005) [1], along with rate coefficients of CH-He collisions from Marinakis et al. (2019). The rate coefficients included for CH-He collisions has been reduced to only cover the lowest 32 hyperfine states of CH (covering 4 rotational levels), which matches the range of rate coefficients in the CH-H and CH-H_2 data. Unfortunately, at the time of writing there was no hyperfine resolved collision data available for CH collisions with electrons for the 32 lowest states of CH.

The chemical network used is the 128 species chemical network included with the stock code, and each of the simulations uses a one dimensional, constant density model. The gas-to-dust ratio for the majority of the trials is considered to be 124, which is assumed to be the average gas-to-dust ratio of the ISM (Li and Draine 2001). The metallicity is assumed to be 1 (i.e., equal to the metallicity for the Sun).

[1] https://home.strw.leidenuniv.nl/ moldata/

The model determines the species abundance from 10^{-5} to 10^{1} mag extinction with a high extinction resolution across an exponential series of steps. Each of the steps increases the exponent term by 0.0125, therefore each order of magnitude has about 80 steps for a total of 482 steps.

8.2 CH Flat Model

The flat model simulates a region of space with constant density and a UV radiation source on one side similar to the PDR illustrated in figure 1.1. The code was run for densities between $10^{1.7}$ and $10^{2.7}$ cm^{-3} (~ 50.12 and ~ 501.2 cm^{-3}) covering much of the range of densities in diffuse clouds, and the initial UV radiation field is either 0.57, 1.70, or 5.1 Draines (Draine 1978), corresponding to the standard interstellar radiation field (ISRF) and a factor of three change in the standard ISRF in either direction (Heays, Bosman, and van Dishoeck 2017). The extinction in the models is modeled from the edge of the cloud, and is not comparable to measured extinction.

8.2.1 Abundance and Temperature

The majority of the trials had gas temperatures which were usually within the range of temperatures for a diffuse cloud (30 to 100 K) in Snow and McCall (2006). The exceptions were the trial with 0.57 Draine UV radiation field for the $10^{2.7}$ cm^{-3} density model and the 5.10 Draine radiation field trials at low density. As expected, the gas temperatures increase with an increase in the initial UV radiation field intensity and a decrease in the gas density. The temperature usually increases slightly after the molecular hydrogen becomes self-shielding, and then drops to near or at the minimum temperature of 10 K at high extinction due to enhanced molecular cooling. In some of the high UV radiation field trials at low densities, the

temperature would drop after H_2 becomes self-shielding instead of increasing. Unfortunately, when the gas temperature drops to the minimum temperature allowed by the simulation (10 K), as seen in figure 8.1, the results of the simulation in that region are corrupted and are no longer useful.

Figure 8.2 illustrates how the abundance changes with density for the 5 species in the ISM we are primarily interested in (H, H_2, CO, OH and CH). At low extinction before H_2 self-shielding, the abundance of the 4 diatomic species tends to be higher if the density is higher, with H_2 having the highest abundance, followed by CO and OH at 6 orders of magnitude lower abundance, and CH at approximately 8 orders of magnitude lower abundance. H_2, CO and CH increase in abundance with an increase in density for the majority of the extinction space, however, the OH abundance tends to decrease with an increase in density shortly after H_2 becomes self-shielding due to OH being consumed in chemical reactions.

Figure 8.3 shows the abundance for varying UV field strength at 0.57, 1.70, and 5.10 Draines and varying density from $10^{1.7}$ to $10^{2.7}$ cm^{-3}. As the UV radiation field strength is increased and/or the density is decreased, H_2 will become self-shielding at higher extinction. In all cases, the CH abundance, at least initially, will closely match the increase in the H_2 abundance as the H_2 becomes self-shielding. Formation of CH begins with the radiative association of C^+ and H_2 through the reaction

$$C^+ + H_2 \rightarrow CH_2^+ + h\nu \tag{8.1}$$

which is followed shortly by the ion-molecule reaction

$$CH_2^+ + H_2 \rightarrow CH_3^+ + H \tag{8.2}$$

The combination of dissociative recombination of CH_2^+ and CH_3^+ through the reactions

$$CH_2^+ + e^- \rightarrow CH + H \tag{8.3}$$

and

$$CH_3^+ + e^- \rightarrow CH + H_2 \tag{8.4}$$

forms CH (Danks, Federman, and Lambert 1984) The plentiful C^+ in diffuse clouds (as seen in figure 8.3) along with the quick reactions in the CH formation network suggests that the population of CH will be closely linked to the population of H_2, which is reflected in the model results.

The boundary between diffuse and translucent clouds can be defined as the point where half of the carbon in the gas is contained in C^+ ions (Snow and McCall 2006). The densest model ($10^{2.7}$ cm^{-3}) does not reach this boundary before the model reaches the 10 K lower limit, so according to this model that boundary likely occurs at higher densities than the ones sampled in this chapter.

Most of the molecular species we are interested in increase with increasing extinction, however OH usually decreases in abundance after a small increase at low extinction as the molecule is consumed to create more complex molecules. When there is a very low radiation field, OH abundance immediately decreases after H_2 becomes self-shielding.

The CH/H_2 ratio in the model is shown in figure 8.4. The high density and/or UV radiation field trials tend to have CH/H_2 ratios on the order of 10^{-8} and 10^{-7}, which are consistent with the observed N(CH)/N(H_2) ratio of approximately 5×10^{-8} (Liszt and Lucas 2002; see chapter 2). The CH/H_2 ratio varies depending on the initial conditions, and across the extinction space the ratio is not constant but generally does not vary by more than two orders of magnitude. It changes more with increases in the UV

ISRF and decreases in the density. In each case, the CH/H_2 ratio ends up within an order of magnitude of 5×10^{-8} at high extinction ($10^0 - 10^1$ mag).

8.2.2 Excitation

The plots showing how the excitation temperature changes across the photodissociation region are shown in figure 8.5. The excitation temperature at each point in the PDR is shown in red and the axis is on the right side of the figure. The spikes in excitation temperature are an unresolved issue in the calculations of the CH level populations by the 3D-PDR program. Before the H_2 self-shielding region, the excitation temperature varies significantly with varying density and UV radiation field. Due to the relation between the level population ratio and the excitation temperature, the changing excitation temperature is discussed in terms of the population ratio of levels 2 and 4 of the ground state. As the density increases, the upper level (4) becomes more populated, often resulting in negative excitation temperatures, and at low densities the lower level (2) is more populated, resulting in positive excitation temperatures. For all cases, the excitation temperature drops to near the background temperature at high extinction.

If the collisions with helium are ignored, then it appears collisions with atomic hydrogen tend to populate the upper ground state and collisions with molecular hydrogen tends to populate the lower ground state, mirroring the observations of Bouloy, Nguyen-Q-Rieu, and Field (1984). In this case the singularity occurs in the H_2 self-shielding region as the H_2 density rapidly increases. Collisions with helium tend to populate the upper half of the ground state, resulting in more negative excitation temperatures and causes the singularity in the excitation temperature to occur at higher extinction after H_2 becomes self-shielding. The inclusion of helium colliders also causes the slope near the singularity to be more gradual at higher UV radiation intensities, with the slope becoming steeper as the UV radiation field decreases.

Helium is not very reactive in the ISM so its relative population does not change significantly across the flat photodissociation region, so its effect does not appear to strongly depend on the position within the pdr.

Observations of molecular clouds have led to calculations of the CH main line excitation temperature; some studies have derived high excitation temperatures (e.g. Rydbeck et al. 1976), while others have derived low excitation temperatures (e.g. Dailey et al. 2020). While the excitation temperature of the main line is usually determined to be inverted, the excitation temperature of the ground state doublet has been measured to be positive for some lines of sight (Lien 1984; Jura and Meyer 1985). However, the excitation temperature of the doublet includes all 4 hyperfine states from the upper and lower halves of the lambda doubled ground state, which may not be identical to the main line excitation temperature.

The model excitation temperatures are usually positive at higher extinctions, where the majority of the CH is. Observations of the CH main line have shown that the excitation temperature is generally inverted, so it is unlikely that the excitation temperatures in this model are accurate. If the CH-electron collisions are the only major collision partner that is neglected, then the collisions with electrons likely cause the upper states to become populated, similar to collisions with atomic hydrogen. Atomic oxygen and C^+ have similar abundances to electrons, so they may also be important collision partners.

Figure 8.5 also shows the observed velocity-integrated brightness temperature of a hypothetical observation of the PDR. Point W(CH) is calculated from the column density and excitation point at each point in the extinction space, where the column density is the density multiplied by a 0.1 parsec path length. Actual observations will sample the outer portion of the PDR up to the maximum extinction for that line of sight. To determine what influence this has on observations, figure 8.5 shows the cumulative W(CH) of a hypothetical observation of the PDR in green. The cumulative excitation temperature is

shown in orange, and is determined from the column density of N(CH) and the cumulative W(CH). The distance into the modeled region as a function of the extinction is shown in figure 8.5 as a black line. In each trial, the relation between the distance and extinction is linear and increases with decreasing density.

When observing at 3.3 GHz, the Arecibo 305-m telescope has a beam size of about 1.4 arcminutes. If observing a cloud that is 170 pc away, such as MBM 16 (Zucker et al. 2019), then the beam is observing an area 0.07 pc across. At this distance, the H_2 self-shielding region is contained within the beam. At high densities the transition from H_2 being unshielded to self-shielding is quick and occurs over an order of magnitude of distance between 10^{-5} to 10^{-3} pc. The transition is more gradual at low densities, and occurs over an order of magnitude of distance between approximately 10^{-3} to 10^{-1} pc. At a density of $10^{1.7}$ cm^{-3} and the standard UV radiation field (1.70 Draines), the H_2 self shielding transition could occupy the entire beam at 170 pc.

For a line to be detectable in a reasonable amount of time, W(CH) has to be on the order of 10^2 mK km s^{-1}. The model is able to replicate detectable levels of W(CH) (cumulative W(CH) of at least 10^2 mK km s^{-1}), however when CH is measurable, the cumulative excitation temperature does not reflect observed main line excitation temperatures which are generally negative. The model assumes that the observation is made normal to the surface of the cloud, but if the cloud is observed at an angle, then the observable CH signal could be detectable with a shallower PDR. To have excitation temperatures close to what has been observed, the cloud would have to be positioned so that a PDR is observed to have a $1-2$ order of magnitude greater CH velocity-integrated brightness temperature, which would require the cloud to be at a steep angle relative to the observer. Alternatively, the transition region could extend over several beams.

In order to reach detectable levels in very diffuse gas at densities of $10^{1.7}$ cm^{-3}, the PDR will have to be at least about $1 - 10$ parsecs deep, assuming that the actual excitation temperature of CH does not significantly change W(CH). At densities of $10^{2.7}$ cm^{-3}, CH is able to be detected in a PDR which is between 10^{-2} and 10^{-1} pc deep depending on the radiation field intensity.

Either the model is not producing an accurate model of the excitation temperature in the photodissociation region due to missing collision data, or the photodissociation region cannot be accurately modeled as a constant density region. Given that collisions with atomic hydrogen and helium tend to populate the upper half of the CH lambda-doubled ground state and collisions with molecular hydrogen tend to populate the lower half of the ground state, then perhaps the observations of an inverted excitation temperature for the CH main line implies that there is another important collider which is currently unaccounted for. Despite the model's inability to predict the CH excitation temperatures, it is able to show that CH should be detectable in low density gas where CO is not adequately self-shielded, as long as the actual excitation temperature is not close to 2.8 K which would significantly reduce W(CH), which is consistent with our results in chapters 5 and 6.

8.2.3 Gas/Dust Effects

To determine the effects of the relative densities of gas and dust may have on the excitation of CH; the gas-to-dust ratio was assumed to be either 50, 100, 124, or 500 for 4 trials. The gas-to-dust ratios 100 (i.e. Magnani and Shore 2017) and 124 (Li and Draine 2001) are average values for the ISM. The outer values at 50 and 500 are based on the measured gas-to-dust ratios in a sample of galaxies with varying metallicity in Leroy et al. (2011). In the simulation the metallicity will be assumed to be 1.

The model results of the abundances and excitation temperatures are shown in figure 8.6 and 8.7. Each of the trials had a density of $10^{2.7}$ cm^{-3} and 1.7 Draine UV radiation field. Dust is very important for the formation of molecular hydrogen, since H_2 forms very slowly in the gas phase, so H_2 is primarily formed when two hydrogen atoms bond on the surface of a dust grain (Snow and McCall 2006). The trials which had more dust (low gas-to-dust ratio) had more H_2 produced initially due to the increased H_2 production rate and also became self-shielding at lower extinction than the higher gas-to-dust ratio trials. The more abundant H_2 leads to higher abundances of CH and CN, but the initial abundances of CO and OH are nearly constant across each trial. CO and OH do not seem to be effected much by the variations in the gas-to-dust ratio except at the H_2 self-shielding region, where the abundance of CO and OH increase slightly at high dust levels but barely increase at all when there is less dust.

The excitation temperatures of each trial along with the estimated W(CH) are shown in figure 8.7, and the plots are similar to the plots in figure 8.5. The majority of the trial's excitation temperatures are not consistent with observations, since the excitation temperatures are positive by the time that the CH signal is observable in the trials for the lower gas-to-dust ratios. The lower state of CH becomes increasingly more populated after H_2 becomes self shielding due to the increase in H_2 collisions. The abundance of H_2 is strongly linked with the gas-to-dust ratio due to molecular hydrogen's reliance on dust for formation, so when the gas-to-dust ratio is high, like in the 500 gas-to-dust ratio trial, there is less H_2 at the point CH is detectable, so the lower state is less populated at that point compared to the lower gas-to-dust ratio trials. The simulated excitation temperatures are able to be consistent with observations very high gas-to-dust ratios.

According to the simulation, the excitation temperature of an observation can vary depending on the gas-to-dust ratio of the cloud. A lower gas-to-dust ratio will result in the lower state being more populated

at the point the CH signal is detectable, and a higher gas-to-dust ratio will cause the lower state to be less populated. Unless the gas-to-dust ratio is much higher than the average in the PDR of molecular clouds, it is likely that the simulation is missing the collision data for other important colliders for CH.

8.3 Variable Density Model

The gas in a molecular cloud is not expected to be at a constant density as we had in the flat model, but will instead steadily increase in density. The diffuse portion of the cloud will have densities between 100 and 500 cm^{-3}, and translucent portions will have densities from 500 to 5000 cm^{-3} (Snow and McCall 2006). To model the increasing density within the cloud, the density increases as extinction increases by a function of r^{-1}, where r is the distance from the center of the cloud, for two sets of trials based on the density increasing from 50 to 500 cm^{-3} and 10^2 to 10^4 cm^{-3}. Since the flat trials showed that the model tends to break down at high extinction, the upper limit of the extinction is reduced to 10^0 mag for the variable density trials.

8.3.1 Abundance and Temperature

The temperatures for each of the trials shown in figures 8.8a, 8.8b, 8.9a, and 8.9b are similar to the results in section 8.2.1, the initial temperature of the gas is higher at higher UV radiation field intensities, and the temperature will increase after H_2 becomes self-shielding, but drops to the minimum temperature at high extinction.

At low extinction, the abundances in the variable density models in figures 8.8c, 8.8d, 8.9c, and 8.9d are very similar to the flat models at similar densities. The largest difference between the abundances

predicted in the flat model and the variable model is the abundance of CO and C^+. At the high densities in the 10^2 to 10^4 cm^{-3} model, the CO overtakes C^+ and becomes the dominant carbon species, marking the transition from diffuse to translucent. As expected, this transition occurs at lower extinctions in the low UV radiation field trials. The 50-500 cm^{-3} model does not show this transition, but the CO abundance at high extinction is similar to the CO abundance at high extinction in the $10^{2.7}$ cm^{-3} flat density model.

8.3.2 Excitation

The excitation temperatures predicted by the variable model shown in figures 8.8e, 8.8f, 8.9e and 8.9f are very similar to what is predicted by the flat models. This is due to the H_2 self-shielding region occurring at very low extinction where the density is almost constant. When the density increases at the higher extinctions, the point W(CH) and the cumulative W(CH) also increase due to the increase in density since the excitation temperature does not change much compared to the flat model.

8.4 Conclusion

The modified 3D-PDR model was unable to reproduce observed excitation temperatures with the initial conditions in the trials. This likely indicates that CH-H, CH-H_2, and CH-He collisions are not sufficent to describe why the CH excitation temperature is often measured to be inverted. Possibly collisions with electrons, atomic oxygen or C^+ may be causing the upper half of the lambda doubled ground state to become overpopulated, but collision data for each of those species with CH would be needed to determine their effect on the CH main line excitation temperature in this model.

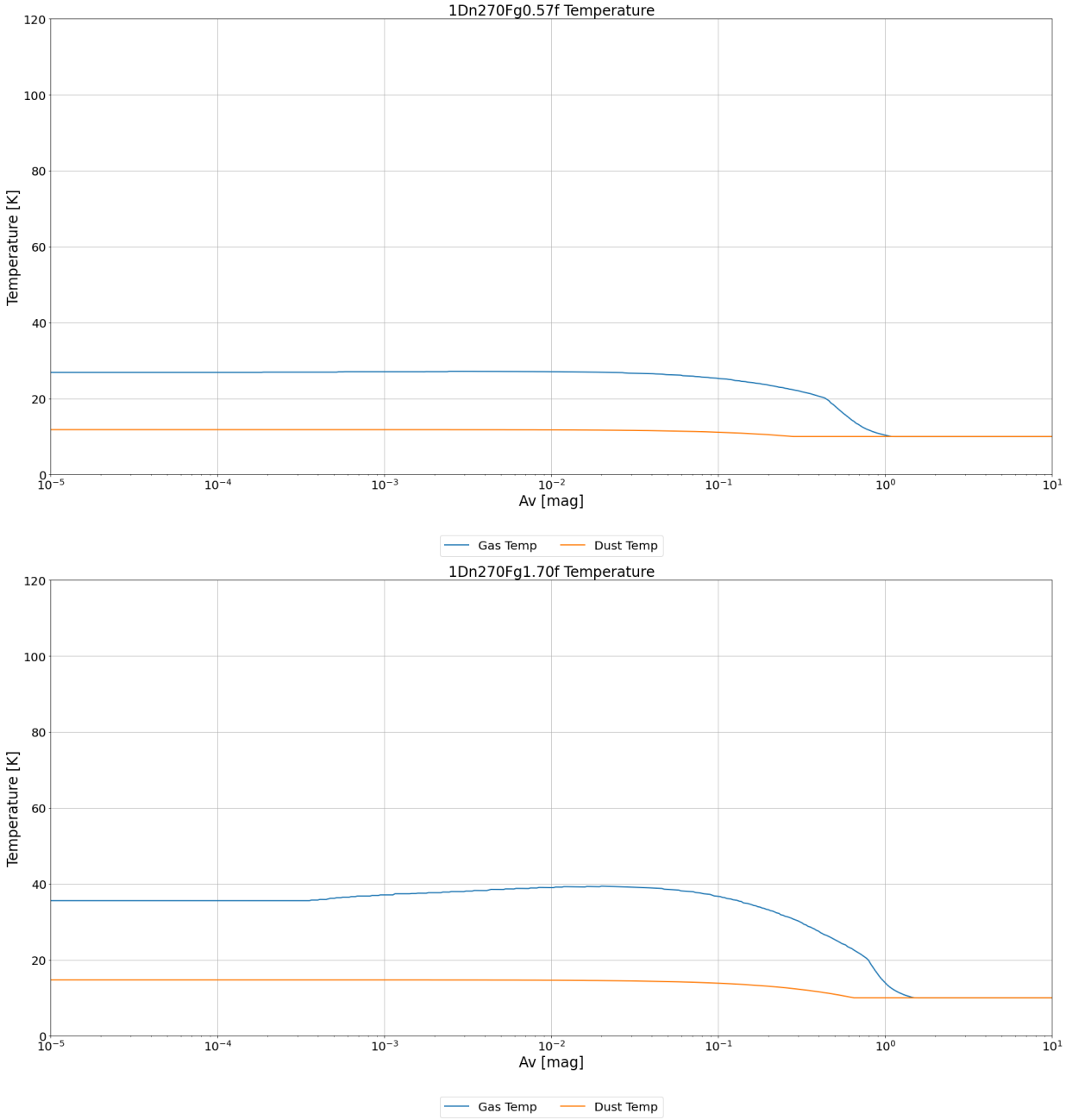

Figure 8.1a: Model gas temperatures in the cloud at $n_H = 10^{2.7}$ cm^{-3}, 0.57 and 1.70 Draine initial UV radiation field

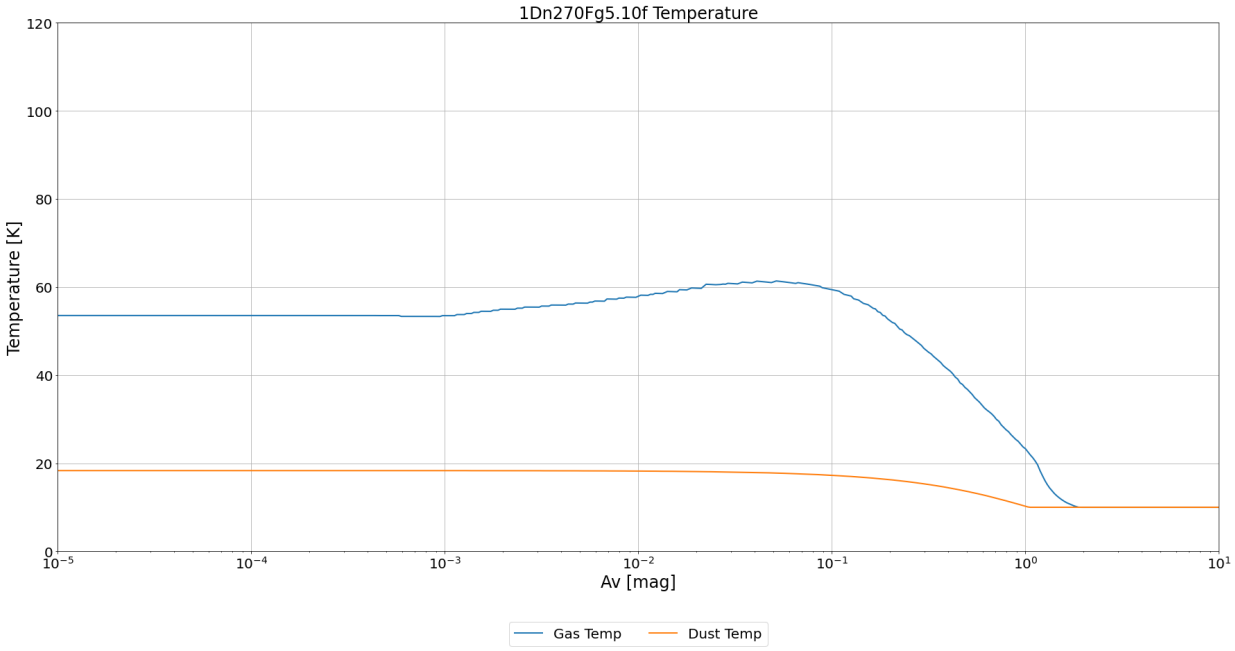

Figure 8.1b: Model gas temperatures in the cloud at $n_H = 10^{2.7}$ cm^{-3}, 5.10 Draine initial UV radiation field

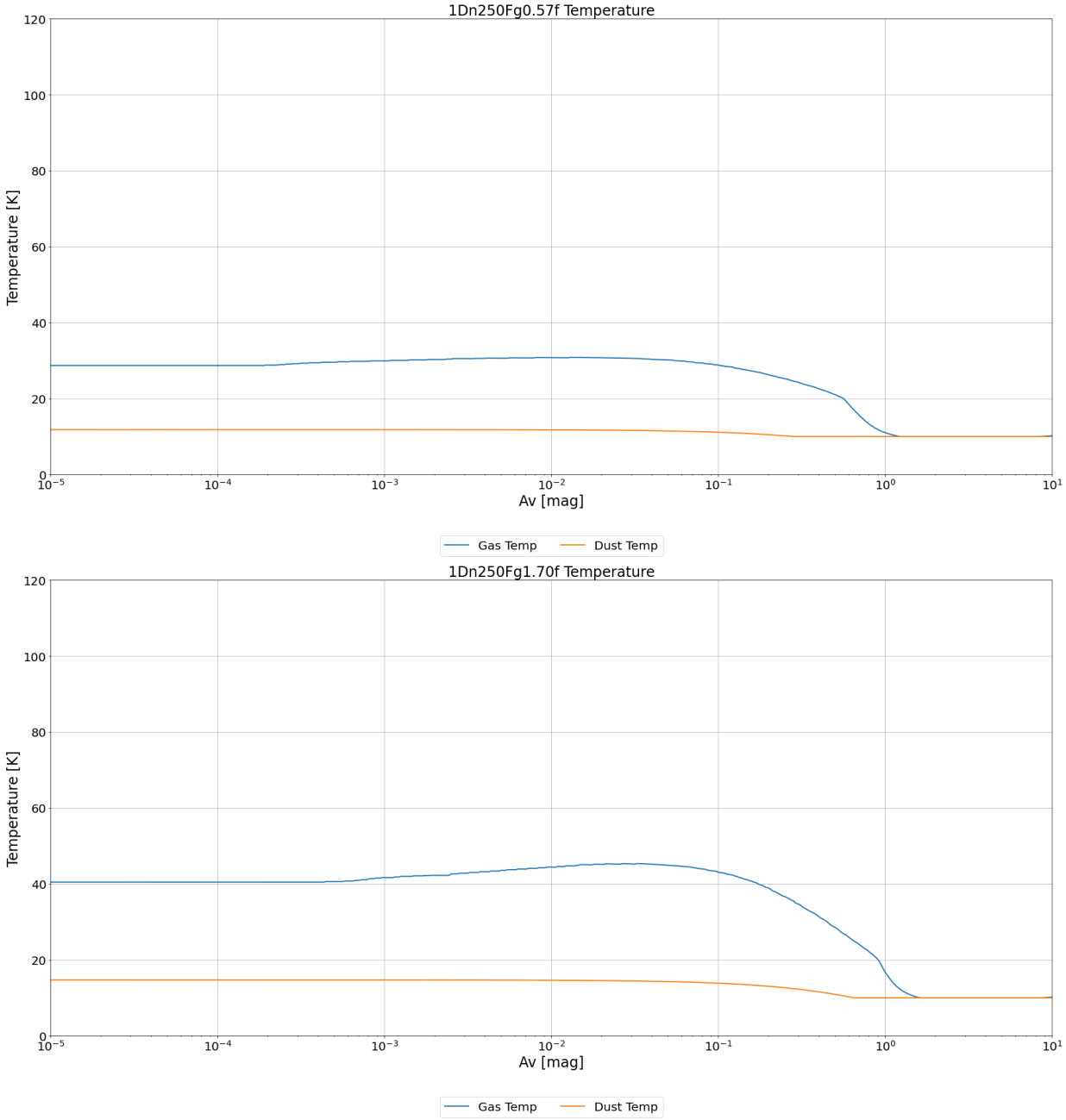

Figure 8.1c: Model gas temperatures in the cloud at $n_H = 10^{2.5}$ cm^{-3}, 0.57 and 1.70 Draine initial UV radiation field

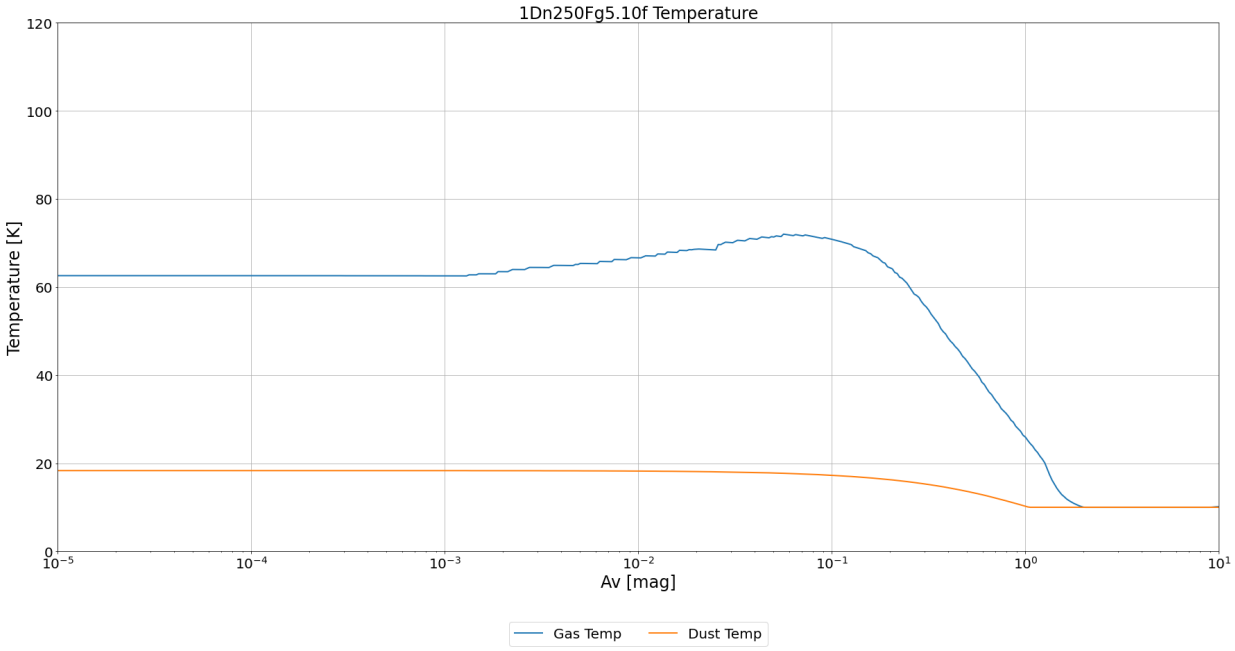

Figure 8.1d: Model gas temperatures in the cloud at $n_H = 10^{2.5}$ cm^{-3}, 5.10 Draine initial UV radiation field

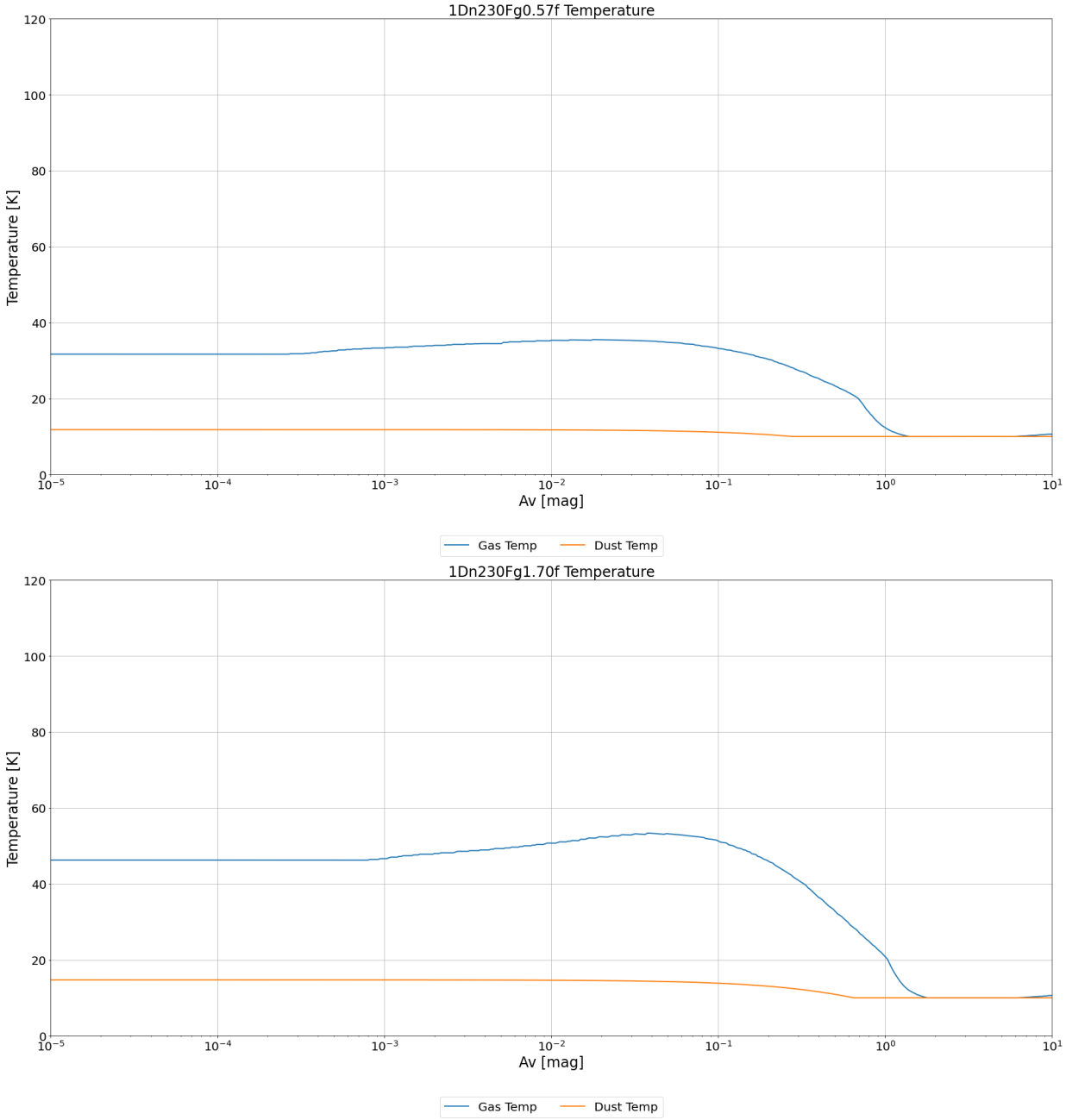

Figure 8.1e: Model gas temperatures in the cloud at $n_H = 10^{2.3}$ cm^{-3}, 0.57 and 1.70 Draine initial UV radiation field

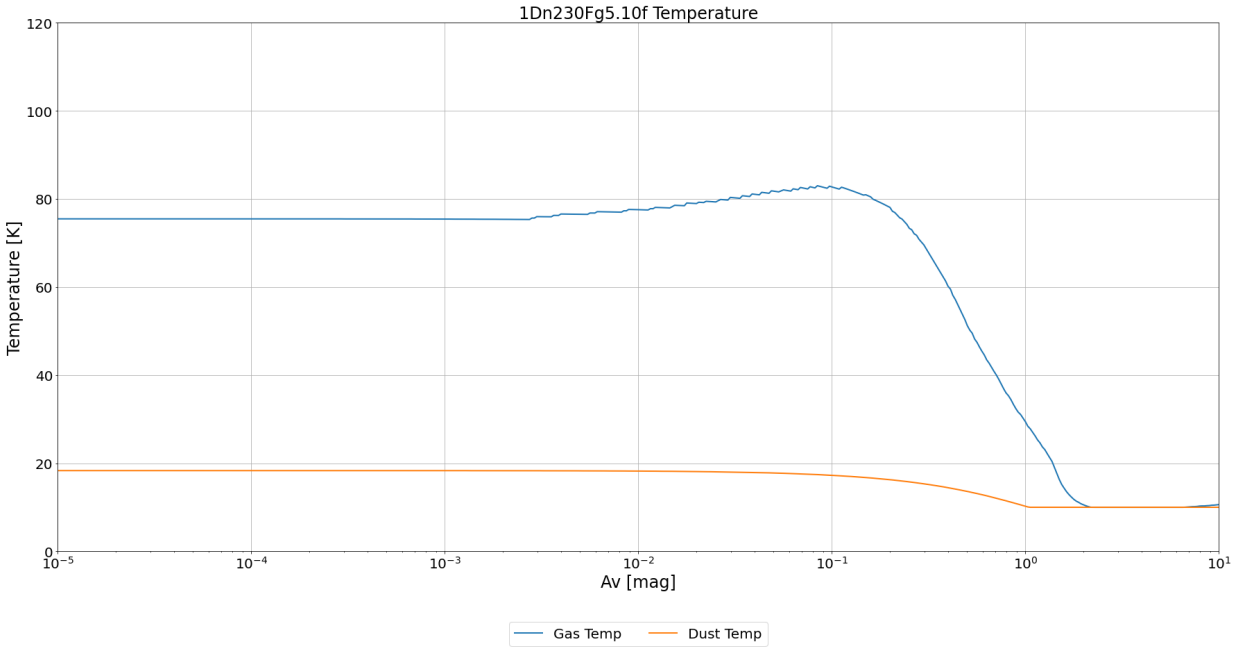

Figure 8.1f: Model gas temperatures in the cloud at $n_H = 10^{2.3}$ cm^{-3}, 5.10 Draine initial UV radiation field

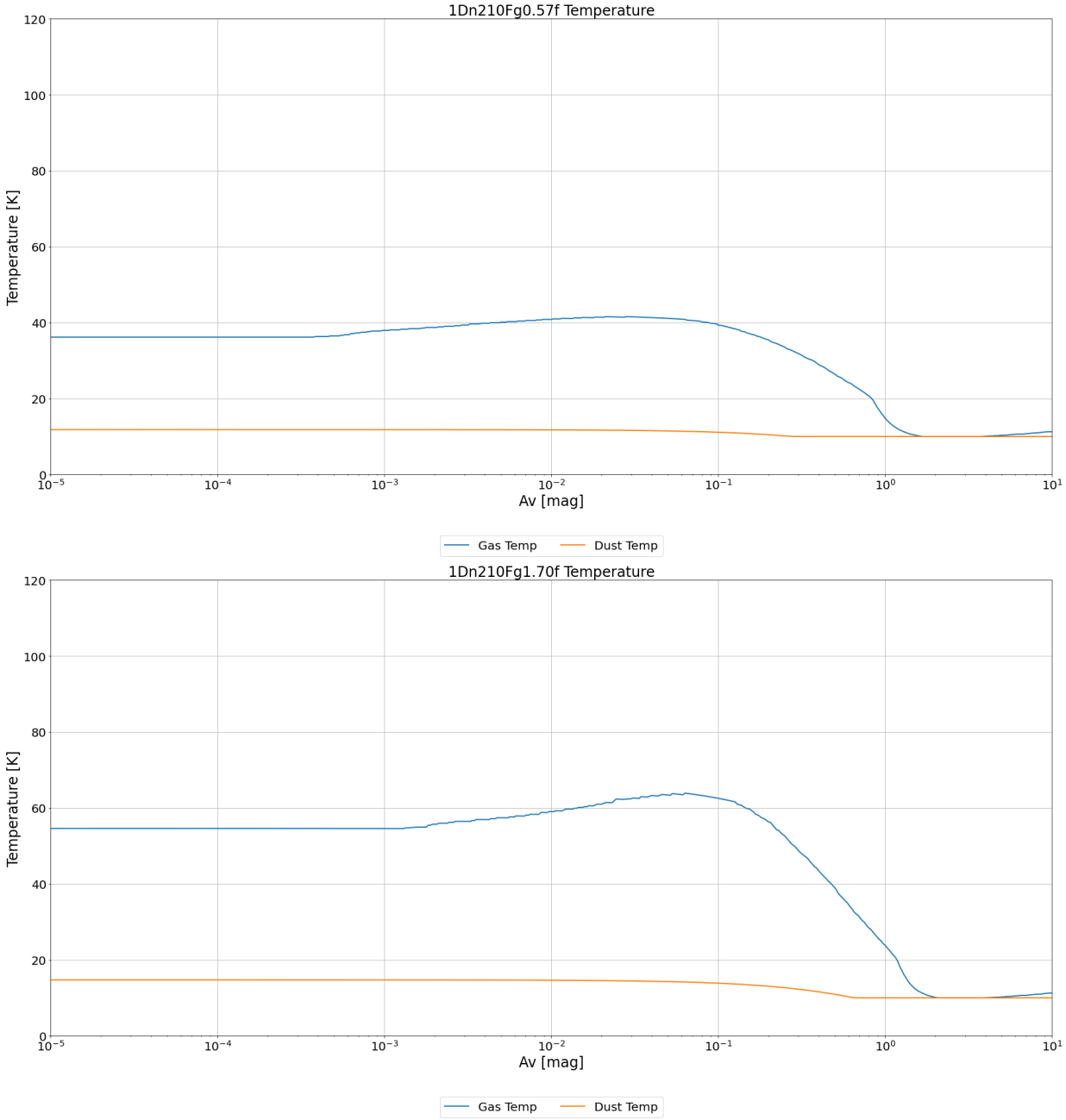

Figure 8.1g: Model gas temperatures in the cloud at $n_H = 10^{2.1}$ cm^{-3}, 0.57 and 1.70 Draine initial UV radiation field

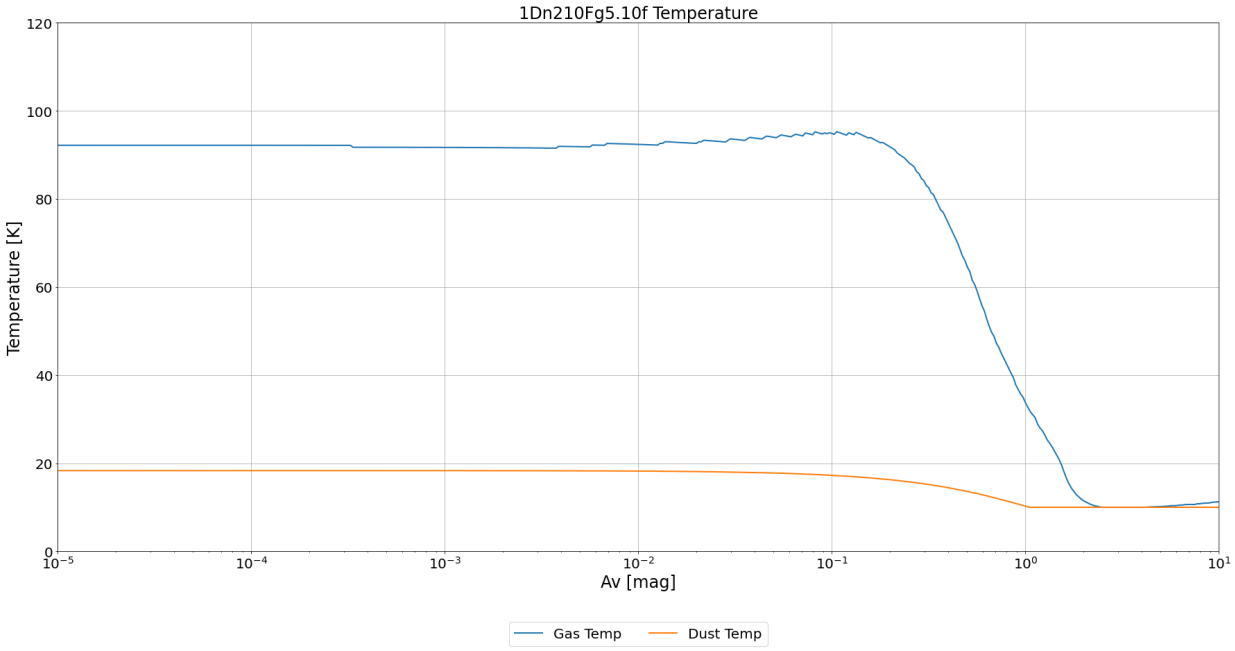

Figure 8.1h: Model gas temperatures in the cloud at $n_H = 10^{2.1}$ cm^{-3}, 5.10 Draine initial UV radiation field

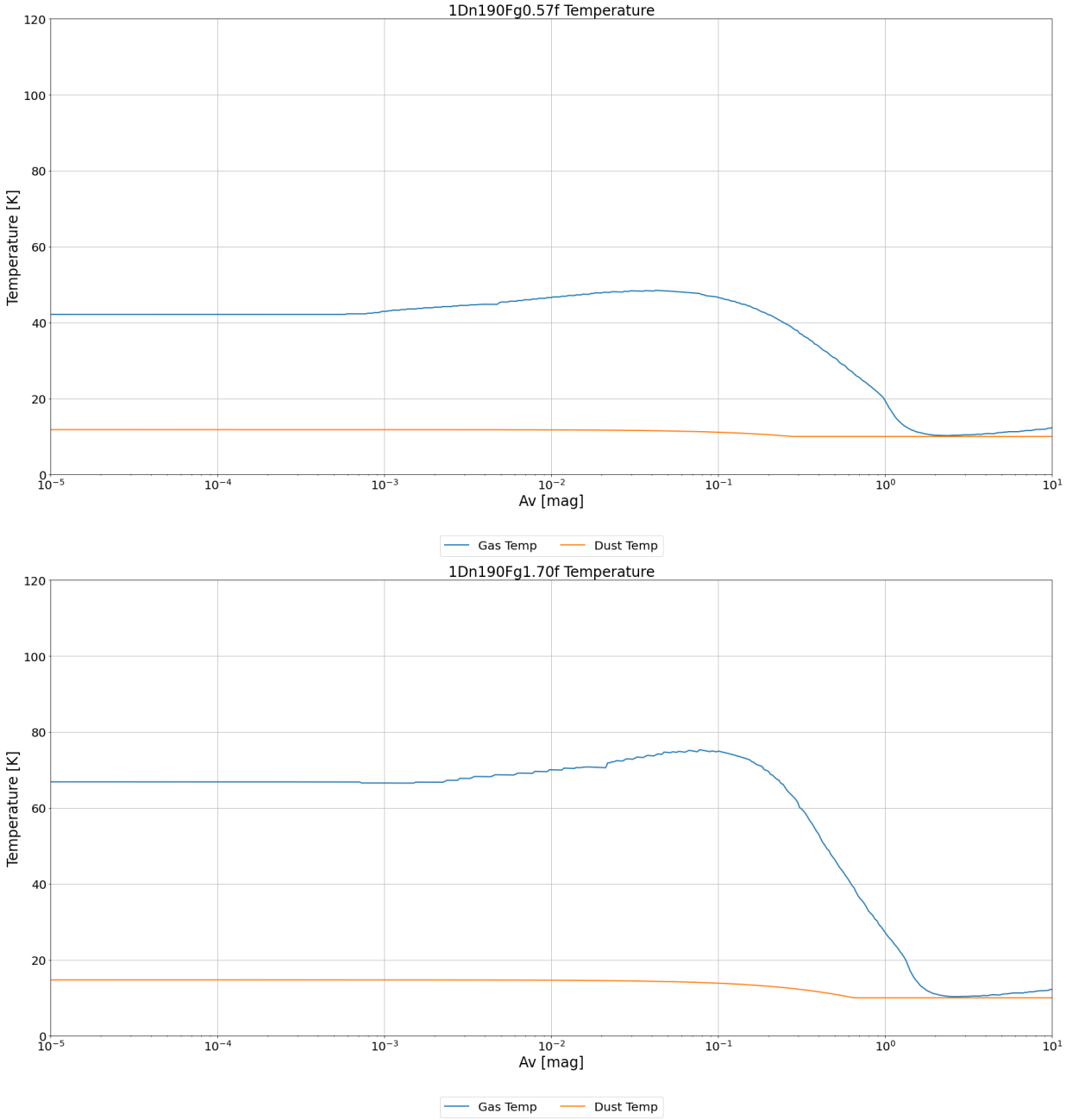

Figure 8.ii: Model gas temperatures in the cloud at $n_H = 10^{1.9}$ cm^{-3}, 0.57 and 1.70 Draine initial UV radiation field

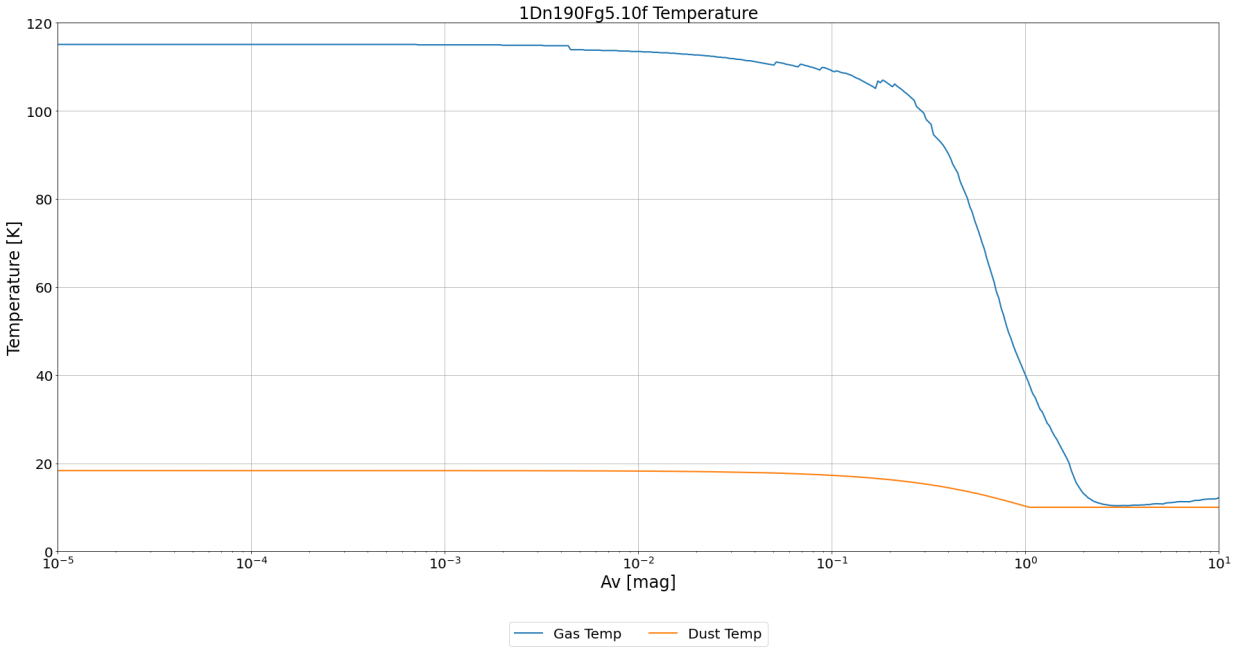

Figure 8.1j: Model gas temperatures in the cloud at $n_H = 10^{1.9}$ cm^{-3}, 5.10 Draine initial UV radiation field

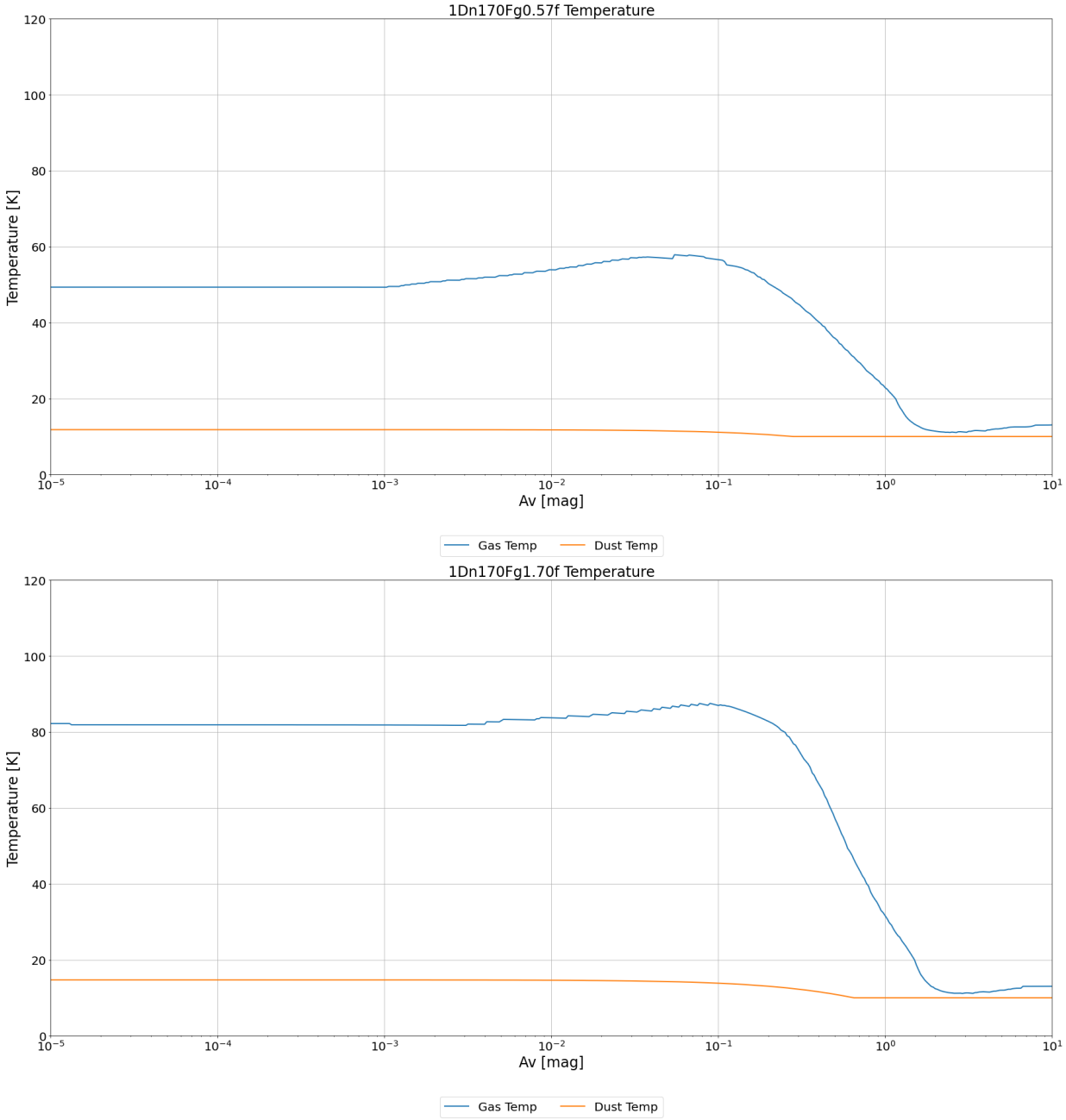

Figure 8.1k: Model gas temperatures in the cloud at $n_H = 10^{1.7}$ cm^{-3}, 0.57 and 1.70 Draine initial UV radiation field

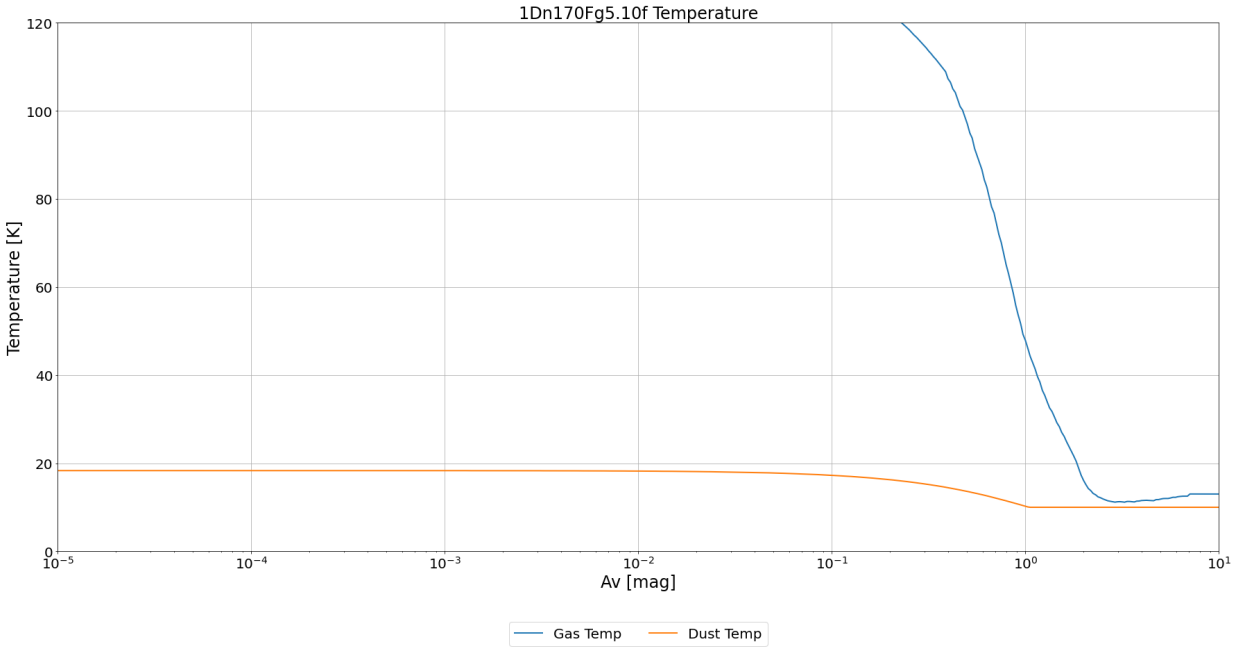

Figure 8.1l: Model gas temperatures in the cloud at $n_H = 10^{1.7}$ cm^{-3}, 5.10 Draine initial UV radiation field

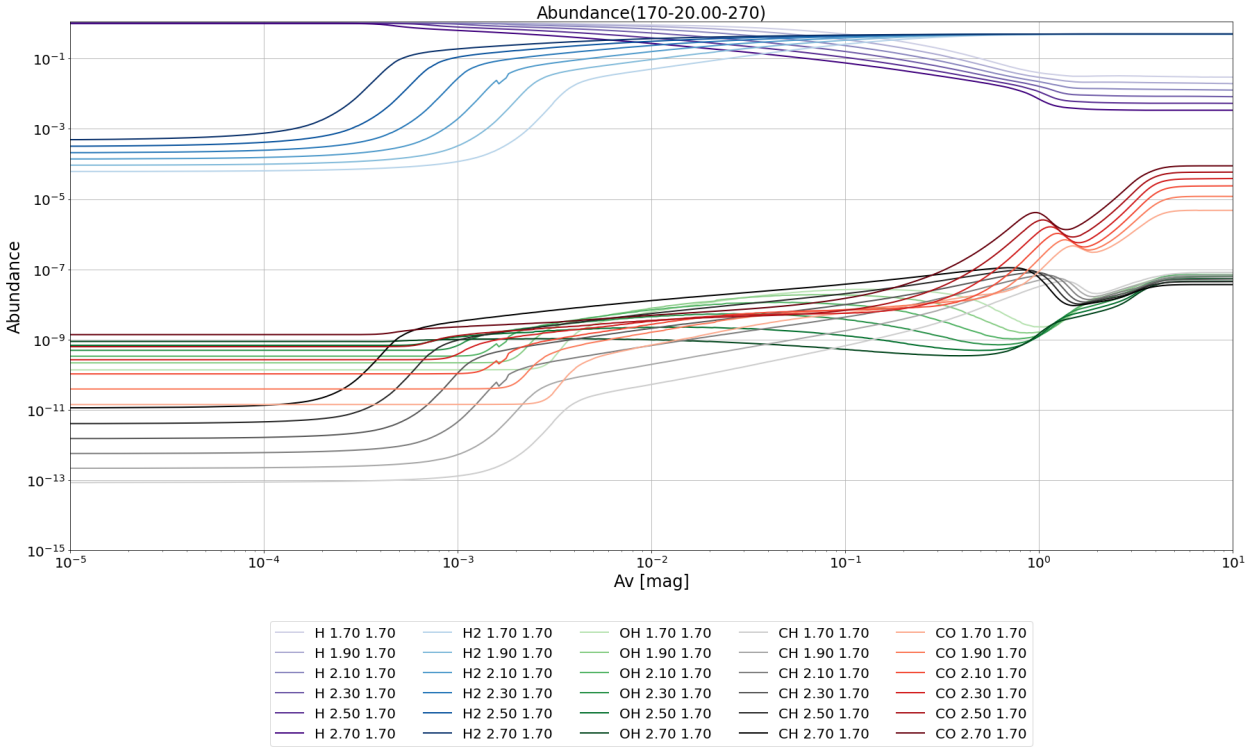

Figure 8.2: Abundance
Abundance of H, H_2, CO, OH and CH in various flat density models between $10^{1.7}$ cm^{-3} and $10^{2.7}$ cm^{-3} with a standard radiation field (G_0 = 1.7 Draines or χ = 1.0 Draines). The various colors represent the abundances of the species as the density varies, with the lighter colors corresponding to simulations with low density and darker colors for simulations with high density.

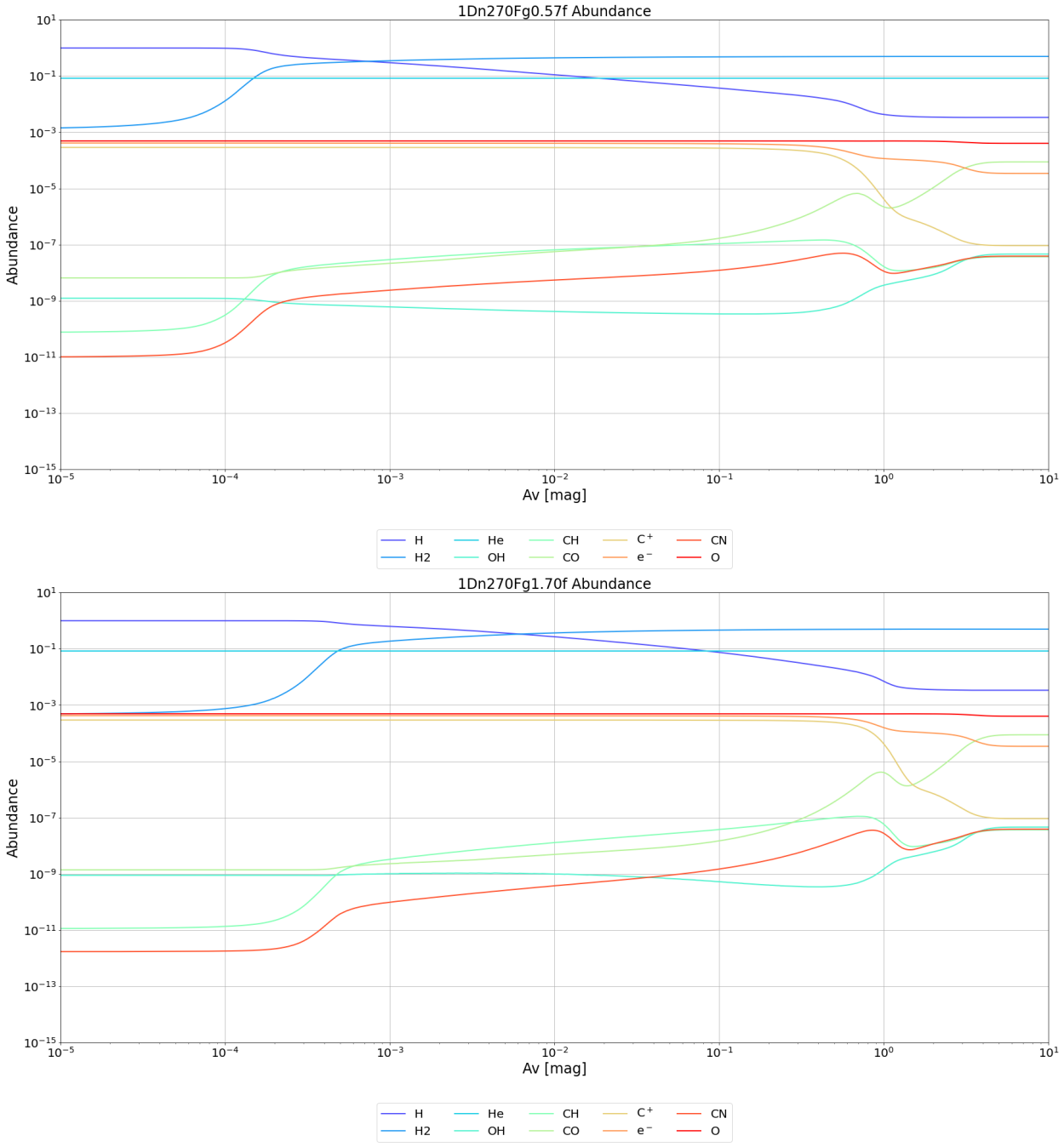

Figure 8.3a: Model abundances in the cloud at $n_H = 10^{2.7}$ cm^{-3}, 0.57 and 1.70 Draine initial UV radiation field

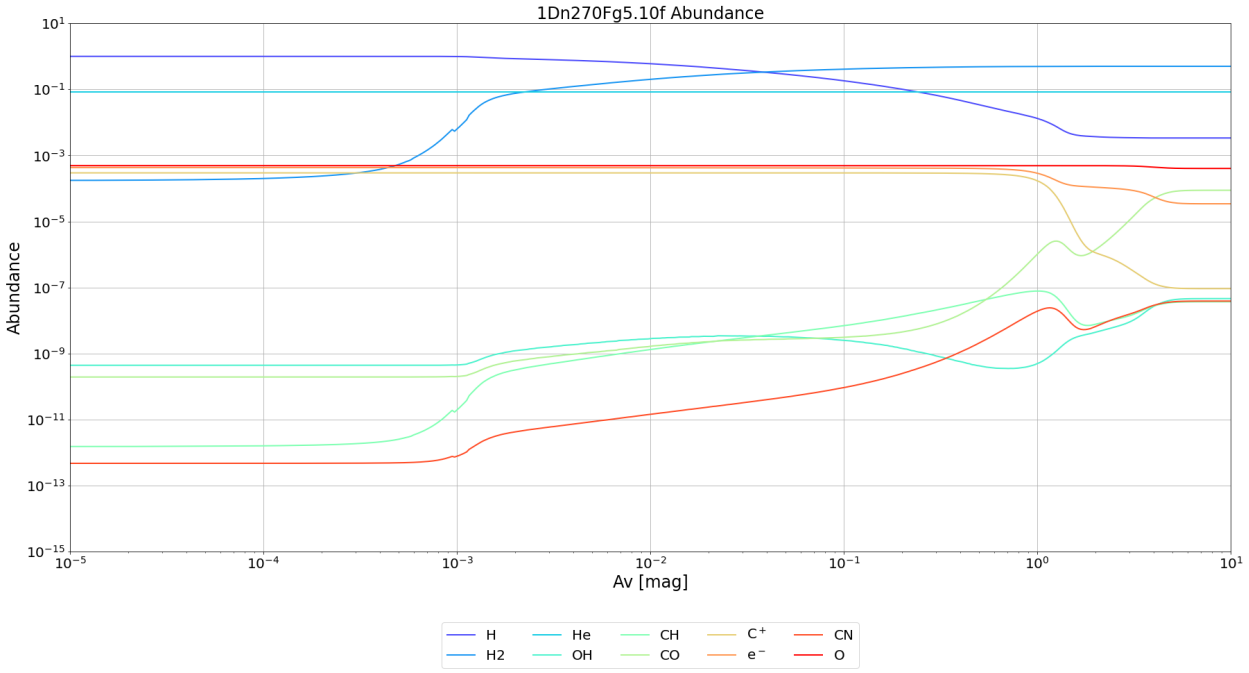

Figure 8.3b: Model abundances in the cloud at $n_H = 10^{2.7}$ cm^{-3}, 5.10 Draine initial UV radiation field

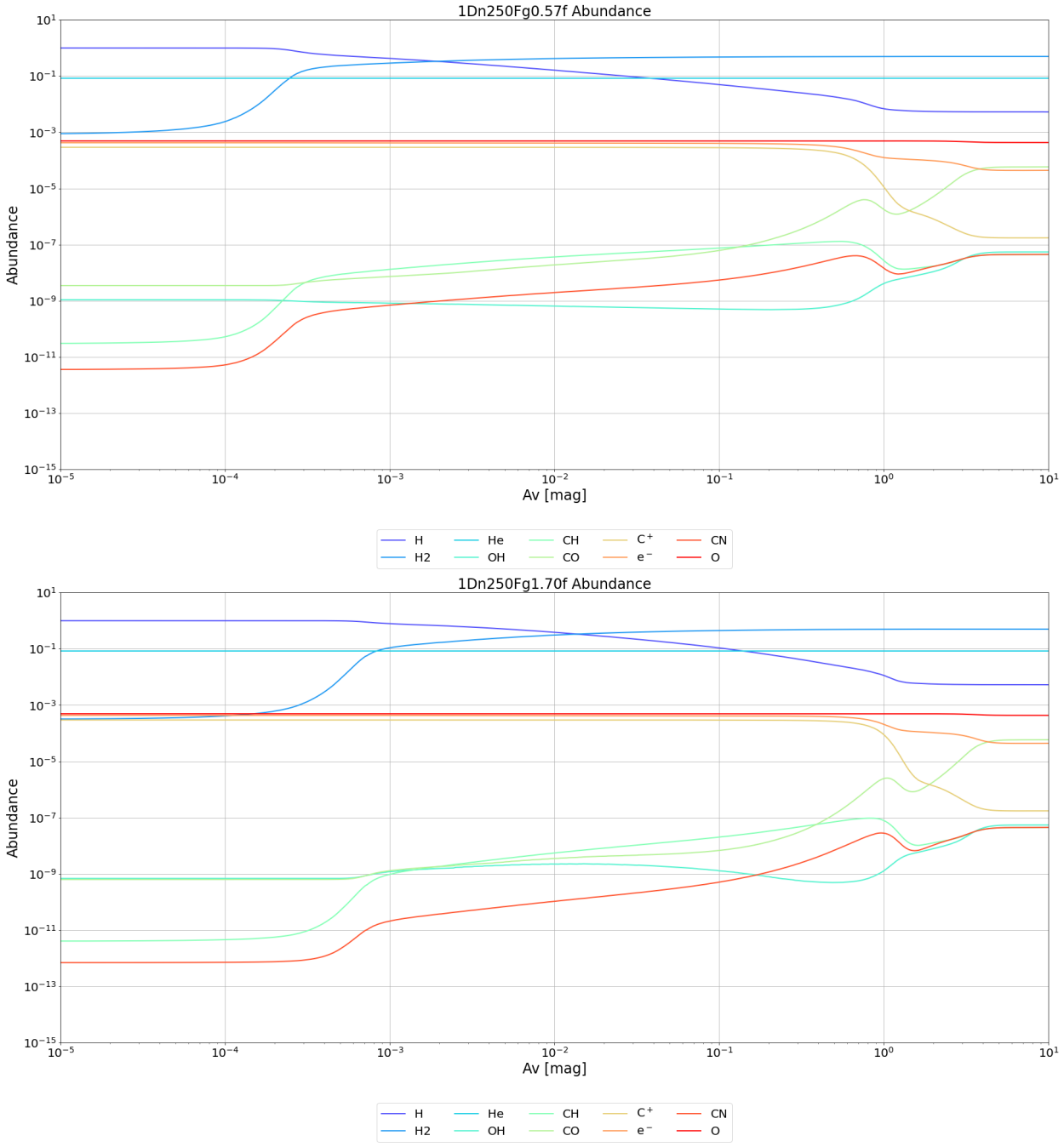

Figure 8.3c: Model abundances in the cloud at $n_H = 10^{2.5}$ cm^{-3}, 0.57 and 1.70 Draine initial UV radiation field

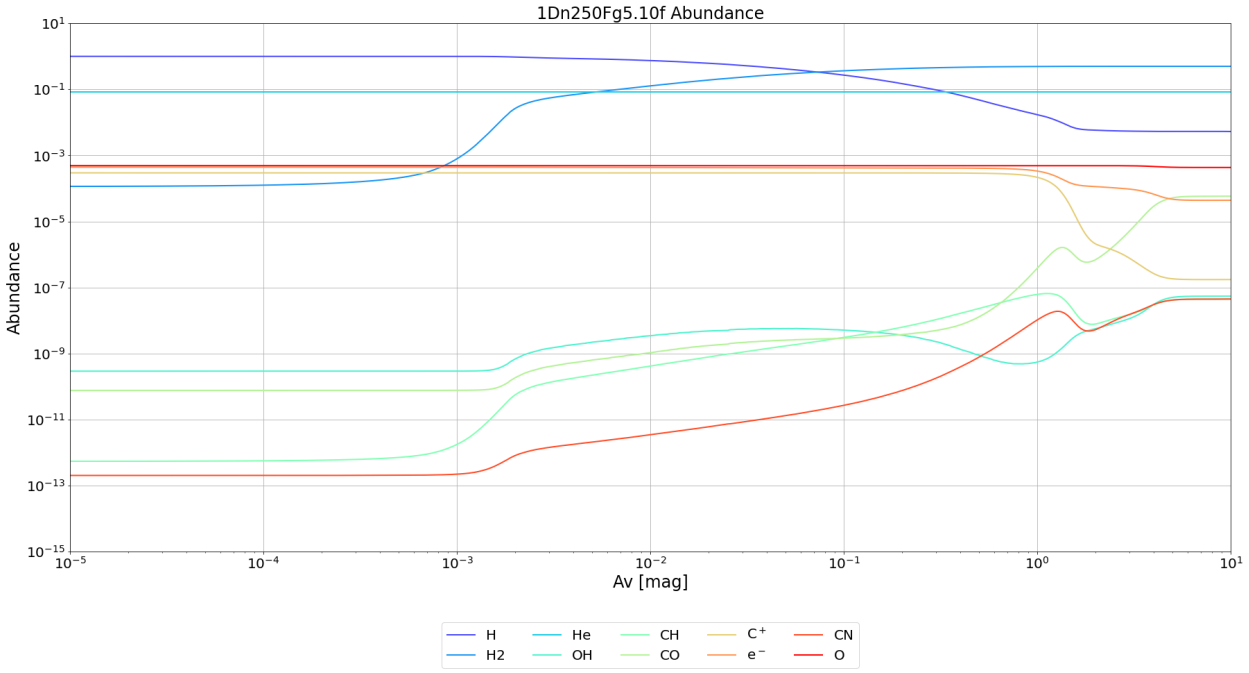

Figure 8.3d: Model abundances in the cloud at $n_H = 10^{2.5}$ cm^{-3}, 5.10 Draine initial UV radiation field

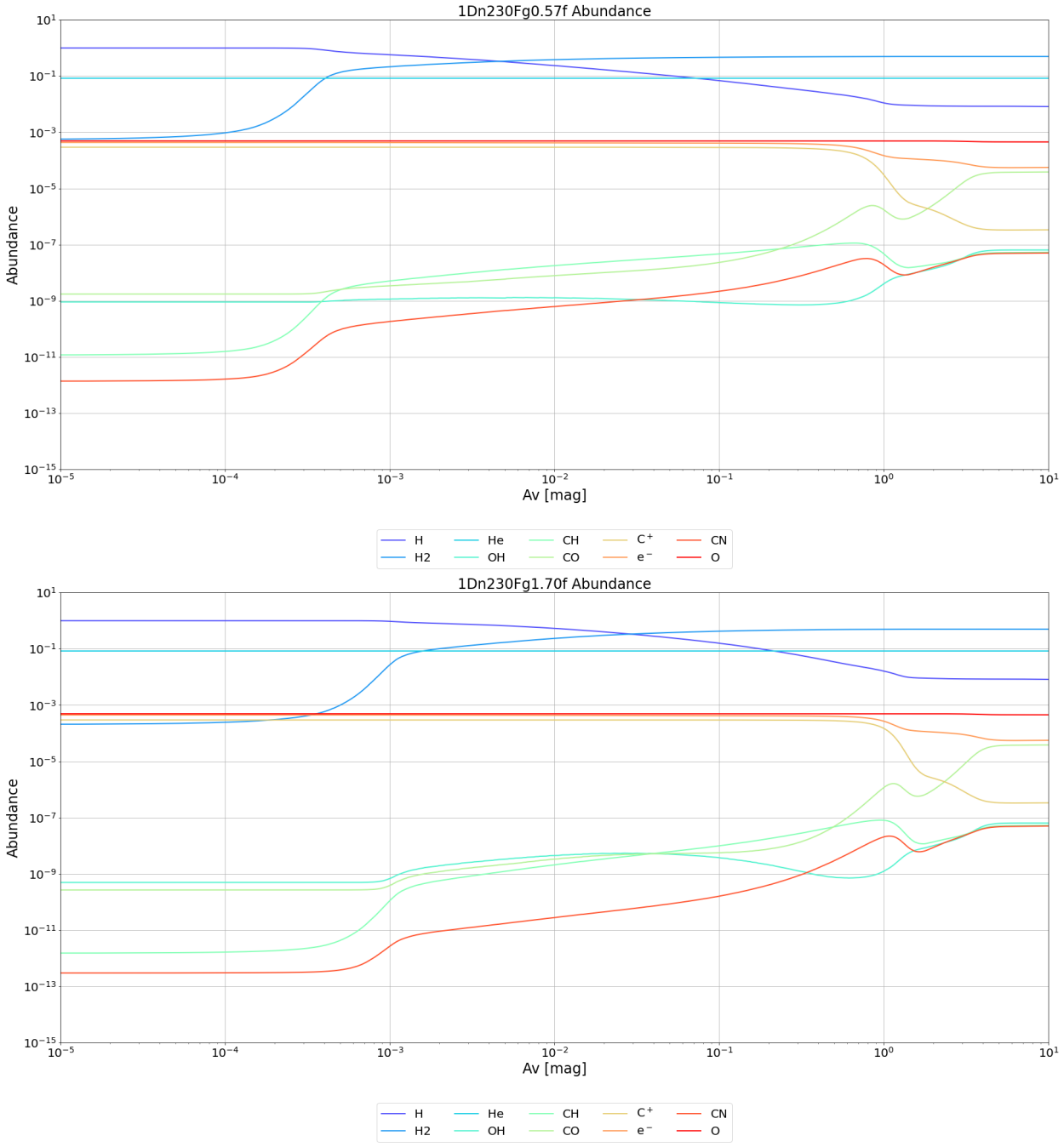

Figure 8.3e: Model abundances in the cloud at $n_H = 10^{2.3}$ cm^{-3}, 0.57 and 1.70 Draine initial UV radiation field

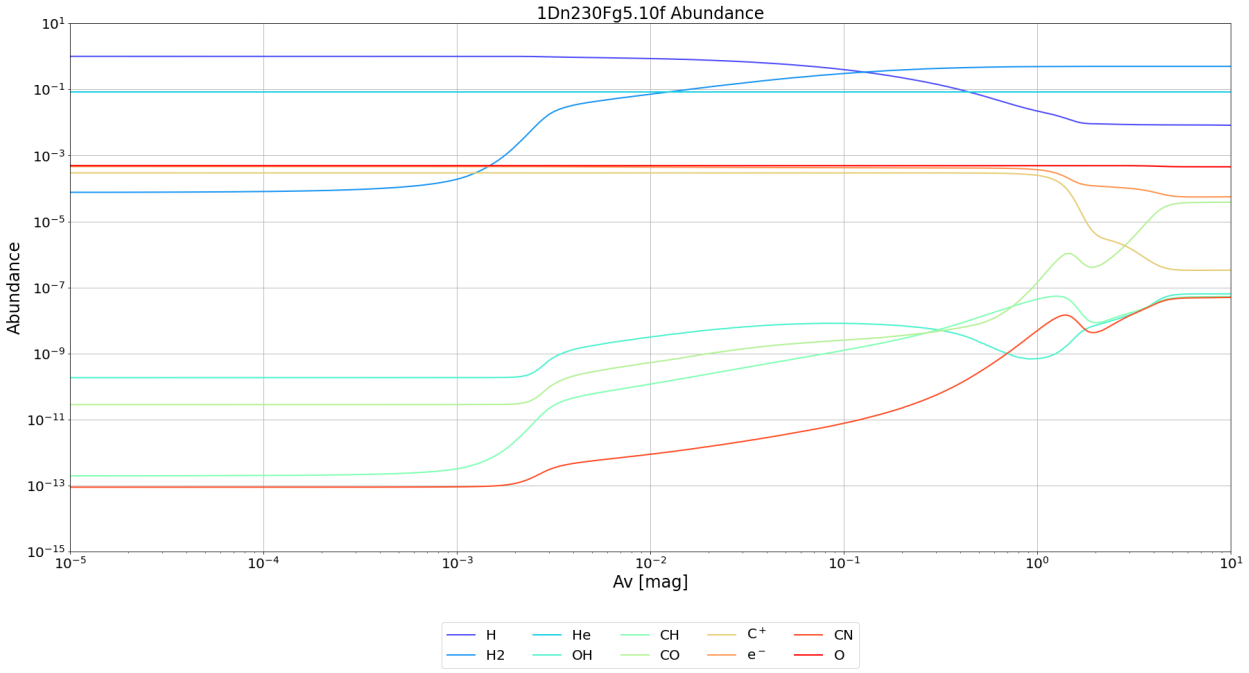

Figure 8.3f: Model abundances in the cloud at $n_H = 10^{2.3}$ cm^{-3}, 5.10 Draine initial UV radiation field

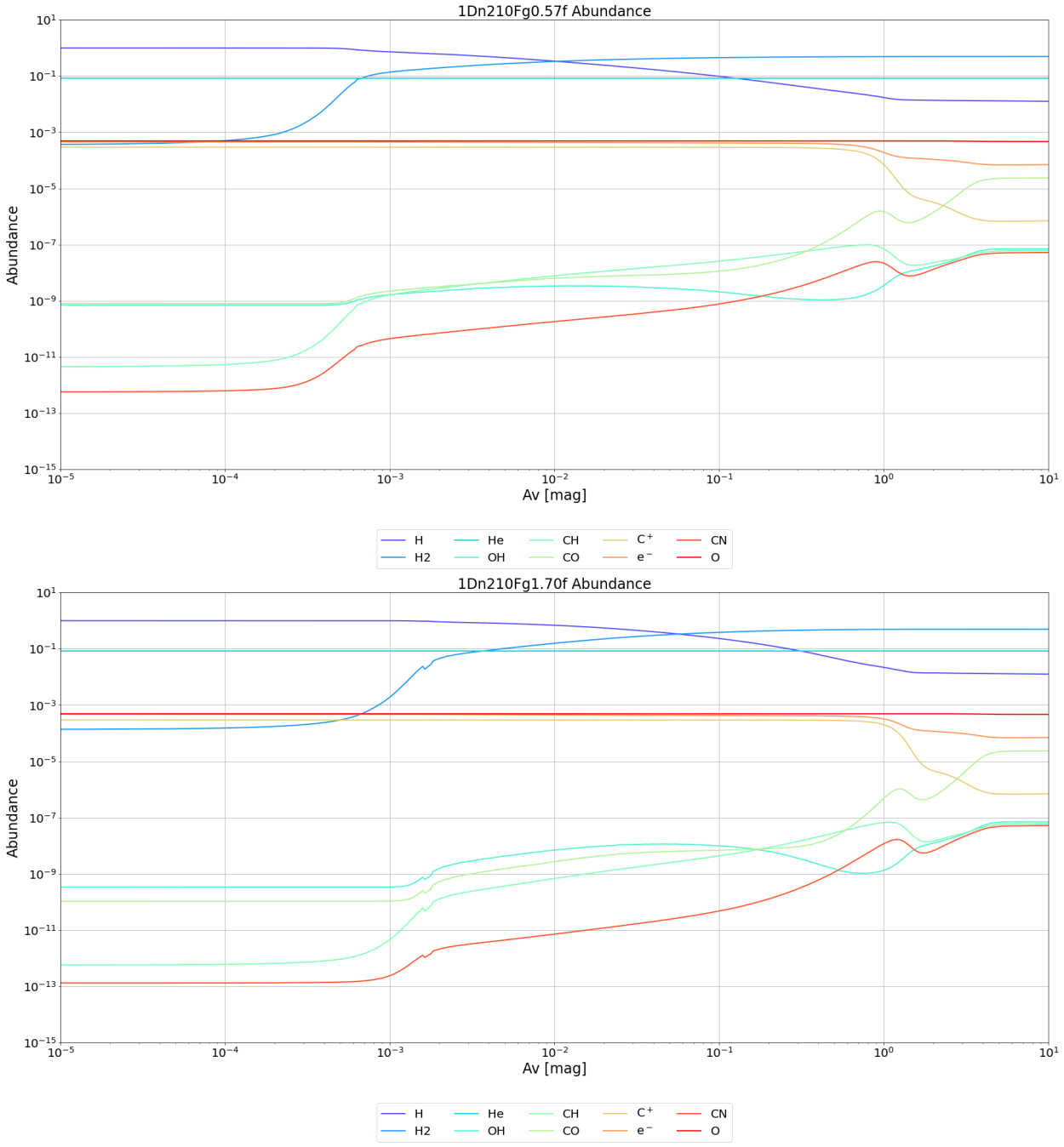

Figure 8.3g: Model abundances in the cloud at $n_H = 10^{2.1}$ cm^{-3}, 0.57 and 1.70 Draine initial UV radiation field

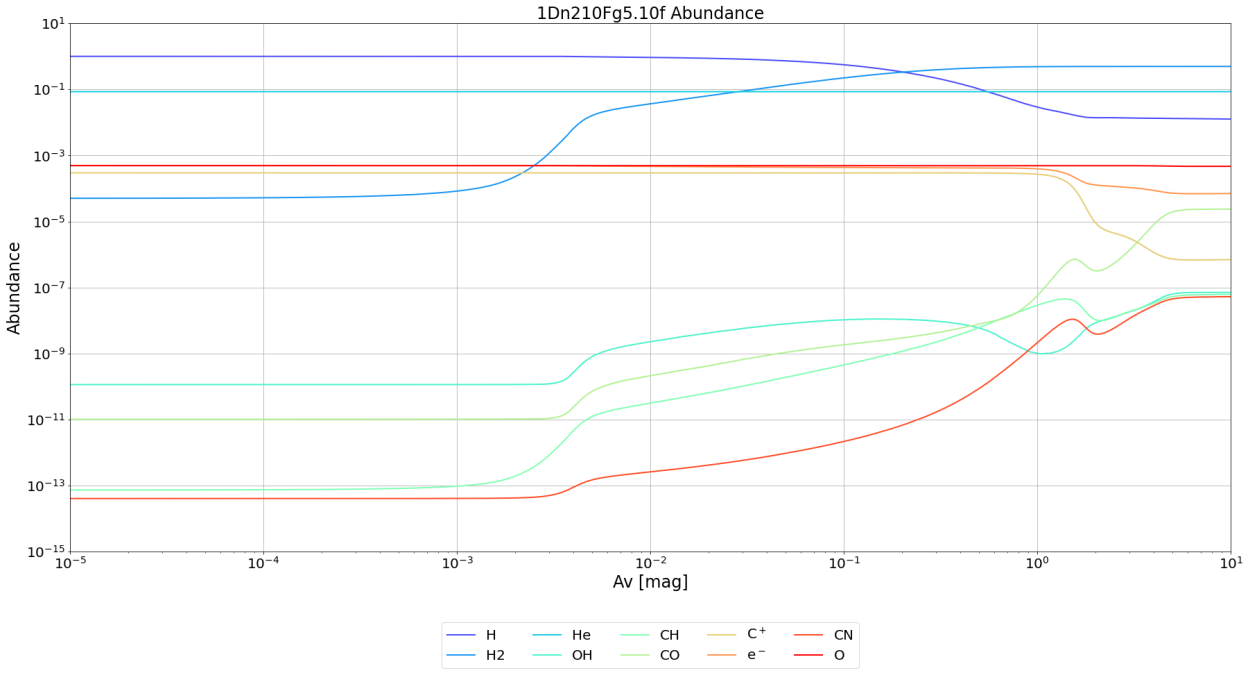

Figure 8.3h: Model abundances in the cloud at $n_H = 10^{2.1}$ cm^{-3}, 5.10 Draine initial UV radiation field

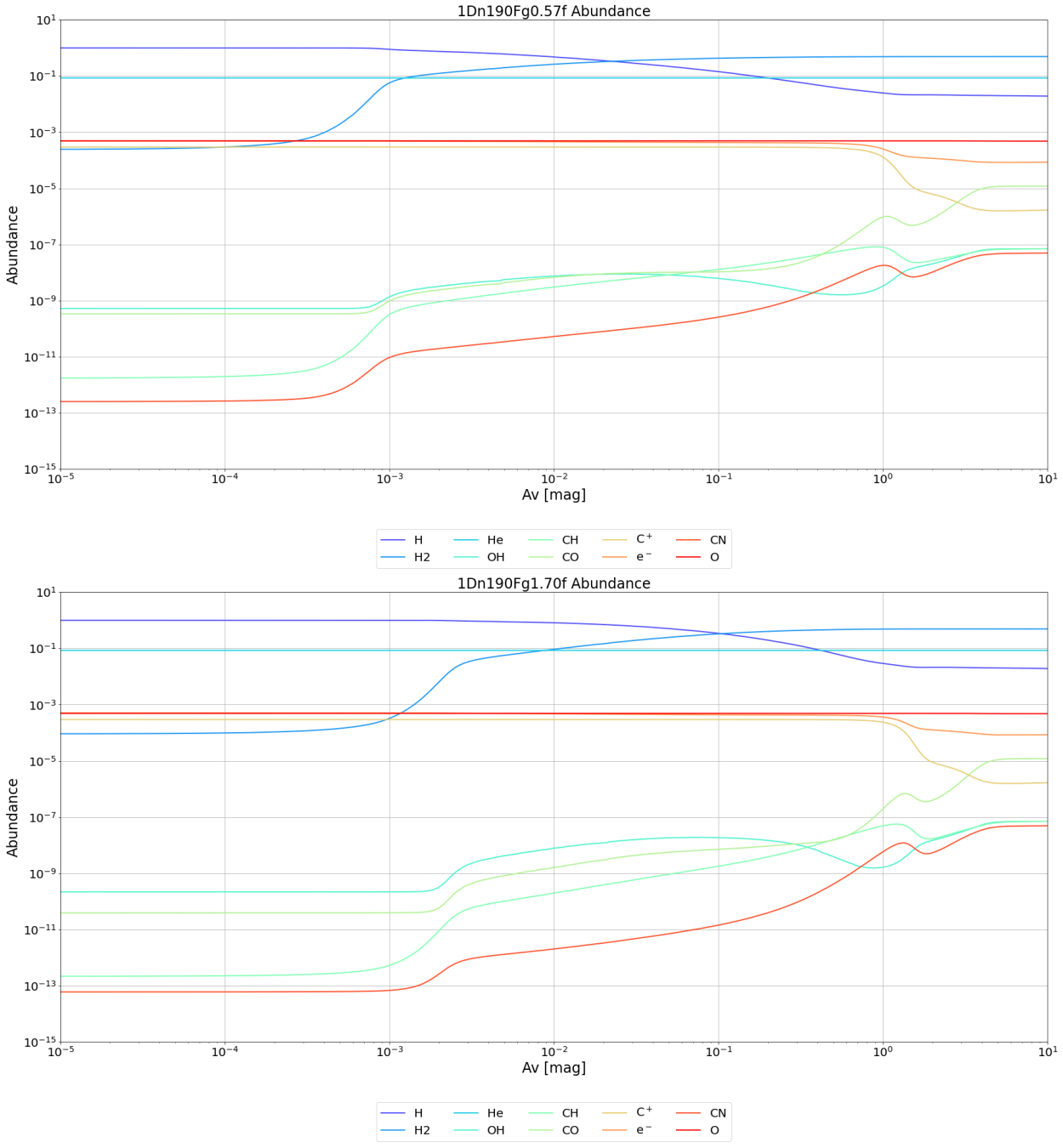

Figure 8.3i: Model abundances in the cloud at $n_H = 10^{1.9}$ cm^{-3}, 0.57 and 1.70 Draine initial UV radiation field

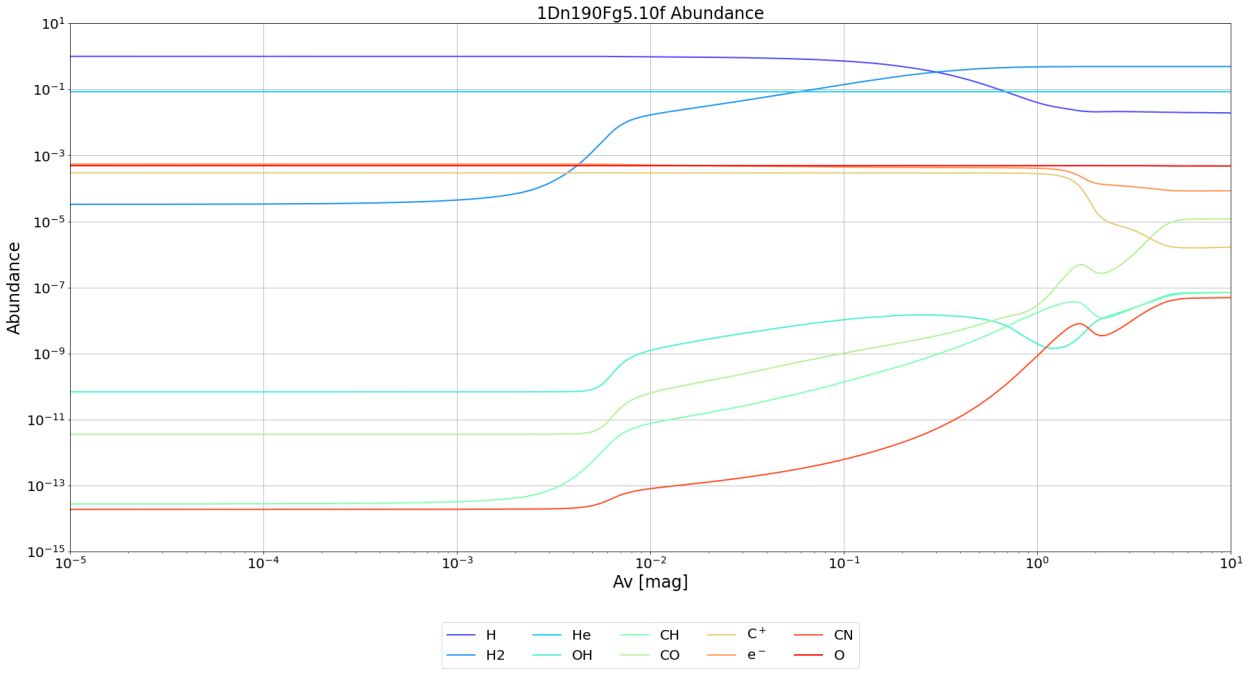

Figure 8.3j: Model abundances in the cloud at $n_H = 10^{1.9}$ cm^{-3}, 5.10 Draine initial UV radiation field

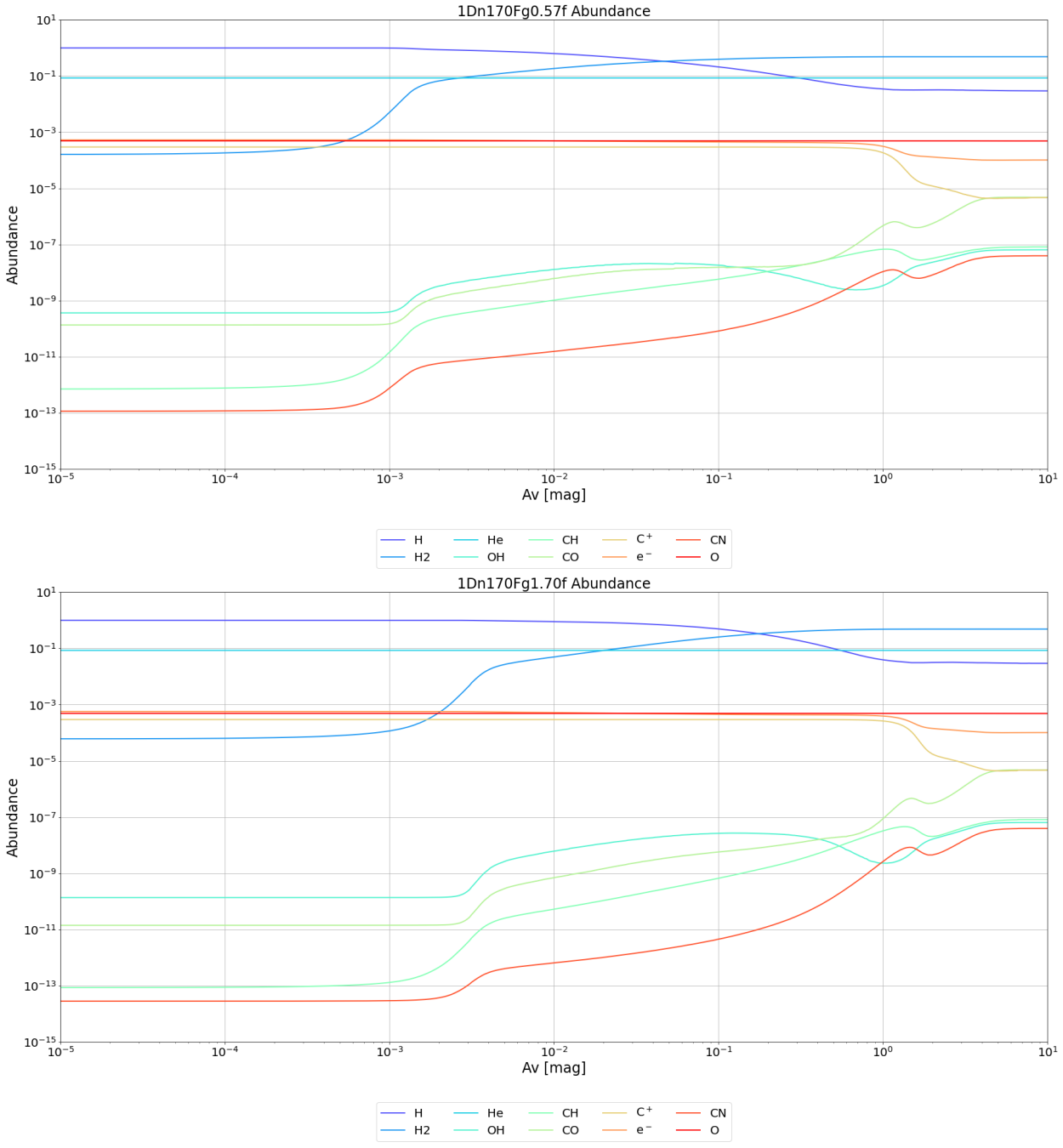

Figure 8.3k: Model abundances in the cloud at $n_H = 10^{1.7}$ cm^{-3}, 0.57 and 1.70 Draine initial UV radiation field

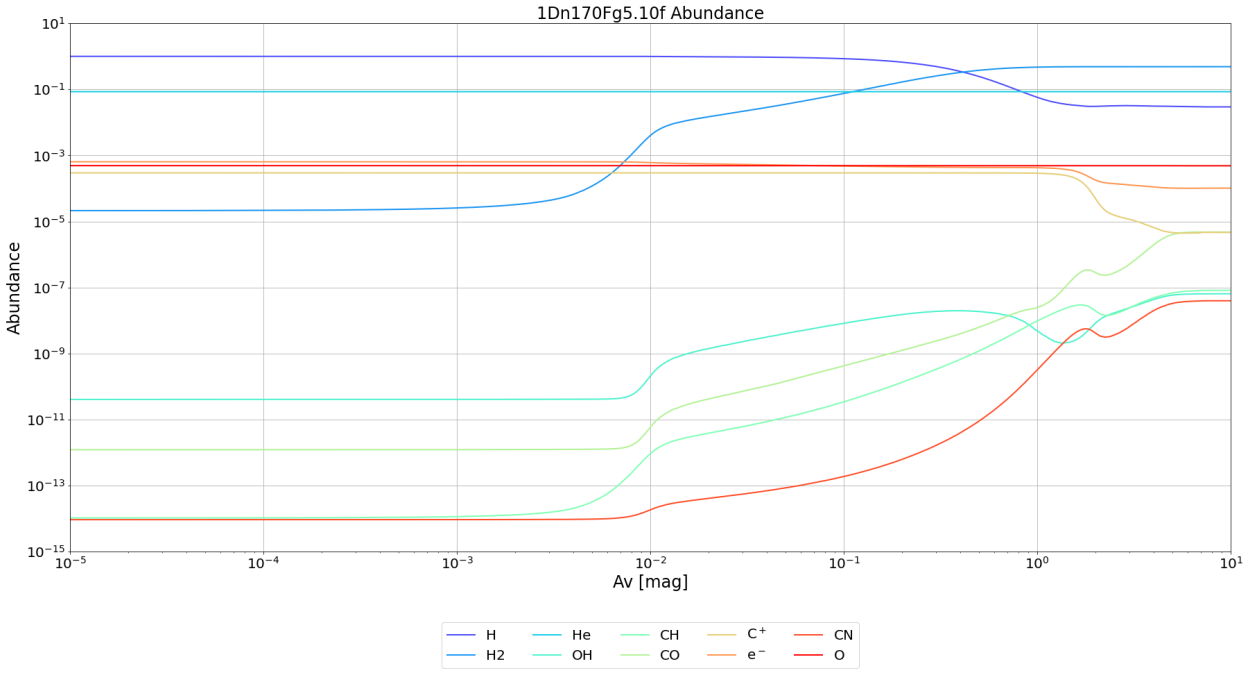

Figure 8.3l: Model abundances in the cloud at $n_H = 10^{1.7}$ cm^{-3}, 5.10 Draine initial UV radiation field

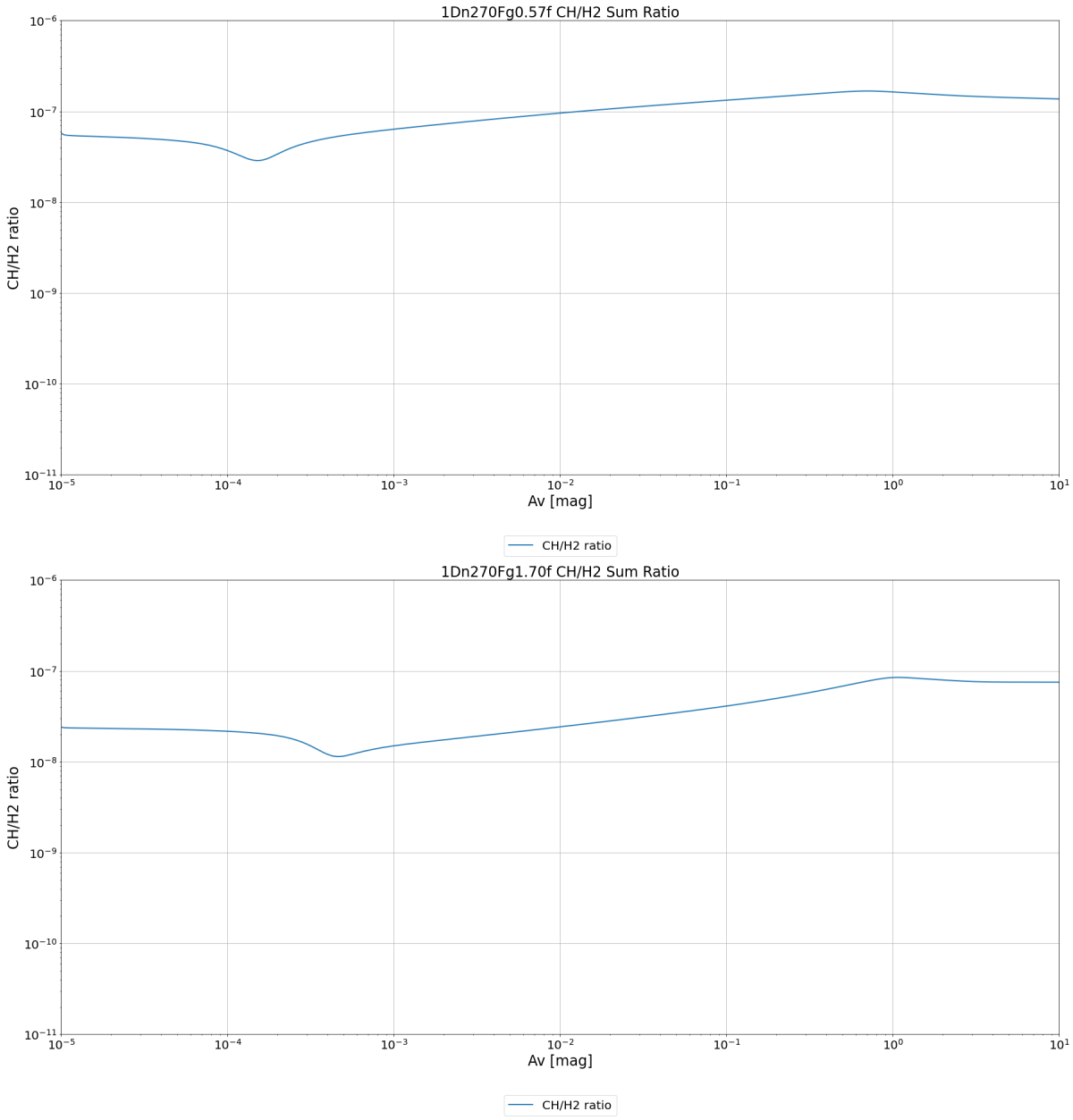

Figure 8.4a: Model CH/H_2 ratio in the cloud at $n_H = 10^{2.7}$ cm^{-3}, 0.57 and 1.70 Draine initial UV radiation field

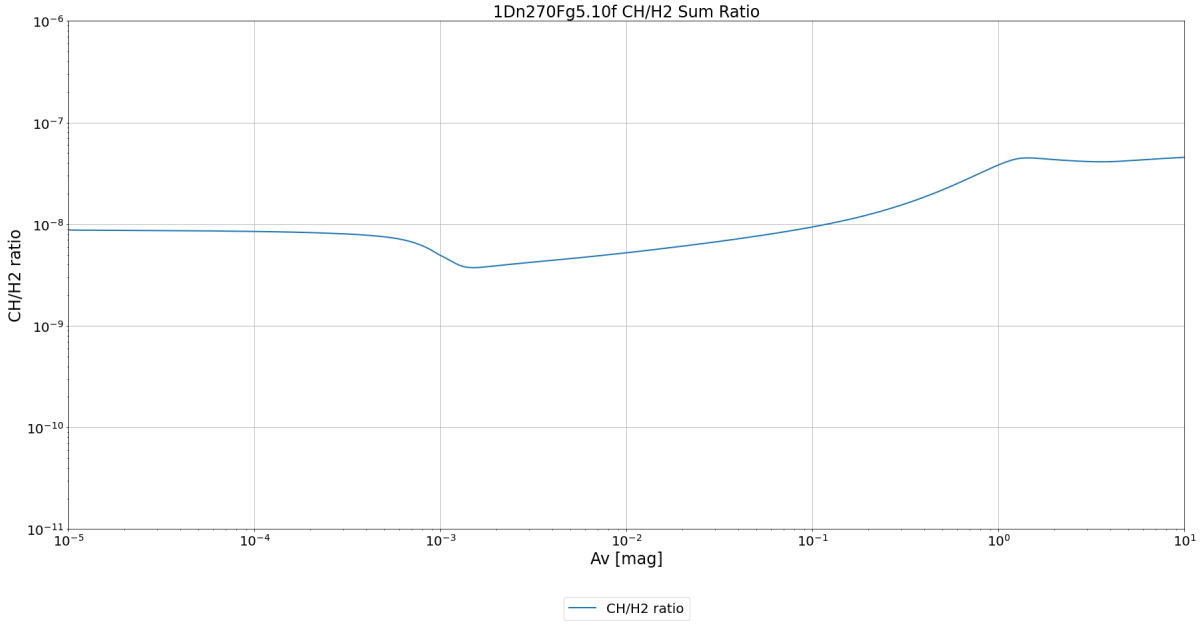

Figure 8.4b: Model CH/H_2 ratio in the cloud at $n_H = 10^{2.7}$ cm^{-3}, 5.10 Draine initial UV radiation field

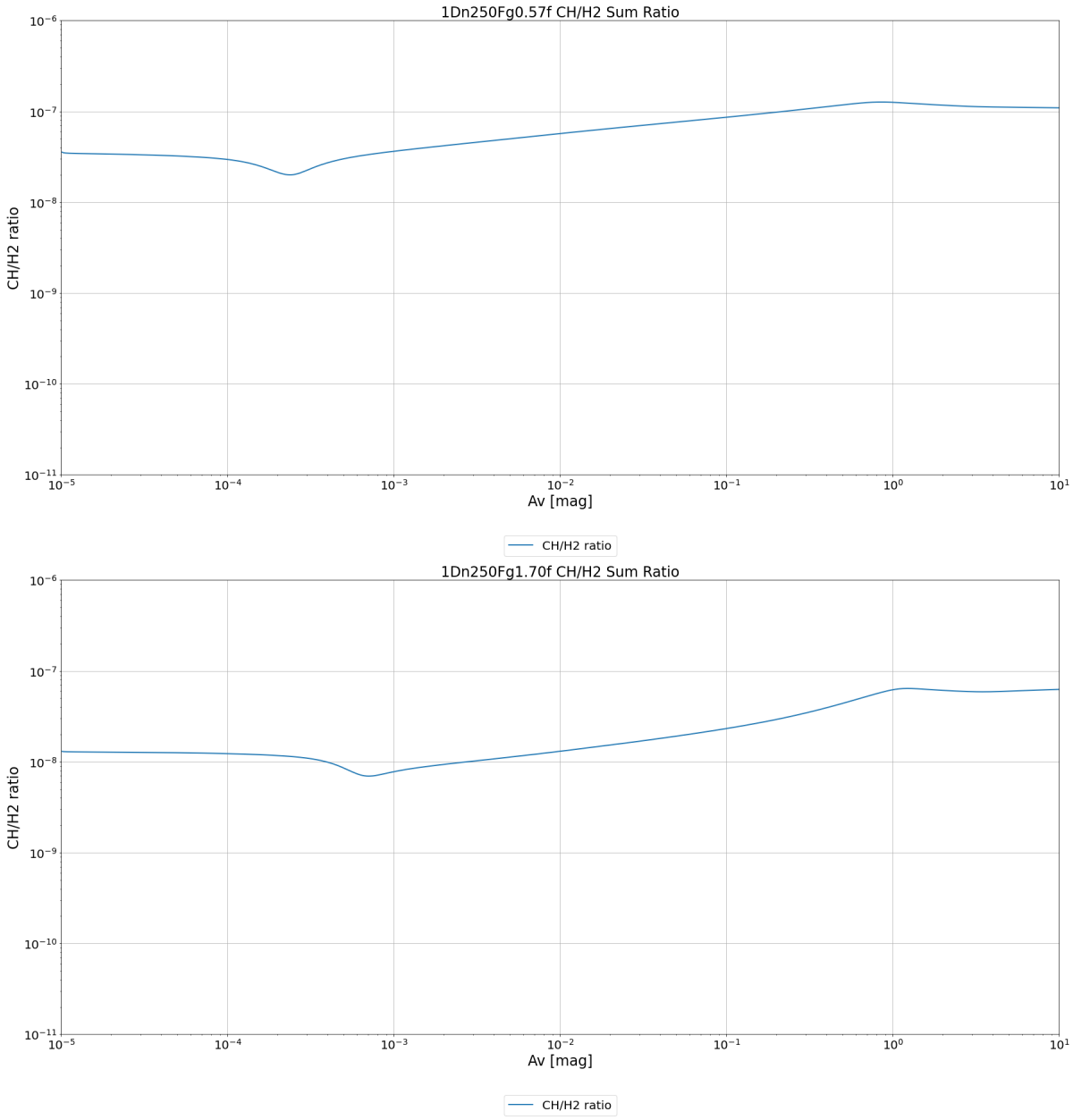

Figure 8.4c: Model CH/H_2 ratio in the cloud at $n_H = 10^{2.5}$ cm^{-3}, 0.57 and 1.70 Draine initial UV radiation field

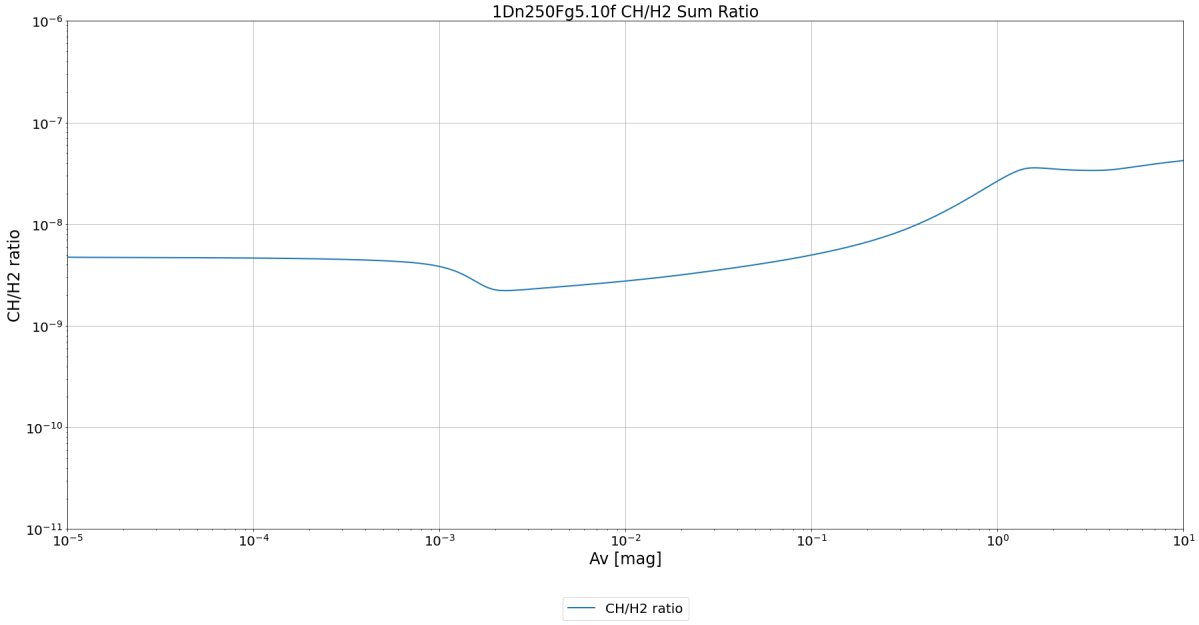

Figure 8.4d: Model CH/H_2 ratio in the cloud at $n_H = 10^{2.5}$ cm^{-3}, 5.10 Draine initial UV radiation field

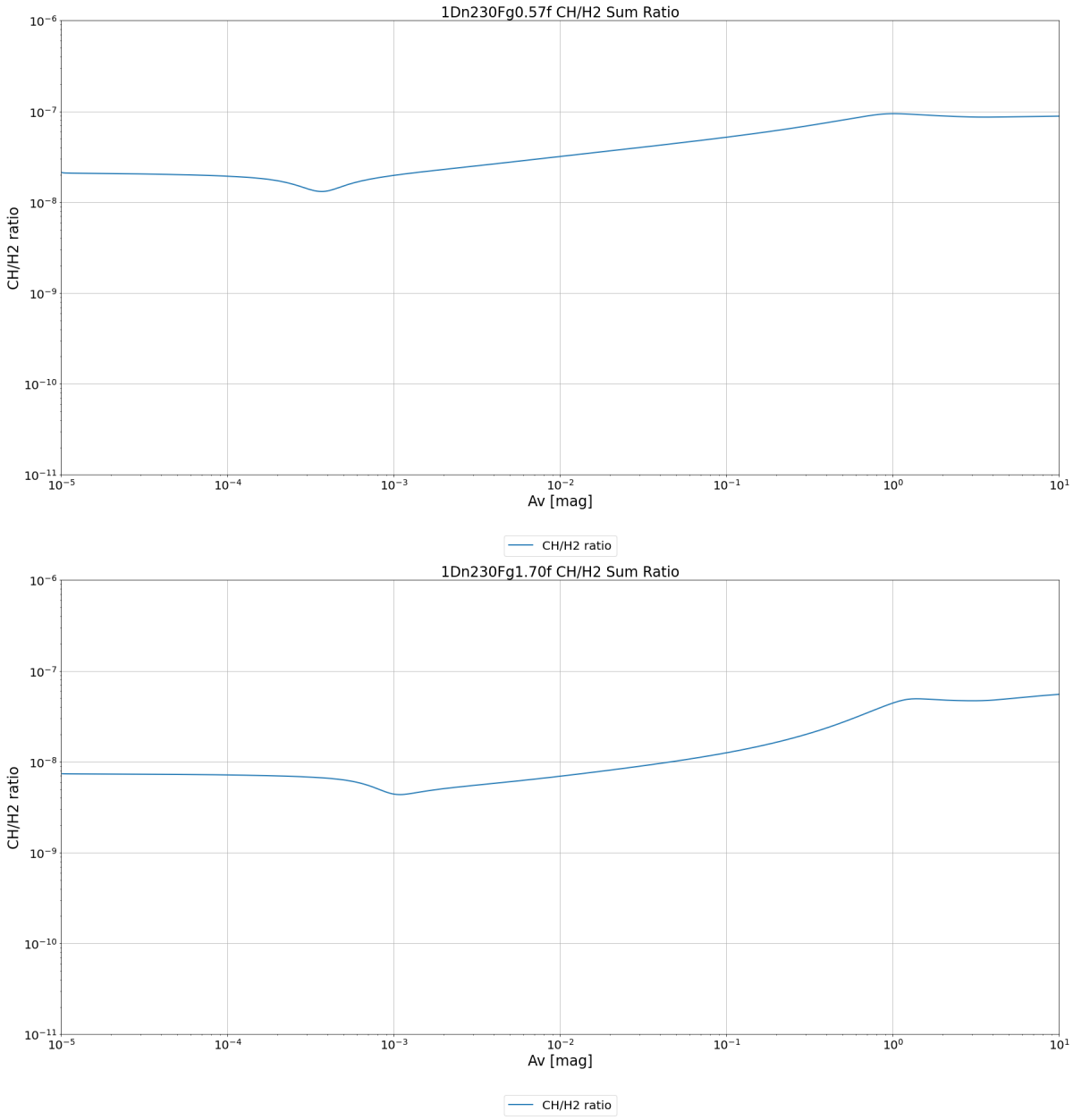

Figure 8.4e: Model CH/H_2 ratio in the cloud at $n_H = 10^{2.3}$ cm^{-3}, 0.57 and 1.70 Draine initial UV radiation field

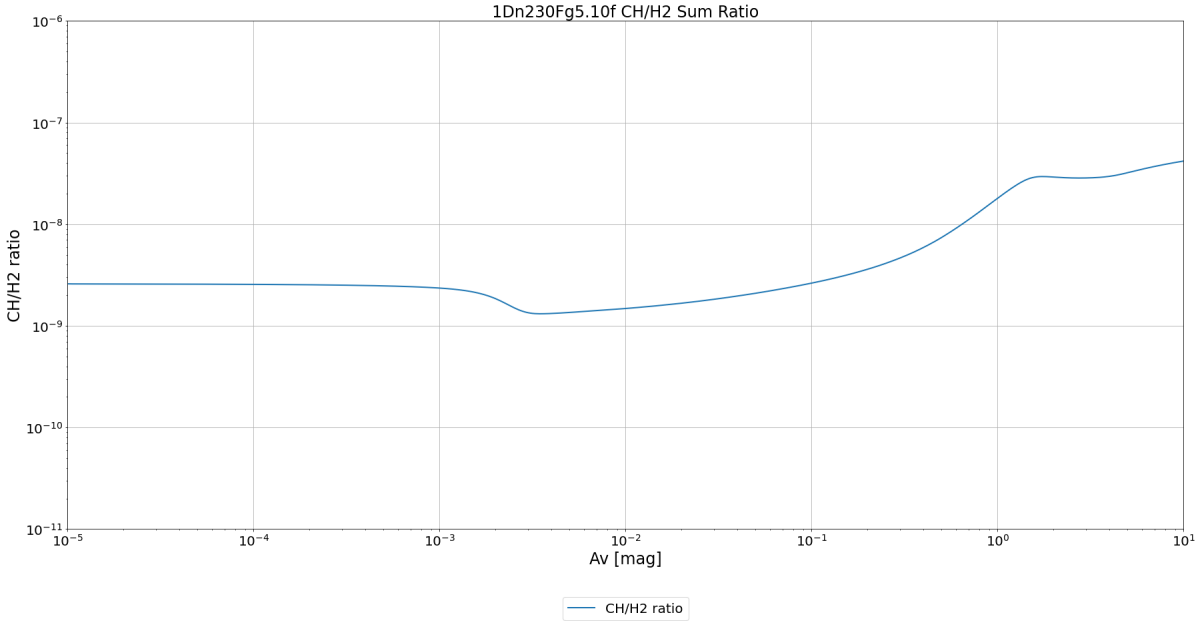

Figure 8.4f: Model CH/H_2 ratio in the cloud at $n_H = 10^{2.3}$ cm^{-3}, 5.10 Draine initial UV radiation field

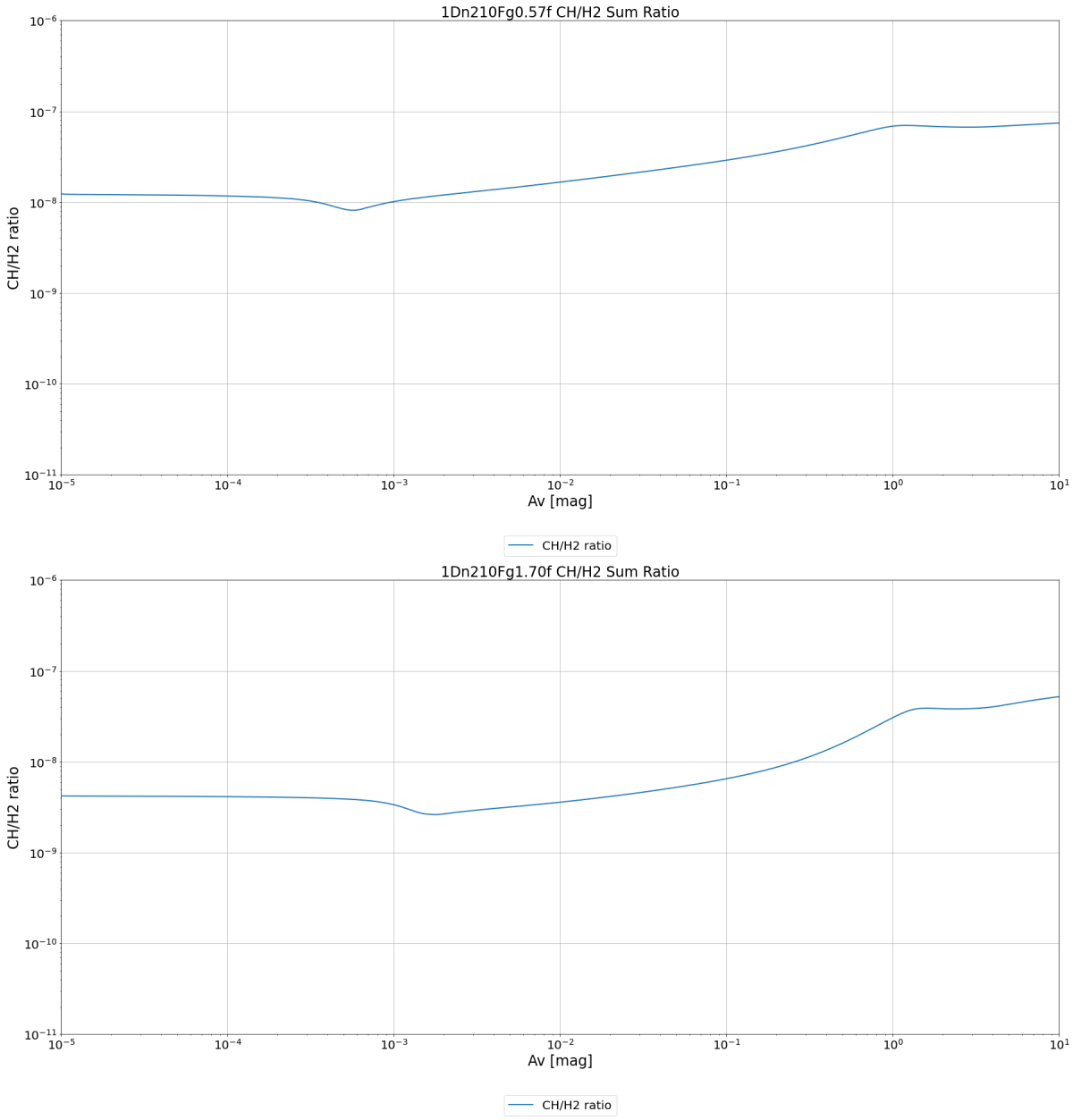

Figure 8.4g: Model CH/H_2 ratio in the cloud at $n_H = 10^{2.1}$ cm^{-3}, 0.57 and 1.70 Draine initial UV radiation field

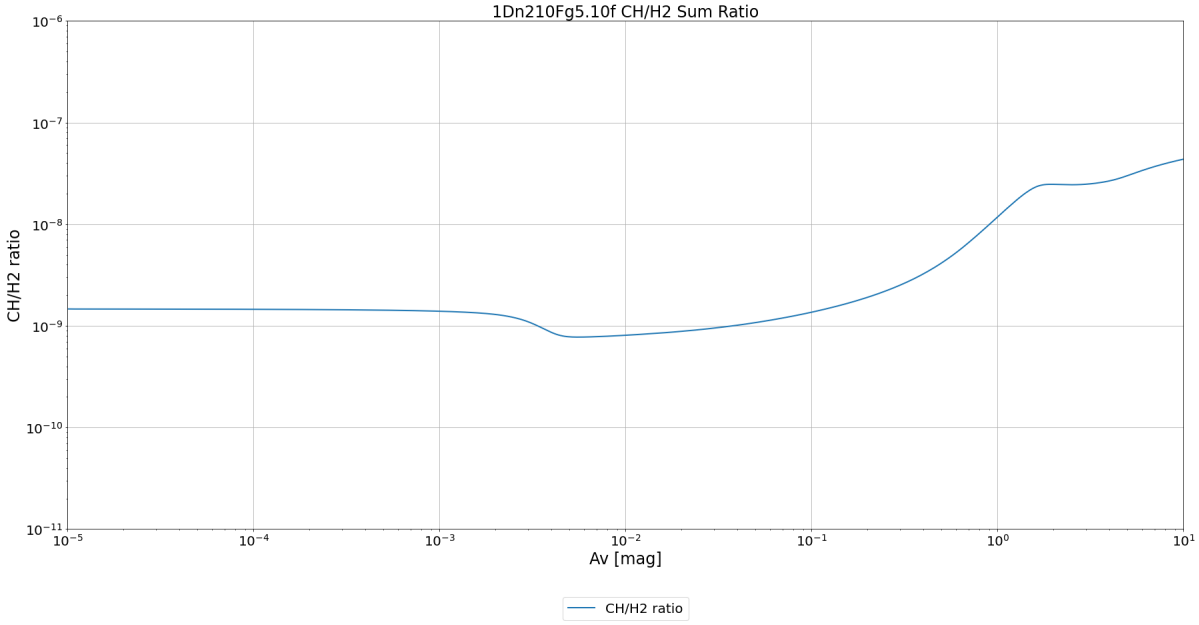

Figure 8.4h: Model CH/H_2 ratio in the cloud at $n_H = 10^{2.1}$ cm^{-3}, 5.10 Draine initial UV radiation field

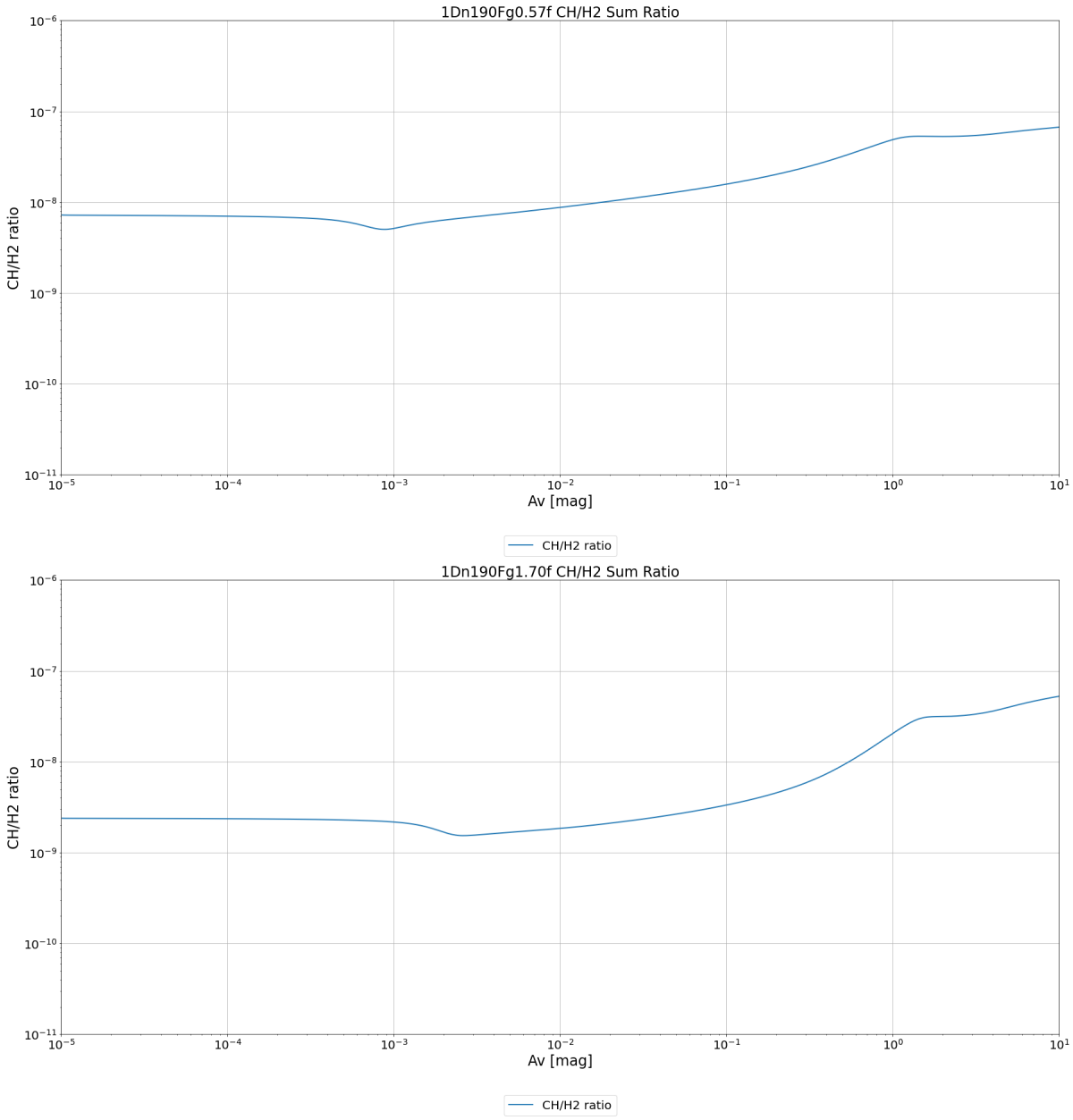

Figure 8.4i: Model CH/H_2 ratio in the cloud at $n_H = 10^{1.9}$ cm^{-3}, 0.57 and 1.70 Draine initial UV radiation field

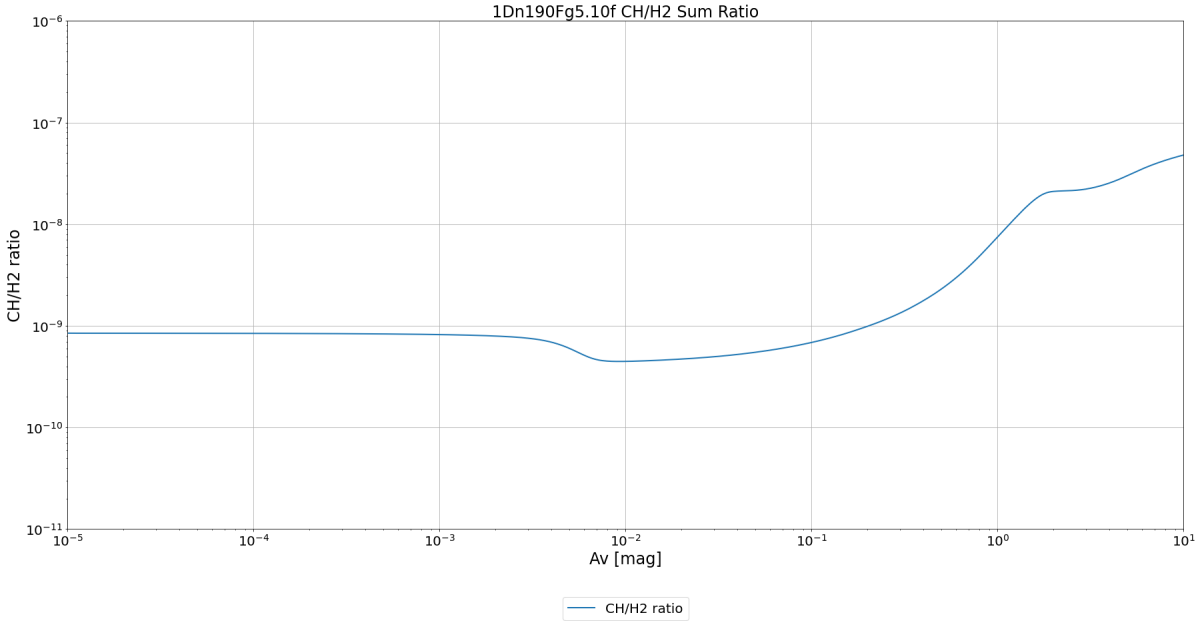

Figure 8.4j: Model CH/H_2 ratio in the cloud at $n_H = 10^{1.9}$ cm^{-3}, 5.10 Draine initial UV radiation field

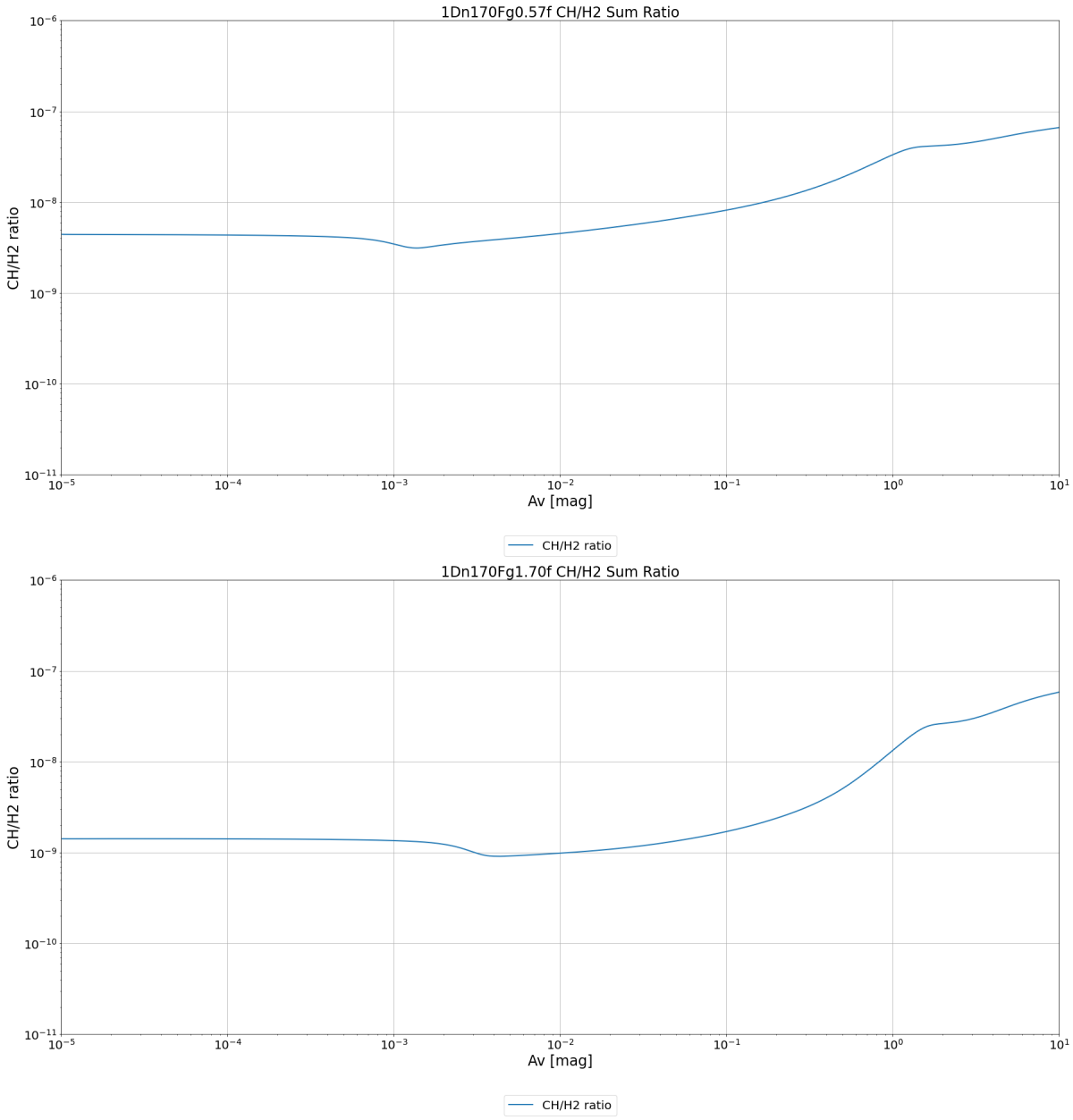

Figure 8.4k: Model CH/H_2 ratio in the cloud at $n_H = 10^{1.7}$ cm^{-3}, 0.57 and 1.70 Draine initial UV radiation field

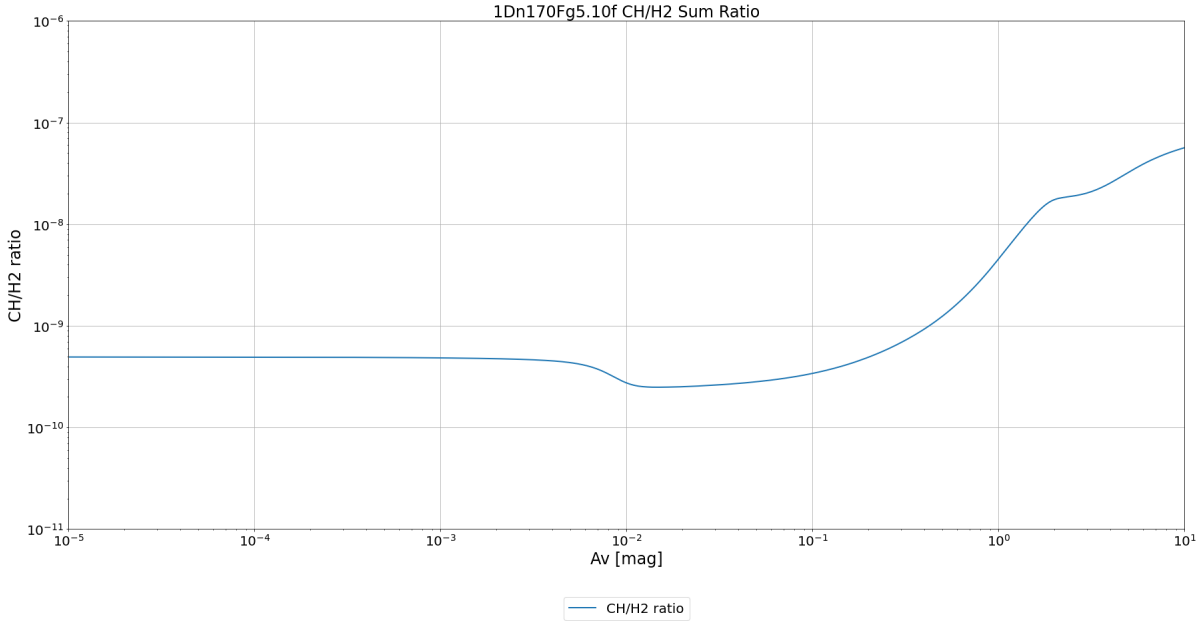

Figure 8.4l: Model CH/H_2 ratio in the cloud at $n_H = 10^{1.7}$ cm^{-3}, 5.10 Draine initial UV radiation field

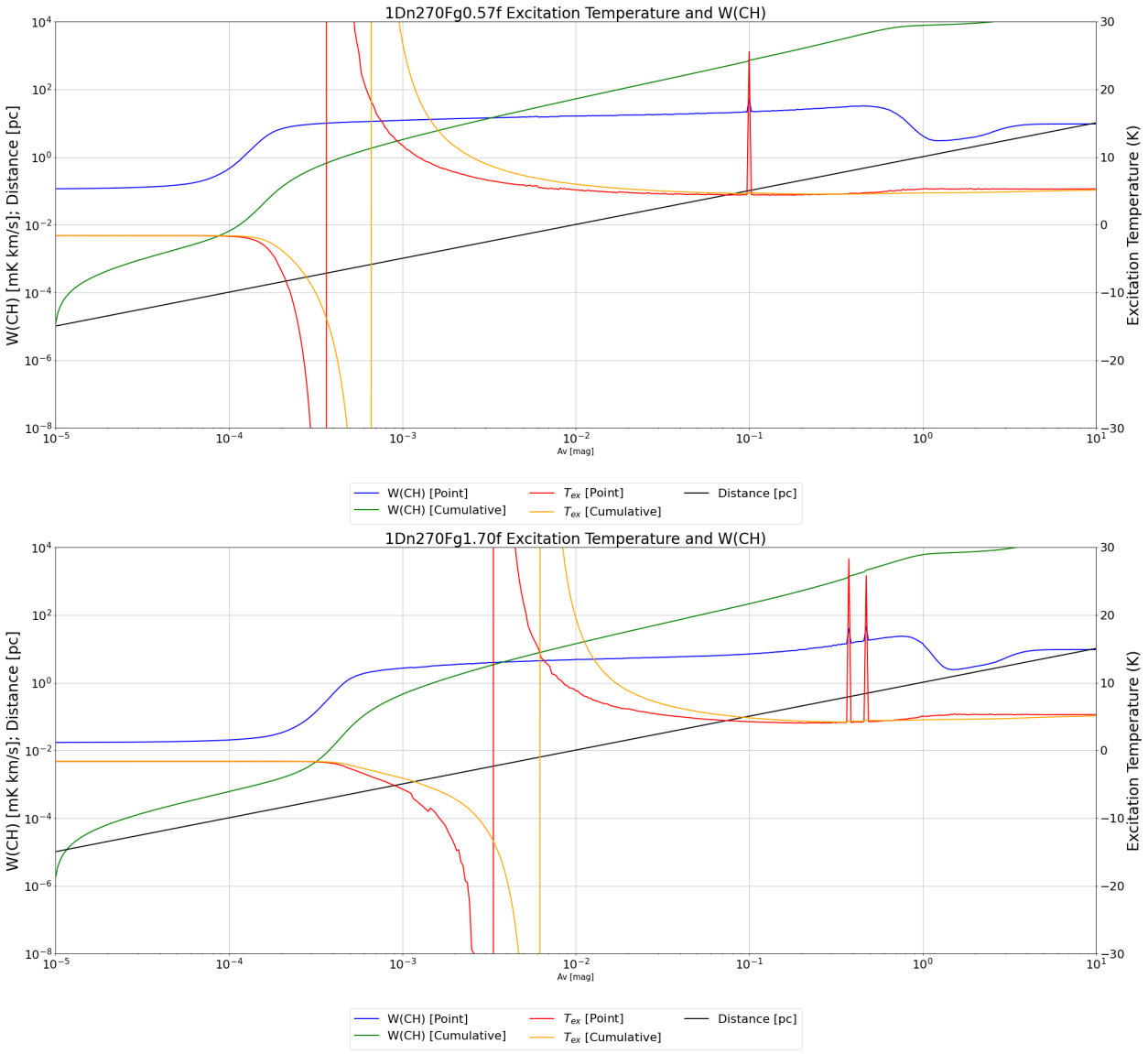

Figure 8.5a: Model excitation temperatures and W(CH) at $n_H = 10^{2.7}$ cm^{-3}, 0.57 and 1.70 Draine initial UV radiation field

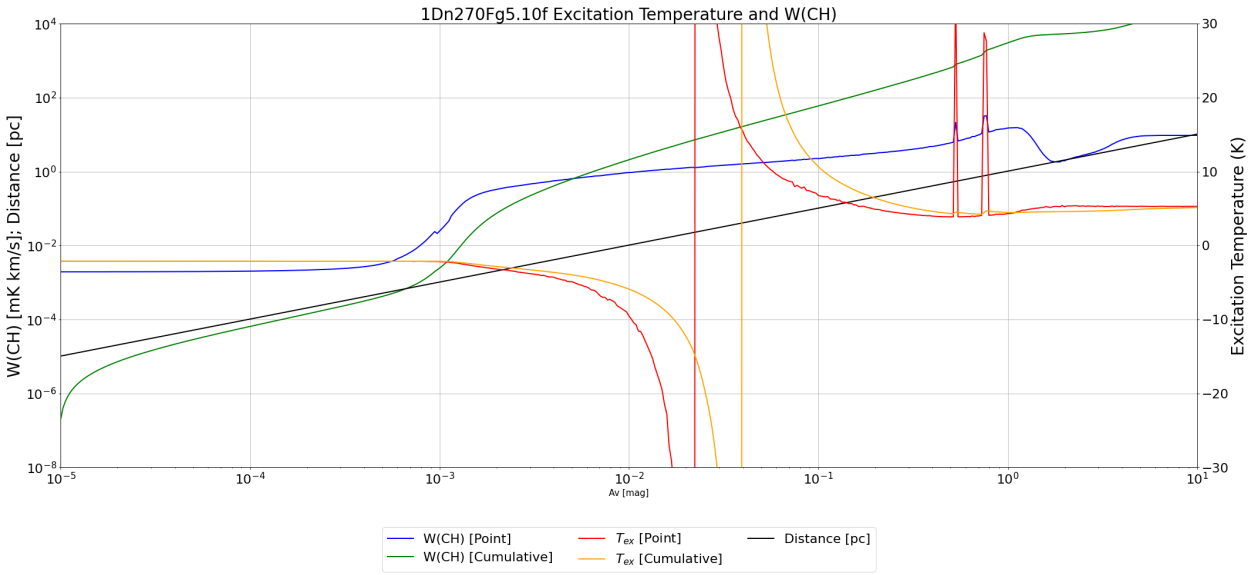

Figure 8.5b: Model excitation temperatures and W(CH) at $n_H = 10^{2.7}$ cm^{-3}, 5.10 Draine initial UV radiation field

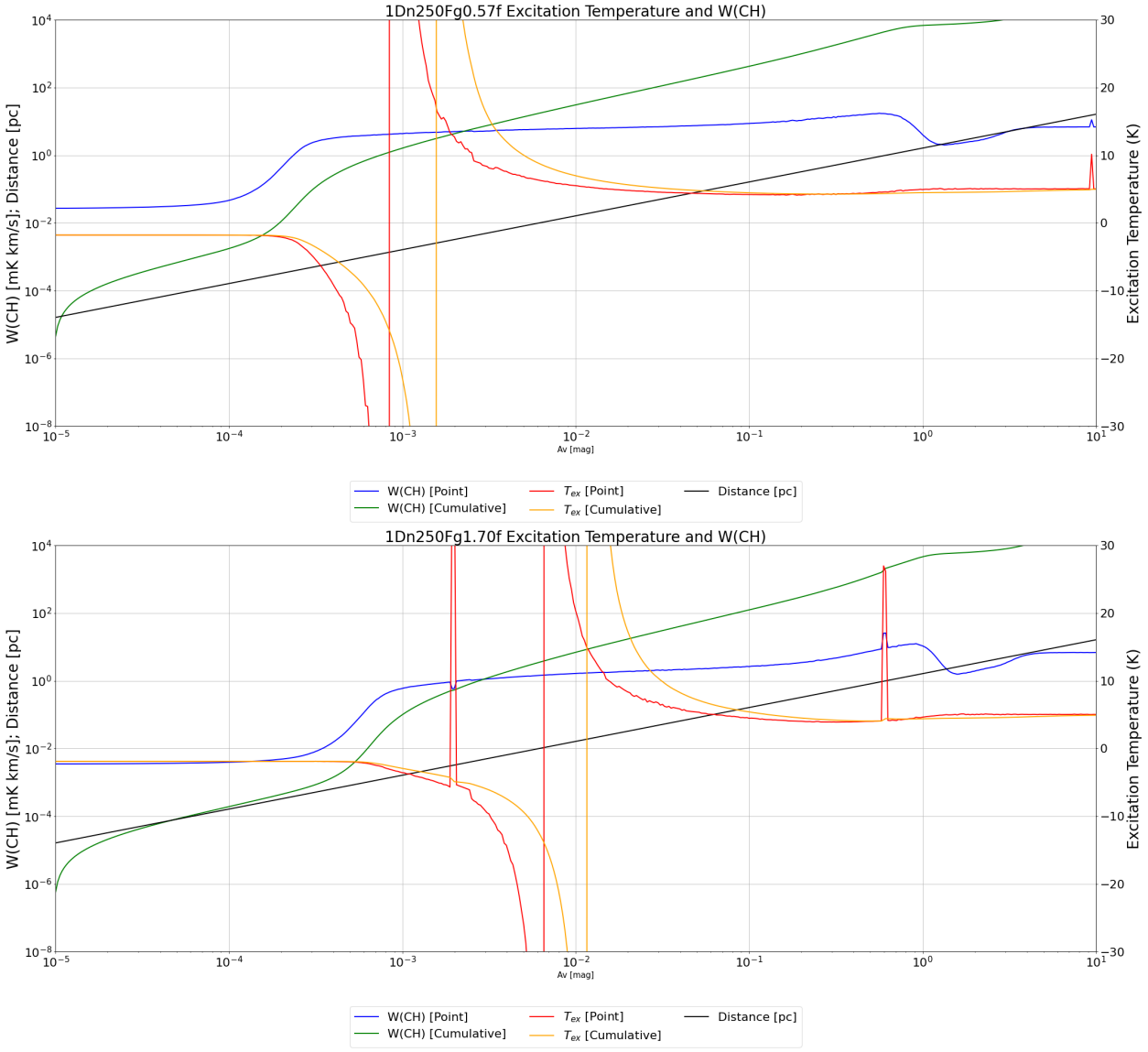

Figure 8.5c: Model excitation temperatures and W(CH) at $n_H = 10^{2.5}$ cm^{-3}, 0.57 and 1.70 Draine initial UV radiation field

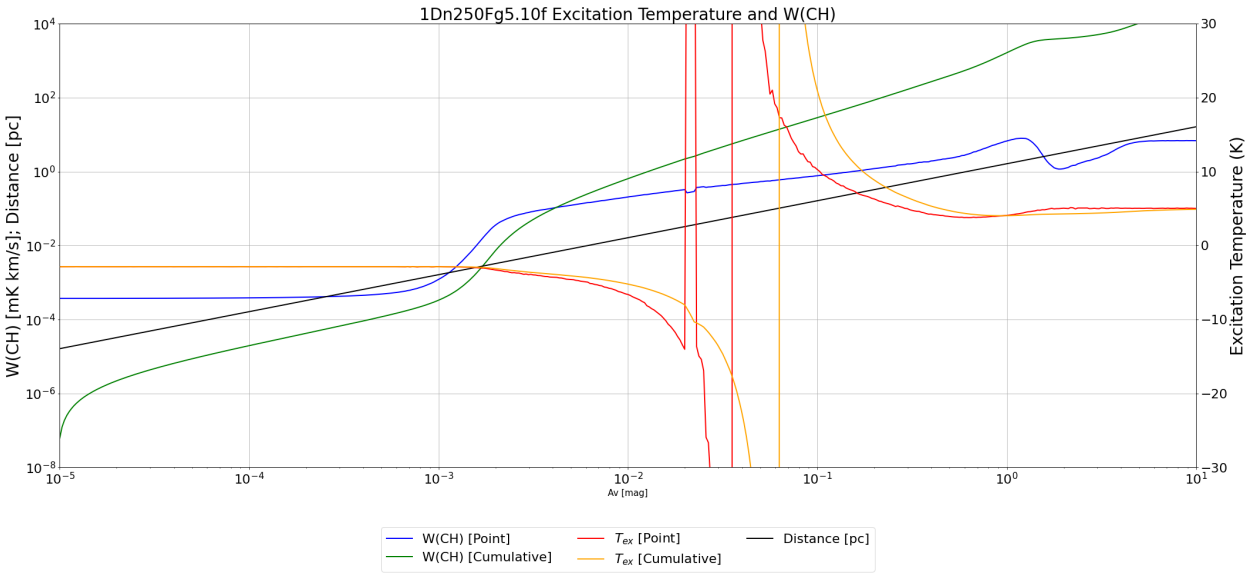

Figure 8.5d: Model excitation temperatures and W(CH) at $n_H = 10^{2.5}$ cm^{-3}, 5.10 Draine initial UV radiation field

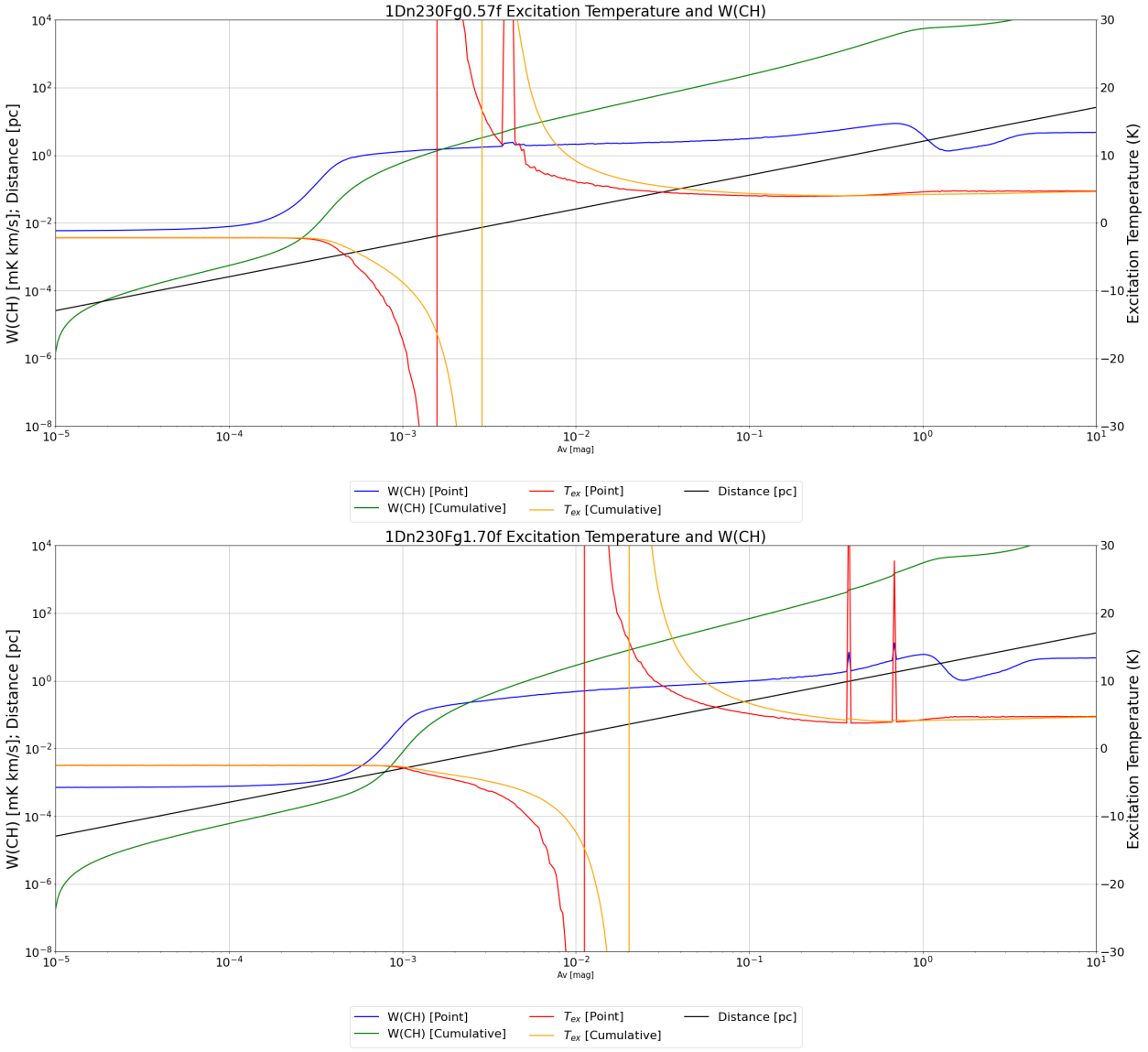

Figure 8.5e: Model excitation temperatures and W(CH) at $n_H = 10^{2.3}$ cm^{-3}, 0.57 and 1.70 Draine initial UV radiation field

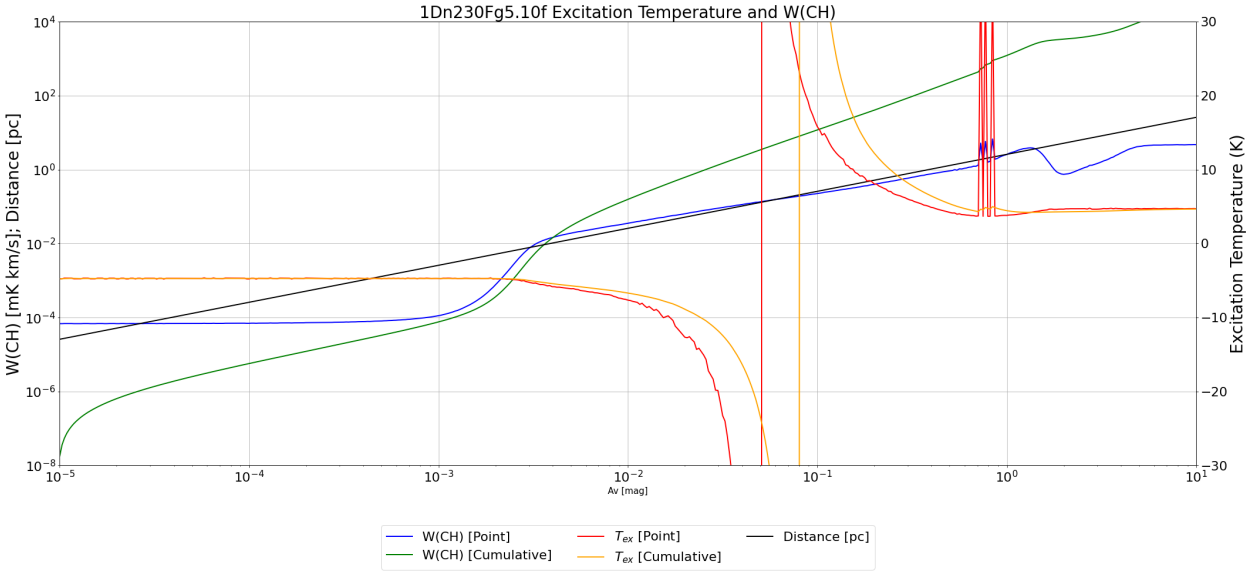

Figure 8.5f: Model excitation temperatures and W(CH) at $n_H = 10^{2.3}$ cm^{-3}, 5.10 Draine initial UV radiation field

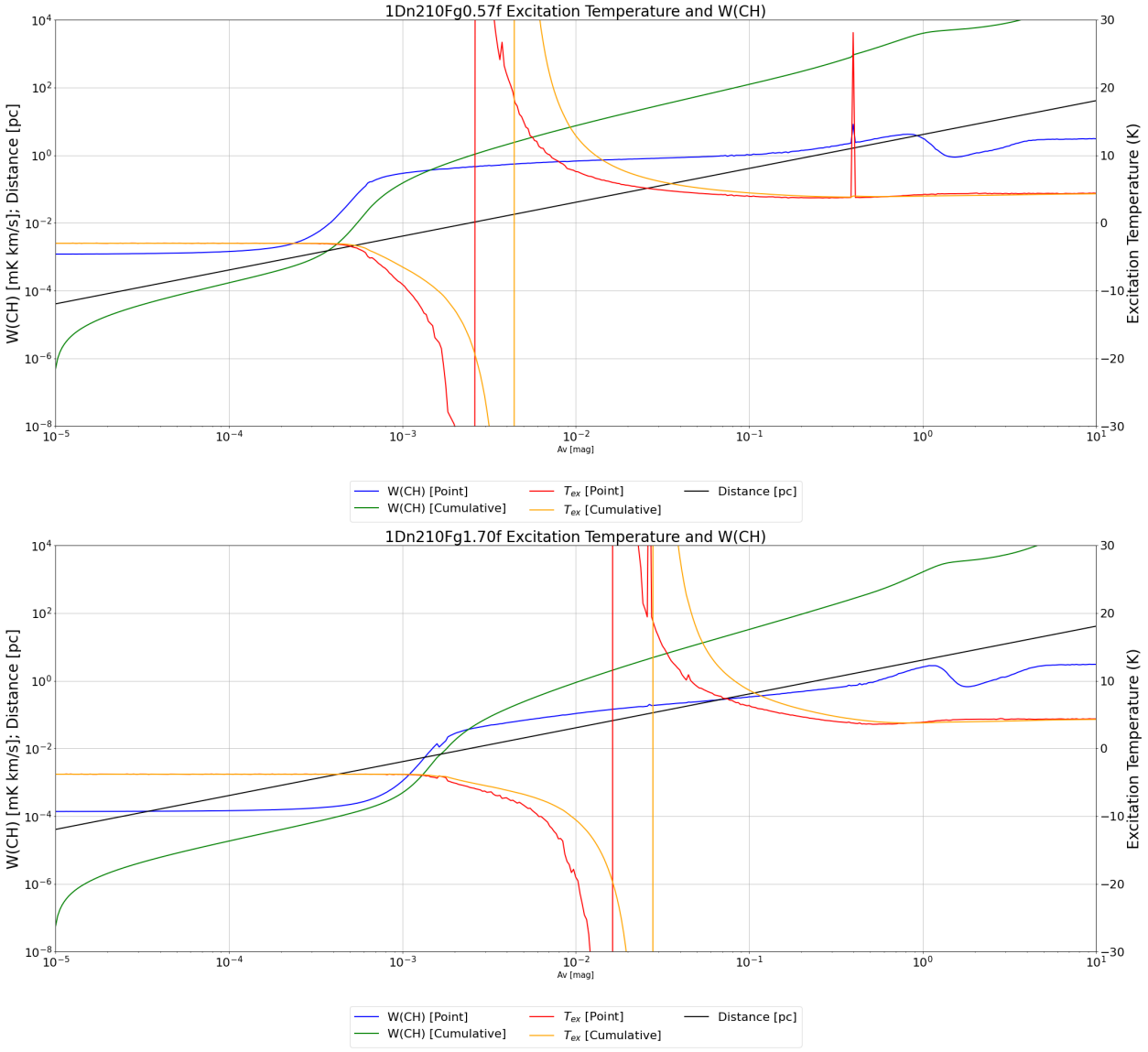

Figure 8.5g: Model excitation temperatures and W(CH) at $n_H = 10^{2.1}$ cm^{-3}, 0.57 and 1.70 Draine initial UV radiation field

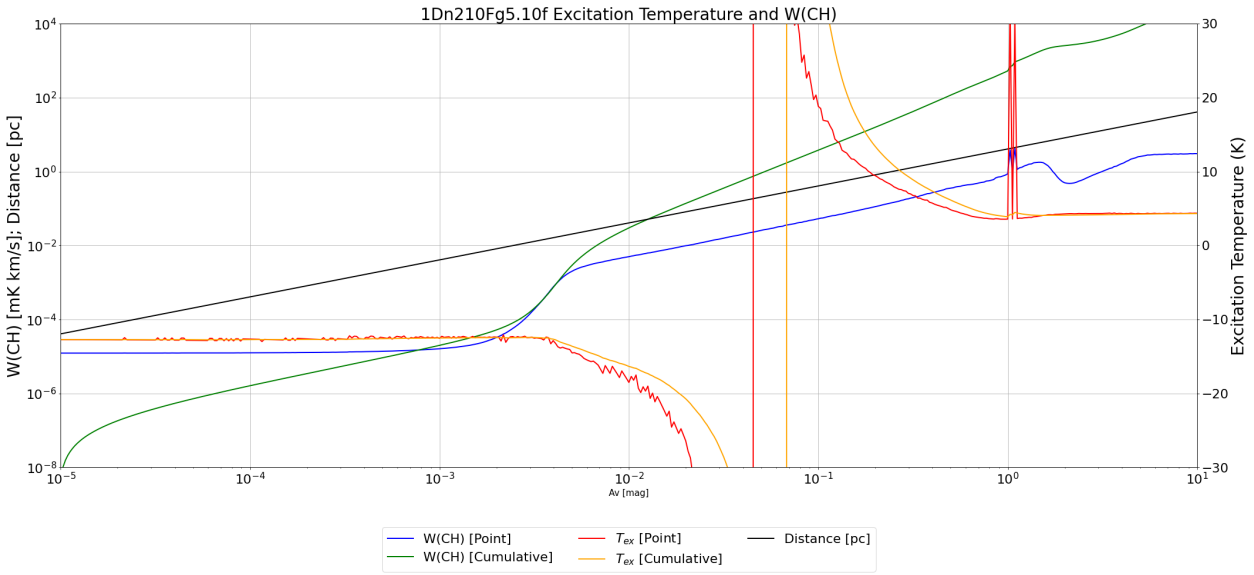

Figure 8.5h: Model excitation temperatures and W(CH) at $n_H = 10^{2.1}$ cm^{-3}, 5.10 Draine initial UV radiation field

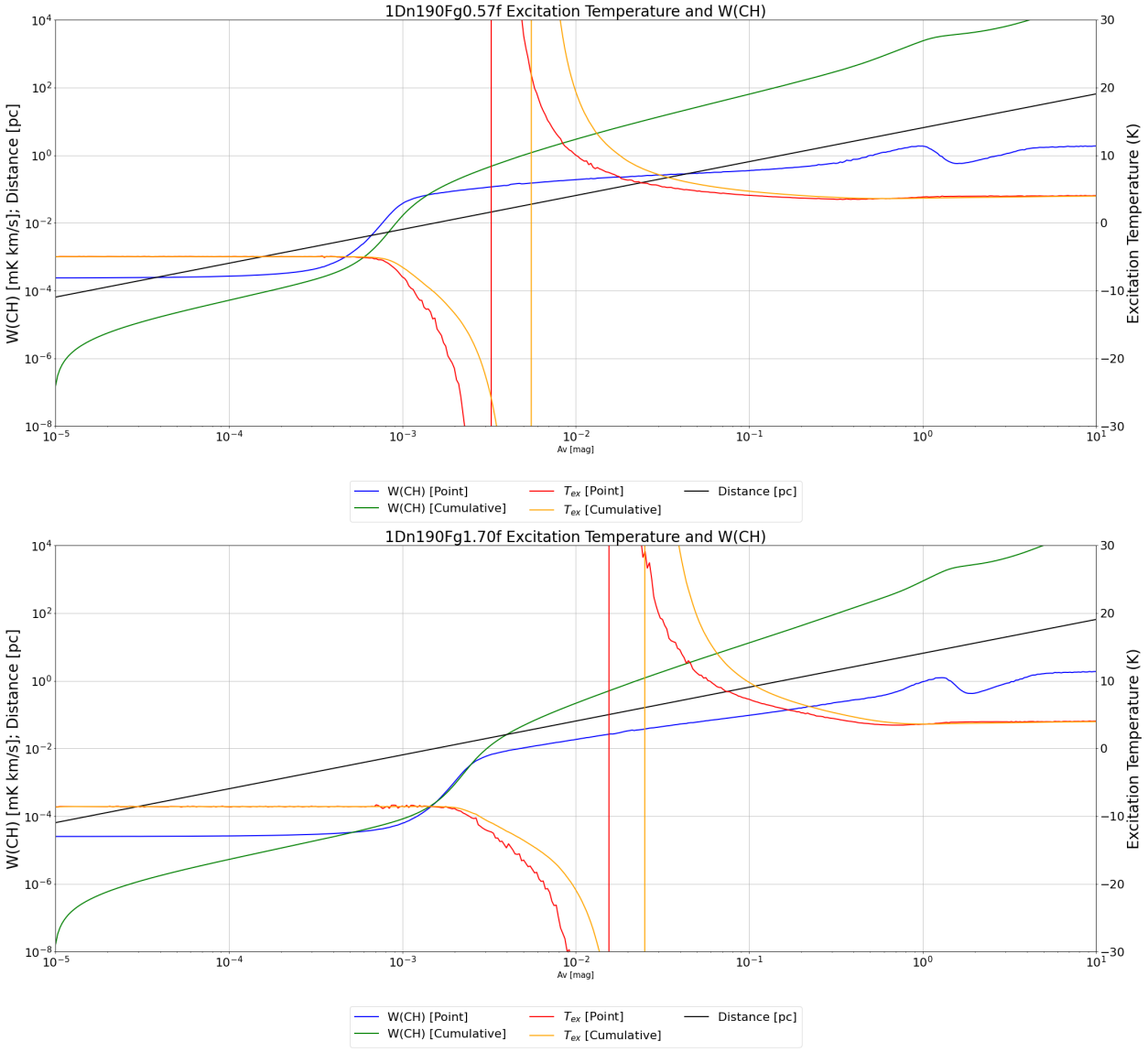

Figure 8.5i: Model excitation temperatures and W(CH) at $n_H = 10^{1.9}$ cm^{-3}, 0.57 and 1.70 Draine initial UV radiation field

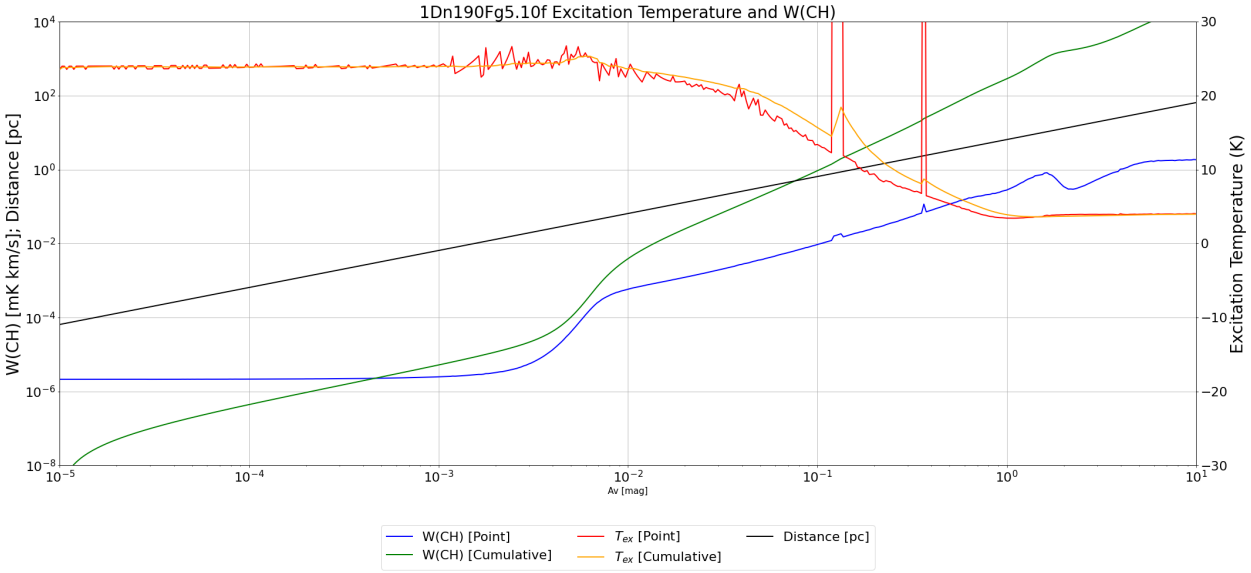

Figure 8.5j: Model excitation temperatures and W(CH) at $n_H = 10^{1.9}$ cm^{-3}, 5.10 Draine initial UV radiation field

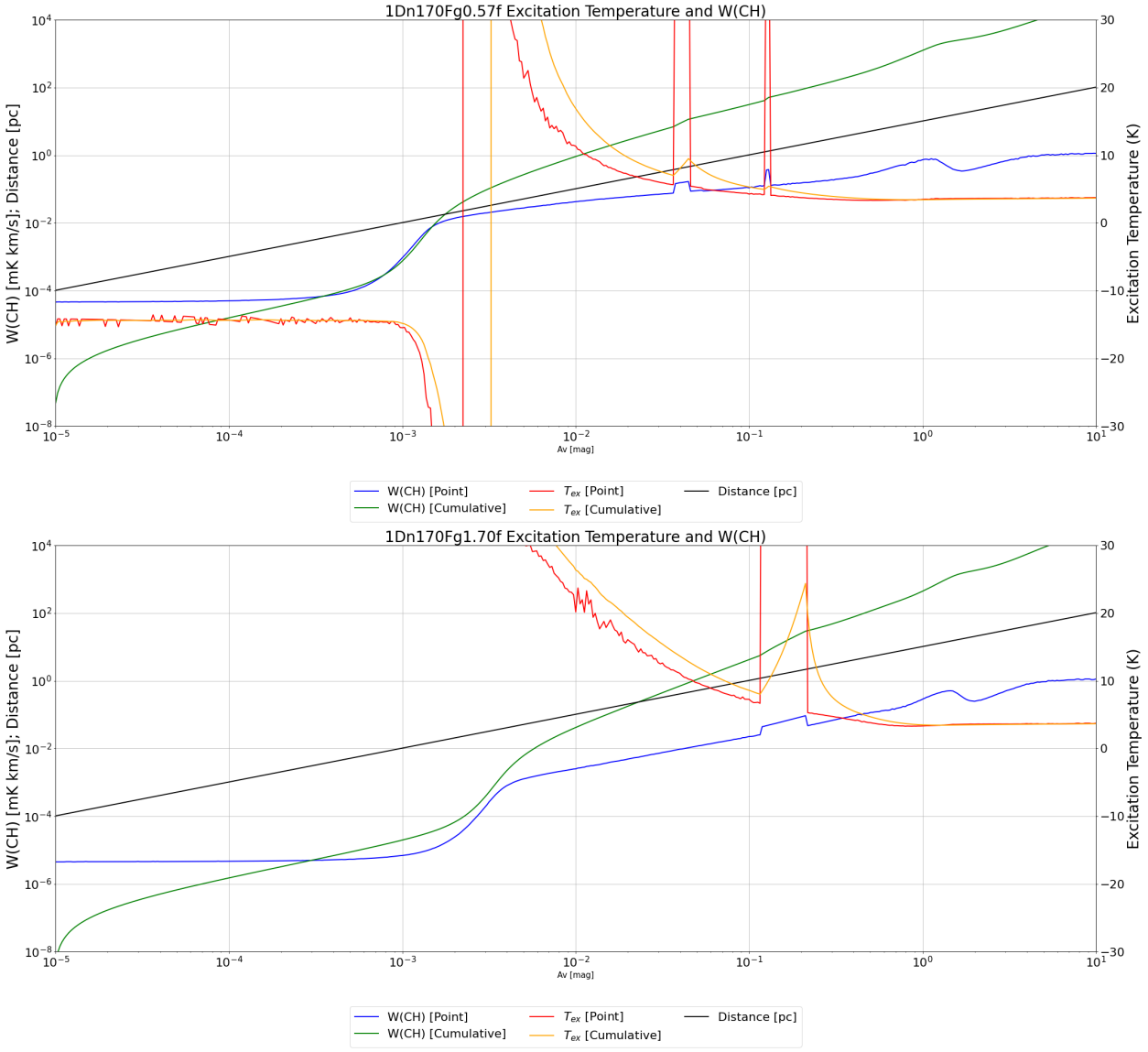

Figure 8.5k: Model excitation temperatures and W(CH) at $n_H = 10^{1.7}$ cm^{-3}, 0.57 and 1.70 Draine initial UV radiation field

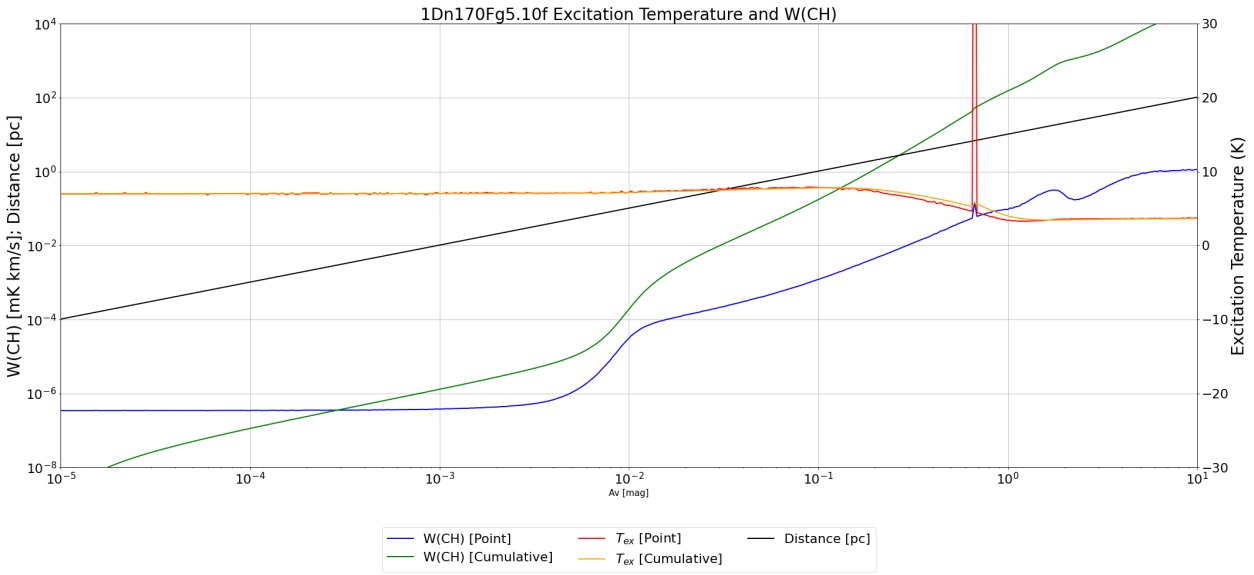

Figure 8.5l: Model excitation temperatures and W(CH) at $n_H = 10^{1.7}$ cm^{-3}, 5.10 Draine initial UV radiation field

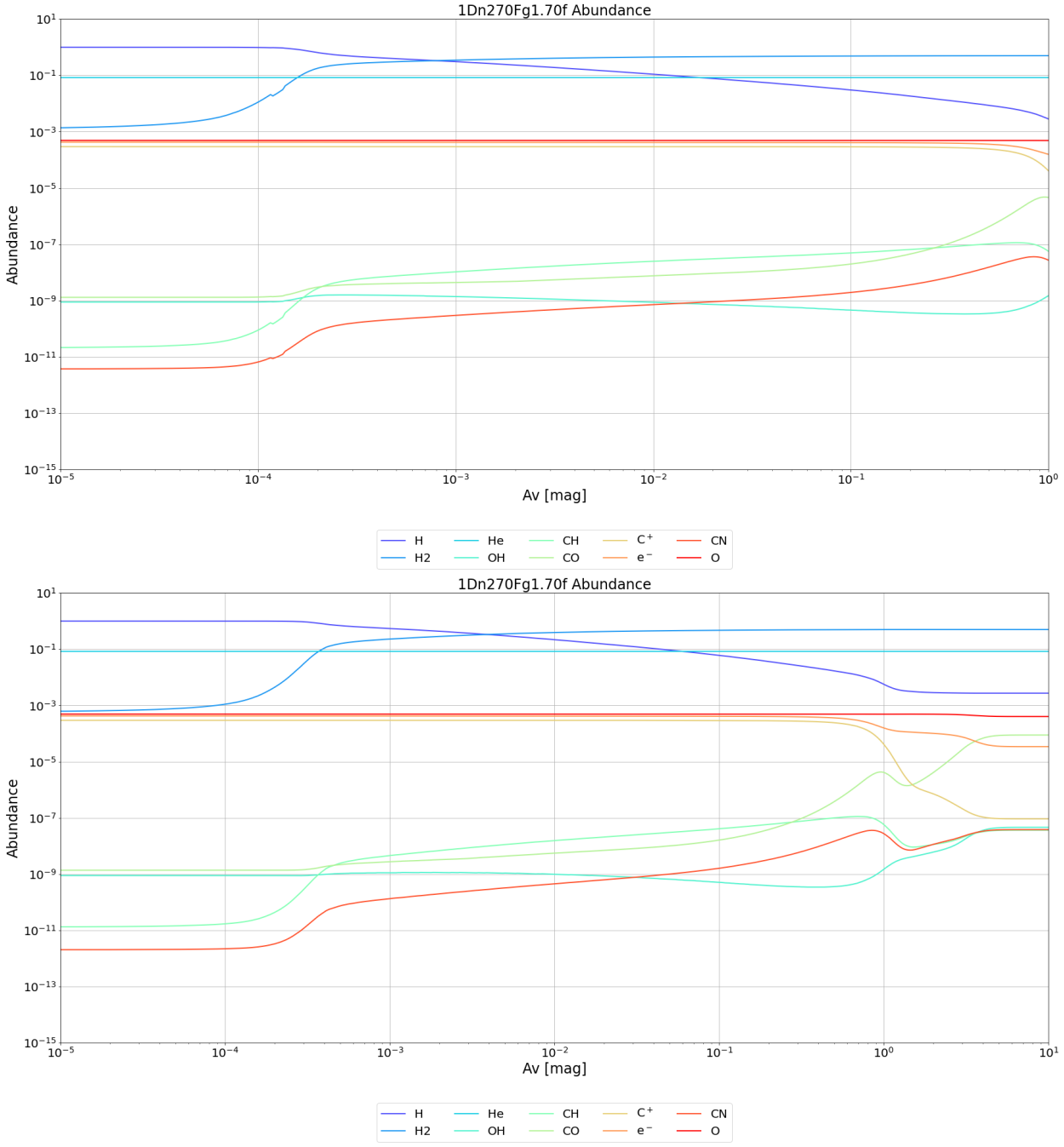

Figure 8.6a: Model abundances at various G/D ratios
Top plot has a gas-to-dust ratio of 50 and the bottom plot has a gas-to-dust ratio of 100.

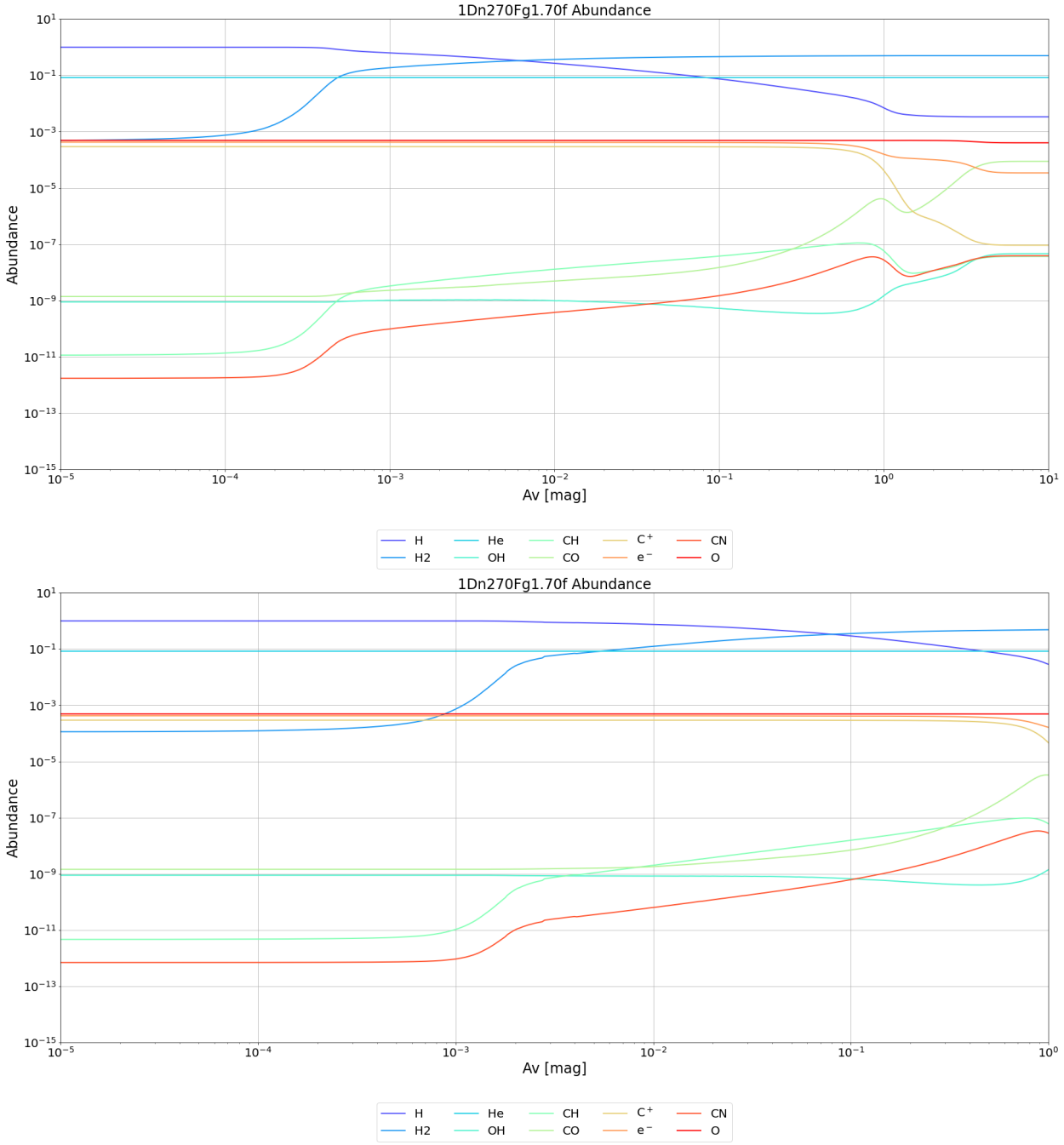

Figure 8.6b: Model abundances at various G/D ratios
Top plot has a gas-to-dust ratio of 124 and the bottom plot has a gas-to-dust ratio of 500.

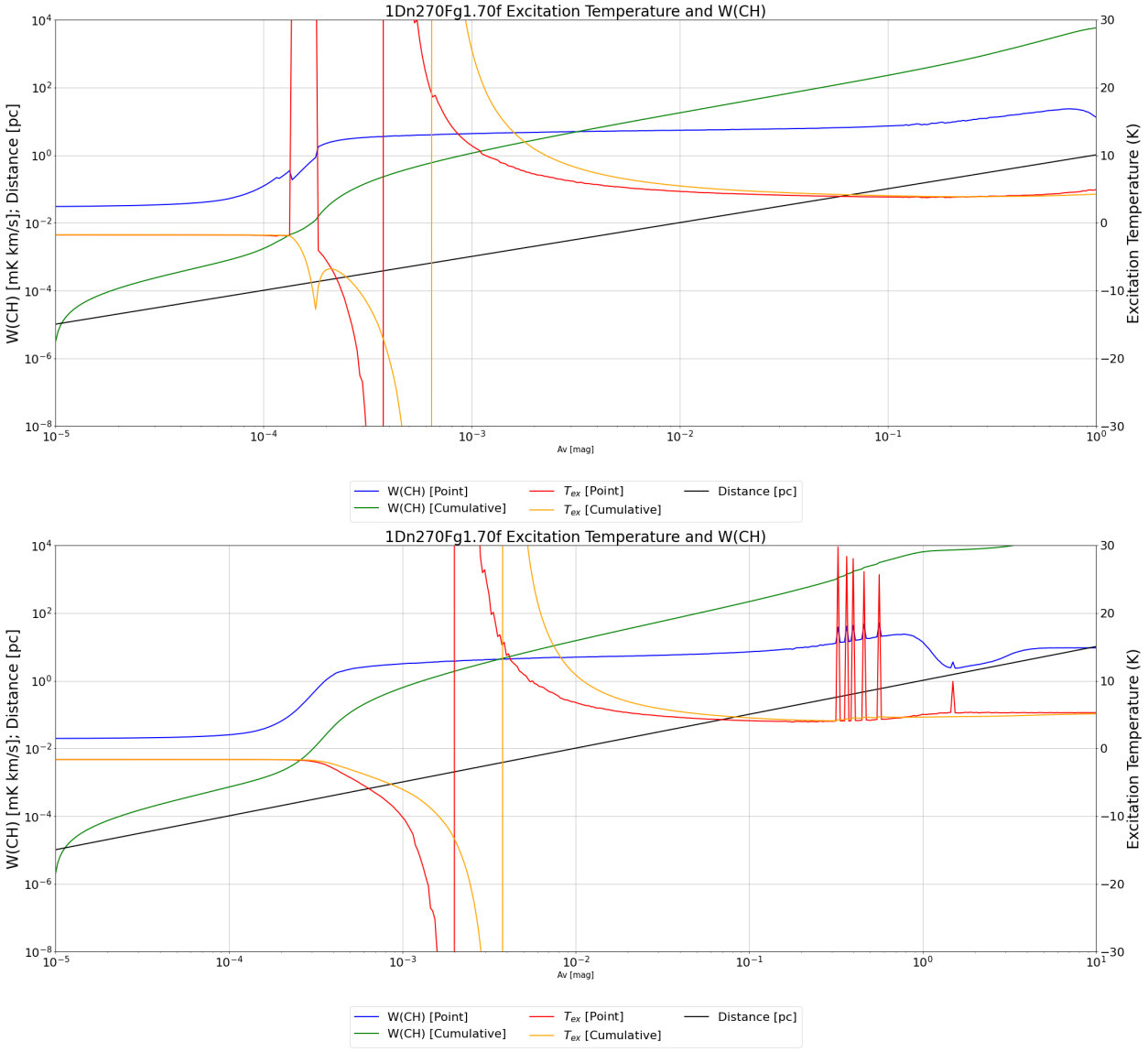

Figure 8.7a: Model excitation temperatures and W(CH) at various G/D ratios
Top plot has a gas-to-dust ratio of 50 and the bottom plot has a gas-to-dust ratio of 100.

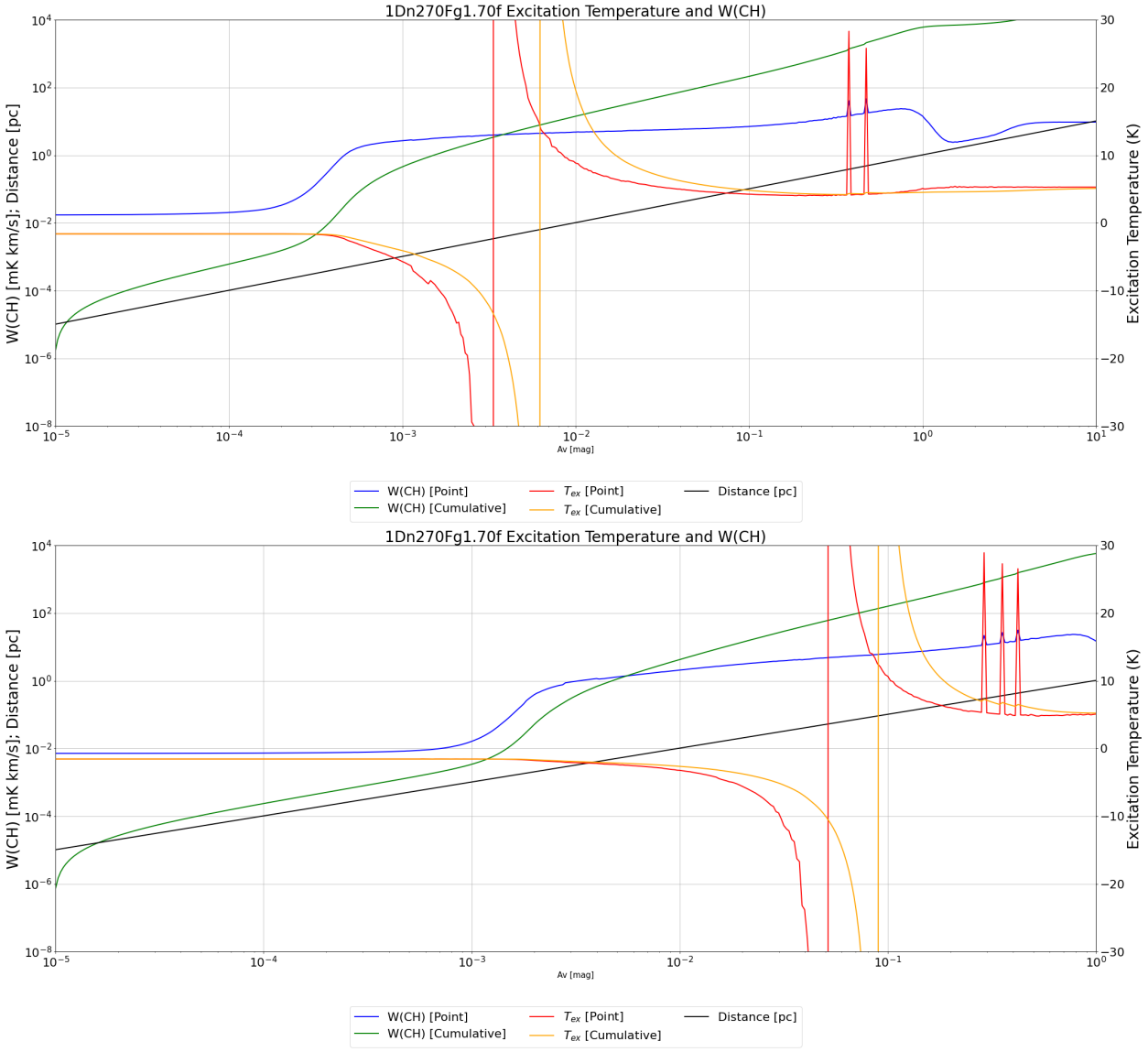

Figure 8.7b: Model excitation temperatures and W(CH) at various G/D ratios
Top plot has a gas-to-dust ratio of 124 and the bottom plot has a gas-to-dust ratio of 500.

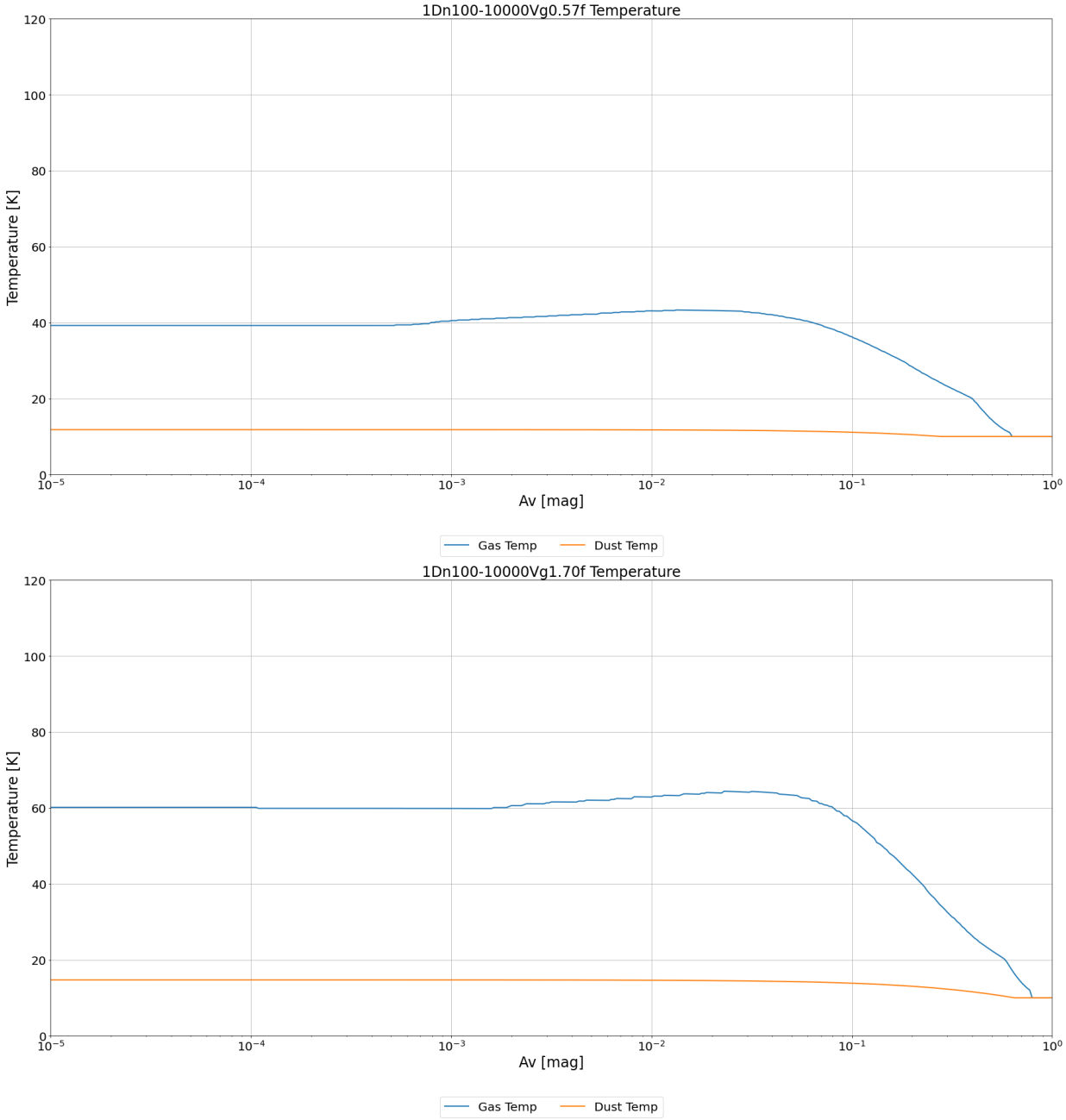

Figure 8.8a: Variable model temperatures in the cloud from 10^2 to 10^4 cm^{-3}, 0.57 and 1.70 Draine initial UV radiation field

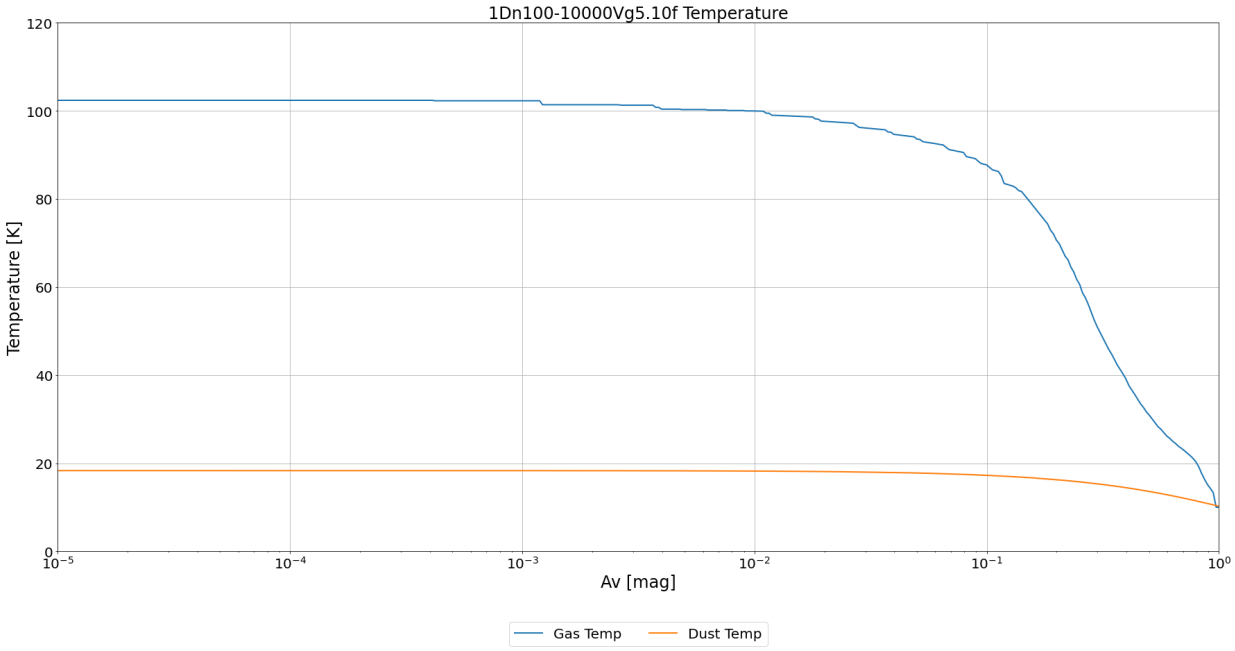

Figure 8.8b: Variable model temperatures in the cloud from 10^2 to 10^4 cm^{-3}, 5.10 Draine initial UV radiation field

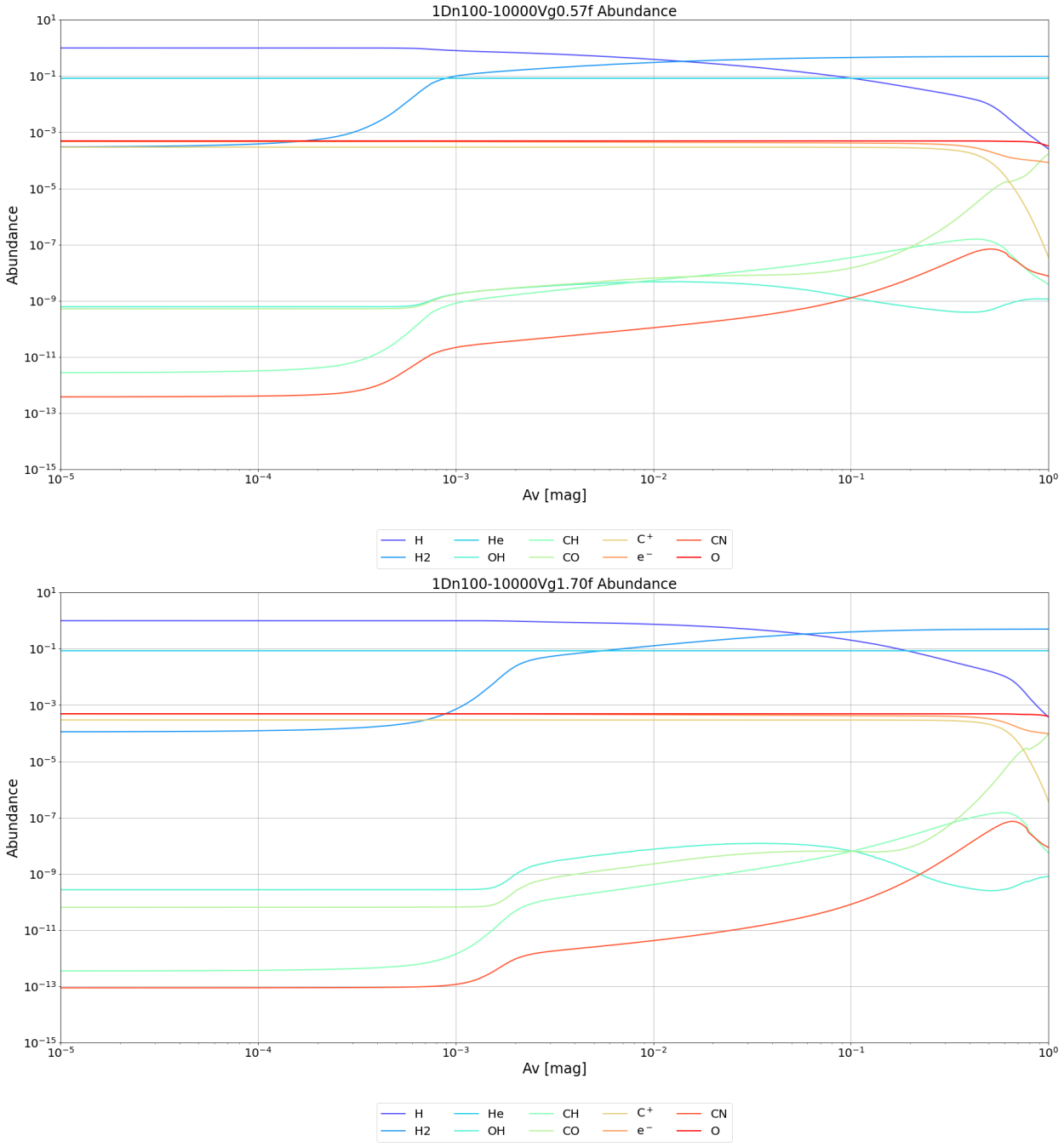

Figure 8.8c: Variable model abundances in the cloud from 10^2 to 10^4 cm^{-3}, 0.57 and 1.70 Draine initial UV radiation field

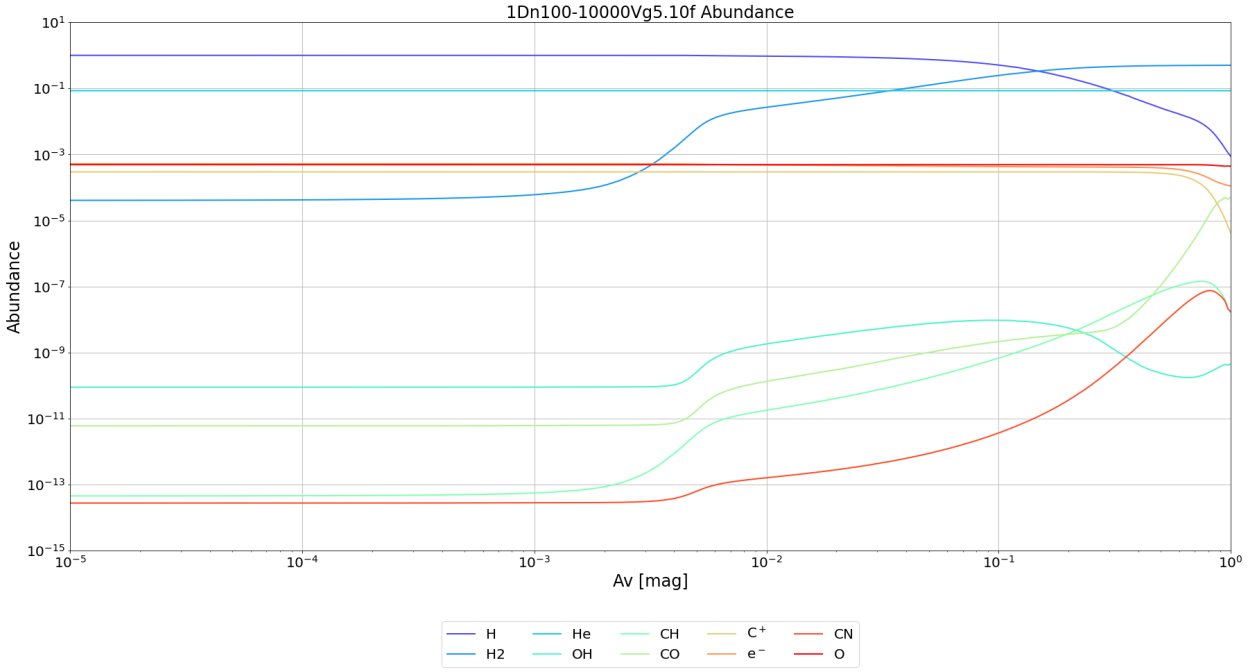

Figure 8.8d: Variable model abundances in the cloud from 10^2 to 10^4 cm^{-3}, 5.10 Draine initial UV radiation field

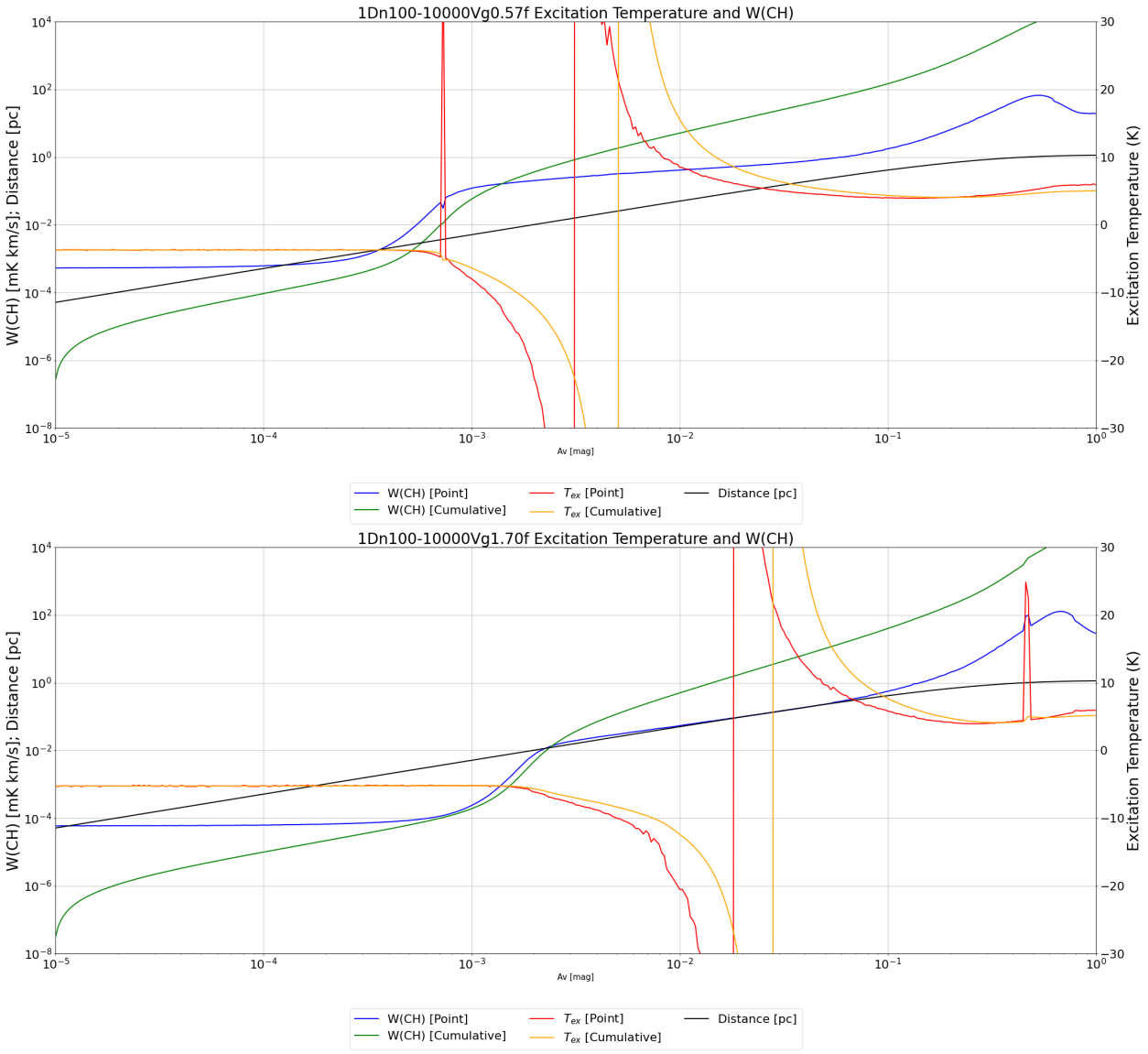

Figure 8.8e: Variable model excitation temperatures and W(CH) for n_H from 10^2 to 10^4 cm^{-3}, 0.57 and 1.70 Draine initial UV radiation field

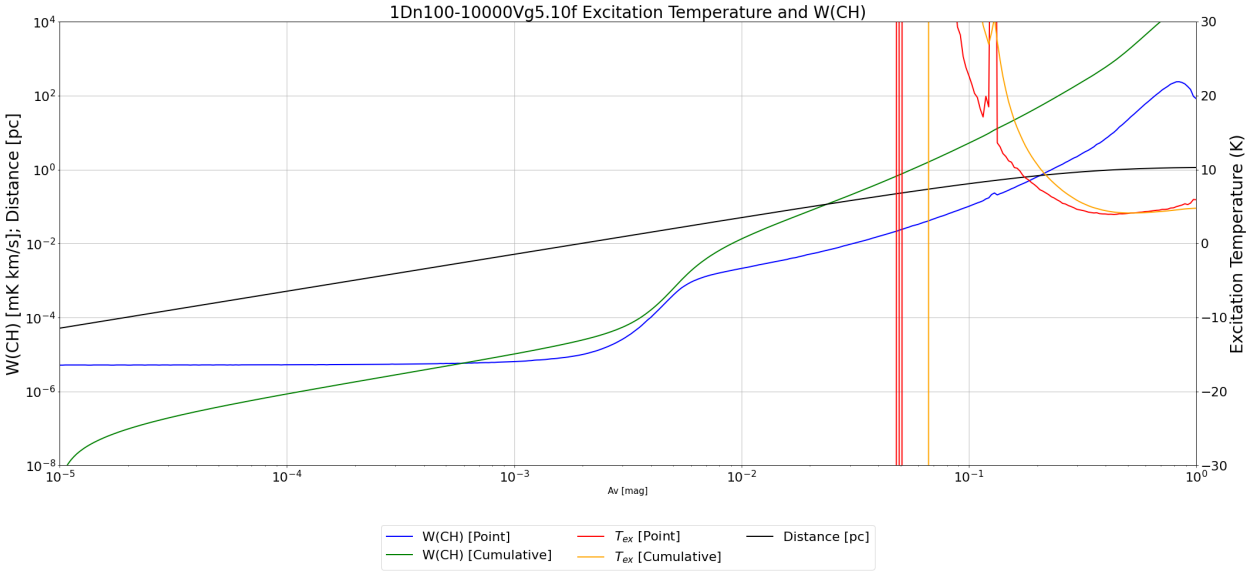

Figure 8.8f: Variable model excitation temperatures and W(CH) for n_H from 10^2 to 10^4 cm^{-3}, 5.10 Draine initial UV radiation field

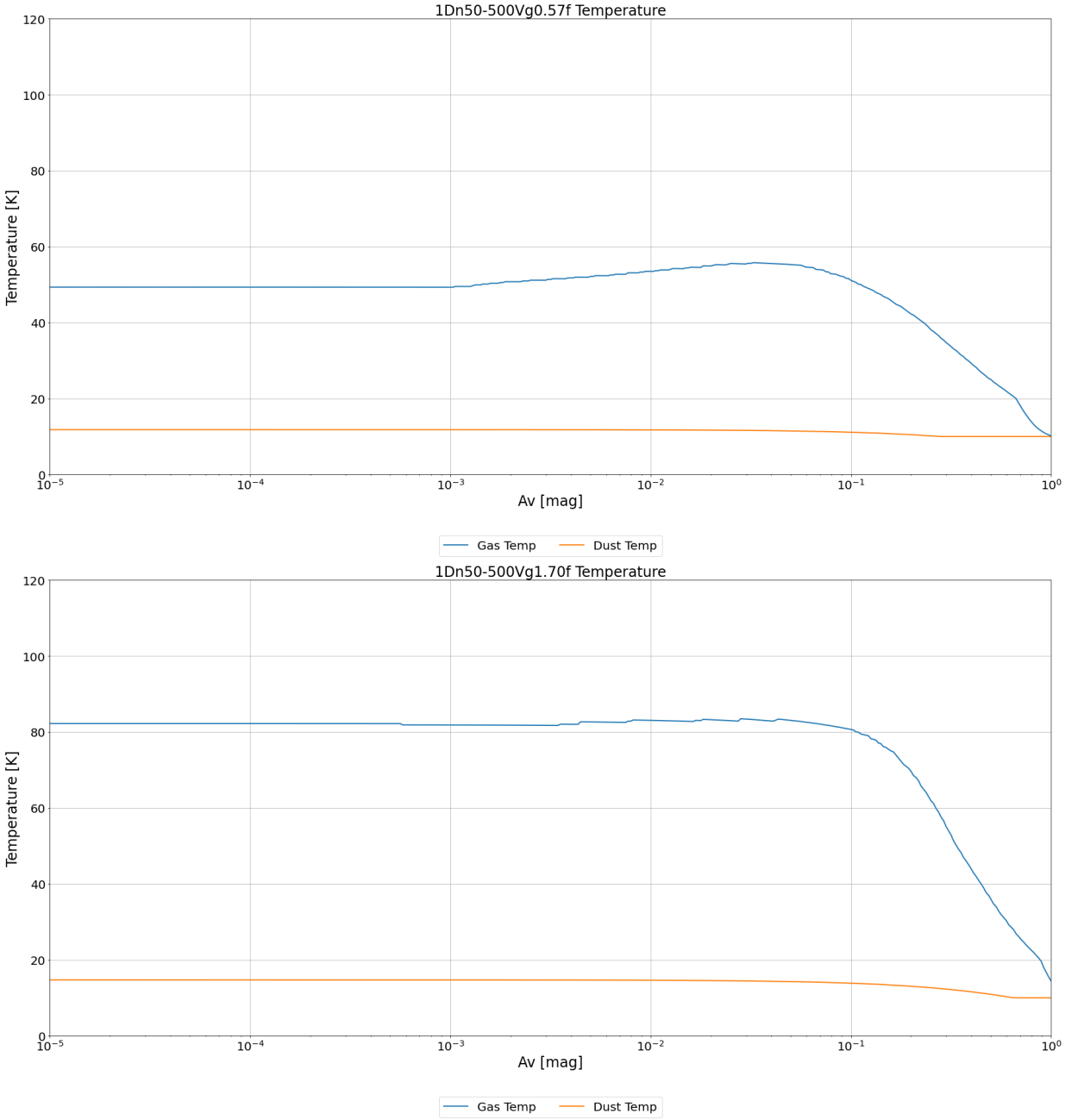

Figure 8.9a: Variable model temperatures in the cloud from 50 to 500 cm^{-3}, 0.57 and 1.70 Draine initial UV radiation field

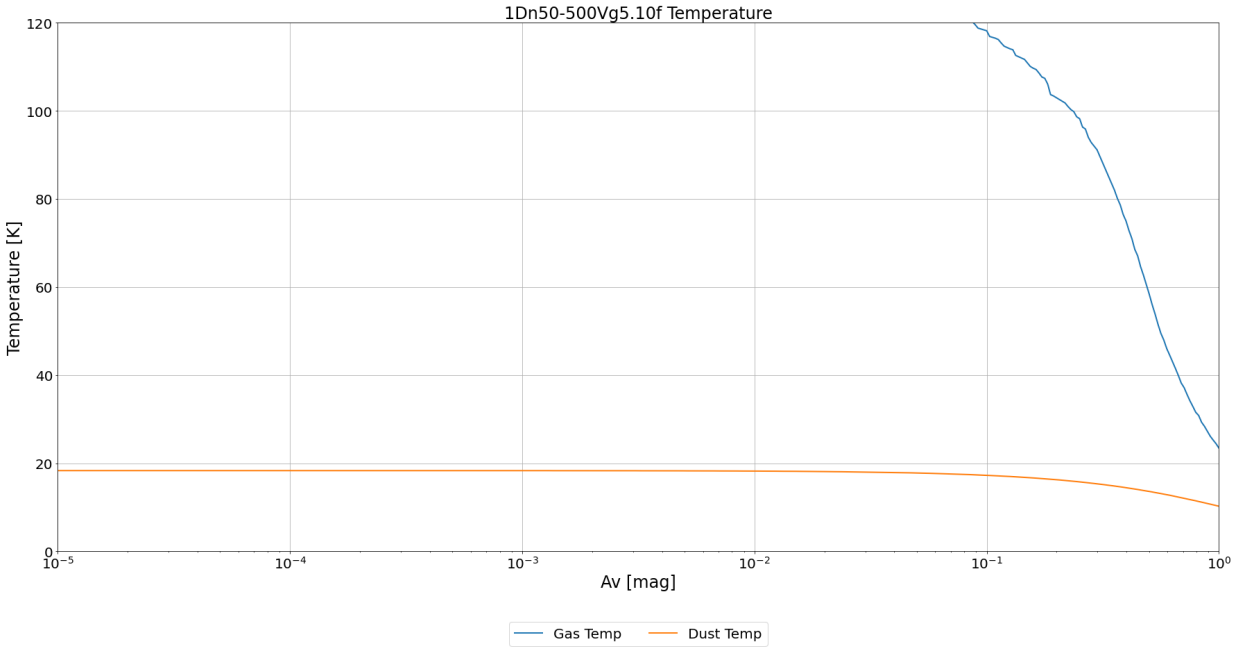

Figure 8.9b: Variable model temperatures in the cloud from 50 to 500 cm^{-3}, 5.10 Draine initial UV radiation field

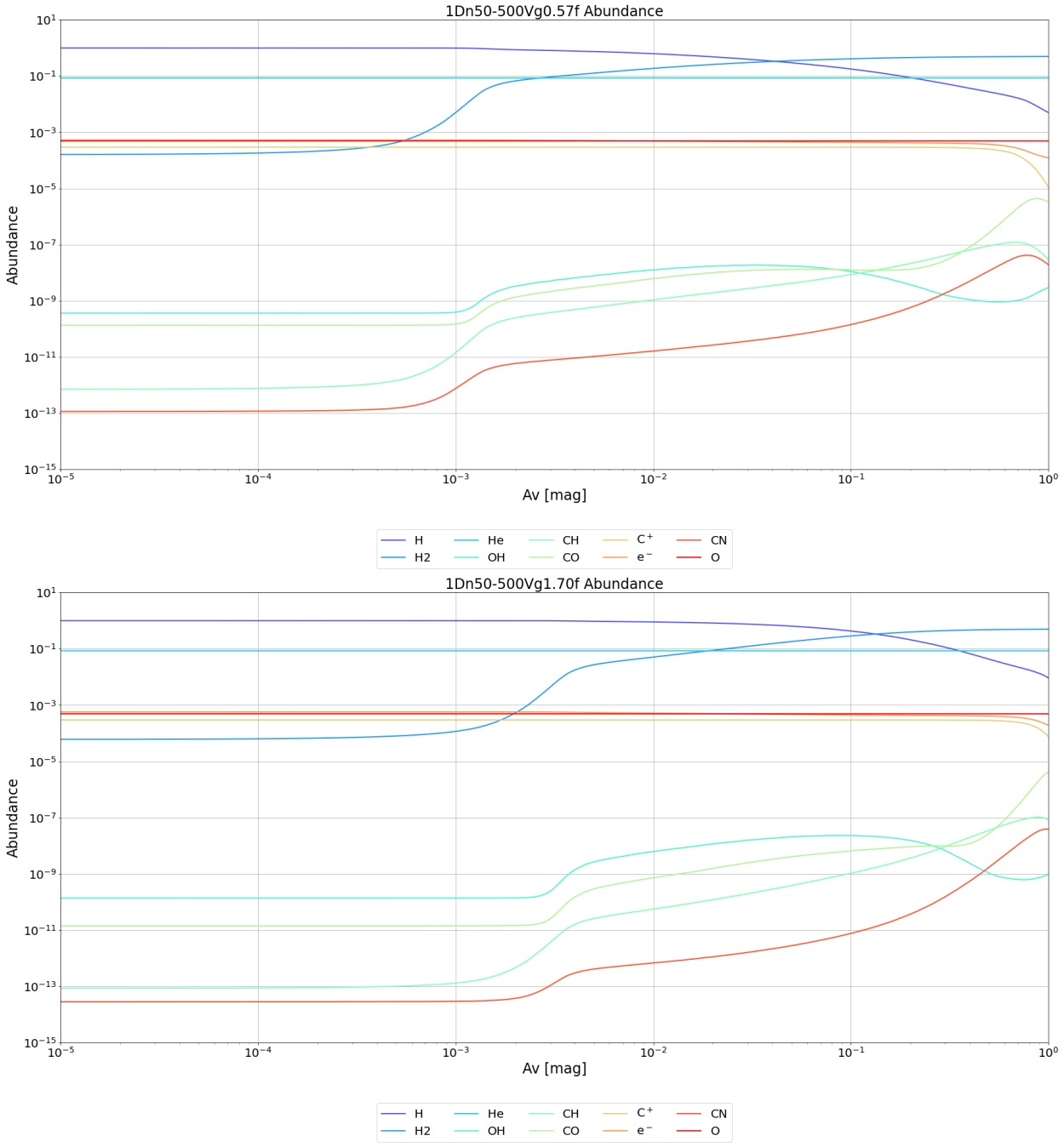

Figure 8.9c: Variable model abundances in the cloud from 50 to 500 cm^{-3}, 0.57 and 1.70 Draine initial UV radiation field

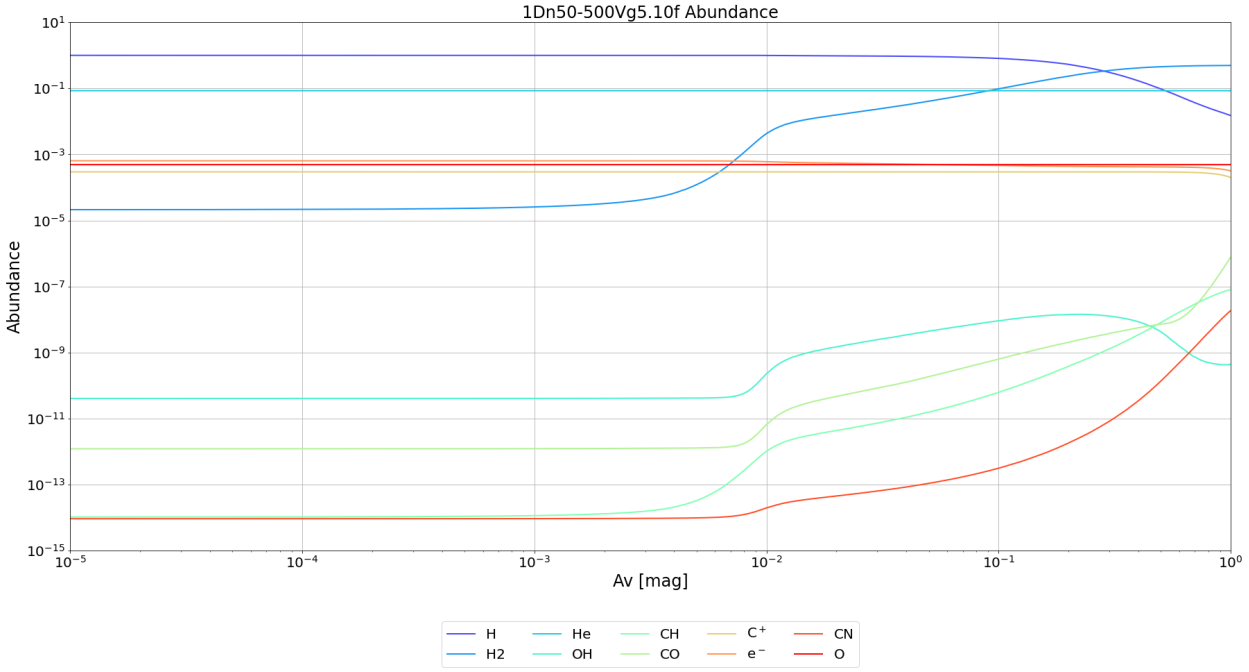

Figure 8.9d: Variable model abundances in the cloud from 50 to 500 cm^{-3}, 5.10 Draine initial UV radiation field

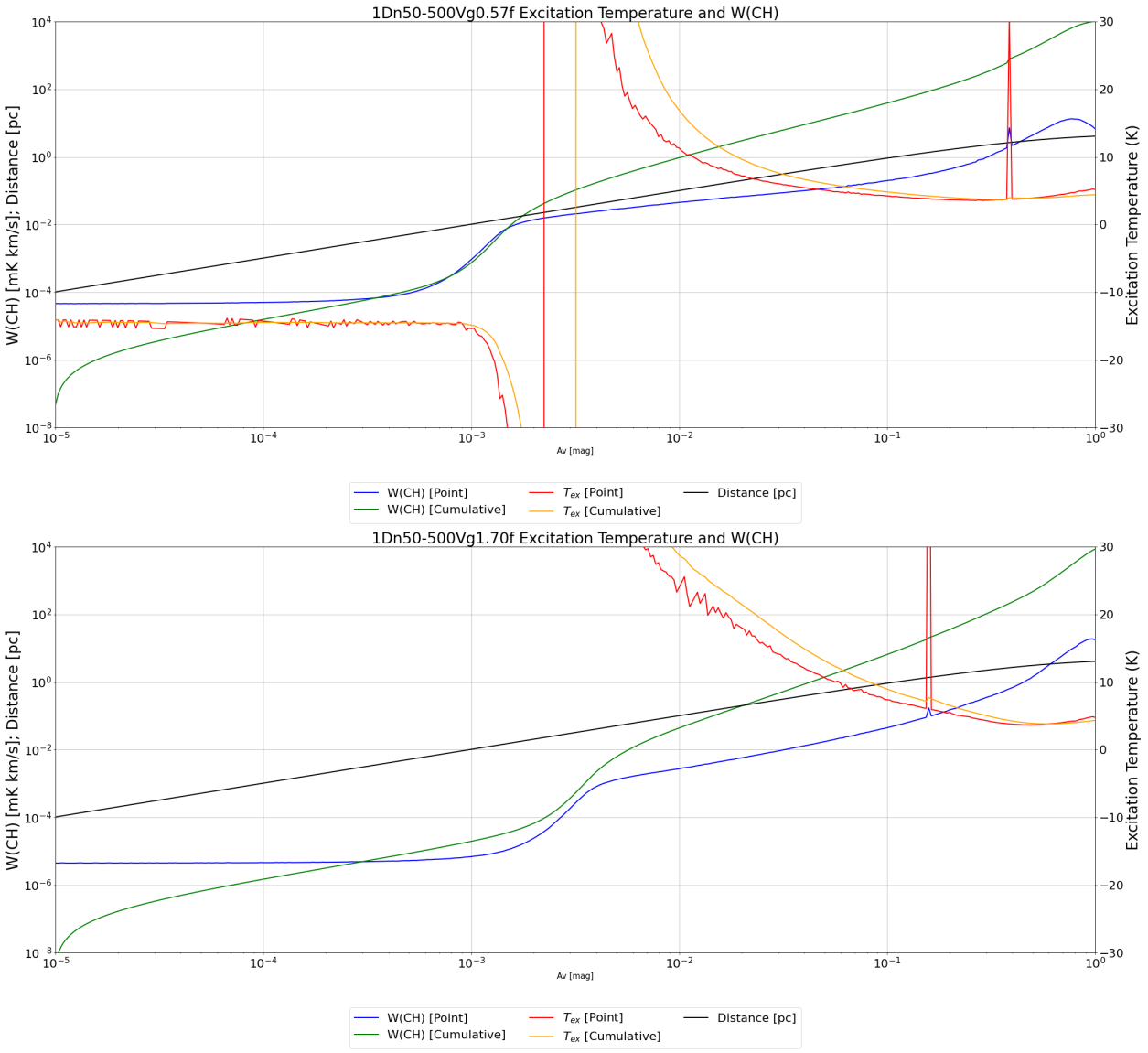

Figure 8.9e: Variable model excitation temperatures and W(CH) for n_H from 50 to 500 cm^{-3}, 0.57 and 1.70 Draine initial UV radiation field

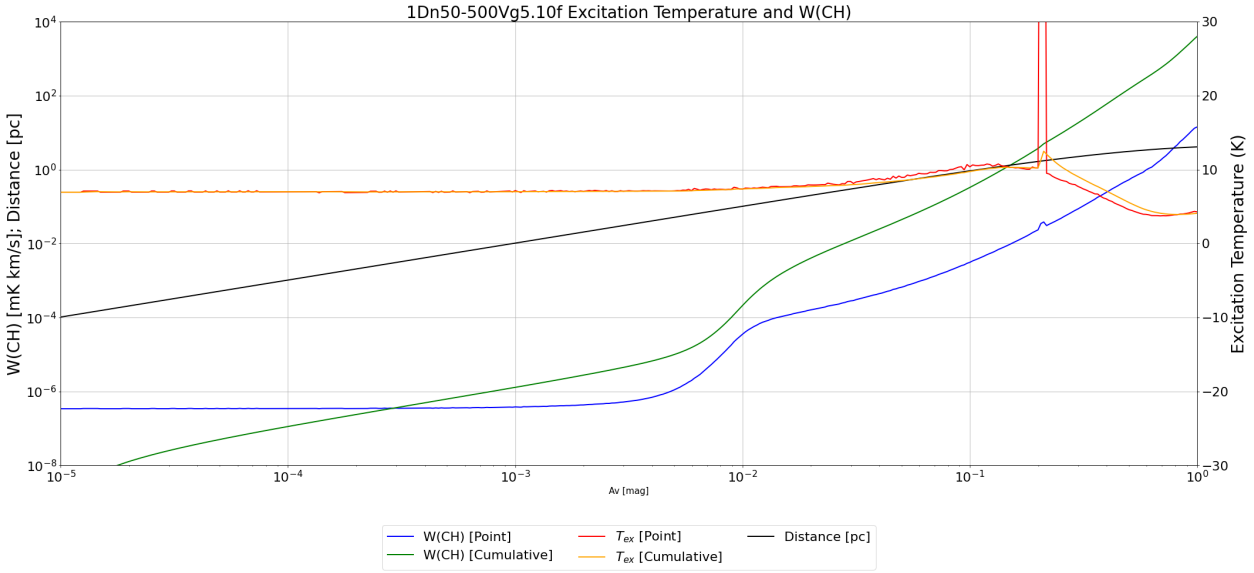

Figure 8.9f: Variable model excitation temperatures and W(CH) for n_H from 50 to 500 cm^{-3}, 5.10 Draine initial UV radiation field

Chapter 9

Conclusion

This thesis has been primarily studying CH in the ISM, with a focus on measuring or simulating the excitation temperature of the CH main line. We have also tested using the CH 3335 MHz emission line as a potential method for tracing CO-faint gas in diffuse molecular clouds.

In chapter 2 we examined the relationship CH has with extinction and molecular hydrogen in order to estimate the average excitation temperature. With a sample of optical and UV data collected from the literature, we found that N(CH)/N(H_2) = $4.75 \pm 2.20 \times 10^{-8}$ where the uncertainty is the standard deviation, which is similar to the value determined by Liszt and Lucas (2002), N(CH)/N(H_2) = $4.3 \pm 1.9 \times 10^{-8}$. Using radio observations, where N(H_2) is calculated from extinction and N(HI), the slope of N(CH)/N(H_2) = $8.73 \pm 6.11 \times 10^{-8}$. The descrepency between the two relations may be due to the excitation temperature, in the radio-derived N(CH)/N(H_2) calculation, N(CH) was determined assuming $T_{\rm ex} \gg T_{\rm bg}$. A small value of $T_{\rm ex}$ will cause N(CH) to be reduced, and given the optical/UV and radio derived relations, N(CH) is likely reduced by a factor of approximately 0.57. This is equivalent to an excitation temperature of 3.7 K with a background temperature of 2.8 K.

N(H_2) was derived indirectly instead of measured from observations of the molecule itself, so the N(CH)/$E(B-V)$ relation was also determined for both data sets. This comparison was complicated by the different fractional H_2 abundance present in the lines of sight for each group, but it is unlikely that the difference in f(H_2) could account for the difference in optical/UV and radio derived N(CH)/$E(B-V)$. The slopes of the two CH and color excess relations indicate there is a similar drop in the CH column density of approximately 0.52, which is equivalent to $T_{\rm ex} = -3$ K with $T_{\rm bg} = -2.8$ K.

We determine the excitation temperature of a few lines of sight more directly in chapter 3. If the CH column density and the velocity-integrated brightness temperature of a line of sight are known, then $T_{\rm ex}$ can determined. We use optical and UV observations of stars in the literature to find N(CH), and we observed those lines of sight using the Arecibo 305-m telescope to determine W(CH). Unfortunately, due to the limited number of suitable stars for measuring absorption lines of CH, this method is limited to those lines of sight.

From the 16 lines of sight observed, we were able to effectively determine $T_{\rm ex}$ for 5 lines of sight. In this small sample, $T_{\rm ex}$ varied between the individual lines of sight. HD24534 and HD26571 both had very low excitation temperatures, while HD21483 and HD27778 had excitation temperatures which are much greater than the background temperature. In order to draw more far-reaching conclusions, the data set would have to be greatly expanded.

We discuss other methods of determining $T_{\rm ex}$ in chapter 4; on-source and off-source observations of radio continuum sources and the 4300 Å blended CH line. The former method is the one traditionally used by radio astronomers to determine $T_{\rm ex}$ of the 3335 MHz line. It was these measurements that led to the widespread belief in the radio community that $|T_{\rm ex}| \gg T_{\rm bg}$. Our result for J0530 + 13 showed a $T_{\rm ex}$ of -21.0 ± 11.2 K, which is somewhat consistent with earlier results and indicative of a population

inversion. To test how well observations of the 4300 line can determine the excitation temperature of the lambda doublet, we created several synthetic spectra based on the gaussian profiles of the doublet. Due to the logarithmic nature of the excitation temperature equation, low excitation temperatures can be determined fairly easily, but the noise in actual observations makes it impossible to reliably determine high excitation temperatures.

In chapters 5 and 6 we examine CH in MBM 16 and MBM 53 to determine its potential as a tracer of CO-faint gas. This issue may be the most important question in current molecular cloud research. In MBM 16, there is a small clump of CO at l=170.66°, b=−37.32° which is not seen in extinction. The H_2 column density seems to be roughly constant over the sampled region when determined from extinction and HI survey data and from CH detections, so it is likely the CO peak shows the transition from poorly-shielded CO to well-shielded CO. In the regions where CO is poorly shielded it does not trace H_2 effectively, so CH is a better tracer of this material. There are clear indications from this study that CH, in some cases, is a better tracer of molecular gas than the CO$(1-0)$ line.

In MBM 53, we observed several sets of 13 points along a grid over the cloud. The gas is more diffuse, between half to a tenth of the value of N(H_2) in MBM 16, which makes it difficult to detect CH. CH was only detected in sets where CO was detected, which would seem to imply that, in this instance, CH is not able to trace the gas as well as CO. However, the 13 individual lines of sight within each set were usually not filled fully by CO observations. The sets of observations at G92431 and G93534 both had lines of sight which did not have CO detections, but CH was able to be detected. Due to how faint the CH line is, CH is only able to trace CO faint gas as long as there is enough H_2 for a detectable CH signal.

In addition to the OH observations collected by Donate, White, and Magnani (2019), they collected but never analyzed high resolution and high signal to noise HI observations of MBM 53. In chapter 7

we analyze these data primarily by decomposing the gaussians to determine the velocity structure of the clouds along the line of sight. We find that, in the sampled portions of MBM 53, more than half of the neutral atomic hydrogen is in the thermally unstable warm neutral medium, consistent with Gazol et al. (2001). It appears that the high signal-to-noise data from the A3021 observations and the GALFA-DR2 data have similar results, but the A3021 data suggest there is less HI in the thermally unstable warm neutral medium than the GALFA data (52 and 59 percent). In the sampled region, a large portion of the WNM is unstable (86 percent), which could suggest that there is a lot of turbulence in the cloud.

Finally, in chapter 8 we used a modified version of the 3D-PDR code (Bisbas et al. 2012) to simulate the photodissociation region of a molecular cloud to calculate the excitation temperature for a variety of conditions. We simulated constant density clouds and clouds where the density increases as r^{-1} with initial UV radiation fields between 5.1 and 0.57 Draines. While the simulation is able to reproduce detectable quantities of CH, the simulated main line excitation temperatures are not consistent with observations, which may suggest that there is another collision partner of CH which is important for populating the upper half of the lambda-doubled ground state.

The above work demonstrates both the appeal and frustration of studying CH in the diffuse ISM with the 3335 MHz line. On one hand there are clear indications that, in some regimes, this line can trace low-density, low-extinction gas more effectively than the traditional CO($1-0$) line. On the other hand, the lower abundance and weakness of the 3.3 GHz lines makes observations difficult and time consuming. Some of the more intriguing issues raised in this thesis, particularly in chapter 5 and 6, merit a more thorough study. CH remains an excellent tracer of H_2 in the diffuse ISM and its study using the 3.3 GHz lines is worth pursuing.

Bibliography

Adams W.S. 1941, ApJ, 93, 11

Alexander M., 2008, MsT

Allen R.J., Ivette Rodríguez M., Black J.H., Booth R.S., 2012, AJ, 143, 97

Allen R.J., Hogg D.E., Engelke P.D., 2015, AJ, 149, 123

Andersson B-G, Wannier P.G., 1993, ApJ, 402, 585

Andersson B-G., Wannier P.G., Crawford I.A., 2002, MNRAS, 334, 327

Arce H.G., Borkin M.A., Goodman A.A., Pineda J.E., Beaumont C.N., 2011, ApJ, 742, 105

Arnal E.M., Bajaja E., Larrarte J.J., Morras R., Pöppel W.G.L., 2000, A&AS, 142, 35

Astropy Collaboration, Robitaille T.P., Tollerud E.J., Greenfield P., Droettboom M., Bray E., Aldcroft T., et al., 2013, A&A, 558, A33

Astropy Collaboration, Price-Whelan A.M., Sipőcz B.M., Günther H.M., Lim P.L., Crawford S.M., Conseil S., et al., 2018, AJ, 156, 123

Audit E., Hennebelle P., 2005, A&A, 433, 1

Baird K.M., Bredohl H., 1971, ApJL, 169, L83

Bajaja E., Arnal E.M., Larrarte J.J., Morras R., Pöppel W.G.L., Kalberla P.M.W., 2005, A&A, 440, 767

Barriault L., Joncas G., Lockman F.J., Martin P.G., 2010, MNRAS, 407, 2645

Bertojo M., Cheung A.C., Townes C.H., 1976, ApJ, 208, 914

Bisbas T.G., Bell T.A., Viti S., Yates J., Barlow M.J., 2012, MNRAS, 427, 2100

Black J.H., van Dishoeck E.F., 1988, ApJ, 331, 986

Bohlin R.C., Savage B.D., Drake J.F., 1978, ApJ, 224, 132

Bolatto A.D., Wolfire M., Leroy A.K., 2013, ARA&A, 51, 207

Bowen D.V. et al., 2008, ApJS, 178, 59

Bouloy D., Nguyen-Q-Rieu, Field D., 1984, A&A, 130, 380

Burgh E.B., France K., McCandliss S.R., 2007, ApJ, 658, 446

Burton W.B., Hartmann D., 1994, Ap&SS, 217, 189

Cartledge S.I.B., Lauroesch J.T., Meyer D.M., Sofia U.J., 2004, ApJ, 613, 1037

Ĉernis K., 1993, BaltA, 2, 214

Chaffee F.H., 1974, ApJ, 189, 427

Chaffee F.H., 1975, ApJ, 199, 379

Cotten D.L., Magnani L., Wennerstrom E.A., Douglas K.A., Onello J.S., 2012, AJ, 144, 163

Crane P., Lambert D.L., Sheffer Y., 1995, ApJS, 99, 107

Crutcher R.M., Watson W.D., 1976, ApJL, 203, L123

Dagdigian P.J., 2018, MNRAS, 475, 5480

Dahlstrom J. et al., 2013, ApJ, 773, 41

Dailey E.M., Smith A.J., Magnani L., Andersson B-G., Reach W.T., 2020, MNRAS, 495, 510

Dame T.M., Hartmann D., Thaddeus P., 2001, ApJ, 547, 792

Danks A.C., Federman S.R., Lambert D.L., 1984, A&Ap, 130, 62

Dickey J.M., Lockman F.J., 1990, ARA&A, 28, 215

Diplas A., Savage B.D. 1994, ApJ, 427, 274

Donate E., Magnani L. 2017, MNRAS, 472, 3169

Donate E., White J., Magnani L., 2019, MNRAS, 486, 4414

Douglas A.E., Herzberg G., 1941, ApJ, 94, 381

Draine B.T., 1978, ApJS, 36, 595

Ducati J.R., 2002, VizieR Online Data Catalog, 2237

Dunham T., 1937, PASP, 49, 26

Dunham T., Adams W.S., 1937*a*, Publ.Am.Astr.Soc., 9, 5[1]

Dunham T., Adams W.S., 1937*b*, PASP, 49, 26[2]

Evenson K.M., Radford H.E., Moran M.M., 1971, Appl. Phys. Lett. 18, 426

Ewen H.I., Purcell E.M., 1951, Natur, 168, 356

Fan H. et al., 2017, ApJ, 850, 194

Federman S.R., Glassgold A.E., Kwan J., 1979, ApJ, 227, 466

Federman S.R., Glassgold A.E., Jenkins E.B., Shaya E.J., 1980, ApJ, 242, 545

Federman S.R., 1982, ApJ, 257, 125

Fitzgerald M.P., 1970, A&A, 4, 234

Fixsen D.J. et al., 2011, ApJ, 734, 5

Fruscione A., Hawkins I., Jelinsky P., Wiercigroch A., 1994, ApJS, 94, 127

Gaia Collaboration, Prusti T. et al., 2016, A&A, 595, A1

Gaia Collaboration, Brown A.G.A. et al., 2018, A&A, 616, A1

[1] This citation appeared in the published paper, but should be Dunham T., Adams W.S., 1939, Publ.Am.Astr.Soc., 9, 5

[2] This citation appeared in the published paper, but should be Dunham T., 1937, PASP, 49, 26

Gazol A., Vázquez-Semadeni E., Sánchez-Salcedo F.J., Scalo J., 2001, ApJL, 557, L121

Genzel R., Downes D., Pauls T., Wilson T.L., Bieging J., 1979, A&A, 73, 253

Gerin M., Neufeld D.A., Goicoechea J.R., 2016, ARA&A, 54, 181

Ginsburg A., Mirocha J., 2011, ascl.soft

Grenier I.A., Casandjian J.M., Terrier R. 2005, Science, 307, 1292 (GCT)

Habart E., Walmsley M., Verstraete L., Cazaux S., Maiolino R., Cox P., Boulanger F., et al., 2005, SSRv, 119, 71

Harris et al. 2020, Natur, 585, 357

Hartmann D., Burton W.B., 1997, "Atlas of Galactic Neutral Hydrogen", Cambridge, UK, Cambridge University Press

Haud U., Kalberla P.M.W., 2007, A&A, 466, 555

Heays A.N., Bosman A.D., van Dishoeck E.F., 2017, A&A, 602, A105

Heiles C., 2001, ApJL, 551, L105

Heiles C., Troland T.H., 2003, ApJ, 586, 1067

Herzberg G., 1950, "Molecular Spectra and Molecular Structure. Vol. 1: Spectra of Diatomic Molecules", New York, Van Nostrand Reinhold

HI4PI Collaboration, Ben Bekhti N., Flöer L., Keller R., Kerp J., Lenz D., Winkel B., et al., 2016, A&A, 594, A116

Hiltner W.A. 1956, ApJS, 2, 389

Hjalmarson Å. et al., 1977, ApJS, 35, 263

Hobbs L.M., Blitz L., Penprase B.E., Magnani L., Welty D.E., 1988, ApJ, 327, 356

Hg E. et al., 2000, A&A, 335, L27

Hube D.P., 1970, Mem. RAS, 72, 233

Hunter J.D., 2007, CiSE, 9, 90

Johansson L.E.B., 1979, Onsala Space Observatory Research Report, 136

Jura M., Meyer D.M., 1985, ApJ, 294, 238

Kalberla P.M.W. et al., 2005, A&Ap, 440, 775

Kenyon S.J., Dobrzycka D., Hartmann, L., 1994, AJ, 108, 1872

Knapp G.R., Kerr F.J., 1974, A&Ap, 35, 361

Kuntz K.D., Snowden S.L., Verter F., 1997, ApJ, 484, 245

Indriolo N., Neufeld D.A., Seifahrt A., Richter M.J., 2013, ApJ, 764, 188

Lacour S. et al., 2005, A&Ap, 430, 967

Lada E.A., Blitz L., 1988, ApJ, 326, 69

Lang K.R., Willson R.F., 1978, ApJ, 224, 125

Larson R.B., 1981, MNRAS, 194, 809

Larsson M., Siegbahn P.E.M., 1983, JChPh, 79, 2270

Leroy A.K., Bolatto A., Gordon K., Sandstrom K., Gratier P., Rosolowsky E., Engelbracht C.W., et al., 2011, ApJ, 737, 12

Lesh J.R., 1968, ApJS, 17, 371

Li D., et al., 2018, ApJS, 235, 1

Li A., Draine B.T., 2001, ApJ, 554, 778

Lien D.J., 1984, ApJ, 224, 125

Liszt H., Lucas R., 2001, A&A, 370, 576

Liszt H., Lucas R., 2002, A&A, 391, 693

Liszt H.S., 2008, A&A, 492, 743

Liszt H., 2014*a*, ApJ, 780, 10

Liszt H., 2014*b*, ApJ, 783, 17

Lockman F.J., Condon J.J., 2005, ApJ, 129, 1968

Magnani L., Blitz L., Mundy L., 1985, ApJ, 295, 402

Magnani L.A., 1987, PhDT, University of Maryland

Magnani L., Lada E.A., Sandell G., Blitz L., 1989, ApJ, 339, 244

Magnani L., Carpenter J.M., Blitz L., Kassim N.E., Nath B.B., 1990, ApJS, 73, 747

Magnani L., Sandell G., Lada E.A., 1992, A&AS, 93, 509

Magnani L., Onello J.S., 1993, ApJ, 408, 559

Magnani L., Onello J.S., 1995, ApJ, 443, 169

Magnani L., Hartmann D., Holcomb S.L., Smith L.E., Thaddeus P., 2000, ApJ, 535, 167

Magnani L., Chastain R.J., Kim H.C., Hartmann D., Truong A.T., Thaddeus P., 2003, ApJ, 586, 1111

Magnani L., Shore S. N., 2017, "A Dirty Window: Diffuse and Translucent Molecular Gas in the Interstellar Medium", GmbH Germany, Springer-Verlag

Maloney P., 1990, ApJL, 348, L9

Mangum J.G., Shirley Y.L., 2015, PASP, 127, 266

Marinakis S., Kalugina Y., Kłos J., Lique F., 2019, A&A, 629, A130

Mattila K., 1986, A&A, 160, 157

Mattila K., 1989, A&Ap, 210, 389

McClure-Griffiths N.M., et al., 2009, ApJS, 181, 398

McKellar A., 1940, PASP, 52, 187

Mookerjea B., 2016, MNRAS, 459, 2822

Mora A., et al., 2001, A&A, 378, 116

Morgan W.W., Keenan P.C., 1973, ARA&A, 11, 29

Neufeld D.A., Zmuidzinas J., Schilke P., Phillips T.G., 1997, ApJL, 488, L141

Neufeld D.A., Wolfire M.G., Schilke P., 2005, ApJ, 628, 260

Neufeld D.A., Sonnentrucker P., Phillips T.G., Lis D.C., de Luca M., Goicoechea J.R., Black J.H., et al., 2010, A&A, 518, L108

Oja T., 1991, A&AS, 89, 415

Oja T., 1993, A&AS, 100, 591

Ortiz-León G.N., et al., 2018, ApJ, 865, 73

Pan K., Federman S.R., Sheffer Y., Andersson B.-G., 1978, ApJ, 633, 986

Peek J.E.G., Heiles C., Douglas K.A., Lee M.-Y., Grcevich J., Stanimirović S., Putman M.E., et al., 2011, ApJS, 194, 20

Peek J.E.G, 2017, "GALFA-HI DR2 Wide data cubes", Harvard Dataverse, V1

Peek J.E.G., Babler B.L., Zheng Y., Clark S.E., Douglas K.A., Korpela E.J., Putman M.E., et al., 2018, ApJS, 234, 2

Penprase B.E., 1993, ApJS, 88, 433

Pesch P., 1967, ApJ, 148, 781

Pety J., Liszt H.S., Lucas R., 2011, EAS, 52, 151

Pickett H.M., Cohen E.A., Drouin B.J., Pearson J.C., 2003, "Submillimeter, Millimeter, and Microwave Spectral Line Catalog"

Rachford B.L., et al., 2002, ApJ, 577, 221

Reach W.T., Heiles C., Bernard J.-P., 2015, ApJ, 811, 118

Rydbeck O.E.H., Elldér J., Irvine W.M., 1973, Natur, 246, 466

Rydbeck O.E.H., Kollberg E., Hjalmarson Å., Sume A., Elldér J., Irvine W.M., 1976, ApJS, 31, 333

Sandell G., Stevens M.A., Heiles C., 1987, A&A, 179, 255

Savage B.D., Bohlin R.C., Drake J.F., Budich W., 1977, ApJ, 216, 291

Schlafly E.F., Finkbeiner D.P., 2011, ApJ, 737, 103

Schlafly E.F., Green G., Finkbeiner D.P., Rix H.-W., Bell E.F., Burgett W.S., Chambers K.C., et al., 2014, ApJ, 786, 29

Schlegel D.J., Finkbeiner D.P., Davis M., 1998, ApJ, 500, 553

Sheffer Y., Federman S.R., Andersson B.-G., 2003, ApJL, 597, L29

Sheffer Y., Federman S.R., 2007, ApJ, 659, 1352

Sheffer Y., Rogers M., Federman S.R., Abel N.P., Gredel R., Lambert D.L., Shaw G., 2008, ApJ, 687, 1075

Schöier F.L., van der Tak F.F.S., van Dishoeck E.F., Black J.H., 2005, A&A, 432, 369

Slettebak A., 1982, ApJS, 50, 55

Smoker J., Ledoux C., Jehin E., Keenan F.P., Kennedy M., Cabanac R., Melo C., 2014, MNRAS, 438, 1127

Snow T.P., McCall B.J., 2006, ARA&A, 44, 367

Solomon P.M., Rivolo A.R., Barrett J., Yahil A., 1987, ApJ, 319, 730

Sota A., Maíz Apellániz J., Walborn N.R., Alfaro E.J., Barbá R.H., Morrell N.I., Gamen R.C., Arias J.I., 2011, ApJS, 193, 24

Stock J., Nassau J.J., Stephenson C.B., 1960, Hamburger Sternw., Warner & Swasey Obs., C02, 0

Stricklan A., 2019, MsT, University of Georgia

Swings P., Rosenfeld L., 1937, ApJ, 86, 483

Tang N. et al., 2017, ApJ, 839, 8

Tashiro L.M., Ubachs W., Zare R.N., 1989, J. Mol. Spectrosc., 138, 89

Thorburn J.A. et al., 2003, ApJ, 584, 339

Truong A.T., Magnani L., Hartmann D., 1997, AAS, Abstract, Vol 29, 1220

Truppe S., Hendricks R.J., Tokunaga S.K., Hinds E.A., Tarbutt M.R., 2014, J. Mol. Spectrosc., 300, 70

van Belle G.T., von Braun K., 2009, ApJ, 694, 1085

van Dishoeck E.F., Black J.H., 1986, ApJS, 62, 109

van Dishoeck E.F., Black J.H., 1988, ApJ, 334, 771

van Dishoeck E.F., Black J.H., 1989, ApJ, 340, 273

van Leeuwen F., 2007, A&A, 474, 653

Virtanen P., et al., 2020, Nat. Methods, 17, 261

Wakker B.P., van Woerden H., 1997, ARA&Ap, 35, 217

Wannier P.G., Andersson B,-G, Federman S.R., Lewis B.M., Viala Y.P., Shaya E., 1993, ApJ, 407, 163

Weinreb S., Barrett A.H., Meeks M.L., Henry J.C., 1963, Natur, 200, 829

Wenger M. et al., 2000, A&AS, 143, 9

Weselak T., Galazutdinov G.A., Musaev F.A., Krelowski J., 2008, A&A, 484, 381

Weselak T., Galazutdinov G.A., Beletsky Y., Krełowski J., 2010, MNRAS, 402, 1991

Weselak T., Galazutdinov G.A., Gnaciński & Krelowski J., 2014, Acta Astronomica, 64, 277

Weselak T., 2019, A&A, 625, A55

Wiesemeyer H., et al., 2018, A&A, 612, A37

Willson R.F., 1981, ApJ, 247, 116

Winkel B., Kerp J., Flöer L., Kalberla P.M.W., Ben Bekhti N., Keller R., Lenz D., 2016, A&A, 585, A41

Wu C., Yu J.Z., 2018, AMT, 11, 1233

Xu D., Li D., Yue N., Goldsmith P.F., 2016, ApJ, 819, 22

Xu D., Li D., 2016, ApJ, 833, 90

Yamamoto H., Onishi T., Mizuno A., Fukui Y., 2003, ApJ, 592, 217

Zucker C., Schlafly E.F., Speagle J.S., Green G.M., Portillo S.K.N., Finkbeiner D.P., Goodman A.A., 2018, ApJ, 869, 83

Zucker C., Speagle J.S., Schlafly, E.F., Green G.M., Finkbeiner D.P., Goodman A.A., Alves J., 2019, ApJ, 125, 20